TICMET'22

8-10 SEPTEMBER, 2022
YTÜ DAVUTPAŞA CONGRESS AND CULTURE CENTER

The 4th International Conference of Materials and Engineering Technology

4. Uluslararası Malzeme ve Mühendislik Teknolojileri Konferansı

PROCEEDING BOOK

E-ISBN: 978-625-00-0969-7

www.ticmet.org

CONFERENCE OBJECTIVE

The 4th International Conference of Materials and Engineering Technology (TICMET'22) will be held on 08-10 September 2022 in partnership with Yıldız Technical University, Hasan Kalyoncu University and Gaziantep University.

The main purpose of TICMET'22 is to present the latest research and results of scientists related to materials and engineering technologies. This conference provides different field delegates with opportunities to exchange new ideas and application experiences, build business or research relationships, and find global partners for future collaboration. Due to Covid-19 that shook the world, in addition to face-to-face sessions, ONLINE presentation will be provided to our participants. After this science feast, your abstract/full texts will be published in congress books with ISBNs and will be brought to the world science literature with open access and significant contributions will be made to the scientific field.

Webinars will be used in online presentations and will be broadcast live. All participants will be able to ask questions to be answered in the presentations. In the event that more than one session takes place at the same time, it will be possible to follow from parallel rooms.

The conference organizing committee is pleased to invite prospective authors to send their original texts to TICMET'22. All papers will be reviewed and evaluated by the referees in the field, based on their technical and I or research content I depth,accuracy, relevance to the conference, contributions and readability.

Selected papers presented (face to face or online) at the conference will be proposed to publish in one of the following journals:

* Sigma Journal of Engineering and Natural Sciences (Sigma) (E-SCI)
* Acta Mechanica et Automatica (E-SCI)
* El Cezeri Journal of Science and Engineering (ECJSE) (TR Dizin)
* Journal of Sustainable Construction Materials and Technologies (JSCMT) (TR Dizin)
* International Journal of Materials and Engineering Technologies (TIJMET) (Dergipark)

TICMET'22 Conference is funded within the framework of Tübitak 2223-B.

PROGRAM COMMITEES

Honorary Chair

Prof. Dr. Tamer Yilmaz, Yildiz Technical University - TR

Prof. Dr. Türkay Dereli, Hasan Kalyoncu University - TR

Prof. Dr. Arif Ozaydin, Gaziantep University – TR

Chair

Prof. Dr. Necip Fazıl Yılmaz, Gaziantep University – TR

Organizing Committee

Prof. Dr. Necip Fazil Yilmaz, Gaziantep University - TR

Prof. Dr. Hassan Jumaa, Universitätsklinikum Ulm - DE

Prof. Dr. Mehmet Lutfi Yola, Hasan Kalyoncu University - TR

Assist. Prof. Dr. Yigit Arabul, Yildiz Technical University - TR

Prof. Dr. Metin Bedir, Gaziantep University - TR

Prof. Dr. Adem Kurt, Gazi University - TR

Prof. Dr. Ali Riza Yildiz, Uludag University - TR

Prof. Dr. Mustafa Bakkal, Istanbul Technical University - TR

Prof. Dr. Murat Oduncuoglu, Yildiz Technical University - TR

Assoc. Prof. Dr. Halil Ibrahim Kurt, Gaziantep University – TR

Assist. Prof. Dr. Erhan Durur, Gaziantep University - TR

Lect. Aykut Bilici, Gaziantep University – TR

Lect. Musa Yilmaz, Gaziantep University - TR

Hakan Yilmaz, Secreteriat – TR

Scientific Committee (National Committee)

Prof. Dr. Abdulkadir Eksi, Cukurova University - TR

Prof. Dr. Abdulkadir Cevik, Gaziantep University – TR

Prof. Dr. Ahmet Erklig, Gaziantep University – TR

Prof. Dr. Ali Gursel, Duzce University – TR

Prof. Dr. Emrah Ozahi, Gaziantep University – TR

Prof. Dr. Enver Atik, Celal Bayar University - TR

Prof. Dr. Ismail Saritas, Selcuk University - TR

Prof. Dr. Mehmet Cengiz Kayacan, Süleyman Demirel University - TR

Prof. Dr. Mete Kalyoncu, Konya Technical University - TR

Prof. Dr. Mustafa Bakkal, Istanbul Technical University - TR

Prof. Dr. Mustafa Cigdem, Yildiz Technical University - TR

Prof. Dr. Oguzhan Yilmaz, Gazi University - TR

Prof. Dr. Omer Eyercioglu, Gaziantep University - TR

Prof. Dr. Rahmi Unal, Gazi University - TR

Prof. Dr. Serdar Salman, National Defense University - TR

Prof. Dr. Suleyman Can Kurnaz, Sakarya University – TR

Prof. Dr. Sultan Ozturk, Karadeniz Technical University - TR

Prof. .Dr. Ugur Cem Hasar, Gaziantep University - TR

Prof. Dr. Yahya Bozkurt, Marmara University – TR

Assoc. Prof. Dr. Abdulcabbar Yavuz, Gaziantep University – TR

Assoc. Prof. Dr. Kursat Gov, Gaziantep University – TR

Assoc. Prof. Dr. Esin Sarioglu, Gaziantep University - TR

Assist. Prof. Dr. Ali Yasar, Selcuk University - TR

Assist. Prof. Dr. Aziz Baris Basyigit, Kirikkale University - TR

Dr. Engin Ergul, Dokuz Eylul University – TR

Scientific Committee (International Committee)

Prof. Dr. Andrey Tsarkov, Moscow State Technical University - RU

Prof. Dr. Bekir Sami Yilbas, King Fahd University of Petroleum and Minerals - SA

Prof. Dr. Fabienne Delaunois, University Of Mons - BE

Prof. Dr. Hazman Seli, University Of Sains Malaysia - MY

Prof. Dr. Heiba Zein, Ain Shams University - EG

Prof. Dr. Marwan K Khraisheh, Hamad Bin Khalifa University - QA

Prof. Dr. Mohamed Elsayed Yahia, International University of Sarajevo - BA

Prof. Dr. Muammer Koç, Hamad Bin Khalifa University - QA

Prof. Dr. Ramazan Asmatulu, Wichita State University - US

Prof. Dr. Senay Simsek, North Dakota State University - US

Prof. Dr. Tai Cheng Chen, Institute Of Nuclear Energy Research Iner - TW

Prof. Dr. Vincent Ji, University Of Paris Sud - FR

Prof. Dr. Yousef Haik, Hamad Bin Khalifa University Hbku - QA

Prof. Dr. Yusuf Ozturk, San Diego State University - US

Prof. Dr. Zakaria Boumerzoug, University Of Biskra - DZ

Assoc. Prof. Dr. Ahmad Azmin Mohamad, University Of Sains Malaysia - MY

INVITED SPEAKERS

Muzaffer Şeker 1961 yılında İzmir'de doğdu. 1986'da Uludağ Üniversitesi Veteriner Fakültesi'nden mezun oldu. 1995 yılında İngiltere'de Leicester Üniversitesi Tıp Fakültesi'nde İnsan Anatomisi üzerine doktora derecesi aldı. 2000 yılında doçent, 2006 yılında da profesör oldu. Birleşik Arap Emirlikleri'nde iki yıl öğretim görevlisi olarak çalıştı. Selçuk Üniversitesi Meram Tıp Fakültesi Tıp Eğitimi ve Bilişimi Ana Bilim Dalı Başkanı olarak da görev yapan Şeker, 2008-2010 yılları arasında İstanbul Medipol Üniversitesi Kurucu Mütevelli Heyeti'nde de görev aldı. Aynı zamanda Kamu Yönetimi Lisans mezunu olan Şeker, Aralık 2010 yılında Konya Üniversitesi'ne kurucu rektör olarak atandı. Necmettin Erbakan Üniversitesi Rektörlüğüne Aralık 2014 yılında ikinci dönem için tekrar atandı. TÜBA Asli Üyesi ve TÜBA Konsey Üyesi, TÜBİTAK Bilim Kurulu Üyesi, Üniversitelerarası Kurul (ÜAK) Tıp Sağlık Eğitim Konsey Üyesi, Sağlık Bakanlığı Sağlık Turizmi Üst Kurul Üyesi, Üniversitelerarası Kurul (ÜAK) Doçentlik Konsey Üyesi, Yükseköğretim Kurulu (YÖK) Engelli Öğretim Komisyon Üyesi, KOP Bölgesi Üniversiteler Birliği (UNİKOP) Dönem Başkanı, Üniversite Hastaneler Birliği Yönetim Kurulu Asil Üyesi, Ahmet-Nezahat Keleşoğlu Eğitim Vakfı Mütevelli Heyet Üyesi, Selçuklu Otizmli Bireyler Eğitim Vakfı (SOBE) Kurucu Mütevelli Üyesi, İstanbul İlim ve Eğitim Vakfı (İSİLEV) Kurucu Mütevelli Üyesi, Birlik Vakfı Danışma Kurulu Üyesi ile İNNOPARK Yönetim Kurulu Üyesidir. Türkiye Sağlık Enstitüleri Başkanlığı (TÜSEB) Aziz Sancar Bilim, Hizmet ve Teşvik Ödülleri, TÜBA-GEBİP Teşvik Ödülleri, TÜBİTAK Bilim, Hizmet ve Teşvik Ödülleri seçici kurullarında idari görev yürüttü. G20 ülkelerinin 2017 Science '20 Zirvesi'nde ve 2018 World Science Forum Jordan'da ülkemizi temsil etti. Ayrıca 2002 yılından bu yana üyesi olduğu Türk Anatomi ve Klinik Anatomi Derneği ile Temel Tıp Bilimleri Platformu yönetimlerinde farklı görevler yürüten Şeker, evli ve üç çocuk babasıdır.

Krzysztof Jan Kurzydłowski was born on 29 August 1954, in Lublin. Polish physicist, professor of technical sciences, vice-rector of the Warsaw University of Technology in 1993-1999, undersecretary of state in the Ministry of Education and Science in 2005-2006, undersecretary of state in the Ministry of Science and Higher Education in 2006-2007, Director of the National Research and Development Center in 2011-2016.

Professor Kurzydłowski graduated from the Warsaw University of Technology Faculty of Technical Physics and Applied Mathematics. He later earned his doctorate (1981) and postdoctoral (1989) degrees at the Warsaw University of Technology. In 1995, he received the title of professor of technical

sciences. In his scientific work, he deals with materials engineering, modeling the structure and properties of materials, nanomaterials, and the degradation of structural and functional materials.
He is the European consultant in the field of operational safety of industrial plants. He held position of research associate at the University of Manitoba in Canada, and visiting professor at Brunel University in Great Britain, and École Nationale Supérieure des Mines de Saint-Étienne in France. He has published more than 500 scientific papers and several monographs. He supervised over70 doctoral theses. He is a member of Senate of E-MRS. Received a gold medal of FEMS. Professor Kurzydłowski is married and has two sons.

Radovan Kopecek obtained his Diploma in Physics at the University of Stuttgart in 1998. In addition, he studied at Portland State University (Oregon, USA), where he obtained a Master of Science in 1995. In 2002 he finalizes his PhD dissertation in Konstanz in the field of thin film crystalline photovoltaics.
Until the end of 2006 he was a group leader at University of Konstanz. One of the founders of ISC Konstanz, Dr. Kopecek has been working at the institute as a full time manager and researcher since 2007 and is currently a managing director and the head of the Advanced Solar Cells department. Dr. Kopecek was since 2016 in the board of directors of EUREC (Association of EU´s R&D centers involved in renewables). He is co-founder of ATAMOSTEC in 2018 – an R&D center for desert modules and systems in Chile and since 2022 in board of directors. In 2022 Dr. Kopecek was elected also for the board of directors of ESMC (European Solar Manufacturing Council).

Muammer Koç, Prior to his appointment as a founding professor of sustainability at HBKU in 2014, Professor Koç held professor, director, chair and dean positions at different universities in Turkey and the USA between 2000-2014. He has a PhD degree in Industrial and Systems Engineering from the Ohio State University (1999) and an Executive MBA degree from the University of Sheffield, UK (2014). He has published 130+ publications in various international journals and conferences; edited three books; organized, chaired, and co-chaired various international conferences, workshops and seminars on design, manufacturing and product development. In addition to his academic and educational activities, he provides consulting services to industry, government and educational institutes for strategic transformation, business optimization, organizational efficiency, lean operations, restructuring and reengineering initiatives. He has taught courses across a range of subjects, including product/process/business innovation and development; medical design and production; energy and efficiency; computer-aided engineering, design and manufacturing; modern manufacturing technologies; manufacturing system design; material forming plasticity; and the mechanical behavior of materials.

PROGRAM OVERWIEV **Location:** Yıldız Technical University - Davutpaşa Congress and Culture Center		
08.09.2022 - THURSDAY		
09:00 – 10:00	Registration	Conference Registration Desk
10:00 – 11:15	Opening Ceremony	Yildiz Technical University – Main Hall
11:15 – 12:00	Invited Speakers Session	Prof. Dr. Muzaffer ŞEKER – President of TUBA
12:00 – 13:30	Launch	
13:30 – 15:15	Plenary Session	Prof.Dr. Krzysztof Jan KURZYDŁOWSKİ – Bialystok University of Technology
		Prof.Dr. Radovan KOPECEK – CTO and Co-Founder / ISC Konstanz
		Prof.Dr. Muammer KOÇ – Founding Professor, Sustainability, Hamad Bin Khalifa University
15:15 – 15:30	Coffee Break	
15:30 – 16:45	Session I	Yildiz Technical University - Hall 1 (Face to Face) - Hall 2 & Hall 3(Online)
16:45 – 17:00	Coffee Break	
17:00 – 18:15	Session II	Yildiz Technical University - Hall 1 (Face to Face) - Hall 2 & Hall 3(Online)
19:30 – 21:00	Gala Dinner and Plaque Presentation	
09.09.2022 - FRIDAY		
09:30 – 10:45	Session III	Yildiz Technical University - Hall 1 (Face to Face) - Hall 2 & Hall 3(Online)
10:45 – 11:00	Coffee Break	
11:00 – 12:30	Session IV	Yildiz Technical University - Hall 1 (Face to Face) - Hall 2 & Hall 3(Online)
12:30 – 14:30	Launch	
14:30 – 17:00	Session V	Yildiz Technical University – Main Hall - **Special R&D Session**
19:30 – 21:00	Conference Dinner	
10.09.2022 - SATURDAY		
ALL DAY	Social Event – Free Time for Participants	

CONTENTS

ELEKTRİKSEL EROZYON İLE DELİK DELME İŞLEMİNİN ANFIS İLE MODELLENMESİNDE DENEY PLANININ ETKİSİ

ALİ GÖÇMEN[1], ALİ TOLGA BOZDANA[2,*]

[1]Gaziantep Üniversitesi, Fen Bilimleri Enstitüsü, ÜR-GE ve Tasarım Mühendisliği, Gaziantep, Türkiye
[2]Gaziantep Üniversitesi, Mühendislik Fakültesi, Makine Mühendisliği Bölümü, Gaziantep, Türkiye
[*]bozdana@gantep.edu.tr

Özet

Uyarlamalı Ağ Tabanlı Bulanık Çıkarım Sistemi (*Adaptive Neuro-Fuzzy Inference System*), Bulanık Mantık (*Fuzzy Logic*) ve Yapay Sinir Ağları (*Artificial Neural Networks*) araçlarının bütünsel kullanıldığı bir yapay zekâ yöntemidir. ANFIS ile oluşturulan bulanık model, adaptif ağ yapısı sayesinde öğrenebilmekte ve kendini güncellemektedir. Modelin eğitilmesinde kullanılan veriler, modelin öğrenme ve güncelleme performansı açısından oldukça önemlidir. Bu çalışmada, ANFIS kullanılarak Elektriksel Erozyon ile Delik Delme (*Electrical Discharge Drilling*) işleminde girdi-çıktı ilişkisini tahmin edebilen bulanık modeller geliştirilmiştir. Farklı küme tiplerine ve sayılarına sahip modeller, Merkezi Kompozit Tasarım (*Central Composite Design*) ve Ortogonal Dizi (*Orthogonal Array*) deney planına göre elde edilen deneysel veriler doğrultusunda oluşturulmuş ve eğitilmiştir. Validasyon deneyleri sonucunda MKT deney planı ile oluşturulan modellerin OD deney planına kıyasla daha doğru ve tutarlı sonuçlar verdiği gözlemlenmiştir.

Anahtar Kelimeler: Elektriksel Erozyon ile Delik Delme, ANFIS, Deney Planı.

1. Giriş

Elektriksel Erozyon ile Delik Delme – EDD (*Electrical Discharge Drilling*) işlemi, Elektriksel Erozyon ile İşleme – EDM (*Electrical Discharge Machining*) prosesinin delik delme işlemleri için kullanıldığı bir türüdür. EDD sayesinde elektriksel iletkenliğe sahip metalik malzemelerde elektrik deşarjları vasıtasıyla belirli derinliğe sahip küçük çaplı delikler üretilebilmektedir. Bu işlem, özellikle sert ve kırılgan malzemeler için tercih edilmektedir. Türbin kanatlarındaki soğutma deliklerinin delinmesinde, dizel enjektörlerde, kesici takımların soğutma kanallarında, kalıp menfezlerinde ve benzeri uygulamalarda kullanılmaktadır. Şekil 1'de görüldüğü üzere bu işlemde, bir tutucu vasıtasıyla kendi ekseni etrafında sabit hızda dönen ve içerisinden dielektrik sıvı akan boru şeklinde silindirik elektrotlar kullanılmaktadır. Belirli voltaj ve deşarj akım altında elektrotun iş parçasına yaklaştırılması suretiyle elektrot ile iş parçası yüzeyi arasında meydana gelen elektrik deşarjı vasıtasıyla hem elektrot hem de iş parçasından küçük parçacıklar koparılmaktadır. Bu sayede, elektrot çapı büyüklüğünde delikler delinebilmektedir. EDM ve EDD prosesleri; girdi parametrelerinin fazla olması, bu parametrelerin proses çıktıları üzerindeki tekil ve birleşik etkilerinin matematiksel olarak ifade edilememesi, iş parçası ve elektrot malzemesinin fiziksel ve elektriksel özellikleri, vb. faktörlerden dolayı kompleks yapıya sahiptir. İşlem performansının farklı girdi parametrelerine direkt ve/veya dolaylı şekilde bağımlı olması sebebiyle işlem çıktılarının hesaplanması, modellenmesi ve tahmin edilmesi zordur.

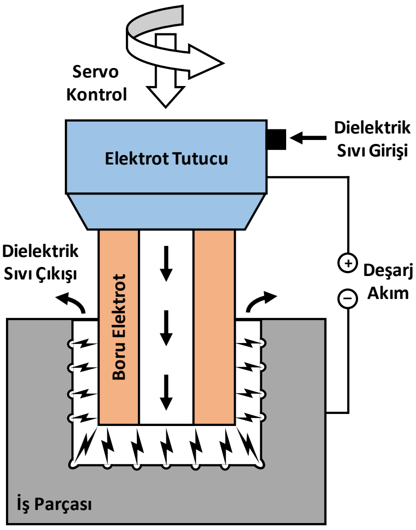

Şekil 1. EDD işleminin şematik gösterimi [1]

Bu amaçla, EDM/EDD işleminde farklı yaklaşımlar kullanılarak girdi-çıktı ilişkileri belirlenmeye çalışılmıştır. Bunlar arasında, mühendislik problemlerinin çözümünde etkin şekilde kullanılan Adaptif Ağ Tabanlı Bulanık Çıkarım Sistemi – ANFIS (*Adaptive Neuro-Fuzzy Inference System*) dikkat çekmektedir. ANFIS; Bulanık Mantık – BM (*Fuzzy Logic*) ve Yapay Sinir Ağları – YSA (*Artificial Neural Networks*) araçlarının bütünsel kullanıldığı yapay zekâ yöntemidir. Şekil 2'de gösterildiği üzere altı katmandan (*layer*) oluşmaktadır. Öncelikle girdi parametreleri belirlenir ve bu parametreler için bir üyelik fonksiyonu (*membership function*) seçilir. Sonrasında EĞER-İSE şeklinde belirli sayıdaki kurallar oluşturulur. Kural katmanından elde edilen sonuçların etki seviyeleri (*weights*), bir sonraki katmanda normalize edilir. Arındırma katmanında, normalize edilmiş etkilere karşılık gelen değerler toplanır ve çıktı parametresinin değeri bulunur. Bu süreçte oluşturulan model, adaptif ağ yapısı sayesinde öğrenebilmekte ve kendini güncellemektedir.

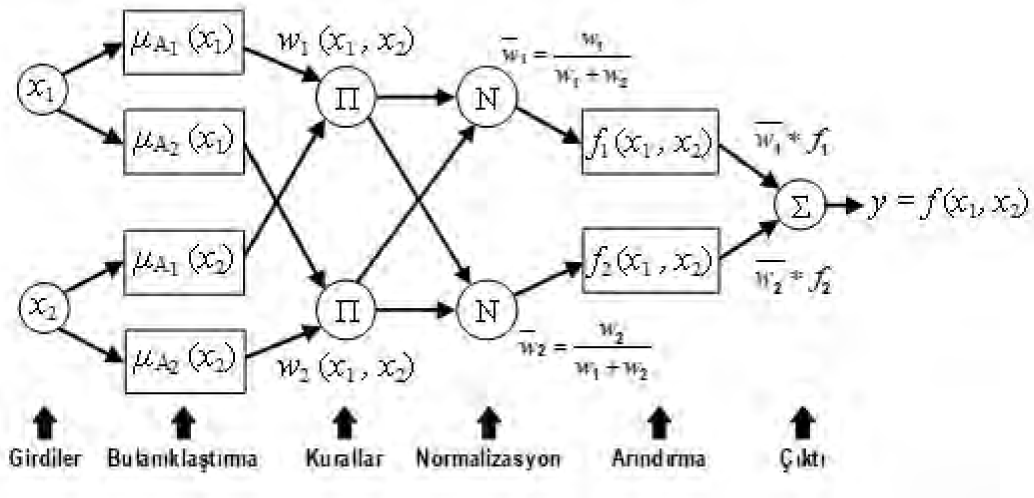

Şekil 2. ANFIS ile oluşturulan modelin ağ yapısı [2]

ANFIS'te modelin eğitilmesinde kullanılan veriler, modelin öğrenme ve güncelleme performansı açısından oldukça önemlidir. Verilerin sayısına ve parametre değerlerine karar verebilmek oldukça zordur. Bu bağlamda, rastgele veriler kullanmak yerine spesifik veriler doğrultusunda prosesin modellenmesine yönelik çalışmalar yapılmaktadır. Deney Tasarımı/Planı (*Design of Experiment*); gerçekleştirilecek deneylerin asgari sayısını, hangi sıralamada yapılacağını, parametre değerlerini, vs. belirlemek amacıyla kullanılan bilimsel bir yaklaşımdır [3]. İşlem değişkenlerinin azaltılması, süreç/proses optimizasyonu, maliyetin düşürülmesi, vb. avantajlar sağlamaktadır. Burada amaç; belirli parametre değerleri ile spesifik bir sıralamada gerçekleştirilecek deney sayısını ve etken faktörleri belirlemek, bu sayede girdi-çıktı ilişkisini tahmin edebilmektir. İşlem parametrelerinin sayısına, parametreler arasındaki ilişkilere, öngörülen sonuçların hassasiyet ve doğruluk derecesine, vb. göre hangi deney tasarımının daha uygun olacağına karar verilmektedir.

Mühendislik uygulamalarında Merkezi Kompozit Tasarım – MKT (*Central Composite Design*) ve Ortogonal Dizin – OD (*Orthogonal Array*) sıklıkla tercih edilen tasarımlar arasında yer almaktadır. MKT, Tepki Yüzey Metodolojisi – TYM (*Response Surface Methodology*) yönteminde kullanılan deney tasarımı yaklaşımıdır. Taguchi yönteminde ise OD deney tasarımı kullanılmaktadır. Her iki tasarımda temel amaç asgari deney veri seti ile girdi-çıktı ilişkisinin tahmin edilmesidir, ancak deney sayıları ve deneylerde kullanılacak parametre değerleri açısından farklılıklar içermektedir.

Literatürde EDM/EDD işleminde girdi-çıktı ilişkisinin ANFIS ile tespitinde Taguchi/OD ve TYM/MKT deney tasarımlarının kullanıldığı çalışmalar mevcuttur. Sharma vd. [4], TYM ve ANFIS sayesinde EDM girdi parametrelerinin proses çıktılarına etkilerinin belirlenmesi ve en uygun parametre değerlerinin tespiti üzerine çalışmışlardır. Inconel 625 alaşım malzemesinde TYM-L_{27} deney tasarımı doğrultusunda gerçekleştirilen deneyler sonucunda proses çıktıları olarak Malzeme Kaldırma Oranı – MKO (*Material Removal Rate*), Elektrot Aşınma Oranı – EAO (*Electrode Wear Rate*) ve Yüzey Pürüzlülüğü – YP (*Surface Roughness*) incelemişlerdir. Phate vd. [5,6] çalışmalarında Taguchi OD-L_{18} deney planı kapsamında gerçekleştirilen deneylerden elde edilen veriler doğrultusunda Al-Cu-Ni alaşımının EDM ile işlenmesinde ANFIS yöntemi ile EAO ve YP değerlerini tahmin edebilen modeller geliştirmişlerdir. Agarwal vd. [7] çalışmalarında EDD prosesinde hibrit algoritmalar kullanarak YP'nin tahmini ve eniyilemesi üzerine bir çalışma gerçekleştirmişlerdir. TYM-L_{30} deney planına göre Titanyum 685 alaşımında belirli çapta delikler delinmiştir. ANFIS yöntemi ile modeller oluşturulmuş, sonrasında Rao ve Jaya algoritmaları kullanılarak optimizasyon çalışması gerçekleştirilmiştir. Bhiradi vd. [8] ise mikro-EDD prosesi ile gümüş plakalar üzerinde küçük çapta deliklerin delinmesinde girdi parametrelerinin MKO, EAO ve delik çapında büyüme üzerine etkilerini araştırmışlardır. Taguchi OD-L_{16} ile gerçekleştirilen deneylerden elde edilen verilerden yola çıkarak ANFIS'te modeller geliştirmişlerdir.

Gaz destekli veya toz katkılı EDM/EDD üzerine çalışmalar da literatürde yer almaktadır. Singh vd. [9], D3 kalıp çeliğinin helyum-destekli EDM ile işlenmesinde MKO ve YP çıktılarının tahmini ve eniyilemesi üzerine karşılaştırmalı bir çalışma gerçekleştirmişlerdir. MKT-L_{31} tasarımı ile gerçekleştirilen deneylerin ANOVA varyans analizleri yapılmıştır. Girdi parametrelerinin çıktılar üzerindeki etkilerinin tahmin edilmesi amacıyla ANFIS, YSA ve TYM yöntemleri kullanılarak modeller geliştirilmiştir. En iyi modelin sonuçlarından yola çıkılarak Genetik Algoritma – GA (*Genetic Algorithm*) ile proses çıktıları için en uygun değerler belirlenmiştir. Goyal vd. [10] tarafından yapılan çalışmada, nano-grafen toz katkılı EDD işleminde Inconel 718 alaşımında delinen deliklerin dairesellik ve pürüzlülük özellikleri incelenmiştir. Taguchi OD- L_{27} tasarımına göre gerçekleştirilen deneyler doğrultusunda ANOVA varyans analizi sonucunda etken parametreler belirlenmiş, BM ve ANFIS ile oluşturulan modellerin performansları irdelenmiştir.

Bir diğer çalışmada (Hourmand vd. [11]), nano-toz katkılı EDD prosesi ile Al-Mg_2Si metal matris kompozit malzeme üzerinde delik delme işlemleri gerçekleştirilmiştir. MKT-L_{27} tasarımına göre delinen deliklerde ANFIS ve TYM kullanılarak girdi parametrelerinin MKO üzerindeki etkileri araştırılmıştır. Singh ve Sharma [12], toz-katkılı EDM prosesi ile tungsten karbür malzemenin işlenmesinde MKT-L_{30} tasarımı kullanarak gerçekleştirilen deneyler doğrultusunda proses çıktıları incelemişlerdir. GRA ve ANFIS yaklaşımları ile MKO, EAO ve YP'nin tahmini ve optimizasyonu gerçekleştirilmiştir. Tungsten karbür ile ilgili bir diğer çalışmada (Singh [13]) ise toz karışımlı EDM işleminde proses parametrelerinin çok amaçlı optimizasyonu için Grey-ANFIS yöntemi kullanılmıştır. Taguchi OD-L_{27} deney tasarımına göre deneyler gerçekleştirilmiş, bu doğrultuda MKO ile EAO için en uygun değerler elde edilmiştir.

Buna ilaveten, Tel Erozyon (WEDM) prosesinde de ANFIS ile modellemede deney tasarımından yararlanılmıştır. Natarajan vd. [14] tarafından gerçekleştirilen çalışmada WEDM işleminde Alüminyum 7075 alaşımının YP optimize edilmiştir. OD-L_{27} tasarımı ile gerçekleştirilen deneyler sonucunda ANFIS'te modeller oluşturulmuş, GTO yaklaşımı ile YP'nin eniyilemesi yapılmıştır. Bir diğer çalışmada (Phate vd. [15]), Taguchi OD-L_{27} tasarımı kullanılarak ANFIS-TYM hibrit yöntem sayesinde Al/Gr/Cp5 metal matris kompozit malzemenin WEDM prosesi ile işlenmesinde girdi parametrelerinin YP üzerindeki etkisi incelenmiştir. Kumar vd. [16], Ti-6Al-4V alaşımının WEDM ile işlenmesinde girdi-çıktı ilişkilerinin modellenmesi ve optimizasyonu için ANFIS ve GRA tekniklerini kullanmışlardır. Taguchi OD-L_{18} deney planına göre deneyler gerçekleştirilerek MKO ve YP çıktılarının modellenmesi ve eniyilemesi üzerine çalışmışlardır. WEDM ile işlemede AISI 1050 karbon çeliğinde beyaz katman kalınlığının ANFIS ile tespiti üzerine gerçekleştirilen bir çalışmada (Maher vd. [17]) deney planı olarak Taguchi OD-L_{18} kullanılmıştır. Azhiri vd. [18], Al-SiC metal matris kompozit malzemenin WEDM ile işlenmesinde kesme hızının ve YP'nin modellenmesi ve eniyilemesi üzerine çalışmışlardır. Taguchi OD-L_{27} deney planına göre elde edilen deneysel veriler ile ANFIS'te modeller oluşturulmuş, GRA yöntemi kullanılarak çıktılar optimize edilmiştir. Abhilash ve Chakradhar [19] ise WEDM prosesinde deşarj voltajındaki değişimin işleme kalitesine ve tel kopmasına olan etkisini araştırmışlardır. Inconel 718 alaşımında MKT-L_{31} tasarımı kullanılarak elde edilen deneysel verileri ANFIS'te kullanılmışlardır.

Literatürde yer alan çalışmalardan görüldüğü üzere EDM/EDD/WEDM proseslerinde girdi-çıktı ilişkilerinin belirlenmesi amacıyla ANFIS'te oluşturulacak modeller için çeşitli deney tasarımları kullanılmıştır. Buna karşın, söz konusu çalışmalarda spesifik bir deney planı seçilmiş olup diğer deney tasarımları ile kıyaslanmamıştır. Bir diğer deyişle, seçilen deney planının etkinliği ve performansı ölçülmemiştir. Dolayısıyla, belirli şartlar altında proses çıktılarının modellenmesi ve tahmininde hangi deney planının uygun olduğunun tespiti üzerine bir çalışma bulunmamaktadır. Bu çalışmada, EDD prosesi ile Inconel 718 alaşım malzemesinde gerçekleştirilen delik delme işlemleri için iki farklı deney planı kullanılmıştır. MKT ve OD tasarımları kullanılarak spesifik parametre değerleri ile gerçekleştirilen deneyler sonucunda elde edilen veri setleri kullanılarak ANFIS ile modeller oluşturulmuştur. Farklı küme tiplerine ve sayılarına sahip modellerin çıktı performansları, validasyon (doğrulama) deneyleri doğrultusunda karşılaştırılmıştır.

2. Materyal ve Metot

Bu çalışmada, Ø2 mm çapında pirinç boru elektrotlar kullanılarak Inconel 718 alaşım malzemeden yapılmış 6 x 11 x 35 mm boyutlarındaki numuneler üzerinde delikler delinmiştir. Delik delme işlemleri, otomatik kontrol sistemine ve dijital eksen okuyucuya sahip tezgâhta gerçekleştirilmiştir (Şekil 3). Değişken ve sabit deney parametreleri Tablo 1'de gösterilmektedir. Tüm deneylerde;

deşarj akım – I (*discharge current*), vurum süresi – T_{on} (*pulse-on time*), bekleme süresi – T_{off} (*pulse-off time*) ve kapasitans – C (*capacitance*) değişken parametrelerdir. Dielektrik sıvı basıncı, voltaj seviyesi ve elektrot dönüş hızı ise sabit tutulmuştur. Değişken parametrelerin kademe değerleri, tezgâh üzerindeki kontrol panelinden seçilmektedir. Ön çalışma kapsamında gerçekleştirilen deneylerde 5-9 arasındaki kademelerin en uygun seviyeler olduğu saptanmış, dolayısıyla tüm delik delme işlemleri bu kademelerde gerçekleştirilmiştir.

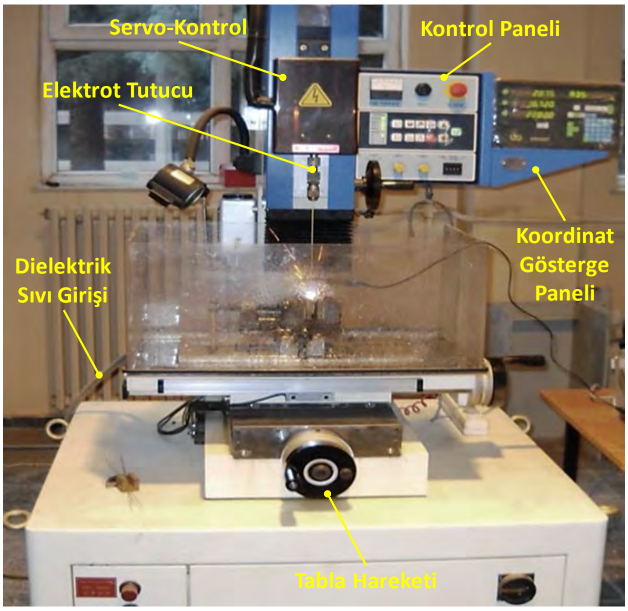

Şekil 3. Delik delme deneylerinde kullanılan EDD tezgâhı

Tablo 1. Delik delme deneylerinde kullanılan değişken ve sabit parametreler

Değişken Parametreler				
Kademe	**I (A)**	**T_{on} (µs)**	**T_{off} (µs)**	**C (µF)**
5	8,2	27	16	1100
6	8,8	30	18	1217
7	10,2	35	20	1316
8	11,5	38	23	1422
9	12,0	44	26	1476

Sabit Parametreler	
Voltaj:	27 V
Dielektrik Sıvı:	deiyonize su
Dielektrik Basıncı:	100 bar
Elektrot Dönüş Hızı:	200 devir/dk

EDD işleminde, proses performansının ölçülebilmesi adına farklı çıktı parametreleri incelenebilir. MKO ile EAO; birim zamanda iş parçasından kaldırılan malzeme miktarı ve elektrotun aşınma miktarı olarak tanımlanan çıktılardır. MKO'nun olabildiğince yüksek, EAO'nun ise düşük olması istenmektedir. Bu durum, EDD'nin doğası gereği mümkün değildir. Seçilen parametre değerleri, MKO'nun iyileşmesine imkan tanırken EAO üzerinde olumsuz etki yapmaktadır. Dolayısıyla bu çalışmada, iki çıktının bütünleşik olarak değerlendirilebilmesi adına Bağıl Aşınma Oranı – BAO (*Relative Wear Rate*) incelenmiştir:

$$BAO\ (mg/mm) = \frac{MKO\ (mg/dk)}{EAO\ (mm/dk)}$$

MKO'nun hesaplanabilmesi için; her delik delme işlemi öncesinde ve sonrasında iş parçasının ağırlığı ölçülmüş, elde edilen ağırlık farkı delme süresine oranlanmıştır. Diğer taraftan EAO, delme işlemi öncesinde ve sonrasında elektrot boyundaki kısalma miktarının delme süresine oranlanması ile bulunmuştur. Sonuç olarak, her delik delme işleminden sonra elde edilen MKO ve EAO değerlerinden yola çıkılarak BAO değerleri tespit edilmiştir.

MKT-L_{25} ve OD-L_{25} deney planlarına göre hazırlanan ve modellerin eğitilmesinde kullanılan veri setleri Tablo 2'de verilmiştir. Modellerin öğrenme ve çıktı performanslarının sağlıklı şekilde kıyaslanabilmesi açısından her iki veri setinde 25'er adet veri bulunmaktadır. Girdi parametre değerleri olarak tezgâh üzerinde seçilen kademeler kullanılmıştır. MKT veri setinde, deney planının doğası gereği #M1 nolu deney; 7 kez tekrarlanmış olup tekrarlı deneyler sonucunda elde edilen BAO değerlerinin ortalaması (9,130 mg/mm) alınarak tabloda belirtilmiştir.

Tablo 2. Modellerin eğitilmesi için kullanılan veri setleri

Deney Planı (MKT)						Deney Planı (OD)					
#	I	T_{on}	T_{off}	C	BAO (mg/mm)	#	I	T_{on}	T_{off}	C	BAO (mg/mm)
M1	7	7	7	7	9,130	O1	5	5	5	5	6,549
M2	5	7	7	7	9,728	O2	5	6	6	6	7,369
M3	7	5	7	7	8,254	O3	5	7	7	7	9,728
M4	7	7	5	7	9,328	O4	5	8	8	8	12,265
M5	7	7	7	5	10,023	O5	5	9	9	9	13,336
M6	9	7	7	7	13,312	O6	6	5	6	7	10,365
M7	7	9	7	7	9,030	O7	6	6	7	8	14,691
M8	7	7	9	7	11,564	O8	6	7	8	9	13,615
M9	7	7	7	9	12,947	O9	6	8	9	5	9,178
M10	6	6	6	6	6,207	O10	6	9	5	6	9,009
M11	8	6	6	6	8,760	O11	7	5	7	9	12,668
M12	6	8	6	6	8,292	O12	7	6	8	5	8,785
M13	6	6	8	6	10,153	O13	7	7	9	6	9,851
M14	6	6	6	8	12,834	O14	7	8	5	7	7,922
M15	8	8	8	8	14,236	O15	7	9	6	8	10,789
M16	6	8	8	8	12,712	O16	8	5	8	6	9,128
M17	8	6	8	8	15,466	O17	8	6	9	7	11,179
M18	8	8	6	8	15,547	O18	8	7	5	8	13,201
M19	8	8	8	6	9,079	O19	8	8	6	9	14,842
M20	6	6	8	8	12,930	O20	8	9	7	5	10,218
M21	8	8	6	6	8,106	O21	9	5	9	8	14,824
M22	6	8	8	6	8,213	O22	9	6	5	9	15,502
M23	8	6	6	8	15,927	O23	9	7	6	5	14,353
M24	6	8	6	8	13,602	O24	9	8	7	6	9,293
M25	8	6	8	6	9,349	O25	9	9	8	7	11,963

Modellerin validasyonu için kullanılan veri seti Tablo 3'te gösterilmiştir. Validasyon için rastgele girdi değerleri seçilmiş olup toplam 4 adet deney gerçekleştirilmiştir. Bu deneylerde kullanılan girdi parametre değerleri, Tablo 2'de gösterilen her iki deney planında da yer almamaktadır. Bir diğer deyişle, modellerin validasyonu için eğitim veri setlerinden tamamen bağımsız seçilen ve farklı girdi parametre değerlerine sahip deneyler kullanılmıştır. Bu sayede, modellerin çıktı performanslarının sağlıklı şekilde karşılaştırılabilmesi mümkün olabilecektir.

Tablo 3. Modellerin validasyonu için kullanılan veri seti

#	I	T_{on}	T_{off}	C	BAO (mg/mm)
V1	7	8	7	8	11,927
V2	8	7	7	6	9,306
V3	6	8	8	7	9,470
V4	7	9	5	8	14,172

Modellerin oluşturulması, eğitilmesi ve validasyonu için Matlab® ANFIS modülü kullanılmıştır. Girdi parametreleri (I, T_{on}, T_{off}, C) için; yamuk (*trapmf*), çan (*gbellmf*), gaussian (*gaussmf*) ve birleşik sigmoidal (*psigmf*) olmak üzere 4 farklı küme tipi seçilmiştir. Ayrıca, her girdi parametresi için 2 ve 3 kombinasyonlarına göre küme sayıları belirlenmiştir. Dolayısıyla, MKT ve OD için 64'er adet olmak üzere toplamda 128 adet model (Tablo 4) oluşturulmuştur.

Modellerin eğitiminde; En Küçük Kareler Yöntemi (*Minimum Squares Method*) ile Geri Yayılmalı Öğrenme Algoritmasının (*Backpropagation Learning Algorithm*) birleştirildiği Melez Öğrenme Algoritması (*Hybrid Learning Algorithm*) kullanılmıştır. Eğitim hata toleransı (*error tolerance*) için herhangi bir değer atanmamış, böylece asgari hata değeri ile modelin eğitilmesi amaçlanmıştır. Eğitimde kullanılan iterasyon sayısı (*epoch number*), 300 olarak belirlenmiştir. Bunun sonucunda validasyon veri setindeki deney sonuçları ile modelin verdiği çıktı değerleri ile dikkate alınarak Kök Ortalama Kare Hatası – RMSE (*Root Mean Square Error*) hesaplanmıştır.

3. Bulgular ve Tartışma

Yukarıda bahsedildiği üzere toplamda 128 adet model oluşturulmuş ve eğitilmiştir. Validasyon (doğrulama) veri seti kullanılarak modellerin validasyon hata değerleri (RMSE) hesaplanmıştır. Tüm modeller için elde edilen validasyon hata değerleri Tablo 4'de ve Şekil 4'de verilmiştir. Sonuçlardan görüldüğü üzere; #6 nolu model haricinde MKT ile oluşturulan tüm modeller, OD'ye kıyasla daha düşük hata değerlerine sahiptir. Bir diğer deyişle, küme tipi ve sayısından bağımsız olarak MKT deney tasarımının kullanıldığı modeller girdi-çıktı ilişkisinin tespitinde daha doğru tahminler yapabilmektedir. Bunun başlıca sebebi, deney setlerindeki parametre değerlerinin farklı olmasıdır. Tablo 2'den anlaşılacağı üzere MKT, parametre seviyeleri (kademe değerleri) içerisinde öncelikle orta kademe değerini ("7") dikkate almakta ve diğer deneylerdeki değerlerin buna göre belirlenmesine yönelik bir yapıya sahiptir. Bu durumda deneyler, merkez seviye odaklı değerlerle kurgulanmaktadır. Diğer taraftan, OD tasarımında deney kurgusu çok farklıdır. OD ile tasarlanan deneylerde; parametre değerlerinin sıralı dizilime ("5 6 7 8 9") sahip olduğu göze çarpmaktadır. Özetle, MKT ve OD tasarımlarının odağında yer alan seviye değerleri farklıdır. Bu sebepten ötürü ANFIS ile modellemede MKT'nin daha iyi performans sergilediği düşünülmektedir.

Tablo 4. Tüm modellerin validasyon hata değerleri (RMSE)

Model No.	Küme Sayısı	TRAPMF		GBELLMF		GAUSSMF		PSIGMF	
		MKT	*OD*	*MKT*	*OD*	*MKT*	*OD*	*MKT*	*OD*
1	2 2 2 2	0,3934	2,5213	0,6698	2,5085	0,9837	2,4586	0,3582	2,5082
2	2 2 2 3	0,5694	2,3811	0,8056	1,9127	0,9098	1,8420	0,5840	2,3436
3	2 2 3 2	1,6252	4,0928	1,7186	4,2767	1,4101	4,3520	1,6504	4,0501
4	2 3 2 2	1,3008	2,0417	1,6709	2,1656	1,7572	2,1497	1,2815	2,0258
5	3 2 2 2	0,8494	2,2003	1,0338	2,3049	0,9958	2,4762	0,8507	2,2715
6	2 2 3 3	2,0786	1,9172	2,0945	1,8288	2,1128	1,7327	2,0275	1,9022
7	2 3 3 3	1,0212	3,1121	0,8644	2,6091	0,8736	2,5447	1,0122	3,1032
8	2 3 2 3	1,4127	2,3407	1,6779	2,0052	1,8752	1,9523	1,4117	2,3078
9	2 3 3 2	1,8729	3,7465	2,2177	4,0377	1,5995	4,1124	1,6789	3,7142
10	3 3 3 3	1,2052	1,4888	0,9182	1,8460	0,9267	1,8569	1,2971	1,4707
11	3 3 2 2	0,4130	2,4149	0,3487	2,0244	0,4204	2,0220	0,4006	2,4350
12	3 3 3 2	1,7090	2,3497	1,3905	2,5503	1,6025	2,3392	1,6076	2,3619
13	3 2 3 2	0,9030	3,6438	0,8431	3,8002	0,8624	3,9013	0,9786	3,5674
14	3 2 3 3	2,0478	2,7336	1,6100	1,7257	1,5653	1,6702	2,0416	2,6941
15	3 3 2 3	1,0829	2,6192	0,8607	1,7329	0,9612	1,5607	1,1231	2,5450
16	3 2 2 3	1,0740	2,8523	1,0496	2,1705	0,9840	1,9674	1,0541	2,8260

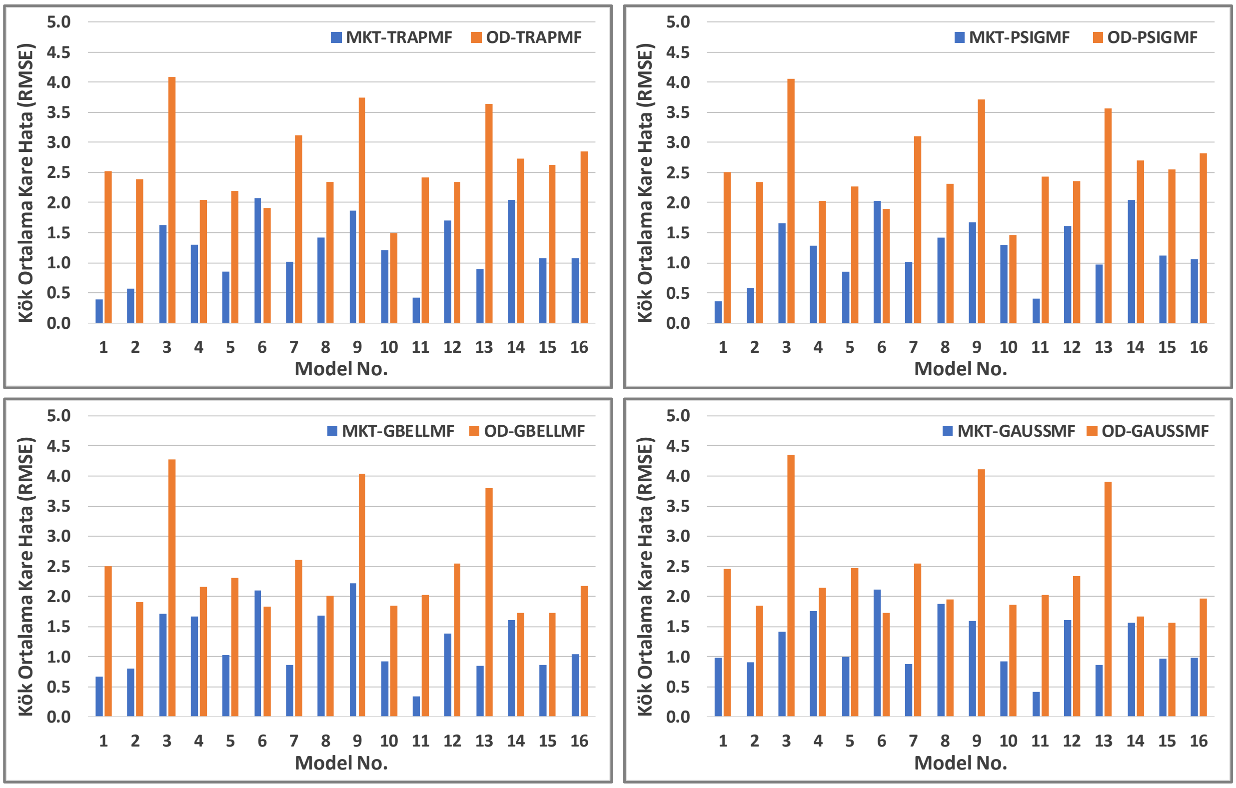

Şekil 4. Validasyon hatalarının (RMSE) karşılaştırılması

Performans karşılaştırması yapabilmek adına tüm modeller içerisinde MKT ve OD ile oluşturulan en iyi modeller seçilmiştir. Tablo 4'deki validasyon hataları dikkate alındığında en düşük hata değerine sahip modellerin; MKT için "GBELLMF-3322" ve OD için "PSIGMF-3333" olduğu görülmektedir. Bu modellerin ağ yapıları Şekil 5 ve Şekil 6'da gösterilmektedir. Ağ yapılarından anlaşılacağı üzere girdi parametreleri (I, T_{on}, T_{off}, C) için küme sayıları "MKT-GBELLMF-3322" modelinde "3 3 2 2" iken "OD-PSIGMF-3333" modelinde "3 3 3 3" olmuştur. Dolayısıyla, kural sayıları sırasıyla 36 ve 81 olarak belirlenmiştir.

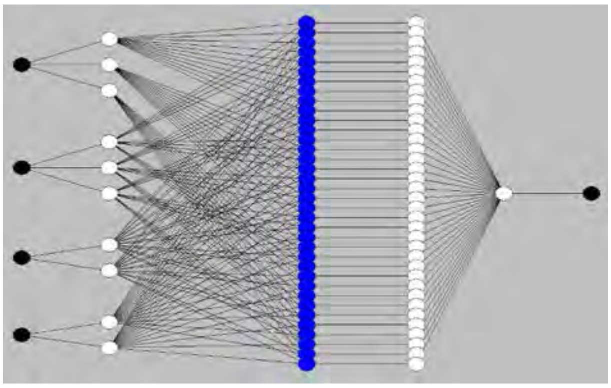

Şekil 5. Model "MKT-GBELLMF-3322"

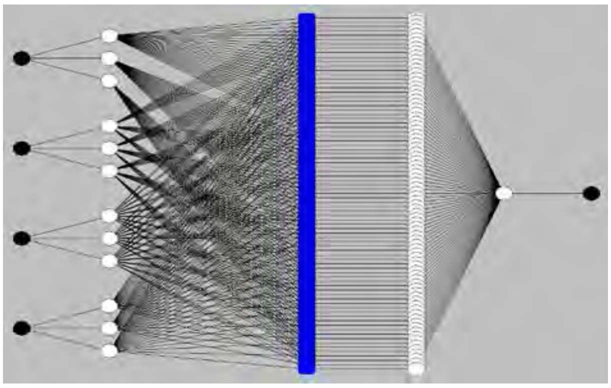

Şekil 6. Model **"**OD-PSIGMF-3333"

Seçilen modellerin, validasyon veri setindeki deneysel sonuçlarla karşılaştırılması ve her bir validasyon deneyindeki hata oranları Tablo 5 ve Şekil 7'de verilmiştir. Sonuçlardan görüldüğü üzere MKT ile oluşturulan modelin OD'ye kıyasla çok daha düşük hata yüzdeleri ile sonuçları tahmin edebildiği görülmektedir. "MKT-GBELLMF-3322" modelindeki hata payı en fazla %6,2 iken **"**OD-PSIGMF-3333" modelinde hata oranı %16,4'tür.

Tablo 5. Seçilen modellerin validasyon hata değerleri (%)

#	**BAO** (mg/mm) ***DENEYSEL***	**BAO** (mg/mm) ***MKT-GBELLMF-3322***	**Hata** (%)	**BAO** (mg/mm) ***OD-PSIGMF-3333***	**Hata** (%)
V1	11,927	11,953	0,2	12,436	4,3
V2	9,306	8,945	3,9	7,775	16,4
V3	9,470	10,058	6,2	7,999	15,5
V4	14,172	14,269	0,7	12,201	13,9

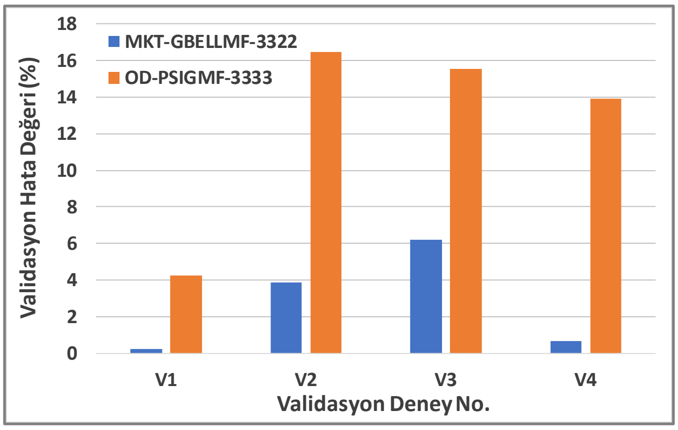

Şekil 7. Seçilen modellerin validasyon hatalarının karşılaştırılması

Şekil 8'de seçilen modellerin validasyon değerlerinin deneysel sonuçlara göre regresyonları gösterilmektedir. Lineer regresyon değerleri (R^2); "MKT-GBELLMF-3322" modelinde 0,9721 iken **"**OD-PSIGMF-3333" modelinde ise 0,8135 olarak elde edilmiştir. OD modeline kıyasla daha yüksek regresyon değerine sahip MKT modeli doğru ve tutarlı sonuçlar vermektedir.

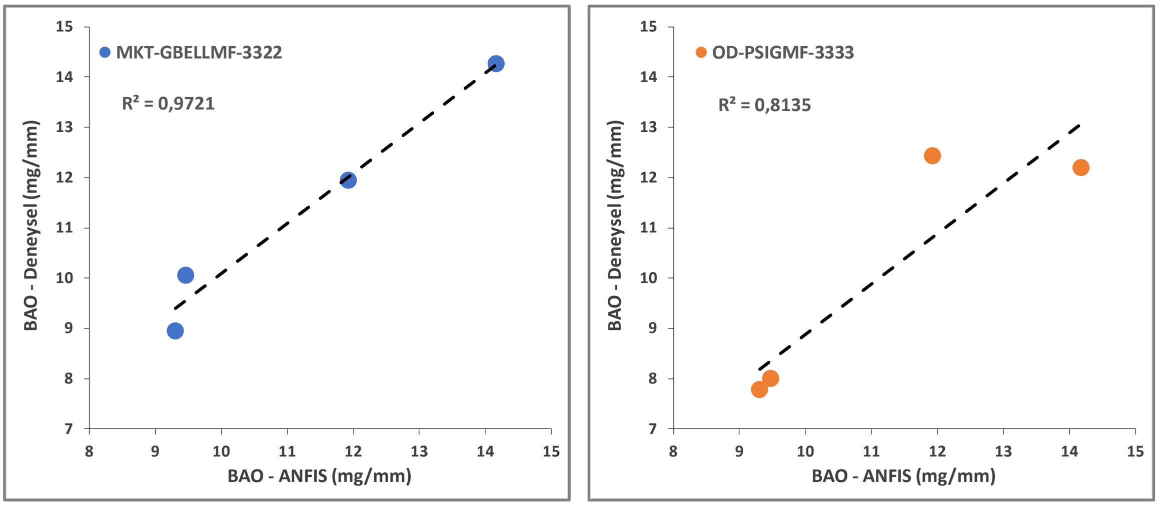

Şekil 8. Seçilen modellerin validasyon değerlerinin regresyonu

4. Sonuçlar

Bu çalışmada, deney planının EDD işleminde girdi-çıktı ilişkisinin ANFIS ile modellenmesindeki etkisi araştırılmıştır. Deney planının etkinliğinin sağlıklı şekilde belirlenebilmesi amacıyla eşit sayıda deney yapılmasını öngören veri setleri (MKT-L25 ve OD L25) kullanılmıştır. Farklı küme sayıları ve küme tiplerine sahip toplam 128 adet model oluşturulmuş ve bu veri setleri kullanılarak eğitilmiştir. Modellerin validasyonu, eğitim için kullanılan veri setlerinde bulunmayan tamamen farklı deneyler doğrultusunda gerçekleştirilmiştir.

Elde edilen sonuçlar şu şekilde özetlenebilir:

- Küme sayısı "2233" olan model hariç tüm modellerde MKT'nin OD'ye kıyasla daha düşük hata oranı ile sonuçları tahmin edebildiği görülmüştür.
- Validasyon hata değerleri göz önüne alındığında en düşük RMSE hatasına sahip modellerin "MKT-GBELLMF-3322" (36 kural, çan küme tipi) ve "OD-PSIGMF-3333" (81 kural, birleşik sigmoidal küme tipi) olduğu belirlenmiştir.
- Seçilen modeller karşılaştırıldığında MKT ile oluşturulan modelde en yüksek hata oranı %6,2 iken OD modelinde bu oran %16,4 seviyesindedir.
- Validasyon deneylerinde lineer regresyon sonuçlarına göre MKT modelinde R^2 değeri 0,9721 iken OD modelinde bu değer 0,8135 olarak tespit edilmiştir.

Özetle, ANFIS ile modellemede kullanılacak eğitim veri setinin belirlenmesinde deney tasarımının rolü büyüktür. OD tasarımı ile oluşturulan modellere kıyasla MKT'ye göre oluşturulan modellerin daha doğru ve tutarlı sonuçlar verdiği gözlemlenmiştir.

Kaynaklar

1. Bozdana, A.T., Ulutas, T., The effectiveness of multichannel electrodes on drilling blind holes on Inconel 718 by EDM process, Materials and Manufacturing Processes, **2016**, 31(4):504-513.
2. Jang, J.S.R., ANFIS: Adaptive-Network-Based Fuzzy Inference System, IEEE Transactions on Systems, Man, and Cybernetics, **1993**, 23(3):665-685.
3. Montgomery, D.C., Design and Analysis of Experiments, John Wiley & Sons, **2020**.
4. Sharma, D., Bhowmick, A., Goyal, A., Enhancing EDM performance characteristics of Inconel 625 superalloy using response surface methodology and ANFIS integrated approach, CIRP Journal of Manufacturing Science and Technology, **2022**, 37:155-173.
5. Phate, M., Toney, S., Phate, V., Modelling and investigating the impact of EDM parameters on surface roughness in EDM of Al/Cu/Ni Alloy, Australian Journal of Mechanical Engineering, **2020**, 1-14.
6. Phate, M., Bendale, A., Toney, S., Phate, V., Prediction and optimization of tool wear rate during electric discharge machining of Al/Cu/Ni alloy using adaptive neuro-fuzzy inference system, Heliyon, **2020**, 6(10), e05308.
7. Agarwal, N., Shrivastava, N., Pradhan, M.K., Hybrid ANFIS-Rao algorithm for surface roughness modelling and optimization in electrical discharge machining, Advances in Production Engineering and Management, **2021**, 16(2):145-160.
8. Bhiradi, I., Raju, L., Hiremath, S.S., Adaptive neuro-fuzzy inference system (ANFIS): modelling, analysis, and optimisation of process parameters in the micro-EDM process, Advances in Materials and Processing Technologies, **2020**, 6(1):133-145.
9. Singh, N.K., Singh, Y., Kumar, S., Sharma, A., Comparative study of statistical and soft computing-based predictive models for material removal rate and surface roughness during helium-assisted EDM of D3 die steel, SN Applied Sciences, **2019**, 1(6):529.
10. Goyal, A., Sharma, D., Bhowmick, A., Pathak, V.K., Experimental investigation for minimizing circularity and surface roughness under nano graphene mixed dielectric EDM exercising fuzzy-ANFIS approach, Int. J. on Interactive Design and Manufacturing, **2022**, 16(3):1135-1154.
11. Hourmand, M., Sarhan, A.A.D., Farahany, S., Sayuti, M., Microstructure characterization and maximization of the material removal rate in nano-powder mixed EDM of Al-Mg_2Si metal matrix composite – ANFIS and RSM approaches, **2019**, Int. J. of Advanced Manufacturing Technology, 101(9-12):2723-2737.
12. Singh, J., Sharma, R.K., Modeling and optimization of multi-performance characteristics of powder-mixed EDM of tungsten carbide alloy using intelligent decision-making tools, Journal of Advanced Manufacturing Systems, **2017**, 16(2):101-128.
13. Singh, J., Multi-objective optimization of powder-mixed EDM parameters using hybrid Grey-ANFIS artificial intelligence technique, Int. J. on Interactive Design and Manufacturing, **2022**, *in press*.
14. Natarajan, E., Kaviarasan, V., Lim, W.H., Ramesh, S., Palanikumar, K., Sekar, T., Mok, V.H., Gorilla Troops Optimizer combined with ANFIS for wire cut EDM of aluminum alloy, Advances in Materials Science and Engineering, **2022**, 3072663.
15. Phate, M., Toney, S., Phate, V., Response Surface Modelling and Effective Application of Adaptive Neuro-Fuzzy Inference System to Analyze Surface Roughness of Al/Gr/Cp5 MMC Machined using WEDM, Australian Journal of Mechanical Engineering, **2021**, *in press*.

16. Kumar, S., Dhanabalan, S., Narayanan, C.S., Application of ANFIS and GRA for multi-objective optimization of optimal wire-EDM parameters while machining Ti-6Al-4V alloy, SN Applied Sciences, **2019**, 1(4):298.
17. Maher, I., Sarhan, A.A.D., Marashi, H., Barzani, M.M., Hamdi, M., White layer thickness prediction in wire-EDM using CuZn-coated wire electrode – ANFIS modelling, Transactions of the Institute of Metal Finishing, **2016**, 94(4):204-210.
18. Azhiri, B., Teimouri, R., Ghasemi Baboly, M., Leseman, Z., Application of Taguchi, ANFIS and grey relational analysis for studying, modeling and optimization of wire EDM process while using gaseous media, Int. J. of Advanced Manufacturing Technology, **2014**, 71(1-4):279-295.
19. Abhilash, P.M., Chakradhar, D., ANFIS modelling of mean gap voltage variation to predict wire breakages during wire EDM of Inconel 718, CIRP Journal of Manufacturing Science and Technology, **2020**, 31:153-164.

PERFORMANCE of CONVENTIONAL GAS CARBURIZATION METHOD APPLIED on AISI/SAE 420 MARTENSITIC STAINLESS STEEL

AZİZ BARIŞ BAŞYİĞİT *1, HALİL İBRAHİM KURT 2

1 Kırıkkale University, Faculty of Engineering and Architecture, Metallurgical and Material Engineering Department, Kırıkkale, TÜRKİYE.
2 Samsun University, Faculty of Aeronautics and Astronautics, Aerospace Engineering Department, Samsun, TÜRKİYE.

Abstract

Martensitic stainless steels are preferentially used in applications where high mechanical properties with satisfactory general atmospheric corrosion resistance are in concern. These alloys are strengthened by heat treating methods generally the same as plain carbon or low alloy steels. The main metallurgical difference can be defined as air cooling is enough for obtaining adequate strength values in these alloys for complete cross-sectional hardening operations. These alloys are also hardened by cooling in oil in many applications with precautions for preventing cracking phenomena. However they can be rarely strengthened up to specific amounts of case depths by surface hardening methods. In this study; Ø24x10 mm in dimensions of 420 martensitic stainless steel samples are conventionally gas carburized in a controlled furnace atmosphere. Applicability of conventional gas carburization technique on 420 alloys is investigated. Gas carburization performance and case depths are studied by micro-vickers hardness tests and micro-structural analysis. The case hardness is determined as 590 HV with an average case depth of approximately 0.66mm while the core hardness value is estimated as 400HV in mean values after heat treatments. AISI 420 alloy can be satisfactorily surface hardened with conventional gas carburization method.

Keywords: Martensitic stainless steels, Surface hardening, Gas carburization.

1. Introduction

AISI 420 martensitic stainless steels are generally defined for their dominant martensitic microstructure when they hardened rather by air as it originates from the term ‘air hardening’. They can be strengthened up to 1900MPa values by quenching and tempering via complete (full) cross-sectional heat treatments [1]. Complete cross-sectional heat treatments can cause to cracking, distortion, stresses or improper micro-structural developments that may result in reducing the service life of mechanical components or parts [2,3].

Therefore as an alternative to complete hardening operation only a specified depth of parts from the surface can be hardened in order to obtain adequate wear resistance for prolongation of service life. Carburizing, nitriding, boriding, induction and flame hardening heat treating methods can be used for such case hardening operations. Among them especially carburizing but also nitriding are two popular case hardening techniques in consequence of determining and adjusting case depth control simply by heat treatments [2, 4].

Carburizing can only be effectively applied on steel groups that have carbon element amounts less than approximately 0.25% by weight [2]. By carburizing core regions of parts have original (raw material) amounts of carbon element in limited values while it is enriched in case regions by an intense carbon ambient inside the furnaces. That's why after carburizing followed by hardening, parts can simply have much more hardness values in case regions as compared to core regions. Upon quenching the high carbon including region transforms rapidly to martensite phase resulting in higher hardness values than the core regions having finally dominant perlitic and ferritic microstructure. Nickel, chromium and molybdenum elements are intentionally added to carburizing steel groups in order to facilitate the carburizing operation. Carburizing can be applied in three common ways. Solid, liquid and gas carburization can be effectively used. As a comparison gas carburization is frequently preferred for easier control of process parameters and accurate management of needs for parts to be heat treated [2, 3].

Carburizing operation is generally applied to steels depending on their compositions in a temperature range of 900-1050°C selected mainly for best diffusion temperatures in austenitic structure of steel although higher temperatures as well as 1095°C can also be used. After the carburizing followed by quenching (or hardening) heat treatment parts must be tempered for relieving the internal stresses originating from thermal shocks and adjusting the final hardness values [2-6].

Commonly, surface treatment of various classes of stainless steels is hard to accomplish. The main reason is the chromium oxide layer or various types of oxides formed naturally on these steels acting as an obstacle to be surface treated. Therefore as a practical solution the surfaces of the samples are machined just before the carburization operation in order to eliminate oxidation for increasing the effectiveness of the carburization [6].

In this study; AISI 420 stainless steel round bar samples are gas carburized and hardened for investigating the applicability of method and determining the effectiveness of case depth and surface hardness values. Micro-structural and micro-hardness tests are applied for identifying the carburization efficiency of samples.

2. Materials and Methods

Experimental material is prepared from AISI/SAE 420 martensitic stainless steel bar to dimensions of Ø24x10 mm. The hardness value of raw 420 alloy is estimated 228 HV1 in mean values as seen in Figure 1.

Spectral analysis result of experimental alloy gained from Amatex Spectromax optical argon emission spectrometer is given in Table 1.

Table 1. Spectral analysis of 420 alloy (%wt.)

C	Si	Mn	P	S	Cr	Mo	Ni	V	N	Fe	Others
0.230	0.51	0.63	0.010	0.002	13.30	0.006	0.13	0.04	0.02	85	0.122

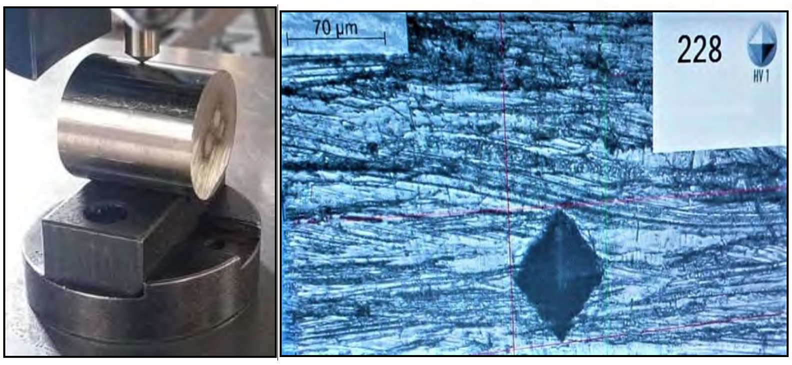

Figure 1. Raw 420 alloy

Experimental material is suitable with the standard document [7]. Micro-vickers hardness testing method is used for obtaining test samples core and case hardness values with a unit cell load of 1 kg [8, 9]. The hardness values are investigated by an Emcotest brand Durascan 20 model micro-vickers hardness testing instrument. Effective case depth and hardness surveys of carburized layer are investigated according to the related standards [8-10].

Gas carburization heat treatment is applied conventionally by carburization followed by quenching in IVA Brand RM300 model controlled atmosphere furnace. Heat treatment parameters are listed in Table 2 as interpreted from literature [1-6].

Table 2. Heat treatment parameters

Pre-heat temperature (°C)	**Time at pre-heating (min.)**	**Carburization temperature (°C)**	**Time at carburization (min.)**	**Hardening Temperature (°C)**
600	60	910	320	1020
Carburization source	**Carbon content (by%vol.)**	**Time at hardening (min.)**	**Quenching media**	**Quenching media temperature (°C)**
Aceytone+methyl alcohol	0.95	25	Oil bath	60

3 samples are prepared for gas carburization operation. Samples are pre-heated for reducing thermal shock probabilities before the carburization at 600 °C in an electrical resistance dry furnace for 60 minutes.
Carburization stage is applied at 910 °C in controlled atmosphere furnace at approximately 320 minutes of duration time by aceytone and methyl alcohol mixture obtained from a gas chamber ensuring the final carbon content of ambient 0.95% by volume. Increasing carburization time increases the carburized layer depth therefore wear resistance is also improved [2-6, 11, 12].

As soon as the carburization stage finishes the temperature of the furnace is increased to 1020 °C with the samples inside for the need of adjusting the samples hardening temperature. After keeping 25 minutes of duration time at hardening stage as estimated according to the samples stock dimensions they were immediately cooled by oil quenchant keeping it with a constant temperature of 60 °C. Until the temperature of samples decreases to the oil bath temperature, they were taken to atmospheric environment for cooling down directly to room temperature.

After the carburization and hardening stages all of the three samples, the hardness values are controlled by micro-vickers hardness instrument with 1 kg unit cell of HV1. Finally, the tempering operation is applied to all samples for stress relieving and adjusting the final hardness values in a dry resistance furnace at 130°C for two hours of time.

3. Results and Discussion

3.1. Micro-structural examinations of samples

Carburized and as hardened state of samples microstructure is given in Figure 2.

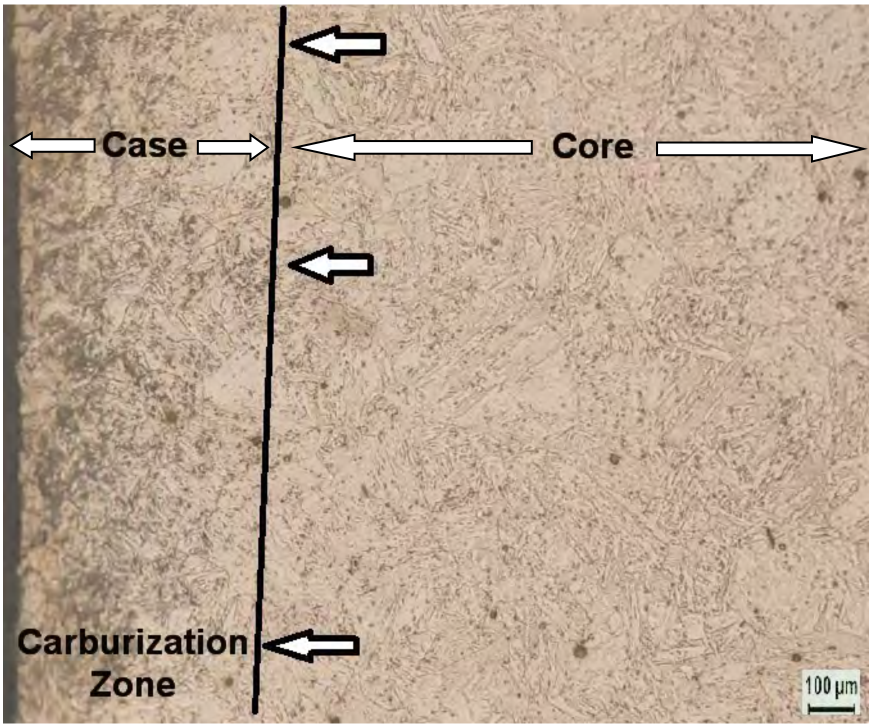

Figure 2. Microstructure of carburized and hardened samples

In core region (right hand side of the micrograph) dominant needle like martensitic (darker) microstructure with delta ferrite (semi-dark) and minor amounts of retained austenite (the lightest) is visible.

However in case region (left hand side of the micrograph) the amount of martensite phase increases, besides grain boundary chromium carbides seem as the darker regions. At some regions of the case sides, the effective case depth changes from place to place most probably in consequence of inhomogeneous carburization operation as clearly seen from Figure 2.

3.2. Micro hardness tests of samples

Effective case depth estimation and hardness surveys by micro-vickers hardness testing
After the carburizing and hardening operations the surface hardness value is estimated as 590HV1. The hardness limit value for determining the effective case depth value is calculated approximately 472 HV1 according to EN 10328 standard document.

Microvickers hardness testing instrument is adjusted for 0.1 mm intervals of indentation points the first one to be 0.15mm away from the surface of case hardened layer. The hardness survey results after heat treatments are listed in Table 3.

Table 3. Micro-hardness test results after the heat treatments

	Distance from the outer case (mm)										Core region (in mean values)	Raw State (in mean values)
	0.1	0.2	0.3	0.4	0.5	0.6	0.7	0.8	0.9	1.0		
Micro hardness value (HV1)	558	543	508	485	474	475	470	472	464	465	400	228

Case depth is estimated approximately as 0.66mm. Core region micro hardness value is determined as 400HV as a result of hardening operation after the carburization. Effective case depth estimation of samples is given in a graph in Figure 3.

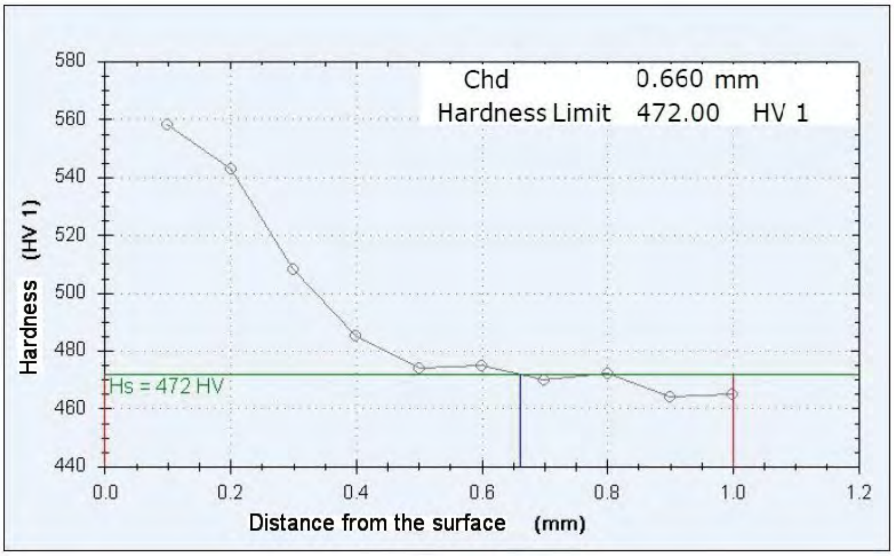

Figure 3. Effective case depth results

4. Conclusions:

- AISI 420 martensitic stainless steel samples are conventionally gas carburized satisfactorily.
- After carburization and hardening operation, raw samples core hardness value is increased from 230HV to 400HV.
- The effective case depth and micro-hardness limit value are calculated according to EN10328 standard document.

- The case hardness is determined as 590 HV value while the effective case depth is found approximately 0.66mm in mean values varying from place to place on samples.

Acknowledgments: Authors present their thanks to Mechanical and Chemical Industries Corporation Heat treatment personnel for heat treating and experimental investigation supports.

References:

1. Lippold, J. C. and Kotecki D, Welding Metallurgy and Weldability of Stainless Steels, 56-57, **2005**, Wiley Interscience.
2. Mandal S.K., Heat treatment of Steels, McGraw Hill Education, **2016**; 237, 263, 298.
3. Thelning K. E., Steel and its Heat Treatment, Butterworh Heinemann, Reprinted **2000;** 168, 344
4. Haimbaugh R. E., Practical Induction Heat Treating, 2nd Edition, **2015**, 192, ASM International.
5. Dossett J.L., Boyer H. E., Practical Heat Treating, 2nd Edition, **2006**, 141-151, ASM International.
6. ASM Handbook Committee, ASM Metals Handbook Volume 4A, Steel Heat Treating Fundamentals and Processes, **2013**, 528-596, Heat Treating Society, ASM International.
7. ASTM A240/A240M, Standard Specification for Chromium and Chromium Nickel Stainless Steel Plate, Sheet and Strip for Pressure Vessels and for General Applications, ASTM International, **2017**, USA.
8. ASTM A370, Test Methods and Definitions for Mechanical Testing of steel Products, ASTM International, **2017**. USA.
9. EN ISO 6507-1, Metallic Materials, Vickers Hardness Testing Method, **2018**, European Standard.
10. EN 10328, Iron and Steel, Determination of the Conventional Depth of Hardening after Surface Heating, **2005**, European Standard, Brussels.
11. Ramli Wu, C.-C., Shaaban, A. Mechanical Properties of Pack Carburized SCM 420 Steel Processed Using Natural Shell Powders and Extended Carburization Time. Crystals **2021**, 11, 1136. https://doi.org/10.3390/cryst11091136.
12. Ramli Wu, C.-C., Effective Case Depth and Wear Resistance of Pack Carburized SCM 420 Steel Processed Using Different Concentrations of Natural Shell Waste Powders and Carburizing Duration. Crystals 2022, 12, 296. https://doi.org/10.3390/cryst12020296.

GROUP IV SEMICONDUCTOR MATERIALS USED FOR INFRARED DEVICES

GÖKÇE KARANFİL[1], MURAT ODUNCUOĞLU[1]

[1]Yildiz Technical University, Science and Arts Faculty, Physics Department, 34220, Istanbul, Turkiye

Abstract

Infrared photonic devices have found numerous applications for detecting longer wavelengths beyond the reach of the human eyes. Different material systems and devices for infrared (IR) technology have been studied for achieving high-performance devices. Semiconductor lasers emitting in infrared portion of the electromagnetic spectrum range have many important applications in high-impact fields of light–matter interaction in different industries. The different materials (Group IV, III-V, and II-VI) and structures of semiconductor-based IR photonic devices have been developed to achieve performance needs. Short-wave infrared (SWIR: 1.5-3 µm), mid-wave infrared (MWIR: 3-8 µm), and long-wave infrared (LWIR: 8-14 µm) bands can be potentially served by all-group IV (Si)GeSn devices. In this study, the material parameters of heterostructures at the desired Sn/Pb content and lattice strain of Si compatible direct bandgap semiconductors of group IV compounds were investigated for high performance. In Si-based technology, Ge-based alloys with low concentrations of Sn, and Pb are the most interesting since it is important to tune the conduction and valence bands without drastic modification of the lattice constant. The simulating and understanding the fundamental properties of materials have been used to create new opportunities for Si-compatible infrared photonic devices and applications. The alloying Ge with other elements from group IV (Ge/Sn/Pb) were potential to IR photonic technology.

Keywords: Germenium, GeSn, GePb, Si photonic, infrared, semiconductor

1. Introduction

The optoelectronics devices made from silicon (Si) and germanium (Ge) are known as silicon (Si) photonics or group IV photonics. Silicon (Si) photonics operating in the infrared regions are attracting great interest because of the intrinsic communications-based, medical and atmospheric sensing applications and on-chip CMOS optoelectronic systems with novel applications [1]. There are many potential applications for silicon photonics in the IR range. The direct and indirect band gaps of Si(GeSn/GePb) were calculated energy-band structure of α-Sn and from the known structures of Ge and Si. The material parametrers are calculated and compared the group IV-elements. The parameters of the binaries Sn1−xGex, Ge1−ySiy and Si1−ySny change linearly with x and y and estimated using Vegard's law by interpolation from the parameters of binaries (GeSn, GePb, SiGe, and SiSn). Ge and Si have common crystal structure, the diamond cubic lattice, and different lattice parameters as 5.43 A for Si and 5.65 A for Ge. The lattice parameter of Ge-Si alloys obeys Vegard's law. This article focuses on the parameters of silicon photonics and briefly summarize the possible applications. Germanium Lead (GePb). The periodic table group IV elements are given in figure below.

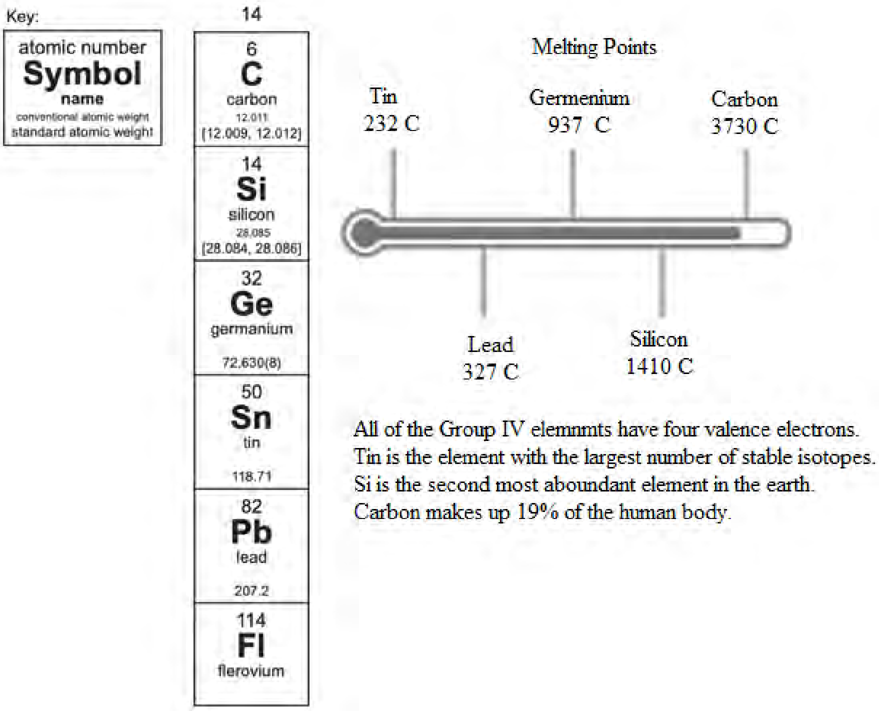

Figure 1. The Group 4 (Group 14) elements.

2. Materials and Methods

Using Vegard's law, band gaps and lattice constants for GeSn and GePb can be calculated. In order to be able to calculate bandgap and lattice constant of GeSn and GePb using Vegard's law we need the parameters of Ge, Sn, Pb [2-5]. The band gaps and lattice constants were calculated. Table 1 shows that the constants of Ge, Sn, and Pb.

Table 1. The band gap and lattice constant of Ge, Sn, and Pb.

Material	Bandgap (eV)	Lattice Constant (A)
Ge	0.67	5.568
Sn	-0.41	6.489
Pb		6.82

3. Results and Discussion

The band structures of GePb and GeSn were calculated to understand and develop Si-based GeSn and GePb devices for low-cost infrared imaging and high-speed detection. The calculated band gap energy and indicate that the Pb and Sn concentration increase, the bandgap energies were decreased. The lattice constant of GeSn and GePb alloys agree with experimental and other theoretical values. The calculated results of GePb and GeSn have the same trend as the concentrations increase, and the increase in GePb is much slower than GeSn.

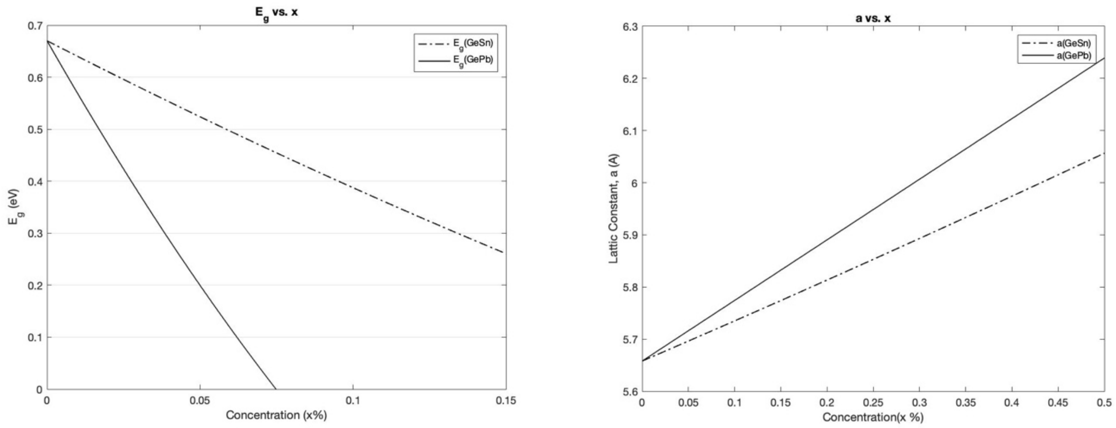

Figure 2. The calculated (a) band gap energy and (b) lattice constant for GeSn and GePb.

4. Conclusions

The group-IV semiconductors Si and Ge have limited active photonic device applications due to indirect band gap. The new technologies and fabrication techniques were open new application windows for group-IV materials. $Ge_{1-x}Sn_x$ and $Ge_{1-x}Pb_x$ alloys development have special interest to develop new integrated room temperature active and passive device applications such as waveguides, sources, detectors, amplifiers, resonators, switches, modulators, and optical parametric devices. These systems were good candidates for a new generation of infrared devices, with the critical advantage that they can be grown directly on Si.

References

1. Soref, R.J.N.p., Mid-infrared photonics in silicon and germanium. 2010. **4**(8): p. 495-497.
2. Huang, W., et al., Comparative studies of clustering effect, electronic and optical properties for GePb and GeSn alloys with low Pb and Sn concentration. Physica B: Condensed Matter, 2014. **443**: p. 43–48.
3. Broderick, C.A., E.J. O'Halloran, and E.P. O'Reilly. Comparative analysis of electronic structure evolution in Ge1-xSnx and Ge1−xPbx alloys. in 2019 International Conference on Numerical Simulation of Optoelectronic Devices (NUSOD). 2019.
4. Huang, W., et al., The band structure and optical gain of a new IV-group alloy GePb: A first-principles calculation. Journal of Alloys and Compounds, 2017. **701**: p. 816-821.
5. Alahmed, H., Growth of GeSn and GePb Alloy Films Using Thermal Evaporator, in Microelectronics-Photonics 2016, University of Arkansas.

EFFECT OF LASER WELDING POWER ON THE MICROSTRUCTURE AND NANOCREEP BEHAVIOR OF TITANIUM ALLOY WELD BEADS

MIRZA NADEEM BAIG [*1], FAHD NAWAZ KHAN [2], TAUHEED SHEHBAZ[2], HUZAIFA ASIF[2], MASSAB JUNAID[3]

[*1] Pakistan Welding institute, P.O. Box 1781, Islamabad 44000, PAKISTAN.
[2] Faculty of Materials and Chemical Engineering, Department of Materials Science, Ghulam Ishaq Khan Institute of Engineering Sciences and Technology, Topi 23640, PAKISTAN.
[3] Faculty of Mechanical Engineering, Ghulam Ishaq Khan Institute of Engineering Sciences and Technology, Topi 23640, PAKISTAN.

Abstract

Laser welding of an alpha-titanium alloy (Ti-5Al-2.5Sn) was performed in a Beed on Plate (BoP) configuration at five different welding currents (140 Amps, 150 Amps, 160 Amps, 170 Amps, 180 Amps) keeping all other laser welding parameters constant using a pulsed Nd-YAG laser welding system. A relationship between the microstructures evolved at different welding parameters and their nanocreep behavior was investigated. The microstructural evaluation reveled the formation of α′-martensite in the fusion zone (FZ) of all the beads. Owing to the presence of α′-martensite and acicular α, the microhardness and nanohardness increased by ~71% and ~58%, respectively from the base alloy (BA) to the FZ. Nanocreep analysis showed that the diffusional creep mechanism was observed in all the specimens except the bead performed at 140 Amps since the calculated stress exponent value was less than 2.

Keywords: Laser Welding, Ti-Alloy, Microstructures, Nano-Indentation, Creep Behavior.

1. Introduction

Titanium alloys possess excellent high strength-to-weight ratios, remarkable resistance to corrosion, wear and high temperature creep. These outstanding properties of Ti-alloys make them ideal for use in high perfromance structural applications. The industries extensively using Ti-alloys include but are not limited to aerospace, petrochemical, automotive, power generation, marine structures and biomedical [1-3].

Titanium alloys are mainly categorized as commercially pure (C_P) titanium, alpha (α) titanium alloys, alpha-beta (α-β) titanium alloys and beta (β) titanium alloys. α-Ti alloys or near α-Ti alloys show superior creep properties and strength at elevated temperatures than α-β and β-Ti alloys [4]. Amongst these alloys, those containing aluminum, tin and/or zirconium are preferred for high temperature applications [5]. When undergoes heating, Ti experiences a phase transformation from HCP (α-phase), to BCC (β-phase) and this transformation temperature is called β-transus temperature. β-transus temperature is different for different titanium alloys and depends on the alloying additions or impurities present in the alloy [6].

One of the promising benefits of the α-Ti alloys is their good weldability because they exhibit better weld properties than the base metal (BM) itself. This attribute of α-Ti alloys is due to the formation of α′-martensite and acicular α within the weld both having higher strength/hardness than the BM. However, in β-Ti alloys, because of the presence of β-stabilizers (like V, W, Mo etc.), the formation of α′-martensite is suppressed thus resulting in welds having lesser strengths than that of the BM [7].

Ti-5Al-2.5Sn is an α-Ti alloy which is mostly used in the aerospace applications requiring high temperature strength [5,8]. Furthermore, it has low cost alloying elements as compared to the wellknown Ti–6Al–4V, which is considered to be the 'workhorse' of aerospace industry [5]. This alloy has outstanding weldability and is frequently used in airframe applications. This is particularly suitable for the aerospace structural components near engines and leading edge of the wings and can withstand temperatures up to 480 ^{o}C [5]. Other characteristics of this alloy include good ductility and fracture toughness at extremely low temperatures (-252 ^{o}C) where the well-known Ti-6Al-4V alloy loses its ductility [9]. This alloy has also been extensively used in annealed conditions for cryogenic equipment such as liquid hydrogen tanks and high pressure vessels, operating at such low temperatures [10-12].

Conventional as well as solid state welding methods have been used in industry for joining Ti-alloys [13]. However, conventional arc welding processes like Tungsten Inert Gas Welding (TIG) are mostly used due to ease of automation and low cost operation [14]. Furthermore, laser beam welding (LBW) has also been established to be very effective due to its focused and dense heat source and low heat input. This high power density of LBW results in high penetration in a single pass and consequently in a reduced overall heat input. Therefore, the grains in the weld zone are relatively fine, hence narrower HAZ and reduced structural distortions are observed as compared to TIG welding process [15]. Nd-YAG Pulsed Laser Beam Welding (P-LBW) is an effective and controllable welding process due to the ease of obtaining desired welding mode by chossing an ideal combination of welding parameters (pulse energy, pulse duration, pulse frequency and welding speed). Furthermore, this pulsation leads to a cooling effect which is intermittent in nature and consequently results in grain refinement of produced welds [16,17]. Due to these characteristics, laser welding is by far the most researched and widely used joining technique for high-performance alloys.

Various researchers have investigated the microstructure, mechanical properties and creep behavior of different Ti-based alloys (e.g., Ti-6Al-4V, Ti-60, CpTi, Ti-5Al-2.5Sn) welded with either Electron Beam or Laser Beam Welding processes [18-21]. However, the nano-creep behaviour of Ti-5Al-2.5-Sn weld beads has not been investigated before. The present work is focused on the effect of laser welding power on the microstructure and nano-creep behaviour of Ti-5Al-2.5Sn alloy beads produced by P-LBW using Bead-on-Plate (BoP) configuration.

2. Materials and Methods

In the present study, a 1.6 mm thick sheet of fully annealed Ti-5Al-2.5Sn alloy was used as BM. The chemical composition of the Ti-5Al-2.5Sn sheet in wt.% is shown in Table 1. Five weld beads were produced using Nd-YAG Pulsed Laser Beam Welding (P-LBW) at five different welding currents/powers in a Bead-on-Plate (BoP) configuration without clamping the BM keeping all the other parameters constant as shown in Table 2. Argon gas was employed as a shielding gas to prevent the alloy surface from oxidation during welding. Wire electric discharge machining (EDM) was used to prepare the specimens for metallography, microhardness and nanoindentation testing in the transverse direction of the weld beads. For microstructural and nanoindentation creep analysis, all specimens were cold mounted and subsequently ground using silicon carbide (SiC) grit paper ranging from 220 to 4000 grit size. Finally, a micro cloth was used along with 0.25 µm diamond paste for polishing purposes. Kroll solution (6 % HNO_3 + 2 % HF + 92 % distilled water) was used for etching purposes. After etching, all the weld beads were examined under Olympus BH2-UMA optical microscope using a sensitive tint filter and polarized light. The morphology of the grains were analysed using Carl Zeiss Evo 15 scanning electron microscope (SEM). The microhardness profiles were measured using a micro-hardness tester (Tukon Model 300) at a load of 200 gf, with 10 s dwell time.

Table 1. Chemical composition of Ti-5Al-2.5Sn in wt.% as measured by EDS.

Ti	**Al**	**Sn**
92.09	5.37	2.54

Nanoindenter (iMicro, Nanomechanics, TN, USA) was used for nanoindentation at room temperature. The nano-hardness and elastic moduli of all the specimens were measured by using a three-sided Berkovich tip, at a constant load of 200 mN in load control mode during nanoindentation. For creep testing, the highest indentation load was 200 mN, with a strain rate of 0.1 s^{-1} and the indenter was held for 200 s to examine the variation of creep depth over time. Afterwards, the indenter was promptly discharged to 10 % of its maximum load and kept for 40 s to observe drift velocity. To conclude the test, the indenter was completely unloaded from the specimen surface. Oliver and Pharr method was used to measure the hardness (H) and modulus of elasticity (E) [22]. The hardness (H) value was calculated using Equation (1), where P is the applied load and A_c is the indentation projected area. The slope of the unloading curve P-h curve was used to estimate the modulus [22].

$$H=\frac{P}{Ac} \tag{1}$$

The creep behaviour in nanoindentation testing was studied using the data obtained by holding the indenter tip for 200 s. Poisl et al. [23] approach was used to calculate the indentation strain rate for the Berkovich indenter as represented by Equation (2):

$$\text{Creep Strain Rate } (\varepsilon^{'}) = \frac{\text{Rate of Indentation Depth}}{\text{Indentation Depth}} = \frac{h^{'}}{h} = \frac{1}{h} = \frac{dh}{dt} \tag{2}$$

After calculating the creep strain rate, the empirical creep model was used to fit the indentation depth rate data on the measured experimental creep rate and this model is expressed in Equation (3) [24]:

$$h = h_i + a(t-t_i)^{\frac{1}{2}} + b(t-t_i)^{\frac{1}{4}} + c(t-t_i)^{\frac{1}{8}} \tag{3}$$

Table 2. P-LBW welding parameters.

Specimen No.	**Power (W)**	**Welding Speed (mm/min)**	**Pulse Duration (ms)**	**Pulse Frequency (Hz)**	**Ar Gas Flow Rate (lit/min)**
S-1	140	300	8.0	10	10
S-2	150	300	8.0	10	10
S-3	160	300	8.0	10	10

S-4	170	300	8.0	10	10
S-5	180	300	8.0	10	10

where t is the creep time, h is the depth of indenter penetration, and a, b, c, h_i and t_i are the best-fitting parameters. Indentation creep stress was calculated by using Equation (4) in the holding stage as given in the literature [22].

$$\sigma = \left(\frac{H}{3}\right)\left(\frac{h_{max}}{h}\right) \tag{4}$$

Where h_{max}, h and σ are maximum loading depth, instantaneous depth and indentation creep stress, respectively.
The creep stress exponent in the steady-state creep stage was measured using the power-law, since it is only valid for the secondary/steady-state creep stage, as given by Equation (5):

$$\varepsilon' = k\sigma^n \tag{5}$$

3. Results and Discussion

3.1 Physical Appearance

A schematic illustration of a pulsed laser weld bead is shown in Figure 1. The weld bead consists of a sequence of spots or patches that overlap each other. P-LBW process is typically used to minimize the heat input during welding as compared to continuous wave (CW) LBW whose power output is constant over time. Consequently, this low heat input associated with P-LBW results in an over all reduced distortion of the weldment.

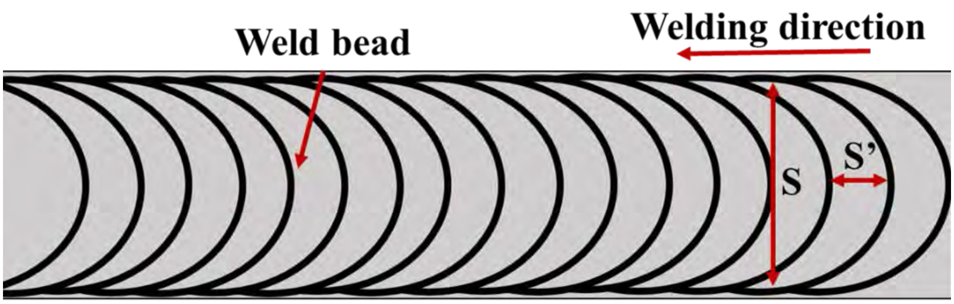

Figure 1. Schematic of P-LBW weld bead consisting of a sequence of overlapped spots

The % Overlap can be calculated by using the Equation (6), where S′ is the length of the weld spot that is not overlapped by the laser welding and S is the major diameter of the weld spot as presented in Figure 1.

$$\%\ \text{Overlap} = \frac{[S\text{-}S']}{S}\times 100 \tag{6}$$

Moreover, heat input (H) in the beads can be measured by using Equation (7) where P_{av} is average power and U is the welding speed.

$$H = \frac{P_{av}}{U} \tag{7}$$

In addition, peak power (P_{peak}) can be related to average power (P_{av}), pulse frequency (f), and pulse duration (t) by using Equation (8). Pulse frequency and pulse duration for all the experiments were kept constant at 10 Hz and 8 ms, respectively.

$$P_{peak} = \frac{P_{av}}{ft} \tag{8}$$

Figure 2 shows the physical appearance of all the beads produced using five different values of laser power. It can be observed from Figure 2 that all the weld beads were free from oxidation and contamination due to the proper use of shielding gas (argon with a purity of 99.999%).

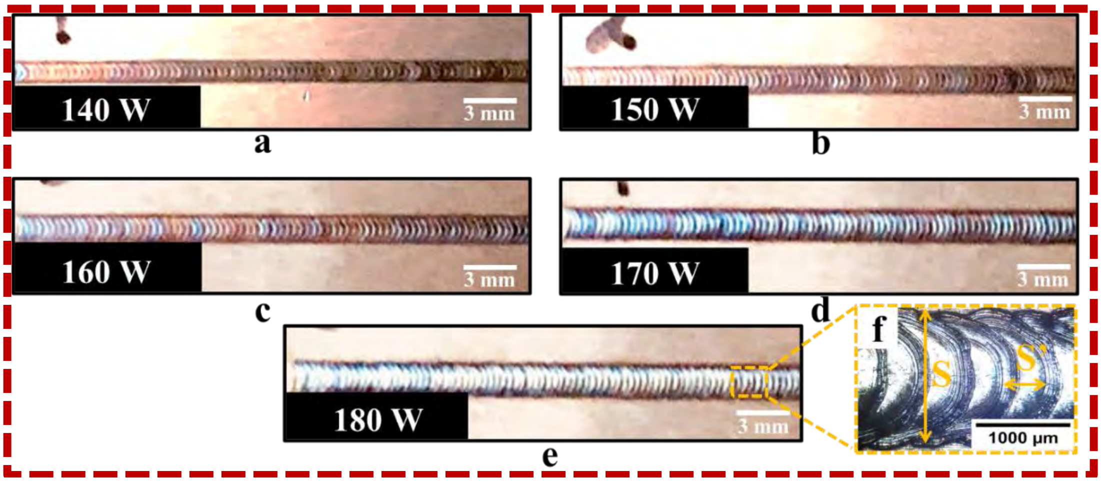

Figure 2. Physical appearance of all the weld beads.

In the present study, only the average power was varied from 140 W to 180 W while welding speed, pulse frequency and pulse width/duration were kept constant as presented in Table 1. Figure 2(f) shows the dimensions of the spots (S' and S**)** which were used to calculate the % overlap using Equation (6). It can be concluded that with the increase in average power from 140 W to 180 W, % overlap increased from ~ 54 % to ~72 % as shown in Table 3. This can be attributed to the increase in heat input and peak power associated with increase in average laser power during welding. Table 3 represents the calculated values of peak power, heat input and spot overlap using Equations (8), (7) and (6), respectively.

Table 3. P-LBW parameters used and calculated.

Sample No.	Average power (W)	Welding speed (mm/min)	Pulse duration (ms)	Pulse Frequency (Hz)	Peak power (kW)	Heat input (J/mm)	Spot overlap (%)
S-1	140	300	8.0	10	1.75	28	53.7
S-2	150	300	8.0	10	1.88	30	59.1
S-3	160	300	8.0	10	2.00	32	62.9
S-4	170	300	8.0	10	2.13	34	68.1
S-5	180	300	8.0	10	2.25	36	71.5

3.2 Microstructural Characterization

Figure 3 shows the microstructure of the Ti-5Al-2.5Sn base alloy (BA) where the equiaxed alpha grains are embedded in the prior beta matrix. ImageJ software was used to measure the average grain size of the base alloy, which was found to be ~10.2 µm, using the linear intercept method.

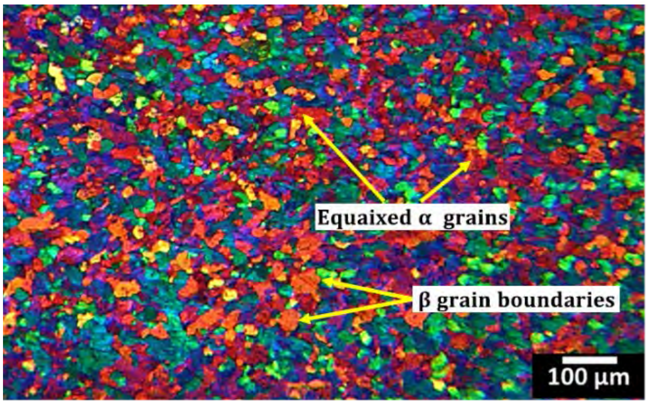

Figure 3: Microstructure of Ti-5Al-2.5Sn base alloy.

Figure 5 (a, c, e, g, i) shows the microstructural variations, weld bead width and penetration as a result of varying heat input per unit length and peak power. it can be observed that the penetration and the width of the weld pool increased from ~ 210 µm to ~ 884.4 µm and ~1257 µm to ~1561 µm, respectively as measured by using imageJ software. This increase in penetration and width of the beads is due to the increase in heat input and peak power since with the increase in power from 140 W to 180 W at constant welding speed and pulse width, the heat input per length and peak power increased from 28 J/mm to 36 J/mm and 1.75 kW to 2.25 kW, respectively as shown in Table 3. Moreover, it can also be observed that near the HAZ/F Z interface, the microstructure of the HAZ varies from equiaxed α grains near the base alloy to a more refined α and α′ martensite in all the beads as shown in Figure 4 (a, c, e, g, i) which is due to the high cooling rate at FZ/HAZ interface [25].

Figure 5 (b, d, f, h, j) presents the effect of average laser power on the evolution of average grain sizes and prior beta grains in the fusion zone (FZ) of all the beads. It has been reported that high cooling rates can be accomplished with relatively low average power and heat input in the welding process [26]. Moreover, it is well-known in the literature that higher is the cooling rate, the less will be the prior beta grain size [27]. In the present study, the bead obtained at 140 W has the minimum grain size (~ 25.6 µm) due to the least peak power and heat input per unit length of 1.75 kW and 28 J/mm, respectively. Owing to the maximum heat input (36 J/mm) and peak power (2.25 kW) achieved at 180 W power which caused a reduction in the cooling rate. Therefore, the largest grain size (~ 85.6 µm) was achieved in a bead obtained at 180 W average power. Furthermore, this increase in grain size is due to the increase in heat input per unit length which leads to a decrease in the cooling rate [26].

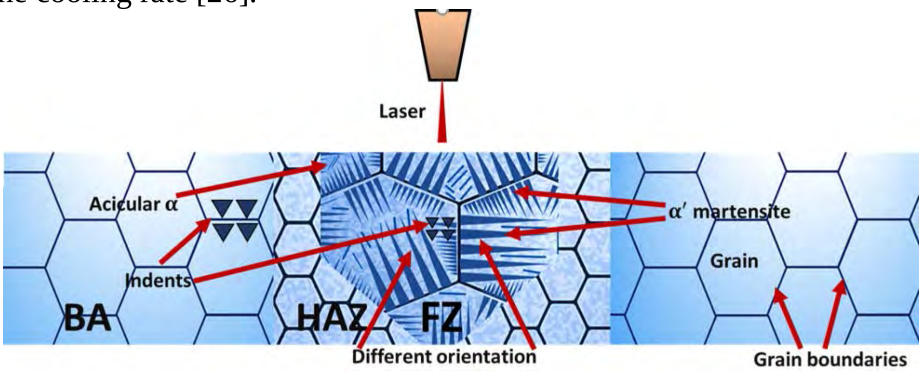

Figure 4. Schematic illustartion of microstructural details of a LBW α-Ti-alloy.

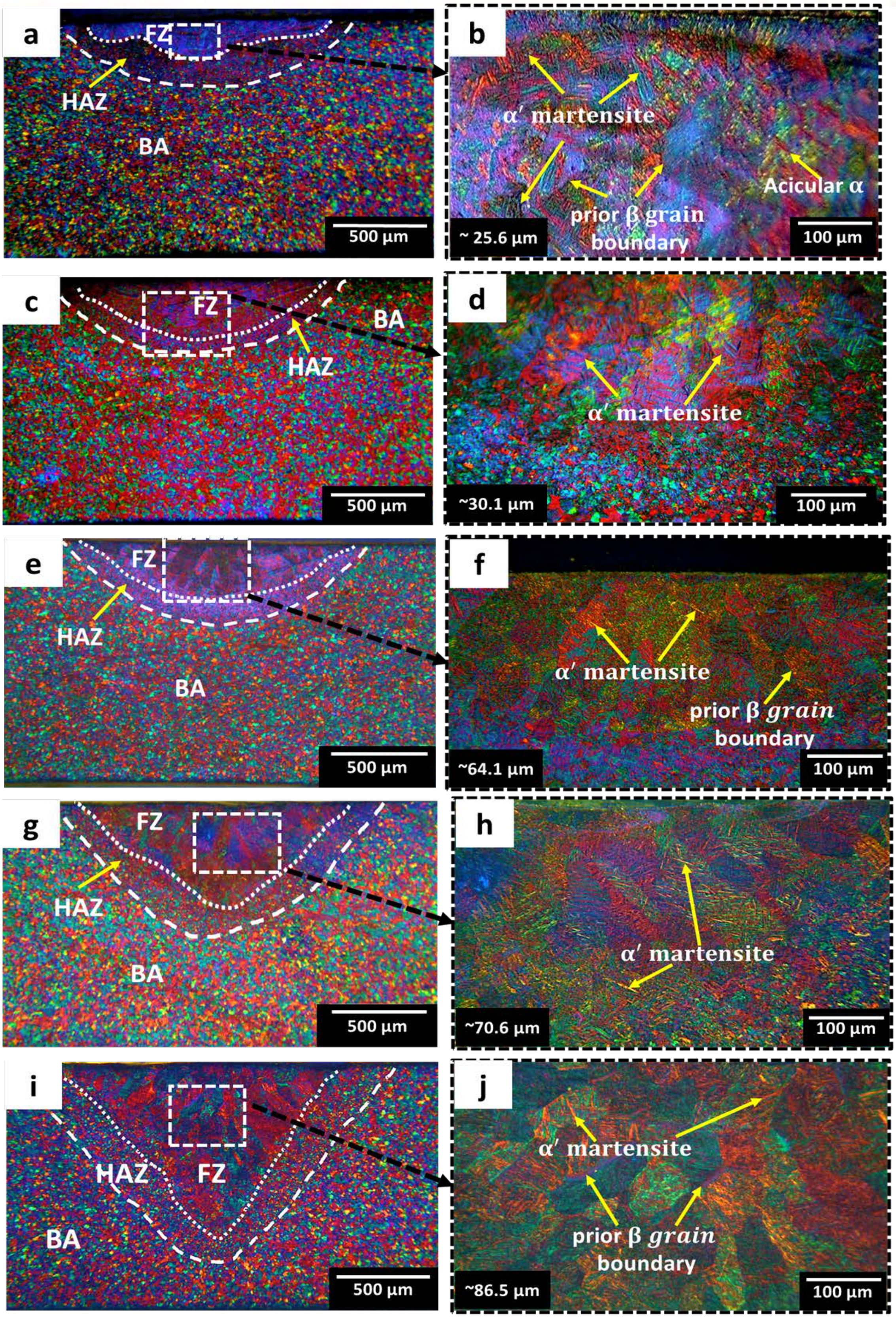

Figure 5. Optical microstructures and magnified images of all weld beads, (a & b) 140 W, (c & d) 150 W, (e & f) 160 W, (g & h) 170 W, (i & j) 180 W.

3.3 Micro-hardness Profiles

Microhardness profiles of all the weld beads can be seen in Figure 6. All the specimens exhibited a gradual increase in hardness from the BA to the FZ. . It has been reported that the increase in microhardness in FZ of laser-welded Ti-5Al-2.5Sn alloy can be due to the presence of acicular α and α′-martensite [28]. It has also been reported that the hardness of different phases in the titanium alloys follow the sequence: α′-martensite > accicular-α > β [29]. Furthermore, the formation of α′-martensite and acicular-α in the FZ depends on the cooling rate. It has been reported that titanium alloys need a cooling rate higher than 410°C/s to complete the α′-martensite transformation in the FZ [27]. The use of a dense laser heat source and the pulsed nature of the heating process are two main reasons which may help in achieving a cooling rate greater than 410^{o}C/s in P-LBW.

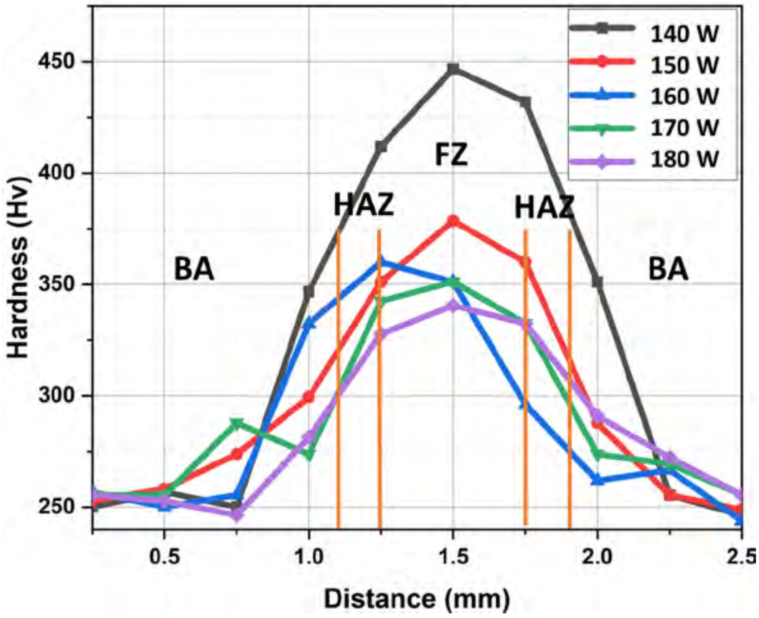

Figure 6. Microhardness profiles of all weld beads.

In the present study, owing to the high proportion of α′-martensite , the maximum microhardness (~ 432 Hv) was achieved in the weld bead obtained at 140 W. This higher proportion of α′-martensite can be confirmed by SEM results as can be seen in Figure 7 (b and c). Moreover, the average grain size (25.6 µm) contributed to the increase in microhardness. However, the minimum microhardness (~ 340 Hv) was achieved in the weld bead deposited at 180 W. It has been reported that with the increase in heat input, the morphology of α′-martensite changed to the accicular-α phase due to the slow cooling rate [30]. Thus, the bead obtained at 180 W had less proportion of α′-martensite and a high proportion of accicular-α. SEM analysis shown in Figure 7 (f and g) confirmed the low proportion of α′-martensite as compared to platelet-like accicular-α.

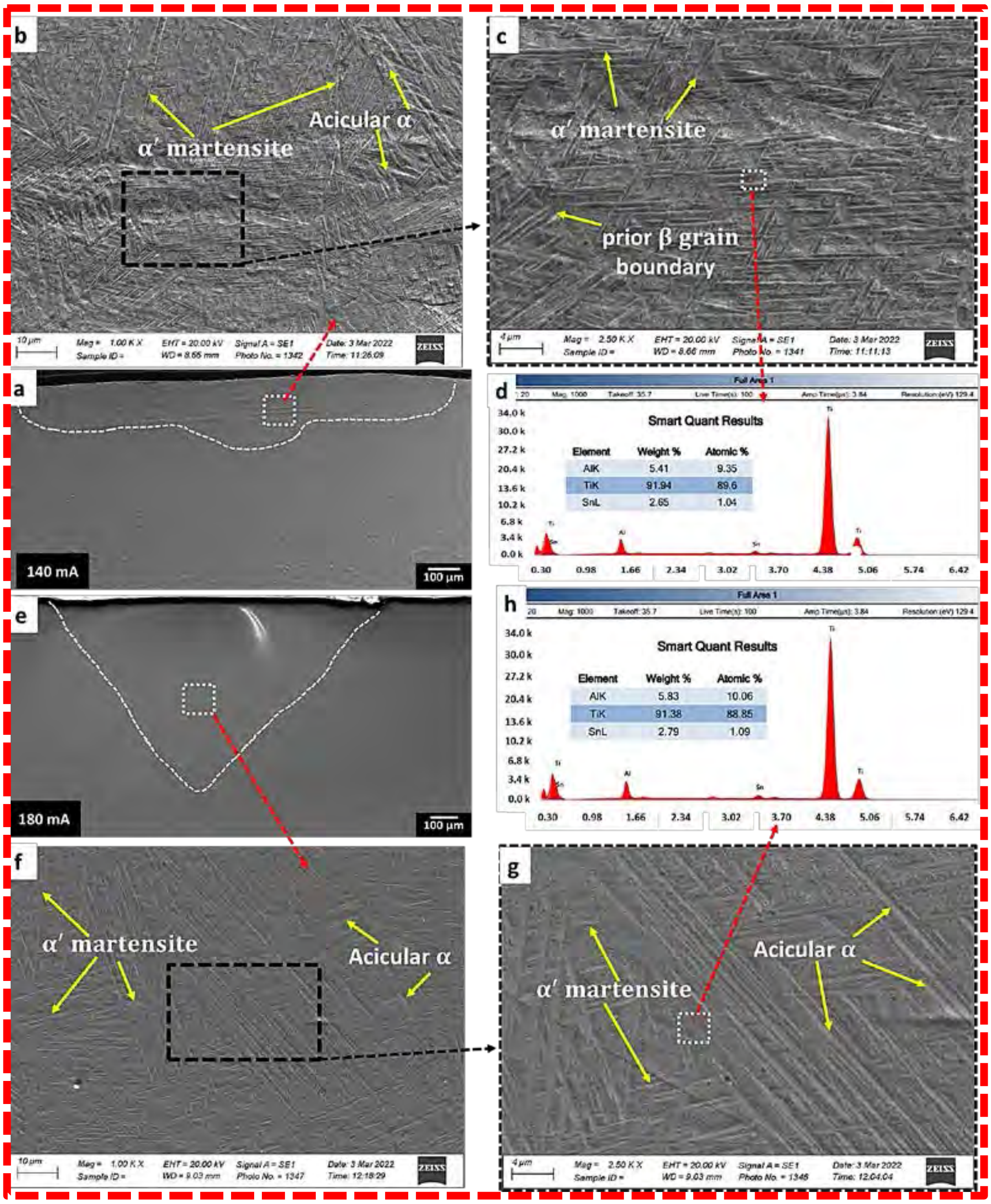

Figure 7. SEM images of specimen at 140 W (a, b, c and d) and 180 W (e, f, g and h). (d) EDS analysis of joint at 140 W and (h) 180 W.

3.4 Nanomechanical Characterization

Nanoindentation was performed to ascertain the nanomechanical properties at room temperature of all the beads. Figure 8(a) shows the micro and nano indents location in the fusion zone of a bead. Based on Oliver and Pharr method [22], P-h curves of all the beads along with the base alloy are presented in Figure 8(b). The elastic-plastic loading and pure elastic unloading deformations occurred as a result of indentation and the variation in the penetration depth can be observed which is associated with the microstructural/phase changes during the LBW process [31]. From Figure 8 (b), it can be concluded that BA has the highest penetration depth and elastic recovery which is

~1772 nm and 32.6%, respectively. Moreover, a pop-in was observed in BA which could be ascribed to the existence of grain boundaries in the indenter's stress field [32]. From the p-h curves, it can be seen that the bead obtained at 140 W has the least penetration depth which is approx. 1453 nm while the highest penetration among the beads was observed in the bead developed at 180 W, which is ~ 1632 nm. This variation in the penetration depth can be due to the indentation effect that occurred at the α′-martensite phase and grain boundaries.

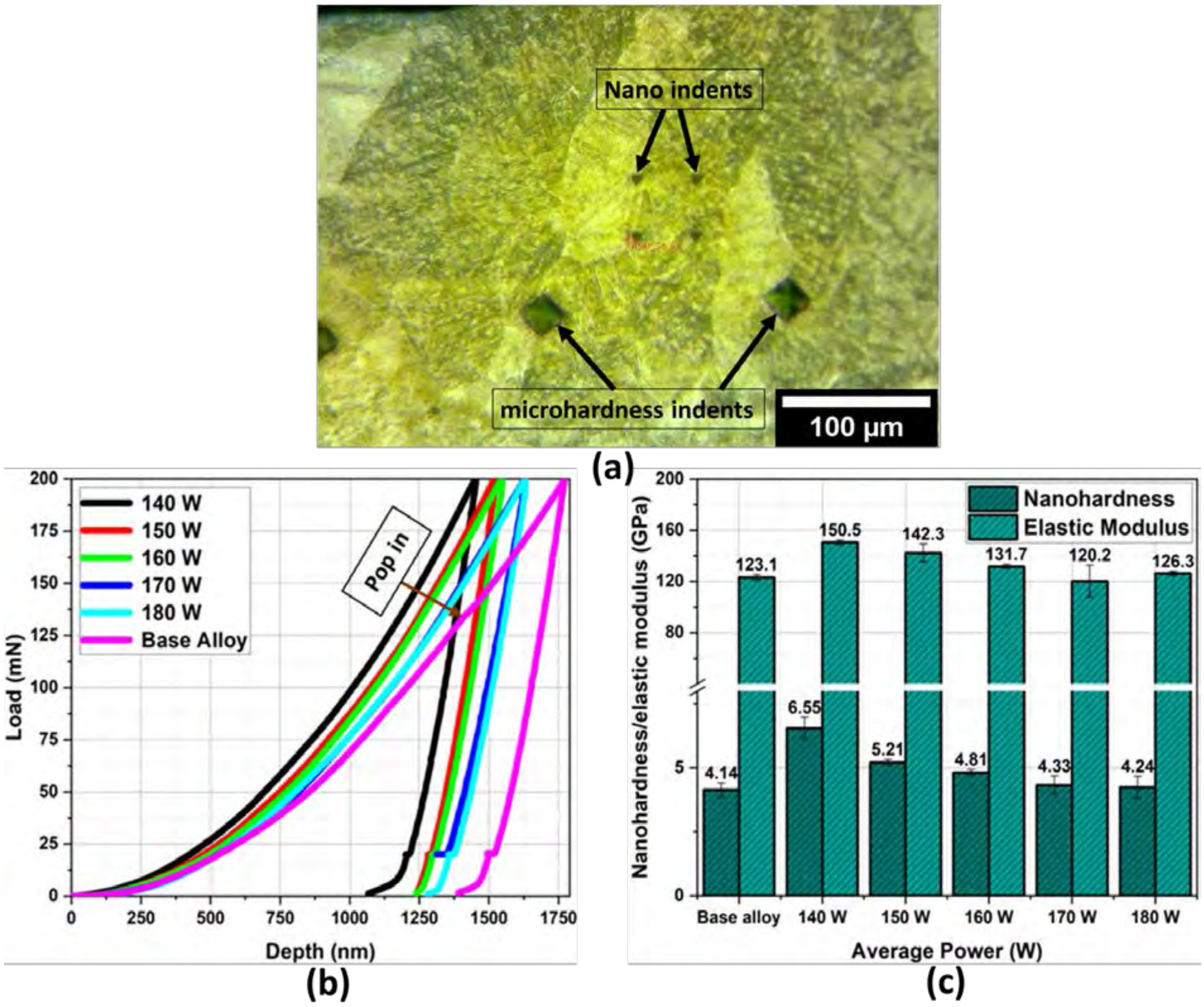

Figure 8. (a) Location of nano and micro indents in the FZ (b) P-h curves (c) nanohardness and elastic modulus of all the weld beads along with BA.

Figure 8(c) presents the nanohardness and elastic moduli of all the weld beads along with the BA. These properties have also been tabulated and are given in Table 4. It can be noticed that with the increase in the average power from 140 W to 180 W, the nanohardness and elastic moduli of all the beads decreased by 35.3 %. The highest hardness (~ 6.55 GPa) was obtained in the bead produced at 140 W which might be due to the least heat input (~ 28 J/mm) and a high cooling rate, resulting in the formation of a higher proportion of the α′-martensite phase. Moreover, the small grain size (~ 25.6 µm) also contributed to the increase in hardness.

Table 4. Nanohardness and elastic moduli variation with average laser power.

Sample No.	Nanohardness (GPa)	Elastic modulus (GPa)	Grain size (µm)
BA	4.14	123.1	~ 10.2
S-1	6.55 ± 0.42	150.5 ± 0.98	~ 25.6
S-2	5.21 ± 0.12	142.3 ± 6.93	~ 30.1
S-3	4.81 ± 0.12	131.7 ± 0.77	~ 64.1
S-4	4.33 ± 0.35	120.2 ± 12.48	~ 70.6
S-5	4.24 ± 0.43	126.3 ± 1.66	86.5

3.5 Nanoindentation Creep

Figure 9 illustrates the typical load-displacement (P-h) and displacement-time (h-t) curves for all the weld beads along with BA. It can be observed that all the P-h curves exhibit a similar trend under load, and indenter displacement rises from ~1560 nm in bead produced at 140 W to ~1940 nm in BA as shown in Figure 9(a).

The resultant creep displacement-time (h-t) as extracted from the constant load (200 mN) and time (200 sec) plateau of P-h curves for BA and all the beads are presented in Figure 9(b). P-h curves of BA and all the beads revealed significant load plateaus, in the holding regime. The maximum creep displacement was achieved from the bead produced at 170 W, while the minimum value was achieved at 140 W, at a constant load and time of 200 mN and 200 sec, respectively. In Figure 9(b) the increased creep deformation is indicated by wider load plateaus in the holding regime. The variation in the creep displacement can be attributed to the presence of different proportions of α′-martensite and accicular-α in the FZ zones of all the beads. In comparison with BA, the bead obtained at 140 W had the highest nanohardness (6.55 GPa) which can be due to the formation of a high proportion of α′-martensite and small grain size (~ 25.6 µm), resulting in the least creep displacement which is approx. 38% of the BA. However, the highest creep displacement was observed at 170 W bead which is ~ 111 % of the BA which can be due to the indentation which might have taken place at the grain boundaries. While owing to the large grain size (~ 86.5 µm) and a less proportion of α′-martensite , the bead produced at 180 W has the least nanohardness resulting in creep displacement which is almost equal to the BA as shown in Figure 9(b).

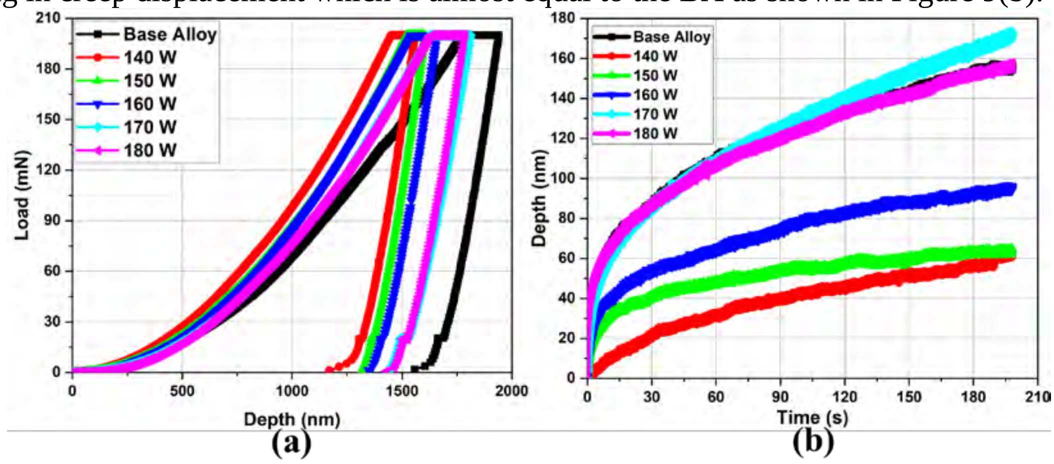

Figure 9. (a) Load-displacement (p-h) curves and (b) displacement-time (h-t) curves of all the weld beads along with BA.

Furthermore, it can also be observed from Figure 9(b) that at the initial stage (primary creep stage) for each weld bead, the indentation depth increased with the holding time, while in the second stage (steady/secondary creep), depth increased linearly with holding time. Unlike the conventional creep, the tertiary creep stage does not occur in indentation creep since the hardness test is a compression test, and the specimen does not fracture, making it impossible to measure a third stage of the curve.

The creep strain rates of all the weld beads were measured by using Eq. (2) and are presented in Figure 10. The creep strain rates were determined after the maximum load, thus the steep decrease in creep strain rates is observed in all the beads. This decrease in creep strain rates might be attributed to the strain hardening produced by plastic deformation. A consistent slope was seen after this region, indicating secondary or steady-state creep, as the creep strain rate steadily declined. Both the strain hardening and recovery took place at the same time and rate within the Ti5-Al2.5-Sn alloy, resulting in steady/secondary state creep.

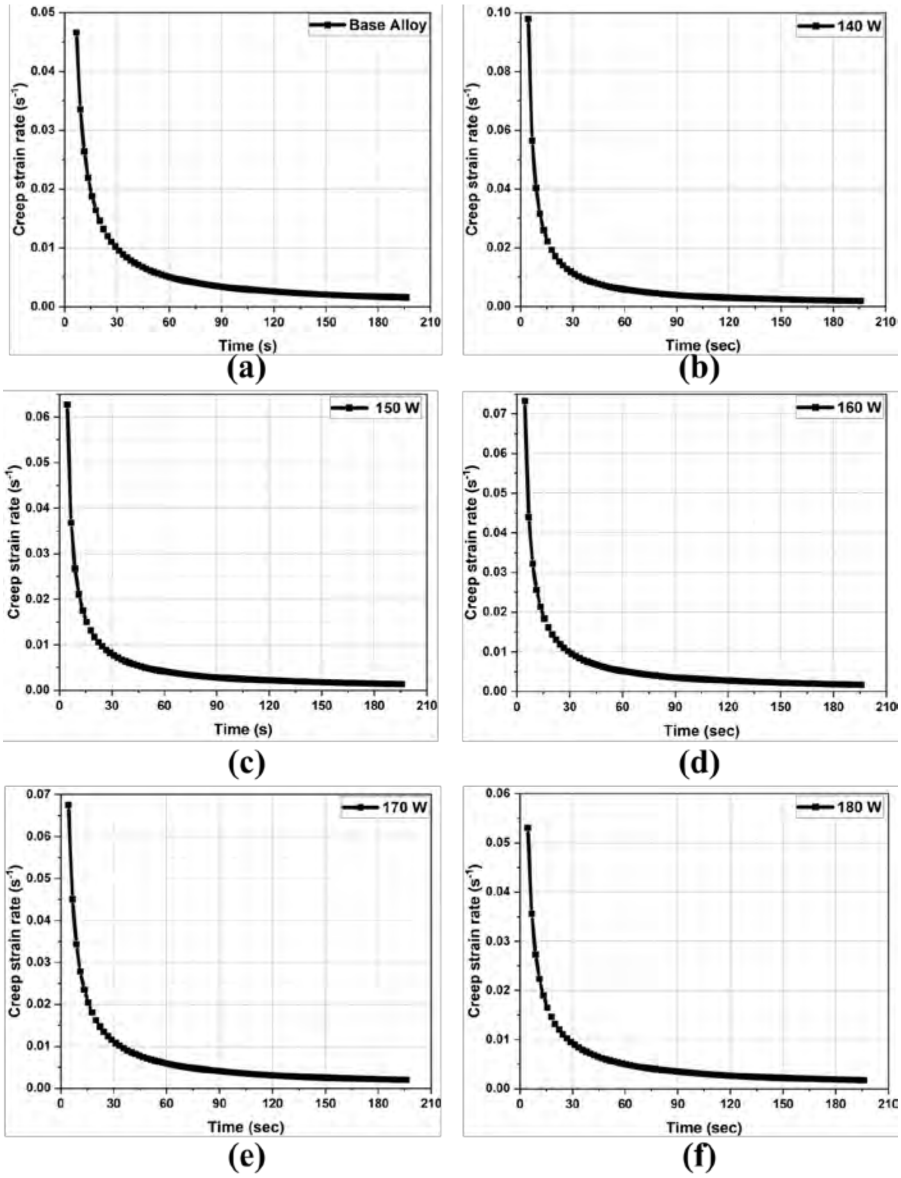

Figure 10. Creep strain rate and time plots of BA and all weld beads.

Figure 11(a) illustrates ln(creep strain rate)-ln(stress) indentation tests for BA and all the weld beads. In linear fitting, the slope of the linear function is equal to the creep stress exponent. The creep stress exponent values indicate the creep behaviour of a material in terms of creep resistance and active creep phenomena as shown in Table 5. Furthermore, creep resistance varies with the variation in creep stress exponent. Higher values of the creep stress exponent are indicative of better creep resistance [50].

Table 5. Creep mechanism related to the creep stress exponent.

Sr. #	Creep mechanism	Creep stress exponent
01	Diffusional creep	Greater than 1
02	Grain boundary sliding creep	2 – 2.9
03	Dislocation climb creep	3 – 5

The creep stress exponents of BA and all the weld beads were measured using the same methodology as given in [33]. The measured stress components of all the weld beads, except that deposited at 140 W, were less than 2 as shown in Figure 11(b).This was owing to the activation of the diffusional creep mechanism where the material deforms plastically over time [33]. While the specimen at 140 W had the creep stress exponent greater than 2 (2.06), suggesting grain boundary sliding as the creep deformation mechanism [33]. However, better mechanical properties were obtained at 180 W bead, since the nanohardness and elastic moduli were almost similar as compared to the BA as shown in Table 4.

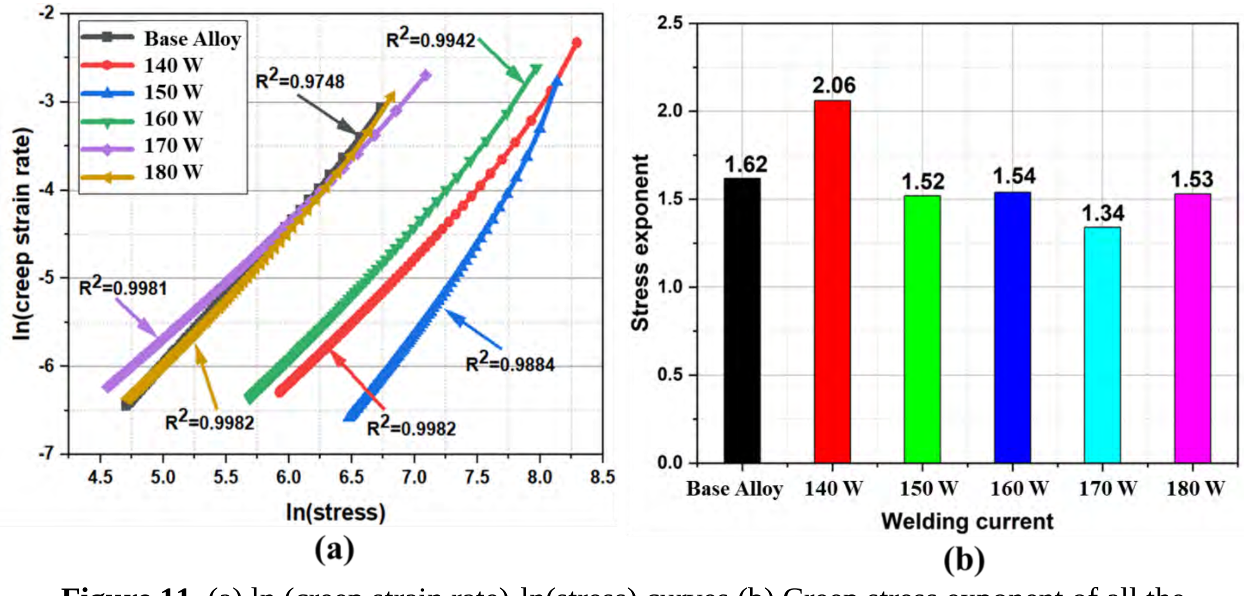

Figure 11. (a) ln (creep strain rate)-ln(stress) curves (b) Creep stress exponent of all the specimens.

4. Conclusions

The following conclusions were drawn, based on the experimentation:

- The microstructure analysis indicated that with the increase in average power from 140 W to 180 W, width and penetration increased by ~ 19 % and ~ 237 %, respectively. Microhardness and nano-hardness increased by ~76% and ~58% from the BA to the FZ at 140 W, respectively. This is due to the high cooling rate which results in the formation of α′-martensite. Moreover, owing to low heat input and high cooling rate, the high proportion of α′-martensite, maximum nano and microhardness was achieved in the bead obtained at 140 W.

- Owing to the slow cooling rate at 180 W, less proportion of α′-martensite and a high proportion of acicular-α phases were formed. Thus, the bead obtained at 180 W exhibited superior properties (comparable to BA) in terms of nanohardness, elastic moduli and creep behaviour.
- Base alloy and other beads on the plate, except 140 W show the diffusional creep mechanism since the calculated creep stress exponent was less than 2. However, the calculated creep stress component in the 140 W specimen was higher than 2, indicative of grain boundary sliding as the creep mechanism.

References:

1. Luo, S. D. and Qian, M., Microwave processing of titanium and titanium alloys for structural, biomedical and shape memory applications: Current status and challenges, Materials and Manufacturing Processes, **2016**, 33(1):35-49.
2. Khorev, A.I., Development of titanium sheet alloys for welded structures working at high temperatures, Welding International, **2016**, 30(5):389-394.
3. Revathi, A., Magesh, S., Balla, V.K., Das, M., and Manivasagam, G., Current advances in enhancement of wear and corrosion resistance of titanium alloys-a review, Materials Technology, Advanced Performance Materials, **2016**, 31(12):696-704.
4. Calderon-Moreno, J.M., Vasilescu ,C., Drob, S.I., Ivanescu, S., Osiceanu, P., Drob, P., et al., Microstructural and mechanical properties, surface and electrochemical characterisation of a new Ti-Zr-Nb alloy for implant applications, Journal of Alloys and Compounds, **2014**, 612:398-410.
5. Boyer, R.R. An overview on the use of titanium in the aerospace industry, Materials Science and Engineering: A, **1996**, 213(1-2):103-114.
6. Muhammad, S., Junaid, M., Khan, F.N. , Taimoor, A.A., and Baig, M.N., A comparative study of electrochemical corrosion behavior in Laser and TIG welded Ti–5Al–2.5Sn alloy, Journal of Materials Research and Technology, **2019**, 8(1):87-98.
7. Chamanfar, A., Pasang, T., Ventura, A., and Misiolek, W.Z., Mechanical properties and microstructure of laser welded Ti-6Al-2Sn-4Zr-2Mo (Ti6242) titanium alloy, Materials Science and Engineering: A, **2016**, 663:213-224.
8. Hosseini, S., Mirdamadi, S., and Nemati, A., Porous Ti6Al4V scaffolds for dental implants: microstructure, mechanical, and corrosion behavior, Proceeding of the Institution of Mechanical Engineers, Part L: Journal of Materials: Design and Applications, **2015**:1-7.
9. Billinghurst Jr., E.E., Tensile properties of cast titanium alloys: Titanium-6Al-4V ELI and Titanium-5Al-2.5Sn ELI, NASA Technical Paper, **1992**.
10. Tan, M.J., Chen, G.W., and Thiruvarudchelvan S., High temperature deformation in Ti-5Al-2.5Sn alloy, Journal of Materials Processing Technology, **2007**, 192-193:434-438.
11. Sun, Q.Y., and Gu, H.C., Tensile and low-cycle fatigue behavior of commercially pure titanium and Ti-5Al-2.5Sn alloy at 293 and 77 K, Materials Science and Engineering: A, **2001**, 316 (1-2):80-86.
12. Sun, Q.Y., Song, S.J., Zhu, R.H., and Gu, H.C., Toughening of titanium alloys by twinning and martensite transformation, Journal of Materials Science, **2002**, 37:2543-2547.

13. Lu, W., Shi, Y., Lei Y, and Li, X., Effect of electron beam welding on the microstructures and mechanical properties of thick TC4-DT alloy. Materials & Design, **2012**, 34:509-515.
14. Short, A.B., Gas tungsten arc welding of α+β titanium alloys: a review. Materials Science and Technology, **2009**, 25(3):309-324.
15. Gao, X.L., Zhang, L.J., Liu, J., and Zhang, J.X., A comparative study of pulsed Nd:YAG laser welding and TIG welding of thin Ti6Al4V titanium alloy plate, Materials Science and Engineering: A, **2013**, 559:14-21.
16. Costa, A., Miranda, R., Quintino, L., and Yapp, D., Analysis of beam material interaction in welding of titanium with fiber lasers, Materials and Manufacturing Processes, **2007**, 22 (7-8):798-803
17. Ghaini, F.M., Hamedi, M.J., Torkamany, M.J., and Sabbaghzadeh, J., Weld metal microstructural characteristics in pulsed Nd: YAG laser welding, Scripta Materialia, **2007**, 56 (11):955-958.
18. Chen, Z., Li, J., Liu, J., Wang, Q., Liu, J., and Yang, R., Creep behavior of fusion zone and base metal of the electron beam weldments of a near-alpha titanium alloy, Journal of Materials Science and Technology, **2010**, 26(6):564-571.
19. Peng, H., Fang, W., Dong, C., Yi, Y., Wei, X., Luo, B., and Huang, X., Nano-mechanical properties and creep behavior of Ti6Al4V fabricated by powder bed fusion electron beam additive manufacturing, MDPI Materials, **2021**, 14(11), 3004.
20. Junaid, M., Khan, F. N., Rahman, K., and Baig, M. N., Effect of laser welding process on the microstructure, mechanical properties and residual stresses in Ti-5Al-2.5Sn alloy, Optics and Laser Technology, **2017,** 97:405-419.
21. Luo, L., Zhao, X., Liu, X., and Yang, X., Creep behavior of UFG CP Ti at room temperature, IOP Conference Series: Materials Science and Engineering, **2017**, 250, 012062.
22. Oliver, W.C., and Pharr, G. M., An improved technique for determining hardness and elastic modulus using load and displacement sensing indentation experiments, Journal of Materials Research, **1992**, 7:1564-1583.
23. Poisl, W.H., Oliver, W.C., and Fabes, B.D., The relationship between indentation and uniaxial creep in amorphous selenium, Journal of Materials Research, **1995**, 10:2024-2032.
24. Liu, X., Zhang, Q., Zhao, X., Yang, X., and Luo, L., Ambient-temperature nanoindentation creep in ultrafine-grained titanium processed by ECAP, Materials Science and Engineering: A, **2016**, 676:73-79.
25. Squillace, A., Prisco, U., Ciliberto, S., and Astarita, A., Effect of welding parameters on morphology and mechanical properties of Ti-6Al-4V laser beam welded butt joints, Journal of Materials Processing Technology, **2012**, 212(2):427-436.
26. Akman, E., Demir, A., Canel, T., and Sinmazçelik, T., Laser welding of Ti6Al4V titanium alloys," Journal of Materials Processing Technology, **2009**, 209(8):3705-3713.
27. Ahmed, T., and Rack, H. J., Phase transformations during cooling in α + β titanium alloys, Materials Science and Engineering A, **1998**, 243(1-2):206-211.
28. Junaid, M. Khan, F.N., Baksh, N., Baig, M.N., and Rahman, K., Study of microstructure, mechanical properties and residual stresses in full penetration electron beam welded Ti-5Al-2.5Sn alloy sheet, Materials and Design, **2018**,139:198-211.
29. Zeng, L., and Bieler, T.R., Effects of working, heat treatment, and aging on microstructural evolution and crystallographic texture of α, α′, α″ and β phases in Ti-6Al-4V wire, Materials Science and Engineering: A, **2005**, 392:403-414.
30. Su, X., Tao, W., Chen, Y., and Fu, J., Microstructure and tensile property of the joint of Laser-MIG hybrid welded thick-section TC4 alloy, **2018**, Metals (MDPI), 8(12).

31. Hainsworth, S.V., Chandler, H.W., and Page, T.F., Analysis of nanoindentation load-displacement loading curves, Journal of Materials Research, **1996,** 11(8):1987-1995.
32. Pöhl, F., Pop-in behavior and elastic-to-plastic transition of polycrystalline pure iron during sharp nanoindentation, Scientific Reports, **2019**, 9(1).
33. Shehbaz, T., Khan, F.N., Junaid, M., and Haider, J., Investigating nanoindentation creep behavior of pulsed-tig welded inconel 718 and commercially pure titanium using a vanadium interlayer, Metals (MDPI), **2021**, 11(9).

THE ANALYSIS AND CHALLENGES OF 2D BORON: BOROPHENE

MURAT ODUNCUOĞLU[1]
[1]Yildiz Technical University, Science and Arts Faculty, Physics Department, 34220, Istanbul, Turkiye

Abstract

Recent developments on the single layer of boron atoms that form various crystalline structures, borophene, provides a remarkably unique anisotropic flexibility and metallicity. Borophene has been realised on substrates and is creating a new class of synthetic, thin covalently bonded boron sheet materials. Borophene is a novel quantum material that has many lattice configurations and each with different characteristics allowing for flexibility. This combines unique mechanical properties and structural tunability with anisotropic metallicity. Borophene can serve as a prototype for ongoing efforts to discover and exploit synthetic 2D materials. In this work, we explored the recent progress and future opportunities for borophene and investigated the challenges of two-dimensional novel quantum material. Research on borophene with electronic, mechanical, and photonic properties as an encouraging platform for discovery of several materials opens the door for innovative experiments and revolutionize the sensors, batteries, several flexible and transparent electronics, and environmental and energy production applications.

Keywords: Borophene, material science, 2D, boron

1. Introduction

The growths of borophene material have attracted interests in material science and related industrial applications. The molecular, bulk, or low dimensional structures of boron remains one of the less studied elements. The boron in different dimensions: 3D (bulk), 2D (borophene), 1D (nanotube), and 0D (molecule). Boron forms a wide variety of chemical bonds with each other, making crystalline allotropes for the development of photonics. Boron is the fifth chemical element of the periodic table, which has valence orbitals like that of carbon and is the only group 13 (i.e., 3A) element with semiconducting properties [1]. The next-generation two-dimensional (2D) layered materials were investigated to provide a novel, scientifically interesting wide range of applications. A different 2D materials have been theoretically predicted and synthesized and new era have brought towards the next generation devices [2]. The material field has made great improvements in 2D materials, due to its ability to form spheres, tubes, sheets, and a variety of unusual shapes. The 2D borons - monoatomic (monatomic) sheet of boron - known as borophenes were investigated to tune the material's properties such as strain and doping. The borophene was first synthesized on Ag substrates in late 2015 with different properties and striped pattern compering to other 2D materials [3-5]. The properties (electronic, optical, and mechanical) of 2D materials are investigated for nanoscale devices, energy storage, sensing, electrodes for rechargeable batteries and photo-catalysis applications for hydrogen storage applications. The properties (stronger, flexible, conductive (electrical and heat), and superconductive) depending on the material's orientation and vacancies have led to superior electronic, mechanical, and magnetic applications. The first promising materials for electronic devices in the form of single atomic layers

represented by graphene (carbon based) and the other is borophene (boron-based) with their physical and chemical properties [6].
In this study, we were focus on the borophene, and briefly summarize the possible applications in materials.

2. Materials and Methods

The low-dimensional structure of boron, borophene, synthesized in different structures with different properties. In Table 1, some borophene studies both theoretically predicted and synthetised experimentally are collected for potential applications as

Table 1. The studies based on borophene

Author	Study	Reference
Zhou et al.	Dirac cone structure	[7]
Mannix et al.	Anisotropic and has high conductivity property	[4]
Xu et al.	Field emission and fast response properties	[8]
Penev et al. and Zhao et al.	Superconductor property	[9], [10]
Mortazavi et al.	Borophene in lithium storage by molecular dynamics method	[11]
Zhang et al.	Infrared plasma sensor property	[12]
Feng et al.	Dirac fermions with quantum effects	[13]
Wang et al.	Hydrogen storage performance	[14]
Chen et al.	P doped borophene	[15]
Tu et al.	Li doped borophene	[16]
Thanh et al.	Charge doping effects	[17]
Zhang et al.	Electronic and magnetic properties of borophene	[18]

The properties of borophene have expanded with its rich structure. P_{mmn} borophene, α borophene and β_{12} borophene were predicted for different properties with different characteristics such as Dirac cones, isotropic, anisotropic, respectively. The low dimensional boron have the larger surface area, linear band structures, enhanced quantum confinement effect of monoatomic layered 2D nanosheets [19]. Different configurations of reconstructed, buckled, icosahedral and few low-symmetry hybrid borophene structures were studied by researchers.

The borophene research began through theoretical simulations [20] for various new materials and a best example for the material genome project [21]. This method can improve the synthesis efficiency, minimize the cost, and increase the research material design production rate.

3. Results and Discussion

Experimental studies were very limited but the examination of different structure of boron was started using new computer simulations. The scientific research groups have proved the novel structures of boron and the developed mechanical properties. The borophene has a potential material for applications in various fields. The metallic features are useful for the sensing of various small molecules and gases. Researchers were started to show sensor properties of borophene for detection of several molecules and their atoms. The features of borophene with its capabilities play significant role in novel photonic and optoelectronic devices.

4. Conclusions

The single-atom layer of boron, stronger and more flexible than graphene, could change the industries with sensors, batteries and applications in material sciences and chemistry. The research on borophene has grown fast in the fields of physics, chemistry, material science, and nanotechnology. Finally, the challenges and outlooks in different field are presented with its current development.

References

[1]. Forte, G., et al., Ab initio prediction of boron compounds arising from borozene: structural and electronic properties. 2010. 5(1): p. 158-163.
[2]. Kambe, T., et al., Liquid crystalline 2D borophene oxide for inorganic optical devices. Nature Communications, 2022. 13(1): p. 1037.
[3]. Zhang, Z., et al., Substrate-Induced Nanoscale Undulations of Borophene on Silver. Nano Letters, 2016. 16(10): p. 6622-6627.
[4]. Mannix, A.J., Synthesis of borophenes: anisotropic, two-dimensional boron polymorphs. Science, 2015. 350.
[5]. Liu, Y., E.S. Penev, and B.I. Yakobson, Probing the synthesis of two-dimensional boron by first-principles computations. Angew. Chem. Int. Ed., 2013. 52.
[6]. Brotchie, A., Borophene: Served on a silver platter. Nature Reviews Materials, 2016. 1(11): p. 16083.
[7]. Zhou, X.-F., et al., Semimetallic two-dimensional boron allotrope with massless Dirac fermions. 2014. 112(8): p. 085502.
[8]. Xu, J., et al., Ultrathin Single-Crystalline Boron Nanosheets for Enhanced Electro-Optical Performances. 2015. 2(6): p. 1500023.
[9]. Penev, E.S., A. Kutana, and B.I.J.N.l. Yakobson, Can two-dimensional boron superconduct? 2016. 16(4): p. 2522-2526.
[10]. Zhao, Y., S. Zeng, and J.J.P.R.B. Ni, Superconductivity in two-dimensional boron allotropes. 2016. 93(1): p. 014502.
[11]. Mortazavi, B., et al., Borophene as an anode material for Ca, Mg, Na or Li ion storage: a first-principle study. 2016. 329: p. 456-461.
[12]. Zhang, J., et al., Infrared plasmonic sensing with anisotropic two-dimensional material borophene. 2021. 11(5): p. 1165.
[13]. Feng, B., et al., Dirac fermions in borophene. 2017. 118(9): p. 096401.
[14]. Wang, J., Y. Du, and L.J.I.J.o.H.E. Sun, Ca-decorated novel boron sheet: A potential hydrogen storage medium. 2016. 41(10): p. 5276-5283.
[15]. Chen, H., et al., First principles study of P-doped borophene as anode materials for lithium ion batteries. 2018. 427: p. 198-205.
[16]. Tu, X., et al., First-principles study of pristine and Li-doped borophene as a candidate to detect and scavenge SO2 gas. 2021. 32(32): p. 325502.
[17]. Thanh, V.V., et al., Charge-induced high-performance actuation of borophene. 2020. 54(10): p. 105504.
[18]. Zhang, X., et al., Modulating the electronic and magnetic properties of bilayer borophene via transition metal atoms intercalation: from metal to half metal and semiconductor. 2018. 29(30): p. 305706.

[19]. Tang, H. and S.J.P.R.B. Ismail-Beigi, First-principles study of boron sheets and nanotubes. 2010. 82(11): p. 115412.
[20]. Boustani, I., Z. Zhu, and D.J.P.R.B. Tománek, Search for the largest two-dimensional aggregates of boron: An ab initio study. 2011. 83(19): p. 193405.
[21]. Ou, M., et al., The emergence and evolution of borophene. 2021. 8(12): p. 2001801.

QUANTUM COMPUTING AND SIMULATION OF MATERIALS

BILAL EROL[1], MURAT ODUNCUOĞLU[2]
[1]Yildiz Technical University, Department of Aviation Electronics, 34220, Istanbul, Turkiye
[2]Yildiz Technical University, Science and Arts Faculty, Physics Department, 34220, Istanbul, Turkiye

Abstract

The multidisciplinary field of quantum computing and related next-generation technology has the potential to advance industry applications and our daily life. Recent advances and opportunities in material sciences with quantum computing include novel issues in synthesis, fabrication, material characterization, and simulation. Quantum computing were using the quantum bits and properties of subatomic particles. The superposition, entanglement, and interference to extend the computational capabilities are the examples of these quantum properties. In this study, we were investigated and highlighted the potential impact of quantum computations on certain roles of material science for the future of a growing industrial sector. The application of quantum computers provided exponential performance benefits in processing and simulating the quantum systems within many ranges with ease. The simulations of material systems with the state of a many particle molecules at the thermodynamic limit involving lots of degrees of freedom. The properties and simulations of these materials were described by using quantum mechanics that are sped up by a quantum computer. Some quantum problems in material sciences were solved by using a wide range of quantum algorithms. There are many different ideas and components to test a slew of proposals in real quantum computational platforms for solving the open problems. The quantum hardware and computational methods have been actively researching and is set to continue to develop in the future, and the new computational subjects are used to the study of material sciences.

Keyword: Quantum computing, material science, qubit

1. Introduction

A computer is described as a universal computational device to process information by executing algorithms and simulate physical systems. Quantum computers are quantum systems which can be initialized, appropriately controlled, and measured, in order to perform a computational task [1]. The quantum computing is still novel subject. Recent development of quantum computers, introduced by Richard Feynman in the 80's [2-4], open door for practical application of quantum algorithms. The quantum computers were used a fundamentally different instructions set comparing to the classical computers [5]. The quantum computer could theoretically store and process a lot more information than a conventional computer. The quantum-mechanical phenomena like superposition, nonlocality, entanglement, interference, and other quantum mechanical effects are used in quantum computers to perform computation solving problems. The quantum systems were simulated on classical computers and some complex approximation methods have been developed. They could run different algorithms that use quantum effects. The quantum computers promise to competently produce accurate results for many important problems in material science by manipulating the quantum states. The initial algorithms and computers were changing the computational models. Quantum computers perform high speed computations for solving problems in different fields to develop new applications in near future [3, 6, 7]. The quantum computing and used quantum algorithms and applications in different areas for improving computational tasks were provided the exponential performance benefits in processing, the speed up the solution of optimization problems, energy distribution and optimization, quantum cryptography, cybersecurity, drug discovery and simulation of elements in real-life [8-10]. The synthesis, characterization, and modelling of materials have many exciting improvements in recent years and will become increasingly significant. The reasons for this increase directly related to the funding for quantum technologies that is increasing rapidly all over the world from both government and corporate sources. The quantum computing methods were used in investigation of nanoparticles, material/molecule innovation, design of new material/molecule, drug discovery, pattern recognition, and classification. The relevant use in different disciplines were opening new windows, and results discoveries. The potential of quantum computing presents a considerable challenge in the performance and motivated the researchers for research and development in different industries.

The quantum computing was changed the way and algorithms, the implementation and controlling the applications in comparison to the traditional programming methods and models. The scientists require a different technique to predict and solve today's complex problems. These outcomes are based on different frameworks, algorithms, computational platforms, and new tools. The working quantum computers with several tens of qubits are implemented the developed quantum algorithms [11-13]. Quantum computers consist of qubits (quantum bits) and related quantum properties of subatomic particles. These devices have some restrictions such as the number of logic gate operations and the number of qubits [14]. The main part of quantum computer is the set of quantum logic gates to specify the prepared quantum algorithm. These algorithms involve the rotation of these qubits on a Bloch sphere and the entanglement of qubits. Quantum algorithms need to be executed on the computers to simulate and develop conventionally unmodelled complex material systems. Efficient numerical characterization is a key problem in analysis of materials. The characterisation and simulation of complex materials and composites were difficult task. Especially, development of programming interfaces and quantum calculation platforms resulted in the development of various applied quantum algorithms for real world problems. The quantum algorithms were solved problems and developed applications in fields such as material science, quantum chemistry and quantum machine learning. More complicated, multi-qubit systems were started to operate, and the materials science continue to emerge new research challenges and opportunities.

In this study, we were investigated the current state of materials science progress and obstacles for quantum computing platforms. These algorithms, systems and quantum computers were required more development to live up to this potential. The realization of the potential of quantum computers will require a multidisciplinary effort. We were not cover the topics of building quantum computer theoretically or practically, and quantum error-correction and others. Finally, we investigate recent challenges, their affects, and future study trends in realizing quantum computing systems in material science.

2. Materials and Methods

The basic algorithms were constructed to store information in bits, which take superposition of zeroes and ones. The quantum system is coded in a well-defined quantum state system can take quantized values of the qubit into the |0> (ground) state or the qubit is in the |1> (excited) state, and any complex superposition of these two states. The quantum bits are interconnected through quantum entanglement and have nonlinear structures. The measurement of the final state of a qubit determines the results.

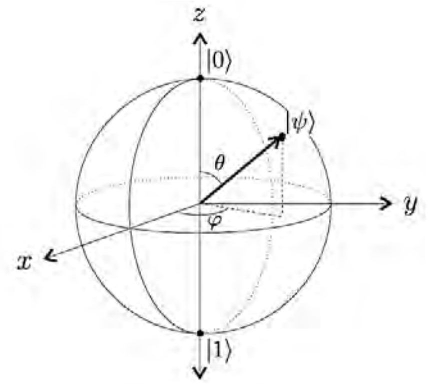

Figure 1. State of a qubit on the Bloch sphere.

The state of a photon '0' is given by the vector $\binom{1}{0}$ and of '1' by the vector$\binom{0}{1}$. In classically, the photon will be in state |0> or |1>. The traditional bit can be described either 0 or 1. The computation model were designed on the principles of quantum mechanics. According to the quantum mechanics, the superposition of states was described mathematically by a vector as

$$|\varphi\rangle = \alpha_0|0> +\alpha_1|1>= \alpha_0\binom{1}{0} + \alpha_1\binom{0}{1} \quad (1)$$

The measurement of the photon state will be |0> state with probability $|\alpha_0|^2$, and in |1> with probability $|\alpha_1|^2$. The $r_0 = |\alpha_0|$ and $r_1 = |\alpha_1|$ is given in the equation as $r_0e^{i\varphi_0}$ and $r_1e^{i\varphi_1}$, respectively. The north and south poles on the Bloch sphere of states $|0>$ and $|1>$ with spherical angles are $(\theta, \phi) = (0, 0)$ and $(\theta, \phi) = (\pi, 0)$. Since the photon in exactly one state as

$$|\alpha_0|^2 + |\alpha_1|^2 = 1 \quad (2)$$

The probability of state was calculated by multiplying the equation by its 'state vector'. The probability of the state |0> is ½ and the state |1> is ½ . The photon after first operation then its state remains by the matrix

$$\frac{1}{\sqrt{2}}\begin{bmatrix}1\\ i\end{bmatrix} \quad (3)$$

where i denotes $\sqrt{-1}$. These quantum principles of superposition and entanglement were used for complex algorithms and protocols for computing and provide for an enormous increase in computational capacity and possibility of new and quick way of solving computational problems. The effective solution and computability were required to describe, characterize, and model each problem/system for qubit system. The development of the algorithms of are based on these studies and computing models on the 'quantum scale' of individual atoms, electrons, and photons [15]. The solutions of problems and systems were resulted by the qubit operations. The coefficients are estimated with an algorithm mixing universal network of quantum gates. The set of different gates were used to construct a gate network, called as circuit, in terms of vectors and matrices.

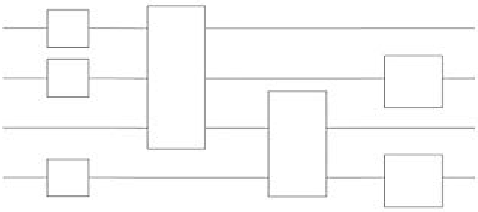

Figure 2. A circuit of depth 4, space (width) 4, and having a total of 7 gates.

A quantum circuit is a graphic representation of a quantum algorithm. The input from the left, were processed the information, and the right exits the results and continues its course. The gate processing is done by multiplying the unitary matrix. The gates were given in the form as

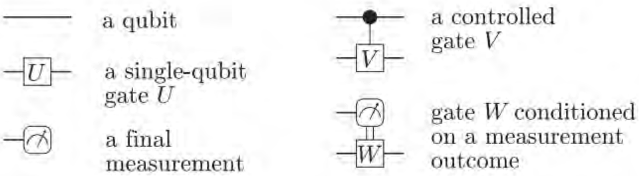

Figure 3. The components of a quantum circuit.

name	symbol	matrix representation	name	symbol	matrix representation
Pauli X	$\boxed{X}$	$\begin{pmatrix} 0 & 1 \\ 1 & 0 \end{pmatrix}$	X rotation	$\boxed{R_x(\theta)}$	$\begin{pmatrix} \cos\left(\frac{\theta}{2}\right) & -i\sin\left(\frac{\theta}{2}\right) \\ -i\sin\left(\frac{\theta}{2}\right) & \cos\left(\frac{\theta}{2}\right) \end{pmatrix}$
Pauli Y	$\boxed{Y}$	$\begin{pmatrix} 0 & -i \\ i & 0 \end{pmatrix}$	Y rotation	$\boxed{R_y(\theta)}$	$\begin{pmatrix} \cos\left(\frac{\theta}{2}\right) & -\sin\left(\frac{\theta}{2}\right) \\ \sin\left(\frac{\theta}{2}\right) & \cos\left(\frac{\theta}{2}\right) \end{pmatrix}$
Pauli Z	$\boxed{Z}$	$\begin{pmatrix} 1 & 0 \\ 0 & -1 \end{pmatrix}$	Z rotation	$\boxed{R_z(\theta)}$	$\begin{pmatrix} e^{-i\frac{\theta}{2}} & 0 \\ 0 & e^{i\frac{\theta}{2}} \end{pmatrix}$
Hadamard	$\boxed{H}$	$\frac{1}{\sqrt{2}}\begin{pmatrix} 1 & 1 \\ 1 & -1 \end{pmatrix}$	cNOT	$\bullet$ / $\oplus$	$\begin{pmatrix} 1 & 0 & 0 & 0 \\ 0 & 1 & 0 & 0 \\ 0 & 0 & 0 & 1 \\ 0 & 0 & 1 & 0 \end{pmatrix}$
S gate	$\boxed{S}$	$\begin{pmatrix} 1 & 0 \\ 0 & i \end{pmatrix}$	cU	$\bullet$ / $\boxed{U}$	$\begin{pmatrix} 1 & 0 & 0 & 0 \\ 0 & 1 & 0 & 0 \\ 0 & 0 & u_{00} & u_{01} \\ 0 & 0 & u_{10} & u_{11} \end{pmatrix}$
T	$\boxed{T}$	$\begin{pmatrix} 1 & 0 \\ 0 & e^{i\frac{\pi}{4}} \end{pmatrix}$	Z measurement		$p(k) = \lvert\langle k \vert \Psi\rangle\rvert^2$

Figure 4. Examples of quantum gate operations and circuit elements.

3. Results and Discussion

The exponential complexity of quantum systems resulted the complex, and advantageous quantum algorithms for generating useful results. The scalable, fault-tolerant quantum algorithms have been developed in the last decade for solving and simulating the quantum systems, number theoretic problems, integer factorization, and certain types of search problems. The potential of quantum principles and new algorithm have been studied extensively and multidisciplinary.

Table 1. The chronological steps on study.

Deutsch,1985	One-bit Boolean function at two points simultaneously by exploiting the superposition of zeroes and ones	Quantum parallelism
Deutsch, 1989	on quantum circuits	Quantum gates
Deutsch and Jozsa, 1993	Quantum algorithm	Properties of Boolean function
Bernstein and Vazirani, 1993	The algorithm used in the set	Specific Boolean function
Simon, 1994	New quantum algorithm	Quantum algorithms
Peter Shor	Quantum algorithms	Factoring large numbers and computing discrete logarithms [7]
Grover, 1996	Quantum algorithm for finding the unique inputs to a given function	Quantum search algorithms [16]

The algorithm for quantum factoring, finding hidden structure, and quantum phase estimation is the quantum Fourier transform (QFT). The classical Fourier transform turns a signal represented as a function of time into its corresponding signal represented as a function of frequency. The method is based on analysing the tomography image to simulate the material on the microscopic scale and involves 3D Fourier transforms of large data domain. This results a longer computation time due to Fourier transform complexity and need large memory. This transformation is reversible via the inverse Fourier transform for any operation on a quantum computer.

The simulations of materials were best described using quantum mechanics. These famous quantum algorithms were simulated a system with many quantum degrees of freedom, with applications including problems in chemistry, materials science, and physics. The simulations used to determine the structure of a substance, or the results of interacting particles. The solutions have been used for different applications for developing new industrial materials. The Hamiltonian (energy operator) describing all elements and interactions of the system were used in simulations. The quantum phase estimation was a stage in many quantum algorithms and enables measurements of the ground and excited energy levels. The physical system

$$|\psi_t\rangle = e^{-iHt}|\psi_0\rangle \tag{4}$$

where H is the Hamiltonian of the system, $|\psi_0\rangle$ is the initial state and t is time. The material simulations were prepared by solving Hamiltonian on a quantum computer [17]. Hamiltonian simulation is used or solving complex correlated material problems that have many applications [18, 19]. The kinetics of chemical reactions for chemical processes were also calculated and proved by these calculations. The quantum computer was used to simulate experiments on quantum systems in thermal equilibrium. The minimally entangled typical thermal state (METTS) algorithm implemented via the quantum imaginary time evolution algorithm [20].
The quantum eigenvalue problems were solved by using the variational quantum eigen solver (VQE) [21, 22]. The Variational Quantum Eigensolver is the foundation algorithm that could simulate molecules and chemical reactions. A related approach is the quantum approximate optimization algorithm (QAOA) [23, 24], an algorithm for preparing a variational guess of a wave function that satisfies an optimization problem that has the similar procedure with VQE algorithm. The quantum unconstrained binary optimization and Ising problems effectively solved on quantum computers. The algorithms were built for traveling salesman, scheduling problems, optimal

placement problems, graph colouring problems, and even game optimization. Some other quantum algorithms are related to the machine learning. The classical computers were process and analyse the data to find and classify data patterns by using machine learning. A new field has emerged showing a new possibility of finding patterns using quantum computers or algorithms. The quantum machine learning has been developing quantum versions of known classical machine learning algorithms. Research is going into finding the quantum versions of k-nearest neighbour methods, support vector machines, and other classical ML algorithms. As a disadvantage of error correction in quantum computers have looked for new approaches. A solution for this problem is to use quantum/classical hybrid algorithms for the simulation of many-body systems such as molecules and materials [25] and optimization [26, 27].

We have described a some of quantum algorithms with remarkable contributions that were used in quantum computers. These algorithms were high impact on applications and used in quantum chemistry (applied in pharmaceutics), and materials science [28, 29]. These applications were extend to quantum computing applications of fertilizer production, polymerization catalysis and clean energy processes applications [30].

4. Conclusions

In this study, we surveyed the quantum computation and the used quantum algorithms for materials science. The solutions and quantum algorithms for physical simulation were developing fast and rapidly. Quantum computers are able change our world with creating more accurate simulations. There are many open source ideas, components and algorithms were shared to solve these problems. The quantum computers and algorithms were developing by the help of theory of physics, chemistry, and material science. The material simulations were prepared using quantum computers accurately. A quantum computer was required perfect, and long coherence times qubits to perform complex material simulations. Many scientists and researchers from all over the world were investigating to quantum computing technology. The quantum technologies were an interesting field with a potential to open new window in material science. The quantum computers can be said to be emerging stars in calculating tools that enable the "quantum jump" current stage of material science. The quantum computers and algorithms were continued to develop, and we focus on the new developments in quantum algorithms. The beginning of new computational disciplines dedicated to the study of chemistry, materials, and physics on quantum computers.

References

[1]. Nielsen, M.A. and I. Chuang, Quantum computation and quantum information. 2002, American Association of Physics Teachers.
[2]. Feynman, R.P., Simulating physics with computers, in Feynman and computation. 2018, CRC Press. p. 133-153.
[3]. Feynman, R.J.J.T.P., Internat. 1982. 21: p. 467-488.
[4]. Feynman, R., Quantum mechanical computers. Foundation of Physics, 1985. 16(6): p. 507-531.
[5]. Benenti, G., et al., Principles of quantum computation and information: a comprehensive textbook. 2019: World Scientific.
[6]. Arute, F., et al., Quantum supremacy using a programmable superconducting processor. Nature, 2019. 574(7779): p. 505-510.
[7]. Shor, P.W. Algorithms for quantum computation: discrete logarithms and factoring. in Proceedings 35th Annual Symposium on Foundations of Computer Science. 1994.
[8]. Hempel, C., et al., Quantum chemistry calculations on a trapped-ion quantum simulator. 2018. 8(3): p. 031022.

[9]. Aspuru-Guzik, A., et al., Simulated quantum computation of molecular energies. 2005. 309(5741): p. 1704-1707.
[10]. Peruzzo, A., et al., A variational eigenvalue solver on a photonic quantum processor. 2014. 5(1): p. 1-7.
[11]. IBM Q Experience: https://quantumexperience.ng.bluemix.net/qx/editor (2019). Accessed 26 Mar 2019.
[12]. Friis, N., et al., Observation of entangled states of a fully controlled 20-qubit system. Phys. Rev. X, 2018. 8.
[13]. Song, C., et al., 10-qubit entanglement and parallel logic operations with a superconducting circuit. Phys. Rev. Lett., 2017. 119.
[14]. Preskill, J., Quantum computing in the NISQ era and beyond. Quantum, 2018. 2.
[15]. Phillip Kaye, R.L., Michele Mosca, An Introduction to Quantum Computing. 2007, Oxford University Press Oxford New York. p. xii+ 276.
[16]. Grover, L.K. A fast quantum mechanical algorithm for database search. in Proceedings of the twenty-eighth annual ACM symposium on Theory of computing. 1996.
[17]. Privman, V., D.V. Mozyrsky, and S.P. Hotaling. Hamiltonians for quantum computing. in Photonic Quantum Computing. 1997. SPIE.
[18]. Altman, E., et al., Quantum simulators: Architectures and opportunities. 2021. 2(1): p. 017003.
[19]. Bauer, B., et al., Quantum Algorithms for Quantum Chemistry and Quantum Materials Science. Chemical Reviews, 2020. 120(22): p. 12685-12717.
[20]. Motta, M., et al., Determining eigenstates and thermal states on a quantum computer using quantum imaginary time evolution. 2020. 16(2): p. 205-210.
[21]. Sawaya, N.P. and J.J.T.j.o.p.c.l. Huh, Quantum algorithm for calculating molecular vibronic spectra. 2019. 10(13): p. 3586-3591.
[22]. O'Malley, P.J., et al., Scalable quantum simulation of molecular energies. 2016. 6(3): p. 031007.
[23]. Zhou, L., et al., Quantum approximate optimization algorithm: Performance, mechanism, and implementation on near-term devices. 2020. 10(2): p. 021067.
[24]. Streif, M., M.J.Q.S. Leib, and Technology, Training the quantum approximate optimization algorithm without access to a quantum processing unit. 2020. 5(3): p. 034008.
[25]. Ma, H., Electronic Structure of Molecules and Materials from Quantum Simulations. 2020, The University of Chicago.
[26]. Moll, N., et al., Quantum optimization using variational algorithms on near-term quantum devices. 2018. 3(3): p. 030503.
[27]. McClean, J.R., et al., The theory of variational hybrid quantum-classical algorithms. 2016. 18(2): p. 023023.
[28]. Butler, K.T., et al., Machine learning for molecular and materials science. 2018. 559(7715): p. 547-555.
[29]. Endo, S., et al., Hybrid quantum-classical algorithms and quantum error mitigation. 2021. 90(3): p. 032001.
[30]. Reiher, M., et al., Elucidating reaction mechanisms on quantum computers. 2017. 114(29): p. 7555-7560.

WORKING OF A SINGLE PHASE INDUCTION MOTOR AS ALTERNATOR AND INVESTIGATING THE OUTPUT VOLTAGE VARIATON ACCORDİNG TO EXCITATION CAPACITY AND OHMIC, INDUCTIVE LOADS

MEHMET ALİ ÖZÇELİK*[1], AHMET AYCAN[1]

[1]Gaziantep University, Technical Science, Department Electric and Energy, Gaziantep, Turkey.

Abstract

Asynchronous motors are the most widely used machines in the industry. In the study, a single-phase asynchronous motor with main winding and auxiliary winding was rotated by a drive motor. By connecting the capacitor to the main winding ends, it is provided to operate as a one-phase alternator. The synchronous speed of a single-phase asynchronous motor is 1500 rpm at 50Hz mains frequency. First, a single-phase asynchronous motor was rotated by a three-phase asynchronous machine with a synchronous speed of 1500 rpm, and various capacitance values were connected to the main winding ends. At values below 124 µF, the received voltage is 6.75 V. At capacitance values of 124 µF and above, the output voltage increases, above 206 µF it decreases, and the asynchronous motor working as an alternator is loaded. In this case, the frequency decreases as the current drawn from the grid increases and the machine speed decreases.

Keywords: Asynchronous motor, Asynchronous generator, Synchronous Machine, frequency, remenance voltage

1. Introduction

Due to the developments and needs in technology, the need for energy is increasing day by day. However, with the limited reserves in energy resources such as oil and coal, the tendency for renewable energy sources such as wind, solar, and geothermal is increasing day by day. The electrical energy obtained from renewable energy sources varies according to factors such as ambient speed, temperature, light, and pressure [1]. When this situation is evaluated by considering synchronous and asynchronous machines, the ability of asynchronous machines to convert power at different speeds has made them more prominent [2].

Recently, asynchronous generators have been widely used in the power generation sector, especially in wind turbines. In the operation of an asynchronous machine as a generator, the mechanical power taken from the rotor is evaluated and this mechanical power taken from the input is converted into electrical energy [3-4].

The current through the motor windings creates a rotating magnetic field on the rotor. The flux interaction between the rotor and stator windings causes torque. If we rotate the rotor at a speed higher than the synchronous speed, the direction of the current and torque induced in the rotor will be opposite to the motor running condition. In this case, the machine works as a generator, and for the machine to work as a generator it must be rotated at a speed higher than the synchronous speed.

2. Material and Method

The equivalent circuit of a self-excited induction generator is shown in Figure 1 with the excitation capacitor and the load impedance. R1 is stator resistance, X1 is stator leakage reactance, R2 is rotor resistance, X2 is rotor reactance, Rc is core loss resistance, Xm is asynchronous generator magnetization reactance. The asynchronous generator speed is expressed as v and its frequency F.

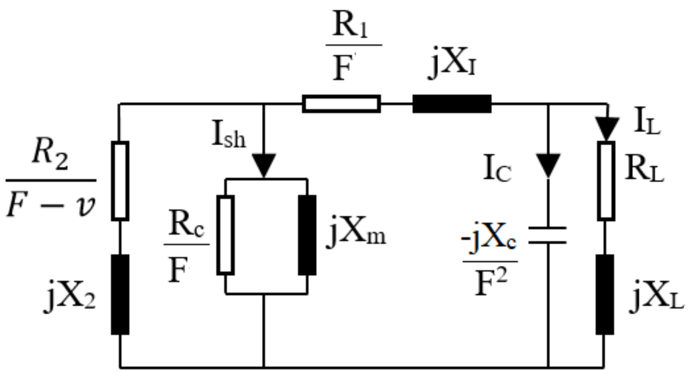

Figure 1. Equivalent circuit of a single-phase asynchronous generator

2.1. Experimental Setup

In the experimental setup, the 3-phase asynchronous motor and the universal motor are coupled. The incandescent lamp is used as ohmic load, the coil is used as inductive load, and capacitors are used as capacitive load. The experimental setup is shown in Figure 2.

.

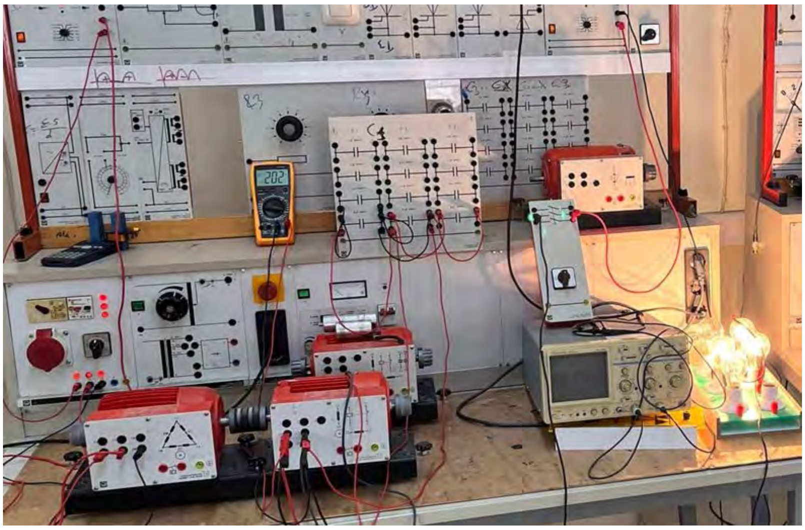

Fig. 2. Experimental Setup

The connection diagram of the experimental setup is shown in Figure 3. Voltmeter, amper-meter and frequency-meter were used as measuring instruments.

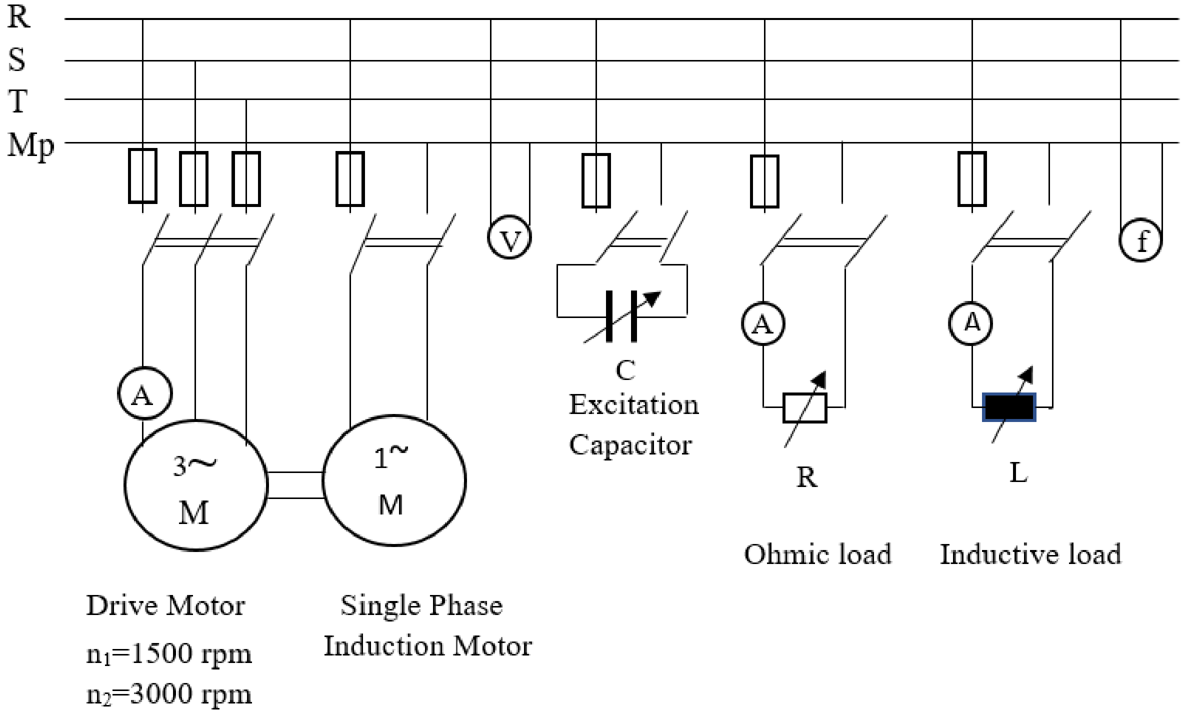

Figure 3. Connection of the system

When an asynchronous motor with a synchronous speed of n=1500 rpm is rotated by another motor with the same speed, the variation of the voltage taken from the main winding ends according to the capacitance values is seen in figure 4. However, it is seen that the voltage at the ends of the main winding remains at a very small value due to the residual magnetism. After the capacitance value exceeds 124 µF, the generated voltage increases depending on the capacitance value. However, after 182 µF, the generated voltage decreases, and both the single-phase asynchronous motor working as an alternator and the drive machine are forced and the current drawn from the network increases.

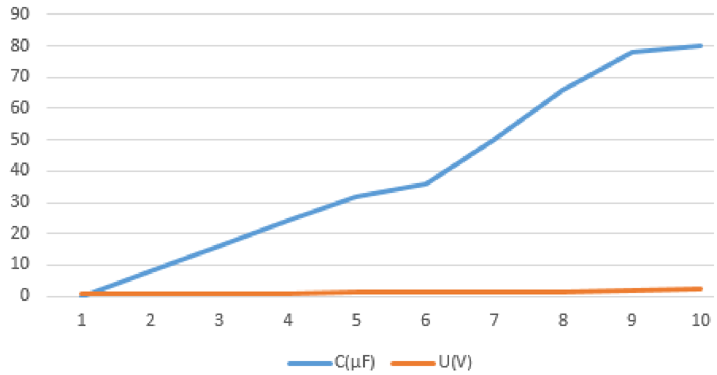

Figure 4. Voltage taken from the main winding ends according to the capacitor value (n=1500 rpm)

A one-phase asynchronous motor was rotated by another three-phase motor with a synchronous speed of 3000rpm, and capacitors of various capacities were connected to the ends of the main winding. A voltage of 12 V was taken below 28 µF. At 36 µF, the output voltage was 223 V. Then, the capacitance value was increased up to 52 µF, and it was observed that the generated voltage increased to 249 V as the capacitance value increased. However, as the capacity value continued to be increased, the output voltage started to decrease this time, and it was observed that the three-phase motor rotating the one-phase asynchronous motor working as a generator was forced, and the current drawn from the grid increased, and the frequency of the generated voltage decreased.

After a certain value of the capacitance, the generated voltage decreases. When an asynchronous motor with a synchronous speed of n=3000 rpm is rotated by another motor with the same speed, the variation of the voltage taken from the main winding ends according to the capacitance values is seen in Figure 5. It is seen that the voltage at the ends of the main winding increases according to a certain capacitance value.

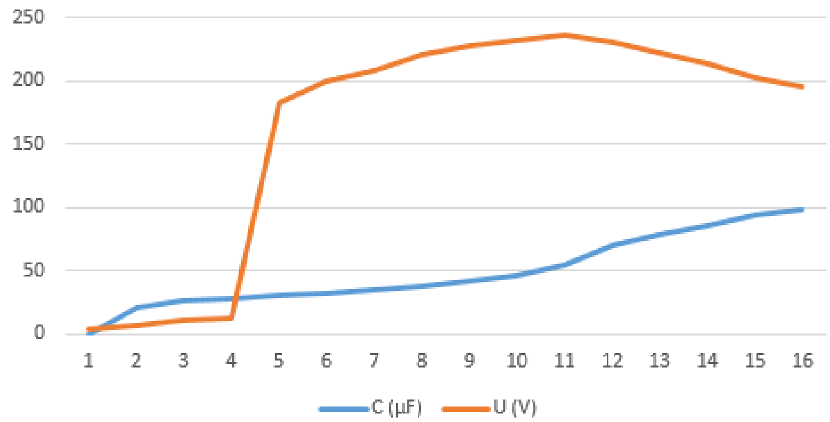

Figure 5. Voltage taken from the main winding ends according to the capacitor value (n=3000 rpm)

When a phase motor working as an alternator exceeds a certain capacity value, the current drawn by the capacitors increases, the load of the asynchronous motor working as a single phase alternator increases, and thus the drive machine is forced to increase the current drawn by this machine from the mains, and the frequency decreases as the number of speed decreases. The variation of the current drawn by the motor that rotates the asynchronous motor according to the capacity is shown in Table 1.

Table 1. Current values drawn by the drive motor

C (µF)	U (V)	f (Hz)	I (A)
54	237	46	0.8
70	231	43	1.1
78	222	42	1.3
86	214	40	1.45
94	202	38	1.6
98	195	37	1.7

It has been observed that as the ohmic load at the single-phase asynchronous generator ends increases, the output voltage decreases, the frequency decreases slightly, and naturally the current drawn by the drive motor from the grid increases. The decrease in the voltage at the load ends was compensated by increasing the capacitance value. That is, when the capacitance value increases, the decrease in the output voltage can be compensated, and the capacitance value increases when the load is loaded. Ohmic and inductive loads are connected to the single-phase asynchronous generator terminals.

Table II shows the variation of the voltage produced, the current drawn by the driving machine, and the frequency when various values of ohmic and inductive loads are connected to the output of one phase motor operating as an alternator.

Table 2. Variation of electrical parameters for ohmic load

Current drawn from the grid by the driving machine (A)	Single phase alternator output voltage (V)	Excitation capacity (μF)	Alternator load current (A)	Frequency of the generated voltage (Hz)	Type of load
0.6	229	38	0	49	No load
0.66	215	38	0.38	48	Ohmic
0.72	198	38	0.57	47	Ohmic
0.75	170	38	0.9	47	Ohmic
0.75	229	46	0.3	47	Ohmic
0.85	216	46	0.61	47	Ohmic
0.92	197	46	0.87	46	Ohmic

Table III shows the variation of the voltage produced, the current drawn by the driving machine, and the frequency when various values of inductive load has been connected to the output of one phase motor operating as an alternator.

Table 3. Variation of electrical parameters for inductive load

Current drawn from the grid by the driving machine (A)	Single phase alternator output voltage (V)	Excitation capacity (μF)	Alternator load current (A)	Type of load
0.6	229	38	0	no load
0.6	213	38	0.22	inductive
0. 58	190	38	0.4	inductive
0.68	222	46	0.45	inductive

3. Conclusion

This study aims to understand better the working of single-phase asynchronous motors as generators. When an induction motor with a synchronous speed of 1500 rpm is rotated by another motor with a synchronous speed of 1500 rpm, although various capacities are connected to the output of the main winding, the voltage taken from the output of the main winding could no longer exceed the voltage caused by the magnet. One-phase asynchronous motor is rotated with another asynchronous motor with a synchronous speed of 3000rpm, it has been observed that the voltage produced increases as the capacity increases, up to a certain capacity value. However, if the capacity value is continued to be increased, the voltage produced (taken from the ends of the main winding) decreases, and at the same time the driving machine is forced, and the frequency of the generated voltage decreases.

When Ohmic and inductive load is connected to the main winding output of a single-phase asynchronous motor, it has been observed that the voltage decreases compared to the no-load situation. It has been understood that the capacity should be increased to compensate for this decrease and, the capacity value should be increased with each load increase. The decrease in voltage at the output of the main winding in ohmic and inductive loads is approximately close to each other for the same current values.

References

1. Özçelik, M. A., Aycan, A. Bilezikli Asenkron Motorda Kaymanın Rotor Gerilimi ve Rotor Frekansına Etkisinin İncelenmesi . Kahramanmaraş Sütçü İmam Üniversitesi Mühendislik Bilimleri Dergisi, 2017, 20 (4), 134-142. DOI: 10.17780/ksujes.349408
2. Ünal, S., Özdemir M., Üç Fazlı Kendinden Uyartımlı Asenkron Generatörün Farklı Yük ve Hız Değerleri İçin Sürekli ve Geçici Durum Davranışının İncelenmesi, Doğu Anadolu Bölgesi Araştırmaları; 2004. 2(2), 124-129.
3. M. H. Haque, A Novel method of evaluating performance characteristics of a self-excited induction generator", IEEE Trans. on Energy Conversion, Vol. 24, No. 2, 2009, pp. 358-365.
4. Haque, M. H. Maximum Power Delivery Capability of a Three Phase Self-Excited Induction Generator, 8th International Conference on Electrical and Computer Engineering 20-22 December, 2014, Dhaka, Bangladesh, pp.465-468.

DESIGN AND CONSTRUCTION OF PVC PACKAGING MACHINE

NECIP FAZIL YILMAZ[1, 2], IBRAHIM HUWARI[1]

[1] Gaziantep University, Engineering Faculty, Mechanical Engineering Department, Gaziantep, TÜRKİYE.
[2]Hasan Kalyoncu University, Board of Trustees, 27010, Gaziantep, TÜRKİYE.

Abstract

The PVC industry is an economical and versatile thermoplastic polymer widely used in the building and construction industry to produce door and window profiles, pipes, cable insulation, and medical devices. In light of the rapid development in our world where most industries have been automated, the profile packaging department is still manual in most factories, and every PVC production line needs at least two workers to wrap the PVC profiles. In some applications, the weight of the profiles is too great and it is difficult to wrap them and then transport them, with the possibility of injury to the workers responsible for the packaging. That's led to an increase in cost in both money and time. The purpose of this study is to design and manufacture PVC packaging machines that can automate packaging to reduce the manpower required in the PVC profile packaging department. The packaging process consists of four basic stages, starting with the process of arranging the profiles transferring them to the waiting stage, and then wrapping, ending with placing the envelope in the designated place.

Keywords: PVC Profile, Packaging Machines, Automation, Wrapping Machine, Packaging Machine Design

1. Introduction

Polyvinyl chloride (PVC) [1] is the world's third-most widely produced synthetic polymer of plastic (after polyethylene and polypropylene) [2], About 40 million tons of PVC are produced each year, in most factories, the PVC production line works automatically without any interference. After PVC profiles are produced. The packaging process is considered to be one of the most important processes, many clients need their PVC profiles to be shipped internationally because PVC profiles need to be packed very well for several reasons, including protecting them from weather corrosion, damage, accumulation, dust, and scratches. The packaging [3] process of PVC products is done in various methods, one of the methods is manual, Manual packaging requires two workers, firstly, they put a long piece of plastic which is usually 1.5 meters longer than the profile in each end on a stacking table, and then the workers place the PVC profiles on the plastic piece and arrange the profiles, and finally the plastic piece is folded over the profiles and then the adhesive tape is applied, in this method, the packaging is very difficult and requires physical strength, not to mention the possible injuries during carrying the profiles. Also, the workers wait for a long time estimated at 12 minutes for each packaging, the worker can make a mistake in calculating the number of profiles in each packaging, PVC production line works under continuous conditions, so this can be challenging to follow up each production line for big factories, so this method led to an increase in cost in both money and time [4-5].

Another method is using a semi-automatic machine, also in this method workers are required to carry the profiles from the production line to the stacking table and arrange the profiles in an orderly manner so as not to take up space, and then the packaging process is done by one of the two machines, which are either wrapping machine [6] or flow pack machine [7], in both cases, the workers must be present to put the wrapped profiles in another place for the new packaging, In addition, the flow pack machine method needs heat shrink [8] machine to reduce the size of the plastic bag after the packaging process is done, which makes the production process of the plastic profile not fully automated, this negatively affects the quality, speed, and cost of the production process. The importance of this study is coming from several sides such as; controlling the length of the production-line layout, automated packaging means reducing the number of workers needed in the factory, and the worker's efficiency will be increased due to focusing on other sensitive tasks during the process such as monitoring, reducing the number of workers leads to cost reduced which means more competitive in the market place, and the time of production will be reduced. PVC Packaging prototype machine parts were designed and assembled by using CAD programs which is SOLIDWORKS, simulations will be done in the future for structure and effectiveness analysis, and finally, the prototype will be done in reality so it can be tested preparing it for the mass production that makes it possible to place the final product to the market.

2. The Designing of PVC Packaging Machine

The machine was designed and assembled using SOLIDWORKS 2022 and the material that the machine will be made from is mostly made of iron ST36 with sheet metal technology where a laser machine is cutting the sheets of metal to the required shapes then the bending process takes place to bend the parts preparing them to the assembly. Other parts will be made using a turning machine, weldment cut, and CNC machine. The machine's main parts and final assembly were designed by CAD program and are explained in detail in the following section. These parts will be assembled using different techniques such as; welding, screwing, and fitting. The method used in this study will be both computational and experimental methods by applying many suitable simulations to avoid the possible mistakes that can be shown up when making the prototype. The machine is consisting of 3 main assemblies which contain nearly 105 unique parts assembled as shown in figure 1;

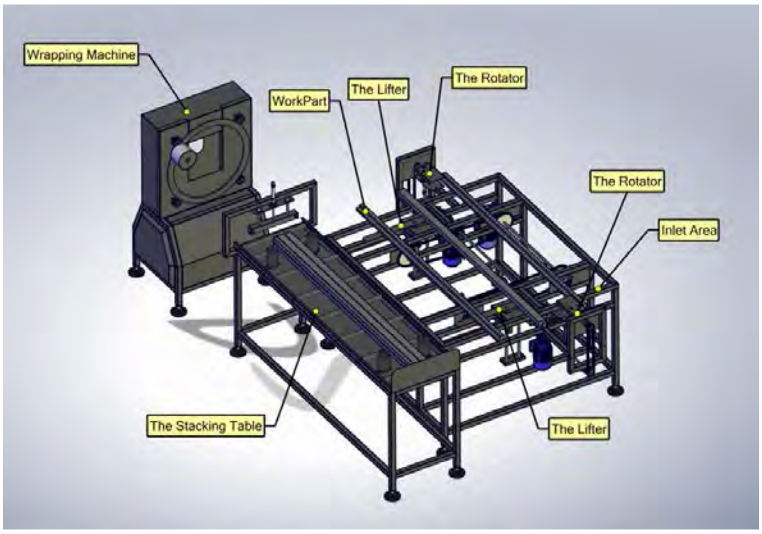

Figure 1. Automatic PVC Packaging Machine

2.1 The Rotator

After the PVC is cut with the required meters the PVC Cutting machine sends a single to the PVC packaging system, the machine will slide the PVC profile to the left to a certain distance by electric motor and sprocket with a chain and plastic piece (soldiers) as shown in figure 2 where the rotators can hold the profile.

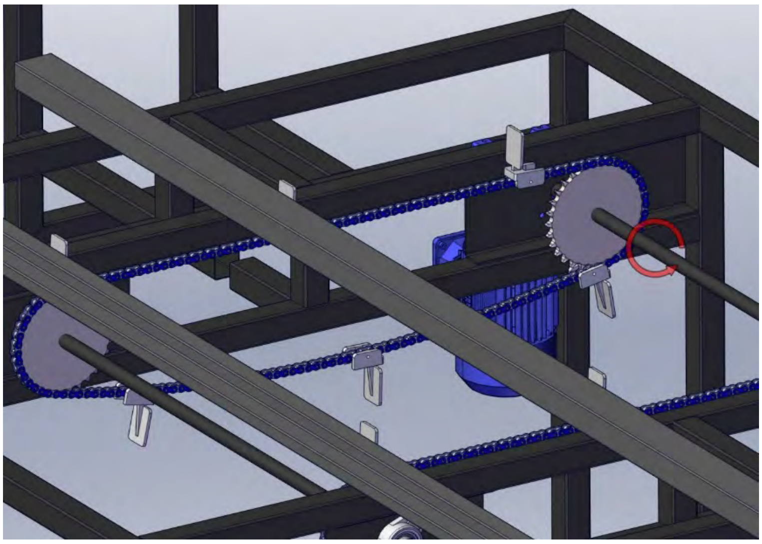

Figure 2. Moving Left Motion

The soldiers have a very unique motion they slide the profiles once the soldier reach the sprocket the solider moves downward to leave the profile gently so that the profile does not get pulled down and crash. The rotators (as shown in figure 4) are on the sides of the machine symmetrically and they consist of a pneumatic piston [9] and color detection sensor are equipped on the top of them, once the sensor detected the PVC profile passing throw, the pneumatic piston will hold the profile while it is rotating, both rotators have the same motion since they are equipped on the same electric motor. The PLC will decide if it will rotate the PVC profile or not and the angle required for the part to be rotated. For example, when the “L” shape of the PVC profile is produced the best fit arrangement can be as shown in figure 3.

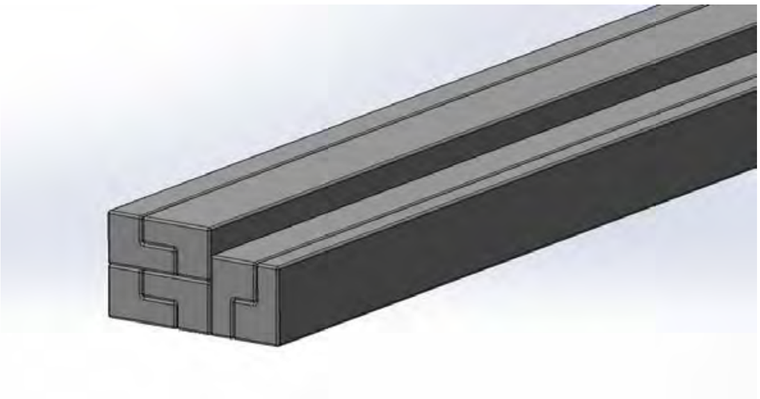

Figure 3. "L" shape Profiles are fits in each other

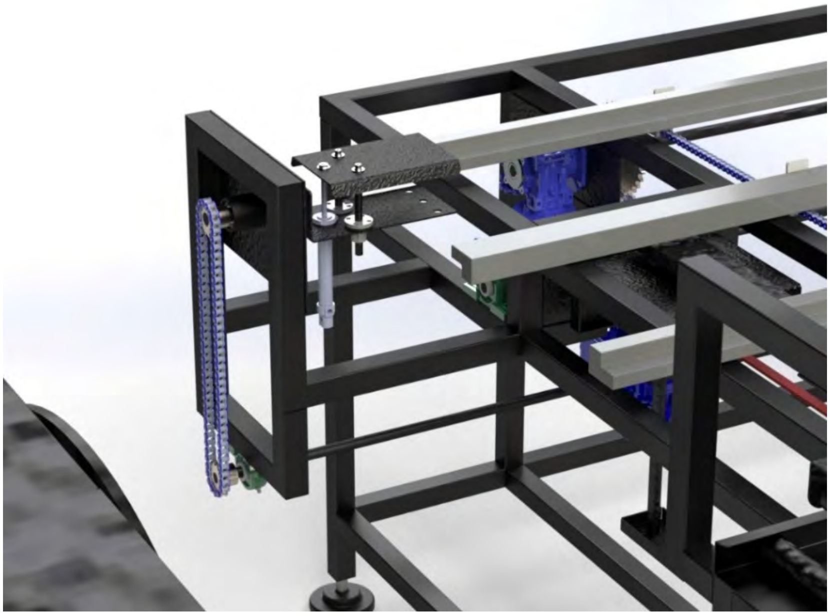

Figure 4. The Rotator at (180°)

2.2 The Lifter

In this stage, three PVC profiles in a row are arranged and waiting to be transformed to the next stage of the packaging process. There are two lifters on both sides left and right, the lifters' function is to lift the three profiles upward by an electric motor and then to move forward by another electric motor to the stacking table, the function upward for the left & right sides of the machine are on the same electric motor as well as the moving forward function so that neither side lags behind the other side, this process will be performed two times so the total number of PVC profiles is six, in our case the total number of PVC profile will be four. The lifter assembly is as shown in figure 5;

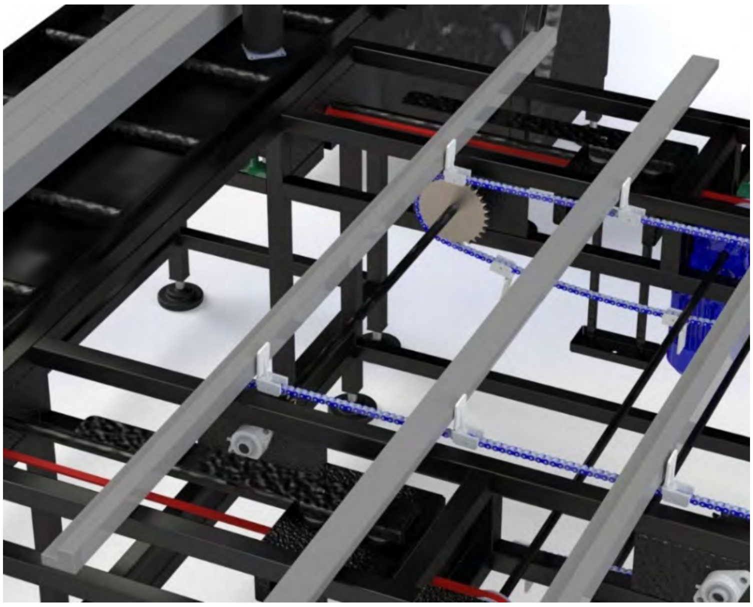

Figure 5. The Lifter

2.3 The Stacking Table

The stacking table has very important functions, firstly it will wait until the PVC profiles are assembled on it, then the pneumatic pistons will apply pressure to the PVC profiles in three directions, left, right and above so it is set tight, and the electric motor will rotate in the reverse direction so the profiles will hit the starting point, the electric motor will rotate at a certain speed in the direction of the wrapping machine with a constant speed, the pressure applied on the profiles will stable the profiles while the wrapping machine warps the PVC profiles together, therefore the wrapping machine will have higher speed working.

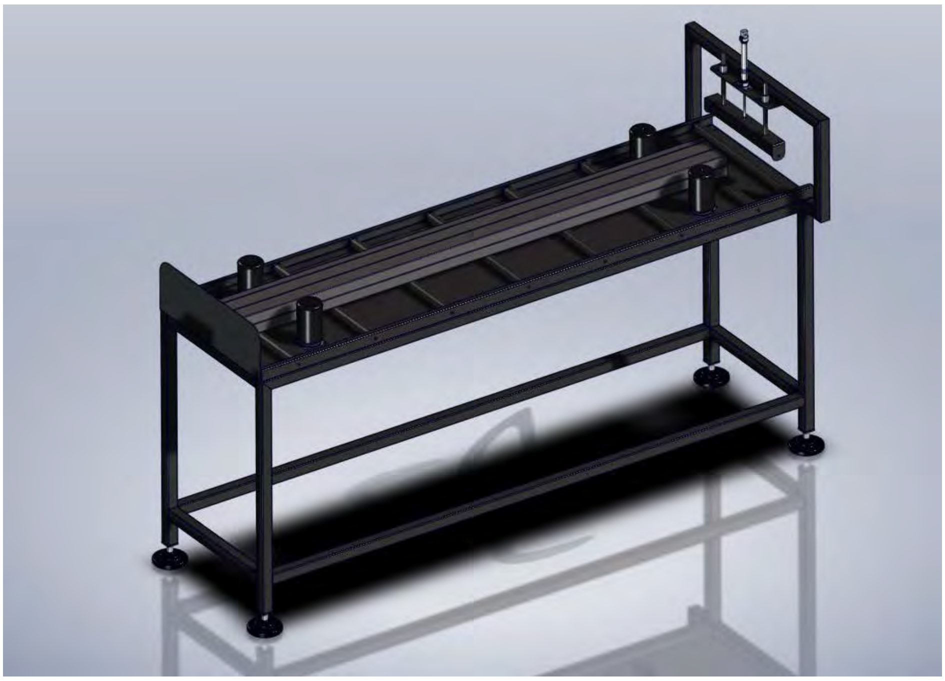

Figure 6. The Stacking Table

2.4 Wrapping Machine

The final process in this prototype is the wrapping machine [10], it has a big roll on the end of the coil [11] as shown in figure 7, the electric motor is equipped on the machine to rotate the coil, and while the PVC profiles are moving forward a color sensor [12] will detect the profiles, the coil will start to rotate at a constant speed, the profiles will be wrapped tightly, by changing the speed of the wrapping machine the thickness of the wrap will be changed after the profiles are packed a piston will cut the stretch so the packed profiles free from the starch.

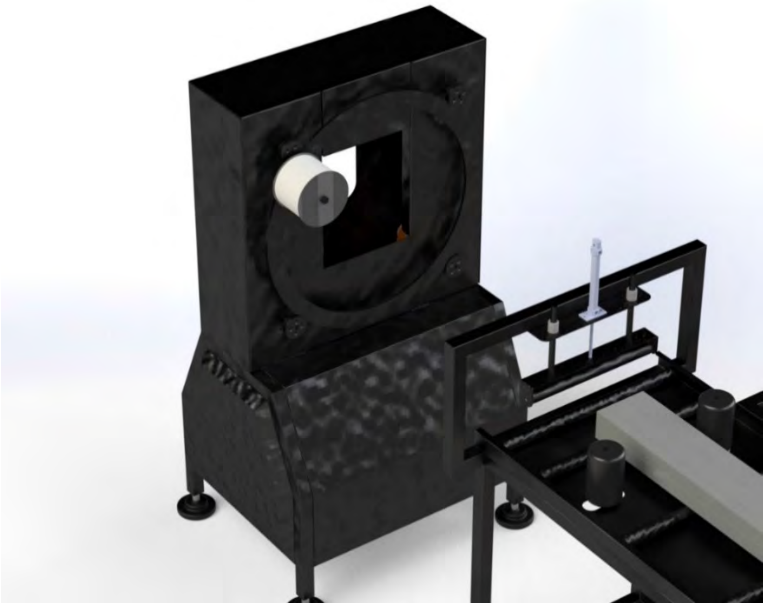

Figure 7. Wrapping Machine.

3. The Benefits of PVC Packaging Machine

Rising demand of PVC profiles is a sign that PVC industry business is doing something right. More orders mean that you have satisfied customers and can look forward to making more profit. However, as any production manager will attest to, rising demand can bring its own problems if your company does not have the capacity to cope. Extra labor costs, staff shortages, missed deadlines, and quality problems if you sacrifice accuracy for speed can lead to less profit. Automation can help you scale up production quickly, especially if you anticipate growth. In the PVC Profile business, two workers (or more) for each production line can be expensive, especially when you factor in the payroll tax, holiday pay, sick pay, training, and superannuation. Packaging machines can pay for themselves because machines need only a few operators. Also, repetitive jobs can be mentally tiring and lead to repetitive strain injuries and accidents simply because people lose their focus. Apart from the moral issues, this can result in time off work, paying sick wages, and compensation if a tribunal finds a company negligent. Automation removes workers from repetitive tasks and reduces the amount of heavy lifting, increasing productivity while reducing injury and accidents. The PVC packaging machine can be a solution to the space problem in factories, simply one packaging machine can work for more than one production line because of the nature of the PVC extruder's work.

The machine has three separate assemblies as shown in figure 8, and each has many functions, which shortage the number of weldments cut profiles, the space needed, the ease to move it, and the cost of machines.

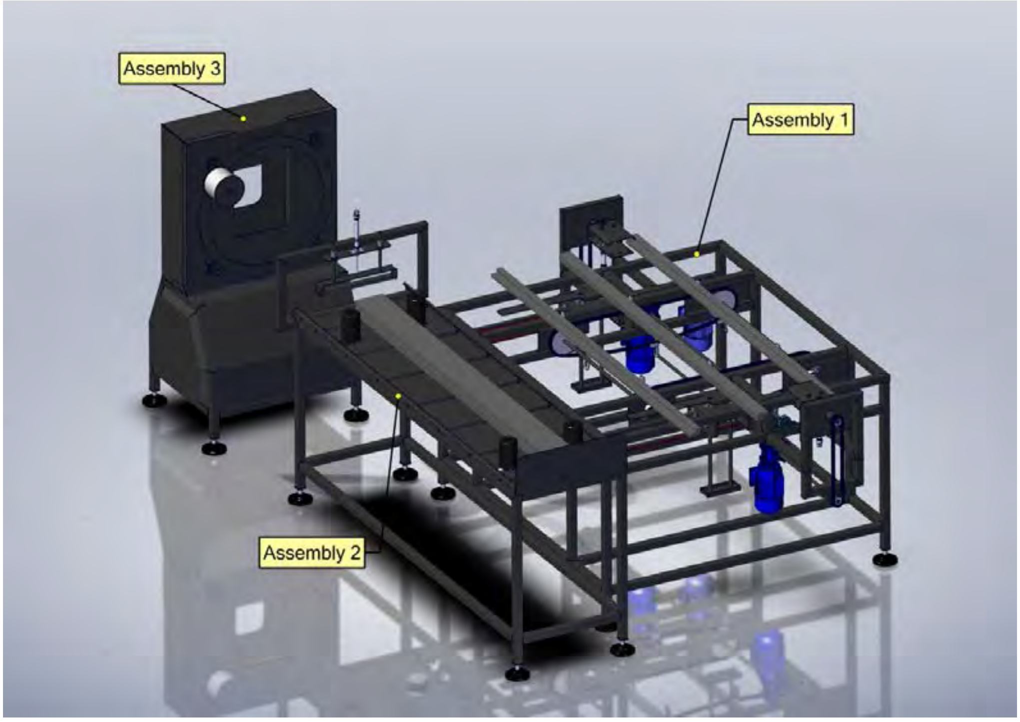

Figure 8. PVC Packaging Machines Assemblies

For instant, the first assembly has four functions, firstly the machine waits the PVC profile to reach the required length, secondly slide the profiles toward the stacking table, thirdly, while the machine in the first function it rotates the profiles to fit with the best nesting shape, finally moving the row of PVC profile to the stacking table. These functions are compatible and linked with each other so that each of them is accomplished in accordance with the other functions. Basically, the PVC profile will be produced at a constant speed which is nearly 3 m/min, once the PVC profile reaches the first assembly table than it is cut to the required length then the cutting machine sends a single to the packaging machine PLC system, soldiers will move to the left side forcing the profile to slide, the rotator will detect the profile while it sliding, the soldiers will stop immediately, the system will decide the best nesting shape to be packed with, the rotator gets in action and rotates the profile to the required angle in most cases it is (0°,90°,180°), in this stage, the next profiles are coming continuously, the system will wait until it gets another single from the cutting machine and the machine will repeat the procedure we mentioned before, normally the profiles are packed as 6 profiles 2 columns and 3 in a row, to get that shape the machine will left the first 3 profiles in raw to the stacking table than it will left the second 3 profiles in row above the first 3 profiles. Substantially, timing is key and the PVC packaging machine gets the benefit of the continuous production speed which is relatively slow. There is one disadvantage of the rotator, which is the length of the PVC profile, the rotator can work only with a certain length of the profile, a longer PVC profile length will cause the machine to stop working, and a shorter PVC profile length the machine can work but it loses the benefit of the rotator. Fortunately, the global standard profile length is 6 meters and it can't be longer than 6 meters because it doesn't fit in the container while shipping, and less than 6 meters is rarely needed.

Moving to the second assembly which is the stacking table, the benefits of the stacking table are: firstly, re-line the profiles so that they are all on the same starting line then applying a certain pressure to the PVC profiles so they are tight grip with minimal space, thirdly moving the profiles forward at a constant speed, and finally holding the profiles for the wrapping machine while the profiles are moving forward. All these functions are together in the same assembly, other companies are performing those tasks manually or by two assemblies which led to losing space and time and more importantly in cost, simply buying one machine with too many functions is cheaper than too many machines with the same number of functions.

Lastly, the third assembly of this study is the wrapping machine, which is the most important part of the PVC packaging machine, the electric motor is equipped with an inverter which means the speed of the rotation can be changed, according to the stretch properties and the number of the PVC profiles the manager can change the speed of the machine so the stretch layers can be changed, increasing the speed increases the stretch layers and decreasing the speed decrease the layers. One of the advantages of using a wrapping machine is that it can stretch wrapping film much further than a human can, wrapping machines can stretch film by up to 300%, depending on the settings, while manually stretching typically only yields a 50% stretch, having the ability to stretch wrapping film six times more will provide significant savings to the materials expenditure. Not only that, but machine wrapping will eliminate the inconsistencies of manual wrappings so you will know exactly how many profiles you can wrap with a roll of film, allowing you to plan your ordering more effectively. Also, it will ensure that the PVC profiles are securely wrapped to avoid any potential damage from dirt, dust, or moisture.

4. Conclusion

In this article, we designed a PVC packaging machine that will rearrange the product so it can be fitted with the best nesting shape while sliding to the packaging spot so it will minimize the volume of the final packages, which means this machine offers a new space solution inside the inventories of the factory, the final products that were packaged automatically will be safer, tighter, and more manageable while carrying and transporting during the supply chain from the factory to the place of construction, the machine will be tested computationally and experimentally to save work effort, cost, and time during the packaging and handling, the machine is designed to be suitable for continuous and mass production type, because the PVC extruder works under continuous conditions, the problem of having many workers in the PVC packaging process will be solved by designing a new and unique machine to package the PVC product 100% automatically, there should be another stacking table after the wrapping machine to pull out the packed PVC profiles and transporting them. Furthermore, there will be in the future a new design to pack the standard PVC profile length which is 6 meters based on the prototype design.

References

1. Arjen, S. What is PVC, Wayback Machine. **2017**.
2. Allsopp, M.W., and Vianello,G. Poly (Vinyl Chloride), Ullmann's Encyclopedia of Industrial Chemistry. **2012**.
3. Persona, A., Azzi, A., Battini, D., and F. Sgarbossa, Packaging Design: General Framework and Research Agenda, Packaging Technology and Science. **2012**, 25(8):435-456.
4. Jeffrey, L.P., and Fish K.H. A Commentary on Packaging Machines, American Journal of Hospital Pharmacy.**1965**, 22(9):532-537.

5. Hooper, J.H. An introduction to packaging machines, Confectionery Packaging Equipment. **1999**,1-10.
6. Fromm Packaging, [Online] Available: https://www.youtube.com/watch?v=eUjFLwzvh08.
7. Park Industrial Packaging, [Online] Available: https://www.youtube.com/watch?v=dJF0e18lDQI.
8. Sun, T. Heat shrink formation of a corrugated thin film thermoelectric generator, Energy Conversion and Management. **2015**, 103:674-680.
9. Kalekin, V.S., and Kalekin, D.V. Experiments on a piston pneumatic motor with self-acting valve, Chemical and Petroleum Engineering. **2009**, 648-653.
10. Lin, J.C. The design and manufacture of an automatic wrapping machine, Proceedings IEEE Conference on Industrial Automation and Control Emerging Technology Applications. **1995**.
11. Oestreich, J. M., Tolley, W.K., and Rice, D.A. Design And Study Of Outside Wrapping Machine Of Sewing Thread, Advanced Materials Research. **2013**, 706-708:1266-1269.
12. Oestreich, J. M., Tolley, W.K., and Rice D.A. The development of a color sensor system to measure mineral compositions, Minerals Engineering. **1995**, 8(1-2):31-39.

POLİMER TEMELLİ SİKLOİD DİŞLİLERDE SONLU ELEMANLAR ANALİZİ

NECİP FAZIL YILMAZ*[1,3], HASAN MİTHAT DELİBAŞ[2], MAHMUT FURKAN KALKAN[3]

[1]Hasan Kalyoncu Üniversitesi, Mütevelli Heyeti, Gaziantep, TÜRKİYE
[2]Hasan Kalyoncu Üniversitesi, Mühendislik Fakültesi, Makine Mühendisliği, Gaziantep, TÜRKİYE
[3]Gaziantep Üniversitesi, Mühendislik Fakültesi, Makine Mühendisliği Bölümü, Gaziantep, TÜRKİYE

ÖZET

Sikloid dişlilerin geleneksel dişlilere kıyasla yüzey basıncı açısından daha büyük bir kuvvet taşıma potansiyeline sahip olduğu gerçekleştirilen literatür çalışmaları ile ispatlanabilen bir gerçektir. Ancak çok hassas imalat gerektiren bu parçaların kullanımı, gerekli tolerans hassasiyetlerinin karşılanamamasından dolayı, yeterince yaygınlaşamamıştır. Metal bazlı sikloid dişlilerden ziyade polimer bazlı malzemelerden imal edilen sikloid dişlilerde bu tolerans hassasiyetlerinin daha rahat sağlanabildiği, imalat adımlarının ve bu sayede maliyetin azaltılabileceği dikkat çekmektedir. Bu bilgiler ışığında, bu çalışmada klasik bir sikloid dişlinin farklı polimer temelli malzemelerde ve farklı kuvvet değerleri altında hangi davranışları sergileyeceği incelenmiştir. Sikloid dişli modelleme parametrelerine sadık kalınarak klasik bir sikloid dişlinin üç boyutlu modellemesi gerçekleştirilmiştir. Oluşturulan bu model aracılığı ile sikloid dişlinin malzeme özellikleri değiştirilerek farklı devir/dakika'lardaki stres, gerinim ve yer değiştirme değerlerinin analizi sonlu elemanlar metodu temel alınarak gerçekleştirilmiştir. Analiz malzemeleri olarak geleneksel dişli imalatında da sıkça kullanılan polimer türleri olan Delrin ve Nylon belirlenmiştir, seçilen bu malzemelere literatür çalışmaları doğrultusunda karar verilmiştir. Modellenen sikloid dişli boyutlarına uygun ve gerçekçi bir kuvvet yüklemesi yapabilmesi amacı ile, 12 V motorların da çalışma aralığında bulunan, 100, 200, 350 rpm hızları sonlu elemanlar analizi için uygun görülmüştür. Çalışmanın sonunda her bir sistem elemanı için ayrı ayrı kuvvet dağılımlarına yer verilmiş olup elde edilen bu sonuçların yorumlanması bir bütün olarak gerçekleştirilmiştir. Sonlu elemanlar analizinden elde edilen veriler bize en yüksek yer değiştirme oranının malzeme cinsinden bağımsız olarak dış yatak dişlerinde gerçekleştiğini, stres ve gerinimin ise nispeten homojen olarak dağılmasına rağmen dış yatak diskinin, sikloid dişin ve alt şaft dişlerinin üzerine yoğunlaştığını göstermektedir.

Anahtar Kelimeler: Sikliod Dişliler, Sonlu Elemanlar Analizi, Polimer Dişli Malzemeleri, Stres Analizi, Eksantrik Analiz.

1. Giriş

Sikloid redüktörler alman mühendis Lorenz Braren tarafından geliştirilmiş olup, planet grubuna ait bir dişli tipidir. Sikloid redüktörler başta endüstriyel robotik olmak üzere otomotiv, havacılık mühendisliği ve hassas makine takımlarının kullanıldığı farklı endüstriyel alanlarda yaygın olarak kullanılmaktadır (1). Sikloid dişli redüktörlerin en büyük avantajı sıfır veya sıfıra yakın diş boşluğuna sahip olmasıdır. Bu özellik sikloid redüktörlerin büyük ölçüde hassas pozisyonlanabilme ihtiyaçlarının olduğu robotik uygulamalarda önemli ve ihtiyaç duyulan bir redüktör tipi olmasını sağlamaktadır (2). Bunun yanı sıra kompakt tasarım, yüksek verimlilik, düşük gürültü, darbelere karşı dayanıklılık, düşük enerji kaybı ve yüksek tahvil oranlarına sahip olmasıyla diğer redüktör tiplerine karşı önemli bir avantaj sağlamaktadır (3).

Sikloid redüktörler genellikle talaşlı imalat yöntemi ile üretilen kompleks parçalardan oluşan bir sikloid yapıda dişli redüktör tipidir (4). Avantajlarının yanında talaşlı imalat ile üretimlerinde ortaya çıkabilecek faktörlerden kaynaklı diş boşluğu oluşabilmektedir (5). Bu durum yüksek hızlarda sikloid redüktörlerde dengenin bozulmasına, gürültü ve titreşimin ortaya çıkmasına sebebiyet verebilmektedir (6). Eğer ideal ölçümlerde üretim gerçekleştirilirse diş boşluğu oluşmayacak ve belirtilen kusurların gerçekleşmeyeceği bilinmektedir. Sikloid redüktör parçalarının işlenmesinde kullanılan kesici takım ve tezgahların imalat sektöründe yaygın kullanılan standart takım ve tezgahlar olmaması sikloid redüktörlerin istenilen hassasiyette üretilememesinde önemli bir etkiye sahiptir (7,8). İdeal ölçümlerde üretim gerçekleştirilebilmesi için geleneksel olmayan yöntemlerle üretim yapılması tavsiye edilmektedir (6). Bu durum bizlere yalnızca geleneksel yöntemler dışında kalan talaşlı imalat yöntemlerine sahip işletmeler ile üretim yapabileceğini göstermektedir. Literatürde yapılan çalışmalarda talaşlı imalat yöntemlerinin ve parametrelerinin geliştirilmesi üzerine çalışmalar bulunmaktadır (2,9,10). Yapılan çalışmalar, kompleks yapıdaki diş geometrilerinin daha hassas üretilebilmesi, pürüzlülüğün azaltılması, yorulmaya karşı direncin geliştirilebilmesi gibi konular yoğunluk göstermektedir(11,12).

Polimer malzemelerin kullanımı, eklemeli imalatın kullanımının artmasıyla birlikte endüstride de gitgide yaygınlaşmaktadır. Polimer tabanlı malzemelerin kullanılmasının tasarımsal, teknolojik ve ekonomik sebeplerden kaynaklı farklı avantajları bulunmaktadır. Metal esaslı malzemelere göre daha düşük seviyede gürültü üretmesi ve uygun fiyatlı üretim yöntemleri kullanılarak üretilebilmesi en büyük avantajlarındandır. Bazı araştırmacılar sikloid dişli redüktörlerin üretilmesinde çelik yerine plastik malzemelerin kullanılmasına yönelik çalışmalar gerçekleştirmişlerdir(13–15). Optimum çalışma basınç değerlerine göre tasarlanmış plastik malzemelerle üretilmiş olan sikloid redüktörlerin sağlıklı olarak çalışabileceği gösterilmiştir.

Kapsamlı literatür araştırmalarında, sikloid dişli üretimi için eklemeli imalat yöntemlerine dair gerçekleştirilen çalışmaların eksikliği dikkat çekmektedir. Aynı zamanda sikloid dişli analizlerinde polimer temelli malzemelerin kalıtsal davranışlarının incelemesinde de yetersiz kalındığı göze çarpmaktadır. Bu iki temel eksiklik göz önüne alındığı zaman metal esaslı üretime kıyasla üretim maliyetlerini düşürmek, parça hassasiyetini arttırmak ve üretim adımlarını azaltmak amacıyla polimer temelli malzemelerin kullanılması durumunda ortaya çıkacak olası sonuçların analizlerinin yapılmasının sektörün geleceği için hayati bir öneme sahip olduğu görülmektedir. Bu değerlendirmeler ışığında gerçekleştirilen çalışmada sonlu elemanlar yöntemi kullanılarak polimer tabanlı malzemelerle tasarımı gerçekleştirilmiş olan sikloid redüktörlerin farklı devir/dakika'lardaki stres, gerinim ve yer değiştirme değerleri modellenerek incelenmiştir. Modellenen sikloid dişli boyutlarına uygun ve gerçekçi bir kuvvet yüklemesi yapabilmesi amacı ile, 12 V motorların da çalışma aralığında bulunan, 100, 200, 350 rpm hızları sonlu elemanlar analizi için uygun görülmüştür. Gerçekleştirilen analizlerle birlikte farklı polimer temelli malzemelerden üretilen sikloid dişli redüktörlerinin farklı yükler altındaki mekanik özellikleri birbirleri ile kıyaslanarak, gelecekteki çalışmalara zemin hazırlanması amaçlanmıştır.

2. Materyal ve Metot

Çalışma kapsamı bağlamında sikloid dişli profili ile gerçekleştirilecek olan sonlu elemanlar analizi için seçilen polimer malzemeler, literatürde de dişli imalatları için en sık yararlanılan polimer malzemeler olan Polihekzametien (Nylon) ve Polioksimetilen (Delrin) adı verilen termoplastiklerdir. Sertlik ve boyut hassasiyeti gerektiren küçük parça uygulamalarında sıklıkla kullanılan bu malzemeler imalat sonrasında aşınmaya ve kimyasal etkilere karşı dayanıklı olması sebebiyle literatür çalışmalarında sıklıkla kullanılmaktadır. Bu malzemeler aynı zamanda eklemeli imalatta kullanılan polimer filamentlerin temel elemanları arasında yer almaktadır. Nylon ve Delrin'in malzeme özellikleri Tablo 1'de gösterildiği üzeredir.

Tablo 1. Nylon ve Delrin malzeme özellikleri.

	Elastikiyet Modülü (N/m^2)	**Poisson Oranı**	**Gerilme Mukavemeti (N/m^2)**	**Akma Mukavemeti (N/m^2)**	**Kütle Yoğunluğu (g/cm^3)**	**Erime Sıcaklığı (^oC)**
Nylon	$8300x10^6$	0.28	$142,5x10^6$	$139x10^6$	1.15	~190
Delrin	$2900x10^6$	0.3	$40,7x10^6$	$63x10^6$	1.41	~170

Analizde kullanılan sikloid dişli redüktörü temek olarak 4 elemandan oluşmaktadır. Bu elemanlar Şekil 1'de görüldüğü üzere sırasıyla bir bakıma rulman görevi gören dış yatak (a), eksantrik hareket aktarımını ileten çıkış mili (b), dişli görevini üstlenen sikloid diş (c) ve son olarak tahrik mekanizmasından gelen gücün eksantrik biçimde dişliye aktarılmasını sağlayan giriş mili (d) olarak betimlenebilmektedir. Dış yatak toplam 9 yatak dişine sahiptir ve sikloid dişlinin hareket ekseni bu yatak dişlerinin değme noktalarına teğet olacak biçimdedir. Dış yatak iç yarıçapı 21 mm dış yarıçapı ise 30 mm olarak ayarlanmıştır. Yatak dişleri ise 3 mm yarıçapında ve 40'ar derecelik açılar ile yerleştirilmiştir. Sikloid dişli 10 mm et kalınlığına ve 8 adet diş eğrisine sahiptir. Diş eğrilerinin eğri üstü yarıçapı 23.42 mm, eğri altı yarıçapı ise 20.5 mm olarak alınmıştır. Çıkış miline uyumlu bir biçimde 90 derecelik açılarla merkeze 15 mm yarıçapı uzaklıkta 4 adet mil boşluğu bırakılmıştır. Giriş milinin merkezi ile sikloid dişli merkezi arasında 1.5 mm sapma bulunaktadır. Bu durum sistemin düzgün çalışması için ihtiyaç duyduğu eksantrikliği sağlamaktadır. Bu modelleme standart sikloid dişli şablonları yardımı ile yapılmıştır.

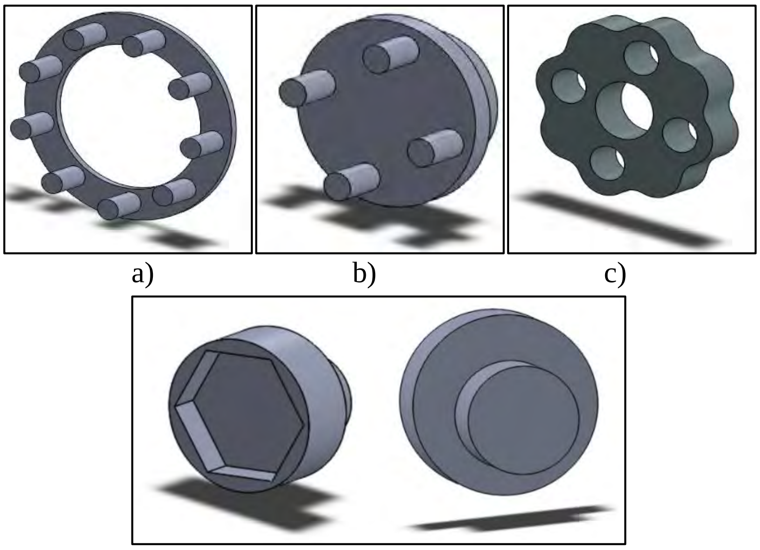

a) b) c)

d)

Şekil 1. Sikloid dişli redüktörünün temel elemanları

Şekil 2'de ise sikloid dişli redüktörünün montaj durumundaki görünümü görülmektedir. Çalışma verileri 80 W gücüne sahip 12 V ile çalışan bir tahrik motoru dikkate alınarak 100, 200, 350 rpm dönme hızlarında elde edilmiştir.

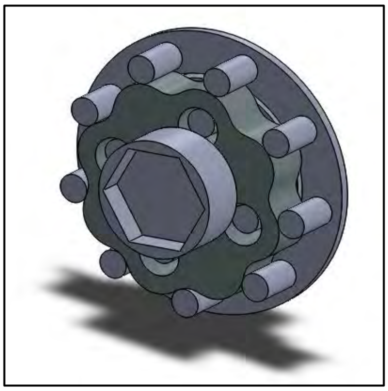

Şekil 2. Sikloid dişli redüktör montajı.

3. Sonlu Elemanlar Modeli

Modelleme, montaj ve sonlu elemanlar simülasyonları Solidworks programı aracılığı ile gerçekleştirilmiştir. Redüktör modellemesi standart sikloid dişli şablonları yardımı yapılmıştır. Montaj aşamasından sonra simülasyon işlemleri doğrusal olmayan dinamik yöntemi ile 100 adım ve 100 döngü için gerçekleştirilmiştir. Malzeme türü olarak nylon ve delrin seçilmiştir. 80 W gücüne sahip 12 V bir motorda 100,200 ve 350 rpm dönme hızlarının her biri için stres, yer değiştirme ve gerinim analizleri gerçekleştirilmiştir. Analizler sistem elemanlarının tümünün aynı malzemeden üretildiği varsayımı ile etüt edilmiştir. Analizin mesh yapısı Şekil 3'de verildiği üzeredir.

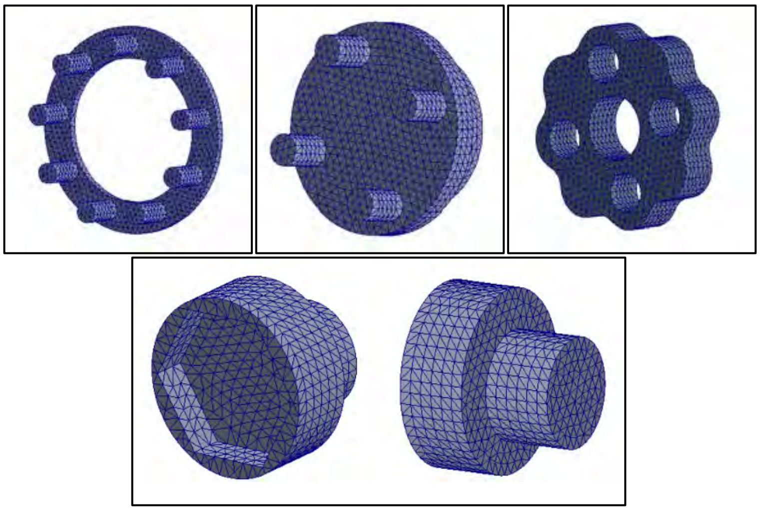

Şekil 3. Sonlu elemanlar analizi mesh yapısı.

4. Bulgular ve Tartışma

4.1. Stres Analizi

Çalışma kapsamında nylon ve delrin yapılı malzemelere sahip olan bir sikloid dişli redüktörünün sistem elemanları için 100, 200 ve 350 rpm hızlarındaki stres analizi gerçekleştirilmiştir. 100 rpm hızına sahip nylon temelli bir sikloid dişli redüktörü için elde edilen sonlu elemanlar modellemesi Şekil 4'de, yine aynı değere sahip delrin temelli bir redüktör için elde edilen modelleme yapısı ise Şekil 5'de gösterildiği üzeredir. Analiz sonuçları doğrultusunda nylon temelli modelleme için maksimum stres 115,2 N/m^2 olarak bulunurken, delrin malzemeye sahip modellemede maksimum stres 181,7 N/m^2 olarak bulunuştur.

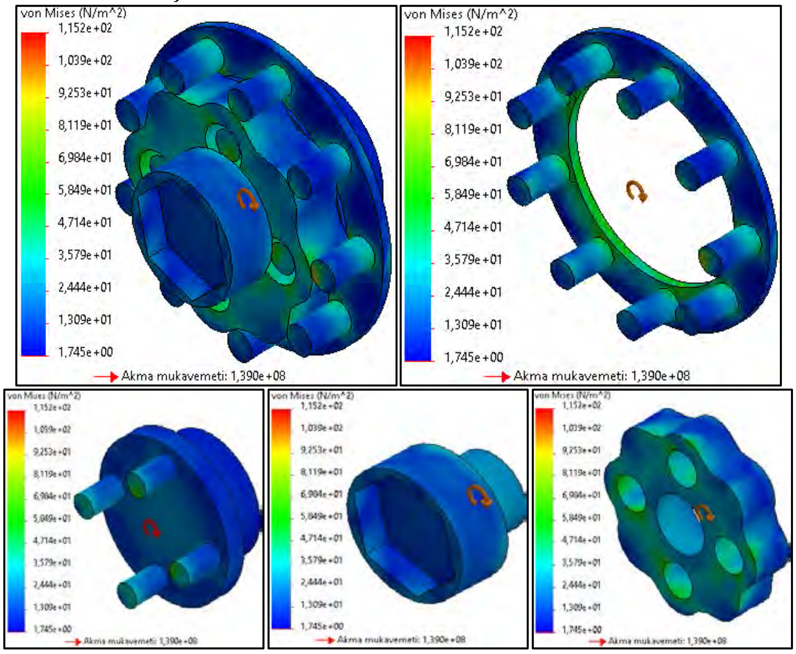

Şekil 4. 100 rpm hızında nylon temelli sikloid dişli için stres analizi.

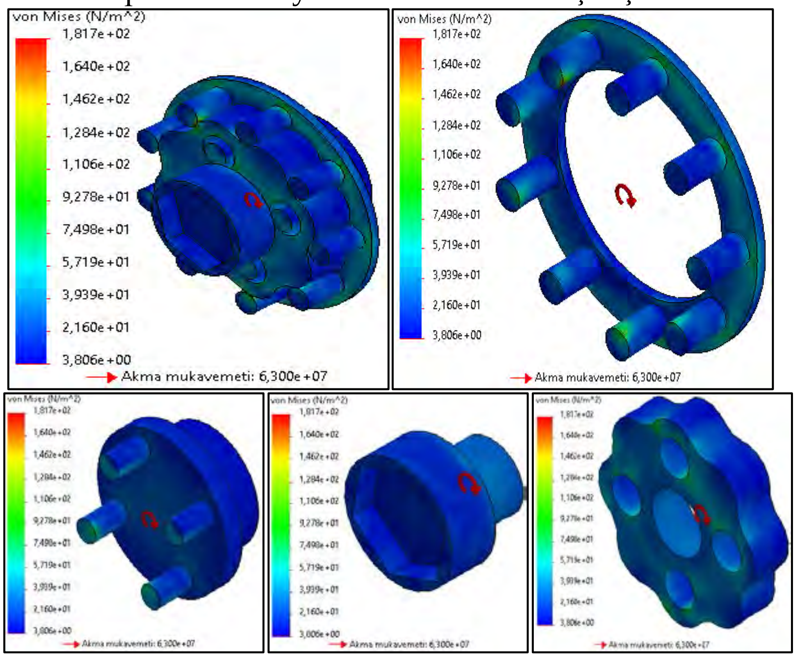

Şekil 5. 100 rpm hızında delrin temelli sikloid dişli için stres analizi.

200 rpm hızına sahip nylon temelli bir sikloid dişli redüktörü için elde edilen sonlu elemanlar modellemesi Şekil 6'de, yine aynı değere sahip delrin temelli bir redüktör için elde edilen modelleme yapısı ise Şekil 7'de gösterildiği üzeredir. Analiz sonuçları doğrultusunda nylon

temelli modelleme için maksimum stres 338,6 N/m^2 olarak bulunurken, delrin malzemeye sahip modellemede maksimum stres 418,5 N/m^2 olarak bulunuştur.

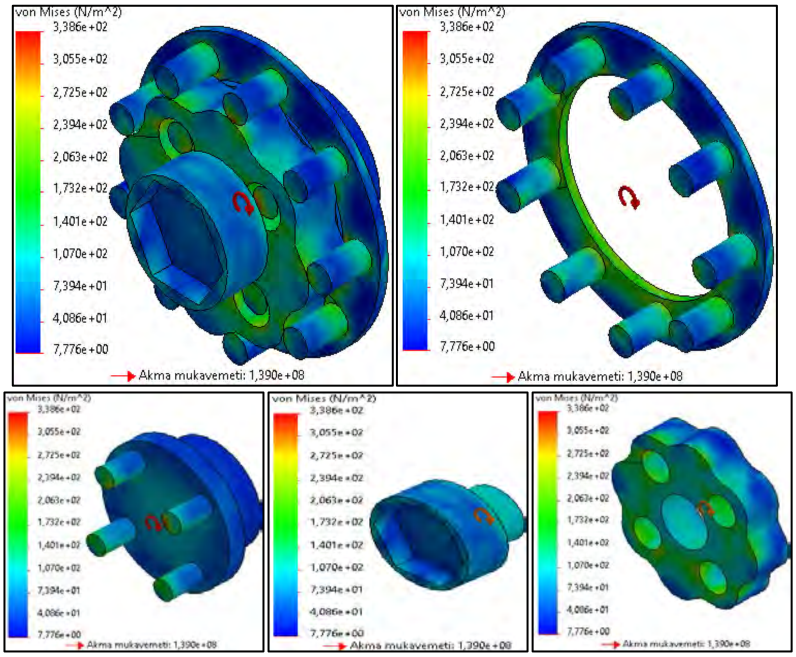

,

Şekil 6. 200 rpm hızında nylon temelli sikloid dişli için stres analizi.

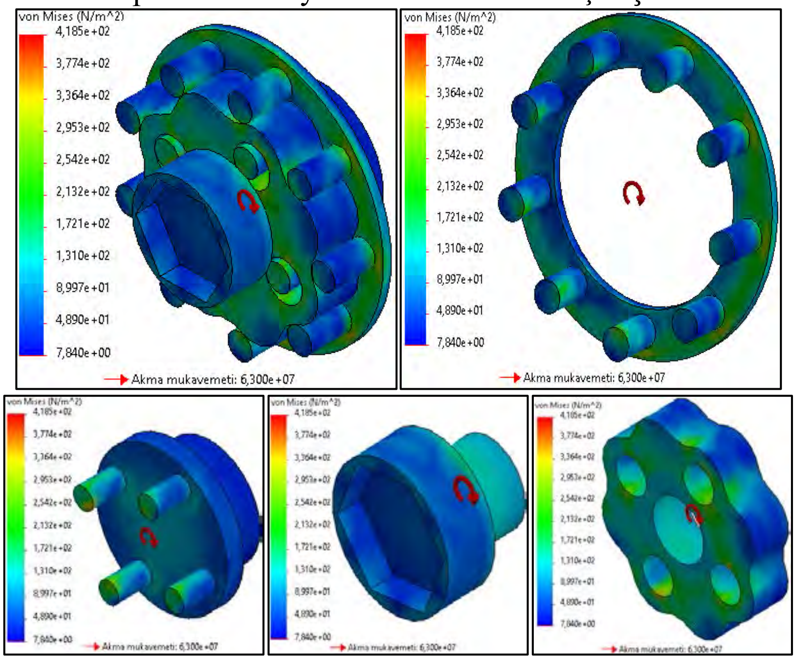

Şekil 7. 200 rpm hızında delrin temelli sikloid dişli için stres analizi.

350 rpm hızına sahip nylon temelli bir sikloid dişli redüktörü için elde edilen sonlu elemanlar modellemesi Şekil 8'de, yine aynı değere sahip delrin temelli bir redüktör için elde edilen modelleme yapısı ise Şekil 9'de gösterildiği üzeredir. Analiz sonuçları doğrultusunda nylon temelli modelleme için maksimum stres 1037 N/m^2 olarak bulunurken, delrin malzemeye sahip modellemede maksimum stres 1313 N/m^2 olarak bulunuştur.

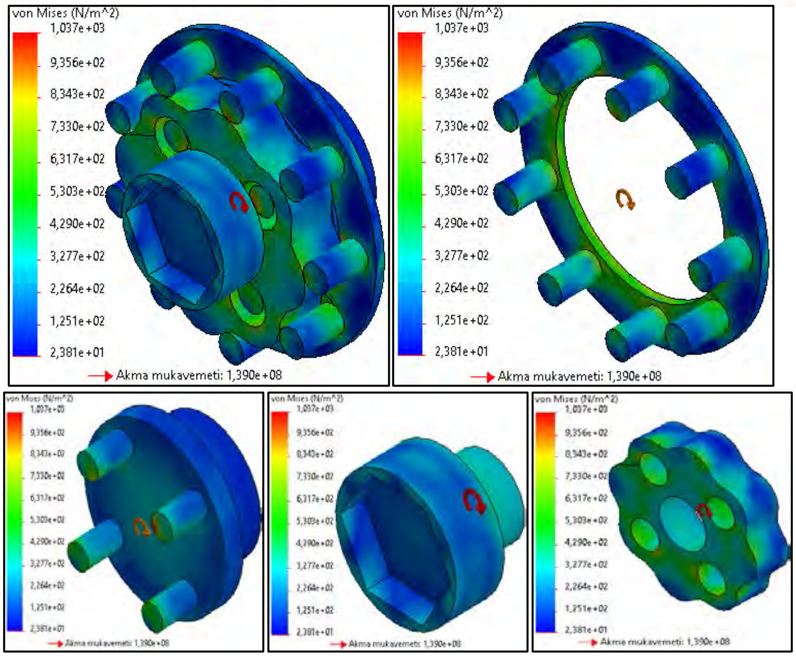

Şekil 8. 350 rpm hızında nylon temelli sikloid dişli için stres analizi.

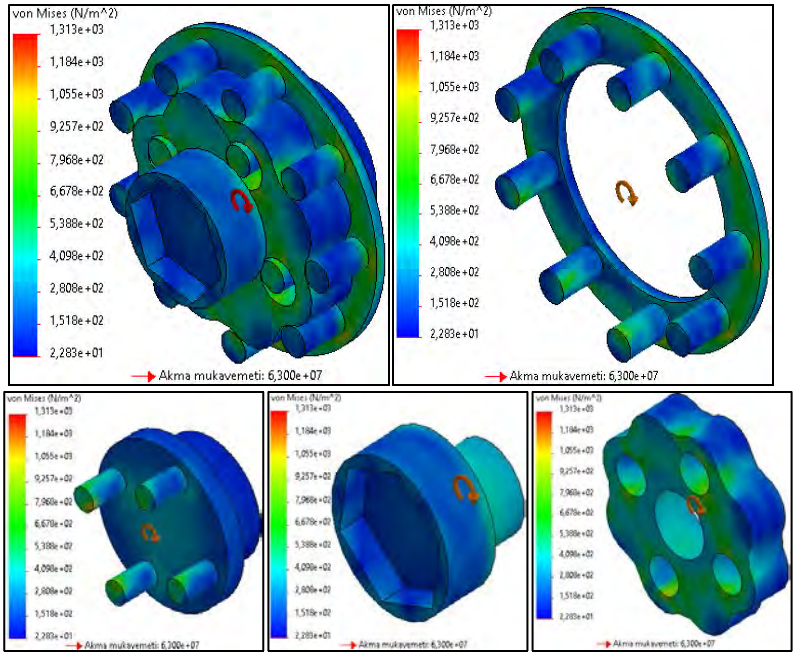

Şekil 9. 350 rpm hızında delrin temelli sikloid dişli için stres analizi.

Sonlu elemanlar yöntemi kullanılarak elde edilen stres analizi sonuçları Grafik 1'de gösterildiği üzeredir. Elde edilen sonuçlara göre ve malzeme özellikleri doğrultusunda da beklenildiği gibi, tüm rpm değerleri için maksimum stres değerinin delrin bazlı numunelerde daha yüksek olduğu ortaya çıkmaktadır. Aynı zamanda elde edilen grafik, dönme hızı artışı ile stres değeri artışlarının yaklaşık olarak aynı oranlarda gerçekleştiği çıkarımının yapılabilmesine olanak sağlamaktadır. Yine yapılan analizler doğrultusunda her iki malzeme tipine sahip numuneler için de en yüksek stres dağılımına sahip sistem elemanlarının dış yatak yüzeyi ve sikloid diş olduğu görülmektedir.

Grafik 1. Stres analizi sonuçları

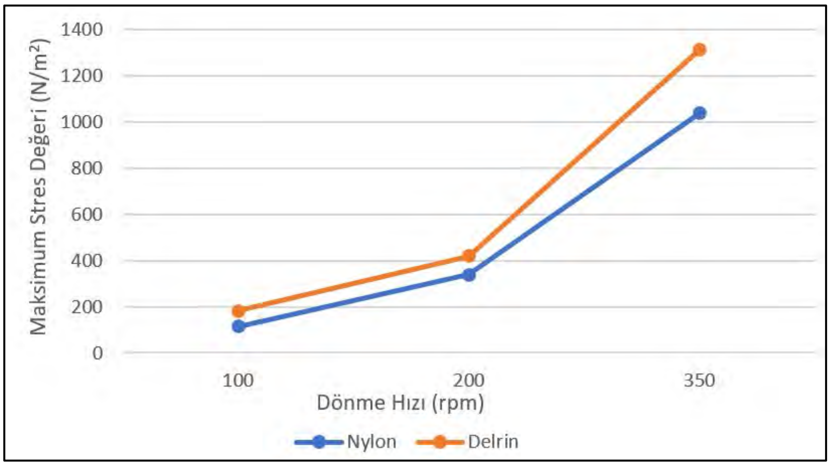

Grafik 1'deki değerler doğrultusunda açıkça görülmektedir ki her iki malzeme ve tüm rpm değerleri için elde edilen stres gerilmeleri kabul edilebilir sınırlar içerisinde yer almaktadır. Bu durum bizlere stres dayanımı noktasında termoplastik temelli sikloid dişli redüktörlerinin, metalik sikloid dişli redüktörlerine iyi bir alternatif oluşturabileceğini göstermektedir. Yine aynı zamanda termoplastik malzemelerin kütle yoğunluğunun, çelik veya dökme demir gibi metalik malzemelerin kütle yoğunluğundan yaklaşık 5 kat daha düşük olduğu göz önüne alındığında redüktör kütlesinden de oldukça büyük bir kazanç sağlanabileceği açıkça görülmektedir. Çalışmada tercih edilen iki polimer dikkate alındığında, delrin temelli polimer malzemelerin, nylon temelli polimer malzemelere kıyasla yarı yarıya daha uygun olduğu göze çarpmaktadır. Ancak öte yandan nylon hem kütlesel yoğunluğunun daha düşük olması hem de daha yüksek sıcaklıklara dayanabilmesi açısından delrinden daha avantajlı bir durumdadır. Gerekli çalışma koşullarının optimizasyonu neticesinde her iki malzemenin de sikloid dişli üretimi için iyi bir alternatif olabileceği görülmektedir.

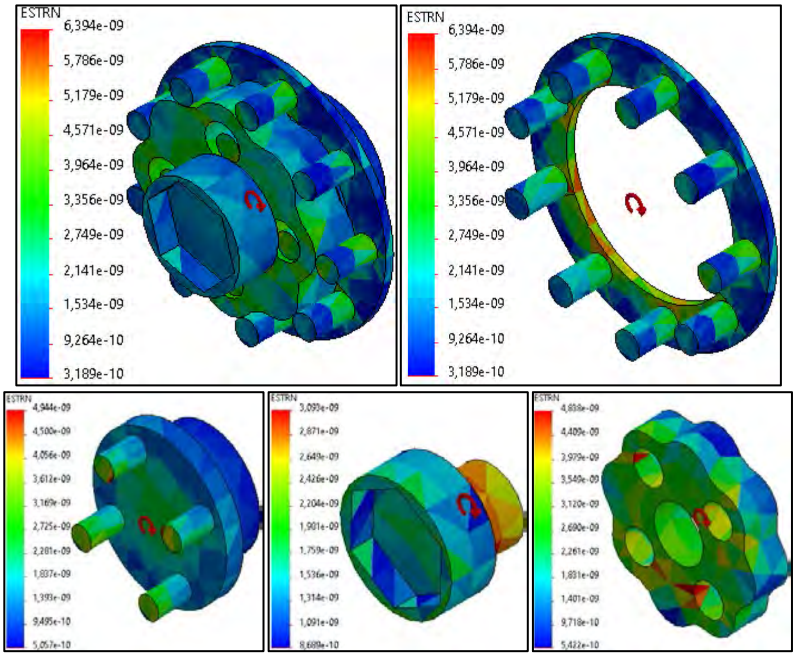

Şekil 10. 100 rpm hızında nylon temelli sikloid dişli için gerinim analizi.

4.2. Gerinim Analizi

Çalışma kapsamında nylon ve delrin yapılı malzemelere sahip olan bir sikloid dişli redüktörünün sistem elemanları için 100, 200 ve 350 rpm hızlarındaki gerinim analizi gerçekleştirilmiştir. 100 rpm hızına sahip nylon temelli bir sikloid dişli redüktörü için elde edilen sonlu elemanlar modellemesi Şekil 10'da, yine aynı değere sahip delrin temelli bir redüktör için elde edilen modelleme yapısı ise Şekil 11'de gösterildiği üzeredir. Analiz sonuçları doğrultusunda nylon temelli modelleme için maksimum gerinim $0{,}64x10^{-8}$ olarak bulunurken, delrin malzemeye sahip modellemede maksimum gerinim $2{,}46x10^{-8}$ olarak bulunuştur.

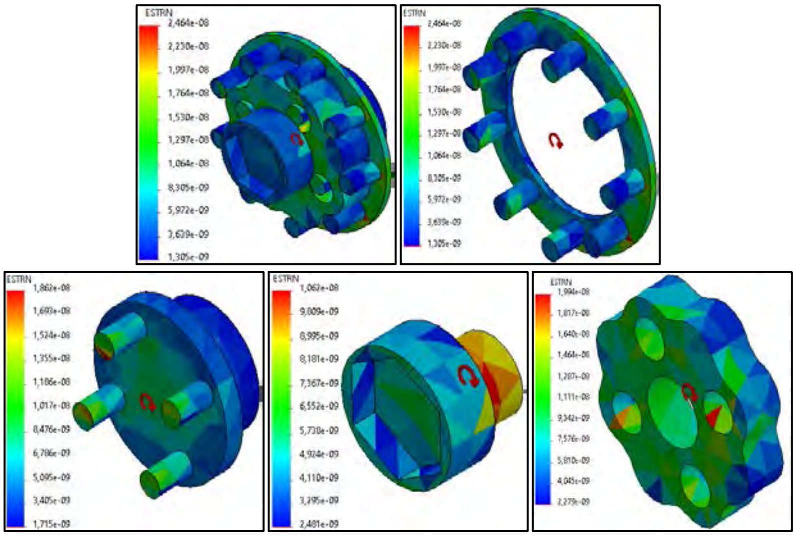

Şekil 11. 100 rpm hızında delrin temelli sikloid dişli için gerinim analizi.

200 rpm hızına sahip nylon temelli bir sikloid dişli redüktörü için elde edilen sonlu elemanlar modellemesi Şekil 12'de, yine aynı değere sahip delrin temelli bir redüktör için elde edilen modelleme yapısı ise Şekil 13'de gösterildiği üzeredir. Analiz sonuçları doğrultusunda nylon temelli modelleme için maksimum gerinim $2{,}58x10^{-8}$ olarak bulunurken, delrin malzemeye sahip modellemede maksimum gerinim $9{,}51x10^{-8}$ olarak bulunuştur.

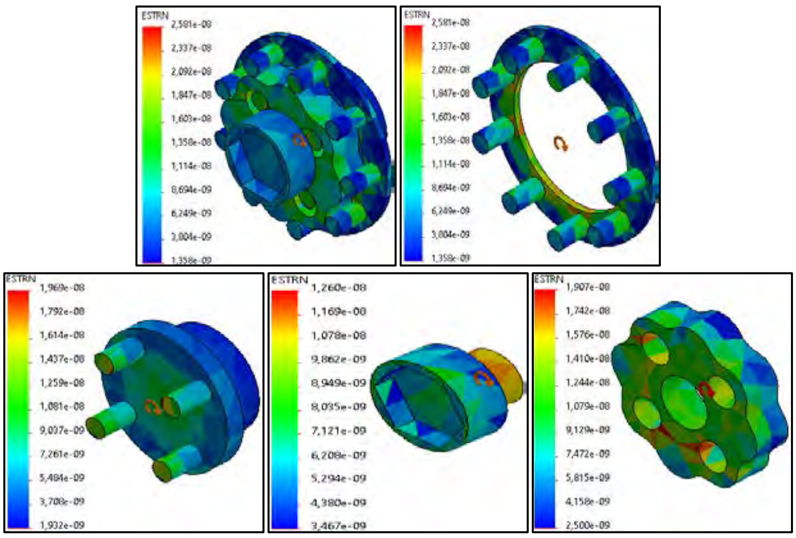

Şekil 12. 200 rpm hızında nylon temelli sikloid dişli için gerinim analizi.

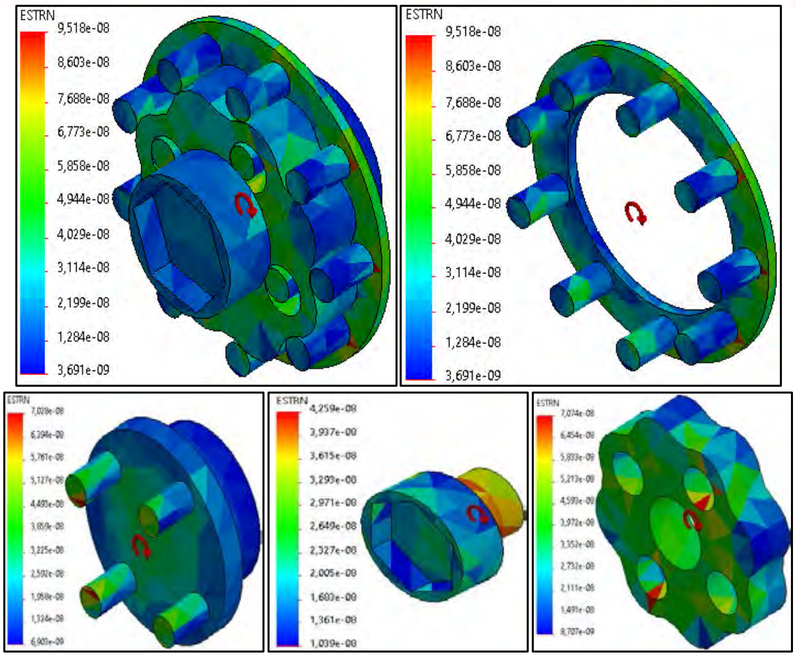

Şekil 13. 200 rpm hızında delrin temelli sikloid dişli için gerinim analizi.

350 rpm hızına sahip nylon temelli bir sikloid dişli redüktörü için elde edilen sonlu elemanlar modellemesi Şekil 14'de, yine aynı değere sahip delrin temelli bir redüktör için elde edilen modelleme yapısı ise Şekil 15'de gösterildiği üzeredir. Analiz sonuçları doğrultusunda nylon temelli modelleme için maksimum gerinim 7,90x10^{-8} olarak bulunurken, delrin malzemeye sahip modellemede maksimum gerinim 29x10^{-8} olarak bulunuştur.

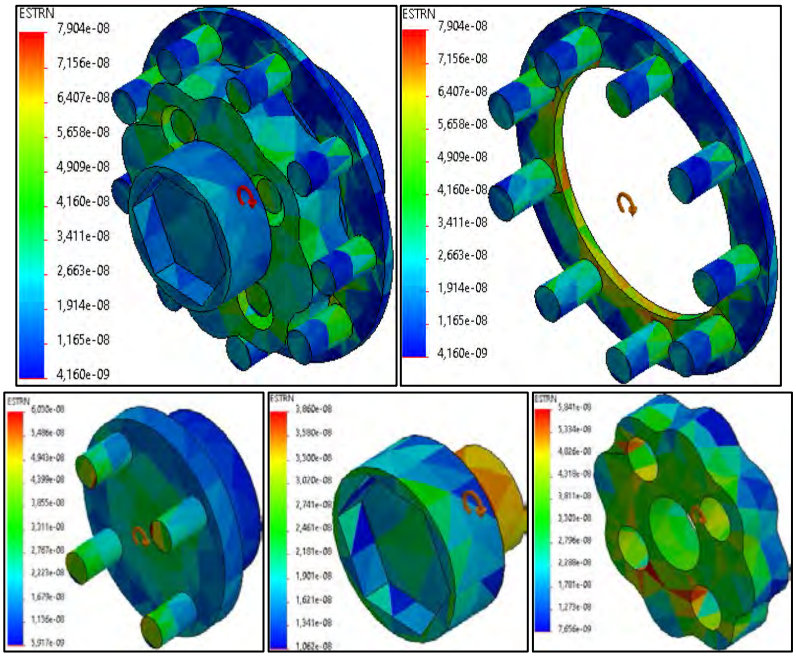

Şekil 14. 350 rpm hızında nylon temelli sikloid dişli için gerinim analizi.

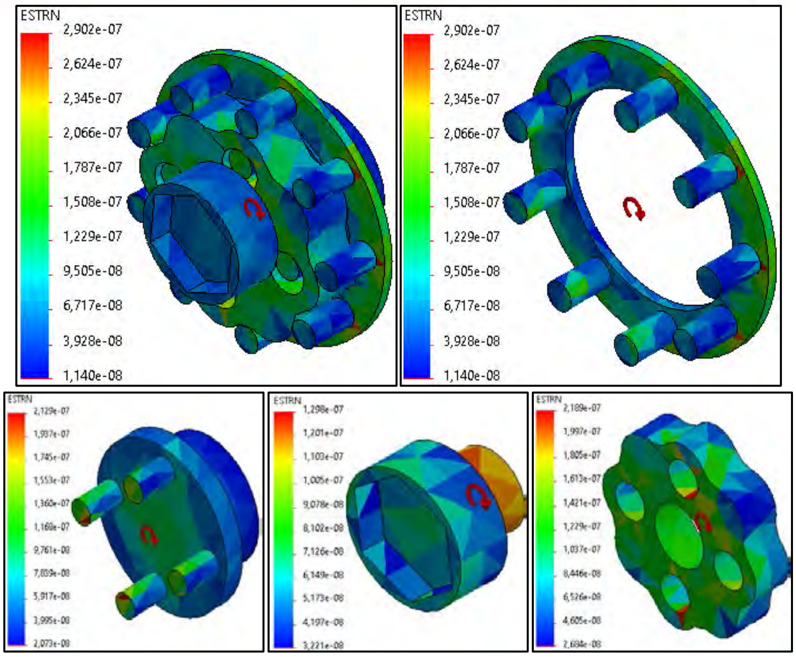

Şekil 15. 350 rpm hızında delrin temelli sikloid dişli için gerinim analizi.

Sonlu elemanlar yöntemi kullanılarak elde edilen stres analizi sonuçları Grafik 2'de gösterildiği üzeredir. Elde edilen sonuçlara göre ve malzeme özellikleri doğrultusunda da beklenildiği gibi, tüm rpm değerleri için maksimum gerinim değerinin delrin bazlı numunelerde daha yüksek olduğu ortaya çıkmaktadır. Aynı zamanda elde edilen grafik, gerinim değerleri artış oranının dönme hızı artış oranından daha yüksek değerlerde olduğu çıkarımının yapılabilmesine olanak sağlamaktadır. Yani dönme hızının lineer artışında gerinim oranı eksponansiyel artış eğilimine girmektedir. Yine yapılan analizler doğrultusunda her iki malzeme tipine sahip numuneler içinde en yüksek gerinim dağılımına sahip sistem elemanlarının sırsıyla dış yatak, sikloid dişli ve giriş milinin bağlantı kısımları olduğu görülmektedir.

Grafik 2. Gerinim analizi sonuçları

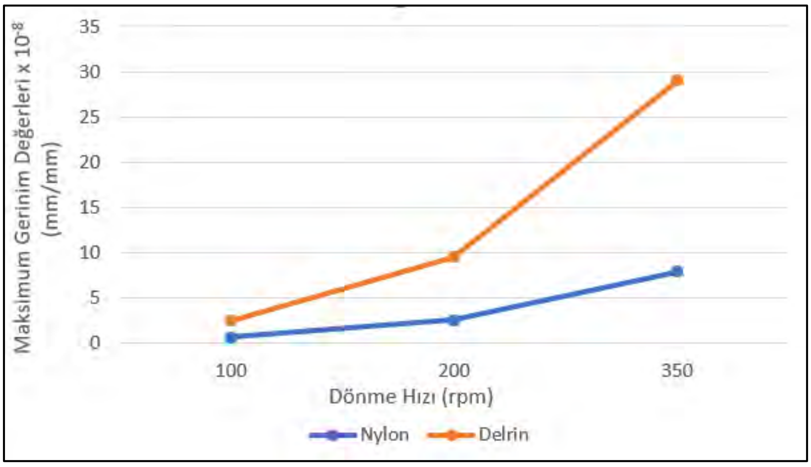

Grafik 2'deki değerler doğrultusunda açıkça görülmektedir ki her iki malzeme ve tüm rpm değerleri için elde edilen gerinim değerleri kabul edilebilir sınırlar içerisinde yer almaktadır. Bu durum bizlere gerinim dayanımı noktasında termoplastik temelli sikloid dişli redüktörlerinin, metalik sikloid dişli redüktörlerine iyi bir alternatif oluşturabileceğini göstermektedir.

4.3. Yer Değiştirme Analizi

Çalışma kapsamında nylon ve delrin malzemelere sahip olan bir sikloid dişli redüktörünün sistem elemanlarının yer değiştirme analizi 350 rpm değeri için gerçekleştirilmiştir.

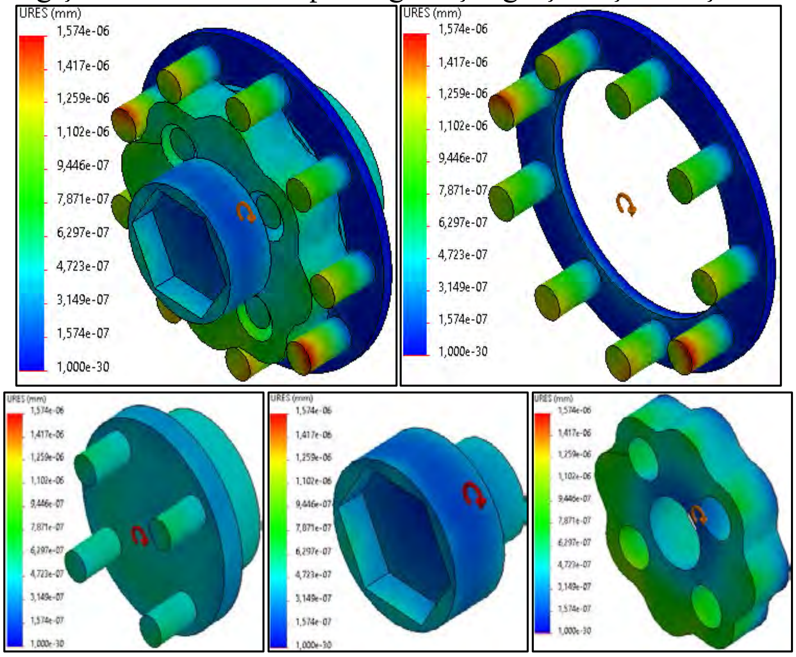

Şekil 16. 350 rpm hızında nylon temelli sikloid dişli için yer değiştirme analizi.

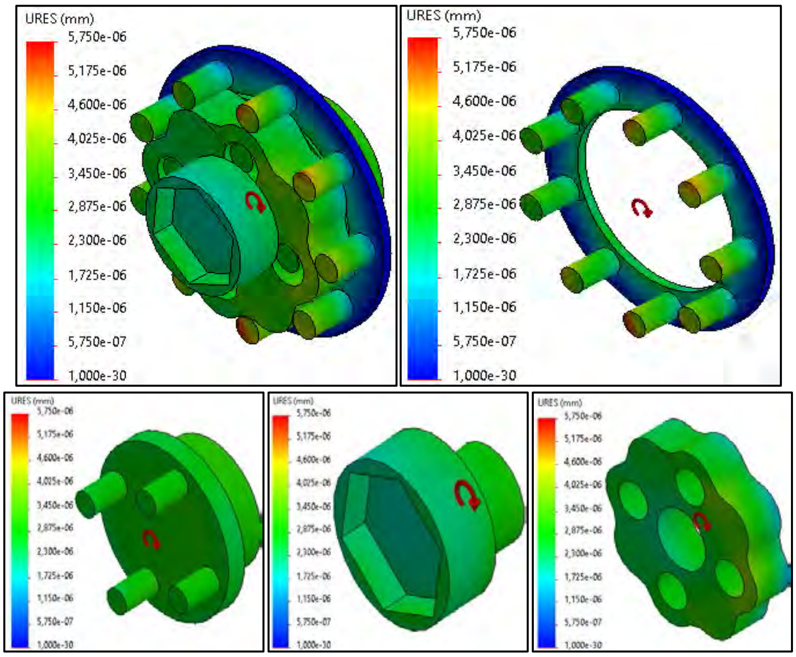

Şekil 17. 350 rpm hızında delrin temelli sikloid dişli için yer değiştirme analizi.

350 rpm hızına sahip nylon temelli bir sikloid dişli redüktörü için elde edilen sonlu elemanlar modellemesi Şekil 16'de, yine aynı değere sahip delrin temelli bir redüktör için elde edilen modelleme yapısı ise Şekil 17'de gösterildiği üzeredir. Analiz sonuçları doğrultusunda nylon temelli modelleme için maksimum gerinim $1{,}57\times10^{-6}$ mm olarak bulunurken, delrin malzemeye sahip modellemede maksimum gerinim $5{,}75\times10^{-6}$ mm olarak bulunuştur.

Sonlu elemanlar yöntemi kullanılarak elde edilen yer değiştirme analiz sonuçları, 350 rpm hız değeri için nylon ve delrin temelli malzemelerde gerçekleştirilmiştir. 100 ve 200 rpm hızlarındaki yer değiştirme oranı ihmal edilebilecek derecede küçük miktarlarda olduğundan dolayı çalışma verileri içerisinde gösterilmemiştir. Ancak 350 rpm hızına sahip numunelerin, redüktördeki olası yer değiştirmelerin hangi bölgelerde ve hangi oranlarda oluşabileceğinin gösterilmesi ve ayrıca redüktördeki kritik noktalar hakkında fikir vermesi açısından önemli olduğu düşünülmektedir. Analiz sonuçları dikkate alındığı zaman delrin temelli malzeme ile üretilmiş olan numunede daha yüksek miktarda yer değiştirme oranı oluşurken bu durum malzeme özellikleri doğrultusunda da beklenildiği gibi gerçekleşmiştir. Yine yapılan analizler doğrultusunda her iki malzeme tipine sahip numuneler içinde en yüksek yer değiştirme dağılımına sahip sistem elemanlarının sırasıyla dış yatak dişlileri, sikloid dişli, giriş milinin bağlantı kısımları ve çıkış milinin dişlileri olduğu görülmektedir.

5. Sonuçlar

Bu çalışmada geleneksel dişli imalatında da sıkça kullanılan polimerlerden olan nylon ve delrin esaslı malzemelere sahip bir sikloid dişli redüktörü modellendikten ve montajlandıktan sonra sonlu elemanlar analizi gerçekleştirilmiştir. Modelleme standart sikloid dişli şablonları yardımı yapılmıştır. Modellenen sikloid dişli boyutlarına uygun ve gerçekçi bir kuvvet yüklemesi yapabilmesi amacı ile, 12 V motorların da çalışma aralığında bulunan, 100, 200, 350 rpm hızları sonlu elemanlar analizinde parametre değerleri olarak tercih edilmiştir. Simülasyonlar Solidworks Simülation programı yardımıyla ve doğrusal olmayan dinamik modelleme etüdü ile 100 adım ve 100 döngü için gerçekleştirilmiştir.

Elde edilen sonuçlar ve bu sonuçlar ile oluşturulan grafikler doğrultusunda açıkça görülmektedir ki her iki malzeme ve tüm rpm değerleri için elde edilen stres, gerinim ve yer değiştirme değerleri kabul edilebilir sınırlar içerisinde yer almaktadır. Bu durum bizlere termoplastik temelli sikloid dişli redüktörlerinin, metalik sikloid dişli redüktörlerine iyi bir alternatif oluşturabileceğini göstermektedir. Yine aynı zamanda termoplastik malzemelerin kütle yoğunluğunun, çelik veya dökme demir gibi metalik malzemelerin kütle yoğunluğundan yaklaşık 5 kat daha düşük olduğu göz önüne alındığında redüktör kütlesinden de oldukça büyük bir kazanç sağlanabileceği açıkça gözükmektedir. Çalışmada tercih edilen iki polimer dikkate alındığında, delrin temelli polimer malzemelerin, nylon temelli polimer malzemelere kıyasla yarı yarıya daha uygun maliyetli olduğu göze çarpmaktadır. Ancak öte yandan nylon hem kütlesel yoğunluğunun daha düşük olması hem de daha yüksek çalışma sıcaklığı değerlerine ulaşabiliyor olması tercih sebebi olabilmektedir. Yine çalışma sonuçları neticesinde nylon esaslı redüktörün tüm deney parametrelerinde delrinden daha iyi sonuçlar vermesi nylon esaslı redüktörleri, delrin esaslı redüktörlerden daha avantajlı bir duruma getirmektedir.

Gerçekleştirilen bu çalışmada, gerekli çalışma koşullarının optimizasyonu sağlanarak her iki termoplastik malzemenin de sikloid dişli üretiminde metalik esaslı redüktörler için iyi bir alternatif olabileceği literatüre katkı sağlaması amacıyla sunulmuştur. Göze çarpan olası bir diğer yöntemin ise kritik redüktör elemanlarının imalatlarının nylon esaslı, diğer elemanların ise delrin esaslı malzemelerden üretilerek optimizasyonun sağlanabilecek olabilmesidir.

6. Kaynakça

1. Blagojević M, Marjanović N, ĐORĐEVIĆ Z, STOJANOVIĆ B. STRESS AND STRAIN STATE OF SINGLE–STAGE CYCLOIDAL SPEED REDUCER. In: The 7th International Conference Research And Development Of Mechanical Elements And Systems IRMES-2011. 2011. p. 553–8.

2. Li T, An X, Deng X, Li J, Li Y. A new tooth profile modification method of cycloidal gears in precision reducers for robots. Appl Sci. 2020;10(4):1266.
3. Li K, Bird J, Kadel J, Williams W. A flux-focusing cycloidal magnetic gearbox. IEEE Trans Magn. 2015;51(11):1–4.
4. Bao J, He W, Lu Q, Li L. Research of output-pin-wheel cycloid drive reducer. In: 2010 WASE International Conference on Information Engineering. IEEE; 2010. p. 307–10.
5. Chu X, Xu H, Wu X, Tao J, Shao G. The method of selective assembly for the RV reducer based on genetic algorithm. Proc Inst Mech Eng Part C J Mech Eng Sci. 2018;232(6):921–9.
6. Blanche JG, Yang DCH. Cycloid drives with machining tolerances. 1989;
7. Cihan Ö, ORTAÇ Y, GÜRGENÇ T. Yağ Pompasında Kullanılan Sikloidal Dişlilerin Parmak Freze ile CNC Freze Tezgâhlarında İmalatının Araştırılması. Fırat Üniversitesi Mühendislik Bilim Derg. 2017;29(2):97–110.
8. Lai T-S. Design and machining of the epicycloid planet gear of cycloid drives. Int J Adv Manuf Technol. 2006;28(7):665–70.
9. Li H, Tang Z, Liu Z, Zhi C. Evaluating flexibility and wearability of flexible energy storage devices. Joule. 2019;3(3):613–9.
10. Wu K-Y, Shih Y-P, Lee J-J. Kinematic error analysis of the rotor vector gear reducer with machining tolerances. J Brazilian Soc Mech Sci Eng. 2020;42(11):1–16.
11. Wang R, Gao F, Lu M, Liu T. Meshing efficiency analysis of modified cycloidal gear used in the RV reducer. Tribol Trans. 2019;62(3):337–49.
12. Bo W, Jiaxu W, Guangwu Z, Rongsong Y, Hongjun Z, Tao H. Mixed lubrication analysis of modified cycloidal gear used in the RV reducer. Proc Inst Mech Eng Part J J Eng Tribol. 2016;230(2):121–34.
13. Biernacki K. New construction of cycloidal gear unit made of plastics. Proc Inst Mech Eng Part C J Mech Eng Sci. 2021;235(5):800–11.
14. Biernacki K. Selection of the optimum tooth profile for plastic cycloidal gears. Proc Inst Mech Eng Part C J Mech Eng Sci. 2014;228(18):3395–404.
15. Krawczyk J, Stryczek J. Construction and experimental research on plastic cycloidal gears used in gerotor pumps. In: Fluid Power Systems Technology. American Society of Mechanical Engineers; 2014. p. V001T01A006.

Farklı Isıl İşlem Sıcaklıklarının Boraks Takviyeli Alüminyum Metal Matris Kompozitler Üzerindeki Korozyon Davranışına Olan Etkisi

Suat ÖNAL

Osmaniye Korkut Ana Üniversitesi, Osmaniye Meslek Yüksek Okulu, Osmaniye, Türkiye

Abstract

Günümüzde alüminyum alaşım ve kompozitlerinin düşük yoğunluk ve yüksek mukavemet özelliklerinden dolayı endüstrideki kullanımı giderek artmaktadır. Alüminyum bazlı metal matris kompozitler otomotiv, havacılık ve nükleer endüstrilerde büyük ilgi görmektedir. Al bazlı metal matris kompozitleri kullanmanın ana zorluklarından biri, takviye partiküllerinin korozyon direnci üzerindeki etkisidir. Bu çalışmada karıştırarak döküm yöntemi ile üretilmiş %15 boraks takviyeli alüminyum bazlı metal kompozitin korozyon davranışı incelenmiştir. Korozyon davranışı incelenecek numuneler soğuk olarak haddelendikten sonra farklı sıcaklıklarda ısıl işleme tabi tutulmuşlardır. Korozyon testleri tuz ortamında gerçekleştirilmiştir. Karakterizasyon çalışmalarıyla birlikte ısıl işlem sıcaklıklarının boraks takviyeli alüminyum metal matris kompozitlere olan etkileri araştırılmıştır.

Anahtar Kelimeler: Metal Matrisli Kompozitler, Alüminyum, Boraks, Korozyon

1. Giriş

Alüminyum ve alaşımları yaygın olarak kullanılan ve endüstrinin neredeyse her alanında sıkça karşılaşılan bir malzeme grubudur. Bu malzeme grubunun bu kadar yaygın olarak kullanılmasının en önemli sebeplerinden birisi düşük yoğunlukla birlikte yüksek mukavemete sahip olmasıdır [1]. Bununla birlikte alüminyum alaşımlarının yüzeyinde oluşan alüminyum oksit tabakasının sağladığı korozyon direnci bu talebi ciddi oranda etkilemektedir. Alüminyum takviye elementlerle alaşım hale getirildiğinde mekanik özellikleri ciddi oranda değişmektedir[2,3]. Piyasada çokça karşılaşılan alaşımlarda kullanılan elementler başlıca bakır, silisyum, magnezyum ve çinko olarak gösterilebilir.

Son dönemlerde metal, seramik veya organic bileşiklerle güçlendirilmiş alüminyum metal matrisli kompozitler dikkat çekmektedir. Metal matris kompozitler döküm, sürtünmeli karıştırma tekniği, basınçlı infiltrasyon, toz metalurjisi, elektrodepozisyon ve eklemeleri imalat yöntemleri gibi tekniklerle üretilebilmektedir [4]. Mevcut alaşımı güçlendirme amaçlı kullanılan takviye elemanları, alüminyum matris içerisinde dağıtılarak kullanılmaktadır. Günümüzde bu tip kompozit malzemeler düşük termal genişleme, yüksek mukavemet ve düşük yoğunluklara sahip olduklarından endüstride bir çok alanda kullanılmaktadır [5]. Yılmaz ve arkadaşları [6], 1000 °C altında farklı oranlarda B_4C takviyesi ve farklı bekleme sürelerinde üretilmiş alüminyum metal matris kompozitlerin mekanik özellikleri araştırmışlardır. %20 oranında B_4C takviyeli alüminyum matris kompozitin ergimiş halde 45 dakika bekletilmesiyle darbe mukavemetinde saf alüminyuma

kıyasla %100 lük bir artış sağlandığını gözlemlemişlerdir. Pul [7], farklı oranlarda SiC, B_4C ve TiB_2 takviyesinin Alüminyum 7075 matrisli metal kompozitlerde mekanik özelliklere olan etkisini araştırmıştır. Çalışmada takviye oranlarının artışına bağlı olarak gözeneklerin oluştuğu ve bunun mekanik özelliklere etkilerinin olduğu gözlemlenmiştir. Üç takviye elemamanında da en yüksek sertlik değerinin ağırlıkça %20 olduğu numunelerde ortaya çıktığı tespit edilmiştir. Mazahery ve arkadaşları [8], nano seviyede Al_2O_3 takviyesinin alüminyum metal matrisli kompozitlerde olan mekanik özelliklerini araştırmışlardır. Sharma ve arkadaşları, alüminyum 6082 matrisli kompozitlerde grafen takviyesinin mekanik özelliklere iyi gelmediğini göstermişlerdir [9].
Metal matrisli kompozitlerde destek elemanı olarak bor türevleri yaygın olarak kullanılmaktadır. En bilinen bor türevli destek elemanları B_4C, AlTiB, BN ve boraks olarak görülmektedir [10–12]. Yılmaz ve Öztürk [13] farklı sıcaklık, bekleme süresi ve farklı oranda boraks oranı kullanarak bir çalışma gerçekleştirmiştir. Gerçekleştirdiği çalışmada optimum parametreleri mekanik test sonuçlarına göre belirlemiştir. Ayrıca, gerçekleştirilen çalışmada Al-B bileşiminin alüminyum mikroyapısında ortaya çıktığını gözlemlemiştir. Şu an ki çalışmada, bulunan optimum üretim parametreleri kullanılarak döküm işlemi gerçekleştirilmiştir. Döküm işlemi gerçekleştirilerek üretilen numuneler üzerinde haddeden geçirilerek farklı sıcaklıklarda ısıl işlem sıcaklıklarının etkisi araştırılmıştır.

2. Materyal ve Yöntem

Çalışmada kullanılan ticari olarak ağırlıkça %99.95 saflıkta alüminyum kullanılmıştır. Matrisi güçlendirmek üzere %10 oranında boraks tozu kullanılmıştır. Alüminyum külçeler, döküm işlemi öncesinde yüzeyindeki kirleticileri gidermek için asetonlu ultrasonik banyoda temizlendi. Döküm işlemi, elektrik rezistanslı bir fırında 1000 °C altında 45 dakika bekletilerek gerçekleştirilmiştir. Ergitme işlemi esnasında alüminyum külçeler ve boraks tozu gafit pota içerisinde ısıltıldı. Kullanılan prosedür ve parametreler bir önceki çalışmanın optimum parametrelerinden alınmıştır. Döküm cürufu ergimiş alümünyum ve boraks karışımın yüzeyinden alındıktan sonra yaklaşık 20 saniye kadar karıştırılmak üzere grafit çubuk kullanıldı. Karıştırma işleminden sonra ergiyen metal hemen kokil kalıba döküldü.
Boraks takvieli alüminyum metal matrisli kompoziti, sertleştirilmiş bir silindir ile haddelenmiştir. Gerçekleştirilen soğuk hadde işleminden sonra dökümden elde edilen boraks takviyeli alüminyum metal matrisli kompozitin kalınlığı 2 mm olarak ölçüldü. Elde edilen haddelenmiş numune 2x2 cm olacak şekilde eşit boylarda kesilmiştir. Yeniden kristalleştirme işleminin gerçekleşebilmesi için numuneler 60 dakika süre ile farklı sıcaklıklar altında (290 °C, 320 °C, 350 °C, 380 °C, 410 °C, 440 °C ve 470 °C) ısıl işlem fırınında tutulmuştur. Her farklı sıcaklık için üç farklı numune ısıl işleme tabi tutulmuştur. Isıl işlem sonrası tüm numuneler oda sıcaklığında soğutuldu.
Mikroyapısal analizlerin gerçekleştirilebilmesi için numuneler ilk olarak bakalite alınmıştır. Bakalite alınan numuneler sırasıyla 240, 600, 800, 1000 ve 200 mesh SiC zımpara kağıtları ile zımparama işleminden geçirilmiştir. 6µ elmas süspansiyon yardımı ile parlatma çuhası yardımı ile ışığı yansıtan yüzeye sahip numuneler elde edilmiştir. Zımparalama ve parlatma işlemlerinde Forcipol 2V zımparalama ve parlatma makinesi kullanılmıştır. Mikroyapının görünebilmesi için son adım olan dağlama işleminde numuneler 0.5 ml hidrofilorik içeren 100 ml saf su karışımı içerisinde 45 saniye kadar bekletilmiştir. Dağlama işlemi sonrasında alkol ile yıkanan yüzeyler hava kurutma makinesi ile kurutulmuştur. Mikroskobik analizler için Nikon LV150Nl optic mikroskop kullanılmıştır. Çalışmada kullanılan bir diğer analiz ise XRD analizidir. Isıl işleme tabi

tutulan numuneler XRD analizleri Sütçü İmam Üniversitesi bünyesinde bulunan ÜSKİM labaratuvarında bulunan Cu-Kα radyasyonu kullanan Panalytical X'Pert Pro MPD cihazı kullanılmıştır. Difraksiyon grafikleri 20°≤2θ≤90° açıları arasında 0.44ºdk^{-1} tarama hızında kaydedilmiştir. Korozyon çalışmaları AMETEK VERSASTAT 3-200 potentiostat cihazı ve döngüsel polarizasyon tekniği oda şartlarında kullanılarak gerçekleştirilmiştir. Döngüsel polarizasyon tekniğinde saf su içerisinde ağırlıkça %3.5 oranında NaCl karışımı elektrolit olarak kullanılmıştır. Gümüş/gümüş klorür elektrodu voltajı ölçmek üzere kullanılmıştır. Testten önce tüm numuneler saf su ile temizlenmiştir. Döngüsel polarizasyon işlemi -1 V ile +1 V arasında 2mV/s tarama hızında iki döngü olarak gerçekleştirilmiştir. Sertlik ölçümleri oda sıcaklığı altında Vickers elmas piramidi 0.2 kg yük uygulanarak gerçekleştirildi. Testlerde LHV-1 Micro Vickers test cihazı kullanılmıştır. Her bir numune için 5 farklı ölçüm gerçekleştirilip ortalamaları alınmıştır.

3. Bulgular ve Tartışma

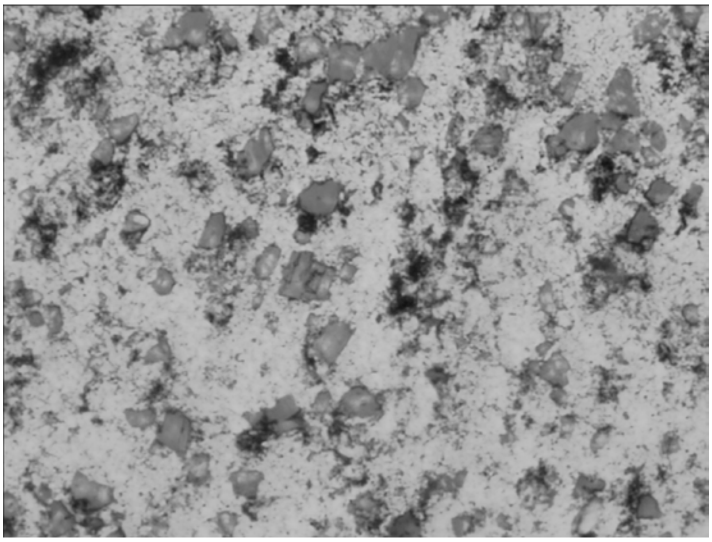

Şekil 1. Boraks ile güçlendirilmiş alüminyum metal matris kompozitin mikroskobik görüntüsü

Şekil 1 boraks takviyeli alüminyum metal matrisli kompozitin mikroskobik görüntüsünü vermektedir. Görüntü 1000x büyütme kullanarak alınmıştır. Boraks parçacıkları gri ve köşeli partiküller halinde görülmektedir. Mikroskobik görüntüde boraks partiküllerinin homojen olarak dağılım gösterdiği görülmektedir.

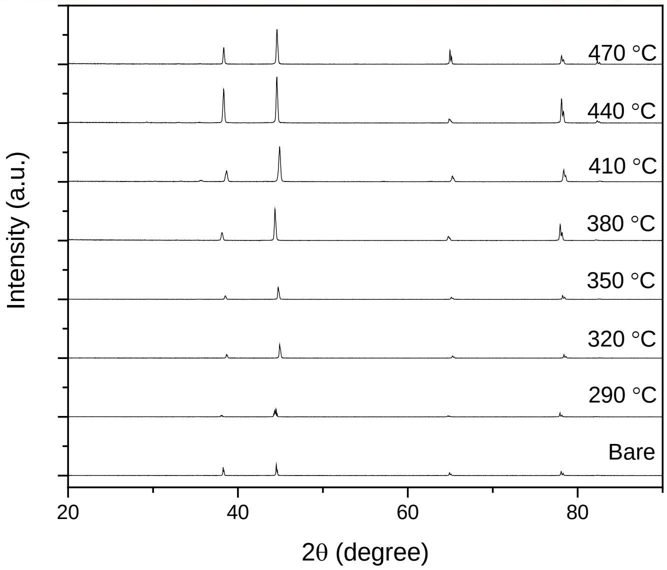

Şekil 2. Isıl işlem görmemiş ve farklı sıcaklıklarda ısıl işlem görmüş numunelere ait XRD grafikleri

Isıl işlem görmemiş ve ısıl işlem görmüş kompozit numunelerin XRD grafikleri Şekil 2 de verilmiştir. Tüm numunelere ait X-ışını kırınımları incelendiğinde dört farklı pik belirgin olarak gözükmektedir. Bu piklere ait açılar sırasıyla 38.85°, 44.72°, 64.85° ve 78.14° olarak görülmüştür. Bu piklere ait kristal yapısının hekzagonal yapıda olduğu düşünülmektedir. Belirlenen piklerin literatürde alüminyum a ait X-ışını piklerine ait olduğu saptanmıştır. Yine bu piklere ait yönelimler sırasıyla (111), (200), (220) ve (311) olduğu görülmüştür [14]. Isıl işlem sıcaklıklarının artmasıyla X-ışını kırınımlarında karşılaşılan pikler incelendiğinde malzemedeki kristal yoğunluğunun arttığı gözlenmektedir. Bununla birlikte AlB_2 ye ait bir pike rastlanmamıştır. Bu durum mikroyapı analizi ile birlikte değerlendirildiğinde boraks takviyeli alüminyum metal matrisli kompozitin üretiminde AlB_2 bileşiği oluşmadığı ve malzemenin alaşımdan ziyade kompozit olduğu gözlenmiştir.

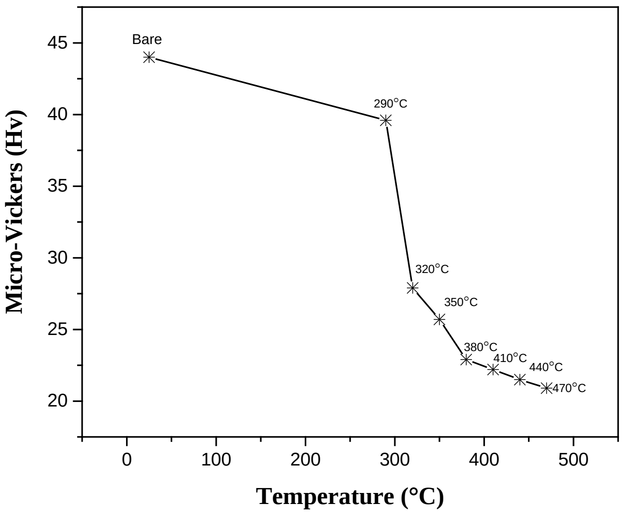

Şekil 3. Farklı sıcaklıklar altında ısıl işleme tutulmuş numunelerin sertlik grafiği

Sertlik değerleri Şekil 1'de gösterildi. Soğuk haddelenmiş alüminyum boraks bileşiğinin sertlik değeri 44 Hv ölçüldü. 290, 320, 350, 390, 410, 440 ve 470 °C'de tavlama işlemlerinden sonra sertlik ölçümleri için diğer sertik sonuçları 39.6, 27.9, 25.7, 22.9, 22.2, 21.5, 20.9 Hv olarak elde edildi. Sonuçlar dikkate alındığında ısıl işlem sıcaklığının artmasının hadde sonrası sertliği azalttığı tespit edilmiştir. Sertlik değeri 290 °C tavlama sıcaklığı uyglandığında diğer sıcaklıklara nazaran önemli ölçüde sertlik düşüşü gözlenmemiştir. 320 °C de gerçekleşen ısıl işlem sonrasında sertlik değerlerinde ciddi bir kırınım görülmüştür. Bu sıcaklığın üzerinde gerçekleşecen sıcaklıklarda ölçülen sertlik değerlerinde bir miktar azalma olduğu görüldü. Yüksek sıcaklıklardaki ısıl işlemlerin, soğuk haddeleme işlemi sonucunda oluşan numunelerin sertliğini düşürdüğü kaydedildi.

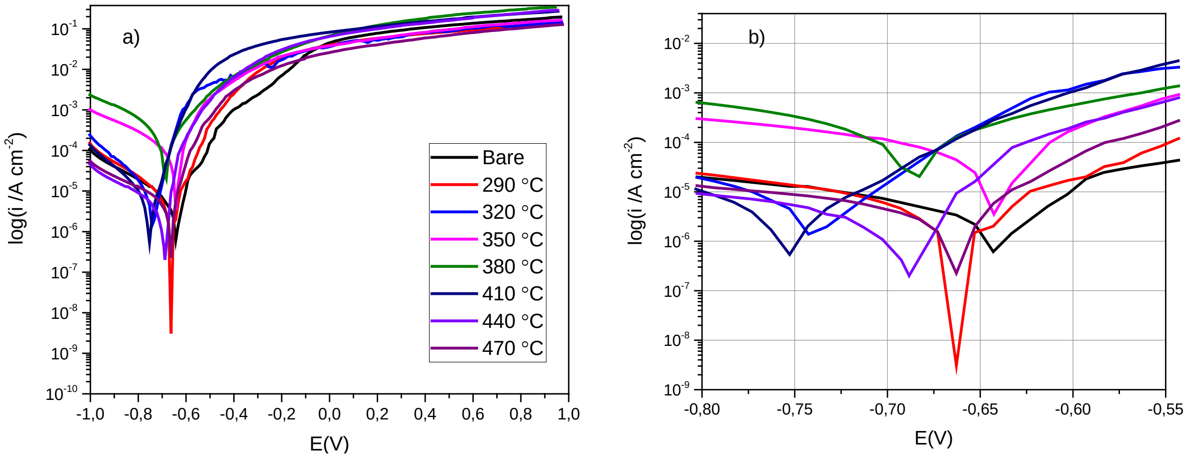

Şekil 4. a) Tafel polarizasyon eğrilerinin farklı ısıl işlem sıcaklıklarına bağlı ilk döngüsü **b)** Tafel polarizasyon eğrilerinin yakınlaştırılmış görüntüsü

NaCl korozif ortamında uygulanan boraks takviyeli alüminyum kompozit malzemelerin negatif yönden pozitif yöne doğru oksidasyonuna ait Tafel grafiği Şekil 4a ve Şekil 4b ile gösterilmiştir. Şekil 4b numunelere ait E_{corr} ve I_{corr} değerlerinin daha iyi anlaşılabilmesi için verilmiştir. Grafikten elde edilen verilerin sayısal değerleri Tablo 1 de verilmiştir.Tablo 1 de gösterilen akım yoğunluğu (I_{corr}) değerleri test edilen numunelern Tafel grafindeki polarizasyon eğrilerinin anodik ve katodik dallarının kesiştiği noktadan elde edilir. Korozyon potensiyel (E_{corr}) değerleri ise anodic ve katodik eğrilerin uzatılması ile elde edilen noktadan bulunur.

İlk Tafel eğrisinde en düşük korozyon potansiyeli ısıl işlem görmemiş metal matrisli kompozit numunede -0.642 V olarak bulunmuştur. 290 ℃, 320 ℃, 350 ℃, 380 ℃, 420 ℃, 450 ℃ ve 470 ℃ altında ısıl işlem görmüş numunelerde sırasıyla -0.642 V, -0.664 V, -0.743 V, -0.643 V, -0.683

V, -0.753 V, -0.689 V ve -0.662 V olarak bulunmuştur. Korozyon akım değerleri ise ısıl işlem görmemiş, 290 ℃, 320 ℃, 350 ℃, 380 ℃, 420 ℃, 450 ℃ ve 470 ℃ altında ısıl işlem görmüş numunelerde sırasıyla 1.76 µA cm^{-2}, 0.24 µA cm^{-2}, 3.05 µA cm^{-2}, 15.1 µA cm^{-2}, 45.8 µA cm^{-2}, 1.94 µA cm^{-2}, 0.89 µA cm^{-2}, 0.97 µA cm^{-2} olarak bulunmuştur. En yüksek korozyon direnci 290 ℃ altında ısıl işlem görmüş numunede görülmüşken en düşük korozyon direnci ise 380 ℃ altında ısıl işlem görmüş numunede gözlenmiştir. Bununla birlikte 450 ℃ ve 470 ℃ altında ısıl işlem görmüş numunelerdede korozyon direnci 380 ℃ ye yakın olarak bulunmuştur.

Tablo 1. İlk Tafel polarizasyon eğrisinden elde edilen E_{corr} ve I_{corr} verileri

Numune	**E_{corr} (V)**	**I_{corr} (A cm^{-2})**
Bare	-0.642	$10^{-5.75}$
290 ℃	-0.664	$10^{-6.62}$
320 ℃	-0.743	$10^{-5.52}$
350 ℃	-0.643	$10^{-4.82}$
380 ℃	-0.683	$10^{-4.34}$
410 ℃	-0.753	$10^{-5.71}$
450 ℃	-0.689	$10^{-6.05}$
470 ℃	-0.662	$10^{-6.00}$

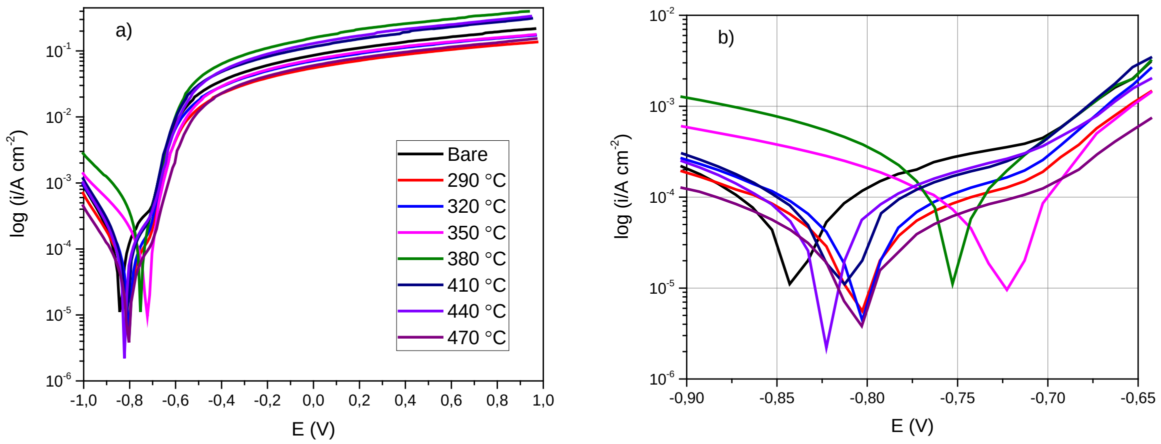

Şekil 5. a) Tafel polarizasyon eğrilerinin farklı ısıl işlem sıcaklıklarına bağlı ikinci döngüsü **b)** Tafel polarizasyon eğrilerinin yakınlaştırılmış görüntüsü

NaCl korozif ortamında uygulanan boraks takviyeli alüminyum kompozit malzemelerin negatif yönden pozitif yöne doğru oksidasyonuna ait ikinci döngüdeki Tafel grafiği Şekil 5a ve Şekil 5b ile ortaya koyulmuştur. Şekil 4b ile verilen Tafel eğrilerinin yakından gösterimi numunelere ait E_{corr} ve I_{corr} değerlerinin daha iyi anlaşılabilmesi için verilmiştir. Grafikten elde edilen verilerin sayısal değerleri Tablo 2 de verilmiştir.

Tablo 2. İkinci Tafel polarizasyon eğrisinden elde edilen E_{corr} ve I_{corr} verileri

Numune	Ecorr (V)	Icorr (A cm-2)
Bare	-0.843	10-4.49
290 °C	-0.802	10-4.59
320 °C	-0.801	10-4.66
350 °C	-0.723	10-4.24
380 °C	-0.752	10-3.98
410 °C	-0.813	10-4.30
450 °C	-0.823	10-4.47
470 °C	-0.803	10-4.71

İkinci Tafel eğrisinde en düşük korozyon potansiyeli 350 °C altında ısıl işlem görmüş metal matrisli kompozit numunede -0.723 V olarak bulunmuştur. Isıl işlem görmemiş, 290 °C, 320 °C, 350 °C, 380 °C, 420 °C, 450 °C ve 470 °C altında ısıl işlem görmüş numunelerde sırasıyla -0.843 V, -0.802 V, -0.801 V, -0.723 V, -0.752 V, -0.813 V, -0.823 V ve -0.803 V olarak bulunmuştur. Korozyon akım değerleri ise ısıl işlem görmemiş, 290 °C, 320 °C, 350 °C, 380 °C, 420 °C, 450 °C ve 470 °C altında ısıl işlem görmüş numunelerde sırasıyla 32.6 µA cm^{-2}, 25.8 µA cm^{-2}, 21.5 µA cm^{-2}, 58.1 µA cm^{-2}, 103.4 µA cm^{-2}, 49.8 µA cm^{-2}, 33.9 µA cm^{-2}, 19.4 µA cm^{-2} olarak bulunmuştur. İkinci Tafel eğrisinde en yüksek korozyon direnci 470 °C altında ısıl işlem görmüş numunede görülmüşken en düşük korozyon direnci ise 380 °C altında ısıl işlem görmüş numunede gözlenmiştir. İkinci polarizasyon eğrisinde korozyon akımlarının tüm numunelerde daha düşük seviyelerde olduğu gözlenmiştir. Bunun sebebinin ilk polarizasyon eğrisi sonrasında numune yüzeylerinde pasif tabaka oluşmasından kaynaklanabileceği düşünülmektedir [15].

4. Sonuçlar

Metal matrisli kompozitlerin kullanımı endüstride gittikçe yaygınlaşmaktadır. Farklı matris ve farklı güçlendirici elemanlarla metal matris kompozit malzemeler kolayca üretilebilmektedir. Kompozit malzemelerle ilgili haddeleme ve ısıl işlem parametrelerininde kompozit içeriği kadar önemli olduğu düşünülmektedir. Bu çalışmada boraks takviyeli alüminyum metal matris kompozitin hadde ile kalınlığı indirildikten sonar farklı sıcaklıklar altında ısıl işlem sıcaklıklarının korozyona olan etkisi araştırılmıştır. Korozyon sonuçlarıyla birlikte mikroyapı, XRD ve sertlik analizleri yapılıp tartışılmıştır. Farklı ısıl işlem sıcaklıkları belirtilen sürede mikroyapı üzerinde bir etkisi bulunmamıştır. X-ışını kırınımlarında ısıl işlem sıcaklıklarına bağlı olarak numunelerin kristal yoğunluklarında artış olduğu gözlenmiştir. Bununla birlikte kristal yoğunluklarının sıcaklık değişimlerinde farklı piklerde oluştuğu gözlenmiştir. Sertlik değerleri ısıl işlem sıcaklığı arttıkça düşme meyili gösterdiği görülmüştür. Korozyon sonuçları incelendiğinde bazı sıcaklıklarda ısıl işlemin korozyon direncini arttırmak yerine azalttığı tespit edildi. İki korozif döngünün sonunda en iyi korozyon direncinin 440 °C ve 470°C sıcaklıklarda oluştuğu görüldü.

Referanslar

1. Ma, K., Lavernia, E.J., Schoenung, J.M. Particulate reinforced aluminum alloy matrix composites-a review on the effect of microconstituents. Rev Adv Mater Sci 2017;48:91–104.
2. Salama, E.I., Abbas, A., Esawi, A.M.K. Preparation and properties of dual-matrix carbon nanotube-reinforced aluminum composites. Compos Part A Appl Sci Manuf 2017;99:84–93.
3. Mamoon, A., Al-Jaafari, A. Fatigue behavior of aluminum SIC Nano composites material with different reinforcement ratio. IOP Conf. Ser. Mater. Sci. Eng., vol. 870, IOP Publishing; 2020, p. 12159.
4. Singh, L., Singh, B., Saxena, K.K. Manufacturing techniques for metal matrix composites (MMC): an overview. Adv Mater Process Technol 2020;6:441–57.
5. Senthil, S., Raguraman, M., Manalan, D.T. Manufacturing processes & recent applications of aluminium metal matrix composite materials: A review. Mater Today Proc 2021;45:5934–8.
6. Yilmaz, N.F., Yilmaz, M., Kalkan, M.F. Experimental study on investigation of mechanical and microstructural properties of al b4c composite material. Int. Conf. Mater. Eng. Technol., Gaziantep: 2019, p. 906–12.
7. Muharrem PUL. Alüminyum 7075 Matrisli Kompozitlerde SiC, B4C Ve TiB2 takviye elemanlarının mekanik özelliklere etkilerinin karşılaştırılması. Düzce Üniversitesi Bilim ve Teknol Derg 2019;7:180–93.
8. Mazahery, A., Ostadshabani, M. Investigation on mechanical properties of nano-Al2O3-reinforced aluminum matrix composites. J Compos Mater 2011;45:2579–86.
9. Sharma, P., Sharma, S., Khanduja, D. Effect of graphite reinforcement on physical and mechanical properties of aluminum metal matrix composites. Part Sci Technol 2016;34:17–22.
10. Lu, L., Dahle, A.K. Effects of combined additions of Sr and AlTiB grain refiners in hypoeutectic Al–Si foundry alloys. Mater Sci Eng A 2006;435:288–96.
11. Kaya, C., Avcıoğlu, S., Kaya, F. Low temperature synthesis and characterization of high purity nano boron carbide (B4C) structures 2018.
12. Antonov, M., Hussainova, I., Kers, J., Kulu, P., Kübarsepp, J., Veinthal, R. Advanced

multifunctional materials and their applications. Res Est Present Futur n.d.:146.

13. Yilmaz, N.F., Öztürk, M. Improvement of mechanical properties of AA1070 aluminium by the addition of borax under different holding conditions. Materwiss Werksttech 2012;43:1006–18.
14. Davey, W.P. Precision measurements of the lattice constants of twelve common metals. Phys Rev 1925;25:753.
15. Yavuz, A., Kalkan, M.F., Yilmaz, N.F. The corrosion effect of cuo and zno formations on brass surface. Int J Mater Eng Technol n.d.;4:117–24.

EFFICIENCY IMPROVEMENT THROUGH LEAN MANUFACTURING AND PROBLEM-SOLVING TECHNIQUES

DİLAN ÇELİK[1], MEHMET HADİ KUZU[1], UMUT KARANFİL[1], CAN DENİZ UYGUN[1], ÖNER SUFİOĞLU[1], MERT DÖKMECİ[1], ERDEM AZ[2], HASAN AYTUĞ KURT[2], ALPER YETER[2], MUSTAFA BAKKAL[1]

[1]Istanbul Technical University Mechanical Engineering Department, Istanbul/TURKEY
[2]Yılmaz Machine, Istanbul, TURKEY

Abstract

In order to survive in today's competitive market, it is necessary to produce with high efficiency. It is possible to increase productivity by analyzing the errors that occur during manufacturing, finding the root causes, and solving them. In this project, the efficiency of a cutting machine line was examined over the 6-month. Among the 6-month data, the errors that caused the downtime in production were determined with the help of Pareto analysis. There are 4 main defect types and the root causes of these defects were found with the help of fishbone diagrams. Then, using problem-solving techniques and considering the financial effects, solution suggestions were made. As a result of the study production efficiency improved by 55% and cost savings were obtained.

Key Words: Production Efficiency, Lean Manufacturing, Data Science, Cost Saving, Problem Solving, Fishbone Diagram, Pareto Chart, FMEA.

1. Introduction

Today, customer demands vary greatly compared to the industrial revolution in the 1950s. Such that customers demand better quality products at cheaper prices and faster. This situation drives the market into an increasingly competitive environment. Under these conditions, companies/manufacturers must be able to meet these demands in order to survive.

Companies that can respond to these demands will continue to make a profit, while companies that cannot develop their technology in this direction and keep up with this competitive market will perish. There are two vital elements that companies should pay attention to survive in this challenging market. One of them is the necessity of putting themselves in continuous improvement to meet the demands and the other is the necessity of reviewing the quality standards and quality control processes. At this point, the most important philosophy to be considered is lean production. The Pareto chart is beneficial for data, such as classification, type or cause and is convenient to arrange where process changes or action taken should be focused and is also used to classify the wastage and downtimes of machine. It uses Bar diagrams to sort problems based on frequency, severity, nature, or source and displays them size which problems are vital ones [1,2] A fishbone diagram can be helpful in identifying possible causes for a problem that might not otherwise be considered by directing the team to look at the categories and think of alternative causes. If it is the Pareto chart that helps us to prioritize our efforts and focus attention on the most pressing problem or symptom, it is the cause-and-effect diagram that helps to lead us to the root cause of the problem [3, 4]

The Company Information

The manufacturing company was founded in 1977 as an establishment aiming to meet the demand for production, assembly, technical service & maintenance, fault detection, and spare parts. The company continues its sales and production activities in different continents and countries with its export volume to more than 85 countries around the world. *The manufacturing company* has adopted the principle of development by using the technologies of its solution partners in the fields of mechatronics, pneumatics, and hydraulic hydropneumatic, by providing services in the fields of research, development, design, production, sales, and after-sales for changing needs. *The company* takes the chances of investments to increase its country, sector, and production volume. At the same time, it pays attention to sectoral, social, and individual interests. *The* Company, which bases its activities on honest, respectful, socially friendly, humane, superior quality and principles, aims to continue on its way with the principle of "trust".

Line Details

Improvements within the scope of the project were applied to the MNT-02 line. There are 18 stations and 6 operators on the MNT 02 line. In addition, there is a line leader and a relief operator. An aluminum profile cutting machine is produced in this line. In total, 7 different models of machines are produced. There were approximately 28 sub-models due to differences in electrical and mechanical connections. The planned production time for the line in 1 day is 520 minutes but 420 minutes is achieved. Availability of the line is calculated as 0,80 from this information. The production rate of the line is 14 machines per day but there are 1 scrap/rework machine in March.

2. IMPLEMENTATION

Data Processing

After getting all data sets, data analysis was started and data analysis steps were applied. PYTHON program was used for data analysis.

```
import numpy as np
import pandas as pd
import matplotlib.pyplot as plt
import seaborn as sns
from matplotlib.ticker import PercentFormatter
import datetime
import matplotlib as mpl
from matplotlib.pyplot import figure
```

Figure 1: Libraries which is used in Python code.

Preparing Data Frame

	Date	Category	Error_Type	Comment	Process	Model	Takt	Stop_Time	Machine Loss	Labor Loss
0	2021-10-01	Planlı_Duruş	Lojistik	-	-	Planlı Duruş	NaN	115.0	NaN	NaN
1	2021-10-01	Planlı_Duruş	Lojistik	-	-	Planlı Duruş	NaN	135.0	NaN	NaN
2	2021-10-01	Planlı_Duruş	Lojistik	-	-	Planlı Duruş	NaN	140.0	NaN	NaN

Excel data has been made suitable for processing in python.
"Date","Category","Error_Type","Comment","Process","Model","Takt","Stop_Time","Machine Loss","Labor Loss"
Data were categorized using sub-names.
Data Cleaning Phase

```
model = df_error.groupby('Model').size()
print(model)

Model
-                1
AÇK 420        206
CA 601          35
FR 220 - 221    63
FR 223          26
FR 223S         14
FR 225 - 226    31
KM 211          17
KM 215          49
MK 420           5
MK 450          36
Planlı Duruş    28
ST 264          12
TK 503          73
TK 505          60
ÇK 412          52
dtype: int64
```

```
model = df_error.groupby('Model').size()
print(model)

Model
AÇK 420        206
CA 601          35
FR 220 - 221    63
FR 223          26
FR 223S         14
FR 225 - 226    31
KM 211          17
KM 215          49
MK 420           5
MK 450          36
ST 264          12
TK 503          73
TK 505          60
ÇK 412          52
dtype: int64
```

Figure 2: Cleaning on model column.

Using Python functions and libraries, dirty data started to be cleaned. As can be seen above, the model name was found in different names that are not related to the model name in the fields that need to be specified. This dilemma was resolved by cleaning the data, and only the model names were provided in the data set.

```
category = df_error.groupby('Category').size()
print(category)

Category
Diğer                             202
Elektrik_Ön_Montaj                 50
Hat_Arızaları                      15
Kalite                            132
Lojistik                          130
Operatör_Hatası                    98
Planlı_Duruş                        2
Proses_Öğrenme__Öğretme            22
Tasarım_Geliştirme_Faaliyetleri     4
Tip_Değişimi                       24
dtype: int64
```

```
category = df_error.groupby('Category').size()
print(category)

Category
Elektrik_Ön_Montaj                 50
Hat_Arızaları                      15
Kalite                            132
Lojistik                          130
Operatör_Hatası                    98
Planlı_Duruş                        2
Proses_Öğrenme__Öğretme            22
Tasarım_Geliştirme_Faaliyetleri     4
Tip_Değişimi                       24
dtype: int64
```

Figure 3: Cleaning on category column

Here, the parts that should not be in the error modes were cleaned and a clearer understanding of the error modes was provided in the next stages.
Before the data cleaning total data size was 708 Rows and 10 Columns after the implementation of data cleaning methods total data size was reduced to 477 Rows and 6 Columns.

	Date	Category	Error_Type	Process	Model	Stop_Time
8	2021-10-05	Kalite	Arızalı Parça	-	FR 225 - 226	22.0
9	2021-10-05	Kalite	Arızalı Parça	-	FR 225 - 226	9.0
10	2021-10-05	Operatör_Hatası	Montaj Hatası	3. Proses	FR 225 - 226	9.0
...	...	...	...	...	...	...
704	2022-04-26	Kalite	Arızalı Parça	13. Proses	AÇK 420	7.0
706	2022-04-27	Elektrik_Ön_Montaj	Hatalı Kablo Bağlantısı	-	AÇK 420	13.0
707	2022-04-27	Hat_Arızaları	Mekanik Arıza	-	AÇK 420	5.0

After cleaning and ordering the data, the visualization phase of the data was started.

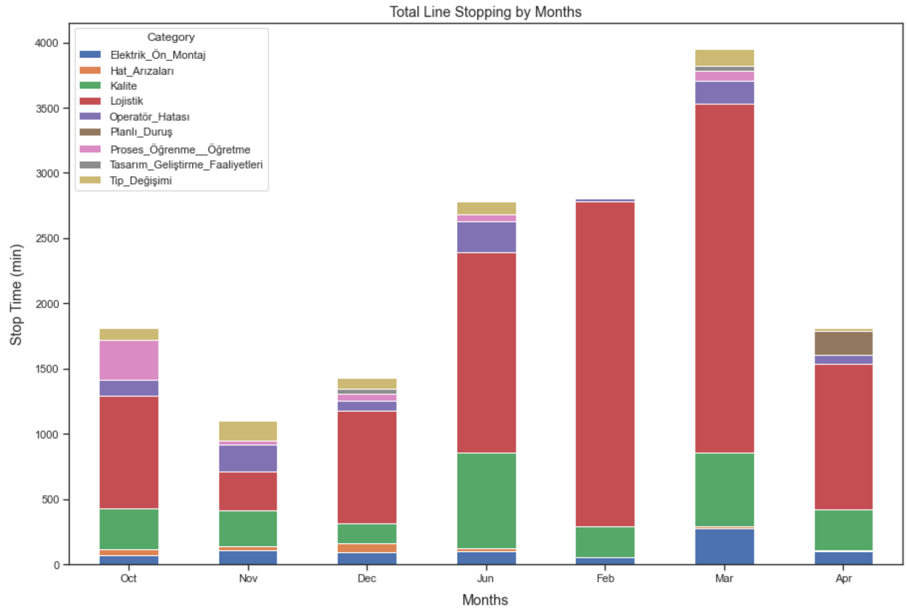

Figure 4: Total line stopping time by months

While visualizing the data, the analysis was primarily done on a monthly basis. It was examined whether there was a monthly trend in the error modes that emerged in the month-based visualization. As a result, although there was no change in the order of error modes on a monthly basis, it was observed that logistics errors took up a large place, especially in months 2 and 3.
For further review, error modes were reviewed and visualized individually on a monthly basis.

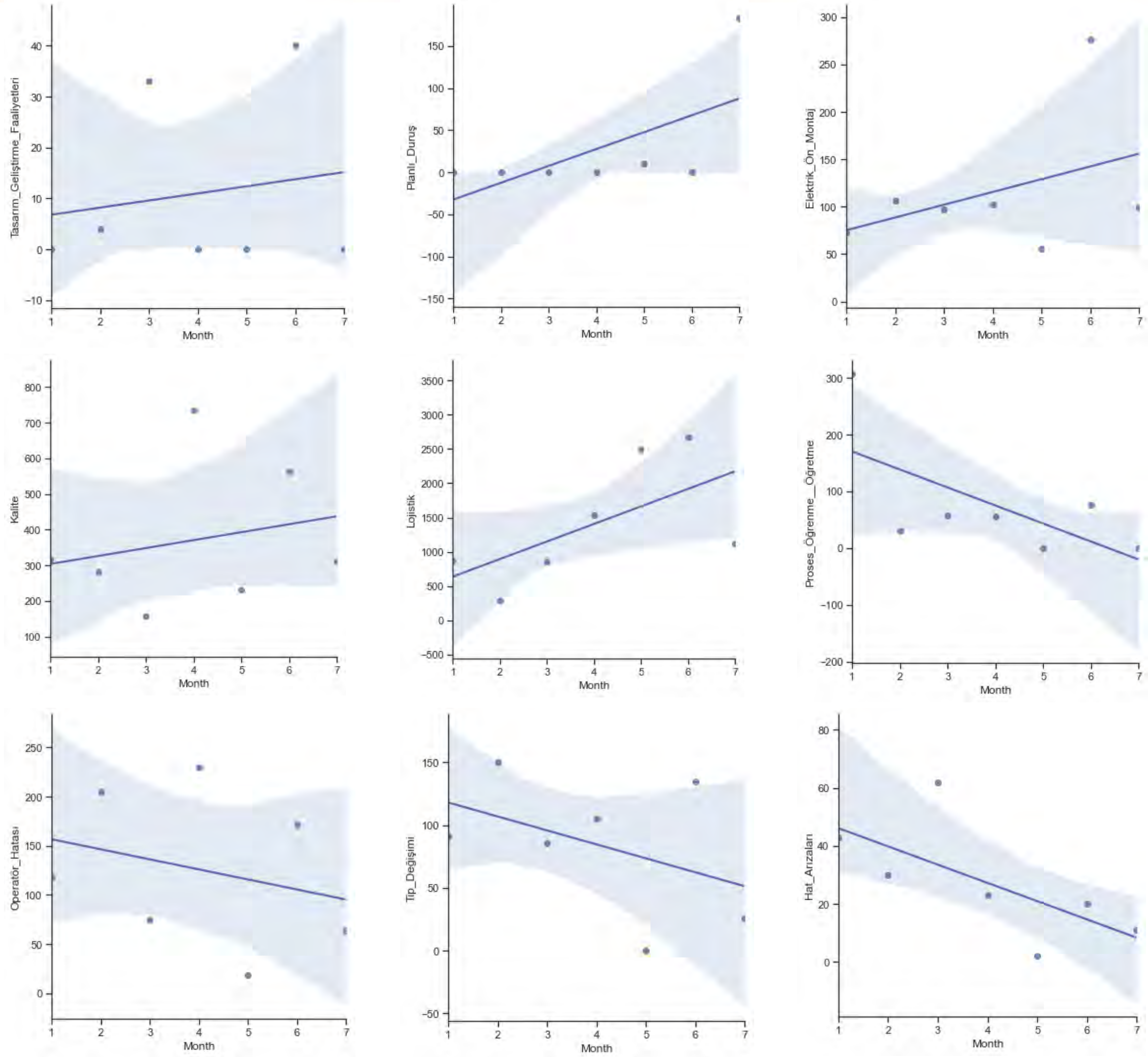

Figure 5: Trendlines of main errors in last six months.

Figure 6:

When the error modes were examined one by one over a 6-month period, no trend could be found. However, when the graphs are examined, it can be determined that all error modes decrease between the 2nd and the 5th month. The reason for this is the decrease in production numbers between these months.

Pareto Analysis

After the data is visualized and cleaned, a Pareto Analysis was performed to obtain the most problematic errors. The Pareto analysis results can be seen below;

The data which represents the stopping times in the production line is analyzed manually via excel and automatically via a python programming language. The data is sorted out by the pivot table. By looking into the pivot table, the priority order is made and a graph is drawn. Pareto Analysis suggests only 20 % of the factors that affect the process generate 80 % of the problem. According to this approach, the most important factors are selected.

According to Pareto Analysis results based on [7];

- Set Waiting
- Defective Part
- Cable Connection Fault
- Electrical Part Failure

These problematic factors are sorted according to the importance level. These 4 factors nearly cause 80 % of the stopping in this production line. Problem solving suggestions will be made to these 4 problems only because focusing on them is much more profitable than dealing with all of the factors. After these most-impact problems are solved, the analysis will be done again and the new problems will be solved. This cycle will be repeated constantly according to continuous improvement (Kaizen) logic.

FMEA Analysis

After the Pareto Analysis, Failure Mode Effect Analysis is performed to calculate the importance number (RPN). This number gave idea to the team to where to start and which to focus.
Severity Values: Set waiting has the biggest severity of them all so it is ranked with 10 points. According to Set Waiting, the Severity of the Functionally Failed Part is significantly lower. Because it does not stop all processes and the part which is defective can be changed in a short notice. So, it will be ranked 2/10. Wrong Cable Connection Error has the least Severity in the group. It can easily be solved such as and does not require a complex procedure. It is ranked 1.5/10. The logistics error has the same impact as Set Waiting. So, the Severity of Logistics error is also 10/10.
Occurrence Values: According to the data which was given by the company, occurrence values are rated. Most frequent of them is Set Waiting and it is ranked 9/10. Other Occurrence values are given according to this.
Detectability: Detectability in these problems varies a lot but the Set Waiting error is the hardest to detect because the production line workers are not aware of the situation in the warehouse and supply. So it is ranked 10/10. Secondly, Logistics errors are more predictable because they are related to the suppliers and the factory can gather information from them about whether they will deliver late or not. Logistics is ranked 8/10. And Functionally Failed Part is also hard to detect because the part is incorrect visual conditions but does not work. It is also rated 8/10. The wrong cable connection is easy to detect because there is a quality control station in the production line which is also responsible for checking the electrical connections. So, it was ranked 2/10.

- Set Waiting; S=10, O=9, D=10 RPN=900
- Functionally Failed Part; S=2, O=8, D=8 RPN=128
- Wrong Cable Connection; S=1.5, O=4, D=2 RPN=12
- Logistics; S=10, O=1, D=8 RPN=80

It can be clearly seen that the most important problem is Set Waiting. Set waiting is a time past while waiting for all the components to get ready for the assembly. Incomplete delivery of a box called “Set” which includes all the components required to assembly in a specific station. This problem is directly connected to the Kanban system in the production line and supplier delays.
The second most important problem was Functionally Failed Part. It means a part which is correct in terms of dimensions but cannot perform its functions.

Third one was Logistics. A part which is correct in terms of dimensions but cannot perform its functions. Set Waiting and Logistics are sometimes connected because when the Suppliers doesn't meet the demand, the set is also delayed.
The last problem is Wrong Cable Connection. It is caused by the operator mistakes and can be detected easily. But these problems occur too much and take a lot of time.

Fishbone Diagram

After the FMEA, team decided to create a fishbone diagram to obtain the root-causes of the 4 major problems. After all of the root-causes were written in the diagram, most important ones are determined.

Set Waiting:

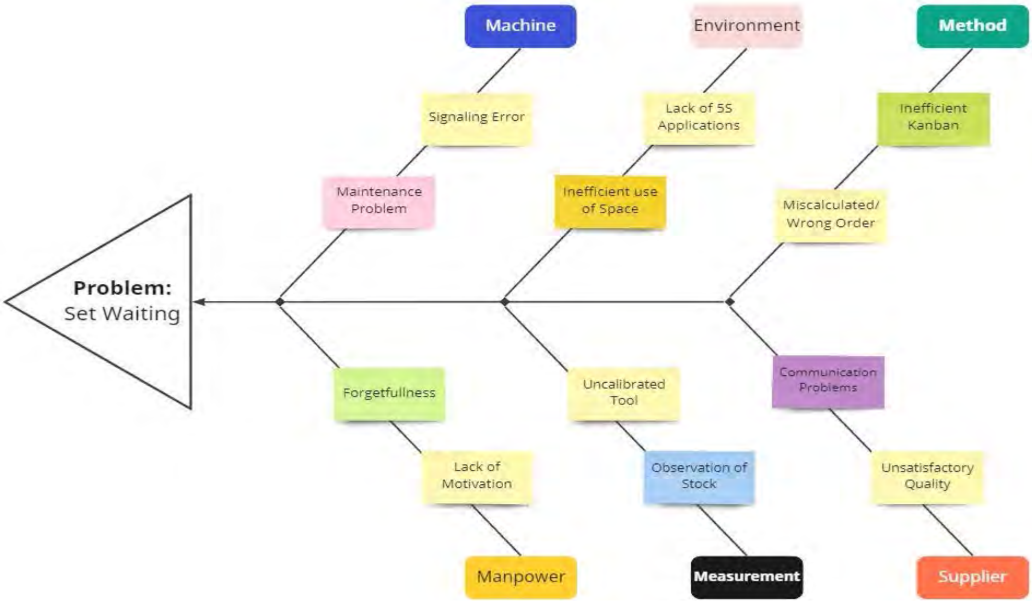

Figure 7: Fishbone diagram for set waiting error.

These most important root-causes of Set Waiting are as follows;

- Inefficient Kanban Method
- Forgetfulness of the Warehouse
- Supplier Communication Problems

Functionally Failed Part:

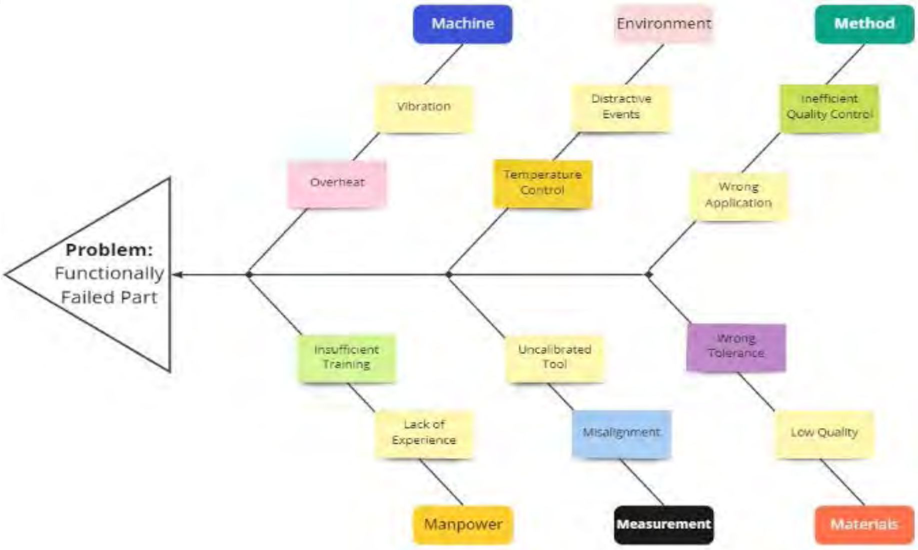

Figure 8: Fishbone diagram for functionally failed part error.

The most important root-causes of Functionally Failed Parts are as follows;

- Low quality products from the suppliers
- Insufficient training in production workers
- Machine tool problems in the part production
- Maintenance problems in the part production
- Insufficient quality control

Logistics:

Figure 9: Fishbone diagram for logistic error.

The most important root-causes of Logistics are as follows;

- External supplier problems
- Legal restrictions and health issues caused by COVID-19 pandemic
- Transportation problems
- Wrong batch sizes

Wrong Cable Connections:

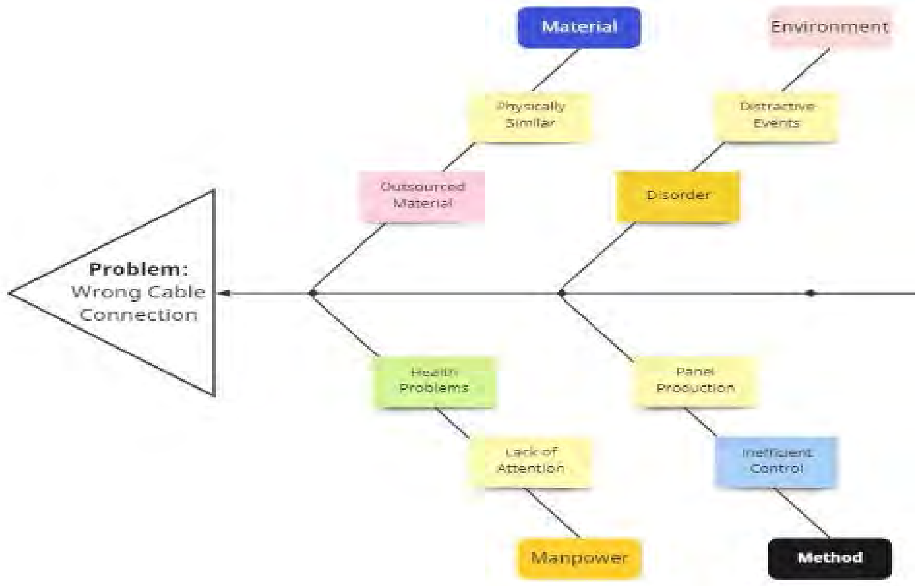

Figure 10: Fishbone diagram for wrong cable connection error.

The most important root-causes of Wrong Cable Connections are as follows;

- Visually similar materials
- Lack of attention in assembly process
- Distractive Events
- Inefficient control

3. Results and Discussion

By using data analysis, the problems in production were determined correctly. The possible gains in case the recommendations are implemented will be evaluated.

Table 1: Time and machine saving.

Problem	Saving (Time)	Saving (Machine)
Hydro-check Error	162	7
Kanban System	2000	101
Cable Connection	282	12,8
Stop Button	-	-
Saw Error	80	4
Ruler Error	60	3

Hydro-check Error: With the reduction of the possibility of repetition of the Hydro-check failure with the measures, an estimated 162 minutes, i.e. 7 machines, were saved.

Kanban System: Kanban system is a problem in every manufacturing factory. Thanks to the possibilities brought by digitalization, these problems are gradually decreasing and contribute to an increase in production output. With the establishment of a new Kanban system for the company, this system is compatible with the software used by the company, and the tracking process for both in-plant material handling and parts coming from suppliers has become easier, and possible delays can be determined beforehand. In this way, in case of a possible delay, losses will be minimized with the type rotation of the line, and production will continue in the lean production philosophy. Possible wins are shown in the table as machines and minutes, and it can be considered natural to have wins above and below them. The variability in this output is completely related to the system and it can be said that a higher-cost system will bring higher returns. Here, it is recommended to carefully examine the return on investment and choose a suitable system for it.

Cable Connection: This proposal, which can contribute to the production output with a simple solution, can increase 12 machines in 6 months. There is no cost item in the solution of this problem, which was resolved with the implementation of poke yoke.

Stop Button: Although this proposal does not increase production output, it is of great importance in terms of measuring and examining employee effectiveness. How skilled an employee is at their job can be measured by how many stop buttons are pressed at stations, and it is possible to produce better quality products with a correct rotation and to obtain more qualified employees.

Saw and Ruler Error: Although the outputs of the proposed solutions to these problems are not very large, it is expected to yield approximately 7 machines in 6 months.

OEE Comparison

The overall equipment efficiency based on [5, 6], described in section 2, is calculated to understand how effective the improvements are. For this, the situations before and after the implementation of the project are compared.

a- Before Suggested Implementation

Availability:

The company gives a 1-hour lunch break and a total rest break of 30 minutes.

Theoretical Production Time = 8 Hours = 28.800

Net production time = 6.5 Hours = 23.400

Efficiency:

Daily maximum Output = 21

Daily Actual Output = 15

Quality:

Daily parts produced = 14

Daily parts produced meet quality standards = 13

b- After Suggested Implementation

The implementation of the project does not affect the quality and availability components of OEE. So these parameters remain as they were calculated in the first case.

Efficiency:

Daily maximum Output = 21

Daily Actual Output = 18

After eliminating the errors in the production line, the production line can produce at maximum capacity. Therefore, this project is a capacity improvement study. As a result of the improvements made, the efficiency rate, which was 66% in the previous situation, increased by 19% and became 85%

Timeline	**Availability**	**Efficiency**	**Quality**	**OEE**
Before Project Implementation	0,81	0,66	0,93	0,49
After Project Implementation	0,81	0,85	0,93	0,64

The estimated gains of the solutions have been studied above. The estimated values given during these examinations may vary depending on many parameters. However, it should be noted that the production numbers, which have decreased due to the supply and pandemic experienced in recent years, show a tendency to increase rapidly with the supply system that is gradually normalized and improved.

For this reason, since the 6-month production data examined is in low production numbers, the earnings remained low at this amount. Since the number of errors is related to the number of productions, it is expected to be aware that higher returns will come with the increase in the number of productions.

4. CONCLUSIONS

In this paper, the efficiency of assembly line MNT02 of *the manufacturing company* has been studied using lean manufacturing tools. The objective of the study was to provide a new insight to bring suggested solutions to existing problems of *the manufacturing company* using the before-mentioned lean tools and to demonstrate the advancements these suggested solutions would contribute to eliminating waste. The results obtained in this study are in line with the hypotheses in the literature. Upon analyzing the 6-month data using data science it was apparent that the biggest losses were recorded about errors such as set waiting, functionally failed parts, logistics, and operator errors.

Set waiting on its causes 9070 minutes of stoppage time in the assembly line over the course of 6 months. To solve the set waiting error electronic kanban system was introduced in the previous chapter and implementing this solution only saves 44% of the total stoppage time, and eliminates the waste of 101 machines, which translates to a major profit for the company.

An example can be given on the solution that was suggested to solve wrong cable connection errors. This solution was inspired by the Poka-Yoke method. Application of color codes to solve cable connections might seem like a minor effort to increase efficiency but according to the analysis presented in chapter 5, it would eliminate the waste of 12.8 machines in 6 months, regaining 282 units of time out of 502 that is currently being lost due to wrong cable connection error.

Furthermore, in light of the third most significant result of this paper, the solution to hydro-check errors can lead to savings of 7 machines in 6 months and reduces the cycle time.

Lastly, evaluation and acknowledgment must be made of the limitations of this study. One of the biggest obstacles was in obtaining data from the company and being able to comprehend them. To reach lean and smart solutions, the most important step is to understand the problem. Accumulating data of the error types is an essential step leading to an accurate problem definition. According to observations made in visiting the factory, further research is needed to establish a more efficient data-keeping system in *The manufacturing company* assembly lines. The outcome of this study might have been superior if the data inputs in the assembly line were written more carefully and without missing information. To conclude, improvements in efficiency using lean manufacturing and data analysis are demonstrated using evidence obtained in this study. In implementing all solutions given in this study, the company can eliminate the waste of 127.8 machines and save up to 2584 minutes of production time.

REFERENCES

1. Ishikawa, K. (1985). What is total quality control? New Jersey: Prentice Hall.
2. Hristoski, Ilija & Kostoska, Olivera & Kotevski, Zoran & Dimovski, Tome. (2017). Causality of Factors Reducing Competitiveness of e-Commerce Firms. Balkan and Near Eastern Journal of Social Sciences (BNEJSS), ISSN: 2149-9314. Vol. 3. pp. 109-127.
3. Gregory H. Watson and Ekaterina A. Spiridonova (2019), "Fish (Bone) Stories: Reimagining the Fishbone Diagram for the Digital World," *Quality Progress*, 52:8, pp. 14-23
4. Devor, R. E, Chang, T., & Sutherland, J. W. (2007). Statistical quality design and control: Contemporary concepts and methods. 2nd Edition, Pearson Prentice Hall.
5. Amedy, W. Y., Awaj, Y. M., Singh, A. P., International Journal for Quality Research 7(1) 107–126 ISSN 1800-6450
6. (S. J. Benjamin, M. S. Marathamuthu, and U. Murugaiah, "The use of 5-WHYs technique to eliminate OEE's speed loss in a manufacturing firm," J. Qual. Maint. Eng., vol. 21, no. 4, pp. 419–435 Oct 2015)
7. Bhade, S., & Hegde, S. (2020). Improvement of Overall Equipment Efficiency of Machine by SMED. Materials Today: Proceedings, 24, 463-472.

SURFACE AND STRUCTURAL PROPERTIES OF MARTENSITIC STAINLESS STEEL –GLASS POWDER COMPOSITE MATERIALS PREPARED BY POWDER METALLURGY METHOD

AYŞE NUR ACAR[1*], DOĞAN KAYA[2], ABDUL KADIR EKŞİ[3], AHMET EKİCİBİL[2]

[1]Çukurova University, Ceyhan Engineering Faculty, Department of Mechanical Engineering, Adana-TÜRKIYE
[2] Çukurova University, Art and Sciences Faculty, Department of Physics Adana-TÜRKIYE
[3]Çukurova University, Engineering Faculty, Department of Mechanical Engineering Adana-TÜRKIYE
*anacar@cu.edu.tr

Abstract

X12Cr13 stainless steel provides excellent strength, toughness, and corrosion resistance. So it has been preferred for the cutting tools, valves, and valve plates with martensitic and ferritic phases in the alloy structure. Glass powder is acquired via grinding waste glass cracks and applied as an additional agent in structural materials owing to its chemical composition (alkali and alkaline earth oxides, such as SiO_2, Al_2O_3, Na_2O, MgO, *etc*.). In this study, the effect of glass powder on the surface and structural properties of X12Cr13 martensitic stainless steel has been investigated. A homogeneous mixture was formed by mixing martensitic stainless steel and 10 % (wt) glass powders, this homogeneous mixture was pressed under 12-ton pressure, and then, a heat-treatment process was applied at 1250 °C temperature for 2 hours. The physical property of this composite material, such as hardness measurement, surface topography, and microstructural properties, were determined using optical microscopy, scanning electron microscopy images, energy dispersive X-ray spectroscopy spectrums, and X-ray diffraction analysis performed to determine the crystal structure. It was observed that there was a reaction between martensitic stainless steel and glass powder and phase transformation occurred in this composite structure.

Key Words: Martensitic Stainless Steel, Glass Powder, Composite Material, Structural Property, Phase Transformation

1.Introduction

Stainless steel is classified into four main groups consisting of ferritic, austenitic, martensitic and duplex stainless steel in terms of their chemical compositions and microstructures. Martensitic stainless steel has a body-centered cubic crystal structure and is a heat-treatable alloy [1, 2]. These stainless steels are used in industrial areas, such as automobiles, aerospace, aerospace, etc. due to their good strength, toughness and corrosion resistance [2-4]. X12Cr13 stainless steel used in this study has semimartensitic stainless steel including martensitic and ferritic phases and is widely applied to use pumps, valve shafts, etc. [4, 5]. Solid waste management and waste usage are more important environmental issues due to the scarcity of space for landfilling and its ever-increasing cost. The utilization of waste products provides reduces annihilation problems and performs economically [6]. Glass powder is obtained by grinding waste glass cracks. This powder has alkali and alkali earth chemical composition (SiO_2, Al_2O_3, Na_2O, MgO, etc.), and is used to additive raw material into structural materials such as concrete and steels [6, 7]. In this study, the effect of glass powder on the structural and morphological properties of martensitic stainless steel was examined and with this study, it was aimed that the utilization of glass powder could be evaluated.

2.Material and Method

The chemical composition of X12Cr13 martensitic stainless steel powder obtained from Shi Jia Zhuang Daye Powder Factory in China was given as 13.3% Cr, 0.83% Si, 0.83% Mn, 0.041% C, 0.02% P, 0.02% S and in balance Fe. The chemical composition of glass powder obtained from Acar Frit, Masse and Industrial Raw Materials Industry and Trade Limited Company in Kütahya, Türkiye were given as 68.92% (±0.50) SiO_2, 1.81% (±0.08) Al_2O_3, 0.10% (±0.01) Fe_2O_3, 0.06% (±0.02) $TİO_2$, 8.19% (±0.014) CaO, 4.07% (±0.05) MgO, 16.00% (±0.27) Na_2O, 0.042% (±0.02) K_2O and 0.49% (±0.02) other substances. Glass powder was dehydrated in an oven at 100 °C temperature for 24 hours before it mixed with stainless steel powder [7]. Martensitic stainless steel powder was mixed with 10% (wt) of this dehydrated glass powder and a homogeneous martensitic stainless-glass powder mixture was obtained. This homogeneous mixture was pressed under 12-ton pressure and then pressed sample tempered at 600 and 900°C temperatures for 30 min to remove oxide, distribute uniform temperature in the furnace [8, 9] and sintered at 1250 °C temperature for 2 hours. The physical properties of this composite material were examined. The hardness measurements of stainless steel-glass powder composite materials were performed via Brinel Hardness test using DigiRock Blue Hardness Tester with a ball diameter of 2.5 mm and ball load of 32.25 N.(ASTM10) Morphological and microstructural properties of this composite sample were investigated via optic microscopy (OM) using Nikon Eclipse MA100, Scanning Electron Microscope (SEM) images, and Energy Dispersive Spectrometry (EDS) by FEI Quanta 650 Field Emission SEM device. The crystal structure of this sample were examined via PANalytical Empyrean X-ray diffraction (XRD) with degree of 20-90° tube voltage of 45 kV, tube current of 40 mA and scanning rate of 0.013°/min, anode material of Cu-$K\alpha$ (λ=1.54 Å).

3.Results and Discussion

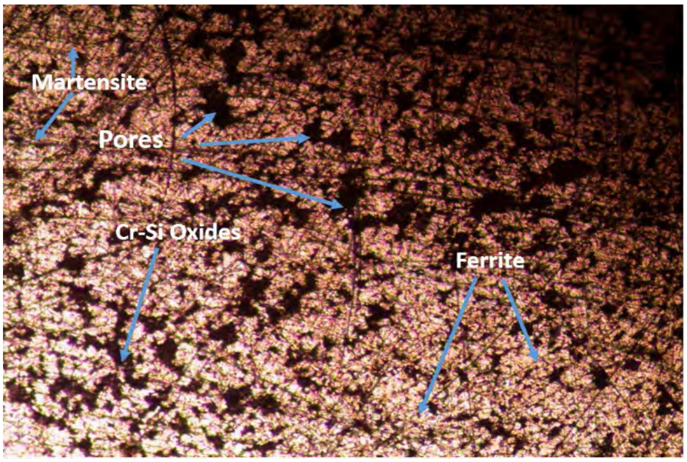

Figure 1. The OM image of X12Cr13 martensitic stainless steel mixing with 10 wt% glass powder sample (50X magnification).

Figure 1 shows OM image of X12Cr13 martensitic stainless steel mixing with 10 wt% glass powder sample. Light and dark regions were referred as ferritic and martensite phases, respectively. Heterogeneous structure was also seen on the surface of this sample. These structures were revealed as pores existences due to powder metallurgy method. It was also considered the regions of the microstructures were defined as Cr-Si oxides formed by segregating Cr to the before glass powder [7]. Also, on these regions, CrN phases were observed. The Brinell hardness value of this sample calculated as 101.90 HB.

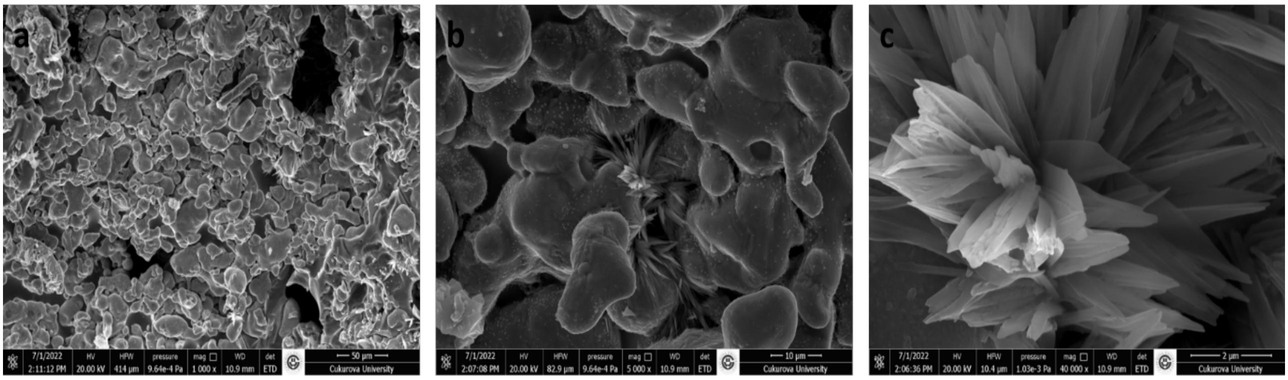

Figure 2. The SEM images of X12Cr13 martensitic stainless steel mixing with 10 wt% glass powder sample ((a) 1 000x, (b) 5 000x and (c) 40 000x magnification).

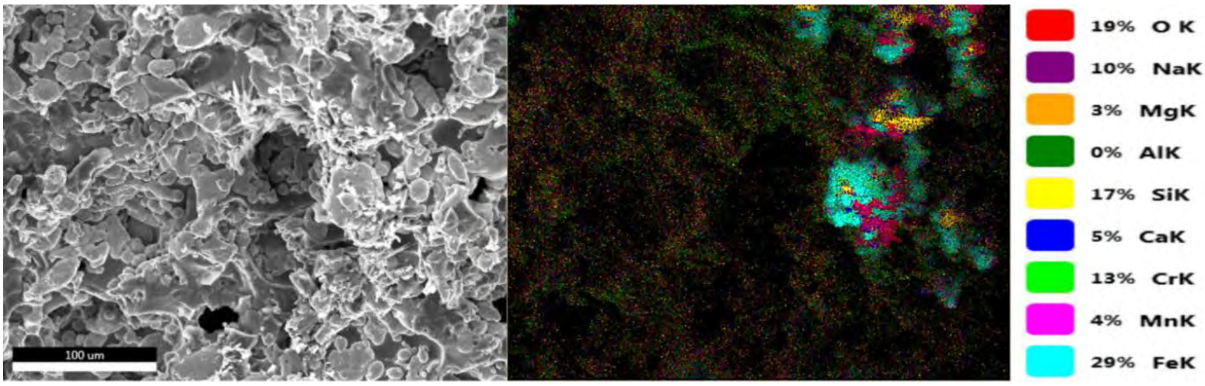

Figure 3. The EDS Mapping of X12Cr13 martensitic stainless steel mixing with 10 wt% glass powder sample

Figure 2 presents the SEM images of X12Cr13 martensitic stainless steel mixing with 10 wt% glass powder sample at 1 000x (a), 5 000x (b) and 40 000x (c) magnifications. Also, the EDS mapping of this sample is given in Figure 3. SEM images of this sample showed large irregular segregates. These are clear on the Figures 2 (a) and (b). An oxygen concentration of 19% was recorded on the all surface of this sample. Cr and Si concentrations were 13% and 17%, respectively. On the surface of this sample, needle-shaped structures were observed. it can be revealed that these structures may be glass powder and have more calcium and alkali content in their structures[10]. Also, carbide precipitation on the surface of this sample was seen. Heat treatment of martensitic stainless steel sample enables to obtain austenite, to the dissolution of the carbides and with cooling to transform the austenite into martensite structures and therefore lead to precipitation of carbide[11].

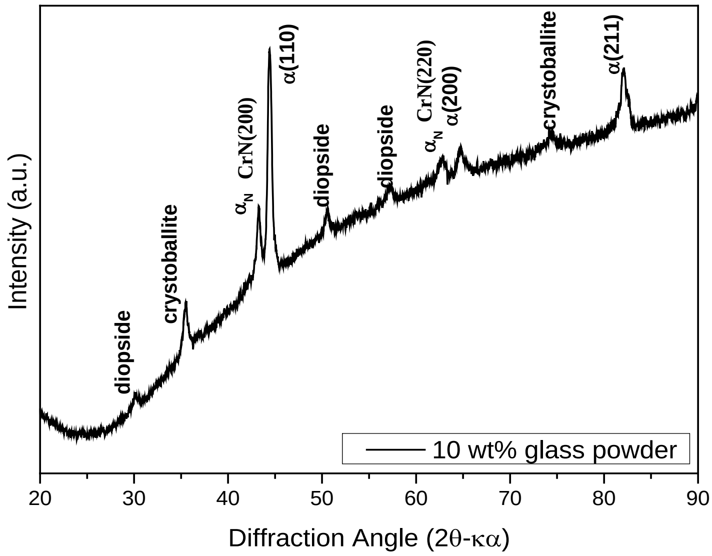

Figure 4. The XRD pattern of X12Cr13 martensitic stainless steel mixing with 10 wt% glass powder sample

Figure 4 shows the XRD diffraction pattern of X12Cr13 martensitic stainless steel mixing with 10 wt% glass powder sample. Diopside phase ($CaMgO_6Si_2$) peaks for 2θ angles of 30.07°, 50.41°, 57.20° and crystoballite ((SiO_2) phase peaks for 2θ angles of 35.43° and 74.54°, α phase peaks for 2θ angles of 44.30° (α(110)), 64.64° (α(200)) and 82.11° (α(211)) recorded [12]. Crystoballite phase forming is based on the reaction enthalpy. This enthalpy is related to the variation of absorbed heat in the form of thermal energy to kinetic energy, in order to occur ionic diffusion in the materials, when temperature increases, crystoballite phases occur [13]. CrN precipitation occurred predominantly at high temperatures [14]. It was considered that peaks on the 2θ angles of 43.12° and 62.68° would be α_N, CrN(200) and CrN(220), respectively [15]. These BCT-α Fe phase peaks for 2θ angles of 44.74°, 65.021° and 82.261° for this martensitic stainless steel powder [15].

4.Conclusion

In this study, the effect of glass powder on the microstructural and surface topography of X12Cr13 martensitic stainless steel prepared by the powder metallurgy method was examined. The following experimental results were given:

- Heterogeneous structures were observed due to porosity existence. Cr-Si oxides occurred between glass powder and stainless steel powder.
- Brinell hardness value of this sample was 101.90 HB.
- Needle-shaped structures on the microstructure of this sample occurred. Carbide precipitations on the microstructure of this sample were also observed.

It is planned this study will be developed in future studies with different features and chemical composition investigations.

Acknowledgement: Authors are greatly thankful to Cukurova University research funding with a Grand Number of FBA-2021-13966.

References

[1] C. Li, T. Bell, A comparative study of low temperature plasma nitriding, carburising and nitrocarburising of AISI 410 martensitic stainless steel, Materials Science and Technology 23(3) (2007) 355-361.
[2] M.K. Alam, M. Mehdi, R.J. Urbanic, A. Edrisy, Mechanical behavior of additive manufactured AISI 420 martensitic stainless steel, Materials Science and Engineering: A 773 (2020) 138815.
[3] A.N. Isfahany, H. Saghafian, G. Borhani, The effect of heat treatment on mechanical properties and corrosion behavior of AISI420 martensitic stainless steel, Journal of alloys and compounds 509(9) (2011) 3931-3936.
[4] X. Chen, Q. Li, J. Pan, J. Liu, X. Wei, S. Chen, Experimental study on stress corrosion of X12Cr13 stainless steel in natural gas environment, Journal of Materials Research and Technology 9(3) (2020) 3064-3074.
[5] Z. Hou, S. Chen, Q. Sun, X. Wei, W. Lv, Experimental research on fatigue characteristics of X12Cr13 stainless steel, Journal of Materials Research and Technology 9(3) (2020) 3230-3240.
[6] B.S. Shekhawat, D.V. Aggarwal, Utilisation of waste glass powder in concrete–A Literature Review, International Journal of Innovative Research in Science, Engineering and Technology 3(7) (2014).
[7] G. Sander, D. Jiang, Y. Wu, N. Birbilis, Exploring the possibility of a stainless steel and glass composite produced by additive manufacturing, Materials & Design 196 (2020) 109179.
[8] S. Butkovic, Sinterability and Tensile Properties of Nickel Free Austenitic Stainless Steel X 15 CrMnMoN 17 11 3, Tehnicki Vjesnik 20(1) (2013) 269-274.
[9] S. Pandya, K. Ramakrishna, A.R. Annamalai, A. Upadhyaya, Effect of sintering temperature on the mechanical and electrochemical properties of austenitic stainless steel, Materials Science and Engineering: A 556 (2012) 271-277.
[10] D. Qin, Y. Hu, X. Li, Waste glass utilization in cement-based materials for sustainable construction: A review, Crystals 11(6) (2021) 710.
[11] C.G.a. de Andrés, G. Caruana, L. Alvarez, Control of M23C6 carbides in 0.45 C–13Cr martensitic stainless steel by means of three representative heat treatment parameters, Materials Science and Engineering: A 241(1-2) (1998) 211-215.
[12] A.N. Acar, K. Doğan, A.K. Ekşi, A. Ekicibil, Structural and Surface Properties of Glass Powder Coated Cr Steels, The International Journal of Materials and Engineering Technology 4(2) 109-116.
[13] A.C. Souza, M.F. Pereira, L.C. Mossin, Thermal and mechanical characterization of blindex glass powder residue® for the production of ecological coating, Journal of Materials Research and Technology 12 (2021) 1794-1803.
[14] L.M. Ferreira, S.F. Brunatto, R.P. Cardoso, Martensitic stainless steels low-temperature nitriding: dependence of substrate composition, Materials research 18 (2015) 622-627.
[15] C. Li, T. Bell, Corrosion properties of plasma nitrided AISI 410 martensitic stainless steel in 3.5% NaCl and 1% HCl aqueous solutions, Corrosion Science 48(8) (2006) 2036-2049.

IMPACT OF INSERTING CAN PIPES ON HEAT TRANSFER IN ASOLAR AIR COLLECTOR

HAMIDOU BENZENINE[a,b], FETHI MOUSSA BOUDJEMA[a], SAID ABBOUDI[c]

[a]Department of Mechanical Engineering, faculty of science and technology, University of BELHADJ Bouchaib, P.O.B. 284 RP, Ain Témouchent, 46000, Algeria
[b]Laboratory of Energetic and Applied Thermal (ETAP), Faculty of Technology,B.P 230, University of Tlemcen, 13000, Algeria
[c]ICB, UMR 6303 CNRS, Department COMM UTBM, University of Bourgogne Franche-Comte, 90010 Belfort Cedex, France

Abstract

In this work, we present an experimental study of the thermal exchanges in forced convection ina solar air collector equipped with pipes with cans in the air stream, intended for the drying of agricultural products. This collector was designed and produced at the University of Ain Temouchent. The results of the graphical analyzes based on measurements of solar flux, air flow and ambient temperature carried out during a few days in June 2021 were presented and interpreted. The influence of the number of rows of can pipes "4 to 14" on the thermal efficiency has been studied and compared with the case of a simple solar collector. The results obtained show that the outlet temperature is markedly improved; it reaches values of 120°C for a row of 14 can lines.

Keyword: Simple air collector, experimental, forced convection, thermal efficiency, can, drying, agricultural products.

1. Introduction

Greater emphasis is being placed on the use of solar energy sources due to economic crises with rising fuel and electricity costs. One of the most used systems to exploit solar energy remains the solar collector. The latter can convert solar radiation into clean thermal energy. This heat transmission system can also be used to improve the performance of drying systems for food products or building materials.

The behavior of turbulent flow and heat transfer has been studied experimentally and theoretically by Azharul et al [1] on different types of solar collectors: plate collector, corrugated fin collector and V-groove collector. The results obtained showed only for the same flow; the dryer equipped with a solar collector with corrugated absorber is more efficient than dryers equipped with a simple or finned collector.

The experimental study conducted by Fakour et al. [2] was made to evaluate the thermal characteristics of a solar collector comprising longitudinal fins fixed on the absorber plate. The results showed that the presence of a network of fine fins increased the transfer surface by almost

66%, which made it possible to obtain an improvement of about 20% in the heat transfer.

An experimental and theoretical study of a natural convection solar collector was carried out by Bahria et al. [3]. The authors examined the effect of the number of baffle rows on the thermal efficiency up to 10 rows placed below the absorber. They indicated that the addition of a row of baffles corresponds to an increase in the air-absorber contact surface, and consequently an efficiency which reaches 32% for 10 rows of baffles.

Essalhi et al. [4] studied a solar collector of an indirect dryer with a new design of the absorber with two corrugated aluminum plates. Their results show that this type of dryer can reach a temperature of 57°C in a natural convection regime and allows the drying of pears and the reduction of their mass from 997.3 g to 135.13 g.

Elsawi [5] and Abhay [6] have studied the thermal performance of a flat V-shaped plate. This type of absorber provides a larger exchange surface compared to a flat absorber. They also found that the corrugated collector had a higher efficiency than a flat plate collector.

The experimental study proposed here falls within this context and aims to analyze a simple flat air collector and to develop a new form of collector integrating aluminum drink cans placed on the absorbent plate. For this, a comparison of two different models with forced convection was carried out: the first is a flat solar collector with simple air and the second model is a collector equipped with pipes with cans. The impact of number of rows of these cans on the improvement of thermal performance of solar collector has been studied and compared with the simple case.

2. Description of the experimental model

The flat air solar collector with different rows of aluminum cans was made at the University of Ain Témouchent, Algeria. The solar collector studied is a single pass flat air collector, length L=1.97 m, width l=0. 98 m and area A=1.93 m² (Fig.1). The 4 mm thick transparent glass plate is placed on the upper side of the frame. On the lower side of the box, an insulator, composed of four layers: wooden plate 2 mm thick, layer of glass wool 2 mm thick, polystyrene sheet 40 mm thick and a sheet of 2mm thick aluminium, was painted math black and used as an absorber.

A row of "used pop" aluminum cans was glued together to form a cylindrical pipe; making a total of 14 rows of 10 cans each, collected in the collector. The cans used have a diameter of 65 mm, a length of 160 mm and a thickness of 0.3 mm. They have been painted in math black, and cut at their ends to let the air flow through.

Figure 1. Solar collector equipped with an absorber with can pipes.

3. Experim0ental procedure

The measurements of the different quantities were carried out from 9 a.m. to 3 p.m. over one day. Over this period, we were able to observe the effect of the inlet temperature of the heat transfer fluid and the solar flux on our system studied by taking measurements of:

- ➢ Solar flux every 60 min.
- ➢ Ambient temperature (inlet) and outlet every 15 min.

Five configurations of solar collectors were studied during this work, namely:

- ❖ Simple collector without cans: **Case 1**
- ❖ Collector with 4 rows of cans: **Case 2**
- ❖ Collector with 8 rows of cans: **Case 3**
- ❖ Collector with 12 rows of cans: **Case 4**
- ❖ Collector with 14 rows of cans: **Case 5**

4. Result and discussion

In order to analyze the five proposed configurations of the solar collector, it is necessary to present the ambient temperature profiles (Tin) and the daily solar fluxes. Figure 2 illustrates the evolution of the entrance temperature and the solar irradiation as a function of time during the days of the month of September.

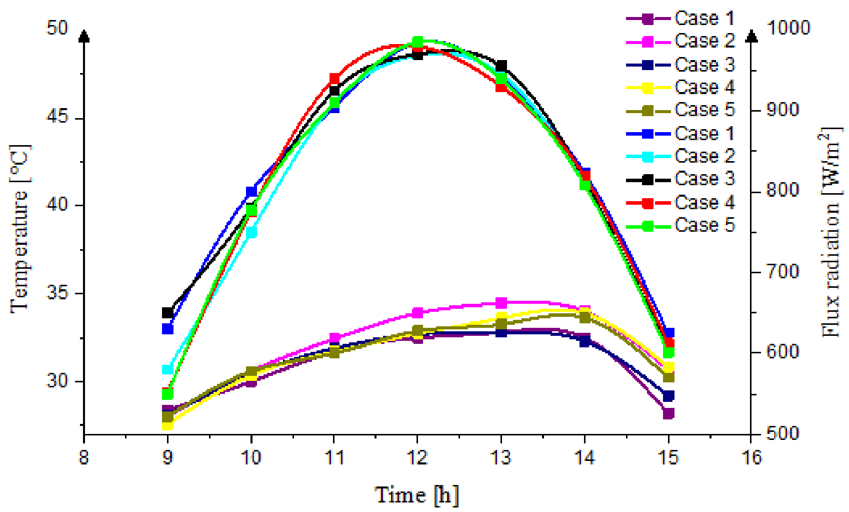

Figure 2. Solar flux and inlet temperature for all the cases studied.

The curves in Figure 2 present the solar flux density and the inlet temperature Tin for all the configurations studied, and as expected, the temperature and flux values reach their maximum between 12 p.m. and 1 p.m. before starting to decrease. until the end of the day. It should be noted that the maximum values of radiation and inlet temperature during the days considered reached 980 W/m2 and 33 °C respectively.

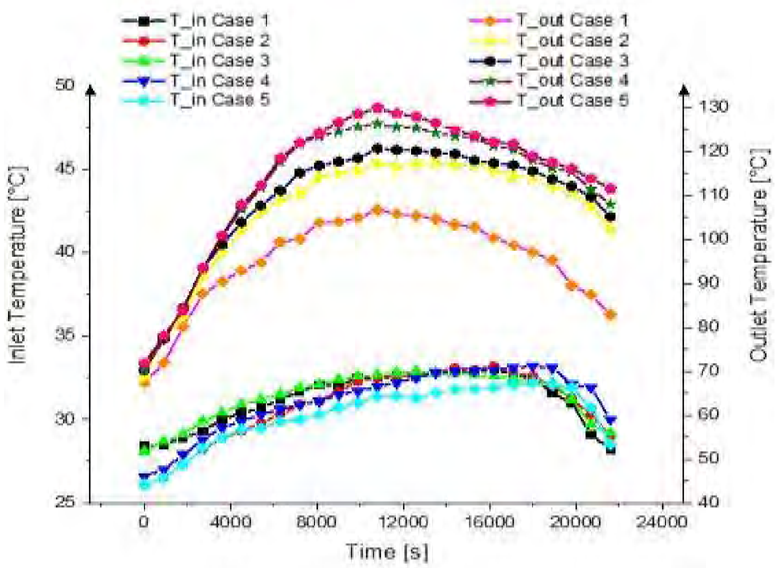

Figure 3. Inlet and outlet temperature for the different cases studied.

According to the graphical representations shown in Figure 3, considerable thermal performance was observed for all the cases of sensors studied. This figure shows the influence of the addition of canned pipes compared to the case of a simple sensor. It is clearly observed that the outlet temperature reaches maximum values in all cases between 12 p.m. and 1 p.m. following a logical evolution over a typical day since the radiation increases and decreases in intensity. It was also found that increasing the number of rows of pipes increases the collector outlet temperature as a function of the solar flux value. The outlet temperature reaches a value of 106°C in the simple case and 130°C in the case of a 14-row sensor; i.e. a recorded difference of 24°C.

5. Conclusion

The results obtained highlight the influence of a new geometry of collectors on the distribution of temperature and air velocities in the air stream. Experience has shown that the presence of canned ducts in the dynamic air stream improves heat exchange compared to the simple case and in addition the increase in the number of ducts makes it possible to obtain a high temperature in the vicinity of the absorber, improvement partly due to the increase in the exchange surface. If we compare our experimental results obtained for the five cases studied, we see that it is case 5 of the 14-row sensor that gives the best performance; i.e. an outlet temperature difference of 24°C compared to a simple solar collector.

References

[1] Md Azharul Karima, M.N.A Hawladerb. Performance investigation of flat plate, v-corrugated and finned air collectors , Energy 31 (2006) 452–470.
[2] M. Fakoor Pakdaman, A. Lashkari, H. Basirat Tabrizi, R. Hosseini. Performance evaluation of a natural-convection solar air-heater with a rectangular-finned absorber plate. Conversion et gestion de l'energie 52(2011)1215-1225.
[3] S. Bahria, M. Amirat. Influence de l'adjonction des chicanes longitudinales sur les performances d'un capteur solaire plan à air. Revue des Energies Renouvelables Vol. 16 N°1 (2013) 51 – 63.
[4] Hajar Essalhi, Rachid Tadili, M.N Bargach. Conception of a Solar Air Collector for an

Indirect Solar Dryer. Pear Drying Test » https://doi.org/10.1016/j.egypro.2017.11.114.

[5] A.M. El-Sawi, A.S. Wifi, M.Y. Younan , E.A. Elsayed , B.B. Basily . Application of folded sheet metal in flat bed solar air collectors. Applied Thermal Engineering 30 (2010) 864–871.

[6] Abhay Lingayat, Chandramohan V.P, V.R.K. Raju. Design, Development and Performance of Indirect Type Solar Dryer for Banana Drying. International Conference on Recent Advancement in Air Conditioning and Refrigeration, RAAR 2016, 10-12 November 2016, Bhubaneswar, India.

SÜRDÜRÜLEBİLİR LİFLERDEN ELDE EDİLEN ÖRME KUMAŞLARIN HAVA GEÇİRGENLİK VE BONCUKLANMA ÖZELLİKLERİNİN İNCELENMESİ

TÜLİN KAYA NACARKAHYA[1], EBRU ÇELİKTEN[1], KUBİLAY ÖZDEN[1], TUĞÇE ÖĞÜT[1*]

[1]Karafiber Tekstil San. ve Tic. A.Ş. Ar-Ge Merkezi, Gaziantep, TURKİYE,

Özet

Dünya nüfusunun artışı, küresel ısınma, arz ve talep dengesinin değişmesi tüm üreticileri sürdürülebilir ürünlerin üretimine sevk etmiştir. Daha sürdürülebilir bir yaşam döngüsüne dahil olabilmek içinde ekolojik üretim prosesleri ve biyobozunur ürünler özellikle son yıllarda tüketiciler tarafından da talep gören bir noktaya gelmiştir. Bu bağlamda, günlük yaşantımızda çok önemli bir yeri olan tekstil ürünlerinin özellikleri de talebe yönelik değişmeye başlamıştır.
Bu çalışmada, sürdürülebilir ve biyobozunur özelliklere sahip olan, %100 Ecocell, %100 Modal, %100 Bambu ve %100 Viskon elyaf içeren Ne 30/1 iplik numarasında Ring ve Vorteks iplik eğirme sistemlerinde üretilen ipliklerden süprem örme kumaş yüzeyleri oluşturulmuştur. Elyaf tipinin ve iplik üretim prosesinin etkisini incelemek amacıyla, gramaj, kalınlık, hava geçirgenlik ve boncuklanma özellikleri test edilmiştir.

Anahtar Kelimeler: Ecocell, sürdürülebilir lifler, hava geçirgenliği, boncuklanma.

1. Giriş

21. yüzyılın en önemli konuları arasında yer alan küresel ısınma ve karbon salınımının artması, tüm üretim sektörlerinde olduğu gibi tekstil sektörünü daha duyarlı bir üretime yöneltmiştir. Giysilerin üretim aşamalarında kullanılan elyaf, boyar madde ve su kullanımı bu açıdan büyük öneme sahiptir. Sürdürülebilir lif sınıfına giren rejenere selülozik liflerin kullanımına yönelik talebin artmasıyla birlikte ekolojik olarak çevreye duyarlı proses adımları tercih edilmektedir. Bu amaçla Ecocell (Lyocell) liflerinin üretim prosesinde kullanılan doğal çözgen olan NMMO (N-metil Morfolin N-Oksit) kullanımı, proses aşamasında % 99,6 oranında sistem içerisinde geri dönüştürülerek kullanılabilmesi bu üretim prosesini diğer rejenere selülozik liflere (Modal, Bambu ve Viskon) kıyasla daha çekici bir elyaf haline getirmiştir. Rejenere selülozik liflerden elde edilen örme ve dokuma kumaşların performans ve konfor özellikleri literatürde birçok araştırmacı tarafından araştırılmıştır.

Çarkıt (2012), 70/30 Bambu-Pamuk, % 100 Pamuk, % 100 Modal, 50/50 Modal-Pamuk içerikli Ne 30/1 iplik numarasında ring iplik eğirme sisteminde üretilen ipliklerden, süprem, lacoste ve ribana örgü yapısında örme kumaşlar üretilmiştir. Üretilen kumaşlara 130 g/l, 100 g/l, 70 g/l' lik NaOH çözeltileri 5, 10 ve 15 dk. boyunca kostik işlem uygulanmış. Elde edilen kumaşların boncuklanma, patlama mukavemeti ve tuşe özellikleri incelenerek bambu içeren kumaşların boncuklanma dayanımının % 100 pamuk kumaştan daha iyi ancak modal içerikli kumaşlardan daha kötü olduğu tespit edilmiştir (1).

Ala ve ark. (2017) yaptıkları çalışmada, 3 farklı iplik numarasında (Ne 12/1, Ne 16/1 ve Ne 20/1) %100 pamuk elyafı içeren iplikler süprem örme kumaşlar elde edilmiştir. Elde edilen bu örme kumaşlara, farklı pH ortamında antipil enzim uygulanmış ve antipil enzim uygulamasında pH derecesinin boncuklanma üzerindeki etkisi araştırılmıştır. Çalışmaya göre, iplik numarası ve kumaşların ilmek yoğunluğunun, kalınlık, hava geçirgenlik ve boncuklanma özellikleri üzerinde etkili olduğu tespit edilmiştir. Ayrıca, antipil enzim uygulamasında flottenin pH değerinin, özellikle pH 6'da antipil enzim uygulanmış olan kumaşlar için antipil enzim uygulanmamış kumaşlara göre daha iyi boncuklanma değerleri elde edilmiştir (2).

Dirgar (2017) çalışmasında, %100 viskon, %100 modal, %100 lyocel ve %100 cupro elyaf içeren Ne 30/1 iplik numarasında üretilen ipliklerden yapılmış süprem örme kumaşların performans özelliklerini (gramaj, kalınlık, patlama mukavemeti, aşınma direnci, esneme, gözeneklilik, hava geçirgenliği ve boncuklanma) incelemiştir. Gerçekleştirdiği çalışmada, en yüksek hava geçirgenliği sonucunu cupro lifinden üretilmiş kumaşlarda, en yüksek patlama mukavemeti değerini lyocel lifi ile üretilmiş kumaşlarda ve en yüksek aşınma direnci değerini modal lifinden üretilmiş kumaşlarda elde etmiştir. Çalışmaya göre, aynı iplik numarasında ve örme tipinde olan farklı elyaf içeriğine sahip olması, kumaşların fiziksel özelliklerini etkileyen önemli bir parametre olduğu tespit edilmiştir (3).

Basit ve ark. (2019), %100 Pamuk, %50/50 Lyocel/Modal, %50/50 Lyocel/Viskon ve %50/50 Lyocel/Bambu, liflerini içeren ipliklerden 120 g/m^2 birim ağırlığında bezayağı dokuma tipinde kumaş üretimleri yapılmıştır. Kumaşların mekanik özellikleri (çözgü ve atkı yönünde çekme ve yırtılma mukavemetleri, boncuklanma ve aşınma direnci) ve konfor özellikleri (hava geçirgenliği, nem yönetimi özellikleri ve termal direnç) analiz edilmiştir. Lyocel/Modal karışımlı kumaşın, incelenen tüm karışımlı kumaşlardan daha yüksek mekanik (gerilme ve yırtılma mukavemeti, boncuklanma ve aşınma direnci) ve konfor özelliklerini (nem yönetimi, termal direnç ve hava geçirgenliği) gösterdiği tespit edilmiştir. Ayrıca Lyocel/Viskon ve Lyocel/Bambu karışımlı kumaşların %100 pamuğa göre daha iyi mekanik ve konfor özellikleri test sonucu verdiği belirlenmiştir (4).

Çeven ve Günaydın (2020), %100 Lyocel, %100 Modal, %100 Cupro ve %100 Umorfil, lifleri içeren Ne 30/1 iplik numarasında kompakt iplik eğirme sisteminde üretilen ipliklerden yapılmış süprem örme kumaşların termal özellikleri (su buharı geçirgenliği, su buharı direnci), hava geçirgenliği ve patlama mukavemeti gibi performans özellikleri incelenmiştir. Çalışmanın sonuçlarına göre, örme kumaşların rejenere selülozik iplik tipi ve işlem tipinin (işlenmemiş ham kumaş veya boyalı kumaş) performans özelliklerine etkisinin olduğu belirtilmiştir. Ayrıca rejenere selülozik liflerin yanı sıra yeni geliştirilen kolajen peptit katkılı Umorfil lifinin de spor giysiler için örme kumaşlarda kullanılabileceğini ve konfor test sonuçlarıyla tespit edilmiştir (5).

Bu çalışmada, %100 Ecocell, %100 Modal, %100 Bambu ve %100 Viskon elyaf içeren Ne 30/1 iplik numarasında Ring ve Vorteks iplik eğirme sistemlerinde üretilen ipliklerden süprem örme kumaş yüzeyleri oluşturulmuştur. Elyaf tipinin ve iplik üretim tekniğinin etkisini incelemek amacıyla, gramaj, kalınlık, çap, may sayısı, hava geçirgenliği, porozite ve boncuklanma özellikleri test edilmiştir.

2. Materyal ve Yöntem

2.1. Materyal

Bu çalışmada, ekolojik lifler sınıfına giren, Ecocell, Modal, Bambu ve Viskon liflerinden %100 oranlarında vorteks ve ring iplik eğirme sistemlerinde iplikler üretilmiştir. Çalışma kapsamında kullanılan liflerin özellikleri (İncelik : TS EN ISO 1973, kopma mukavemeti ve uzaması: TS EN ISO 5079:2021, nem içeriği ASTM D2654 standartlarına göre yapılmıştır) Tablo 1'de gösterilmiştir.

Tablo 1. Kullanılan liflerin özellikleri

Özellik / Elyaf	İncelik (dtex)	Uzunluk (mm)	Yoğunluk (g/cm^3)	Uzama (%)	Kuru Mukavemet (cN/tex)	Yaş Mukavemet (cN/tex)	Nem (%)
Ecocell	1.31	38	1.50	12,9	37,5	32,2	9
Modal	1.33	38	1.53	12,8	32,3	19,0	9
Bambu	1.30	38	1.32	18,3	24,5	14,1	9
Viskon	1.31	38	1.52	16,5	22,7	11,6	9

2.2. Yöntem

Ring ve vorteks iplik eğirme sistemlerinde, Ne 30/1 iplik numarasıyla üretilen ipliklerin üretim parametreleri Tablo 2'de verilmiştir.

Tablo 2. İplik üretim parametreleri

Özellik	Ring	Vorteks
Çıkış hızı (m/dak.)	20	500
Çekim	60	150
İğ hızı (rpm)	16.000	-
Bilezik çapı (mm)	38-40	-
Nozzle tipi	-	M1 eco
Spindle iç çapı (mm)	-	1,2
Hava basıncı (MPa)	-	0,55 bar
Spindle uzaklığı (mm)	-	20

İplik numuneleri test edilmeden önce, 20±2 °C sıcaklıkta ve 65±4% bağıl nemde 24 saat kondisyonlanmıştır. İplik kopma mukavemet ve uzama ölçümleri TS EN ISO 2062 standardına göre Uster® Tensorapid cihazı kullanılarak, her bir iplik tipi için 5'er kopstan 400 m/dk hız ile 500 mm ölçüm uzunluğunda gerçekleştirilmiştir. İplik düzgünsüzlüğü ve iplik hataları TS 2394 ISO 2649 standardına göre Uster® Tester 4 cihazı ile gerçekleştirilmiştir. Hata endeksi iplikte +50 kalın yer, -40 ince yer ve +200 neps'in kümülatif toplamını ifade etmektedir. Çalışma kapsamında iplik hataları "hata endeksi (IPI)" olarak incelenecektir.

Çorap örme makinesinde üretilen örme kumaşlar 20 fine, 3,5´´ pus, LFA: 38 cm de, sıklık faktörü:1,16 ve 25 devir/dk' da üretilmiştir. Süprem örme kumaş numunelerine, Birim Ağırlık ve Kalınlık tayini; "TS 251" standartlarına göre kumaş birim ağırlığı ve "TS 7128 EN ISO 5084" standartlarına göre kalınlık test ölçümleri gerçekleşmiştir. Çap ölçümü Leica S91 sterio mikroskopta yapılmıştır. Hava geçirgenliği testi için; "TS 391 EN ISO 9237" standartlarına göre 5 tekrarlı ölçümler, 100 Pa basınç altında 5 cm2'lik alan üzerine yerleştirilen numunelerin ölçümleri yapılmıştır. Boncuklanma testi için; "TS EN ISO 12945-2" standartlarında 14 cm çapında kesilen numuneler standart sünger ile desteklenerek tutuculara yerleştirilmiştir. Örgü kumaşlar için 9 kPa ağırlık altında 2000 devirde numunelerin boncuklanma testleri yapılmıştır.

3. Bulgular ve Tartışma

3.1. İplik Test Sonuçları

İpliklerin ortalama iplik mukavemeti, uzaması, düzgünsüzlük, hata endeksi değerleri Tablo 3'te verilmiştir.

Tablo 3. İplik Test Sonuçları

Numune No	Üretim Sistemi	Elyaf Tipi	Mukavemet (kgf*Nm)	Uzama (%)	U%	CVm	IPI
1	Ring	%100 Ecocell	28,57	9,93	9,11	11,49	32,5
2	Vorteks		27,42	9,01	8,92	11,26	47,5
3	Ring	%100 Modal	24,76	11,85	8,65	10,91	37,5
4	Vorteks		21,28	9,49	9,56	12,05	23,5
5	Ring	%100 Bambu	15,83	13,82	10,83	13,67	156
6	Vorteks		14,86	9,79	10,62	13,39	255
7	Ring	%100 Viskon	17,59	14,87	9,16	11,56	52,5
8	Vorteks		13,83	9,61	9,67	12,19	80

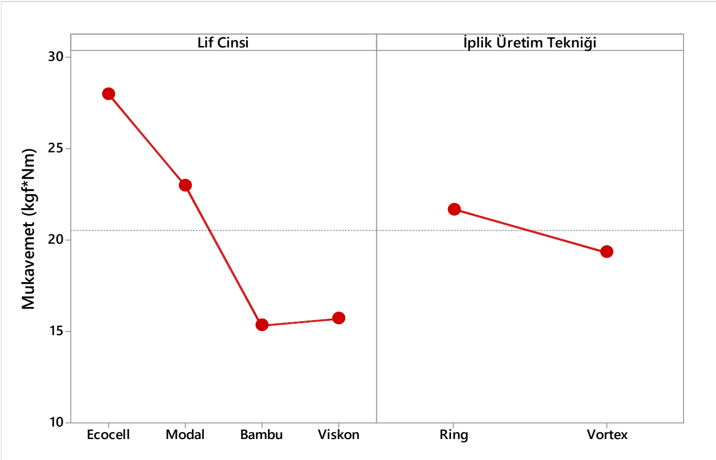

Şekil 1. Mukavemet test grafiği

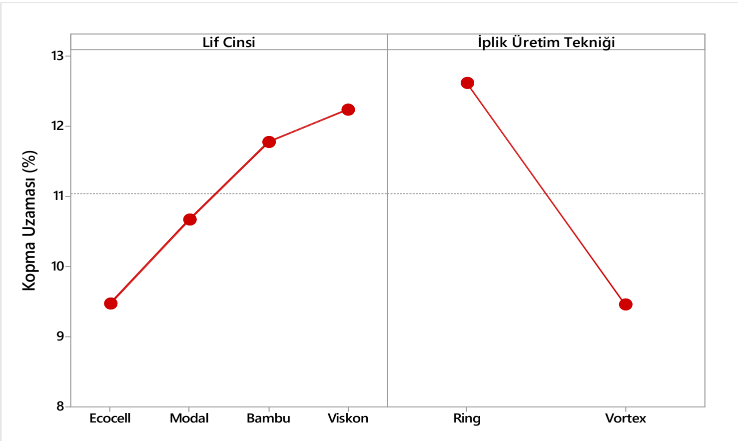

Şekil 2. Uzama test grafiği

Alınan test sonuçlarına göre 20 RKM değeri ortalama sonuç olarak kabul edilmiş ve %100 Ecocell elyafı ring ve vorteks eğirme sisteminde de ortalamanın çok üstünde sonuçlar vermiştir. En düşük sonuçlar bambu ve viskon elyafına ait ipliklerden alınmıştır. Elyaf tipine göre en yüksek uzama sonuçları ise %100 Bambu içerikli ipliklerden elde edilmiştir. İplik mukavemeti ve uzama değerleri, elyaf mukavemeti ve uzama değerleri ile doğrudan ilişkilidir. Elyaf mukavemetinin (Ecocell 37,5 cN/tex) iplik mukavemet değerlerine (%100 Ecocell Ring 28,7 RKM ve Vorteks 27,42 RKM) etki ettiği sonuçlarını desteklemektedir.

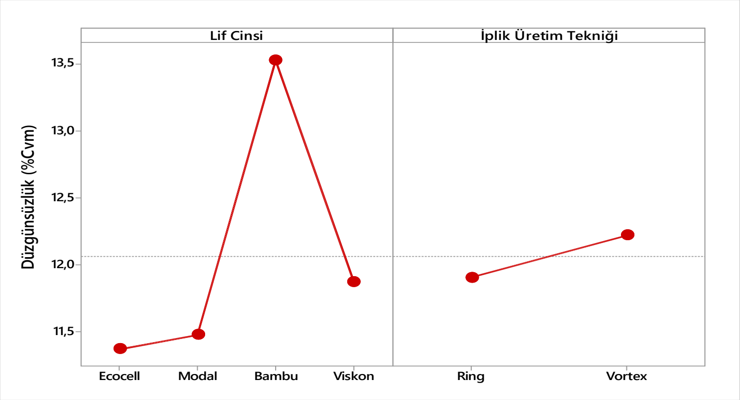

Şekil 3. Düzgünsüzlük test grafiği

Düzgünsüzlük (CVm%) değerini iplik üretim parametrelerinin yanı sıra elyaf morfoloji, krimp tekniği, elyaf üretim tekniğinden etkilenmektedir. Vorteks eğirme tekniği, ring eğirme tekniğine göre daha yüksek düzgünsüzlük sonuçları vermiştir. En iyi sonuçlar her iki eğirme tekniği için de %100 Ecocell ile üretilen ipliklerde olup en düzgünsüz yapının bambu ile üretilen ipliklerde olduğu görülmüştür. Yeknesaklığı kötü alınan liflerin kuagülasyon banyosunda çekimi tamamlanmış olan viskon ve bambu lifleri olduğu düşünülmektedir. %100 Ecocell ipliklerin diğer rejenere selülozik ipliklere kıyasla daha düşük düzgünsüzlük sonuçlar verdiği kaydedilmiştir.

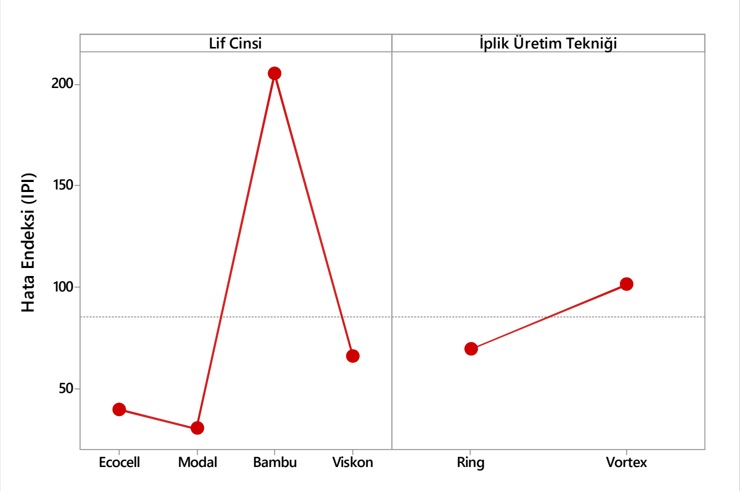

Şekil 4. Hata Endeksi test grafiği

IPI hata endeksi sonuçları, düzgünsüzlük sonuçlarına paralel olarak bambu lifinden üretilen ipliklerde daha yüksek görülmüş, en iyi sonuçların ise modal lifinden yapılmış ipliklerde olduğu gözlemlenmiştir.

3.2. Örme Kumaş Test Sonuçları

Hava Geçirgenliği

Örme veya dokuma kumaşların hava geçirgenlik özellikleri, elyaf tipi ve iplik numarası başta olmak üzere, kumaş kalınlığı, örgü tipi, kumaş sıklığı ve gözenekliliği gibi birçok yapısal özellikten etkilenmektedir (2). Hava geçirgenliği nem/terleme ile oluşan buharın tenden iletilmesinde önemli bir kumaş konfor faktörüdür (6). Numunelerin kalınlık, iplik çapı ve hava geçirgenlik değerleri Tablo 4'te verilmiştir.

Tablo 4. Hava Geçirgenliği Test Sonuçları

Numune No	Üretim Sistemi	Elyaf Tipi	Kalınlık (mm)	Hava Geçirgenliği (mm/s)	İplik Çapı (mm)
1	Ring	%100 Ecocell	0,72	4553,12	0,189
2	Vorteks		0,73	4131,19	0,185
3	Ring	%100 Modal	0,73	4267,39	0,200
4	Vorteks		0,75	3892,10	0,186
5	Ring	%100 Bambu	0,64	4957,14	0,161
6	Vorteks		0,66	4939,59	0,161
7	Ring	%100 Viskon	0,64	4477,67	0,168
8	Vorteks		0,72	4193,05	0,165

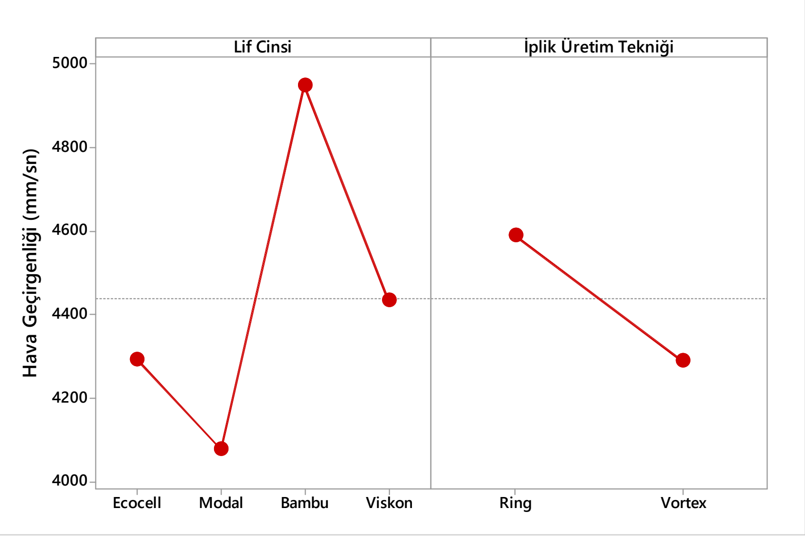

Şekil 5. Hava Geçirgenliği test grafiği

Yapılan test sonucunda kullanılan iplik eğirme sisteminin ve karışım özelliklerinin hava geçirgenliğine etkisi incelenmiştir. Buna göre kullanılan iplik eğirme sistemleri incelendiğinde, ring makinesiyle üretilen kumaşların hava geçirgenliğinin vorteks makinesiyle üretilen kumaşlardan daha yüksek olduğu tespit edilmiştir. Büküm morfolojisinin önemli bir faktör oldugu düşünülmektedir. Farklı lif türleri, farklı iplik çapları oluşturmus ve dolayısı ile farklı gözenek yapıları elde edilmiştir, bu ise farklı hava geçirgenllik sonucları elde edilmesine sebep olmuştur. En yüksek hava gecirgenliği değeri, en düşük çapa sahip bambu lifleri ile elde edilmiştir. En düşük hava geçirgenliği değeri en yüksek çap değerine sahip modal liflerinden örülmüş kumaşta tespit edilmiştir.

Porozite

Gözeneklilik, boşluk hacminin toplam malzeme hacmine oranıdır. Kumaş gözenekliliği, geçirgenlik özelliklerini doğrudan etkiler. Gözeneklilik, Sıkılık, kumaş tipi, iplik yapısı, gibi parametrelerden doğrudan etkilenir (7)

Porozite ölçümü (8);
Eşitlik 1'e göre porozite değerleri hesaplanmıştır.

$$\varepsilon = 1 - \frac{\pi d^2 lcw}{2t} \qquad (1)$$

Burada ε -gözeneklilik, d-iplik çapı, l-ilmek uzunluğu, c-may sayısı, w-çubuk sıklığı, t-kalınlık. İplik yoğunluğu olarak. Sonuçlar Tablo 5'te verilmiştir.

Tablo 5. Hava Geçirgenliği Test Sonuçları

Elyaf Tipi	İplik Üretim Tekniği	İplik Çapı (mm)	İlmek Uzunluğu (mm)	cpc	wpc	Kalınlık (mm)	Gramaj (gr/m^2)	Porozite
%100 Ecocell	Ring	0,189	3,8	11,5	9	0,72	93	0,69
%100 Ecocell	Vorteks	0,185	3,8	14	10	0,73	95	0,61
%100 Modal	Ring	0,200	3,8	12	11	0,73	94	0,57
%100 Modal	Vorteks	0,186	3,8	14	12	0,75	102	0,54
%100 Bambu	Ring	0,161	3,8	11	8,5	0,64	88	0,77
%100 Bambu	Vorteks	0,161	3,8	14	9	0,66	89	0,70
%100 Viskon	Ring	0,168	3,8	12	8,5	0,64	89	0,73
%100 Viskon	Vorteks	0,165	3,8	14	9	0,72	92	0,72

Şekil 6. Porozite grafiği

Modal iplik ile üretilen kumaşlar en az gözeneklilik değerine sahiptir. En yüksek gözeneklilik ise bambu lifleri ile üretilen kumaşlara aittir.
Gözeneklilik grafikleri hava geçirgenliği ile paralel sonuçlar vermiştir. Pearson korelasyonu 0,781 olarak hesaplanmıştır.

Boncuklanma
Boncuklanma, kumaşın yapısında bulunan liflerin iplik veya kumaş yapısı içerisinden çıkarak kumaş yüzeyine yükselmesi sonucunda tuşeyi de etkileyen görüntü bozukluğudur. Özellikle örme kumaşlar örgü yapısından kaynaklı, dokuma kumaş yüzeylerine kıyasla daha fazla boncuklanma eğilimindedirler. Numunelerin birim ağırlık ve boncuklanma değerleri Tablo 6'te verilmiştir.

Tablo 6. Boncuklanma Test Sonuçları

Numune No	Üretim Sistemi	Elyaf Tipi	Boncuklanma Derecesi
1	Ring	%100 Ecocell	1-2
2	Vorteks		1-2
3	Ring	%100 Modal	1-2
4	Vorteks		1-2
5	Ring	%100 Bambu	1-2
6	Vorteks		1-2
7	Ring	%100 Viskon	1-2
8	Vorteks		1-2

Yapılan test sonucunda rejenere selüloz içerikli tüm lif türlerinin ham kumaş pilling değerlerinin aynı olduğu görülmüştür.

4. Sonuçlar

Çalışmanın amacı, sürdürülebilir ve biyobozunur özelliklere sahip olan, %100 Ecocell, %100 Modal, %100 Bambu ve %100 Viskon elyaf içeren Ne 30/1 iplik numarasında Ring ve Vorteks iplik eğirme sistemlerinde üretilen ipliklerden süprem örme kumaşların hava geçirgenlik, gözeneklilik ve boncuklanma özellikleri üzerindeki etkilerini analiz etmektir. Bu amaçla öncelikle üretilen ipliklerin mukavemet, uzama, düzgünsüzlük, hata indeksi, kalınlık, gramaj, iplik çapı, may sayıları özellikleri incelenmiştir.

Genel bir değerlendirme yapıldığında en yüksek mukavemet ve uzama değerlerinin, lif mukavemet ve uzama değerlerine paralel olarak Ecocell lif içeren ipliklere ait olduğu görülmektedir. En düşük hava geçirgenliği değerinin Modal lif ile üretilen kumaşlarda olduğu görüşmüştür. Ham kumaşlar üzerinde yapılan pilling ölçümlerinin tüm lif türlerinde aynı olduğu gözlemlenmiştir.

Referanslar:

1. Çarkıt, G., Bambu-Pamuk Karışımlı Örme Kumaşların Özelliklerinin İncelenmesi, 2012, Erciyes Üniversitesi, Fen Bilimleri Enstitüsü, Tekstil Mühendisliği Anabilim Dalı, Yüksek Lisans Tezi.
2. Ala M.D., Bakici G. G., Abdulvahitoğlu, A., Süprem Örme Kumaşlarda Kalınlık, Hava Geçirgenliği Ve Boncuklanma Özelliklerinin İncelenmesi, Çukurova Üniversitesi Mühendislik Mimarlık Fakültesi Dergisi, 2017, 32(3): 103-109.
3. Dirgar, E., The Performance Properties of The Fabrics Produced From Cupro And Some Other Regenerated Cellulose Fibers, 2017, Tekstil ve Konfeksiyon 27(2):139-144.

4. Basit, A., Latif, W., Ashraf, M, Rehman, A., Iqbal, K., Maqsood, S. H., Jabbar A., Baig, A.S., Comparison of Mechanical and Thermal Comfort Properties of Tencel Blended With Regenerated Fibers and Cotton Woven Fabrics, 2019, Autex Research Journal, Vol. 19, (1):80-85.
5. Çeven, K. E. ve Günaydın, K.G., Evaluation of Some Comfort and Mechanical Properties of Knitted Fabrics Made of Different Regenerated Cellulosic Fibres, 2020, Fibers and Polymers.
6. Karagüzel B., Characterization and Role of Porosity in Knitted Fabrics, 2004, Msc Thesis, North Carolina State University, Department of Textile Engineering, Chemistry and Science.
7. Okur, A., Pamuklu Kumaşlarda Hava Geçirgenliği ile Kumaşın Bazı Yapısal Özellikleri Arasındaki İlişkiler Üzerine bir Araştırma. Tekstil ve Konfeksiyon,1993, 4, 292-299.
8. Serin, M., Oğulata, T.,R., Investigation of Porosity and Air permeability Values of Plain Knitted Fabrics, 2010, Fibers & Textiles in Eastern Europa, Vol.18, No.5 (82) 71-75.

AN INVESTIGATION OF THE CRYSTALLINITY AND OTHER PHYSICAL PROPERTIES OF COMMERCIAL POLYESTER FIBERS

VOLKAN MURAT YILMAZ[1], MEMIK BUNYAMIN UZUMCU[2], TULIN KAYA NACARKAHYA[3]

[1]Bartın University, Central Research Laboratories, Bartın, TURKIYE
[2]Gaziantep University, Department of Textile and Fashion Design, Gaziantep, TURKIYE
[3]Kara Holding, R&D Center, Gaziantep, TURKIYE (Times New Roman 10pt)

Abstract

From its devepolpment in 1940s to now, Polyester fibers became one of the most used fiber types in textile industry. It has lots of properties which make it suitable to build clothings as well as fabrics that can be used for their technical functions. In this study, some of the characteristics and properties of commercial polyester fibers which yarn producers use were investigated. For this reason, 4 different polyester fibers were evaluated in terms of their characteristics and properties. XRD tests were carried out and some physical properties of fibers were used in selection of the most suitable fiber type for yarn production.

Keyword: polyester, characterization, fiber properties, product properties.

1. Introduction

Fiber properties are one of the most important factors that determine the properties of the product produced from it. Other factors are generally related to the process and the differences in the applied processes also affect the product properties. Therefore, in order to develop a suitable product for the need, it is necessary to select the appropriate raw material, determine the systems in which this raw material will be processed most appropriately, and make the settings in these systems depending on the planned product.

The development of polyester, one of the most used fibers in textile industry, took place in 1940s, after a series of research carried out by different scientists. Those days, they named this fiber "Terylene" or "Dacron", as the Dupont used [1]. Its "Low cost, convenient processability, ease of blending with cotton and other natural fibers, convenient recyclability, and excellent and tailorable performance" are the reasons why this fiber type has a great importance for textile manufacturers [2]. However, there are lots of producers for polyester fibers all over the world these days and even the fundementals of its production are the same, some properties may differ from fiber to fiber. Therefore, although they will use the same fiber in practice, the textile manufacturer who will use polyester fiber should have information about the fiber purchased, use the data from the fiber manufacturer and their own analysis, and choose the fiber that will create the best effect for the product and cause minimum disruption in its production.
In this study, different polyester fibers obtained from different producers were comparatively investigated. In order to do this, our initial work was characterization of the fibers. After that, some

properties of the fibers were analysed. The aim was to understand "what to look for in these fibers?" to obtain the results desired.

2. Materials and Methods

We obtained four different commercial polyester fiber types from local and foreign producers. We named these fiber as "P1, P2, P3 and P4". Some of the basic properties of these fibers –which were tested according to the standards- were given by the fiber producers. However, the first thing handled was characterization of the fibers. Therefore, XRD tests were done. (Table 1).

Table 1. Test Standards

Test	Standard
Linear Density	TS EN ISO 1973
Breaking Strength, Breaking Elongation	TS EN ISO 5079:2021

3. Results and Discussion

In this study, properties of commercially available polyester fibers were investigated. For this reason, initially, XRD test was carried out. According to the results of XRD tests, crystallinities (%) of these were calculated. These results are given in table 1.

Table 2. Crystallinity of the fibers

Fiber type	Crystallinity (%)
P1	47.93
P2	54.96
P3	47.74
P4	52.44

Properties of the fibers are affected by how the macromolecules are located in the fiber structure. There are crystalline and amorphous regions in the fiber. The percentage of the crystalline regions is called crystallinity (%). Drawing speed in fiber production affects crystallinity of polymer fibers [3]. According to the calculated crystallinity results 2 of the tested fiber types had crystallinity over 50% and 2 of them below it. This results can affect properties like strength, elongation, stiffness and dye-uptake [4], [5]. XRD graphs of the polyester fibers are given in Figure 1. These graphs shows us that these for fibers are from the same material (peaks are at the same degree), however the their intensities are different, meaning these fibers have different crystallinities, as before mentioned.

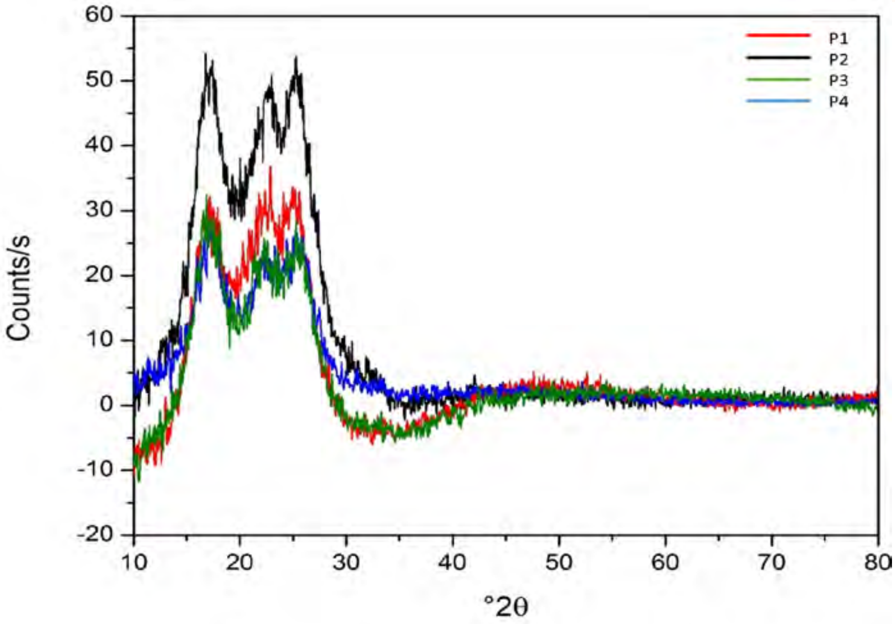

Figure 1. XRD Results

The physical properties of the four types of polyester fibers are given in Table 3.

Table 3. Fiber Properties (mean)

Properties	**Unit**	P1	P2	P3	P4
Linear Density	denier	1,51	1,4	1,45	1,37
Breaking Strength	gpd	5,29	5,1	6	6,48
Breaking Elongation	%	40,48	30	27	21,69
Mean Length	mm	40	38	38	38,1

According to the results, polyester fibers produced by different companies have different properties (Table 1). The main focus of the textile manufacturer that will use these fibers in their goods should be "which properties are the most important one for my product?". In case of breaking strength, P4 polyester fibers have the highest results, while P2 fibers have the lowest. This is an important feature of textile fiber, because the strength of the fiber also effects the strength of the product its used in. If we are speaking about a yarn producer, 30%-70% of yarn tenacity comes from the strength of the fiber [6], [7].

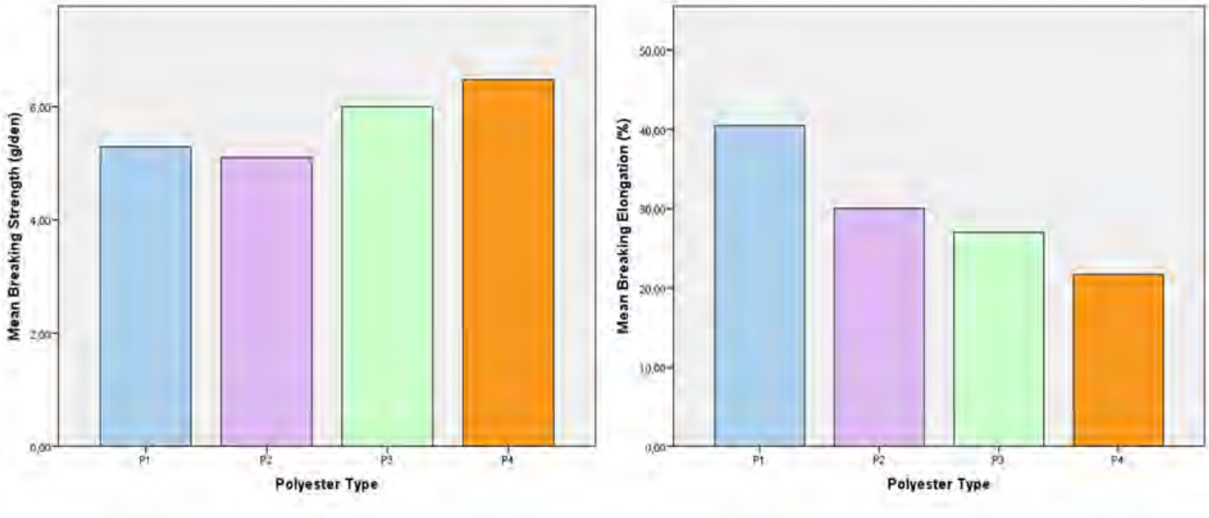

Figure 2. Breaking strength (g/den) and breaking elongation (%) results

Linear density and fiber length are the two properties that can be arranged according to the customer's needs. In our example, in between the four different polyester fibers, mean length results of the fibers are similar except P1. There are statistically important differences between the linear density results of the polyester fiber types ($p<0.05$). This difference means a lot, again for yarn producers. Using finer fibers means more fiber count on cross-section of the yarn, and it results with higher tensile strength on yarns with same twist coefficient. Moreover, twist coefficient can be lowered and it results with improved handle properties in fabrics.

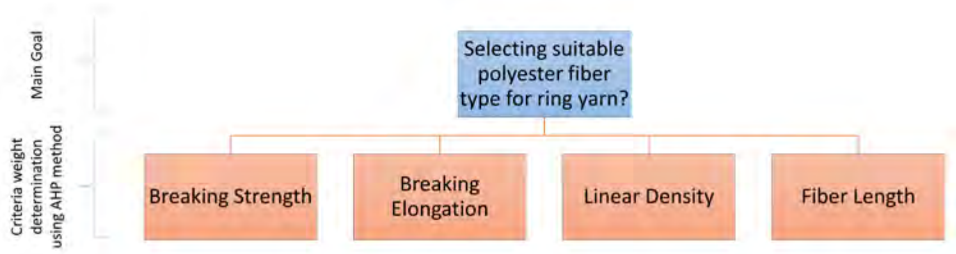

Figure 3. AHP Method

Considering that a yarn manufacturer produces polyester yarn and produces this yarn using ring spinning system, the Analytical Hierarchy Process (AHP) method is used to decide which polyester type to be selected by the producer . This method, developed by Saaty, allows the qualitative estimates elicited from experts to be converted to quantitative ones [8]. Opinions of 5 experts were taken for the criteria matrix created. With this method, fiber properties are weighted. As a result of the analysis, it was determined that the ring yarn manufacturer should pay attention to the strength first and then the fiber length in the selection of polyester material. Breaking elongation was determined as the least important fiber property in the selection. Therefore, in such a decision, the yarn manufacturer can perform the fiber selection by applying a similar method and prioritizing the weights of different fiber properties. For our study and the fiber types we purchased, P4 polyester type is the most suitable fiber type between our samples.

Table 4. AHP criteria matrix

Criteria	Breaking Strength (g/den)	Breaking Elongation (%)	Mean Length (mm)	Linear Density (den)	**Weight**
Breaking Strength (g/den)	1	5	2	2	0,44
Breaking Elongation (%)	0,2	1	0,25	0,33	0,07
Mean Length (%)	0,5	4	1	2	0,29
Linear Density (den)	0,5	3	0,5	1	0,19

λ_{max}	4,0544506
Consistency index (CI)	0,018
Consistency ratio (CR)	0,0205785

4. Conclusions

In this work, it was aimed to determine what does yarn producer have to ask from polyester fibers, before purchase. For this reason, different properties of fibers gathered from different producers. Some tests were carried out for characterization and determining the physical properties of the fibers. According to the results, it is possible to mention that, even the fundamentals of production of these fibers are the same, the outcomes are different. This may be caused by using different parameters during production. Especially, fiber characterization in these fibers are important for the product properties. Even in these four different fiber types, we have seen diferences in fiber crystallinity, which effects strength, elongation, stiffness and dye-uptake. Moreover, we have used AHP method to ease the fiber selection period which have different aspects that can effect the yarn quality.

References

[1] J. E. McIntyre, "Historical background," in *Synthetic fibres : nylon, polyester, acrylic, polyolefin*, 1st ed., J. E. McIntyre, Ed. Boca Raton-Florida: CRC Press, 2005, p. 300.

[2] M. Jaffe, A. J. Easts, and X. Feng, "Polyester fibers," in *Thermal Analysis of Textiles and Fibers*, Woodhead Publishing, 2020, pp. 133–149.

[3] O. Demiryürek and E. Koç, "The mechanism and/or prediction of the breaking elongation of polyester/viscose blended open-end rotor spun yarns," *Fibers Polym.*, vol. 10, no. 5, pp. 694–702, Nov. 2009.

[4] S. Dhouib, A. Lallam, and F. Sakli, "Study of Dyeing Behavior of Polyester Fibers with Disperse Dyes," *Text. Res. J.*, vol. 76, no. 4, pp. 271–280, 2006.

[5] K. Ward, “Crystallinity of Cellulose and Its Significance for the Fiber Properties,” *Text. Res. J.*, vol. 20, no. 6, pp. 363–372, 1950.
[6] J. A. Foulk and D. D. Mcalister, “Single Cotton Fiber Properties of Low, Ideal, and High Micronaire Values,” *Text. Res. J.*, vol. 72, no. 10, pp. 885–891, Oct. 2002.
[7] M. B. Uzumcu, P. Celik, T. Gulumser, and H. Kadoglu, “A Comparison of Color Fastness Properties of Mulberry Silk and Tussah Silk Fabrics in Blends with Cellulosic Fibers,” *J. Nat. Fibers*, vol. 18, no. 11, pp. 1834–1843, Dec. 2021.
[8] V. Podvezko, “Application of AHP technique,” *J. Bus. Econ. Manag.*, vol. 10, no. 2, pp. 181–189, 2009.

INVESTIGATION OF THE PERFORMANCE PROPERTIES OF CONVENTIONAL ACRYLIC AND RECYCLED ACRYLIC

Edanur TURGUT[1]*, M. İdris AKTAŞ[2] & Mehmet TOPALBEKİROĞLU[3]

[1,2] Boyar Kimya San. ve Tic. A. Ş. Gaziantep/Türkiye
[3] Gaziantep Üniversitesi, Tekstil Mühendisliği Bölümü, Gaziantep/Türkiye
[1]*edanur.turgut@boyar.com.tr

Abstract

The textile industry is one of the world's largest and fast-growing sectors. It is the meeting point of many related industries that rely on natural (cotton, wool, flax, silk, etc.) and/or man-made (synthetic) (acrylic, polyester, nylon, etc.) fibers. The worldwide textile market reached a worth of USD 993.6 billion in 2021 and was anticipated to grow at a compound annual rate (CAGR) of 4.0% from 2022 to 2030. During the production of textile products, a large amount of energy, water, and chemicals are utilized in addition to the generation of a large number of soft wastes. In recent years, acrylic fiber has gained a lot of recognition globally since it shares similar properties with wool fiber, however, its environmental impact is immense because acyclic wastes aren't biodegradable and they can remain in the environment for up to 200 years and a huge amount of carbon dioxide and toxic chemicals is accompanied with its production. As a result of the factors mentioned above recycled textile products are of great importance because it minimizes harm done to the environment and helps resolve the planet's resources since recycling consumes less energy than the production of a new product and reduces the number of wastes sent to the landfills. The study aims to contribute to sustainability by expanding the use of recycled products and including products that are originally unusable textile wastes in the production line and delivering them to the buyer. To do so high bulk acrylic yarn with a count of 7.5 Nm with the following blending ratios [(100% conventional acrylic, 0% recycled acrylic)/(85% conventional acrylic, 15% recycled acrylic)/(70% conventional acrylic, 30% recycled acrylic)/ (55% conventional 45% recycled acrylic)] were produced and a comparison between conventional acrylic yarn and blends that contain both conventional and recycled acrylic is to be conducted according to the hairiness, strength, and Uster test (unevenness, CV) of the obtained samples.

Keywords: Conventional acrylic, recycle acrylic, sustainability, strength, hairiness, unevenness.

1. Introduction

Environmental harm has recently become one of the most important issues around the globe and the increased public awareness has forced a lot of industries to change and the need to implement recycling into the production plan has become significant. One of the most important yet have huge negative impact on the environment is the textile industry which has been growing rapidly and enormous growth is expected in the coming years. Fibers are of great importance among textile products since they are the main source for yarn production. Fibers are classified into two groups Natural and Man-made fibers. Natural fibers are divided into 3 different categories: Plant (Cotton, Flax, wool, silk et…). Nylon, Polyester, Acrylic, Rayon, and Carbon fibers are among the most important synthetic fibers. Each one of these fibers possesses unique properties that make it desirable, however, what makes acrylic fiber one of the most important synthetic fibers is that it replicates the properties of the natural wool fiber, and due to this reason, the acrylic fiber production and market share have increased tremendously in the past few years. During the production processes of acrylic fiber, a large amount of waste is generated. This waste is a non-degradable waste and can remain intact in the environment for a very long time therefore the recycling of these wastes is becoming very common and the number of textile recycling companies is increasing. Recycling can be categorized into three main technologies, mechanical, chemical, and biochemical [1-5].

For acrylic fiber, chemical recycling is the most appropriate method of recycling and very few studies have been posted online regarding this matter, [9] came up with a novel method to convert acrylic fiber waste obtained from the manufacturing process to acrylic powder that can be used as acrylic fiber raw material and can be mixed with virgin material to produce yarn with properties that are 100% similar to the conventional acrylic yarn. However, not all recycled yarns have the same properties as conventional acrylic yarn, which depends mostly on the recycling method. The reason for mentioning this is that people hesitate to buy textile products that are recycled (or products produced from blends of recycled and conventional fibers/yarns) and that is because some people came to the conclusion that recycled products are far worse than the original products since they are made mostly from used materials, and to some extent, these claims are true because some fibers experience a loss of strength and other properties. However, this doesn't mean the recycled products are bad or unusable and even though a loss of quality can be present, it should be considered a small price that all of us should pay to sustain and preserve what is left of the environmental resources for us and the upcoming generation. So hairiness, strength, and Uster test (unevenness, CV) were examined to see the differences in performance characteristics between conventional acrylic and recycled acrylic more clearly [6,7,8].

2. Material and Method

2.1. Material

In these studies, the use of recycled acrylic fiber and 7.5 NM yarns with conventional acrylic fiber additives and their usability as tops in knitted fabrics and some of their performance properties were investigated. Yarn count, knitting type and density parameters used to be examined in the study were kept constant. The samples were produced raw, unpainted.

7.5/1 NM yarns were used in the samples. There are differences in the mixing ratios of these yarns. As seen in Table 1, the contents [(100% conventional acrylic, 0% recycled acrylic)/ (85% conventional acrylic, 15% recycled acrylic)/(70% conventional acrylic, 30% recycled acrylic)/ (55% conventional 45% recycled acrylic) acrylic)], 4 samples were produced. Mixing ratios were provided while the products were still in fiber form, and the yarn numbers were kept constant.

Table 1 Conventional acrylic and recycled acrylic mixing ratios of the samples.

	Samples Name	**Conventional Acrylic**	**Recycle Acrylic**
7,5/1 NM	FCA	%100	%0
	MCA	%85	%15
	MRA	%70	%30
	FRA	%55	%45

Different sample names are given for more descriptive purposes for samples with different contents. Sample names are shown in Table 1.

2.2. Method

7.5/1 NM yarns were used in the samples. The contents of these yarns [(100% conventional acrylic, 0% recycled acrylic)/ (85% conventional acrylic, 15% recycled acrylic)/ (70% conventional acrylic, 30% recycled acrylic)/ (55% conventional 45% recycled acrylic)] is in the form. Hairiness, strength, and Uster test (unevenness, CV) tests were performed on the samples obtained. The tests and test standards performed are given in Table 2.

Table 2 Test and standards.

Test	**Standard**	**Tester**
Yarn Strength	EN ISO 2062	Titan 2 Strength Tester
Unevennes (uster)	TS EN ISO 2062	Premier Test 7000 Device

Figure 1 Test machines; a) Premier Test 7000 Device, b) Titan 2 Strength Tester.

Figure 1 shows the devices on which the samples were tested. While performing the tests, Jasmes Heal Titan Universal Strength Tester was used for the yarn strength test and 10 measurements were taken from each sample. In the unevenness test, hairiness measurements of the sample yarns were carried out on Uster Tester 5 devices.

3. Result and Discussion

As seen in Figure 2 and Figure 3, tensile strength and breaking elongation test results are given. The sample with the best tensile strength is seen as the FCA sample. FCA sample consists of 100% conventional acrylic fiber. Although there is not much difference between breaking elongation values, the lowest value is still in FCA sample.

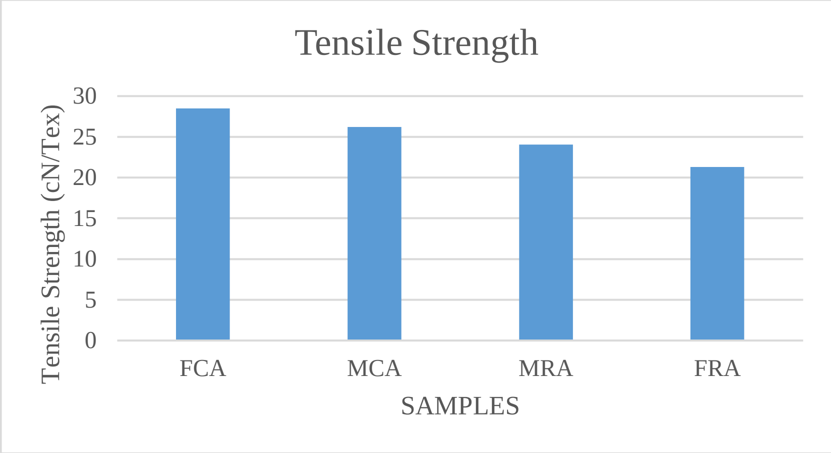

Figure 2 Tensile strength test results.

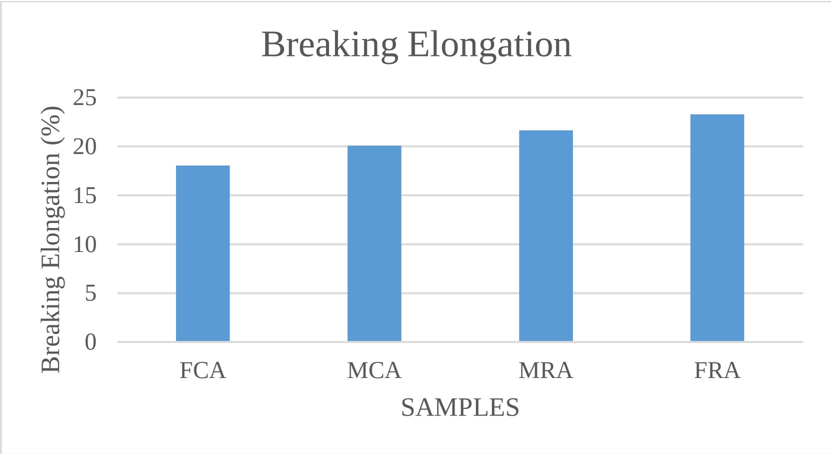

Figure 3 Breaking elongation test results.

As seen in Figure 4 and Figure 5, the unevenness test results are given. It is observed that the test results give close results to each other.

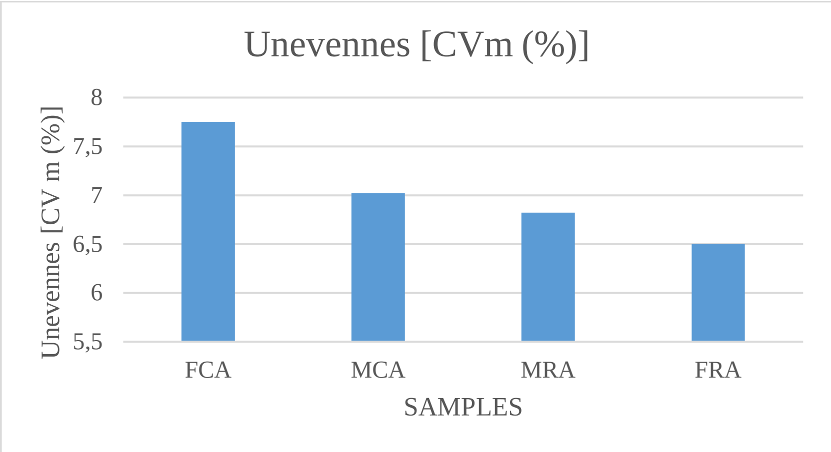

Figure 4 Unevennes [CVm (%)] test results.

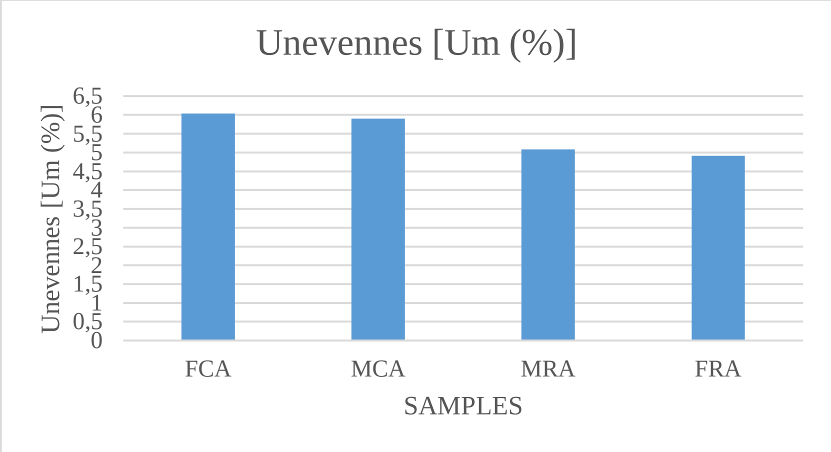

Figure 5 Unevennes [Um (%)] test results.

Hairiness test test results applied to the samples are given in Figure 6. When the hairiness test results are examined, it is observed that the hairiness increases as the recycled acrylic ratio increases between the samples.

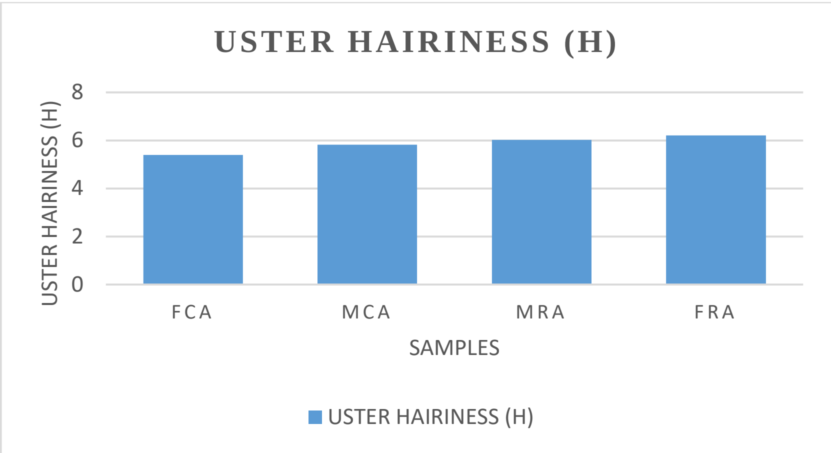

Figure 6 Uster hairiness test results.

4. Conclusion

A number of tests were carried out on conventional acrylic and recycled acrylic blended yarns. When these tests are examined in detail, it is observed that the test results decrease as the ratio of recycled acrylic decreases in tensile strength. The reason for this is that this value is expected to decrease due to the fact that recycled acrylic has been treated before. Although the elongation at break test results are close to each other, when examined in detail, it is seen that the recycling acrylic ratios and elongation at break values give higher results. Unevennes test results are indicated in the test results. In the Unevennes test results, values close to each other were obtained and it was observed that there were no significant differences. When the hairiness test results were observed, the hairiness ratio increased as the recycled acrylic ratios increased between the samples. The reason for this is that since the recycled acrylic has gone through many processes before, wears on the fiber and since the fiber has been processed before, it is predicted that the fiber ends protrude outward and provide diversity. Therefore, as the recycled acrylic ratio increases, it is a possible result that the hairiness ratio will increase. As a result, considering that there are not many differences between recycled acrylic and conventional acrylic for the properties examined, it becomes a good option for potential final customers, considering the contribution of using recycled acrylic to sustainability.

Acknowledgments
This study was carried out by Boyar Kimya Department R&D (Project no: BSET005).

References

1. MACİT H, 2019, Tekstil Sektöründe Geri Dönüşüm Olanakları ve Uşak İli'nde Güncel Durum, Uşak Üniversitesi Fen ve Doğa Bilimleri Dergisi 91-102 (2), 1 Kasım 2019.
2. Gül E, 2021, Konvansiyonel ve Geri Dönüştürülmüş Kumaşlarda Terbiye Etkinliğinin Karşılaştırılması, Bursa Uludağ Üniversitesi Fen Bilimleri Enstitüsü, Bursa.
3. Çolak, S. S, 2020, Kesikli akrilik lif ve karışımlı ipliklerin üretim parametrelerinin iplik ve kumaş özelliklerine etkisi, (Doctoral dissertation, Bursa Uludag University (Turkey)).
4. Bajaj P, Paliwal D.K, 1991, Some recent advances in the production of acrylic fibres for specific and uses, Indian Journal of Fibre & Textile Research, 16: 89-99.
5. McIntyre J.E, 2000, Synthetic fibres: nylon, polyester, acrylic, polyolefin, Woodhead Publishing Limited, England, 167-209, 115-120.
6. Tiyek, İ., and Bozdoğan, F. (2008). Yaş çekim yöntemiyle akrilik lif üretim safhalarında lif içyapısında meydana gelen değişikliklerin geniş açı x-ışını difraksiyonu ile incelenmesi. Tekstil ve Konfeksiyon, 18(1), 15-22.
7. TİYEK, İ., and BOZDOĞAN, F. (2006). Koagülasyon banyo sıcaklığının akrilik liflerinin mikroskobik görünümüne etkisinin incelenmesi. Tekstil ve Konfeksiyon, 16(4), 251-257.
8. Tiyek, İ., and Bozdoğan, F. (2005). AKRİLİK LİF ÜRETİMİNDE KOAGÜLASYON BANYOSUNUN ÖNEMİ. Pamukkale Üniversitesi Mühendislik Bilimleri Dergisi, 11(3), 319-323.
9. ADAB O., and ADAB A. (2012). A process for conversion of grey acrylic fiber waste to acrylic powder. Patent No: WO2013118132A1 WIPO (PCT).

EXAMINATION OF PROCESS IMPROVEMENT IN SOFTENING PROCESSES OF ELASTANE BLENDED ACRYLIC YARNS

Edanur TURGUT[1]*, M. İdris AKTAŞ[2] & Mehmet TOPALBEKİROĞLU[3]

[1,2] Boyar Kimya San. ve Tic. A. Ş. Gaziantep/Türkiye
[3] Gaziantep Üniversitesi, Tekstil Mühendisliği Bölümü, Gaziantep/Türkiye
[1]*edanur.turgut@boyar.com.tr

Abstract

The textile sector is of great importance in Turkey as well as in the rest of the world. The textile sector is an area with a very wide spectrum in the industry. Among these areas, acrylic spinning sees great request. Due to the loss of interest owing to the cost of wool fiber, acrylic fiber, which is equivalent to it, offers a good choice for the consumer as supply and demand. Recently, due to the need for wool, acrylic fiber is mixed with different fiber types to produce a wide variety of acrylic blended yarns. Elastane blended acrylic yarns are highly preferred due to both their performance features, touch and effect they provide. Among these properties in elastane blended acrylic yarns, it is of great importance due to the softness and smooth surface it provides to the touch. This is achieved by the softening processes applied to the fibers or yarns. Softening processes can take place in many different ways. In this study, hank softening, tow (chemical) softening and steam softening processes are discussed. The aim of the study is to obtain the same product of the same quality by reducing the energy, labor and increasing efficiency arising from the process costs in softening processes. In this regard, samples with a high bulk content of 20/2 Nm (85% acrylic, 7% polyamide, 8% polyester) are handled. It is aimed to compare these samples by applying the softening process in three different forms [hank softening, tow (chemical) softening and steam softening]. It is aimed to evaluate the results by looking at the uster test (unevenness), touch, brightness, air permeability and strength values of the produced samples.

Keywords: Elastane blended acrylic yarn, softening process, process improvement, touch, performance properties.

1. Introductıon

The softening process applied in textile finishing processes has a very important place due to the customers' expectation of a good attitude from textile products in general [2-3]. It is known that most of the dyeing and finishing processes take place in the finishing processes, while 35% of these finishing processes are realized in the softening processes [7]. Softening processes affect the fabric handle positively. Fabric attitude is a parameter that determines the quality of the fabric and the quality of the textile products based on the feelings that the person feels when he touches the fabric [5]. There are many parameters that affect the fabric handle. These parameters can include the raw material of the product, yarn, fabric structure, fiber type and applied finishing processes [6]. The purpose of using softener in textile products is to provide a soft touch to the fiber removed during the pre-treatment stage, to regain the soft touch lost due to the elimination of substances such as oil, wax, pectin in natural fibers and the preparation materials in synthetic fibers, and even to obtain a softer surface [4,7,8]. Softener chemicals bring many positive properties to the fabric. Among these features, it provides a positive effect on many features such as flexibility, fullness, draping, abrasion resistance, pilling resistance, static electricity and comfort [8-12].

The softening method is as important as the great importance that softeners provide for a textile product. As it is known, softening processes can be applied to textile products in different forms. While softening can be applied in the form of fabric, softening processes can also be applied to the yarn and fiber form. It is known that the method used as well as the softener used is an effective and decisive parameter on the fabric. Based on this, a textile company tries to give the products a volume and soft touch by applying tow fiber (chemical) softening, hank-form (yarn) softening and steam swelling (yarn) softening processes. It was decided to use elastane mixed acrylic yarn as the product. Handle and softness are important in such final products due to the widespread use of acrylic fiber and generally knitwear and similar products. In addition, flexibility in knitwear is as important as the handle, and this flexibility is usually provided with elastane.

There are process differences between the softening methods to be used. There are methods that have a lot of workload in terms of this process difference and operation. In this study, it is aimed to reduce the process that takes place too much without sacrificing product quality. In this context, three different softening methods are emphasized. Among these methods, chemical softening is carried out by placing the products in large dye machines and softening them with chemicals while they are still in fiber form. In hank softening, after the product undergoes all dyeing and textile processes, it is brought into hank form while in yarn form and subjected to softening processes in hank softening machines. In the steam softening process, after the product is dyed and textile processes, it is softened by volumizing with water vapor in a superba machine at a certain temperature just before the shipment process.

2. Materıal and Method

2.1. Material

Table 1 Yarn contents, yarn number and softening method of the samples.

Sample Names	Yarn Count And Content	Softening Methods
HS	20/2 NM [%85 acrylic, %7 polyamid, %8 polyester]	Hank Softening
TS		Tow Softening
SS		Steam Softening

In this study, as seen in Table 1, 3 different softening methods [hank softening, tow (chemical) softening and steam softening] were applied to elastane mixed acrylic yarns and samples with the same yarn count and same content were obtained after 3 different softening processes. In the section in Table 1, the sample names, HS denotes hank softening, TS denotes tow softening, and SS denotes steam softening.

It is the softening process, which has 20/2 Nm (85% acrylic, 7% polyamide, 8% polyester) contents, which were first applied to the hank softening process on 3 different samples obtained in the study, and which is transferred to the hank transfer machines when they are in the yarn form and carried into the hank form. The second sample is 20/2 Nm (85% acrylic, 7% polyamide, 8%

polyester) in which the tow (chemical) softening process has been applied, and the softening process has been applied while it is in fiber form in large dye machines. Thirdly, in the steam softening process, the yarn with 20/2 Nm (85% acrylic, 7% polyamide, 8% polyester) contents is fed along the machine line with water water at a speed of 360 m/min at 95 °C in the machine called SUPERBA and softened with steam inflation method. Detailed workflow diagrams of these smoothing methods are given in Figure 1.

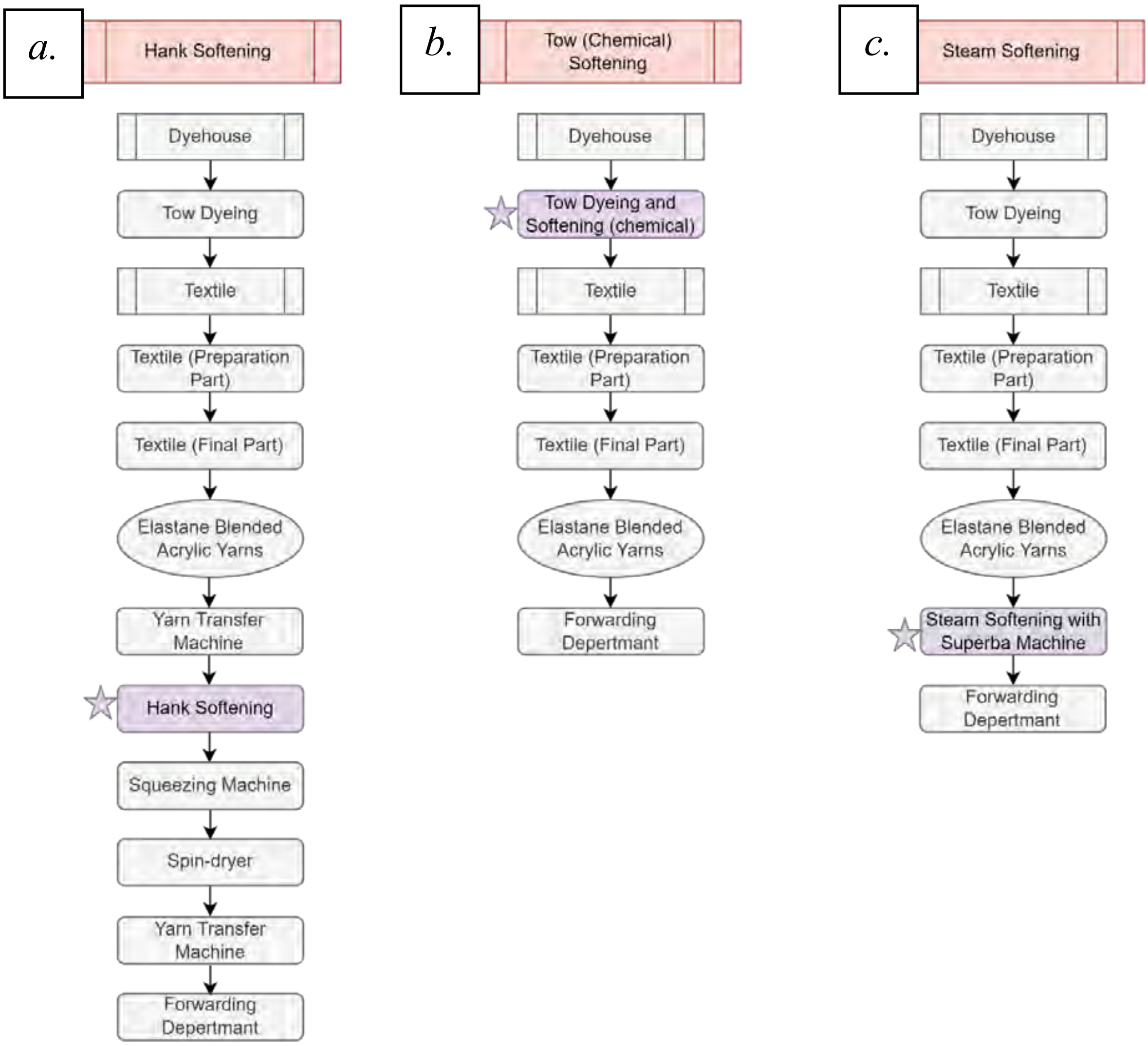

Figure 1 Work flow charts of softening processes; a) hank softening, b) tow softening, c) steam softening.

In tow softening, it is softened at 55-60 C for 1 hour in large paint machines. Temperature and time can vary according to the type or amount of fiber. This is how the tow softening process takes place.

In the hank softening process, as in tow softening, the softening process takes place at 55-60 C for 1 hour. The softening process takes place in fixed hank dyeing machines.

Although softened yarns are obtained in the product final in the softening processes applied, they are very different from each other as a process. As can be seen in Figure 1, the process and work flow in hank smoothing is quite long and tedious, which means extra cost and labor. In the chemical softening process, the softening process is given at the beginning and the workflow is very short. In the steam softening process, the softening process is done just before the shipment, that is, the products are softened at the last point after passing all the stages. While each softening process has advantages in these three different flows, it is investigated which method provides advantages in terms of product quality and cost, and which softening is the optimum softening process.

2.2. Method

20/2 NM yarns are used in the samples. The contents of the yarns used are produced as [85% acrylic, 7% polyamide, 8% polyester] and these yarns have undergone 3 different softening processes. These smoothing processes are as follows; hank softening, tow (chemical) softening and steam softening. Performance evaluations were made by looking at the unevenness, touch, brightness, air permeability and strength values of the samples obtained.For the air permeability test, sample yarns were knitted in plain weave. The samples were knitted on a 12-number manual sample knitting machine.

Table 2 Test and Standarts.

Test	**Standard**	**Tester**
Yarn Strength	EN ISO 2062	Titan 2 Strength Tester
Air Permability	TS 391 EN ISO 9237	SDL Atlas
Unevennes (uster)	TS EN ISO 2062	Premier Test 7000 Device

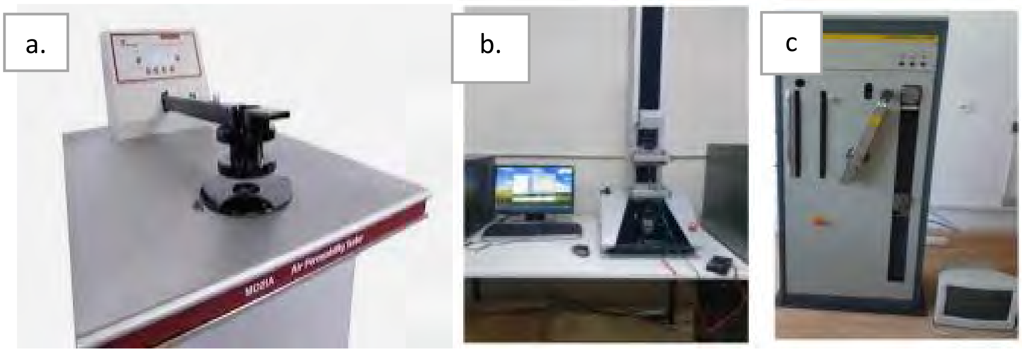

Figure 2 Test Machines; a)SDL Atlas, b) Titan 2 Strength Tester, c) Premier Test 7000 Device.

Figure 2 shows the devices on which the samples were tested. While performing the tests, Jasmes Heal Titan Universal Strength Tester was used for the yarn strength test and 10 measurements were taken from each sample. For the air permeability test, the samples were applied in the M 021A air permeability test device of SDL-Atlas company, based on the TS 391 EN ISO 9237 "Determination of air permeability in textile fabrics" test standard, with a pressure drop of 100 Pa and an area of 20 cm². In the unevenness test, hairiness measurements of the sample yarns were carried out on Uster Tester 5 devices. It is numbered from 1 to 5 by different operators for touch and brightness. (1 no worst 5 exchanges)

3. Result and Discussion

Figure 3 and Figure 4 shows tensile strength and breaking elongation test results. It is observed that the test results are close to each other, but when examined in detail, it is observed that hank softening gives worse results than the other two softening methods.

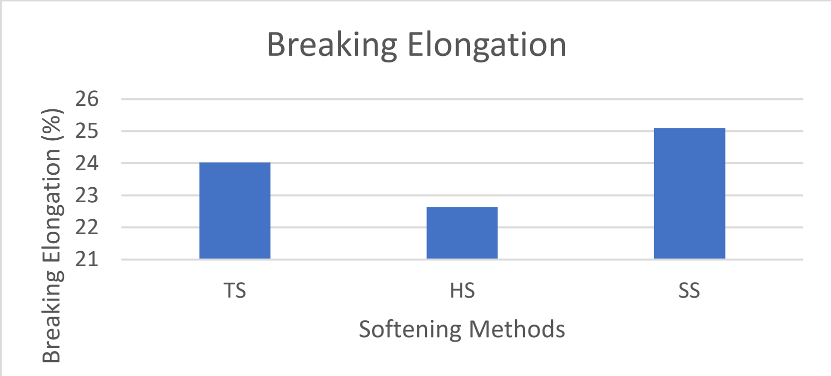

Figure 3 Breaking elongation test results.

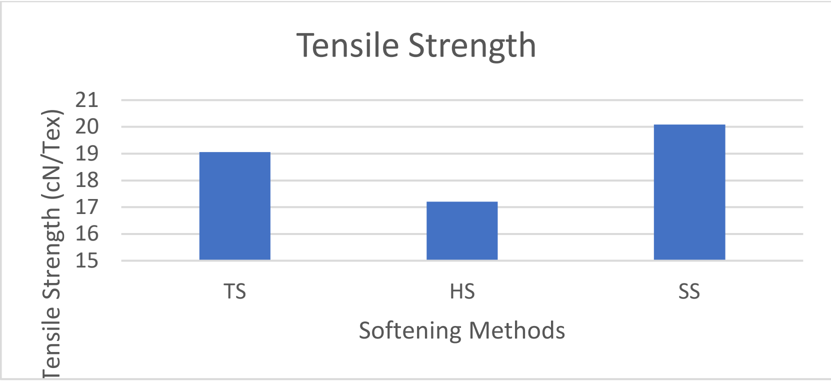

Figure 4 Tensile Strength Test Results.

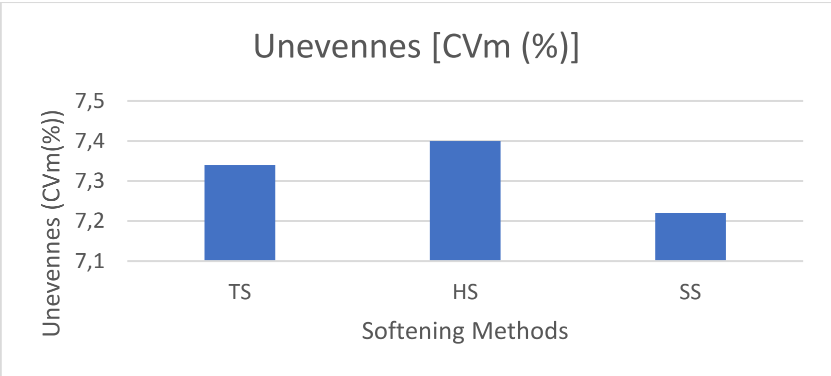

Figure 5 Unevennes (CVm %) test results.

Unevennes test results are given in Figure 5 and Figure 6 . When looking at the unevenness test, all three softening methods give similar results. It can be obtained that softening methods are not an effective parameter on unevenness.

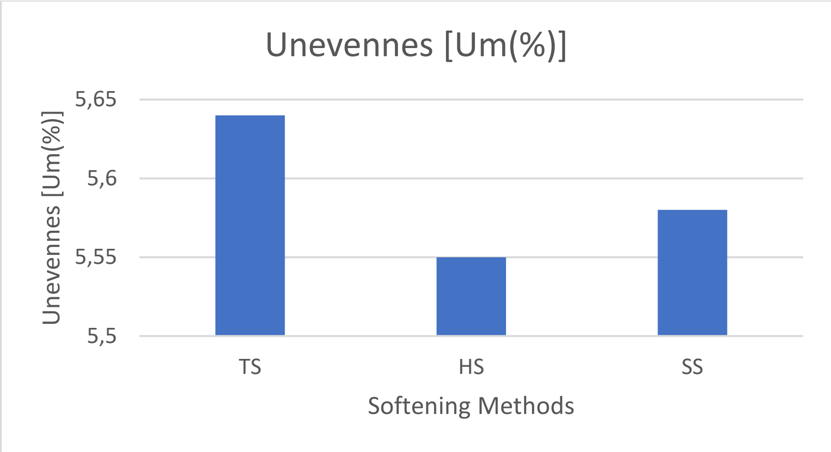

Figure 6 Unevennes (Um %) test results.

Air permeability test results can be observed in Figure 7. When the air permeability test results are examined, it is observed that the hank softening method has the highest air permeability value compared to other softening methods. It is seen in the graph that after hank softening, steam softening has the most air permeability, followed by tow softening.

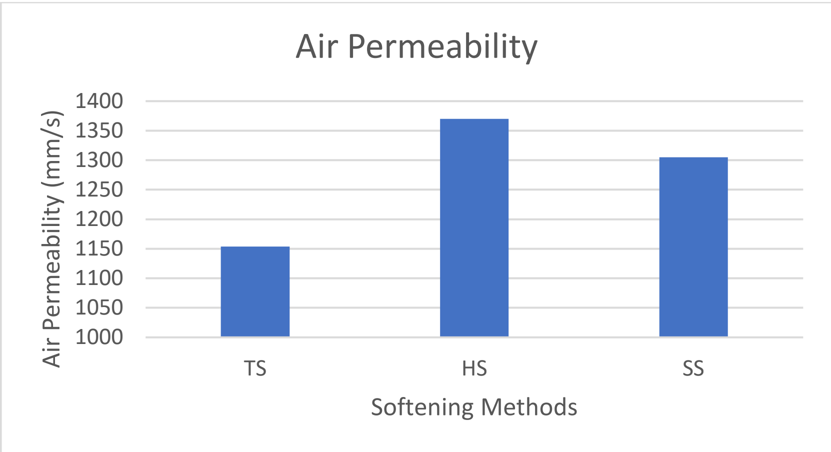

Figure 7 Air permeability test results.

Brightness and touch test results can be observed in Figure 8. During these tests, they are scored and evaluated by different operators. Looking at the test results, it is the sample subjected to the steam softening process with the best brightness and the brightness of the other two softening is evaluated as the same. When looking at the touch, it is observed that the best hand is in the softening of the hank. After hank softening, the best touch is listed as steam softening and tow softening, respectively.

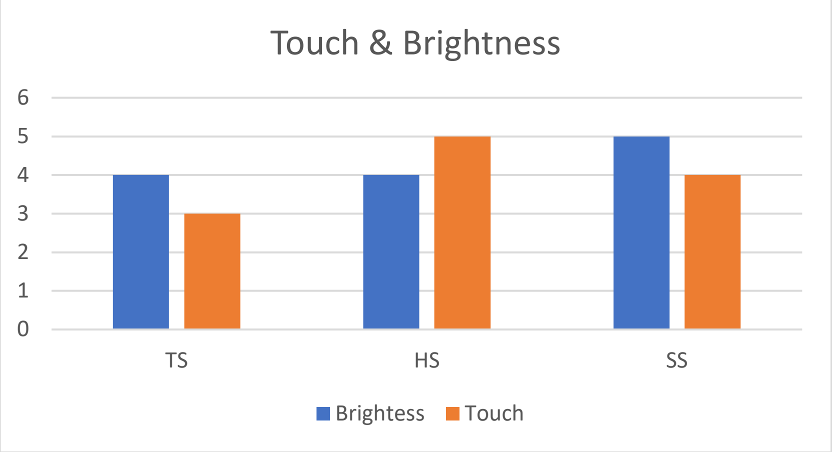

Figure 8 Touch and brightness test results.

4. Conclusıon

The performance properties of the softening method on fabrics and yarns were examined in detail. When the strength values of the samples undergoing different softening are examined, it is observed that there is not much difference between them, but it is seen that hank softening gives worse results than the others. The reason for this is that hank softening has a very long process compared to other softening and it can be predicted that at this stage, the fibers will wear out and give worse results than the others. When looking at the unevenness tests, it is observed in the test results that all the results are close to each other. Based on this, it can be said that the softening method is not an effective parameter on the unevenness. In the air permeability test results, it is seen that the best air permeability is in the sample that undergoes the hank softening process. It is observed that the worst air permeability is in the sample that undergoes tow softening. The reason for this is that while the softening processes applied in the dye machines are carried out, it is known that the pressure inside the machine and before it rises to high temperatures, and starting from this, the fiber length can be shortened and shrinked due to the fact that the fibers are treated at high temperatures beforehand. This can reduce the air passage by reducing the space between the fibers. When looking at the glosses, it is seen from the test results that the brightest sample is the sample subjected to steam softening. The reason for this is that the steam softening process has very short processes and it can be predicted that the brightest sample is the sample that is subjected to steam softening due to the application of the softening process in the last stage. It is thought that the softening process is effective for the yarns, since the yarns are softened in a fairly free form. Therefore, it is foreseen that the sample with the best handle will be the sample that is subjected to hank softening.

Acknowledgments

This study was carried out by Boyar Kimya Department R&D (Project no: BSET004).

References

1. Özdil, N., & Ateş, G. S. M. N. KUMAŞ TUTUMU: SİLİKON ESASLI YUMUŞATICILARIN ETKİSİ. XIII. Uluslararası İzmir Tekstil ve Hazır Giyim Sempozyumu, 2 – 5 Nisan 2014.
2. Çelik, N., Değirmenci, Z. and Kaynak, H.K., Effect of Nanosilicone Softener on Abrasion and Pilling Resistance and Color Fastness of Knitted Fabrics, Tekstil ve Konfeksiyon, 2010, 20(1), 41-47.

3. Periyasamy, S. and Khanna, A. Silicone finishing: softer than a soft touch, Americos Industries, 2007, 54(12), 91-99.
4. Badr, A.A., Performance of Knitted Fabrics Finished with Different Silicone Softeners, Journal of Engineered Fibers and Fabrics, 2018, 13(1), 47-59.
5. Valatkienė, L. and Strazdienė, E., Accuracy and Reliability of Fabric's Hand Subjective Evaluation, ISSN 1392–1320 Materials Science (Medžiagotyra). 2006.Vol. 12, No. 3.
6. Mäkinen, M., Meinander, H., Luible, C., Magnenat and Thalmann, N., Influence of Physical Parameters on Fabric Hand, Proc. of the Workshop on Haptic and Tactile Perception of Deformable Objects, Hanover (HAPTEX'05), 2005, pp. 8-16.
7. Özgüney, A.T., Özkaya, K., Pamuklu Kumaşlarda Parça Baskının Isıl İşlem Koşullarında Meydana Gelen Renk Değişimine Yumuşatıcı Maddelerin Etkisi, Tekstil ve Konfeksiyon, 2008, 2, 121-129.
8. Sancar Beşen, B. and Balcı, O., Investigation of the Effects of Silicone Emulsions Having Different Particle Sizes on Knitted Fabrics Depending on the Type of Yarn, International Journal of Clothing Science and Technology, 2017, 29(3), 394-416.
9. Parvinzadeh, M., Hajiraissi, R., Macro- and Microemulsion Silicone Softeners on Polyester Fibers: Evaluation of Different Physical Properties, Journal of Surfactants and Detergents, 2008, 11, 269–273
10. Balcı, O., Kınoğlu, G.Ö., Sancar Beşen, B., Silicone Oil Based Softeners Including Different Additives – Part I: Characterization of the Softeners and Investigation of Their Effects on Mechanical Properties of the Fabrics, International Journal of Clothing Science and Technology, 2019, 31(1), 130-144.
11. Balcı, O., Kınoğlu, G.Ö., Sancar Beşen, B., Silicone Oil Based Softeners Including Different Additives – Part II: Investigation of Effects of Silicone Softeners on the Comfort Properties of the Fabrics, International Journal of Clothing Science and Technology, 2019, 31(1), 16-31.
12. Şahin, U.K., Cimilli Duru, S., Effects of Softener Applications on Air And Water Vapor Permeabılıty of Cotton Knitted Fabrics Produced With Different Yarns, Tekstil ve Konfeksiyon, 2017, 27(3), 275-282.

AMANYOK ORTAMINDA MEKANOKİMYASAL SENTEZLEME ISLEMİNİN SELESTİT CEVHERİNİN DONUSUM SICAKLIKLARI ÜZERINDEKİ ETKSİ

SUAT ÖNAL, SELMİNE AKYOL*[1], FURKAN ALPTEKİN, KÜRŞAT İÇİN [1], ATABERK YILDIZ[2], SEFA EMRE SÜNBÜL[3], SELMİNE AKYOL[1], SULTAN ÖZTÜRK[1]

[1] Osmaniye Korkut Ata University, Osmaniye Vocational School, Department of Mechanical and Metal Technologies, Osmaniye, TURKEY.
[2] Karadeniz Technical University, Engineering Faculty, Department of Metallurgy and Materials Engineering, Trabzon, TURKEY.
[3] Gaziantep University, Engineering Faculty, Department of Metallurgy and Materials Engineering, Gaziantep, TURKEY.

Özet

Bu çalışma mekanokimyasal sentezleme işleminin selestit cevherinin ve stronsiyum karbonatın dönüşüm sıcaklıkları üzerindeki etkileri araştırılmıştır. $SrSO_4$:$(NH_4)_2CO_3$ 1:1,0 stokiyometrik oranda 10 dakika mekanokimyasal sentezleme işlemi uygulanarak üretilen stronsiyum karbonatın β-SrCO3 dönüşüm ve kalsinasyon sıcaklıkları 833 ve 1005 °C iken 1:2,0 stokiyometrik oran ve 200 dakika mekanokimyasal sentezleme sonrası bu sıcaklıklar sırasıyla 808 ve 894 °C'ye düşmüştür.

Keywords: Mekanokimyasal sentezleme, Termal analizler, Seletit cevheri

1. Giriş

Mekanokimya, mekanik enerjinin etkisiyle tüm agregasyon durumlarındaki tozların kimyasal ve fiziko-kimyasal değişimleriyle ilgilenen bir kimya dalıdır. Mekanokimyasal proses (MCP), kimyasal reaksiyonların, yapısal değişikliklerin ve faz dönüşümlerinin mekanik enerji uygulamasıyla aktive edildiği toz hazırlama ve üretim yöntemidir. Günümüzde mekanokimyasal proses, toz metalurjisi ile üretilmiş katma değeri yüksek ürünler üretmek için ortaya çıkan teknolojiler arasında yer almakta ve son zamanlarda ise proseste zararlı kimyasal ve çözücüler kullanılmamasından dolayı çevreci bir toz üretim yöntemi haline gelmiştir. Mekanokimyasal sentezleme veya mekanik aktivasyon diğer buluşlarda olduğu gibi bir tesadüf eseri öğütme işlemi sırasında reaksiyonların başlatılabildiği gerçeğinin öğrenilmesi sonucu ortaya çıkmıştır.
Mekanokimyasal sentezleme işlemi kısaca, başlangıç malzemelerinden oluşan karışımının tekrarlı olarak deformasyonu, kırılması ve kaynaması adımları ile de ifade edilebilir. Malzemenin uzun süreli öğütülmesi, tane boyutunun azalmasını ve buna bağlı olarak tane yüzey alanının artmasını ve malzemede mekanokimyasal sentezle yeni fazların oluşmasını sağlar [1]. Belirtilen bu olayların çoğu birlikte meydana gelir [1-3].

Mekanokimyasal proses yukarıda da belirtildiği gibi mekanik alaşımlama, mekanik öğütme ve reaksiyonlu öğütme olmak üzere üç farklı şekilde uygulanmaktadır. Bu yöntemlerin her birinde mekanokimyasal prosesin faklı etkileri kendilerini göstermektedir. Bu etkiler aşağıda listelenmiştir.

- Genellikle oksitlerin ince parçacıklar formunda üretimi
- Katı çözünürlüğün artırılması
- Parçacık boyutunun nanometre ölçeğine kadar azaltılması
- Nanokristalli metal veya alaşım tozlarının üretimi
- Yeni kristal veya yarı kristalli fazların sentezlenmesi
- Kristalli malzemelerden amorf fazların geliştirilmesi
- İntermetalik fazların üretimi
- Mineral ve atık işleme proseslerinin geliştirilmesi
- Minerallerden metal rafinasyonunun sağlanması
- Kimyasal yer değiştirme reaksiyonlarının indüklenmesi
- Yanma reaksiyonlarının aktive edilmesi

Bu çalışmada, mekanokimyasal sentezlemenin selestit cevherinin dönüşüm sıcaklıkları üzerindeki etkileri araştırılmıştır.

2. Deneysel Çalışmalar

Selestit cevherinden doğrudan stronsiyum hekzaferrit mıknatıs üretmek için uygulanan mekanokimyasal işlem sırasında, selestit cevherinin stronsiyum karbonata dönüşmesi gerekir. Bu dönüşümün gerçekleşmesi için girdi malzemesi olarak ilave edilecek amonyum karbonatın, $(NH_4)_2CO_3$, miktarı ve mekanokimyasal sentezleme süresi araştırılmıştır.
Stronsiyum hekzaferrit mıknatıs üretiminde stronsiyum kaynağı olarak kullanılacak olan selestit cevherinin mekanokimyasal reaksiyonla stronsiyum karbonata dönüşümünün incelenmesi için Eşitlik 7'de verilen reaksiyona göre stronsiyum sülfat ($SrSO_4$) ile amonyum karbonat $(NH_4)_2CO_3$ harman hazırlanmıştır.

$$SrSO_4+(NH_4)_2CO_3 \rightarrow SrCO_3+(NH_4)_2SO_4 \quad (1)$$

$SrSO_4$ ile $(NH_4)_2CO_3$ arasında 1:1, 1:1,5 ve 1:2 stokiyometrik oranlar ve 10, 100 ve 200 dakikalık sentezleme süreleri belirlenmiştir. Mekanokimyasal sentezleme işlemleri 5 mm çapında WC bilye, 1:10 toz:bilye oranı ve 450 dev/dk sabit dönme hızı parametreleri ile gerçekleştirilmiştir. İşlemler, Fritsch marka Premium Line 5 model gezegen tipi bilyalı değirmende gerçekleştirilmiştir. Mekanokimyasal sentezleme işlemini takabiben 10 °C/s ısıtma hızında 1200 °C'ye kadar koroyucu atmosfer altında termal analizler gerçekleştirilmiştir.

3. Sonuçlar ve Tartışma

Stronsiyum hekzaferrit mıknatıs üretiminde en önemli reaksiyonlardan biri, mekanokimyasal sentezleme prosesi sırasında $SrCO_3$'ın parçalanarak SrO'ün açığa çıkmasıdır ($SrCO_3 \rightarrow SrO + CO_2$). Açığa çıkan bu bileşik hematit ile birleşerek manyetik fazın oluşmasını sağlamaktadır. Bu nedenle, bu aşamada stronsiyum karbonatın parçalanma sıcaklığının belirlenmesi önem arz etmektedir. Bu doğrultuda, farklı stokiyometrilerde ve sentezleme sürelerinde gerçekleşen dönüşüm işlemlerinde $SrCO_3$'ın termal bozunma sıcaklıklarını belirlemek için DTA ve TGA analizleri yapılmıştır.

En düşük stokiyometrik oranı olan $SrSO_4$:$(NH_4)_2CO_3$ 1:1,0'e göre ve 10, 100 ve 200 dakika sürelerde gerçekleştirilen mekanokimyasal dönüşümle üretilen $SrCO_3$ bileşiğine uygulanan DTA ve TGA analizleri sırasıyla Şekil 1 ve Şekil 2'de verilmiştir. 1:1,0 stokiyometrik oranda ve her bir sentezleme süresi için $SrCO_3$'ın faz dönüşümünü ve ısıl bozunmasını gösteren DTA grafiğinde iki farklı pik endotermik görülmektedir (Şekil 1). Bu endotermik piklerin dışında farklı bileşimlere ait dönüşüm pikleri tespit edilmemiştir. Farklı sentezleme sürelerine ait DTA eğrilerindeki dönüşüm sıcaklıklarının, sentezleme süresinin artmasıyla birlikte azaldığı görülmektedir. En düşük sentezleme süresi için stronsiyum karbonatın ısıl bozunmaya başladığı sıcaklık 1005 °C olarak belirlenmişken, sentez süresinin artmasıyla bu sıcaklık önce 886 °C'ye, daha sonra ise 803 °C'ye azalmıştır. Mekanokimyasal sentezleme işleminde parçacıkların sahip olduğu enerjinin sentezleme süresiyle artmasıyla (parçacık boyutunun küçülmesinden dolayı) stronsiyum karbonatın parçalanma (ısıl bozunma) sıcaklığının değişmesine neden olmaktadır. 10 dakikalık sentezleme süresinde temel odak noktası olan 2 numaralı endotermik pikin şiddetinin diğer sentezleme sürelerine (100 ve 200 dakika) göre düşük olması, oluşan $SrCO_3$ miktarının düşük olduğu göstermektedir. Bu da yukarıda SEM ve XRD analizleri ile tespit edilen verileri doğrulamaktadır. 1:1,0 sabit stokiyometride farklı sentezleme süreleri için TGA eğrisi incelendiğinde (Şekil 2); en düşük ağırlık kaybının (%6,8) yine 10 dakikalık sentezleme süresinde görülmesi DTA verilerini doğrulamaktadır. Mekanokimyasal sentezleme süresinin artmasıyla birlikte selestit cevherindeki sülfatlı bileşiğin stronsiyum karbonata dönüşme oranı ve aynı zamanda ağırlık kaybı artmaktadır. Maksimum sentezleme süresi olan 200 dakikada 1200 °C'deki anlık toplam ağırlık kaybı yaklaşık %15,2'dir.

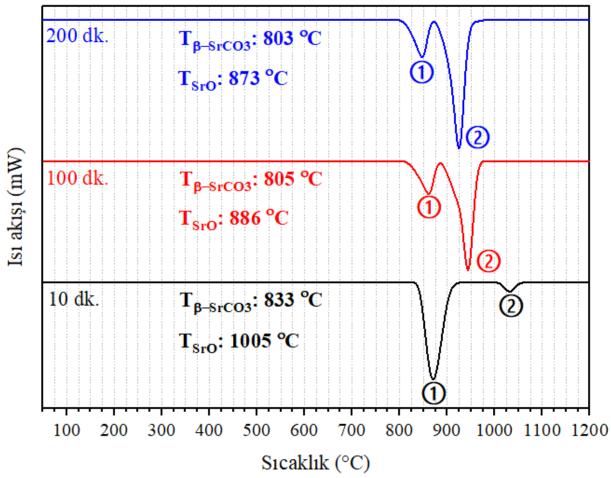

Şekil 1. $SrSO_4$:$(NH_4)_2CO_3$ 1:1,0 stokiyometrik oranına göre farklı sürelerde mekanokimyasal sentezleme işlemi sonrası elde edilen DTA eğrileri.

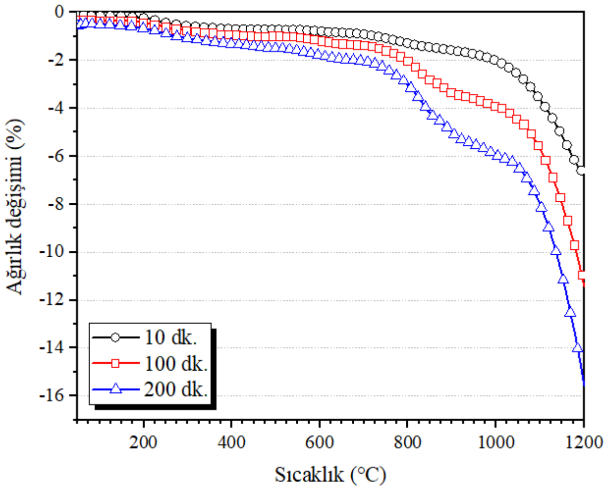

Şekil 2. $SrSO_4:(NH_4)_2CO_3$ 1:1,0 stokiyometrik oranına göre farklı sürelerde mekanokimyasal sentezleme işlemi sonrası elde edilen TGA eğrileri.

Şekil 3 ve Şekil 4'te $SrSO_4:(NH_4)_2CO_3$ 1:1,5 sabit stokiyometrik oranda ve 10, 100 ve 200 dakika mekanokimyasal sentezleme işlemine tabi tutulan selestit cevherinin sentezleme sonrası DTA ve TGA eğrileri sırasıyla verilmiştir. Strokiyometrik olarak daha fazla amonyum karbonat içeren karışımda ilk 10 dakikalık sentezleme süresinde 1:1,0 stokiyometrik oranda olduğu gibi, düşük miktarda oluşan $SrCO_3$ nedeniyle 2 numaralı endotermik pik şiddeti, 100 ve 200 dakikalık sentezleme süresine göre düşüktür. 1:1,5 sabit stokiyometrik oranda $SrCO_3$'ın stronsiyum oksite (SrO) parçalandığı sıcaklık, artan sentezleme süresi ile azalmıştır. 10 dakika mekanokimyasal sentezleme süresinde bu sıcaklık 1003 °C, 100 dakika sentezleme süresinde 880 °C ve en uzun sentezleme süresi olan 200 dakikada ise 868 °C olarak tespit edilmiştir. Bu azalma Şekil 1'de 1:1,0 stokiyometrik oran için verilen DTA eğrileri ile kıyaslandığında, sentezleme sürelerinin aynı olmasına rağmen, artan stokiyometrik oranla birlikte $SrCO_3$'ın ısıl bozunma sıcaklığının azaldığı ortaya çıkmıştır.

Şekil 4'te verilen TGA eğrileri ise, ağırlıktaki değişimin yaklaşık 700 °C'de başlayıp ($SrCO_3$ faz dönüşüm sıcaklığı) 1200 °C'ye kadar devam ettiğini göstermektedir. Ancak, her üç eğride de yaklaşık 800 °C'de ağrılık değişimi hız kazanmaktadır. Bu değişim $SrCO_3$'ın parçalanmasından kaynaklanmaktadır. 10 dakika sentezleme süresinde oluşan stronsiyum karbonat oranı en düşük olmasından dolayı toplam ağırlık değişimi %8 iken, maksimum stronsiyum karbonatın oluşturulduğu 200 dakika sentezleme süresinde bu değer %16 olarak tespit edilmiştir.

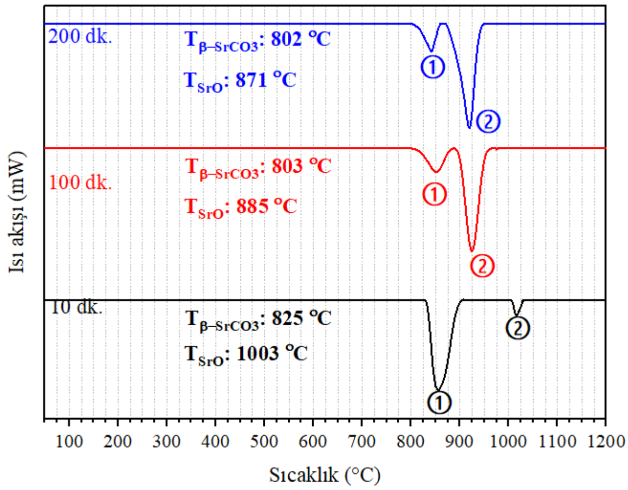

Şekil 3. $SrSO_4$:$(NH_4)_2CO_3$ 1:1,5 stokiyometrik oranına göre farklı sürelerde mekanokimyasal sentezleme işlemi sonrası elde edilen DTA eğrileri.

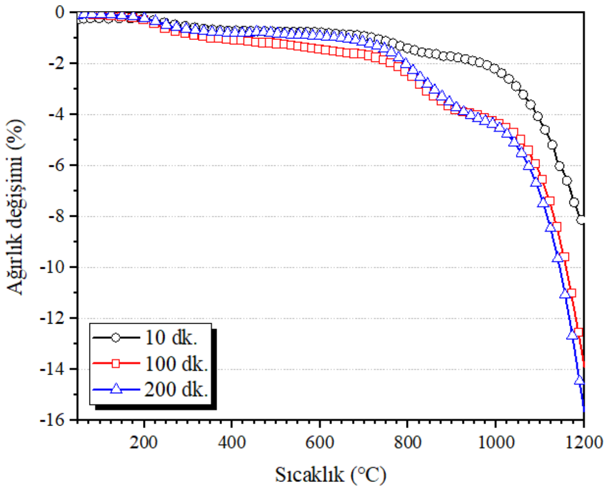

Şekil 4. $SrSO_4$:$(NH_4)_2CO_3$ 1:1,5 stokiyometrik oranına göre farklı sürelerde mekanokimyasal sentezleme işlemi sonrası elde edilen TGA eğrileri.

Şekil 5'de $SrSO_4$:$(NH_4)_2CO_3$ 1:2,0 stokiyometrik oranda gerçekleştirilen mekanokimyasal sentezleme işleminde, sentezleme sürelerine ait faz dönüşümlerini gösteren DTA eğrileri verilmiştir. Buradaki DTA eğrilerinde de yukarıda 1:1,0 ve 1:1,5 stokiyometrik oranlar için verilen DTA eğrilerine benzer şekilde, iki farklı endotermik pik oluşmuştur. 1:2,0 stokiyometrik oran için tespit edilen en önemli değişim, 10 dakikalık sentezleme süresinde gözlenmiştir. Diğer stokiyometrik oranlara göre 10 dakikalık sentezleme süresinde oluşan $SrCO_3$ miktarının artması pik şiddetinin diğer sentezleme süreleriyle (100 dakika ve 200 dakika) yaklaşık olarak aynı çıkmasını sağlamıştır. Burada, stokiyometrik oranın artmasıyla birlikte ortamdaki CO_3^{-2} konsantrasyonun artması sayesinde daha fazla $SrSO_4$ bileşiği $SrCO_3$'da dönüşmüştür. Diğer stokiyometrik oranlarda (1:1,0 ve 1:1,5) olduğu gibi, $SrCO_3$ faz dönüşümü sıcaklığı (1 nolu endtotermik pik) ve ısıl bozunma sıcaklığı (2 nolu endotermik pik), mekanokimyasal sentezleme süresinin artmasıyla birlikte azalmıştır. En düşük sentezleme süresinde bu iki sıcaklık sırasıyla 808

°C ve 894 °C olarak belirlenmiştir. Maksimum mekanokimyasal sentezleme süresinde bu sıcaklıklar 789 ve 868 °C olarak ölçülmüştür.

Şekil 6'de $SrSO_4:(NH_4)_2CO_3$ 1:2,0 stokiyometrik oranda ölçülen TGA eğrileri gösterilmiştir. Şekilde verilen TGA eğrilerinde kütledeki değişim 750 °C'de başlamakta ve 1200 °C'ye kadar devam etmektedir. 1200 °C'de TGA eğrilerindeki toplam ağırlık değişimleri 10 dk, 100 dk ve 200 dk sentezleme süreleri için sırasıyla %11, %17 ve %20 olarak ölçülmüştür.

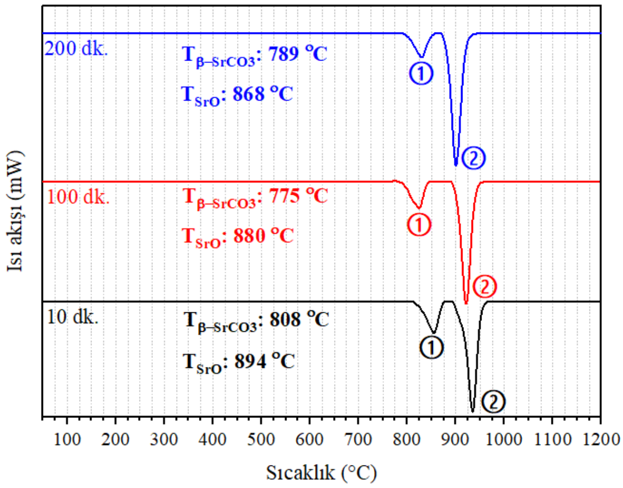

Şekil 5. $SrSO_4:(NH_4)_2CO_3$ 1:2,0 stokiyometrik oranda farklı sürelerde mekanokimyasal sentezleme işlemi sonrası elde edilen DTA eğrileri.

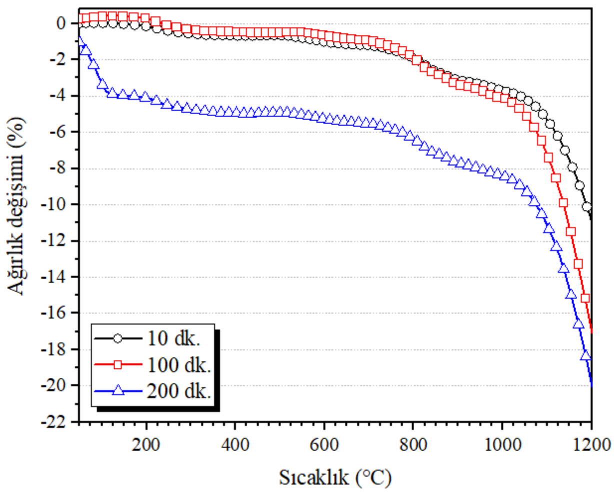

Şekil 6. $SrSO_4:(NH_4)_2CO_3$ 1:2,0 stokiyometrik oranda farklı sürelerde mekanokimyasal sentezleme işlemi sonrası elde edilen TGA eğrileri.

4. Conclusions

- Selestit cevherinden amonyum karbonat kullanılarak 10, 100 ve 200 dakika uygulanan mekanokimyasal sentezleme ile üretilen $SrCO_3$ boyutları sırasıyla 6,721, 4,257, 3,850 µm'a azalmıştır.
- SrSO4:(NH4)2CO3 1:1,0 stokiyometrik oranda 10 dakika mekanokimyasal sentezleme işlemi uygulanarak üretilen stronsiyum karbonatın β-SrCO3 dönüşüm ve kalsinasyon sıcaklıkları 833

ve 1005 °C iken 1:2,0 stokiyometrik oran ve 200 dakika mekanokimyasal sentezleme sonrası bu sıcaklıklar sırasıyla 808 ve 894 °C'ye düşmüştür.

Teşekkür:
Bu çalışma TÜBİTAK tarafından ARDEB 119M111 ve TEYTEB 2210455 proje kodlarıyla; Karadeniz Teknik Üniversitesi BAP Birimi tarafından FBA-2019-8162 ile FDK-2018-7685 numaralı projelerle desteklenmiştir. Maddi desteklerinden dolayı TÜBİTAK ve Karadeniz Teknik Üniversitesi BAP birimi çalışanlarına teşekkürlerimi sunarım.

References

1. Tsuzuki, T.; McCormick, P. G., Mechanochemical synthesis of nanoparticles. *Journal of Materials Science* **2004,** *39* (16), 5143-5146.
2. Dorey, R. A., *Ceramic thick films for MEMS and microdevices*. William Andrew: 2011.
3. Drofenik, M.; Lisjak, D.; Makovec, D. In *The synthesis and properties of magnetic nanoparticles*, Materials Science Forum, Trans Tech Publ: 2005; pp 129-136.

INVESTIGATION OF THE EFFECTS OF TITANIUM ELEMENT ON THE ELECTROCHEMICAL PROPERTIES OF CANTOR ALLOY

FURKAN ALPTEKİN [*1], KÜRŞAT İÇİN [1], SUAT ÖNAL[2], SEFA EMRE SÜNBÜL[3], SELMİNE AKYOL[1], ATABERK YILDIZ[1], SULTAN ÖZTÜRK[1]

[1] Karadeniz Technical University, Engineering Faculty, Department of Metallurgy and Materials Engineering, Trabzon, TURKEY.
[2] Osmaniye Korkut Ata University, Osmaniye Vocational School, Department of Mechanical And Metal Technologies, Osmaniye, TURKEY.
[3] Gaziantep University, Engineering Faculty, Department of Metallurgy and Materials Engineering, Gaziantep, TURKEY.

Abstract

In this study, the effect of Ti addition on microstructure and corrosion properties of Cu-modified Cantor alloy ($CoCuFeNiMnTi_x$) (x=0.0-0.5) produced by vacuum arc melting was investigated. The ratio Ti-rich region formed in the interdendritic region increased with increase of Ti in the $CoCuFeNiMnTi_x$. The E_{corr} and i_{corr} values for CoCuFeNiMn were found to be -0.322 V and $6.30x10^{-7}$ $A.cm^{-2}$, and these values were measured as -0.982 V and $1.16x10^{-3}$ $A.cm^{-2}$ for $CoCuFeNiMnTi_{0.5}$ alloy, respectively. The most important effect of Ti addition on the corrosion properties of the CoCuFeNiMn alloy was determined as the transformation of pitting corrosion to galvanic corrosion.

Keywords: High entropy alloys, corrosion properties, Ti addition effect.

1. Introduction

Over the last two decades, high-entropy alloys (HEAs) have become a remarkable novel type material group due to their unique mechanical [1], thermal [2], corrosive [3], magnetic [4], and electrical properties. Unlike conventional type alloys, which are still used in many industrial applications, high entropy alloys have single-phase structures containing [5] at least five equiatomic or closely equiatomic elements [6]. Different from the traditional ones, many elements with a concentration of 5 to 35 (at.%) are dissolved in basic simple crystal structures in high-entropy alloys [7]. The outstanding properties of the HEAs are defined with four-core effects, such as high entropy, sluggish diffusion, lattice distortion, and cocktail effect [8]. The high entropy effect stabilizes the solid solution phases formed by the dissolved elements in the simple crystal structure [9]. Therefore, the stabilization of the phase in the structure at high operation temperatures is provided by the high entropy effect. The sluggish diffusion effect determines the kinetic behaviors of the high entropy alloys [10]. According to the sluggish diffusion, the diffusion coefficient of the HEAs is slower than pure metals and conventional alloys [8]. The sluggish diffusion effect emerges from phase transformations during the heating of HEAs. The lattice distortion effect arises from the random positioning of many elements in a simple crystal structure. This effect resists the dislocation movements and improves the mechanical properties while negatively affecting the thermal and electrical properties. The final effect seen in high entropy alloys is the cocktail effect proposed by Ranganathan [11]. In high entropy alloys, the cocktail effect has critical importance in alloy design, especially in the determination of alloying elements. Due to this effect, the density of the high entropy alloy can be reduced by the addition or substitution of the low-density elements such as Al, Ti, while refractory elements such as Nb, Ta enable the alloy to work at high temperatures and increase oxidation resistance. However, apart from the individual effects of the elements, the interactions of different elements must also be considered in the design of HEAs properties. In the literature, various high entropy alloys such as CrMnFeCoNi [12, 13], AlCrCoFeNi [14], HfMoNbTaTiVZr [15], TiNbTaZrMo [16] with diverse properties have been produced using different production techniques, including arc melting.

Considering the fact that no study has been found in the literature on the corrosion properties of modified CoCuFeMnNi Cantor alloy prepared by vacuum arc melting method, this current study aims to investigate the electrochemical properties of the CoCuFeMnNi Cantor alloy depending on microstructure. For this purpose, $CoCuFeMnNiTi_x$ (x=0.0-0.5 in at. %) high entropy alloy was prepared by vacuum arc melting method, and the corrosion properties of the alloy were investigated depending on the microstructural variation and oxide layer formation on the surface

2. Materials and Methods

The high entropy alloys with an equimolar composition of $CoCuFeMnNiTi_x$ (x=0.0-0.5 in at. %) (x=0.0, 0.1, 0.2, 0.3, 0.4, 0.5) were synthesized in a vacuum arc melting furnace equipped with a continuous water-cooled copper crucible in an argon atmosphere. The purity of the constituent elements (Co, Cu, Fe, Mn, Ni, and Ti) purchased from Alfa Easer Company was greater than 99.9%, and 50 g of the alloy was prepared for each melting run. In the alloy preparation process, the arc melting furnace pressure was reduced to 10^{-2} mbar, and the melting processes were carried out at high purity argon gas with 400 mbar pressure. The prepared ingot alloys were re-melted five times to ensure chemical homogeneity throughout the ingot, and the ingot was rotated before each re-melting process. The produced ingot alloys were cut in the dimensions of 5x5x2 mm by using the wire erosion process to prepare samples for structural investigations.

Electrochemical properties of $CoCuFeMnNiTi_x$ high entropy alloy samples were tested with Gamry Interface 1010E model device using 3.5% NaCl solution at room temperature. The corrosion tests were carried out with a three-electrode cell system, using Ag/AgCl as a reference electrode, platinum wire as a counter electrode, and high entropy alloy sample as a working electrode. The open-circuit potential (OCP) was applied to all samples before the electrochemical impedance spectroscopy (EIS) and potentiodynamic polarization measurements for a duration of 3600 s. The electrochemical impedance spectroscopy analyses of the produced alloys were performed in the frequency between 10 mHz and 1000 kHz with a scan rate of 10 mV/min. The potentiodynamic-polarization tests were carried out from an initial potential of -1.5 V to a final potential of 1.5 V with a constant scan rate of 10 mV/min. After each corrosion test, the changes in the surfaces of the polished sample were examined by scanning electron microscope (SEM) in seconder electron mode.

3. Results and Discussion

Corrosion is a fundamental science that examines the interaction between material and environment. In this study, in CoCrFeMnNi alloy, Cr was replaced by Cu to prevent Cr decomposition at high temperatures. Also, Ti was doped to improve the high-temperature properties of the alloy, and the corrosion properties of the obtained CoCuFeMnNiTi$_x$ alloy in the NaCl environment were examined, and the results were given in Fig. 1. The potentiodynamic polarization curves, including active and passive corrosion properties in 3.5% NaCl solution for CoCuFeMnNiTi$_x$ (x=0-0.5 at. %) alloys prepared by the arc melting method are shown in Fig. 1.a. As can be seen from the figure, the corrosion potentials (*Ecorr*) of the alloys changed between -0.322 V and -0.982 V, while the corrosion current density ($\dot{I}_{corr}$) increased from 6.30x10^{-7} to 1.16x10^{-3}. With increasing Ti ratio, the E_{corr} decreased, and $\dot{I}_{corr}$ increased, but the rate of increase in $\dot{I}_{corr}$ values was lower for 0.3, 0.4, and 0.5 Ti ratios. While the corrosion rates (mm/year) calculated based on the corrosion current density ($\dot{I}_{corr}$) increased rapidly for 0.0-0.4% Ti ratios in parallel with the $\dot{I}_{corr}$ values, the rate of increase slowed down significantly from 0.4% Ti to 0.5% Ti. When these results were evaluated, it was observed that the corrosion resistance of the alloys decreased with the increasing Ti ratio, and this can be attributed to three different reasons. The first of these is related to how Cu, which has positive mixing entropy compared to other elements in CoCuFeMnNi alloy, affects the corrosion properties of the alloy. When the polarization curves given in Fig. 1.a are examined, it will be seen that the polarization curve of the Ti-free CoCuFeMnNi alloy is quite different from the polarization curves of the Ti-containing CoCuFeMnNiTi$_x$ alloys. With the addition of the Ti element, a passivation layer is formed on the surface of the alloys. In the original CoCrFeMnNi alloy, Cr has a passivating effect [17], and the passivation layer is not formed with the replacement of Cr with Cu in CoCuFeMnNi alloy. Lu et al. [18] stated that the polarization curve of the high-entropy CoCrFeMnNi alloy prepared by vacuum arc melting revealed that the passivation layer was formed. The E_{corr} and I_{corr} values of the CoCuFeMnNi alloy examined in this study and the CoCrFeMnNi alloy tested by Lu et al. [18] in the same corrosion solution (3.5% NaCl) were compared. While E_{corr} and I_{corr} results for CoCrFeMnNi alloy were obtained as -0.268 V and 6.44x10^{-8} A/cm^2, the E_{corr} and I_{corr} values for CoCuFeMnNi alloy were found as -0.322 V and 6.30x10^{-7} A/cm^2, respectively. As can be seen, while the E_{corr} value of the CoCrFeMnNi alloy was higher than that of the CoCuFeMnNi alloy, the I_{corr} value was found to be lower than that of the CoCuFeMnNi alloy, where the Cu element in CoCuFeMnNi alloy caused a decrease in the corrosion properties of the alloy. Here, a passivation layer is formed on the surface with the effect of Cr in CoCrFeMnNi alloy. On the other hand, there is no significant difference in the anodic and cathodic polarization curves of the CoCuFeMnNi alloy containing Cu instead of Cr. This shows that both reactions occur substantially at the same rate. The reason why both reactions proceed at the same speed is due to the fact that the phases formed in the microstructure have approximately the same chemical composition [19]. The second approach related to polarization curves (Fig.1.a) is based on the negative mixing enthalpy between Cr and Cu. In a study made in literature [20], the corrosion properties of

$Co_xCrCuFeMnNi$ alloy produced by the mechanical alloying method were examined, and E_{corr} (-0.787 V) and $\dot{I}_{corr}$ (3.84×10^{-5} A/cm^2) were obtained for x=1 value. The low E_{corr} and high $\dot{I}_{corr}$ values of the $Co_xCrCuFeMnNi$ alloy in comparison to the CoCuFeMnNi alloy produced in this study, caused the corrosion resistance of the $Co_xCrCuFeMnNi$ alloy to be lower than that of the CoCuFeMnNi alloy. In a similar study [21], the corrosion properties, in a 3.5% NaCl environment, of FeCoNiCrCu alloy produced by casting method were investigated. E_{corr} (-0.33 V) and $\dot{I}_{corr}$ (1.32×10^{-6} A/cm^2) values of FeCoNiCrCu alloy show that the corrosion resistance of FeCoNiCrCu alloy is lower than the CoCuFeMnNi alloy produced in this study. In the CoCuFeMnNi alloy, there is a positive mixing enthalpy between Cu and the remaining CoFeMnNi elements. Since there is no Cr element in the CoCuFeMnNi alloy, the negative mixing enthalpy between Cu-Cr does not occur here. The negative mixing enthalpy reduces the corrosion resistance of any alloys by creating regions with different energies that cause galvanic corrosion in the alloy. The third approach is related to phase separation caused by Ti, which is added to the alloy instead of Cr and generally positively affects the corrosion properties [22, 23]. From the potentiodynamic polarization curves given in Fig. 1.a of alloys containing Ti between 0.1-0.5, it is seen that Ti has a significant effect on the corrosion properties of the alloys. With the addition of Ti, similar to the above-mentioned effects of Cr, potentiodynamic curves including passivation have emerged in alloys. There are three different regions in the anode polarization curve given in the figure. The first of these is the active dissolution region, which is seen at a potential close to the E_{corr} value; the second is the passivity region where the alloys tend to passivate; and finally, the anodic dissolution zone formed in the passivation zone, where the passivation layer is corroded. These three regions were found to occur in each Ti-containing alloy. When the polarization curves of the Ti-free CoCuFeMnNi alloy and the Ti-containing $CoCuFeMnNiTi_x$ alloys were compared, it was observed that passivation occurred in the Ti-containing $CoCuFeMnNiTi_x$ alloys. However, this passivation is degraded as the corrosion process continues. It is observed that the ΔE potential at which passivation is observed increases continuously with the increase of the Ti ratio. Increasing the Ti ratio causes segregation in the microstructure of $CoCuFeMnNiTi_x$ alloys. The ratio of dendritic regions (containing primary and secondary dendritic arms) and interdendritic regions formed in the microstructure of alloys increases with increasing Ti ratio. The Ti-rich phase in the interdendritic zones leads to the formation of galvanic regions. The Ti-rich phase, which resists corrosion in the passivation zone, dissolves anodically, leading to a decrease in the corrosion resistance of the alloy. In other words, negative entropy elements such as Ti cause phase separation and the creation of galvanic corrosion in high-entropy alloys. Therefore, increasing the Ti ratio in Ti-containing $CoCuFeMnNiTi_x$ alloys decreased the corrosion resistance. As can be seen in Table 1, with increasing Ti ratio in the alloy, the E_{corr} value increased negatively, while the $\dot{I}_{corr}$ value decreased (approaching zero), indicating a decrease in corrosion resistance. Although the passivation zone widened as the Ti ratio increased, the lack of protection of the formed layer caused the corrosion resistance of the alloy to decrease.

Table 1. The electrochemical measurement results of produced Ti-free CoCuFeMnNi, and CoCuFeMnNiTi$_x$ high entropy alloys.

Alloys	E_{corr} V	i_{corr} A.cm^{-2}	Corrosion rate mm/year
CoCuFeMnNi	-0.322	6.30x10^{-7}	0.00657
CoCuFeMnNiTi$_{0.1}$	-0.401	1.89x10^{-5}	0.190
CoCuFeMnNiTi$_{0.2}$	-0.766	2.99x10^{-5}	0.302
CoCuFeMnNiTi$_{0.3}$	-0.929	2.10x10^{-4}	2.14
CoCuFeMnNiTi$_{0.4}$	-0.961	1.03x10^{-3}	10.5
CoCuFeMnNiTi$_{0.5}$	-0.982	1.16x10^{-3}	11.9

Nyquist, Bode, and phase angle graphs of CoCuFeMnNiTi$_x$ alloys produced by vacuum arc melting, determined by electrochemical impedance spectroscopy method, are shown in Fig. 1.b-d. In the Nyquist plot (impedance plot) in Fig. 1.b, semi-circular curves are formed as a result of redox reactions (oxidation), and the diameters of these curves are equal to the electron transfer resistance. The increase in the diameter of the formed semi-circle indicates that the electron transfer resistance increases, while the smaller diameters indicate that the electron transfer resistance decreases. Therefore, the diameter of the semi-circle at high frequencies is directly related to corrosion resistance. The large semi-circle diameter means high corrosion resistance. When the Nyquist curves of CoCuFeNiMn and CoCuFeNiMnTi$_x$ alloys are compared (Fig. 1.b); it will be seen that the semi-circular diameter of the Ti-free CoCuFeNiMn alloy is larger than the Ti-containing CoCuFeNiMnTi$_x$ alloys, and the semi-circle diameter decreases with the increase of Ti amount in CoCuFeNiMnTi$_x$ alloys. As explained above, since the semi-circle diameter is directly related to the corrosion potential in Nyquist curves, increasing the Ti ratio causes a decrease in corrosion resistance. This result emerging from the Nyquist curves is in good agreement with the polarization curves given in Fig. 1.a. However, the most significant difference between the Nyquist curves obtained as a result of impedance measurements performed in a 3.5% NaCl environment was seen in the CoCuFeNiMn alloy. While material transfer due to ion movement was observed in the low-frequency region in CoCuFeNiMn alloy, this phenomenon was not observed in the CoCuFeNiMnTi$_x$ alloys. When the shapes of the Nyquist curves of CoCuFeNiMnTi$_x$ alloys containing different ratios of Ti are compared, it will be seen that the Nyquist curve of the CoCuFeNiMnTi$_{0.3}$ alloy is flat and has an incomplete semi-circular shape in the high-frequency region. The flat line seen in the Nyquist graph represents the subsequent degradation of the oxidation film, which is formed during the electrochemical measurement and essentially provides corrosion resistance to the material. Here, it is understood that the Ti element doped into the structure reduces the corrosion potential of the alloy. Also, the 0.3 (at. %) Ti ratio can be considered as a critical value for the corrosion resistance of the alloy. For CoCuFeNiMnTi$_x$ alloy, up to 0.3% Ti ratio, the decrease in corrosion resistance is relatively low. This phenomenon can be explained by the segregation that occurs in the structure of the alloy. While low-level segregation occurs in the alloy up to 0.3% Ti, the segregation rate increases for $x>0.3$ conditions. For alloys with low Ti content ($x<0.3$), a protective oxide layer containing Cu and Ni elements is effective. However, at high Ti ratios ($x>0.3$), the increase of Ti-rich regions in the interdendritic regions on the surface of the alloys and the severe galvanic corrosion in these regions cause the deterioration of the TiO_2 film. This phenomenon has been evidenced with the decrease of the semi-circle diameters, which indicates a significant decrease in the corrosion resistance in the Nyquist plots given in Fig. 1.b for 0.4, and 0.5 Ti ratios. Bode and phase angle graphs of $CoCuFeNiMnTi_x$ alloys are shown in Fig. 1.c and 4.d. In the bode plot given in Fig. 1.c, the absolute value of the impedance (|Z|), which corresponds to the constant 10^{-1} frequency, reflects the corrosion resistance of the alloy in 3.5% NaCl solution [24, 25]. Accordingly, the (|Z|) value of the Ti-free CoCuFeNiMn alloy at a frequency of 0.1 (absolute value of impedance) was measured as $4.96x10^2$. The fact that the absolute value of the impedance of the CoCuFeNiMn alloy is higher than that of $CoCuFeNiMnTi_x$ (x=0.1-0.5) alloys confirms the polarization and Nyquist curves given in Fig. 1. a and b. The decrease in the absolute value of impedance by Ti doping to the CoCuFeNiMn alloy shows that the corrosion resistance of Ti-containing alloys ($CoCuFeNiMnTi_x$) decreases. The decrease in the absolute value of impedance is most likely due to the active dissolution of the interdendritic regions depending on the Ti ratio during solidification and the easy charge transfer that occurs on the surfaces of the alloys. Bode curves of $CoCuFeNiMnTi_x$ alloys appeared to form a |Z| plateau after approximately f>20 Hz values. This plateau phenomenon seen in the absolute value of impedance corresponds to the solution resistance, which includes the corrosion cell geometry, electrode resistance, impedances of the conductors used, and reference electrode. The bode curves are given in Fig. 1.c have a frequency between 0.1 and 10 Hz and a linear slope equaling to about -1 in log|Z|. On the other hand, the maximum phase angle is seen below -80° in the same frequency region (Fig. 1.d). This behavior shows the pseudocapacitive nature of the oxide layer formed on the surface of the alloys during corrosion measurements [24]. In other words, the phase angle defines the dielectric properties of the electronically conductive surface layer and is related to the capacitive response of the electrode [26]. The fact that the phase angle is less than -90° indicates that a protective insulating film is not formed on the surface of both Ti-free CoCuFeNiMn and Ti-doped $CoCuFeNiMnTi_x$ alloys. Therefore, there is a possibility of flow leakage between the interdendritic and dendritic regions in the microstructure due to the Ti effect. That is, the phase angle is less than -90° indicates that the oxide layer formed on the surface during corrosion measurements is permeable to the ions coming from the solution. The maximum phase angle value at approximately 1 Hz frequency was determined as -70.5° for the Ti-free CoCuFeNiMn alloy. By doping 0.1% Ti into CoCuFeNiMn alloy ($CoCuFeNiMnTi_{0.1}$), the phase angle decreased to -64.5 ° at the same frequency (1 Hz). Similarly, when the Ti ratio in the alloy was increased to 0.2 ($CoCuFeNiMnTi_{0.2}$), no significant change in phase angle was observed at the same frequency value. It is seen that the log(*f*)-phase angle curve of $CoCuFeNiMnTi_{0.3}$ alloy is different from that of other alloys. It can be said that this is caused by two different oxide layers formed on the surface of the alloy at the ratio of 0.3 Ti, which is defined as critical, as stated above. If the Ti ratio in $CoCuFeNiMnTi_x$ alloy exceeds a certain critical level, it probably causes the formation of a second oxide layer, such as TiO, on the surface of the alloy. Therefore, a second relaxation process was observed at the smaller frequency value (about 0.05 Hz). With the increase of the Ti ratio above the critical level, a relaxation process is seen from the curves. However, the increase in the ratio of the Ti-rich phase in the interdendritic regions of the microstructure led to the formation of a more insulating oxide layer on the surface of the alloys in the low-frequency region. The fact that the phase angle of this layer is less than -90° indicates that it is not protective against the ions coming from the solution.

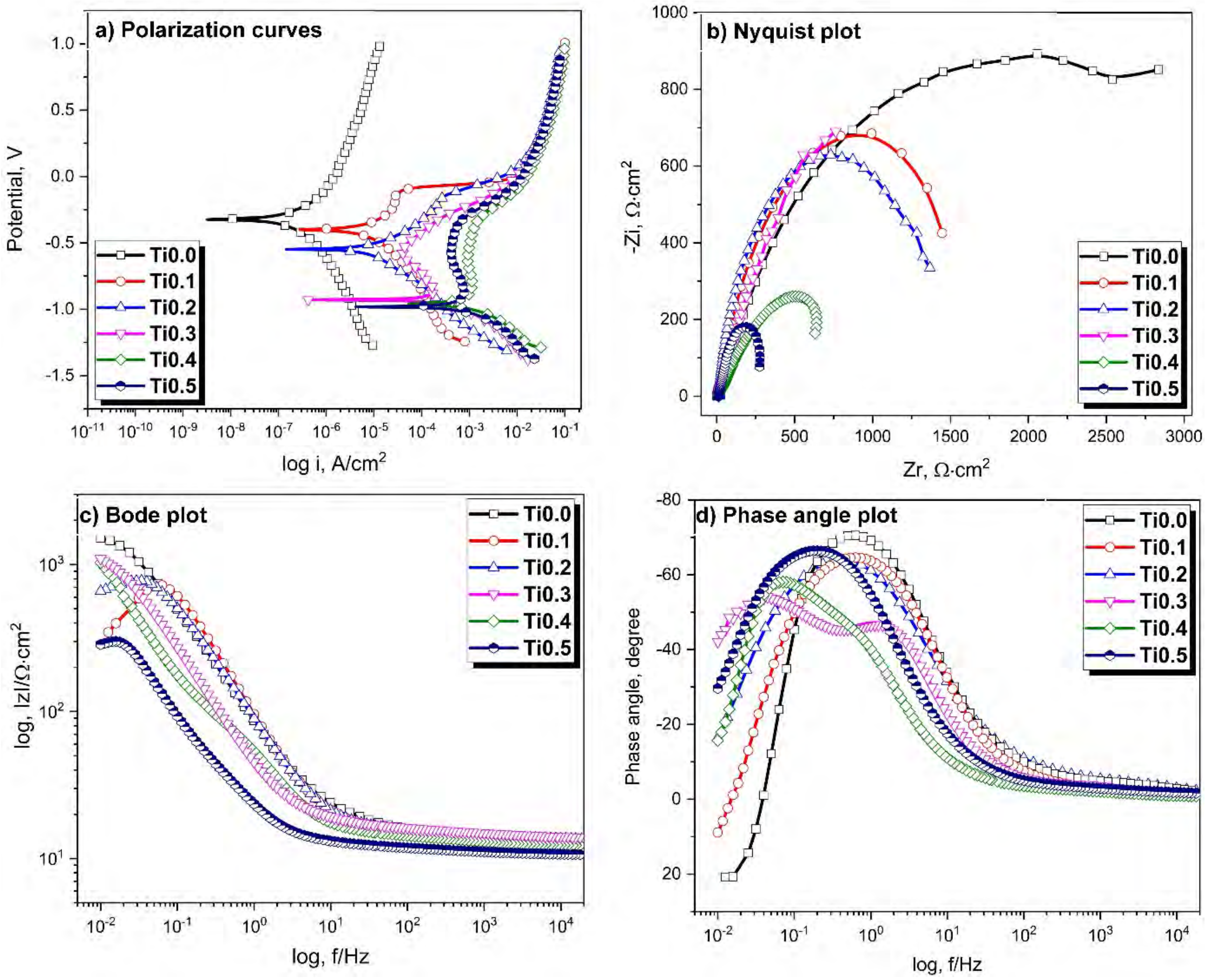

Figure 1. (a) Potentiodynamic polarization curves, (b) Nyquist, (c) bode, (d) phase angle plots of the Cu-modified Cantor alloys and $CoCuFeNiMnTi_x$.

4. Conclusions:

In the present research, Cu-modified high entropy Cantor alloy ($CoCuFeNiMnTi_x$) (x=0.0-0.5) produced by vacuum arc melting method and the effect of Ti addition on microstructure and corrosion properties of the alloy in 3.5% NaCl solution was investigated. The results obtained can be summarized as follows:

- The corrosion resistance of the $CoCuFeNiMnTi_x$ alloys decreased with the increase of Ti addition. The E_{corr} and i_{corr} values for CoCuFeNiMn alloy were found to be as -0.322 V and 6.30×10^{-7} $A.cm^{-2}$, and these values were measured as -0.982 V and 1.16×10^{-3} $A.cm^{-2}$ for $CoCuFeNiMnTi_{0.5}$ alloy, respectively
- Pitting corrosion occurred in the Ti-free CoCuFeNiMn alloy, while the formation of Ti-rich interdendritic zones in the Ti-doped $CoCuFeNiMnTi_x$ alloys caused the corrosion type to turn into galvanic corrosion.

- When the Ti amount in the alloy exceeds a critical ratio, cracks are formed on the insulating TiO_2 passivation layer, which indicates that the oxide layer is not protective, and corrosion progresses towards the inner parts of the alloy.

Acknowledgments:
This study was supported by Karadeniz Technical University, Department of Scientific Research Project, with project numbers of Grand Nos. FYL-2020-9238 and FBA-2021-9396.

References

1. Huang, L.; Sun, Y.; Amar, A.; Wu, C.; Liu, X.; Le, G.; Wang, X.; Wu, J.; Li, K.; Jiang, C.; Li, J., Microstructure evolution and mechanical properties of Al CoCrFeNi high-entropy alloys by laser melting deposition. *Vacuum* **2021,** *183*.
2. He, F.; Wang, Z.; Cheng, P.; Wang, Q.; Li, J.; Dang, Y.; Wang, J.; Liu, C. T., Designing eutectic high entropy alloys of CoCrFeNiNb x. *J Alloy Compd* **2016,** *656*, 284-289.
3. Yang, J.; Wu, J.; Zhang, C. Y.; Zhang, S. D.; Yang, B. J.; Emori, W.; Wang, J. Q., Effects of Mn on the electrochemical corrosion and passivation behavior of CoFeNiMnCr high-entropy alloy system in H2SO4 solution. *J Alloy Compd* **2020,** *819*.
4. Mishra, R. K.; Sahay, P. P.; Shahi, R. R., Alloying, magnetic and corrosion behavior of AlCrFeMnNiTi high entropy alloy. *Journal of Materials Science* **2018,** *54* (5), 4433-4443.
5. Vaidya, M.; Karati, A.; Marshal, A.; Pradeep, K. G.; Murty, B. S., Phase evolution and stability of nanocrystalline CoCrFeNi and CoCrFeMnNi high entropy alloys. *J Alloy Compd* **2019,** *770*, 1004-1015.
6. Zhang, K.; Wen, H.; Zhao, B.; Dong, X.; Zhang, L., Precipitation behavior and its impact on mechanical properties in an aged carbon-containing Al0.3Cu0.5CrFeNi2 high-entropy alloy. *Materials Characterization* **2019,** *155*.
7. Zhang, T.; Xin, L.; Wu, F.; Zhao, R.; Xiang, J.; Chen, M.; Jiang, S.; Huang, Y.; Chen, S., Microstructure and mechanical properties of Fe CoCrNiMn high-entropy alloys. *Journal of Materials Science & Technology* **2019,** *35* (10), 2331-2335.
8. Mohanty, A.; Sampreeth, J. K.; Bembalge, O.; Hascoet, J. Y.; Marya, S.; Immanuel, R. J.; Panigrahi, S. K., High temperature oxidation study of direct laser deposited AlXCoCrFeNi (X=0.3,0.7) high entropy alloys. *Surface and Coatings Technology* **2019,** *380*.
9. Vaidya, M.; Muralikrishna, G. M.; Murty, B. S., High-entropy alloys by mechanical alloying: A review. *J Mater Res* **2019,** *34* (5), 664-686.
10. Bracq, G.; Laurent-Brocq, M.; Perrière, L.; Pirès, R.; Joubert, J.-M.; Guillot, I., The fcc solid solution stability in the Co-Cr-Fe-Mn-Ni multi-component system. *Acta Mater* **2017,** *128*, 327-336.
11. Ranganathan, S., Alloyed pleasures: Multimetallic cocktails. *Current Science* **2003,** *85* (10), 1404-1406.
12. Kawamura, M.; Asakura, M.; Okamoto, N. L.; Kishida, K.; Inui, H.; George, E. P., Plastic deformation of single crystals of the equiatomic Cr−Mn−Fe−Co−Ni high-entropy alloy in tension and compression from 10 K to 1273 K. *Acta Materialia* **2021,** *203*, 116454.
13. Cantor, B.; Chang, I. T. H.; Knight, P.; Vincent, A. J. B., Microstructural development in equiatomic multicomponent alloys. *Materials Science and Engineering: A* **2004,** *375-377*, 213-218.
14. Mitrica, D.; Olaru, M. T.; Dragut, V.; Predescu, C.; Berbecaru, A.; Ghita, M.; Carcea, I.; Burada, M.; Dumitrescu, D.; Serban, B. A.; Banica, I. C., Influence of composition and as-

cast structure on the mechanical properties of selected high entropy alloys. *Materials Chemistry and Physics* **2020,** *242*, 122555.

15. Gao, M. C.; Carney, C. S.; Doğan, Ö. N.; Jablonksi, P. D.; Hawk, J. A.; Alman, D. E., Design of Refractory High-Entropy Alloys. *JOM* **2015,** *67* (11), 2653-2669.
16. Todai, M.; Nagase, T.; Hori, T.; Matsugaki, A.; Sekita, A.; Nakano, T., Novel TiNbTaZrMo high-entropy alloys for metallic biomaterials. *Scripta Materialia* **2017,** *129*, 65-68.
17. Shi, Y.; Yang, B.; Liaw, P. K., Corrosion-Resistant High-Entropy Alloys: A Review. **2017,** *7* (2), 43.
18. Lu, C.-W.; Lu, Y.-S.; Lai, Z.-H.; Yen, H.-W.; Lee, Y.-L., Comparative corrosion behavior of Fe50Mn30Co10Cr10 dual-phase high-entropy alloy and CoCrFeMnNi high-entropy alloy in 3.5 wt% NaCl solution. *Journal of Alloys and Compounds* **2020,** *842*, 155824.
19. Qiang, Y.; Zhang, S.; Guo, L.; Zheng, X.; Xiang, B.; Chen, S., Experimental and theoretical studies of four allyl imidazolium-based ionic liquids as green inhibitors for copper corrosion in sulfuric acid. *Corrosion Science* **2017,** *119*, 68-78.
20. Zhao, R.-F.; Ren, B.; Cai, B.; Liu, Z.-X.; Zhang, G.-P.; Zhang, J.-j., Corrosion behavior of CoxCrCuFeMnNi high-entropy alloys prepared by hot pressing sintered in 3.5% NaCl solution. *Results Phys* **2019,** *15*, 102667.
21. Hsu, Y.-J.; Chiang, W.-C.; Wu, J.-K., Corrosion behavior of FeCoNiCrCux high-entropy alloys in 3.5% sodium chloride solution. *Materials Chemistry and Physics* **2005,** *92* (1), 112-117.
22. Qiu, X. W.; Zhang, Y. P.; Liu, C. G., Effect of Ti content on structure and properties of Al2CrFeNiCoCuTix high-entropy alloy coatings. *Journal of Alloys and Compounds* **2014,** *585*, 282-286.
23. Su, Y.; Liang, X.; Liu, Y.; Dai, Z., Effect of Ti Addition on the Microstructure and Property of FeAlCuCrNiMo0.6 High-Entropy Alloy. *Acta Metallurgica Sinica (English Letters)* **2020,** *33* (7), 957-967.
24. Luo, H.; Li, Z.; Mingers, A. M.; Raabe, D., Corrosion behavior of an equiatomic CoCrFeMnNi high-entropy alloy compared with 304 stainless steel in sulfuric acid solution. *Corros Sci* **2018,** *134*, 131-139.
25. Ray, M.; Singh, V. B., Effect of sulfuric acid on corrosion and passivation of 316 SS in organic solution. *J Electrochem Soc* **2011,** *158* (11), C359-C368.
26. Ruiz-Luna, H.; Porcayo-Calderón, J.; Mora-García, A. G.; López-Báez, I.; Martinez-Gomez, L.; Muñoz-Saldaña, J., Corrosion Performance of AISI 304 Stainless Steel in CO2-Saturated Brine Solution. *Prot Met Phys Chem+* **2019,** *55* (6), 1226-1235.

CUAL10Nİ5FE4 NİKEL ALÜMİNYUM BRONZUNUN MİKROYAPISAL VE TRİBOLOJİK ÖZELLİKLERİNİN İNCELENMESİ

ATABERK YILDIZ[1], ABDURRAHIM METOGLU[2], SUAT ONAL[3], SELMINE AKYOL[1], FURKAN ALPTEKIN[1], SULTAN OZTURK[1], KURSAT ICIN[1], SEFA EMRE SUNBUL[*1,4]

[1] Karadeniz Teknik Üniversitesi, Mühendislik Fakültesi, Metalurji ve Malzeme Mühendisliği Bölümü, Trabzon, Türkiye.
[2] Kartek Metalurji A.Ş.,Üretim Departmanı, İstanbul, Türkiye.
[3] Osmaniye Korkut Ata Üniversitesi, Osmaniye Meslek Yüksek Okulu, Osmaniye, Türkiye.
[4] Gaziantep Üniversitesi, Mühendislik Fakültesi, Metalurji ve Malzeme Mühendisliği, Gaziantep, Türkiye.

Özet

Nikel-alüminyum bronzları (NAB) yüksek korozyon ve iyi aşınma özellikleri nedeniyle endüstride çokça kullanılmaktadır. Ayrıca yağlayıcılık özelliğine de sahip olmalarından dolayı pek çok tribolojik uygulama için tercih edilen bakır alaşımlarındandır. NAB, özellikle ağır yükler altında üstün abrazif aşınma dayanımı ve yüksek korozyon gerektiren uygulamalar için mükemmel malzemeler olarak kabul edilirler. Bu çalışmada, CuAl10Ni5Fe4 bileşimindeki NAB' unun kuru ortam atmosferik koşullarında ve yüksek ve düşük basınçta sürtünme ve aşınma özelliklerinin incelenmesi amaçlanmıştır. Bu amaçla, CuAl10Ni5Fe4 alaşımının mikro yapıları SEM mikroskobu ve sürtünme ve aşınma testleri ise blok-on-disk esaslı bir deney sisteminde gerçekleştirilmiştir. Bu deneyler sonucunda, sürtünme katsayısı değişimleri ve özgül aşınma miktarları belirlenmiştir. 0,5 MPa, 1 MPa ve 1,5 MPa yüklerinde artan yük ile sürtünme katsayısının 0,52, 0,46 ve 0,38' e azaldığı, özgül aşınma miktarının ise artan yük ile sırasıyla $5{,}10\times10^{-5}$, $5{,}25\times10^{-5}$ ve $5{,}63\times10^{-5}$ mm^3/N.m şeklinde arttığı tespit edilmiştir.

Anahtar kelimeler: Nikel alüminyum bronzu, Aşınma, Sürtünme, Mikroyapı

1. Giriş

Nikel alüminyum bronzu (NAB) (CuAl10Ni5Fe4), alüminyum, nikel ve demir metallerinin katkısı ile oluşan bakır esaslı bir alaşımdır. Üstün mekanik özellikleri sayesinde kullanımı sürekli artan bir alaşım çeşididir. Mükemmel korozyon ve aşınma direnci olan NAB aynı zamanda çok iyi sertlik ve mukavemet değerlerine sahiptir. Bu alaşım, üstün özellikleri nedeni ile makine imalatçılarının, gemi sanayinin ve hatta havacılık sektörünün birçok yerde kullandığı bir endüstriyel malzeme haline gelmiştir [1-4].

Nikel alüminyum bronzu (NAB) olarak isimlendirilen CuAl10Ni5Fe4 alaşımı, düşük sürtünme katsayısı, iyi aşınma dayanımı, mükemmel korozyon direnci, iyi kırılma tokluğu, yüksek sönümleme kapasitesi ve iyi yorulma direnci gibi özellikleri yüzünden geniş ölçüde makine imalatında, gemi sektöründe ve hatta havacılık uygulamalarında kullanılan bakır esaslı bir alaşımdır. Nikel alüminyum bronzu esasında bir bronz değildir, tek benzerlikleri her ikisinin de bakır alaşımı olmasıdır. Alüminyum bronzunun bu malzeme ile ismini paylaşması gerçeği ise, bazı geçmiş söylentilerin bir parçasıdır [3-8].

Metalurji uzmanlarının araştırmaları doğrultusunda NAB' ın gemi pervaneleri için kullanımı hızla gelişim göstermiştir. Amerikan nükleer denizaltısı Thresher' ın 1963' teki kaybının bronz döküm hasarından dolayı olduğu düşünülmüş ve bu durum NAB' ın denizaltında kullanımına yol açmıştır. Petrol fiyatlarındaki artış OPEC'i Meksika Körfezi ve Kuzey Deniz'de petrol aramaya itmiş bu da pompa, vana ve yangın kontrol ekipmanları için nikel aluminyum bronzu için yeni talepler ortaya çıkarmıştır. NAB, magnezyum bronz ve paslanmaz çelikten iki kat daha iyi korozyon dayanımına sahip olması 1980'ler ve sonrasında nikel aluminyum bronzlarının, uzay uygulamaları, savunma sanayi, denizcilik, petrokimya endüstrisi gibi sektörlerde aranan bir malzeme haline dönüştürmüştür [9].

Cu-Al alaşımına demir ve nikel eklemenin α faz sahasını genişlettiği bulunmuştur. Ni ve Fe alaşımlama katkıları α ve β fazından karmaşık metaller arası κ fazları çökelmesi ile sonuçlanır ve NAB' nin mekanik özelliklerini önemli ölçüde artırdığı tespit edilmiştir [10].

NAB alaşımlarının alüminyum içeriğinin, %8,8-10 aralığı içerisindeki değerlerde olması mukavemet, sertlik ve korozyon dayanımının artışı ile bağlantılı olmuştur. Bu durum esas olarak, uzamada azalma ile beraber tane sınırları boyunca lamelli κ_{III} fazının varlığına atfedilmiştir. % 9,5 Al içeriği ve ek alaşım elementleri % 5 nikel, % 4 demir ve % 0,5 manganlı alaşımların, pervanelerin imalatı için en iyi özellik kombinasyonları verdiği bildirilmiştir [10,11].

CuAl10Ni5Fe4 alaşımının mikro yapısı bakırca zengin α-fazı, kalıntı β ve çeşitli çökeltiler, toplu olarak Fe_3Al veya NiAl'ye dayanan κ-fazı olarak adlandırılan yapılardan oluşur. α ana yapısı ortalama bakır- %7 aluminyum -%3 nikel -%3 demirden oluşan bileşime sahiptir. β fazı NAB'ın yüksek sıcaklık katı çözelti fazıdır. Bununla birlikte, β ortam sıcaklıklarında stabil bir faz değildir. Çeşitli β dönüşüm ürünleri soğumanın sonucu olarak şekillenir [12-14].

Şekil 1 (a)' da açık gri bölgeler bakırca zengin α fazıdır. α fazı a = 3,64 Å kafes parametresi ile yüzey merkezli kübik kristal yapıya sahip denge terminal katı çözeltisidir. α fazı bir Widmanstatten morfolojisi sergileyebilir. Soğuma süresince yaklaşık 950°C'den başlayarak β fazından preötektoid α şekillenir. Yaklaşık 580°C'de α ve κ_{III} fazlarının karışımı içinde bir ötektoid reaksiyon sonuç verir. Soğuma sonrası, Ni-Fe-Al κ-fazları, α ve β fazlarından çökelir. κ_I fazı, sadece %5 Fe'den daha büyük demir içeriği ile NAB içinde gözlemlenmiş, geniş ve dallantılı (rozet şekilli) parçacıktır. Demirce zengin κ_I parçacıkları, tipik olarak 20 ile 50 µm boyutunda ve α tanelerinin merkezlerinde bulunurlar. κ_I bileşimi ve yapısına benzer κ_{II}, 5 ile 10 µm çapında ve κ_I parçacığından bir miktar küçük olmasına rağmen, demirce zengin dendritik parçacıktır (aynı zamanda küresel veya rozet şekilli). Bununla birlikte geniş κ_{II} parçacıkları κ_I ile kolayca karıştırılabilir. Yaklaşık 800°C'de, κ-fazının nikelce zengin lamelli (veya küresel) ötektoid formu olan κ_{III}, β fazından çökelir. κ_{III}'ün başlangıç çökeltilerinin küresel, sonrakilerin lamelli olduğu gözlemlenmiştir. α taneleri boyunca dağılan ince haç biçiminde, eşeksenli parçacıklar demirce zengin κ_{IV} parçacıklarıdır. Bu çökeltiler 2 µm çapından daha düşük mertebededir [10,11].

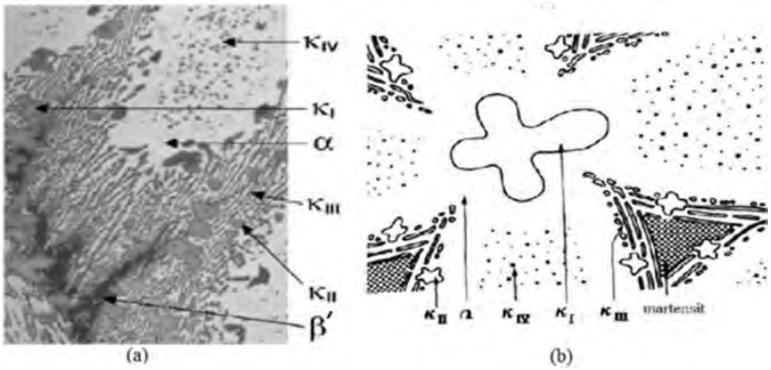

Şekil 1. Ham döküm CuAl10Ni5Fe4 alaşımının mikroyapısı: (a) Kum kalıba dökümde NAB'ın faz dağılımları, (b) Döküm NAB içinde mikroyapı dağılımının şematik gösterimi. (Sürekli soğuma sonrası β fazı, α anayapısı ve κ fazları haline dönüşür.)

Bu çalışmanın amacı, nikel alüminyum bronzu olan CuAl10Ni5Fe4 alaşımının standart karakterizasyon işlemleri ile mikroyapısal ve blok-on disk cihazında sürtünme aşınma testleri ile tribolojik özelliklerinin incelenmesidir.

2. Deneysel Çalışmalar

Bu çalışmada, yatak malzemesi olarak da kullanılan CuAl10Ni5Fe4 nikel alüminyum bronzu(NAB) tercih edilmiştir. Yatak malzemesi olarak kullanılan alaşımın sürtünme-aşınma özellikleri öneminin fazla olmasından dolayı metalografik ve tribolojik özellikleri incelenmiştir. İngot halinde temin edilen alaşımın bileşim oranları ağ.% 78,2Cu, 10Al, 5Ni, 4,8Fe, 1,5Mn ve 0,5 diğer şeklindedir. İngotun mikro yapısını ortaya çıkarmak klasik metalografik işlemlerden sonra, 20ml HCl, 10ml H_2O ve 1gr Fe_3Cl çözeltisi ile 5 saniye süresince numune üzerine damlatma şeklinde dağlama yapılmıştır. Dağlama işleminin ardından mikro yapı incelemeleri Zeiss Evo LS10 model taramalı elektron mikroskobunda (SEM) gerçekleştirilmiştir.

Alaşımın sürtünme ve aşınma özelliklerinin belirlenmesinde blok-on-disk tipi aşınma deney düzeneği kullanıldı. Sürtünme aşınma deneylerinin gerçekleştirildiği düzeneğin görüntüsü Şekil 2' de verilmiştir. Deney düzeneğinde karşı yüzey olarak SAE 4140 çeliğinden imal edilmiş bir disk malzemesi kullanılmış olup yüzey sertliği 55±1 RSD-C, çapı 210 mm ve kalınlığı ise 20 mm' dir. Triboloji testlerine tabi tutulan numunelerin disk ile temas eden yüzeyleri 10×5 mm boyutlarındadır.

Sürtünme katsayısı, serbest uygulanan normal kuvvetle yük hücresi yardımıyla ölçülen sürtünme kuvveti kullanılarak $\mu = F_s / F_n$ eşitliğinden hesaplandı. Malzemelerin aşınma direnci ise belli yük, çevresel hız ve alınan yol (devir) şartlarında oluşan malzeme kaybı olarak değerlendirilmiştir. Her bir numunenin sürtünme katsayısı ve aşınma direnci sabit 0,5 m/s kayma hızında ve 0,5 MPa, 1 MPa ve 1,5 MPa basınç altında deney parametreleriyle tespit edilmiştir. Deneylerde sabit 10000 m değer için ağırlık kaybı ölçülmüştür. Özgül aşınma kaybı, deney sırasında numunedeki kütle kayıplarının ölçülmesiyle belirlendi. Numuneler deney öncesinde ve sonrasında 0,1 mg hassasiyetli elektronik terazide tartıldı ve aşağıda verilen formülle hesaplanmıştır [11]:

$$W = \frac{\Delta m}{\rho . F_n . V . t} \qquad (1)$$

Burada W özgül aşınma miktarı (mm^3/Nm), Δm kütle kaybı (g), ρ yoğunluk (g/mm^3), F_n normal yük (N), V kayma hızı (m/s), t deney süresi (s)' dir. Numunelerin aşınma mekanizmaları, yine SEM' de yapılan aşınma izi (yüzeyi) ve aşınma parçacıklarının incelenmesi ile karakterize edilmiştir.

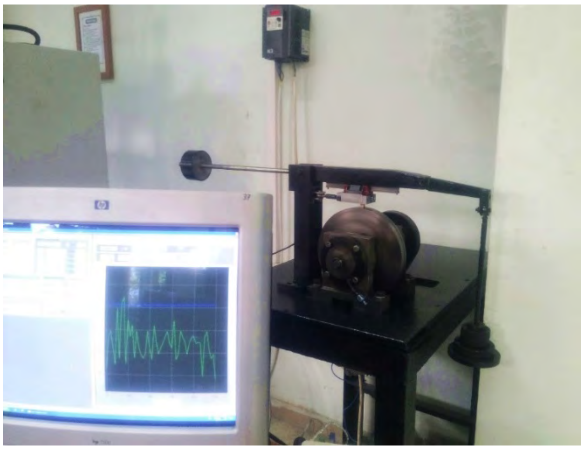

Şekil 2. Sürtünme aşınma deneylerinin gerçekleştirildiği test sistemi.

3. Bulgular ve İrdeleme

NAB alaşımının mikro yapısı SEM' de incelenmiş ve EDS analizleri ile olası fazlar belirlenmiştir. CuAl10Ni5Fe4 alaşımının mikro yapısı görüntüleri Şekil 3' te verilmiştir. Normalde CuAl10Ni5Fe4 alaşımı mikro yapısı α-bakır matrisi içerisinde dağılmış olarak metaller arası bileşik kappa fazlarından (κ_I, κ_{II}, κ_{III}, κ_{IV}) oluşmaktadır. Döküm yoluyla üretilen CuAl10Ni5Fe4 alaşımı yavaş soğuduğundan mikro yapıda herhangi bir martenzitik dönüşüm oluşmamış ve β' martenzit fazı meydana gelmemiştir. Bunun yerine, Şekil 3' te görüldüğü üzere, α-bakır matrisi içerisinde dağılmış durumda κ_{II}, κ_{III}, κ_{IV} metaller arası kappa fazları oluşmuştur. α-bakır matris fazı açık gri renkte olup, bu faz içerisinde dağılmış halde koyu renkte κ_{II}, κ_{III}, κ_{IV} metaller arası bileşik fazları bulunmaktadır. Matris fazı olan α-bakır fazı soğuma süresince yaklaşık 950 °C'den başlayarak β fazından ötektoid öncesi (preötektoid) sıcaklıklarda oluşmaktadır. Preötektoid α fazı yaklaşık 580 °C sıcaklıkta ötektoid reaksiyon sonucu α ve κ_{III} fazlarını içeren bileşimler oluşturmaktadır. Oda sıcaklığına yavaş soğuma sırasında, şekilde koyu gri renkte kontrast oluşturan κ_{IV} fazı α fazı içerisinden çökelmektedir. Öte yandan, κ_I fazı sadece %5'den fazla Fe içeren bir faz olduğundan ve CuAl10Ni5Fe4 alaşımında %4 oranında Fe bulunduğundan ingot mikroyapısında metaller arası bileşik κ_I fazı görülmemiştir [10,11].

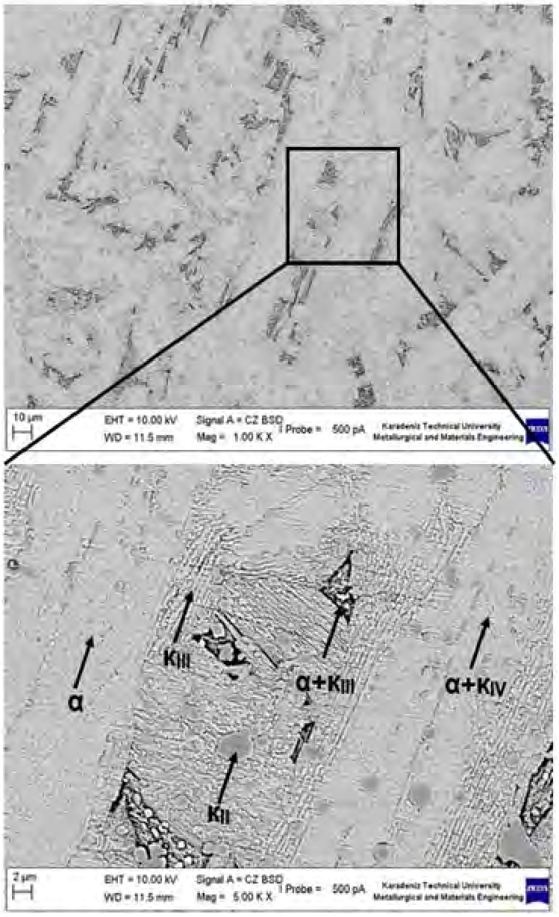

Şekil 3. CuAl10Ni5Fe4 alaşımının mikroyapısı.

CuAl10Ni5Fe4 alaşımının Şekil 4' de gösterilen mikroyapıdaki her bir faz EDS analizine tabi tutulmuş ve sonuçlar Şekil 5-8 arası sunulmuştur. EDS analizi sonucu bulunan element % ağırlık oranları ile literatürde verilmiş olan oranlar, Tablo 1' de sunularak ilgili fazların kimyasal bileşimleri ile karşılaştırılarak ilgili fazlar belirlenmiştir. α fazı içerisinde çökelerek oluşan ve ortalama boyutları 1 – 5 µm arasında değişen demirce zengin parçacıklar (Fe_3Al) κ_{II} fazını oluşturmaktadır. Tablo 1' deki literatüre göre κ_{II} fazı yaklaşık olarak %32 Fe, %19 Cu, %27 Ni ve %19 oranında Al içermektedir. Şekil 4' te verilen κ_{II} fazına ait EDS analiz sonucuna göre bu faz, %32 Fe, % 27 Cu, %16 Ni ve % 11 oranında Al içermektedir. Matris faz olarak tanımlanan α-Cu fazı ise bakır fazını ifade etmektedir ve teorik olarak içerisinde %85 Cu, %8 Al, %3 Fe, %2,5 Ni içerirken, Şekil 5' da sunulan EDS analizine göre ise, %72 Cu, %9 Al, %3 Fe ve %8 oranında Ni içermektedir. Mikroyapıda çok küçük nokta şeklinde ortaya çıkan κ_{IV} fazı üzerinde yapılan EDS analizlerinde ise bu fazın küçük eş eksenli, demirce zengin fazı gösterdiği tespit edilmiştir (Şekil 6). Yapılan EDS analizlerinde diğer analizlerdekine benzer şekilde teorik verilere yakın sonuçlar elde edilmiştir. Buna göre teorik olarak %62 Fe, %15 Al, %14 Cu ve %10 Ni, içeren bu fazın EDS analizi sonucunda yapısında % 68 oranında Fe ve %12 oranında Cu içerdiği görülmüştür. Yapıda ince çubuk şeklindeki fazın ise yapılan EDS analizi sonucu κ_{III} fazı olduğu bulunmuştur. Bu faz üzerinde yapılan noktasal EDS analizi sonucu yapının %27 Cu, %23 Ni, 22 Fe ve %18 Al içerdiği tespit edilmiştir (Şekil 7). Oluşan fazları genel olarak iki gruba ayırmak mümkündür. Birinci grup demirce zengin, ikinci grup ise nikelce zengin metaller arası bileşikleri temsil etmektedir. NAB' da bulunan elementlerin çeşidine ve ağırlıklarına bağlı olarak bu metaller arası bileşikleri kristalize etmek mümkündür (FeAl, Fe_3Al, $(Fe,Cu)_3Al$ ve NiAl, Ni_3Al) [14-16].

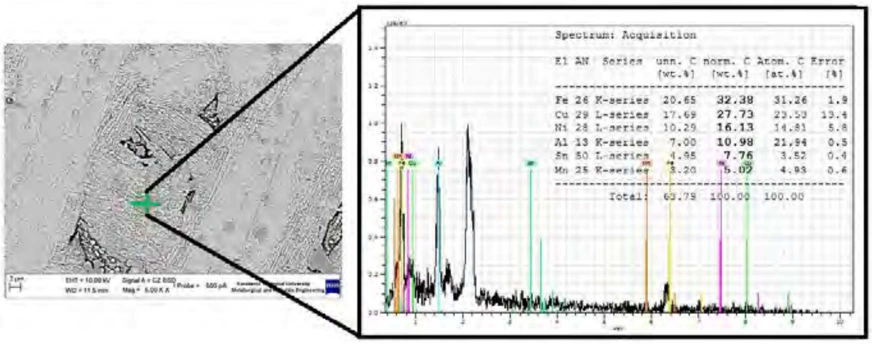

Şekil 4. CuAl10Ni5Fe4 ingot alaşımın yapısında bulunan κII fazının EDS analiz sonuçları.

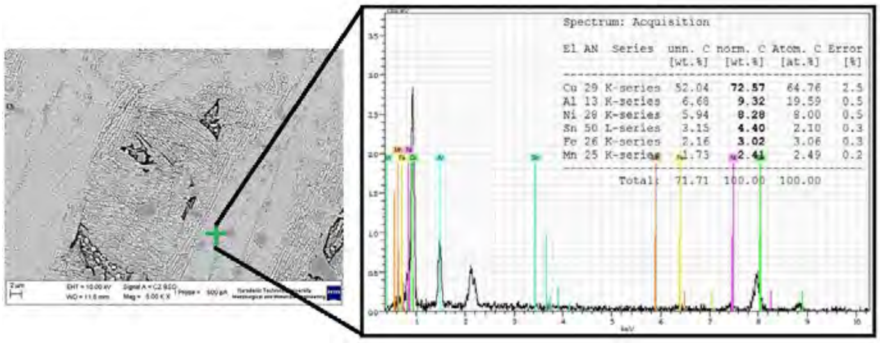

Şekil 51. CuAl10Ni5Fe4 ingot alaşımın yapısında bulunan α-Cu fazının EDS analiz sonuçları.

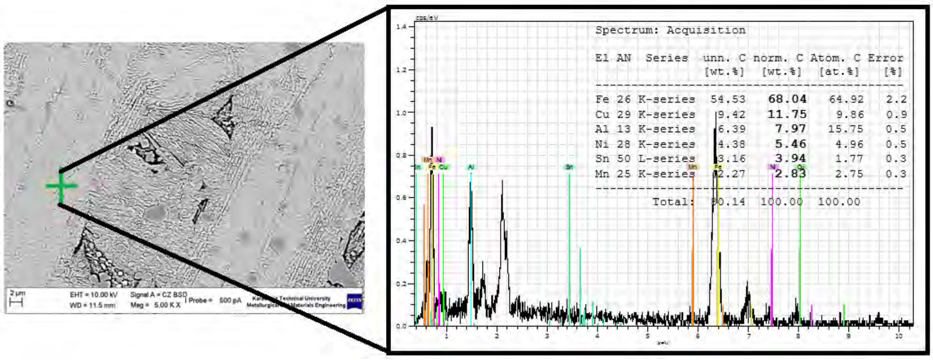

Şekil 6. CuAl10Ni5Fe4 ingot alaşımın yapısında bulunan κIV fazının EDS analiz sonuçları.

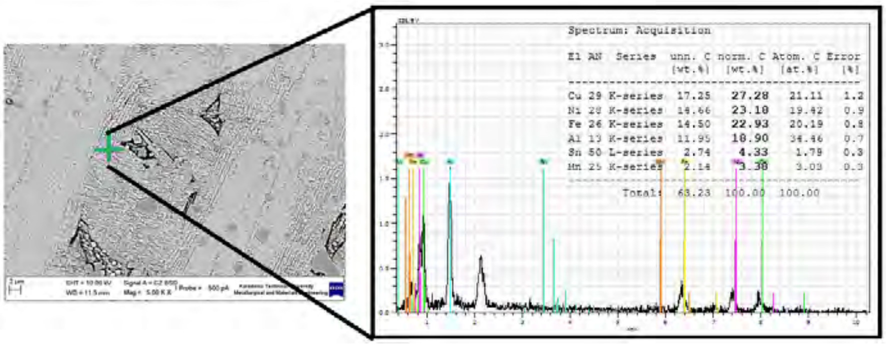

Şekil 7. CuAl10Ni5Fe ingot alaşımın yapısında bulunan κIII fazının EDS analiz sonuçları.

Tablo 1. CuAl10Ni5Fe4 alaşımında bulunabilecek fazların kimyasal bileşimi (% ağırlıkça)

Fazlar	Cu	Al	Fe	Ni	Mn	Referans
α	85,4	8 ±2	2,7 ±2	2,5 ±1,4	1,2 ±0,3	91,92
	85,8	7,2 ±0,4	2,8 ±0,3	3,0 ±0,2	1,1 ±0,1	91,92
	72,57	9,32	3,02	8,28	2,41	Bu çalışma
β	85	8,7	1,6	3,5	1,0	91,92
κ_I	15 ±5	13 ±5	5 5±7	15 ±3	2 ±0,4	91,92
	9,5	10 ±1,3	72 ±14	3,5 ±4	2,9 ±0,5	91,92
κ_{II}	19	19	32 ±3	27 ±5	2	91,92
	12,1 ±3	12,3 ±1,3	61,3 ±4,9	8,0 ±1,8	2 ±0,4	91,92
	27,73	10,98	32,38	16,13	5,02	Bu çalışma
κ_{III}	26 ±4	20 ±4	30 ±3	32 ±2	1,8 ±0,4	91,92
	17 ±5	26,7 ±1	12,8 ±1,6	41,3 ±6	2,0 ±0,4	91,92
	27,28	18,90	22,93	23,18	3,38	Bu çalışma
κ_{IV}	14 ±5	15 ±5	62 ±6	10 ±5	1,3 ±0,4	91,92
	26 ±7	10,5 ±1,7	73 ±2	7,3 ±1,5	2,4 ±0,2	91,92
	11,75	7,97	68,04	5,46	2,83	Bu çalışma

Tablo 2'de CuAl10Ni5Fe4 alaşımının farklı yüke bağlı olarak elde edilen ortalama sürtünme katsayıları ve özgül aşınma değerleri verilmiştir. Şekil 8 ise farklı yüklerdeki ingot malzemesinin sürtünme katsayısının alınan yol (kayma mesafesi) ile değişimini göstermektedir. Şekil 8 ve Tablo 2 birlikte değerlendirildiğinde sürtünme katsayısının artan yük ile azaldığı özgül aşınma miktarının ise artan yük ile artığı görülmektedir. Yükün artması ile sürtünme ısısı artmakta ve bunun sonucunda yüzeyde bir oksit filmi oluşmaktadır. Oluşan bu film yüzeyde kayma etkisi göstererek sürtünme katsayısının düşmesine yol açmaktadır. [17,18].

Tablo 2. Bronz alaşımının farklı yük ve kayma mesafelerindeki ortalama sürtünme katsayısı ve özgül aşınma değerleri

Uygulanan Yük, (MPa)	Ortalama Sürtünme Katsayısı, (µ) (10000m)	Alınan Yol, (m)
		10000 m
		Özgül Aşınma, (mm^3/N.m)
0,5 MPa	0,52	$5{,}10\times10^{-5}$
1 MPa	0,46	$5{,}25\times10^{-5}$
1,5 MPa	0,38	$5{,}63\times10^{-5}$

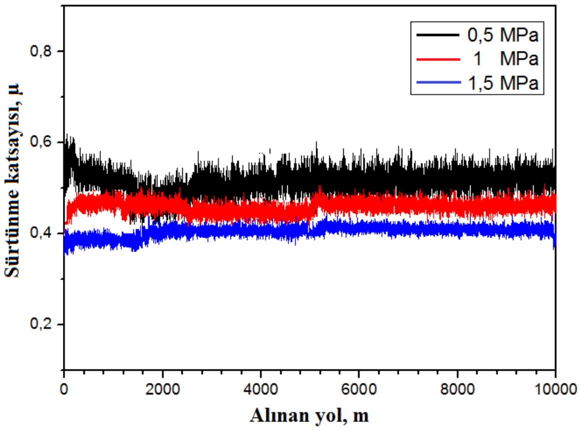

Şekil 8. CuAl10Ni5Fe4 ingot malzemenin farklı yükler altındaki sürtünme katsayısının 10000 metre kayma mesafesi ile değişimi.

Şekil 9-11' de CuAl10Ni5Fe4 alaşımının aşınma testleri sonucunda aşınma yüzeylerinin, Şekil 12-14' te aşınma parçacıklarının SEM görüntüleri verilmiştir. Numune aşınma yüzeylerinin, plastik deformasyon sonucu yüzeye yapışmış durumda bulunan sürtünme film tabakası ve aşınma çiziklerinden oluştuğu görülmektedir. Bu film tabakasının artan basınç ile birlikte genişlediği ve ayrıca artan yük ile beraber daha derin aşınma çiziklerinin ve çukurcukların oluştuğu görülmüştür. Z. Shi vd. [19] CuAl10Ni5Fe4 nikel alüminyum bronzunun sertleştirilmiş çelik üzerinde kuru sürtünme ortamındaki aşınma davranışını incelemiş ve 3 tip aşınmanın (adhezif aşınma, abrazif aşınma ve delaminasyon (tabakalı) aşınma) etkin olduğunu ortaya koymuştur.

Şekil 13-15' te görüldüğü gibi artan basınçla birlikte ortalama aşınma parçacıkların boyutlarının arttığı görülmektedir. Ortalama parçacık boyutları 0,5, 1 ve 1,5 MPa yük değerlerinde sırasıyla 2,84, 3,17 ve 3,81 µm olarak bulunmuştur.

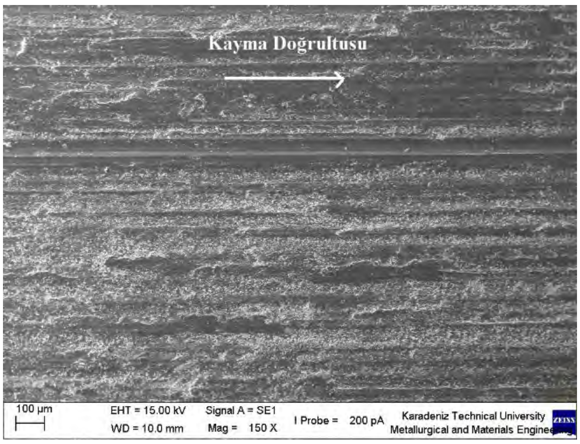

Şekil 9. CuAl10Ni5Fe4 ingot malzemenin 0,5 MPa yük altında, 0,5 m/s kayma hızında ve 10000 metre kayma mesafesi sonucu oluşan aşınma yüzeylerinin SEM görüntüleri.

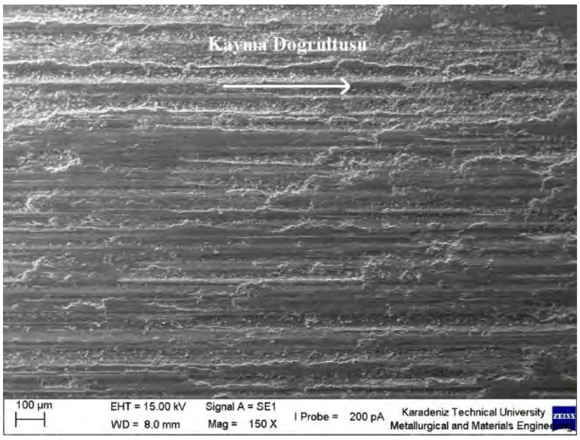

Şekil 10. CuAl10Ni5Fe4 alaşımının 1 MPa yük altında, 0,5 m/s kayma hızında ve 10000 metre kayma mesafesi sonucu oluşan aşınma yüzeylerinin SEM görüntüleri.

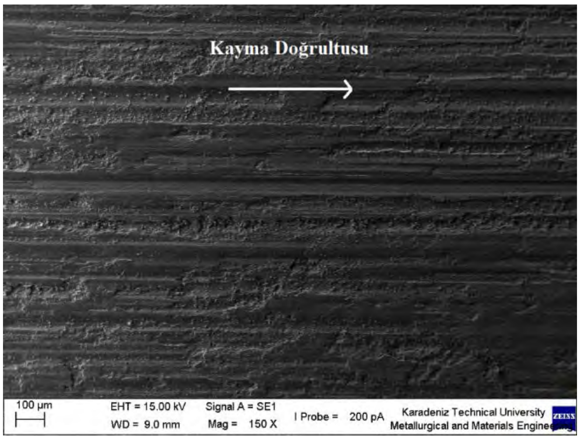

Şekil 11. CuAl10Ni5Fe4 alaşımının 1,5 MPa yük altında, 0,5 m/s kayma hızında ve 10000 metre kayma mesafesi sonucu oluşan aşınma yüzeylerinin SEM görüntüleri.

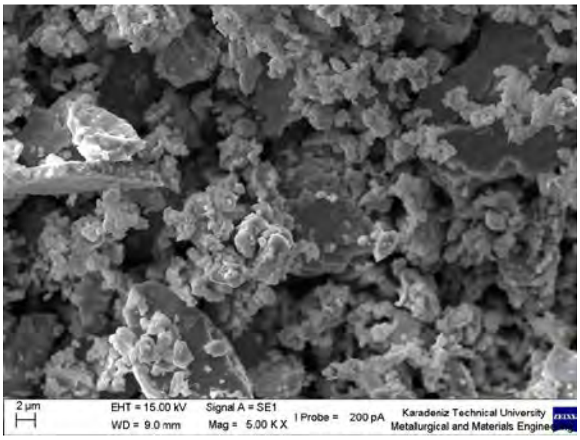

Şekil 12. CuAl10Ni5Fe4 alaşımının 0,5 MPa yük altında, 0,5 m/s kayma hızında ve 10000 metre kayma mesafesi sonucundaki aşınma parçacıkların SEM görüntüsü

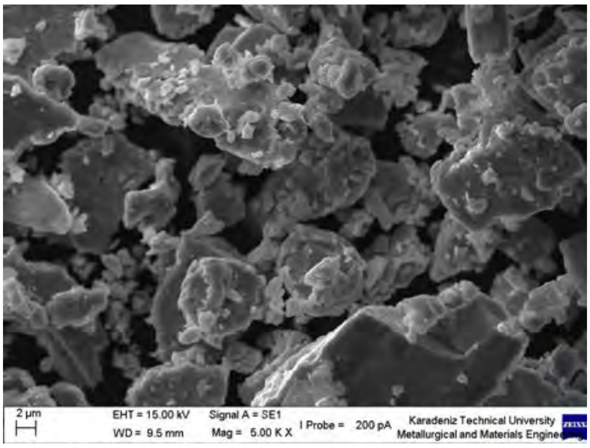

Şekil 13. CuAl10Ni5Fe4 alaşımının 1 MPa yük altında, 0,5 m/s kayma hızında ve 10000 metre kayma mesafesi sonucundaki aşınma parçacıkların SEM görüntüsü

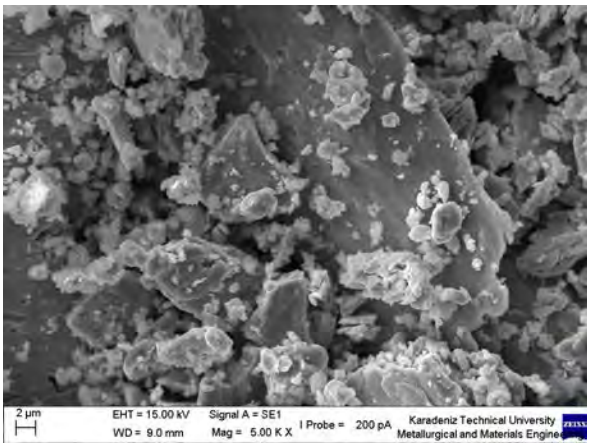

Şekil 14. CuAl10Ni5Fe4 alaşımının 1,5 MPa yük altında, 0,5 m/s kayma hızında ve 10000 metre kayma mesafesi sonucundaki aşınma parçacıkların SEM görüntüsü

4. Sonuçlar

Nikel alüminyum bronzu CuAl10Ni5Fe4 alaşımının metalografik olarak mikro yapısı incelenmiştir. İçerisinde bulunan α ve κ fazları EDS analizi yardımıyla literatür ile karşılaştırılmıştır. EDS ile elde edilen ağırlıkça elementel oranlar literatüre yakın değerlerde bulunmuştur.

Sürtünme katsayısı 0,5 MPa, 1 MPa ve 1,5 MPa yüklerinde artan yük ile sırasıyla 0,52, 0,46 ve 0,38' e azaldığı, özgül aşınma miktarının ise artan yük ile sırasıyla $5{,}10\times10^{-5}$, $5{,}25\times10^{-5}$ ve $5{,}63\times10^{-5}$ mm^3/N.m şeklinde arttığı tespit edilmiştir.

Teşekkür: Bu çalışma, Karadeniz Teknik Üniversitesi Bilimsel Araştırma Projeleri (FBA-2021-9396) tarafından desteklenmiştir.

Kaynaklar

1. Usta, G., Su Jeti Soğutmalı Döner Disk Atomizasyonu Yöntemiyle Hızlı Katılaştırılmış Bronz Alaşımı Toz ve Şeriti Üretiminin İncelenmesi, Yüksek Lisans Tezi, K.T.Ü., Fen Bilimleri Enstitüsü, Trabzon, **2009**.

2. Dawson, R., J., C., Aluminum bronze [J]. Engineering Materials and Design, **1978**, 22(12) 25-28.
3. Callcut V., A., Aluminum bronze for industrial use [J], Metals and Materials, **1989**, 5(3) 128-132.
4. Li, W., S., Wang, Z., P., Lu, Y., Jin, Y., H., Yuan, L., H. ve Wang F., Mechanical and trihological properties of a novel aluminum bronze material for drawing dies [J]., Wear, **2006**, 261(2) 155-163.
5. Tuthill, A., H., Guidelines for the use of copper alloys in seawater [J]. Materials Performance, **1987**, 26(9) 12-22.
6. Barabash, V., Pokrovsky, A. ve Fabritsiev, S., The effect of low-dose neutron irradiation on mechanical properties, electrical resistivity and fracture of NiAl bronze for lTER [J]. Journal of Nuclear Materials, **2007,** 367,370 1305-1311.
7. Wood R., J., K., Erosion-corrosion interactions and their effect on marine and offshore materials [J]., Wear, **2006**, 261, 1012-1023.
8. Li, W., S., Wang Z., P,, Lu Y., Gao, Y. ve Xu J. L., Preparation, mechanical properties and wear behavior of a novel aluminum bronze for dies [J]., Transaction of Nonferrous Metals Society of China, **2006**, 16,3 607-612.
9. Richardson I., 'Guide to Nickel Aluminium Bronze for Engineers' edited by Powell C., Copper Development Association Publication No 222, January **2016**.
10. Cuevas, A., M., Microstructure Characterization of Friction-Stir Processed Nickel Aluminium Bronze Throught Orientation Imanging Microscopy, Thesis, Naval Postgraduate School, Master of Science in Mechanical Engineering, California, September **2002**.
11. Weston, G., M., "Survey of Nickel-Aluminium-Bronze Casting Alloys on Marine Applications," Australia Dept. of Defence Report, DSTO MRL, Melbourne, Victoria, MRL-R-807, **1981**.
12. Hasan, F., Jahanafrooz, A., Lorimer, G., W. ve Ridley, N., The Morphology, Crystallography, and Chemistry of Phases in As-Cast Nickel Aluminium Bronze, Metallurgical Transactions A, **1982**, 13A, 8 1337-1345.
13. Pierce, F., A., The Isothermal Deformation of Nickel Aluminium Bronze in Relation to Friction Stir Processing, Thesis, Naval Postgraduate School, Master of Science in Mechanical Engineering, California, September, **2004**.
14. Hyatt, C., V., Revıew Of Lıterature Related To Mıcrostructure Development Durıng Laser Surface Engıneerıng Of Nıckel Alumınum Bronze, Defence Research Establishment Atlantic, March, **1997**.
15. Pisarek, B., P., Effect of Annealing Time for Quenching CuAl7Fe5Ni5W2Si2 Bronze on the Microstructure and Mechanical Properties, Archives of Foundry Engineering, **2012**, 12,2 187-204.
16. Howell, P., R., On the Phases, Microsconstituents and Microstructures in Nickel Aluminium Bronzes, Department of Materials Science Engineering, The Pennsylvania State University.
17. Özyürek, D., Tekel, S. ve Yılmaz, R., Cu-Al-Ni Alasımlarında Yaşlanmanın Aşınma Davranışı ve Elektrik İletkenliğine Etkisi, 5. Uluslararası İleri Teknolojiler Sempozyumu, **2009**, Karabük, Türkiye.
18. Koçak, T., Ü., Yanar, H., Pürçek, G. ve Birol, F., Bir Nikel Aluminyum Bronzu (CuAl10Ni5Fe4) İle Kalay Bronzunun (CuSn11) Sürtünme Ve Aşınma Özellikleri Açısından Karşılaştırılması, 2. Uluslar arası Demir Çelik Sempozyumu (IISS'15), 1-3 Nisan **2014**, Karabük, Türkiye.

19. Shi, Z., Sun, Y., Bloyce, A. ve Bell, T., Un-lubricated Rolling-Sliding Wear Mechanisms of Complex Aluminium Bronze Against Steel, Wear **1996**, 193,2 235-241.

ERİYİK SAVURMA YÖNTEMİYLE HIZLI KATILAŞTIRILMIŞ CUAL10Nİ5FE4 ALAŞIMI TOZLARINDAN KOMPAKT PARÇA ÜRETİMİ VE TRİBOLOJİK ÖZELLİKLERİNİN İNCELENMESİ

FURKAN ALPTEKIN[1], ABDURRAHIM METOGLU[2], SUAT ONAL[3], SELMINE AKYOL[1], ATABERK YILDIZ[1], SULTAN OZTURK[1], KURSAT ICIN[1], SEFA EMRE SUNBUL[*1,4]

[1] Karadeniz Teknik Üniversitesi, Mühendislik Fakültesi, Metalurji ve Malzeme Mühendisliği, Trabzon, Türkiye.
[2] Kartek Metalurji A.Ş.,Üretim Departmanı, İstanbul, Türkiye.
[3] Osmaniye Korkut Ata Üniversitesi, Osmaniye Meslek Yüksek Okulu, Osmaniye, Türkiye.
[4] Gaziantep Üniversitesi, Mühendislik Fakültesi, Metalurji ve Malzeme Mühendisliği, Gaziantep, Türkiye.

Abstract

Bu çalışmada, bakır esaslı CuAl10Ni5Fe4 alaşımından eriyik savurma yöntemiyle hızlı katılaştırılmış toz üretilmiş, elde edilen tozlardan presleme ve sinterleme işlemiyle kütlesel parçalar elde edilmiş, bu parçaların blok-on disk cihazında sürtünme-aşınma deneyleri gerçekleştirilerek tribolojik özellikler ortaya konmuştur. Eriyik savurma yöntemiyle toz üretme çalışmalarında düz yüzeyli ve dokulu olmak üzere iki farklı profilde diskler kullanılmıştır. Bu tozlar kullanılarak presleme ve sinterleme işlem adımlarıyla kompakt parçalar üretilmiş ve bu parçaların blok-on disk cihazında sürtünme ve aşınma testleri gerçekleştirilmiştir. Üretilen toz ve kompakt parçaların karakterizasyonu kapsamında; SEM'de morfoloji analizleri gerçekleştirilmiş, XRD cihazında faz yapısı belirlenmiştir. Hızlı katılaştırmayla üretilen tozlardan elde edilen kompakt parçaların tribolojik özellikleri oldukça iyidir.

Keyword: CuAl10Ni5Fe4, bronz, tribolojik özellikler, eriyik savurma

1. Giriş

Hızlı katılaştırılmış malzeme üretiminde en yüksek soğuma hızını sağlayan yöntem 'eriyik savurma (ergiyik metal döndürme)' tekniğidir. Bu yöntemin temel prensibi, sıvı metalin çok ince bir kesitten daha soğuk bir yüzeye akıtılması (genellikle basınç etkisiyle) ve çok yüksek hızda soğutulması esasına dayanmaktadır. Eriyik savurma tekniğinde sıvı metal, genellikle yüksek iletkenliğe sahip malzemen imal edilmiş döner bir disk veya tekerlek üzerine belli bir mesafeden, gaz basıncı etkisiyle püskürtülerek ince bir film (şerit) şeklinde katılaştırılır. Diskin yüksek hızlarda dönmesi, yüksek soğuma hızına neden olur. Yapılan işlem bir tür hızlı katılaştırma işlemidir ve ulaşılan soğuma hızı 10^5-10^8 K/s aralığındadır. Alaşım türü başta olmak üzere, disk malzemesi ve boyutları, disk hızı, püskürtme basıncı, nozul genişliği gibi çeşitli parametreler değiştirilerek farklı soğuma hızlarında ve farklı geometrilerde şeritler üretilebilir [1-4].

Eriyik savurma yönteminde genellikle yüzeyi düzgün ve pürüzsüz disk kullanılmaktadır. Disk üzerine akıtılan sıvı metal, yüzeyin kaygan olmasından dolayı ve diskin dönme etkisiyle yüzeyden kayarak sürekli formda ve ince kalınlıkta şerit şeklinde katılaşmaktadır. Disk yüzeyinin bir tür dişli çarkın dişleri gibi pürüzlendirilmesi durumunda şerit yerine toz elde etmek mümkündür. Bu durumda, eriyik savurma yerine atomizasyon işlemi gerçekleşir ve yine şerit yerine toz elde edilir. Demir çelik sektöründe en yaygın kullanım bulan bakır alaşımlarından biri de yatak malzemesi olarak kullanılan bronz alaşımlarıdır. Yatak malzemesi olarak kullanılan ana bronz alaşımları kalay bronzları, alüminyum bronzları, kurşunlu bronzlar ve berilyum bronzları olarak sayılabilir. Alüminyum, demir, mangan, silisyum ve nikel elementlerini içeren alüminyum bronzları ise yüksek sertlik özellikleri ile öne çıkmaktadır. Bu malzemelerden üretilmiş yataklar yüksek darbe ve aşınma dayanımına sahiptir. Bu alaşımlar yüksek sıcaklıklarda mukavemetlerini korur ve 250° C üzerinde çalışan ekipman yataklarında yağlamanın iyi olduğu, yüksek yük ve düşük hız uygulamalarında daha çok tercih edilirler [5].

Nikel alüminyum bronzu (NAB) (CuAl10Ni5Fe4), alüminyum, nikel ve demir metallerinin katkısı ile oluşan bakır esaslı bir alaşımdır. Üstün mekanik özellikleri sayesinde kullanımı sürekli artan bir alaşım çeşididir. Mükemmel korozyon ve aşınma direnci olan NAB aynı zamanda çok iyi sertlik ve mukavemet değerlerine sahiptir. Bu alaşım, üstün özellikleri nedeni ile makine imalatçılarının, gemi sanayinin ve hatta havacılık sektörünün birçok yerde kullandığı bir endüstriyel malzeme haline gelmiştir [6-9].

Nikel alüminyum bronzu (NAB) olarak isimlendirilen CuAl10Ni5Fe4 alaşımı, düşük sürtünme katsayısı, iyi aşınma dayanımı, mükemmel korozyon direnci, iyi kırılma tokluğu, yüksek sönümleme kapasitesi ve iyi yorulma direnci gibi özellikleri yüzünden geniş ölçüde makine imalatında, gemi sektöründe ve hatta havacılık uygulamalarında kullanılan bakır esaslı bir alaşımdır. Nikel alüminyum bronzu esasında bir bronz değildir, tek benzerlikleri her ikisinin de bakır alaşımı olmasıdır. Alüminyum bronzunun bu malzeme ile ismini paylaşması gerçeği ise, bazı geçmiş söylentilerin bir parçasıdır [8-13].

2. Deneysel Çalışmalar

Bu çalışmada, CuAl10Ni5Fe4 nikel alüminyum bronzu (NAB) kullanılmıştır. İngot halinde temin edilen alaşımın bileşim oranları ağ.% 78,2Cu, 10Al, 5Ni, 4,8Fe, 1,5Mn ve 0,5 diğer şeklindedir. Üretimler Karadeniz Teknik Üniversitesi Metalurji ve Malzeme Mühendisliği Bölümü'nde bulunan eriyik savurma cihazı ile gerçekleştirilmiştir (Şekil 1). İki farklı şekilde gerçekleştirilen üretimlerden ilki freon gazı ile soğutulmuş ve yüzeyi düz olan disk ile yapılırken ikincisi düz olan diskin yüzey şekli değiştirilip dokulu hale getirildikten sonra yapılmıştır (Şekil 2). Şerit veya toz üretme işlemleri, her iki disk için de, 0,5x8 mm boyutlarında dikdörtgen kesitli nozul, 52 $m.s^{-1}$'lik disk hızı, 0,6 bar'lık püskürtme gaz basıncı ve 1200 °C sıvı metal sıcaklığı üretim parametreleri kullanılarak gerçekleştirilmiştir. Eriyik savurma ünitesi ile üretilen ince şerit ve tozlar, kaba boyutlu olduklarından dolayı, toz metalürjisi ile dayanımı yüksek parça üretimi açısından, yüksek enerjili bilyeli öğütme işlemi ile öğütülerek boyutları küçültülmüştür. Bilyeli öğütme işlemi, Fritsch Pulverisette 6 model öğütme cihazında, 300 rpm' de 5mm' lik tungsten karbür bilyeler ile 10/1 bilye/toz oranında ve yüzey aktif madde olarak da %1 stearik asit ve aseton altında gerçekleştirilmiştir. Öğütme süresi 20 saat olarak belirlenmiştir. Öğütülen tozlar tek eksenli, tek tesirli hidrolik pres ile 700 MPa basınç altında preslenmiştir. Preslenmiş ham haldeki parçaların sinterlenmesi, argon atmosferi altındaki bir fırında 950 ºC sıcaklıkta ve 3 saat süreyle gerçekleştirilmiştir. Sinterleme sonrası üretilen parçaların mekanik özellikleri açısından makro sertlik ölçümleri gerçekleştirilmiştir. Vickers sertlik ölçümü, batıcı uç olarak tepe açısı 136° olan elmas kare piramit kullanılmış olup, 10 kg yük 25 saniye süresince uygulanmıştır.

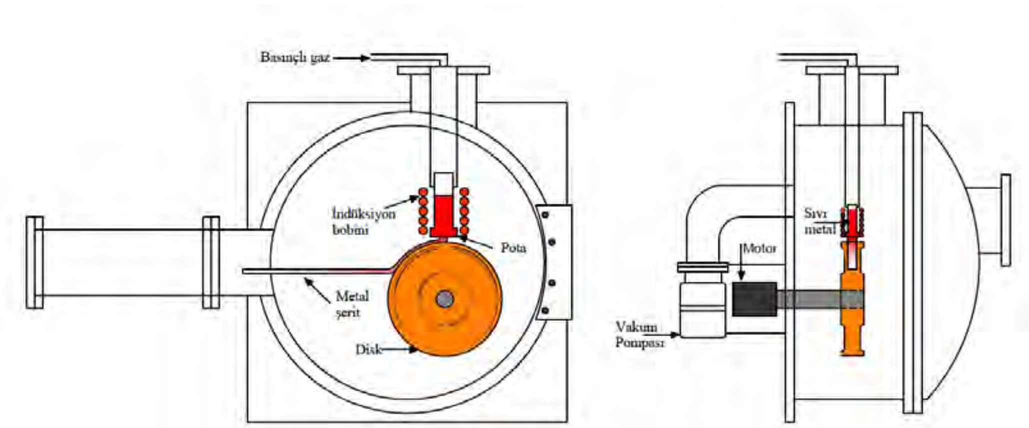

Şekil 1. Deneysel çalışmalarda kullanılan eriyik savurma cihazının şematik resmi.

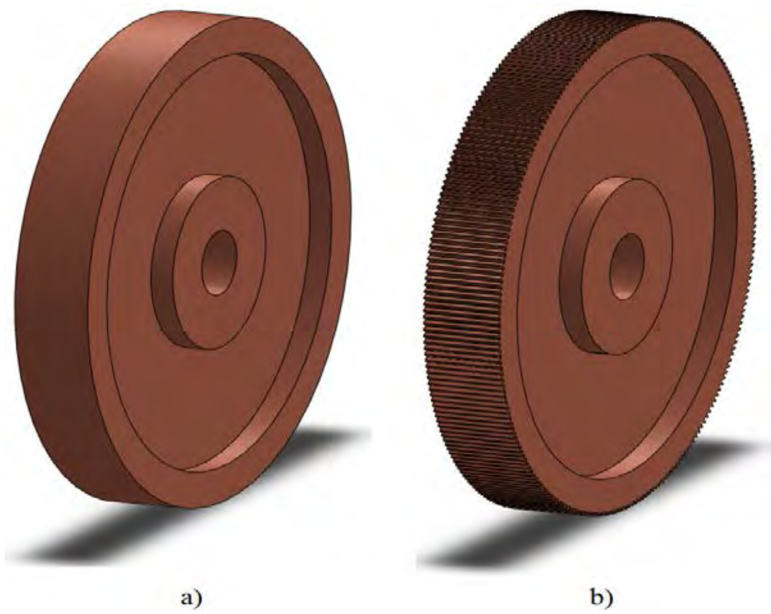

Şekil 2. Kullanılan diskler. a) soğutulmuş düz disk, b) dokulu disk

Eriyik savurma yöntemiyle farklı disklerle üretilen tozlardan presleme ve sinterleme yoluyla elde edilen T/M ürünlerinin sürtünme ve aşınma özelliklerinin belirlenmesinde blok-on-disk tipi aşınma deney düzeneği kullanıldı. Blok-on-disk tipi aşınma deney düzeneğinin görüntüsü Şekil 3'te, verilmiştir. Deney düzeneğinde karşı yüzey olarak SAE 4140 çeliğinden imal edilmiş bir disk malzemesi kullanılmış olup yüzey sertliği 55±1 RSD-C, çapı 210 mm ve kalınlığı ise 20 mm' dir. Triboloji testlerine tabi tutulan numunelerin disk ile temas eden yüzeyleri 10×5 mm boyutlarındadır.

Malzemelerin aşınma direnci ise belli yük, çevresel hız ve alınan yol (devir) şartlarında oluşan malzeme kaybı olarak değerlendirilmiştir. Her bir numunenin sürtünme katsayısı ve aşınma direnci sabit 0,5 m/s kayma hızında, 0,5 MPa, 1 MPa ve 1,5 MPa basınç altında deney parametreleriyle tespit edilmiştir. Deneylerde 2500 m, 5000 m ve 10000 m olmak üzere 3 farklı değer için ağırlık kaybı ölçülmüştür. Özgül aşınma kaybı, deney sırasında numunedeki kütle kayıplarının ölçülmesiyle belirlendi. Numuneler deney öncesi ve deney sonrası 0,1 mg hassasiyetli elektronik terazide tartıldı ve aşağıda verilen formülle hesaplanmıştır [14]:

$$W = \frac{\Delta m}{\rho . F_n . V . t} \tag{1}$$

Burada W özgül aşınma miktarı (mm^3/Nm), Δm kütle kaybı (g), ρ yoğunluk (g/mm^3), F_n normal yük (N), V kayma hızı (m/s), t deney süresi (s)' dir.

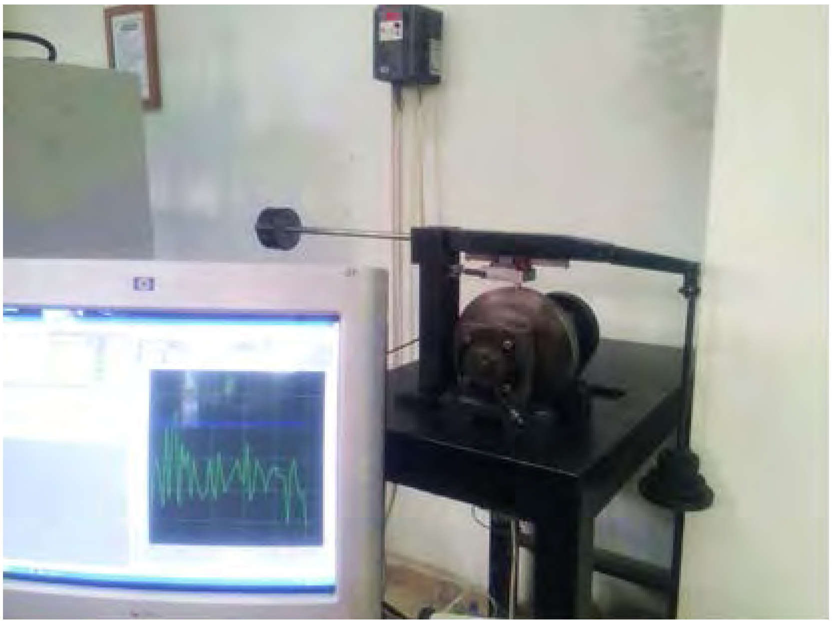

Şekil 3. Blok-on-disk tipi deney düzeneği

3. Bulgular ve Tartışma

Bu çalışmada, yüzeyi düz ve dokulu diskler kullanılarak eriyik savurma yöntemi ile CuAl10Ni5Fe4 alaşımından toz üretimi çalışmasında, üretilen tozlar 36, 45, 63, 90, 125, 180, 250 ve 355 µm'luk elek serisi kullanılarak eleme işlemine tabi tutulmuş ve elde edilen sonuçlardan toz boyutu dağılımı ortaya çıkartılmıştır. Her bir disk için elek aralığına göre elde edilen toz boyutu dağılımları Şekil 4' te verilmiştir. Şekilden görüleceği üzere, yüzeyi dokulu disk ile yapılan üretimde yüzeyi düz diske göre daha ince boyutlu toz elde edilmiştir. Yüzeyi dokulu disk ile üretilen tozların %53,99'u 355 µm altında iken, yüzeyi düz disk ile yapılan üretimlerde bu değer %46,37'dir. Ayrıca yüzeyi dokulu disk ile yapılan üretimlerde 36 µm altında bulunan toz oranı %7,99 iken, yüzeyi düz disk ile üretilen tozlarda bu değer %6,01'dir.

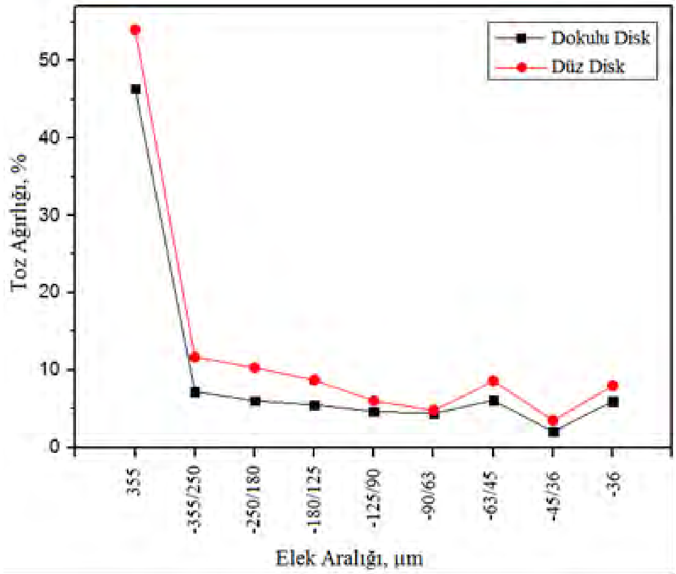

Şekil 4. Eriyik savurma yönteminde farklı yüzey profiline sahip diskler kullanılarak üretilen tozların elek analizi sonuçları.

Hem düz disk hem de dokulu disk kullanılarak NAB alaşımından eriyik savurma yöntemiyle şerit ve toz üretilmiştir. Her iki şekilde üretilen toz numunelerin SEM' de çekilen morfolojileri Şekil 5' te verilmiştir. Şekil 5' te görüldüğü üzere, düz disk ile üretilen tozlar daha küresel şekilli olmakla birlikte çubuksu ve düzensiz tozlar da içermektedir. Dokulu disk ile üretilen tozlar ise nispeten daha yassı, elyafsı, çubuksu ve düzensiz şekildedirler.

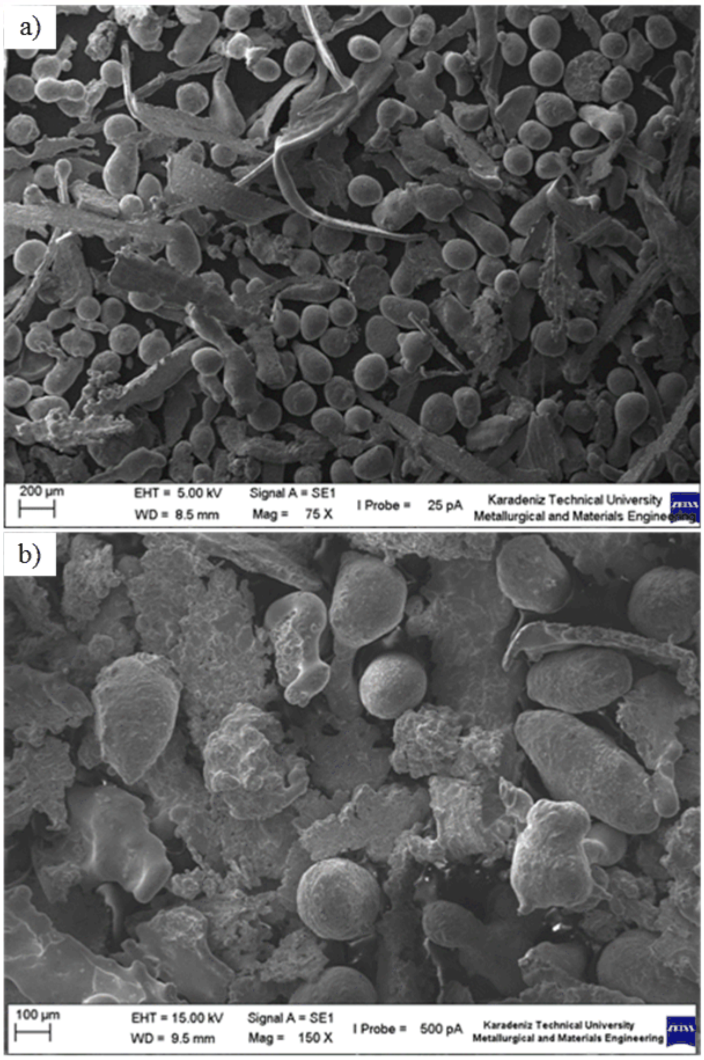

Şekil 5. Eriyik savurma yöntemiyle a) soğutulmuş düz disk, b) dokulu disk kullanılarak üretilen CuAl10Ni5Fe4 alaşımı tozların SEM' de çekilen mikro fotoğrafları.

Eriyik savurma yöntemiyle farklı yüzey profillerinde diskler kullanılarak üretilen CuAl10Ni5Fe4 alaşımı tozlarının boyutlarının, toz metalurjisi yöntemi ile parça üretmeye uygun olmamasından dolayı, bu tozlar öğütme işlemine tabi tutulmuşlardır. Bu amaçla, eriyik savurma sonrası üretilen elyafsı şeritler ve tozlar yüksek enerjili bilyeli öğütme işlemine tabi tutulmuşlardır. Bilyeli öğütme işlemi, alaşım tozlarının oksitlenmeye olan eğilimlerinden dolayı koruyucu özellikteki yüzey aktif madde ortamında (stearik asit+aseton) gerçekleştirilmiştir. Öğütme öncesi çoğunlukla küresel, az miktarda çubuksu ve pulsu şekilde olan tozların, öğütme sonrası düzensiz şekilli, çubuksu ve yassı tozlara dönüştüğü görülmektedir (Şekil 6). 20 saatlik öğütme süresi için ortalama parçacık boyutu yaklaşık 7 µm olarak ölçülmüştür. Mikro fotoğraflardan, öğütülen tozların topaklandığı tespit edilmiştir.

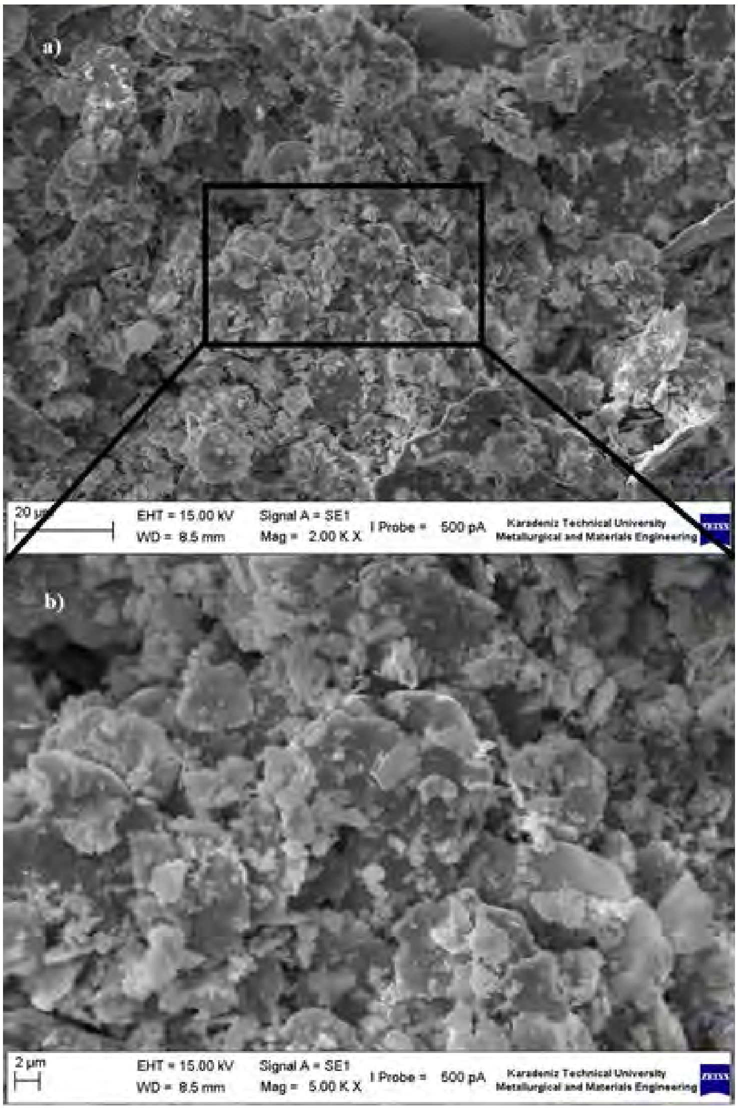

Şekil 6. Üretilen tozların 20 saat öğütme işlemi sonrası SEM' de çekilen mikro fotoğrafları. a) Küçük büyültmedeki görüntü, b)yüksek büyütmedeki görüntü.

Bu çalışma kapsamında çalışılan CuAl10Ni5Fe4 alaşımından eriyik savurma yöntemiyle gerek dokulu disk ve gerekse soğutulmuş düz disk kullanılarak elde edilen tozlardan presleme ve sinterleme ile üretilen kompakt parçaların sinterleme sonrası mikroyapıda olabilecek değişiklikleri ortaya koyabilmek amacıyla SEM' de mikroyapı incelemeleri yapılmış ve XRD çalışmaları gerçekleştirilmiştir. Hem soğutulmuş disk hem de dokulu disk kullanılarak üretilen tozlardan elde edilen kompakt parçaların sinterleme sonrası SEM' de elde edilen mikro yapısı Şekil 7' de gösterilmiştir. Preslenen ham parçalar 950 °C sıcaklıkta 3 saat süreyle sinterlenmişlerdir. Şekil 7' de verilen mikroyapılardan da görüldüğü gibi, tozların hızlı katılaştırma sonucunda oluşmuş mikroyapıları büyük ölçüde değişmiş, hemen hemen ingot mikroyapısına benzer bir yapı oluşmuştur. Bu durumun oluşmasında 950°C gibi nispeten yüksek sıcaklıkta ve 3 saat süreyle sinterlemenin yapılmasının etkili olduğu düşünülmektedir. Sinterleme sonrası mikroyapıda α-bakır matrisi içerisinde dağılmış durumda κ_{II}, κ_{III}, κ_{IV} metaller arası bileşik kappa fazları oluşmuştur. α-bakır matris fazı açık gri renkte olup, bu faz içerisinde dağılmış halde koyu renkte κ_{II}, κ_{III}, κ_{IV} metaller arası bileşik fazları bulunmaktadır.

Eriyik savurma yöntemiyle dokulu ve soğutulmuş düz diskler kullanılarak üretilen CuAl10Ni5Fe4 alaşımı tozlardan elde edilen kompakt parçaların sinterleme sonrası mikroyapılarında bulunan fazları belirlemek amacıyla XRD analizleri yapılmış ve sonuçlar Şekil 8' de verilmiştir. Sinterleme sonrası tozların başlangıç mikro yapılarından farklı, yaklaşık olarak alaşımın ingot yapısı ile aynı faz yapısı elde edilmiştir. XRD kırınım desenlerine göre sinterlenmiş mikroyapının α-matris fazı ve κ_{II}, κ_{III}, κ_{IV} metaller arası bileşik (kappa) fazlarından oluştuğu tespit edilmiştir [15-17].

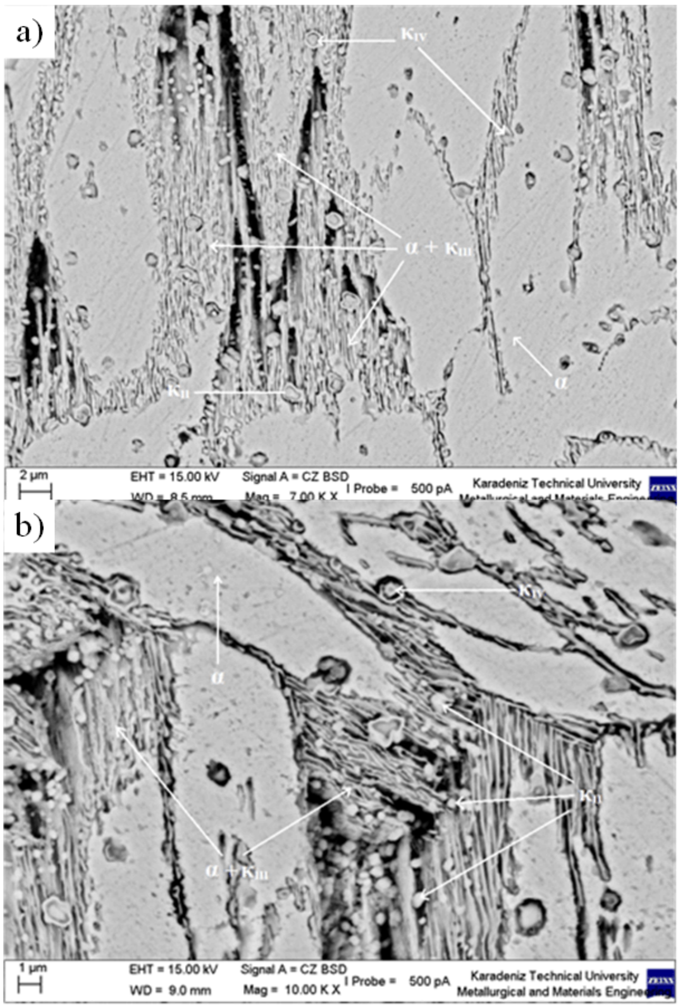

Şekil 7. Eriyik savurma yöntemiyle a) soğutulmuş düz disk b) dokulu disk kullanılarak üretilen CuAl10Ni5Fe4 alaşımı tozlardan elde edilen kompakt parçanın sinterleme sonrası SEM' de çekilen mikroyapısı.

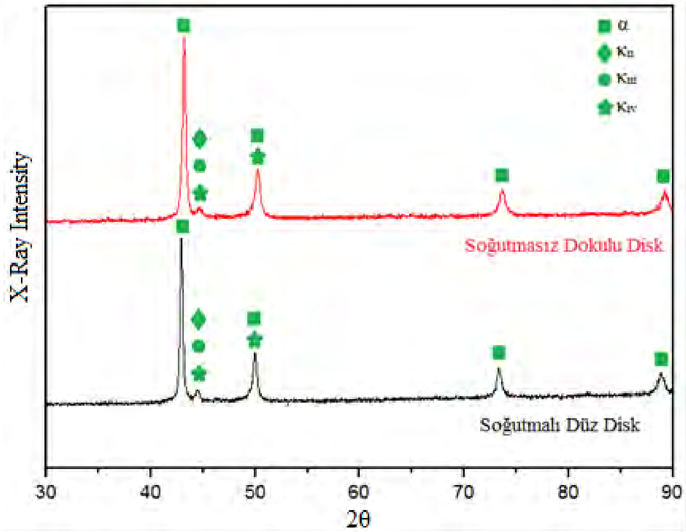

Şekil 8. Eriyik savurma yöntemiyle dokulu ve soğutulmuş düz diskler kullanılarak üretilen CuAl10Ni5Fe4 alaşımı tozlardan elde edilen kompakt parçaların sinterleme sonrası yapılan XRD analizi sonuçları.

Toz metalurjisi yöntemiyle üretilmiş parçaların yoğunlukları, Arşimet suya daldırma tekniği ile Eşitlik 2' de verilen eşitlik yardımıyla tayin edilmiştir. Karmaşık şekillerde, Arşimet suya daldırma tekniği, hacim ve dolaylı olarak yoğunluk ve gözenekliliği ölçmek için kullanılır. Bu teknikte numunenin kuru ortamdaki ağırlığı, yağ emdirildikten sonraki ağırlığı ve bir tel yardımıyla sudaki asılı ağırlığı hesaplanır ve aşağıda verilen formülle yoğunluğu tayin edilir [18]:

$$\rho = \frac{W_1 \cdot Qw}{W_2 - (W_3 - W_w)} \qquad (2)$$

Burada; ρ: gözenekli malzemenin yoğunluğu, W_1: numunenin kuru ağırlığı, W_2: yağ emdirildikten sonraki ağırlığını, W_3: suya daldırıldıktan sonraki ağırlık, Q_w: suyun sıcaklığa bağlı yoğunluğu (Q_w =1,0017-0,0002315T ve T'de, °C olarak suyun sıcaklığıdır), W_w: telin sudaki ağırlığını ifade eder.

Tablo 1' de eriyik savurma yöntemiyle dokulu ve soğutulmuş düz diskler kullanılarak elde edilen tozlardan, presleme ve sinterleme yöntemiyle üretilen parçaların yoğunlukları verilmiştir. Soğutulmuş düz disk ile üretilen tozlardan T/M yöntemiyle üretilen parçaların yoğunluğu 6,13 g/cm^3 iken, dokulu disk ile üretilen tozlardan T/M yöntemiyle üretilen parçalarınki ise 5,95 g/cm^3 bulunmuştur. Ortaya çıkan bu farkın tozların soğuma hızından ve neticesinde oluşan mikro yapıdan kaynaklandığı düşünülmektedir. Öte yandan, ingot haldeki alaşımın yoğunluğu ilgili üretici firma tarafından 7,5 g/cm^3 olarak belirtilmişti. T/M ürünlerinde gözenek oranının nispeten yüksek çıkmasının sebebi tozların presleme işleminin tek eksenli ve tek tesirli sıkıştırma şeklinde olmasından kaynaklanmaktadır [18].

Üretilen kompakt parçalarının makro sertlikleri Brinell & Vickers makro sertlik cihazı yardımıyla ölçülmüş, sertlik değerleri hesaplanmıştır (Tablo 1). En yüksek sertlik değeri ingot malzemede tespit edilmiştir. Eriyik savurma yönteminde soğutulmuş disk ile hızlı katılaştırılan tozlardan üretilen kompakt parçalarının, dokulu disk ile üretilen kompakt parçalara göre sertlik değerlerinin yüksek olmasının sebebi de gözenek yapısının daha az olması ve presleme ve sinterleme öncesi yüksek olan tozların sertliğinin korunamamasından kaynaklandığı düşünülmektedir [18].

Tablo 1. CuAl10Ni5Fe4 ingot alaşımı ve farklı diskler kullanılarak hızlı katılaştırılan tozlardan üretilen kompakt parçalarının yoğunluğu ve makro sertlik değerleri.

Disk Profil Türü	Yoğunluk, (g/cm^3)	Gözenek Oranı, (%)	Vickers Sertlik Değeri, ($\frac{kgf}{mm^2}$)
Dokulu Disk	5,95	20,66	165
Soğutulmuş Düz Disk	6,13	18,26	185
İngot	7,5	-	189

Eriyik savurma cihazıyla dokulu disk kullanarak hızlı katılaştırılmış tozlar üretilmiş olup üretilen tozlardan numuneler kompakt hale getirilmiş ve numunelerin tribolojik özellikleri incelenmiştir. Numunelerin sürtünme ile aşınma özellikleri Tablo 2 ve Şekil 9' da verilmiştir. Burada numunelerin sürtünme katsayısı artan yük ile azalırken özgül aşınma değerlerinde belirgin değişim elde edilememiştir. T/M ile üretilen numunelerin hem sürtünme katsayıları hem de özgül aşınma değerlerinin ingot değerlerine göre daha düşük olduğu tespit edilmiştir. Bunun nedeni öncelikle T/M ile elde edilen parçaların gözenekli olmasına bağlanmıştır. Ayrıca numune yüzeyinden kopan aşınma parçacıklarının tekrar numune yüzeyine yapışması ve yüzeyde daha geniş sürtünme filminin oluşması da diğer bir etken olarak düşünülmektedir [19,20].

Şekil 10' da ise 0,5 MPa, 1 MPa, 1,5 MPa basınç altında, sabit 0,5 m/s kayma hızında ve 10000 metre kayma mesafesi sonunda soğutulmuş düz disk ve dokulu disk kullanılarak üretilen numunelerin aşınma yüzeylerinin SEM görüntüleri verilmiştir. Burada sürtünme tabakasının artan yük ile birlikte arttığı buna ilaveten numune yüzeylerinde çiziklerin de oluştuğu görülmektedir.

Şekil 11' de aşınma testi esnasında oluşan aşınma parçacıkların SEM görüntüleri verilmiştir. 0,5 MPa yük değerinde elde edilen ortalama parçacık boyutu 1,76 µm iken, 1 MPa ve 1,5 MPa basınçlarda bu değerler 2,16 µm ve 2,95 µm' dur. Elde edilen bu değerler CuAl10Ni5Fe4 ingot malzemesiyle yapılan aşınma testleriyle elde edilen sonuçlara nazaran daha düşüktür.

Sürtünme esnasında oluşan aşınma parçacıklarının SEM görüntüleri Şekil 11' de verilmiştir. Aşınma parçacık boyutları 0,5 MPa, 1 MPa ve 1,5 MPa basınç değerlerinde sırasıyla 1,58 µm, 2,07 µm ve 2,69 µm olarak bulunmuştur. Bu değerlerin ingot malzemesi ve dokulu disk ile hızlı katılaştırılan tozlardan üretilen numune aşınma parçacıklarından daha düşük olduğu anlaşılmaktadır.

Tablo 2. Dokulu disk ile hızlı katılaştırılan tozlardan üretilen kompakt parçaların farklı yük ve kayma mesafelerindeki ortalama sürtünme katsayısı ve özgül aşınma değerleri.

Disk Türü	Uygulanan Yük, (MPa)	Ortalama Sürtünme Katsayısı, (μ) (10000m)	Alınan Yol, (m)		
			2500 m	5000 m	10000 m
			Özgül Aşınma, (mm^3/N.m)		
Düz	0,5 MPa	0,39	$1{,}94\times10^{-5}$	$2{,}34\times10^{-5}$	$2{,}46\times10^{-5}$
Dokulu		0,40	$2{,}79\times10^{-5}$	$2{,}82\times10^{-5}$	$2{,}65\times10^{-5}$
Düz	1 MPa	0,33	$2{,}01\times10^{-5}$	$2{,}52\times10^{-5}$	$2{,}68\times10^{-5}$
Dokulu		0,35	$2{,}99\times10^{-5}$	$2{,}67\times10^{-5}$	$2{,}72\times10^{-5}$
Düz	1,5 MPa	0,29	$2{,}49\times10^{-5}$	$2{,}55\times10^{-5}$	$2{,}71\times10^{-5}$
Dokulu		0,30	$2{,}83\times10^{-5}$	$2{,}97\times10^{-5}$	$2{,}88\times10^{-5}$

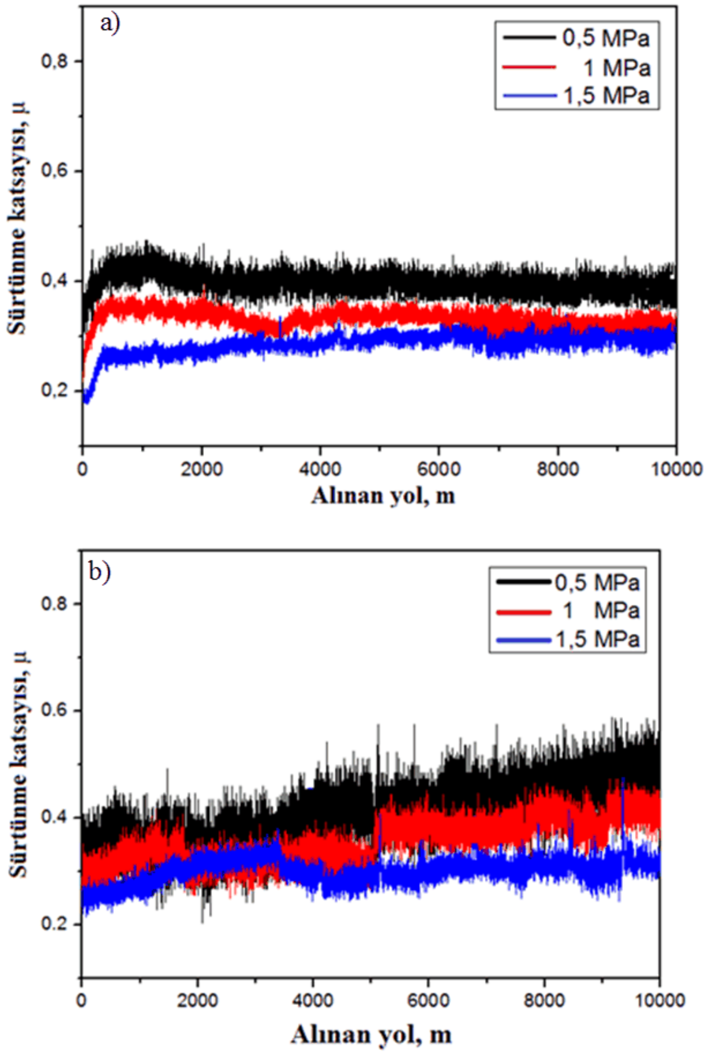

Şekil 9. a)Soğutulmuş düz disk, b) dokulu disk ile hızlı katılaştırılan tozlardan üretilen kompakt parçaların farklı yükler altındaki sürtünme katsayısının 10000 metre kayma mesafesi ile değişimi.

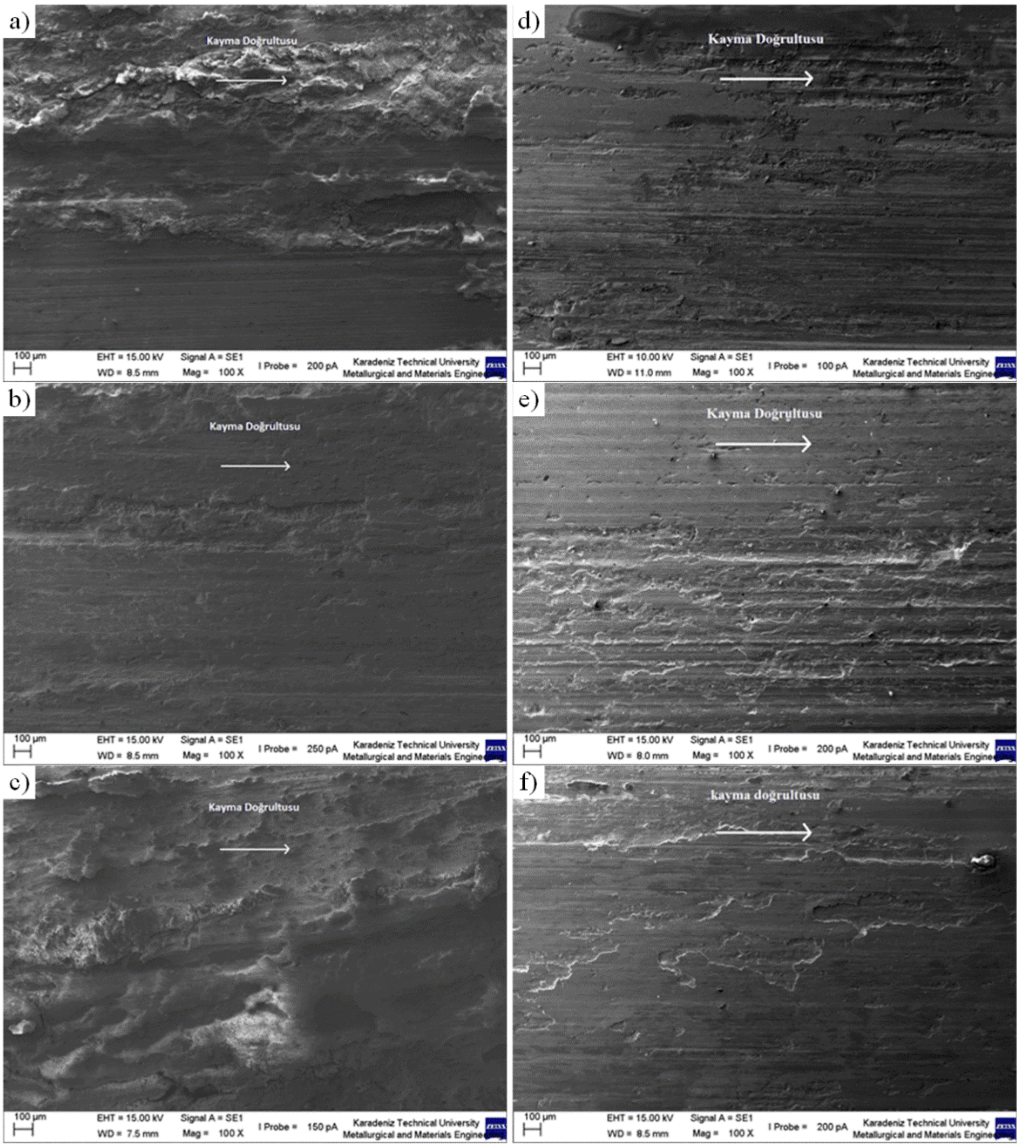

Şekil 10. Soğutulmuş düz disk ile a) 0,5 MPa, b) 1MPa, c) 1,5 MPa basınçlarda; dokulu disk ile d) 0,5MPa, e)1 MPa, f) 1,5 MPa basınçlarda, 0,5 m/s kayma hızında ve 10000 metre kayma mesafesi sonucundaki aşınma yüzeylerinin SEM görüntüsü.

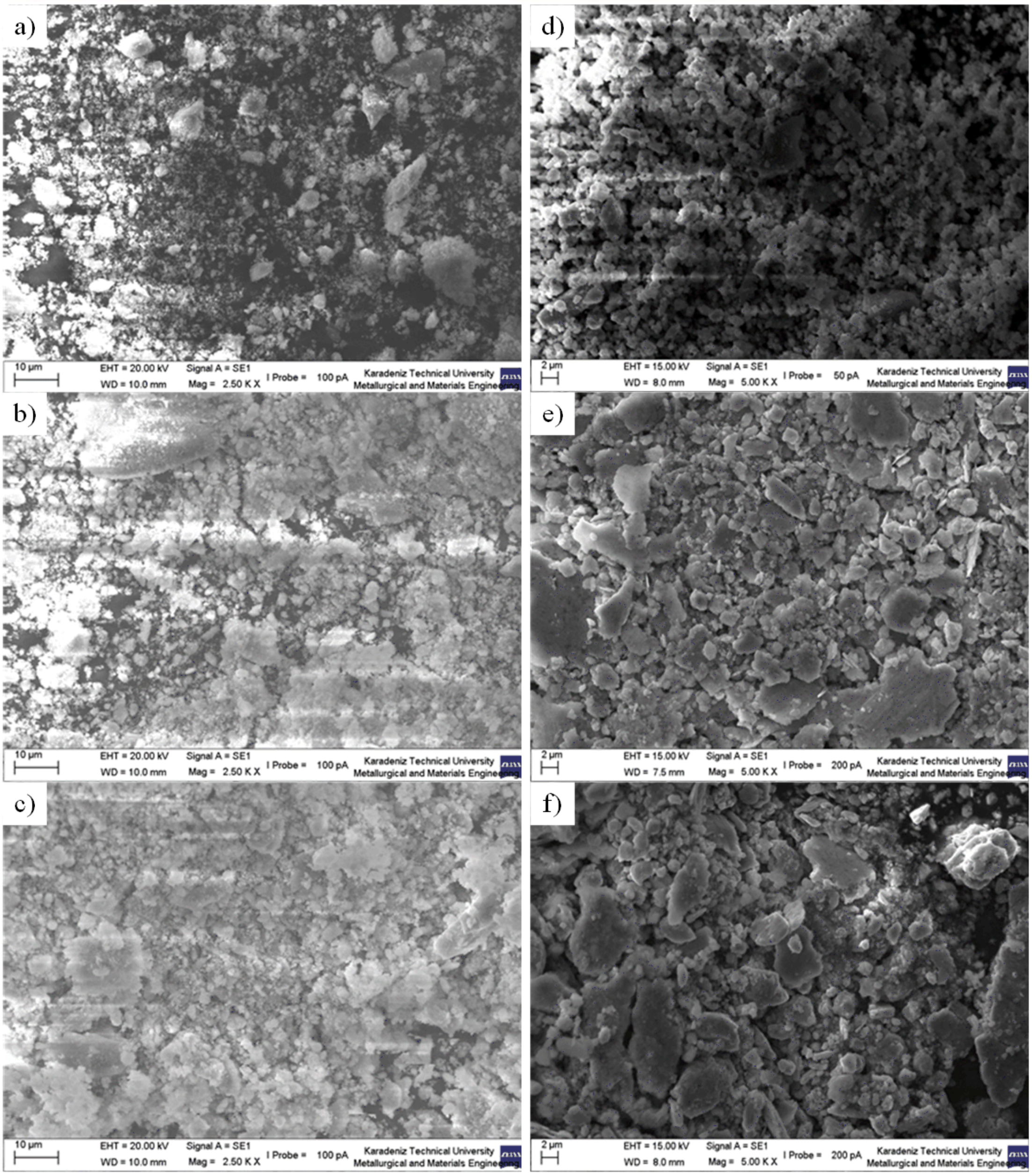

Şekil 11. Soğutulmuş düz disk ile CuAl10Ni5Fe4 tozlarından üretilen kompakt parçaların a) 0,5 MPa, b) 1 MPa, c) 1,5 MPa basınç altındaki; dokulu disk ile CuAl10Ni5Fe4 tozlarından üretilen kompakt parçaların d) 0,5 MPa, e) 1MPa, f) 1,5 MPa basınç altındaki aşınma parçacıklarının SEM görüntüleri.

4. Sonuçlar

- Yüzeyi dokulu disk ile üretilen tozların %53,99'u 355 µm altında iken, yüzeyi düz disk ile yapılan üretimlerde bu değer %46,37'dir. Ayrıca yüzeyi dokulu disk ile yapılan üretimlerde 36 µm altında bulunan toz oranı %7,99 iken, yüzeyi düz disk ile üretilen tozlarda bu değer %6,01'dir.

- Düz disk ile üretilen tozlar daha küresel şekilli olmakla birlikte çubuksu ve düzensiz tozlar da içermektedir. Dokulu disk ile üretilen tozlar ise nispeten daha yassı, elyafsı, çubuksu ve düzensiz şekildedirler.
- Sinterlenmiş mikroyapının α-matris fazı ve κ_{II}, κ_{III}, κ_{IV} metaller arası bileşik (kappa) fazlarından oluştuğu tespit edilmiştir
- Düz disk ile yapılan tozlardan elde edilen tiribolojik sonuçlar, 0,5 MPa yük değerinde elde edilen ortalama parçacık boyutu 1,76 µm iken, 1 MPa ve 1,5 MPa basınçlarda bu değerler 2,16 µm ve 2,95 µm' dur. Dokulu diskten elde edilen tozlardan yapılan bulk numunenin aşınma parçacık boyutları 0,5 MPa, 1 MPa ve 1,5 MPa basınç değerlerinde sırasıyla 1,58 µm, 2,07 µm ve 2,69 µm olarak bulunmuştur.

Teşekkür: Bu çalışma, Karadeniz Teknik Üniversitesi Bilimsel Araştırma Projeleri (FBA-2021-9396) tarafından desteklenmiştir.

Kaynaklar

1. Sünbül, S., E., Eriyik savurma Yöntemiyle AA6060 Alüminyum Alaşımı Şerit ve Toz Üretiminin İncelenmesi, Yüksek Lisans Tezi, K.T.Ü., Fen Bilimleri Enstitüsü, Trabzon, 2015.
2. Suryanarayana, C., Froes, F., H. ve Rowe, R.G., Rapid solidification processing of titanium alloys'. International Materials Reviews, 36,1 (1991) 85-123.
3. Pond, R., B., Maringer, R., E. ve Mobley, C., E., High rates continuous casting of metallic fibers and flaments in new trends in materials fabrication, 1976, ASM Seminar Series, 128–164.
4. Anantharaman T., R. ve Suryanarayana, C., 1987, Rapidly solidified metals: A Technological Overview, 103–124, Trans. Tech. Pub., USA, 1987.
5. Koçak, T., Ü., Yanar, H., Pürçek, G. ve Birol, F., Bir Nikel Aluminyum Bronzu (CuAl10Ni5Fe4) İle Kalay Bronzunun (CuSn11) Sürtünme Ve Aşınma Özellikleri Açısından Karşılaştırılması, 2. Uluslar arası Demir Çelik Sempozyumu (IISS'15), 1-3 Nisan 2014, Karabük, Türkiye.
6. Usta, G., Su Jeti Soğutmalı Döner Disk Atomizasyonu Yöntemiyle Hızlı Katılaştırılmış Bronz Alaşımı Toz ve Şeriti Üretiminin İncelenmesi, Yüksek Lisans Tezi, K.T.Ü., Fen Bilimleri Enstitüsü, Trabzon, 2009.
7. Dawson, R., J., C., Aluminum bronze [J]. Engineering Materials and Design, 22,12 (1978) 25-28.
8. Callcut V., A., Aluminum bronze for industrial use [J], Metals and Materials, 5,3 (1989) 128-132.
9. Li, W., S., Wang, Z., P., Lu, Y., Jin, Y., H., Yuan, L., H. ve Wang F., Mechanical and trihological properties of a novel aluminum bronze material for drawing dies [J]., Wear, 261,2 (2006) 155-163.
10. Tuthill, A., H., Guidelines for the use of copper alloys in seawater [J]. Materials Performance, 26,9 (1987) 12-22.

11. Barabash, V., Pokrovsky, A. ve Fabritsiev, S., The effect of low-dose neutron irradiation on mechanical properties, electrical resistivity and fracture of NiAl bronze for lTER [J]. Journal of Nuclear Materials, 367,370 (2007) 1305-1311.
12. Wood R., J., K., Erosion-corrosion interactions and their effect on marine and offshore materials [J]., Wear, 261 (2006) 1012-1023.
13. Li, W., S., Wang Z., P,, Lu Y., Gao, Y. ve Xu J. L., Preparation, mechanical properties and wear behavior of a novel aluminum bronze for dies [J]., Transaction of Nonferrous Metals Society of China, 16,3 (2006) 607-612.
14. Tan, Z., H., Guo, Zhai, W., K. ve Zhao Z., P., Tribological Characteristics Of Nickel-Aluminium Bronze CuAl10Ni5Fe4 Against 30CrMnSiA Steel After The Prior Corrosion Treatment, Applied Mechanics and Materials Vols. 201,202 (2012) 73-77.
15. Thapliyal, T. ve Dwivedi, D., K., Study of the effect of friction stir processing of the sliding wear behavior of cast NiAl bronze: A statistical analysis, Tribology International, 97 (2016) 124-135.
16. Okolo, B., Kienzler, A., Rothkirch, A., Schulze1, V., Wanner, A., ve Löhe, D., Study of the phase composition and residual stress state in cast nickel aluminium bronze alloy, 1Institute of Materials Science and Engineering, University of Karlsruhe, Germany.
17. Lv, Y., Wang, L., Xu, X. ve Lu, W., Effect of Post Heat Treatment on the Microstructure and Microhardness of Friction Stir Processed NiAl Bronze (NAB) Alloy, Metals, 5 (2015) 1695-1703.
18. German, R. M., Toz Metaluıjisi ve Parçacıklı Malzeme İşlemleri, ed: Sarıtaş, S., Türker, M. ve Durlu, N., Birinci Basım, Türk Toz Metalürjisi Derneği Yayınları:05, Ankara, 2007.
19. Özyürek, D., Tekel, S. ve Yılmaz, R., Cu-Al-Ni Alasımlarında Yaşlanmanın Aşınma Davranışı ve Elektrik İletkenliğine Etkisi, 5. Uluslararası İleri Teknolojiler Sempozyumu, 2009, Karabük, Türkiye.
20. Koçak, T., Ü., Yanar, H., Pürçek, G. ve Birol, F., Bir Nikel Aluminyum Bronzu (CuAl10Ni5Fe4) İle Kalay Bronzunun (CuSn11) Sürtünme Ve Aşınma Özellikleri Açısından Karşılaştırılması, 2. Uluslar arası Demir Çelik Sempozyumu (IISS'15), 1-3 Nisan 2014, Karabük, Türkiye.

NUMERICAL INVESTIGATION OF T6 HEAT TREATMENT FOR A7075 HOT FORGING AND EXPERIMENTAL VERIFICATION

GORKEM TOK *1, MUSTAFA BAKKAL 2

[1] Birinci Otomotiv, 41420, Kocaeli Turkey
[2] Istanbul Technical University, Mechanical Engineering Faculty, 34437, Istanbul, Turkey

Abstract

7xxx series aluminum alloys contain 4-8% Zn and 1-3% Mg and are ideal materials for aircraft, aerospace, defense and automotive industries since they have higher hardness and strength compared to other aluminum alloys. High hardness and strength values in heat treatable 2XXX, 6XXX, 7XXX and 9XXX series aluminum alloys are obtained by precipitation hardening heat treatment consisting of solution, quenching and aging processes, respectively. In this study, it is aimed to model the T6 heat treatment, which will be applied to increase the mechanical properties of the A7075 alloy after hot forging, with the finite element method, to predict the physical experiments to be carried out later. In order to verify the numerical model, results were compared with hardness and tensile test result. In the numerical model, the specimen was modeled in each T6 heat treatment steps and these simulation was performed with Q form UK 10.2.1 in 3D. According to the results of the numerical model, the average hardness value was 199. 789 HB and the tensile strength was 609,319 Mpa, while the experimental data were found to be 189,7 HB and 605,406 Mpa on average.

Keywords: A7075, hot forging, heat treatment, finite element model, experimental verification, closed die, aging, hardness, UTS

1. Introduction

Since aluminum and its alloys have many excellent properties such as low density, good corrosion resistance, machinability, electrical conduction compared to other materials, they are widely used in the aerospace, defense and automotive industries. As seen in Figure 1, high strength light metals are required to be used in the aerospace, defense and automotive industries and some examples are given. 7xxx series aluminum alloys contain 4-8% Zn and 1-3% Mg and are ideal materials for aircraft, aerospace and automotive industries since they have higher hardness and strength compared to other aluminum alloys. [1]

Figure 1: Aluminum Alloy Parts Which are Used in Automotive Industry.

High hardness and strength values in heat treatable 2XXX, 6XXX, 7XXX and 9XXX series aluminum alloys are obtained by precipitation hardening heat treatment consisting of solution, quenching and aging processes, respectively. [7] In this study, it is aimed to model the T6 heat treatment, which will be applied to increase the mechanical properties of the A7075 alloy after hot forging, with the finite element method. Also it is aimed to predict the physical experiments to be carried out later and verify the established numerical model with the physical test results.

2. Materials and Methods

2.1 FEM analysis of the Closed Die Hot Forging

Forging is a plastic deformation process. In forging, the simple billet geometry is transformed into a complex geometry by applying the necessary pressure to the material with the help of forging machines such as hammers and presses.[4] Residual stresses occur on the surface and internal structure of the part due to deformation and thermal gradients that occur during the forming process.[6] Residual stresses in hot forging seriously reduce machining accuracy and stability of parts.[9] This is the main cause of deformation during subsequent machining. Therefore, in this study, in order to model the heat treatment with finite element analysis, the hot forging process should be modeled with the finite element method firstly.

2.1.1 Billet and Material Characterization

Q form has a material database containing chemical composition, physical and mechanical properties of certain metals such as aluminum, copper, magnesium, steel, tool steel. The chemical composition given in the database for 7075 aluminum alloy are shown in Figure 2. As seen in Figure 3, yield stress-strain curves of A7075 alloy, yield stress in the QFORM material database are defined as a function of three variables as in equation (1); strain, deformation rate and temperature:

$$\sigma_s = f(\varepsilon, \dot{\varepsilon}, T) \qquad (1)$$

7075	Cu %	Mg %	Mn %	Si %	Fe %	Cr %	Zn %	Ti %
	1.2-2.0	2.1-2.9	Max. 0.3	Max. 0.4	Max. 0.5	0.18-0.28	5.1-6.1	Max. 0.2

Figure 2: The Chemical Composition of the A7075

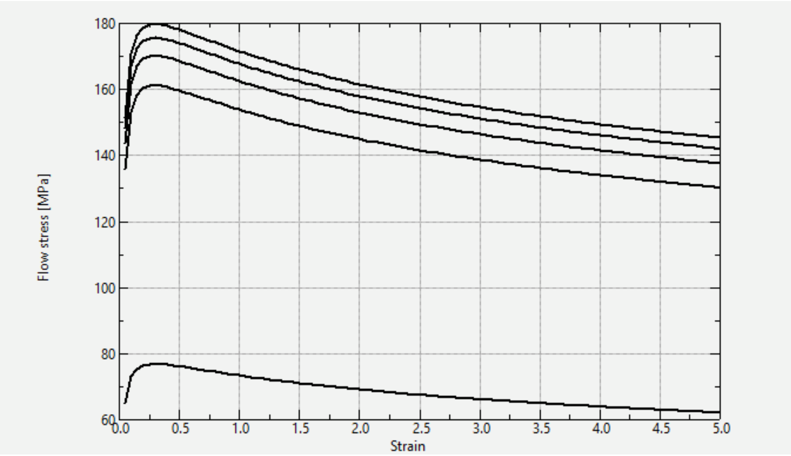

Figure 3: The Flow Stress-Strain Graph of the A7075 in 350°C

The mold material to be used in finite element analysis and experiments is DIN 1.2243. It is a standard hot work tool steel with high thermal conductivity and wear resistance. This steel, which has high impact resistance, can be improved by applying nitration process. Mold material, mold temperature, press bench properties are defined as specified in the boundary conditions.

2.1.2 Boundary Conditions

When modeling with the finite element method, the boundary conditions of the result to be calculated must be defined. When performing hot forging analysis, important boundary conditions such as forging temperature, friction model, and press selection must be defined. Two friction models, Levanov and Siebel, are defined in the Q form. It is stated that A.N.Levanov's friction model is a special case [11, 12]. In addition, when Pavel Petrova's work is examined, it is seen that the Levanov friction model specified in equation 2 and Siebel Prandtl's friction model were compared, and it was stated that Levanov's friction model was successful in modeling the friction between the work piece and mold except in extreme cases. The friction factor coefficient (m) is defined as 0.5, since a mixture of water and graphite is sprayed into the preform and final shape chambers in the forging die in order to prevent sticking and reduce friction during the forging operation. [21]

A.N.Levanov's friction model;

$$\frac{\tau_k}{\tau_{max}} = m\left(1 - \exp\left(-1.25\frac{q}{\sigma_0}\right)\right) \tag{2}$$

In Levanov friction model, $\frac{q}{\sigma_0}$ represents (contact pressure / equivalent yield stress, m represents friction factor coefficient, $\frac{\tau_k}{\tau_{max}}$ normalized friction stress. [21] Obtaining and maintaining suitable preheat metal temperatures in forging aluminum alloys, is a critical process variable which is vital to the success of the machining process. For other alloys that are more difficult to forge, such as the 2xxx and 7xxx series, the change in flow stress associated with the change in work piece temperature is even greater. The main reason aluminum alloys are more difficult to forge is to maintain relatively narrow forging temperature ranges [7] As in Figure 4, the temperature of the work piece is defined as 380°C, in line with the information obtained from the literature and the industrial experience of companies that perform hot forging operations such as Birinci.
In addition to the dies used in forging, forging presses are an important element for forging part production. Mechanical presses are capable of producing a wide variety of forgings. Considering the contact time between the work piece and the mold, mechanical presses are slower than hammers [13]. In this study, a 3150 ton SMERAL LZK3150 crankshaft press, which is called Maxi press in the industry, will be used. In the finite element analysis, the characteristics of the crankshaft press are defined in Q form.

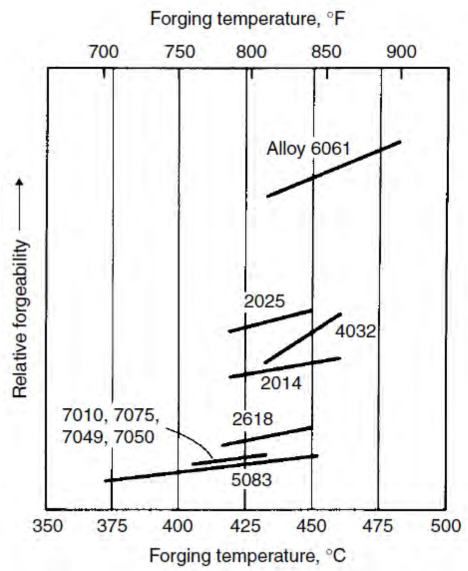

Aluminum alloy	Forging temperature range	
	°C	°F
1100	315–370	600–700
2014	420–460	785–860
2025	420–450	785–840
2219	425–470	800–880
2618	410–455	770–850
3003	315–370	600–700
4032	415–460	780–860
5083	405–460	760–860
6061	430–480	810–900
6069	440–490	825–915
6556	440–490	825–915
7010	370–445	700–830
7033	380–440	720–820
7039	380–440	720–820
7040	360–440	680–820
7049	360–440	680–820
7050	360–440	680–820
7068	380–440	720–820
7075	380–440	720–820
7175	380–440	720–820
7085	360–440	680–820

Figure 4: Forgeability Graph and Forging Temperature Range Table of Aluminum Alloys

As the final boundary condition, the desired amount of burr thickness is defined as the die stop condition. In this study, the burr thickness of the final shape was defined as 5 mm in the last blow.

2.1.3 Analysis of the Closed Die Hot Forging Model

After importing the 3D CAD model and defining boundary conditions and mold stopping conditions, 3 strokes are defined as in Qform as pre-forming, pre-forging and final shaping. Mesh element dimensions of the work piece and molds are defined as maximum 5 mm. When we examine the analysis result, the total number of meshes in the work piece is 572,314.

Figure 5: Numerical result of the Hot Forging

Upon completion of the forging analysis, filling success, burr geometry and burr thickness of the pre-forging and forging blows were examined. Last stage was shown in figure 5. Molds are successfully filled in both pre-forging and forging stages. Although not shown here, the results were simulated step by step and the lap formation of the preform and forging stages was also examined and no lap formation was found on the work piece during the analysis.

2.2 FEM analysis of the T6 Heat Treatment

After the forging processes are completed, the final mechanical properties of the forging (hardness, yield strength, tensile strength, toughness, etc.) are provided by heat treatment.[5] The 2XXX, 6XXX and 7XXX series aluminum alloys are heat treated to achieve the highest mechanical properties. These alloys are somewhat strengthened during forging as they reduce grain size by hot forging. Then, appropriate mechanical properties of the part are developed by heat treatment. After forging, the materials are subjected to solution heat treatment at a temperature just below the solidification temperature, then cooled with water and artificially aged above room temperature for several hours. It has long been known that heat treatment of precipitation hardened aluminum alloys produces high residual stresses [2]. Therefore, in this study, the results obtained by the forging analysis will be linked to the heat treatment analysis and modeled with the finite element method in the Q form program to predict the mechanical properties after heat treatment.

2.2.1 Billet Thermal Characterization

After the part is forged, it undergoes a series of heat treatments to improve its microstructure and material properties (e.g. toughness, strength, creep, fatigue) [6]. In T6 heat treatment modeling, in order to obtain a realistic result, first of all, the part is cooled a little after forging and hot burr cutting is performed, and then it is completely cooled at room temperature. In order to apply T6 heat treatment to the cooled work piece, solution taking, quenching and aging processes are performed respectively as indicated in the temperature time graph in Figure 6.

For precipitation hardening, an alloy with a suitable chemical composition is heated to (α) T1 temperature in order to obtain a single-phase structure and left until all phases in the alloy dissolve in a single phase. Then, it is aged by cooling in water. In precipitation hardening, the diffusion mechanism works in the dissolution and collapse of the atoms forming the precipitate phases. Therefore, temperature and time, which are diffusion parameters, are important factors in precipitation hardening of aluminum alloys [14]. The diffusion conversion mechanism is defined by the Johnson Mehl–Avrami–Koglomorov (JMAK) equation as in equation 3 [15, 16, 17].

$$\xi_{SL} = 1 - \exp(-b \cdot t^{n}) \tag{3}$$

ξ_{SL} is the volume ratio and describes the amount of solution at a given temperature, t is time, b and n are temperature functions. The evolution of this phase transformation can be estimated through an approximate solution using data from Time-Temperature-Transformation diagrams (TTT). The Johnson–Mehl–Avrami equation is valid only for isothermal transformations. In order to calculate the phase transformations by JMA equation and TTT curve, cooling curves are regarded as a series of small isothermal time steps connected by instantaneous temperature changes following constant volume fraction lines. The transformed volume fractions are then calculated isothermally during each time step. For every phase transformation is assumed to occur between certain temperature limits. [15, 16] The amount of dissolved alloy calculated with the help of TTT curve and JMAK equation and the corresponding mechanical strength properties are calculated in Q form with the help of equation 4.

$$d\sigma = d\xi_{SL}(\sigma_{min} - \sigma_{max}) \quad (4)$$

σ_{min} is the tensile strength (UTS) value in T0 phase, σ_{max} is the tensile strength value in T6 phase. These two value can be a coefficient or a function of time. In this study, σ_{min} =230 Mpa. and σ_{max} =610 Mpa.

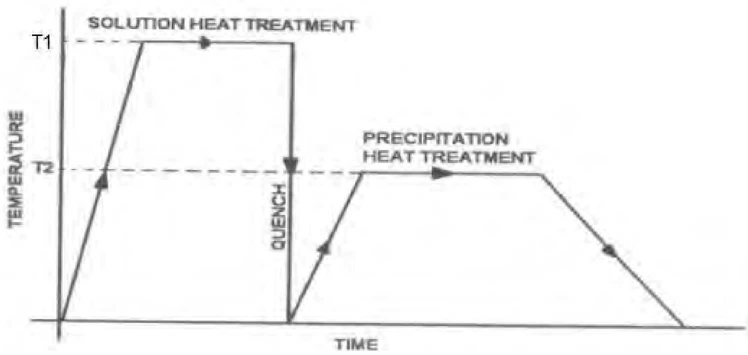

Figure 6. T6 Heat Treatment graph of the Aluminum Alloys

Before applying T6 heat treatment to the trimmed work piece, the T6 phase of the material must be introduced to the Q form for the T6 heat treatment steps. The Time-Temperature-Transformation (TTT) Table, which is in the Q form's library and required for the modeling of the phase transformation, was used.

2.2.2 Analysis of the Heat Treatment Model

After the material characterization is introduced to the Q form, the T6 heat treatment steps are modeled in the order shown in Figure 6 as follows;

Step 1: Heating to a solution heat treatment temperature

An alloy with a structure that dissolves in any ratio in the liquid state and partially in the solid state is heated up to the temperature T1 above the solvus temperature indicated in the phase diagram of the alloy, as shown in Figure 6, in order to obtain a single-phase structure (α), and at this temperature all the components in the alloy are heated. It is left until the phases (α and β) are dissolved in a single phase. In this study, the solution temperature was determined as 480°C. [2, 18, 19, 20]

Step 2: Keeping it at solution temperature for a certain time depending on the profile thickness.

Holding time is also very important. The holding time varies depending on the temperature at which the solution temperature, the annealing method, the type of material and similar factors.

Prolonged holding time causes grain growth, increased diffusion, and color change. Depending on the type of alloy, the holding time starts from 10 minutes for thin pieces and up to 12 hours for thick pieces. For thick parts, a waiting time of 1 hour is accepted for every 1.5 cm of thickness in the section. Since the thickness of the part to be used in this study is 27mm, it will be kept at 480 °C for 2 hours. [18]

Step 3: Rapid cooling in water or polymer glycol solution.

Quenching is done by rapidly cooling the single-phase α solid solution obtained by solution heat treatment from a certain temperature T1 as seen in figure 6, not allowing precipitates to occur. Hardenable alloys are unstable after quenching. Particles that cannot be seen even under the microscope in the precipitation process block the dislocations, also create irregularities in the structure and grain boundaries, and consequently increase the strength of the alloy. In this study, water cooling at room temperature was performed.

Step 4: Waiting for precipitation hardening at room temperature (natural aging) or a suitable temperature (artificial aging).

The last step of the precipitation hardening process, which is applied to obtain high mechanical properties to aluminum alloys that can be hardened by heat treatment, is the aging heat treatment. Artificial aging is carried out by heating the alloy to a temperature determined after the quenching process, taking into account its chemical composition and desired mechanical properties, and cooling it to room temperature in air after it is kept at this temperature for a certain period of time. The applied temperature and time are very important in providing the expected mechanical properties in the aging process. [8] In this study, artificial aging will be done at 120°C for 24 hours, and then it will be stayed to cool automatically at room temperature.

After T6 heat treatment steps were modeled in Q form, when the analysis step size was defined as 0.5 sec in forging analysis and 50 sec in heat treatment analysis. As in forging analysis, mesh element size is defined as maximum 5 mm in heat treatment analysis. When the analysis result was examined, the total number of meshes in the work piece calculated as 572,314. As seen in Figure 7, the hardness values after the heat treatment were calculated as an average of 199.789 HB average tensile strength value of 609,319 Mpa. As a result of the analysis, the most important factor in the hardness of the alloy was determined as the cooling rate and temperature.

3. Results and Discussion

At the end of the numerical and experimental study, mold filling success, burr geometry and burr thickness were investigated. As a result of the forging test performed with the parameters determined in the previous sections, unfilled sections was not observed on the part in both numerical and experimental studies, and the burr geometry is similar in both numerical and experimental studies. While the burr thickness is 5.07 mm in the numerical study, the burr thickness is 5.2 mm as a result of the experimental study. After forging, the geometric dimensions of the work piece are within the forging tolerances determined according to the EN10243 standard. After forging analyzes were confirmed by experimental results, T6 heat treatment was carried out experimentally. Hardness Measurements were done by 3 points and results are given in table 1. BMS 3000-OBC Brinell hardness measuring machine was used for hardness measurement and 3 kg load was applied. Besides, after the hardness measurement, Tensile Test were done and results were given in Table 2. Universal Tensile Test Machine with 1000 KN capacity was used for tensile test.

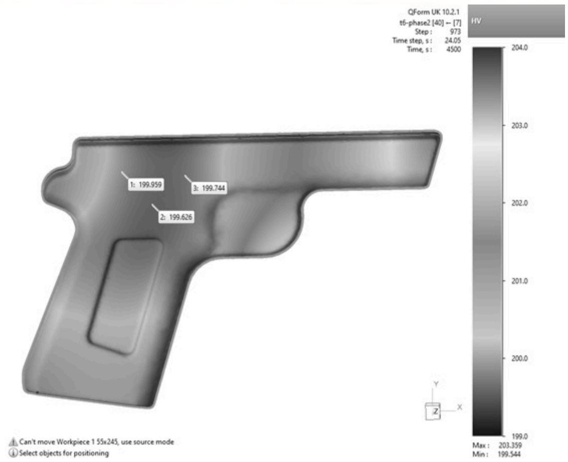

(a)

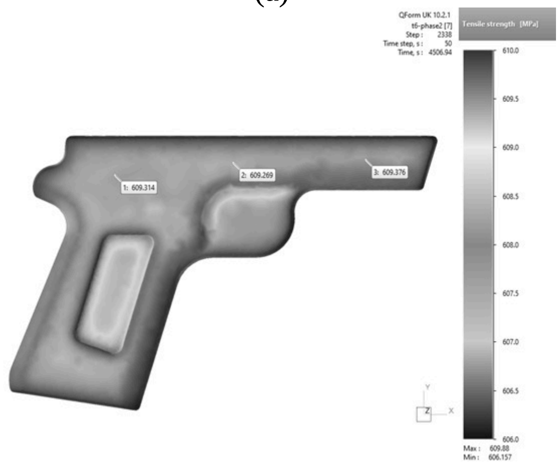

(b)

Figure 7. T6 Heat Treatment Results (a) Hardness (b) Tensile Strength

Table 1. Hardness measurement after T6 Heat Treatment. (Experimental)

Work piece (#)	**Hardness Measurement** 1 (HB)	**Hardness Measurement** 2 (HB)	**Hardness Measurement** 3 (HB)	**Average Hardness Measurement** (HB)	**Numerical Hardness Measurement** (HB)
1	187.8	189.2	186.5	187.8	199.789
2	192,2	192,6	189,9	191,6	

Table 2. Ultimate Tensile Strength (UTS) results after T6 Heat Treatment. (Experimental)

Work piece (#)	**Experimental UTS Measurement** (Mpa)	**Numerical UTS Measurement** (Mpa)
1	598,213	609,319
2	612,581	

4. Conclusions

In this study, closed die hot forging operation and T6 heat treatment operations for A7075 aluminum alloys, were successfully modeled with FEM. When the numerical and experimental results are compared, it is seen that the hardness value and tensile strength values were estimated correctly with a 5% margin of error. After conducting finite element modeling and simulation of hot forging and T6 heat treatment of A7075 aluminum and comparing the results with experimental data, the following conclusions can be drawn:

Forging Temperature of the A7075: 380°C
Friction Rule: Levanov
Coefficient of Friction Factor (m):0.5
Levanov Coefficient: 1,25

- Chemical and material properties of the A7075 was successfully modeled.
- In order to obtain final shape in forging, preforming and pre forging step was successfully modeled.
- Levanov Friction model was used and was successful in modeling the closed die hot forging.
- The Mehl–Avrami–Kolmogorov (JMAK) equation was used and was successful in modeling the T6 heat treatment.

5. References

[1] Yilmaz, Ramazan, Dursun Özyürek, and Erkan KİBAR. "Yeniden çözeltiye alma parametrelerinin 7075 alüminyum alaşimlarinin sertlik ve aşinma davranişlarina etkisi." Gazi Üniversitesi Mühendislik Mimarlık Fakültesi Dergisi 27.2 (2012).

[2] Robinson, Jeremy S., et al. "Residual stress relief in the aluminium alloy 7075." Materials Science and Technology 33.15 (2017): 1765-1775.

[3] DEMİREL, Mehmet Yasin, and İbrahim KARAAĞAÇ. "7075-T6 alaşımının mikroyapı ve mekanik özelliklerine tavlama işleminin etkisinin deneysel olarak araştırılması." Politeknik Dergisi (2019).

[4] Sagara, M. Vidya, and A. Chennakesava Reddyb. "Finite volume analysis of two-stage forging process for aluminium 7075 alloy." International Conference on Advanced Materials and manufacturing Technologies (AMMT). 2014.

[5] Biba, Nikolay, et al. "The implementation of microstructural and heat treatment models to development of forming technology of critical aluminum-alloy parts." AIP Conference Proceedings. Vol. 1960. No. 1. AIP Publishing LLC, 2018.

[6] Srivatsa, Shesh K., and G. E. Aviation. "Modeling of Residual Stress and Machining Distortion in Aerospace Components." Cdn. intechopen. com. (2010).

[7] Kuhlman, G. W. "Forging of aluminum alloys." (2013).

[8] Koç, Funda Gül. "AA7075 alüminyum alaşımına ısıl işlem parametrelerinin endüstriyel koşullarda optimizasyonu." (2019).

[9] Groover, Mikell P. Fundamentals of modern manufacturing: materials, processes, and systems. John Wiley & Sons, 2020.

[10] Özcan, Mehmet Cihat. Thermo-mechanically coupled numerical and experimental study on 7075 aluminum forging process and dies. MS thesis. Middle East Technical University, 2008.

[11] Petrov, Pavel, et al. "Finite-element modelling of forging with torsion: Investigation of heat effect." Procedia Manufacturing 47 (2020): 274-281.

[12] Vianello, Pedro Ivo, et al. "Thermal fatigue analysis of hot forging closed dies." Materials Research 23 (2020).

[13] Makas T. “general overview on hot forging” (2016)

[14] ESER, A. Asım, et al. "ALÜMİNYUM İŞLEM ALAŞIMLARININ T6 ISIL İŞLEMİNDE YAŞLANDIRMA SICAKLIK VE SÜRELERİNİN İNCELENMESİ."
[15] Biba, Nikolay, et al. "The implementation of microstructural and heat treatment models to development of forming technology of critical aluminum-alloy parts." AIP Conference Proceedings. Vol. 1960. No. 1. AIP Publishing LLC, 2018.
[16] Huiping, Li, et al. "FEM simulation of quenching process and experimental verification of simulation results." Materials Science and Engineering: A 452 (2007): 705-714.
[17] Chotěborský, R., and M. Linda. "FEM based numerical simulation for heat treatment of the agricultural tools." Agronomy Research 13.3 (2015): 629-638
[18] Kibar, Erkan. "7075 alüminyum alaşımlarına uygulanan RRA ısıl işlemlerinin mikroyapı ve mekanik özelliklere etkisi." (2010).
[19] Saha, Pradip K. Aluminum extrusion technology. Asm International, 2000.
[20] Demir, Mehmet, Okan Tekin, and Adem Demir. "T6 Yaşlandırma Isıl işlemi Uygulanan Ekstrude AA 7075 Alüminyum Alaşımlarının Mekanik Davranışları." Academic Perspective Procedia 3.1 (2020): 763-771.
[21] Cora, Ömer Necati. Friction analysis in cold forging. MS thesis. Middle East Technical University, 2004.

THE EFFECT OF HA AND BG PARTICLES AIR ABRASIVE BLASTING ON MG-4ZN-0.3CA ALLOY CORROSION RESISTANCE

Hazman Seli[1 *], Nikolaos Silikas[2], Xiaohui Chen[2] and Andrew Thomas[3]

[1]Shool of Chemical Engineering, Universiti Teknologi MARA, 94300 Sarawak, Malaysia
[2]Biomaterials Unit, School of Dentistry, The University of Manchester, Manchester M13 9PL, UK
[3]School of Materials and Photon Science Institute, The University of Manchester, Manchester, M13 9PL, UK
[*]hazmanseli@uitm.edu.my

Abstract

Magnesium based alloys are one group of promising candidates for biodegradable bone implant applications. However, their high rate degradation in human body environment is an obstacle and should be treated. In this study Mg–4Zn–0.3Ca alloy surfaces are blasted with calcium phosphate particles of hydroxyapatite (HA) and bioglass 45S5 (denoted as BG) in order to enhance their corrosion resistance and biocompatibility. Characterization of the blasted surfaces was focused on the microstructure and topography changes. Series of analysis were conducted such as X-ray diffractometer (XRD), scanning electron microscopy (SEM) with energy dispersive X-ray (EDX) and electrochemical measurements using simulated body fluid (SBF) solution. XRD detected mainly the presence of Mg substrate and secondary phase of Ca2Mg6Zn3 with minor embedded calcium phosphate phases on the roughened surface. The SEM results revealed that the deformation of the BG blasted surface is more severe compared to that of HA blasted surface with small portion of impregnated particles. The BG blasted Mg-4Zn-0.3Ca alloy improves the corrosion behaviour due to an increase in the surfaces roughness and partly particles impregnation. In comparison, the BG blasted sample indicates the best corrosion resistance in SBF solution followed by HA blasted and non-blasted samples. This has proven that the calcium phosphate of HA and BG particles air abrasive blasting could enhance the corrosion resistance of the Mg–4Zn–0.3Ca alloy.

Keywords: Mg–4Zn–0.3Ca, alloy, corrosion, blasted

1. Introduction

Magnesium alloys are widely used for structural applications in many structural engineering applications. Despite having high specific strength, magnesium alloys exhibit poor corrosion resistance and do not have a stable passive film for long-term protection from further corrosion. The poor corrosion resistance becomes a major drawback, and many studies have been made on improving this [1-3]. Due to that property, magnesium alloys can be utilized as biomedical temporary implants in corrosive media and act as structural materials in human body where Mg involves in metabolic reactions and physiological mechanisms. Mg ions are imperative to the basic nucleic acid chemistry of living organisms. In comparison to implant materials such as Co, Ti and stainless steel, Mg and its alloys have many advantages such as the low density, low Young's modulus, having almost similar density and elastic modulus of natural bone. Hence, Mg and Mg alloys currently draw the attention to be used as biodegradable implant materials, like cardiovascular or orthopaedic devices [4,5].

Modification on surface of Mg based alloys with biocompatible calcium phosphate coatings in orderto control the corrosion performance might be an effective approach [6,7]. Currently, various calcium phosphates are widely used as bioactive coating for metallic substrates such as Ti alloys [8], stainless steel [9] and Mg alloys [10] especially bioactive glass and hydroxyapatite. They have the major mineral component of human bones and ability to bond chemically with natural bones.

Until now, many attempts have been developed to prepare calcium phosphate coatings on metallic substrates, such as plasma spraying, sol–gel process, electrochemical deposition, biomimetic process, pulsed laser deposition, etc [11–16]. Electrochemical deposition has been receiving more attention for Mg-based implants due to its ease of operation and practicability for coating complex structures [17,18]. Pulsed laser deposition (PLD) technique has also lately shown many successful biomaterials films deposition on metallic substrates[19,20]. The advantages PLD over other techniques are congruent transfer of target composition to coatings, creating good bonding between coating and substrate materials, allowing possibility to control crystallinity and surface roughness. Various target materials could be ablated and almost any substrates could be possibly coated. However this technique is very expensive and needs more safety precautions during coating process.

Apart from coating, changing physical surface of the metallic substrates could possibly improve their corrosion resistance. A long-term interfacial bond between an implant and bone may be improved by creating a rough or porous surface through plastic deformation and micro cutting phenomenon on the implant in order to increase the surface area available for biological bone/implant adhesion [21]. There are many methods to create a rough surface on an implant surface [22]. Air abrasive blasting technique is a simple technique which has ever been attempted to modify surface chemistry of many metals and alloys surfaces. The blasting materials like alumina, zirconia, silica, HA etc. are frequently used as a blasting media. The blasting process applied for the surface properties of titanium based implant materials is widely used in medical applications. Nowadays, zirconia, silica, and HA blasting powders are performed extensively to modify surface topography and improve biocompatibility of the Ti-based implant materials.

In this research, preliminary investigation of the effects of HA and BG particles blastedMg-4Zn-0.3Ca alloy surfaces on their corrosion resistance in simulated body fluids (SBF) is carried out.The calcium phosphate particles air abrasive blasting process is expected to be able to improve the chemical, topographical and biocompatibility characteristics of the magnesium alloys in order to enable the temporal growth of the bone in body fluid.

2. Materials and methods

The experiments were carried out on Mg–4Zn–0.3Ca The Mg–6 wt.% Zn alloy described in Ref. [23] and cut in the form of 1.0 cm X 1.0cm squares of 0.3 cm thickness. Polished surfaces were prepared by abrading the sample surfaces with successively finer silicon carbide papers and then mechanically polishing with1 m diamond paste to a mirror-like finish. The samples were washed in running water and ultrasonically cleaned with distilled water. The samples finely blasted with HA and BG particles with mean sizes of 32 µm and 7.6 µm respectively. The blasted samples were characterized by series of analysis such as scanning electron microscopy (SEM) with energy dispersive X-ray (EDX) and X-ray diffractiometry (XRD). The corrosion resistance of the samples was assessed by electrochemical measurements with pH 7.4 at 310K open to air. The SBF solution was made of 750mL deionized water, 7.996gNaCl, 0.224gKCl, 0.35g NaHCO3, 0.278g CaCl2, 0.228gK2HPO4.3H2O, 0.071gNa2SO4, 0.305g MgCl2.3H2O and 40cm3 1 kmol/m3HCl. The measurements were conducted in a three-electrode cell using a platinum counter electrode and an Ag/AgCl reference electrode. Potentiodynamic polarization curves were measured with a potential sweep rate of 1 mV/s.The samples were also immersed in the SBF solution for 2 hours and 5 hours to preliminary observe the corrosion products development in order to estimate their degradation rates.

3. Results and discussion

Generally, the blasting is based on the mechanical effects generated at the impact of hard particles with metallic surface. The abrasive particles are directed to the substrate surface by means of air jet. As a result, the blasting impact generates surface plastic deformation, microcutting and micro cracking phenomenon.

XRD analysis

X-ray diffraction pattern, exhibited in Fig. 1, indicates that the HA blasted Mg-4.0Zn-0.3Ca alloys microstructure consists of major α-Mg phase and minor phases of MgZn and Ca2Mg6Zn3 from the base alloy as well as have ever been reported [23]. A small contribution of calcium phosphate phases from the remaining blasted particles was also detected. Oxide layer of the alloy could not be detected because of severe surface deformation and impregnation of the blasting. Normally most Mg alloy is covered with thin oxide layer (MgO) that helps protecting the metal from attack by air.

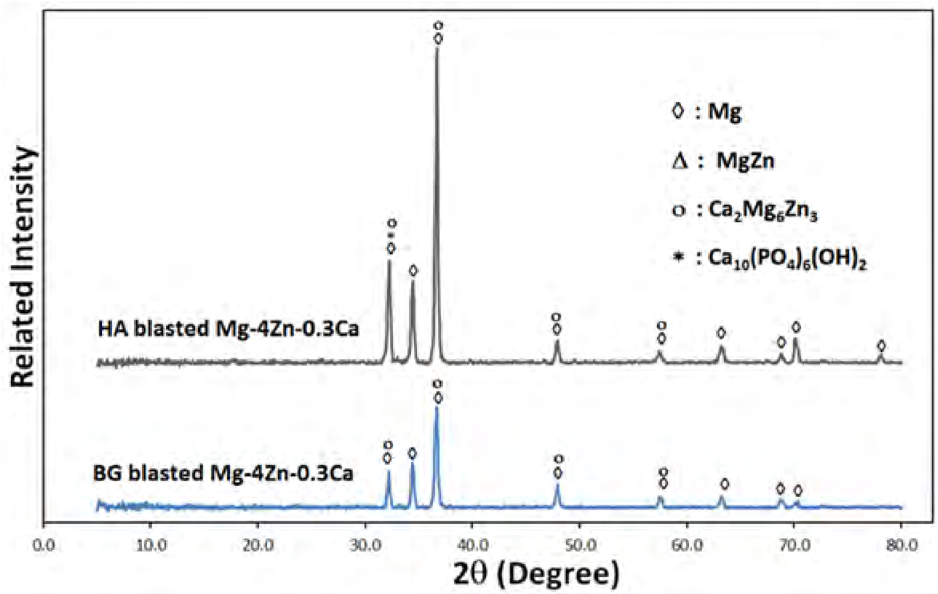

Fig. 1. X-ray diffraction pattern of the HA and BG blasted Mg-4Zn-0.3Ca surface alloy.

But this thin layer is not strong enough to protect the Mg alloy from corrosive body fluids. Typically the surface layer is unstable and breaks away because the crystalline lattice is easily cleaved. The layers have a thickness of some nanometres [24–26]. The structure of this layer was studied by Santamaria et al. [25] in detail using X-ray photoelectron spectroscopy (XPS) and photocurrent spectroscopy (PCS), which indicated that the layer consists of an inner MgO layer of 2.5 nm and an outer Mg(OH)2 layer of 2.2 nm. Seyeux et al. [26] found indications of the existence of MgH2 within this layer.

SEM and EDS analysis

The SEM micrographs of the HA and BG blasted Mg–4Zn–0.3Ca alloy surfaces are shown in Fig. 2(a,b and c) in different magnifications. Fig. 2a shows SEM image of plain grey area of the alloy original surface where the closed up view indicates grain boundary features of the alloy. Whereas for the blasted samples, the SEM analysis reveals an irregular rough typical biphasic structure consisting of bright areas (blasted particles) in a dark matrix (Mg-4Zn-0.3Ca) resulting from the blasting process. As seen in Fig. 2b the HA particles distorted surface structure, were broken and partly stained on it which could act as the corrosion barrier. A closer observation at higher magnification of the HA blasted sample shows the presence stained spots and small broken particles. Fig. 2c shows white BG particles distribution on the BG blasted surface. The higher magnification reveals plastic deformation, microcutting, micro cracking and free broken particles on the BG blasted surface.

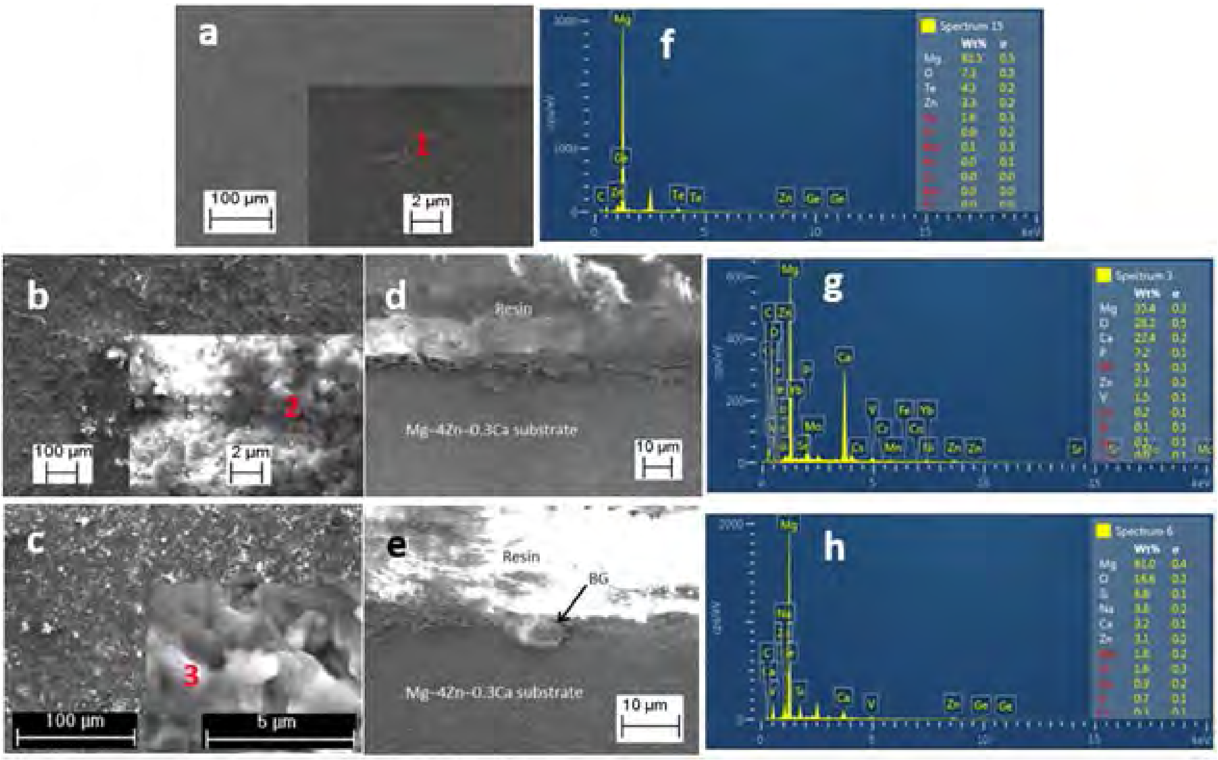

Fig. 2. SEM images of the surface of (a) non-blasted, (b) HA blasted and (c) BG blasted samples. Cross sectional SEM images of (d) HA blasted and(e) BG blasted samples. EDS analysis of (f) point 1, (g) point 2 and point 3.

By comparing the topographical features of the blasted surfaces, BG particles seem to be harder. Fig. 2d and 2ecompares the cross-section micrographs of the two blasted surfaces. It is clearly seen that the BG blasted sample indicates rougher surface with embedded particles compared to that of HA blasted sample. This implies that BG particles are harder than HA particles. Due to that more BG particles embedded on the alloy surface as well as increase the corrosion resistance to the alloy. It is expected that the presence of embedded particles could enhance the in vitro corrosion behaviour.

Apart from improving biological bone/implant adhesion, the stained and embedded HA and BG particles on the alloy surface could also be the main contribution to the corrosion resistance of the magnesium alloy. In summary, BG blasting gives more severe roughing surface compared to that of HA blasting. In order to reveal the chemical composition of the blasted surfaces, EDS was used to analyze the chemical composition and the results are shown in Fig. 2(f, g and h). From the analysis results, it could be figured out that then on-blasted sample (Fig2f) is rich in magnesium, oxygen and a small amount of oxygen, tellurium and zinc, indicating Mg(OH)2 film containing phosphorus tellurium and zinc forms on the surface. Fig. 2g shows that the HA blasted sample has the presence of high magnesium content with minor elements of particularly oxygen, calcium, sodium and phosphorous. Whereas the magnesium content with minor elements of oxygen, zinc, sodium and calcium are detected in the BG blasted surface (Fig. 2h). This implies that the blasting process has slightly altered the chemical composition of the alloy surface and enhances the alloy corrosion resistance.

Corrosion behavior

Potentiodynamic polarization behaviour of Mg–4.0Zn–0.3Ca alloy was depicted in Fig. 3. The non-blasted alloy exhibited a corrosion current density of 4.105 × 10−4 A cm−2with an associated corrosion potential of −1678 mV. Compared to non-blasted sample, the corrosion potential of the HA and BG blasted samples were much more positive, shifting to −1579 mV and −1358 mV respectively.

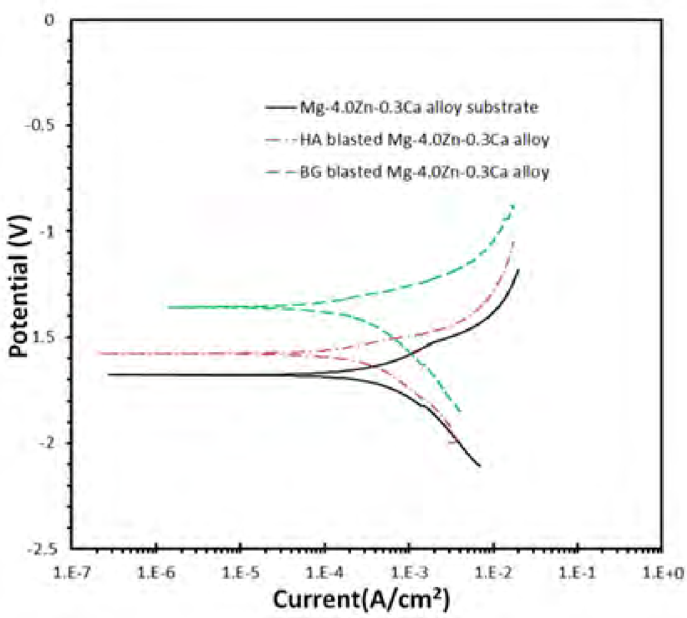

Fig. 3. The potentiodynamic polarization curves of Mg–4.0Zn–0.3Ca alloys in SBF solution.

It was noted that the corrosion current density of the HA and BG blasted samples were slightly less than that of the non-blasted one, suggesting their higher resistance and much less corrosion rate. By comparison, the BG blasted sample has a highest corrosion resistance, followed by HA blasted and non-blasted samples which implies that the blasting and type of blasting particles influence the corrosion behaviour. This has proven that HA and BG particles blasting has tendency to reduce the corrosion rate of the Mg–4Zn–0.3Ca alloy after the air abrasive blasting process.

4. Conclusions

Calcium phosphate of HA and BG blasted Mg–4Zn–0.3Ca surfaces were successfully prepared by means of air abrasive blasting. The results obtained provide a good correspondence between morphological and electrochemical data for calcium phosphate blasted Mg–4Zn–0.3Ca surfaces. By comparison, the BG blasted sample has the highest corrosion resistance, followed by HA blasted and non-blasted samples which implies that the type and hardness of blasting particles influence the topography features and corrosion behaviour as well. It was confirmed that surface modification using air abrasive blasting technique could retard corrosion of Mg–4Zn–0.3Ca alloys.

Acknowledgements

The authors gratefully acknowledge the financial support of this work by the Universiti Teknologi MARA (UiTM), The University of Manchester UK and Ministry of Higher Education, Malaysia.

References

[1] G. Song, Recent Progress in Corrosion and Protection of Magnesium Alloys, Adv. Eng. Mater. 7 (2005) 563-586.
[2] J. E. Gray, B. Luan, Protective coatings on magnesium and its alloys — a critical review, J. Alloys Comp. (2002) 336-388.
[3] G. Song, A. Atrens, Corrosion Mechanisms of Magnesium Alloys, Adv. Eng. Mater. 1 (1999)11-33.
[4] F. Witte, V. Kaese, H. Switzer, A.M. Lindenberg, C.J. Wirth, H.Windhag, In vivo corrosion of four magnesium alloys and the associated bone response, Biomaterials 26 (2005) 3557-3563.
[5] F. Witte, J. Fischer, J. Nellesen, H. Crostack, V. Kaese, A.Pisch, F.Beckmanne, H.Windhagena, In vitro and in vivo corrosion measurements of magnesium alloys, Biomaterials 27 (2006) 1013–1018.
[6] H. Hornberger, S. Virtanen, A.R. Boccaccini, Biomedical coatings on magnesium alloys – a review, Acta Biomater. 8 (2012) 2442–2455.
[7] G.S. Wu, J.M. Ibrahim, P.K. Chu, Surface design of biodegradable magnesium alloys — a review, Surf. Coat Technol. 233 (2012) 2–12.
[8] A. Bigi, M. Fini, B. Bracci, E. Boanini, P. Torricelli, G. Giavaresi, N.N. Aldini,A. Facchini, F. Sbaiz, R. Giardino, The response of bone to nanocrystalline hydroxyapatite-coated Ti13Nb11Zr alloy in an animal model, Biomaterials 29(2008) 1730–1736.
[9] Q.H. Yuan, T.D. Golden, Electrochemical study of hydroxyapatite coatings on stainless steel substrates, Thin Solid Films 518 (2009) 55–60.
[10] C.L. Wen, S.K. Guan, L. Peng, C.X. Ren, X. Wang, Z.H. Hu, Characterization, degradation behavior of AZ31 alloy surface modified by bone-like hydroxyapatite for implant applications, Appl. Surf. Sci. 255 (2009) 6433–6438.
[11] S. Shadanbaz, G.J. Dias, Calcium phosphate coatings on magnesium alloys for biomedical applications: a review, Acta Biomater. 8 (2012) 20–30.

[12] Y. Huang, Y. Qu, B.C. Yang, W. Li, B. Zhang, X.D. Zhang, In vivo biological responses of plasma sprayed hydroxyapatite coatings with an electric polarized treatment in alkaline solution, Mater. Sci. Eng. C 29 (2009) 2411–2416.
[13] D.G. Wang, C.Z. Chen, T. He, T.Q. Lei, Hydroxyapatite coating on Ti6Al4V alloy by a sol–gel method, J. Mater. Sci.: Mater. Med. 19 (2008) 2281–2286.
[14] Z. Grubaˇc, M. Metikoˇs-Hukovi´c, R. Babi´c, Electrocrystallization, growth and characterization of calcium phosphate ceramics on magnesium alloys, Electrochim. Acta 109 (2013) 694–700.
[15] A. Adawy, W.I. Abdel-Fattah, An efficient biomimetic coating methodology fora prosthetic alloy, Mater. Sci. Eng. C 33 (2013) 1813–1818.
[16] J. V. Rau, I. Antoniac, M.Fosca, A. De Bonis, A. I. Blajan, C. Cotrut, V. Craziani, M. Curcio, A. Cricenti, M. Niculescu, M. Ortenzi, R. Teghil, Glass-ceramic coated Mg-Ca alloys for biomedical implant application, Mater. Sci. Eng. C 64 (2016) 362–369.
[17] M.B. Kannan, Enhancing the performance of calcium phosphate coating on a magnesium alloy for bioimplant applications, Mater. Lett. 76 (2012) 109–112.
[18] H.X. Wang, S.K. Guan, X. Wang, C.X. Ren, L.G. Wang, In vitro degradation and mechanical integrity of Mg–Zn–Ca alloy coated with Ca-deficienthydroxyapatite by the pulse electrodeposition process, ActaBiomater. 6 (2010)1743–1748.
[19] J. V. Rau, I. Cacciotti, A. De Bonis, M. Fosca, V. Komlev, A. Latini, A. Santagata, R. Teghil, Fe-doped hydroxyapatite coatings for orthopaedic and dental implant applications, Appl. Surf. Sci. 307 (2014) 301-305.
[20] J. V. Rau, I. Cacciotti, S. Laureti, M. Fosca, G. Varvaro, A. Latini, Bioactive Nanostructured Si-substituted hydroxyapatite coatings on titanium prepared by pulsed laser deposition, J. Biomed. Mater. Res. B Appl. Biomater. 103(8) (2015)1621–1631.
[21] P. Heinl, L. Müller, C. Körner, R.F. Singer, F.A. Müller, Cellular Ti–6Al–4V structures with interconnected macro porosity for bone implants fabricated by selective electron beam melting, Acta Biomater.4(5) (2008)1536–44.
[22] M. Browne, P.J. Gregson, Effect of mechanical surface pre-treatment on metal ion release, Biomaterials 21 (2000) 385–92.
[23] F.Naghdi, R. Mahmudi, Effect of solution treatment on the microstructural evolution and mechanical properties of an aged Mg–4Zn–0.3Ca alloy, Materials Science & Engineering A 631(2015)144–152.
[24] K. Asami, S. Ono, Quantitative X-ray photoelectron spectroscopy characterization of magnesium oxidized in air, J Electrochem Soc.147(4)(2000)1408–13.
[25] M.Santamaria, F. DiQuarto, S. Zanna, P. Marcus, Initial surface film on magnesium metal: a characterization by X-ray photoelectron spectroscopy (XPS) and photocurrent spectroscopy (PCS), Electrochimica53(3) (2007)1315–25.
[26] A. Seyeux, M. Liu, P. Schmutz, G. Song, A. Atrens, P. Marcus, ToF-SIMS depth profile of the surface film on pure magnesium formed by immersion in pure water and the identification of magnesium hydride,Corros.Sci.51 (2009)1883–6.

CRITICAL SIZES OF AG NANOPARTICLES IN WATER AND ETHYLENE GLYCOL BASED NANOFLUIDS OF VARYING VOLUMETRIC FRACTION AND TEMPERATURE

MAHMUT KAPLAN*[1], MELDA OZDINC CARPINLIOGLU[2]

[1] Gaziantep University, Naci Topçuoglu Vocational School, Department of Machine and Metal Technology, Gaziantep, TÜRKİYE.
[2] Gaziantep University, Faculty of Engineering, Department of Mechanical Engineering, Gaziantep, TURKEY.

Abstract

A case study which is founded on the methodology proposed in the previous papers of the authors is presented. In the conducted case study Ag nanoparticles of d_p = 1-10 nm are used at a φ range of 0.5% -2% in W and EG base fluids at T of 333 K and 363 K. Relative thermal conductivity, k_r and dynamic viscosity, μ_r of Ag-W and Ag-EG nanofluids are calculated. The fitted equations of k_r and μ_r with d_p of Ag-W and Ag-EG nanofluids are compared. The form of the equations is as k_r, $\mu_r = a\ (d_p)^b + c$ where a, b and c equation constant. The fitted equations of $k_r = k_r\ (d_p)$ are such that volumetric fraction is effective in reference to varying magnitudes of a and c. At different T for W based fluid magnitude of b is varying while for EG base fluids magnitude of b is independent of T. The fitted equations of $\mu_r = \mu_r\ (d_p\ )$ are such that volumetric fraction is effective in reference to magnitude of a while T is immaterial on the relationship for both W and EG based fluids in reference to the same magnitudes of b and c. The decrease in d_p is associated with increase in k_r so minimum size of d_p = 1 nm is the optimum one. However drastical increase in μ_r is the disadvantage in terms of pumping power requirement with this minimum size. Therefore d_p = 5 nm can be used as the critical size providing acceptable viscous resistance with acceptable thermal enhancement.

Keyword: Ag Nanoparticle, Ag-W Nanofluid, Ag-EG Nanofluid, Temperature, Critical Size, Optimization

1. Introduction

It seems that size and amount- volumetric fraction of nanoparticles which are added to a base fluid and temperature of the base fluid have an interactive influence on the thermophysical properties of the generated nanofluid [1-3]. The decrease in nanoparticle size which is estimated as 20 nm and the increase in the determined volumetric fraction (φ) range of 1%-5% cause an enhancement of water (W) and ethylene glycol (EG) base fluids' thermophysical properties at temperatures (T) of 298 K and 323 K. In the determined range of φ, the critical – minimum possible size of nanoparticles at high temperatures T> 323 K is open to discussion. The relative thermal conductivity of nanofluids (k_r) is calculated by dividing thermal conductivity of nanofluids by thermal conductivity of base fluids. The relative dynamic viscosity of nanofluids

(μ_r) is calculated by dividing dynamic viscosity of nanofluids by dynamic viscosity of base fluids [4].

The utilized equations in terms of nanoparticle Reynolds Number, Prandtl Number, thermophysical properties of nanoparticle and base fluid, d_p, φ and T are given in Table 1.

Table 1. Equations for calculation of k_r and μ_r.

References	**Equations**
[5-22]	$k_r = \Delta_{k_r}\left(\beta_2\varphi^2 + \beta_1\varphi\right) + \beta_0$ $\Delta_{k_r} = \left(\frac{k_p}{k_{bf}}\right)^{0.78}\left[\ln\left(\frac{k_p}{k_{bf}}\right)^{1.25}\right]\left(\frac{h}{d_p}\right)^{1.12}\left(\frac{T}{T_{ref}}\right)^{13.9}\left(\frac{c_{p_{bf}}}{c_{p_{ref}}}\right)^{5.35} Re^{0.1}Pr^{0.24}$ $Re = \frac{\rho_b u_{Br} d_p}{\mu_{bf}}$, $u_{Br} = \sqrt{\frac{18k_bT}{\pi\rho_p {d_p}^3}}$, $Pr = \frac{c_{p_{bf}}\mu_{bf}}{k_{bf}}$ $\beta_2 = 0.00019$, $\beta_1 = 0.0045$, $\beta_0 = 1.033$ for W based nanofluids $\beta_2 = -0.0008$, $\beta_1 = 0.0716$, $\beta_0 = 1.011$ for EG based nanofluids $\mu_r = \Delta_{\mu_r}\left(\eta_2\varphi^2 + \eta_1\varphi\right) + \eta_0$ $\Delta_{\mu_r} = \left(\frac{\rho_p}{\rho_{bf}}\right)^{2.4}\left(\frac{h}{d_p}\right)^{1.8}\left(\frac{T_{ref}}{T}\right)^{8} Re^{-0.11}$ $\eta_2 = 0.3136$, $\eta_1 = 0.5165$, and $\eta_0 = 1.064$ for W based nanofluids $\eta_2 = 0.1167$, $\eta_1 = 0.4717$, and $\eta_0 = 1.064$ for EG based nanofluids

2. Materials and Methods

In the case study water (W) and ethylene glycol (EG) based nanofluids with spherical nanoparticles of Ag with d_p range of (1 nm -20 nm) are used with φ range of (0.5% -2%) and at T = 333 K and T = 363 K. The range of φ and T is determined based on the experimental study [12] related to k_r and μ_r Ag-W nanofluids (φ = 0.3%-0.9% and T = 323-363 K). The thermophysical properties of Ag nanoparticle and W and EG base fluid (T = 333 K and 363 K) are given in Table 2 and Table 3, respectively.

Table 2. Thermophysical properties of Ag nanoparticle.

Nanoparticle	k_p**(W/m K)**	ρ_p**(kg/m^3)**
Ag [23]	429	10500

In reference to Table 1, the magnitudes of k_r and μ_r are calculated. The calculations are expressed as a function of d_p for φ as the governing parameter at T = 333 K and 363 K. The graphical representations of k_r versus d_p and μ_r versus d_p are given for Ag in W-based and EG based nanofluids at T= 333 K, T= 363 K in Figure 1 and 2, respectively. Due to the values of k_r and μ_r, MATLAB semilogy function is used to plot the logarithmic scale in y axis corresponding to $k_r$and μ_r with a linear scale in x axis corresponding to d_p. In Figure 1 and 2, the fitted equations are calculated for by using the power fit in the least-squares sense using MATLAB Curve Fitting Toolbox.

$$k_r,\ \mu_r = a\left(d_p\right)^b + c \tag{1}$$

where a, b and c are constants.

Table 3. Thermophysical properties of base fluids [24].

Base fluids	k_{bf}(W/m K)	ρ_p(kg/m^3)	μ_{bf}(Pas)	$c_{p_{bf}}$(J/kgK)
W (333 K)	0.6536	983.1	0.00047	4185.2
W (363 K)	0.6758	964.9	0.00031	4206.6
EG (333 K)	0.2603	1087.8	0.00522	2561.9
EG (363 K)	0.2613	1071.8	0.00263	2695.8

3. Results and Discussion

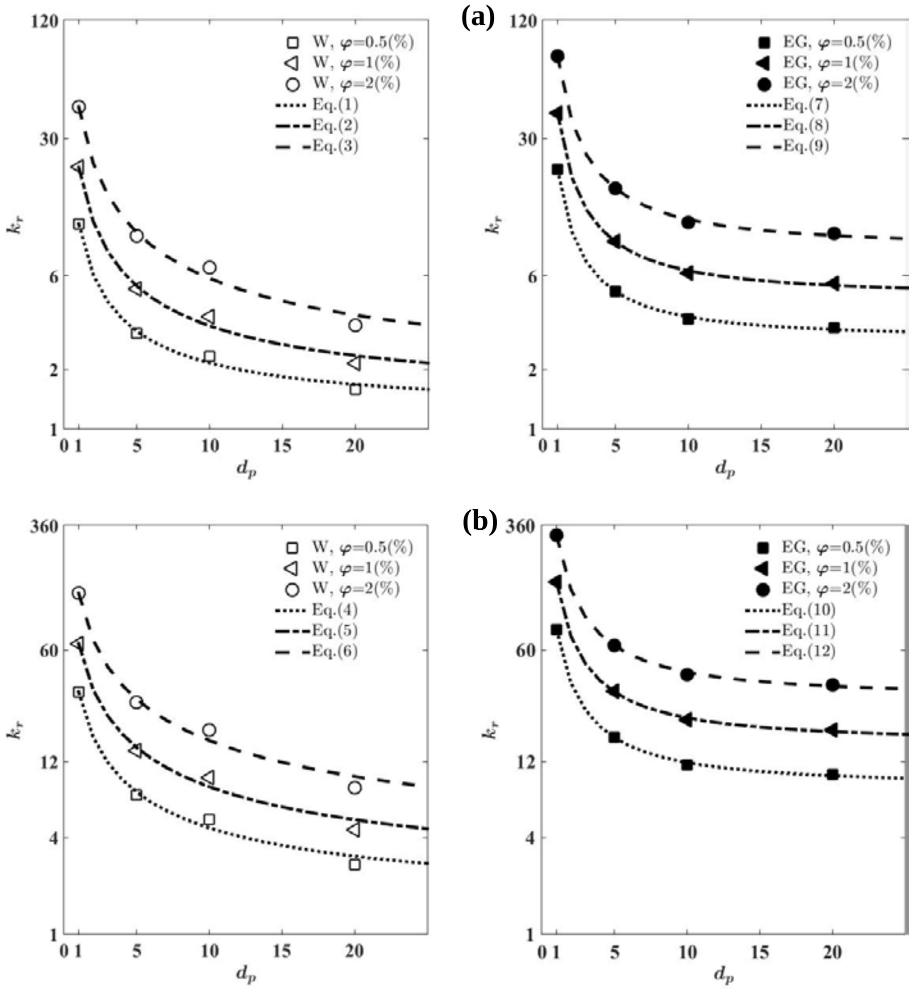

Figure 1. Variation of $k_r$of Ag-W, Ag-EG nanofluids with d_p and φ at (a) 333 K and (b) 363 K

As shown in Figure 1, decreasing d_p and increasing φ enhance k_r of the nanofluids for 333 K and 363 K. Lee et al. [25] points out that despite of thermal conductivity of EG being three times lesser than that of water as shown in Table 3, it shows higher k_r of Al_2O_3 and CuO–EG is higher than k_r of Al_2O_3 and CuO–W. Therefore comparison of k_r values of Ag-W and Ag-EG nanofluids in Figure 1 shows that k_r values of Ag-EG nanofluids are remarkably higher than k_r values of Ag-W nanofluids.

Nanofluid is more effective for EG based fluids having lower thermal conductivity in Table 3. Besides, for d_p (5 nm -10 nm), k_r values do not change significantly independent of φ at 333 K and 363 K. But after d_p = 5 nm, k_r values increase rapidly for both T. 5 nm is critical size due to rapid change of k_r values independent of φ and T. As shown in Figure 1, the maximum values of k_r are obtained with Ag-EG with d_p = 1 nm, φ = 2% and T = 363 K.

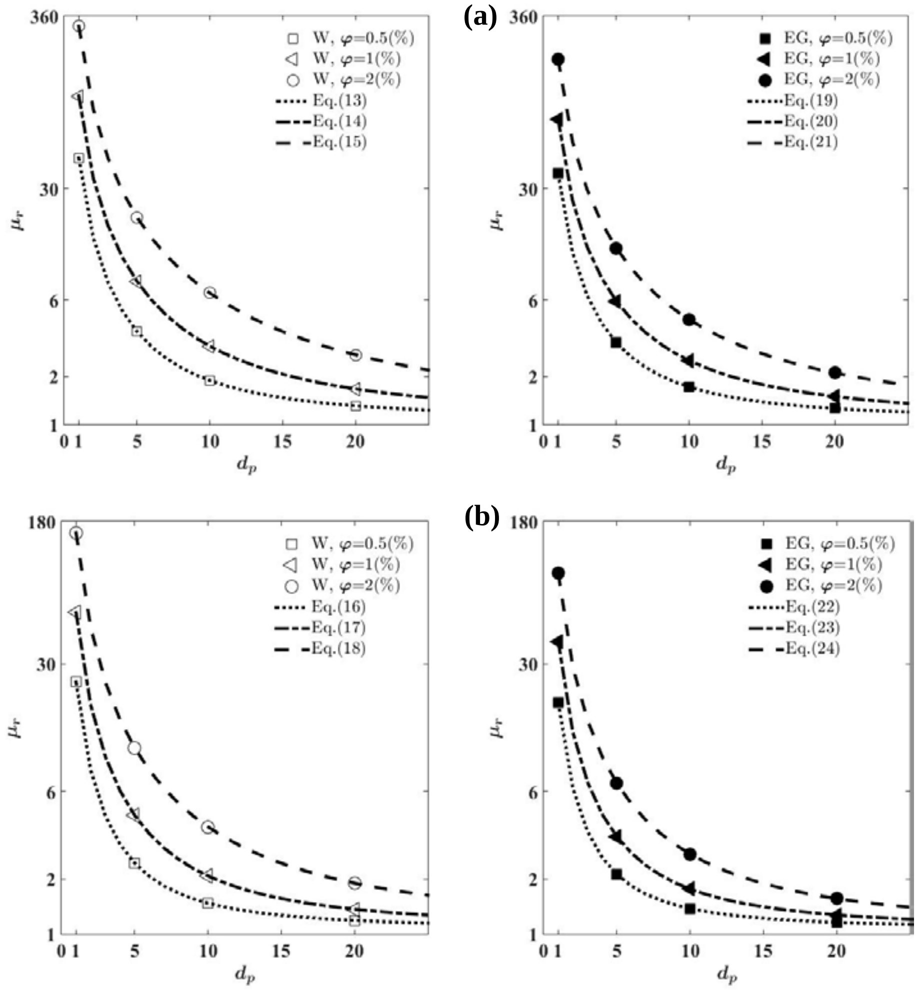

Figure 2. Variation of μ_r of Ag-W, Ag-EG nanofluids with d_p and φ at (a) 333 K and (b) 363 K

As shown in Figure 2, for d_p (5 nm -10 nm), μ_r values increase linearly for φ < 0.5 at 333 and 363 K. But after d_p = 5 nm, μ_r values increase rapidly for both T. But an increase μ_r of nanofluids leads to increase in pressure drop and pumping power. Therefore considering μ_r of nanofluids, optimization is necessary for size of nanoparticles.

Eqs. (2)-(25) shown in Table 4 are obtained by data fitting in Figure 1 and 2.

Table 4. The calculated constants of Eq. (1).

Equations	T (K)	φ(%)	a	b	c	Equation numbers
k_r(W)	333	0.5	9.786	-1.012	1.208	2
		1	19.98	-1.012	1.391	3
		2	41.57	-1.012	1.778	4
	363	0.5	31.15	-1.006	1.536	5
		1	63.58	-1.006	2.06	6
		2	132.3	-1.006	3.17	7
k_r(EG)	333	0.5	17.97	-1.328	2.861	8
		1	35.74	-1.328	4.691	9
		2	70.67	-1.328	8.288	10
	363	0.5	71.87	-1.328	8.433	11
		1	142.9	-1.328	15.77	12
		2	282.6	-1.328	30.2	13
μ_r(W)	333	0.5	45.65	-1.745	1.064	14
		1	112.6	-1.745	1.064	15
		2	310.2	-1.745	1.064	16
	363	0.5	22.79	-1.745	1.064	17
		1	56.19	-1.745	1.064	18
		2	154.8	-1.745	1.064	19
μ_r(EG)	333	0.5	36.29	-1.745	1.064	20
		1	80.57	-1.745	1.064	21
		2	193.1	-1.745	1.064	22
	363	0.5	17.43	-1.745	1.064	23
		1	38.71	-1.745	1.064	24
		2	92.77	-1.745	1.064	25

4. Conclusions

In the case study, the determination of critical sizes of Ag nanoparticles (1-10 nm) of 0.5% - 2% φ in W and EG based nanofluids for 333 K and 363 K is given. The results indicate that for $d_p <$ 5 nm, k_r and μ_r values of Ag-W and Ag-EG nanofluids increase rapidly. Therefore thermal enhancement is given with d_p = 1 nm as the optimum size. However the disadvantage of increased μ_r values of Ag-W and Ag-EG nanofluids for d_p < 5 nm is with increased pumping cost. Therefore the critical size is appeared to be d_p = 5 nm for the acceptable pumping resistance of nanofluids with sufficient thermal enhancement.

Acknowledgment

This work was supported by the Scientific Research Projects Unit (BAPYB) of Gaziantep University (Project numbers: RM.21.01).

References

1. Murshed S.M.S., and P Estellé, A state of the art review on viscosity of nanofluids. Renewable and Sustainable Energy Reviews, 2017, 76:1134-1152.
2. Ahmadi M.H., A. Mirlohi, A.M. Nazari, and R. Ghasempour, A review of thermal conductivity of various nanofluids. Journal of Molecular Liquids, 2018, 265:181-188.

3. Munyalo J.M., and Zhang X. Particle size effect on thermophysical properties of nanofluid and nanofluid based phase change materials: A review. J. Mol. Liq., 2018, 265:77-87.
4. Parashar N. and Yahya S. M. Thermophysical and rheological properties of hybrid nanofuids: a review on recent studies. Journal of Thermal Analysis and Calorimetry, 2022, 147:4411–4449.
5. Masuda H., Ebata A., Teramae K., and Hishinuma N. Alteration of thermal conductivity and viscosity of liquid by dispersing ultra-fine particles (Dispersion of y-A12O3, SiO2, and TiO2 ultra-fine particles. NetsuBussei (in Japanese), 1993, 4:227-233.
6. Wang X., Xu X., and Choi S.U.S. Thermal conductivity of nanoparticles–fluid mixture. J. Thermophys. Heat Transf., 1999, 13(4):474-480.
7. Koo J., and Kleinstreuer C. Laminar nanofluid flow in microheat-sinks. Int. J. Heat Mass Transf., 2005, 48(13):2652–2661.
8. Namburu P.K., Kulkarni D.P., Misra D., andDas D. K. Viscosity of copper oxide nanoparticles dispersed in ethylene glycol and water mixture. Exp. Therm. Fluid Sci., 2007, 32(2):397-402.
9. Duangthongsuk W., and Wongwises S. Measurement of temperature-dependent thermal conductivity and viscosity of TiO2-water nanofluids. Exp. Therm. Fluid Sci., 2009, 33(4):706-714.
10. Mintsa H.A., Roy G., Nguyen C.T., and Doucetet D. New temperature dependent thermal conductivity data for water-based nanofluids. Int. J. Therm. Sci., 2009, 48(2):363-371.
11. Yu W., Xie H., Chen L., and Li Y. Investigation of thermal conductivity and viscosity of ethylene glycol based ZnOnanofluid. Thermochim. Acta, 2009, 491(1):92-96.
12. Godson L., Raja B., Lal D.M., and Wongwises S. Experimental investigation on the thermal conductivity and viscosity of silver-deionized water nanofluid. Exp. Heat Transf., 2010, 23(4):317-332.
13. Murshed S.M.S. Simultaneous measurement of thermal conductivity, thermal diffusivity, and specific heat of nanofluids. Heat Transf. Eng., 2012, 33(8):722–731.
14. Suganthi K.S., and Rajan K.S. Temperature induced changes in ZnO – water nanofluid: zeta potential, size distribution and viscosity profiles. Int. J. Heat Mass Transf., 2012, 55(25):7969–7980.
15. Ghanbarpour M., Haghigi E.B., and Khodabandeh R. Thermal properties and rheological behaviour of water based Al2O3 nanofluid as a heat transfer fluid. Exp. Therm. Fluid Sci., 2014, 53:227-235.
16. Pastoriza-Gallego M.J., Lugo L., Cabaleiro D., Legido J.L., and Piñeiro M.M. Thermophysical profile of ethylene glycol-based ZnOnanofluids. J. Chem. Thermodyn., 2014, 73:23–30.
17. Sundar L. S., Ramana E.V., Singh M.K., and Sousa A.C.M. Thermal conductivity and viscosity of stabilized ethylene glycol and water mixture Al2O3 nanofluids for heat transfer applications: an experimental study. Int. Commun. Heat Mass Transf.., 2014, 56:86-95.
18. Adio S.A., Mehrabi M., Sharifpur M., and Meyer J.P. Experimental investigation and model development for effective viscosity of MgO–ethylene glycol nanofluids by using

dimensional analysis, FCM-ANFIS and GA-PNN techniques. Int. Commun. Heat Mass Transf., 2016, 72:71–83.

19. Zyla G., and Fal J. Viscosity, thermal and electrical conductivity of silicondioxide–ethylene glycol transparent nanofluids: An experimental studies. Thermochim. Acta, 2017, 650: 106–113.
20. Kaplan M., and Carpinlioglu M.O. An extensive review on nanofluids - based on available experimental studies. Proceedings of 2nd International Symposium on Innovative Approaches in Scientific Studies, 2018, pp. 104-116.
21. Kaplan M., and Carpinlioglu M.O. Proposed new equations for calculation of thermophysical properties of nanofluids. Int. Adv. Res. Eng. J., 2021, 5(2):142-151.
22. CarpinliogluM.O.,and Kaplan M. A correlation approach for the calculation of thermal conductivity of nanofluids as a function of dynamic viscosity. J. Braz. Soc. Mech. Sci. Eng., 2021, 43(5):242.
23. Garoosi F. Presenting two new empirical models for calculating the effective dynamic viscosity and thermal conductivity of nanofluids. Powder Technol., 2020, 366:788–820.
24. Bergman T.L., Lavine A.S., Incropera F.P., and DeWitt D.P., Fundamentals of heat and mass transfer, John Wiley & Sons, 2011.
25. Lee S., Choi S., Li S, Eastman J. A. Measuring thermal conductivity of fuids containing oxide nanoparticles. J Heat Transfer, **1999**, 121:280–289.

Nomenclature			
c_p	specific heat, J/kg K	*Subscripts*	
d	nanoparticle diameter, nm	*bf*	base fluid
h	capping layer thickness, nm	*nf*	nanofluid
k	thermal conductivity, W/mK	*p*	particle
k_b	Boltzmann constant, 1.3806 x 10^{-23} J/K	*r*	relative
T	temperature, K	*ref*	reference
Pr	Prandtl number	*Abbreviations*	
Re	Reynolds number	*W*	water
u_{Br}	Brownian velocity (m/s)	*EG*	ethylene glycol
Greek symbols			
β, η	empirical constants		
Δ	correlation term including dimensionless		
μ	dynamic viscosity, Pas		
ρ	density (g/cm^3)		
φ	volume fraction (%)		

BROADBAND MULTILAYER METAMATERIAL MICROWAVE ABSORBER DESIGN USING SOA ALGORITHM

UĞUR CEM HASAR[1], Mona S. S. ALFAQAWI [1]
[1] Gaziantep University, Engineering Faculty, Electric and Electronic Department, Gaziantep, Turkey.

Abstract

In this work the optimization of a scheme based on designing the metamaterial in multi-layered structure to get wideband absorber have been proposed. In the proposed design simple conventional metamaterial shape has been used to ease the fabrication of the proposed design. The absorber is a periodic array of cells which includes three patterns of a resistive films on two dielectric substrates. In the optimization process we choose the Seeker Optimization Algorithm to get the different dimensions of the structure to get the best absorption over the selected band. Our optimized design achieved a 90%-absorption rate over a wide frequency bandwidth of 2.636 GHz to 18.717 under normal incidence. Moreover, the absorber operates over a wide range of incidence angles for obliquely incident waves.

Keyword: Metamaterial, Multilayer, Broad band, Optimization, Seeker Optimization Algorithm.

1. Introduction

Recently, near-optimal solutions for many complex engineering problems have been enabled using efficient computational algorithms. Hence, optimization techniques take their pivotal role in many raising electromagnetic problems. In particular, bioinspired search optimization algorithms have
With the tremendous advancements in electronics industry and wireless communication revolution, new challenges arise to face the accompanying design requirements, such as interference cancellation, limitations on weight and cost, which leads to the need for simple, time saving and efficient design techniques. Recently, near optimal solutions for many complex engineering problems have been enabled using efficient computational algorithms. Hence optimization techniques take their pivotal role in many electromagnetic problems. Bio-inspired search algorithms have been successfully applied in electromagnetic problems, due to their simplicity and robustness [1-11].

Electromagnetic wave absorbers play a pivotal role in several modern military and civil applications, absorbers are those elements that are often used to eliminate the unwanted radiation in the electronic systems. Specifically, they are widely used to reduce the interference between circuit components in near field models, and to create free space conditions as in anechoic chambers. Absorbers also widely used externally to reduce the radar cross section of a target object.

Widespread applications of electromagnetic wave absorbers have inspired RF engineers to exploit more efforts in optimal design using different techniques. Ideally a thin, light weight and wideband absorber is an optimum one, thus many studies have been carried out to meet the optimal design requirements.

In this paper, a multiband unit cell metamaterial has been used to build in a wideband MA consisting of multi-layered resonators. Seeker Optimization algorithm [12] has been used to find the best parameter design for the whole structure. to the best of our knowledge, this is the first work to optimize the MMA using SOA.

The outline of this study is as follows; In section II the theoretical background of the Seeker Optimization Algorithm has been presented. The physical model and the formulation of the problem has been presented in section III. In section IV, designed structures along with the comparisons and verification results are presented. Results and possible advanced studies presented and discussed in section V.

2. Seeker Optimization Algorithm

Due to its computational efficiency, high search capability and easy implementation PSO has been widely applied in solving several engineering optimization problems. Compared to GA, PSO has fewer parameters to adjust; also, it can be considered to be more efficient in maintaining diversity of the swarm. On the other hand, it has no evolution operator such as crossover and mutation.
Seeker Optimization Algorithm (SOA), originally proposed by Dai et al. in 2006 [12] is a new promising technique for the real parameter optimization. SOA is based mainly on the concept of simulating the act of humans intelligent searching with their memory, experience, and uncertainty reasoning. SOA divides the set of solutions (search populations) randomly into K subpopulations with the same size, the individual of this population is called seeker or searcher, where all seekers in the same subpopulation constitute a neighborhood socially sharing the search information. After given start point, search direction, search radius (step length), and trust degree, every seeker moves to a new position (next solution) based on his social learning, cognitive learning, and uncertainty reasoning. SOA operates on a search population of s D-dimensional position vectors [16], which represents the solutions to the optimization problem at hand, i.e., $\vec{x_i} = [x_{i1}, \dots, x_{ij}, \dots, x_{iD}]$; $i = 1, 2, \dots, s$ where x_{ij} is the j^{th} element of $\vec{x}_i$ and s is the population size. The flow chart of the seeker optimization is shown in Figure 1. Firstly, it generates s positions uniformly and randomly in the search space, and calculates the fitness of each seeker, then calculates the search direction $dij(t)$ and the step length $\alpha_{ij}(t)$, for the i^{th} seeker at time step t. Then the j^{th} element of the i^{th} seeker is updated by [19]:

$$x_{ij}(t+1) = x_{ij}(t) + \alpha_{ij}(t) d_{ij}(t)$$

To avoid converging to a local minimum, SOA uses an inter sub population strategy, i.e., the worst k-1 positions of each subpopulation are combined with the best position of each other k-1 subpopulations by the following crossover operator:

$$x_{k_n j,worst} = \begin{cases} x_{lj,best} & if\ R_j \leq 0.5 \\ x_{k_n j,worst} & else \end{cases}$$

Where R_j is a uniformly random real number in the interval [0,1], $x_{k_n j,worst}$ is the j^{th} element of the n^{th} worst position in the k^{th} subpopulation, $x_{lj,best}$ is the j^{th} element of the best position in the l^{th} subpopulation.

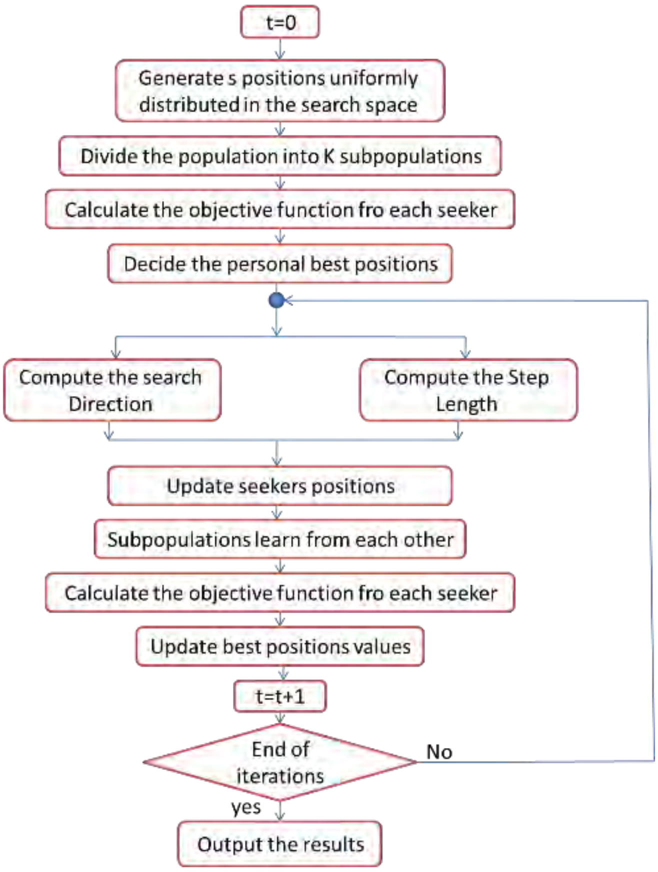

Figure 1: SOA Flow Chart

B. Search Direction

When the fitness function can't be differentiated, a so-called empirical gradient can be used [17] by evaluating the response to increments and decrements in each direction. In this way, the seekers will lead their search. Search direction can be determined by the signum function of a better position minus a worse position, keeping in hand that the seekers must take into consideration their own current or historical positions and their neighbor's positions to determine their search direction. So, SOA models three different behaviors to determine search direction: egotistic, altruistic and proactive.

Egotistic, is an entirely pro self-behavior, in which each seeker i, as a single sophisticated agent, trying to direct toward his historical best position $\vec{p}_{i,best}(t)$ through cognitive learning [18]. Then, an empirical gradient from $\vec{x}_i(t)$ to $\vec{p}_{i,best}(t)$ can be adopted for the i^{th} seeker at time t, and thus each seeker i has an egotistic direction $d_{i,ego}(t) = [d_{i1,ego}, d_{i2,ego}, \ldots, d_{iD,ego}]$ calculated as:

$$\vec{d}_{i,ego}(t) = sgn(\vec{p}_{i,best}(t) - \vec{x}_i(t))$$

On the other hand, based on their altruistic behavior, the neighboring seekers communicate with each other to adjust their behavior to achieve their goal, the neighbors' historical best position $\vec{g}_{best}(t)$ and the neighbors' current best position $\vec{l}_{best}(t)$ are used as the attraction signal source of the self-organized aggregation behavior. Thus, each seeker i is associated with two altruistic directions, i.e., $\vec{d}_{i,alt1}(t)$, $\vec{d}_{i,alt2}(t)$

$$\vec{d}_{i,alt1}(t) = sgn(\vec{g}_{best}(t) - \vec{x}_i(t))$$
$$\vec{d}_{i,alt2}(t) = sgn(\vec{l}_{best}(t) - \vec{x}_i(t))$$

Moreover, seekers exploit the properties of proactiveness, they are able to exhibit a goal-directed behavior [19]. Also, future behavior can be predicted and guided by past behavior [20]. As a result, each seeker will be proactive to vary his search direction and exhibit a goal-directed behavior according to his past behavior. Hence, any seeker i is associated with an empirical direction called proactiveness direction $\vec{d}_{i,pro}(t)$:

$$\vec{d}_{i,pro}(t) = sgn(\vec{x}_i(t_1) - \vec{x}_i(t_2))$$

Where $t_1, t_2 \in t, t-1, t-2$ and $\vec{x}_i(t_1)$ is better than $\vec{x}_i(t_2)$. According to human rational judgment, the actual search direction of the i^{th} seeker, i.e., d_i(t) = [d_{i1} , d_{i2}, …, d_{iD}] is based on a compromise among the aforementioned four empirical directions. In this work, the j^{th} element of $d_i(t)$ is selected by applying he following selection rule:

$$d_{ij}(t) = \begin{cases} 0 & if\ r_j \le p_j^{(0)} \\ +1 & if\ p_j^{(0)} < r_j \le p_j^{(0)} + p_j^{(1)} \\ -1 & if\ p_j^{(0)} + p_j^{(1)} < r_j \le 1 \end{cases}$$

$p_j^m, m \in (0,1,-1)$ is defined as: in the set $(d_{ij,ego}, d_{ij,alt1}, d_{ij,alt2}, d_{ij,pro})$, let $num^{(m)}$ is the number of "m" then $p_j^{(m)}/4$.

A. Step Length

Among the continuous space, there are often fitness points that are closer to the extremum point, such that the fitness values of the input variables are proportional to their distances from the extremum point, so the search must be intensified in regions with relatively good solutions [21]. Hence, from the standpoint of human searching, it could be believed that one may find near-optimal solutions in a narrower neighborhood of the point with lower fitness value and vice versa, less chance to find the optimum in a wider range far away from the points with higher fitness values. Fuzzy systems arose from the need to describe real complex systems by linguistic terms [22]. According to human focusing search aforementioned, the uncertainty reasoning of human searching can be described by natural linguistic variables and a simple control rule as "If fitness value is small" (i.e., the conditional part), then "step length is short" (i.e., the action part). The linguistic description of human search makes the fuzzy system a good candidate for simulating human focusing search behavior.

Optimization problems often have different ranges of fitness values. To design a fuzzy system that can be applicable to a wide range of optimization problems, the fitness values of all the seekers are firstly sorted in descending order and then turned into the sequence numbers from 1 to s as inputs to a fuzzy reasoning system. A linear membership function is then used in the conditional part. The expression is presented as

$$\mu_i = \mu_{max} - \frac{s - I_i}{s - 1}(\mu_{max} - \mu_{min})$$

Where I_i is the sequence number of $\vec{x}_i(t)$ after sorting the fitness values and μ_{max} is the maximum membership degree value that is equal to or little less than 1.0, in this work, $\mu_{max} = 0.95$. In the action part, the Bell membership function $\mu^{\alpha_{ij}^2/2\delta_j^2}$, $(i = 1, \ldots, s; j = 1, \ldots, D)$ is used for the

j^{th} element of the i^{th} seekers step length. For the Bell function, the membership degree values of the input variables beyond $[-3\delta, 3\delta]$ are less than 0.0111 [23]. thus, the minimum value $\mu_{min} = 0.0111$ is often used. Moreover, the parameter δ_j of the Bell membership function is the j^{th} element of the vector $[\delta_1, \delta_2, \ldots, \delta_j]$, which is given by

$$\delta_j = \omega \,.\, abs(\vec{x}_{best} - \vec{x}_{rand})$$

where abs() returns a vector in which each element is the absolute value of the corresponding element in the input vector. The parameter ω is used to decrease the step length with increasing time step such that it gradually improves the search precision. In this work, ω is linearly decreased from 0.9 to 0.1 during the run time. $\vec{x}_{best}, \vec{x}_{rand}$ are the best seeker and a randomly selected seeker in the same subpopulation to which the i^{th} seeker belongs (must differ from $\vec{x}_{best}$,), respectively. Then, the action part of the fuzzy reasoning system gives the j^{th} element of the i^{th} seeker's step length

$$\alpha_{ij} = \delta_j \sqrt{-\log(RAND(\mu_i - 1))}$$

Where δ_j is the j^{th} element of vector δ in equation 2.9, RAND (μ_i,1) returns a uniform random number within the range of [μ_i,1], which is used to improve local search capability.

3. Problem Formulation: Unit Cell Design

Figure 2 shows an initial design of a cell whose array forms a planar multi-layer absorber. This cell is comprised of two dielectric substrates and patterns of thin resistive layers with a surface resistance of Rs imprinted on the surface of substrates.

The dielectric substrates have been separated by an air gap and placed above a metallic ground plate. The substrates are glass-reinforced epoxy (FR4) with a dielectric coefficient of 4.3, a loss tangent of 0.025, and a thickness of 0.5 mm.

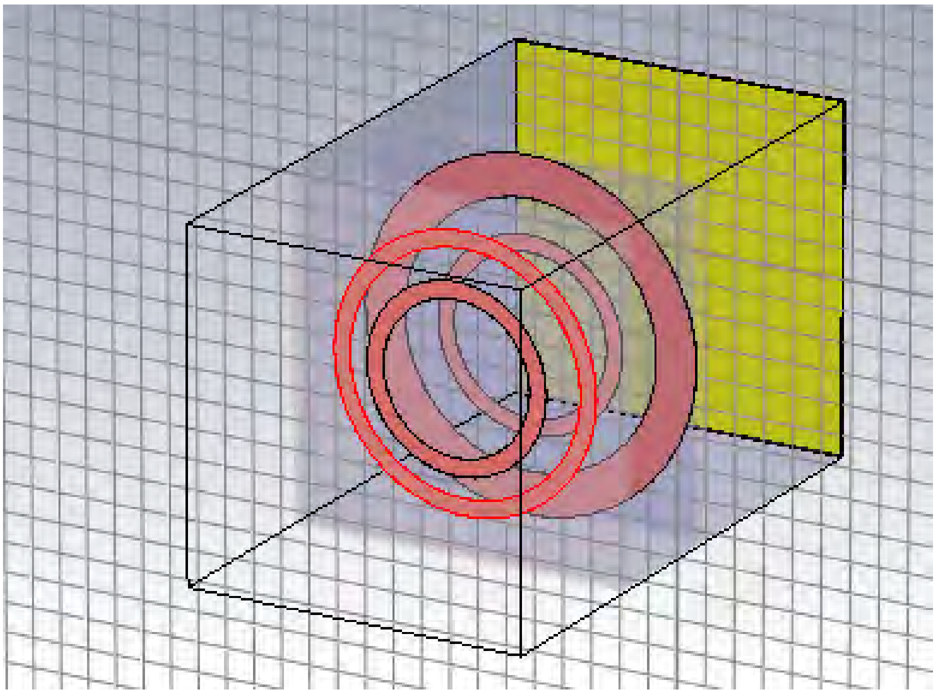

Figure -2: Unicell Design of multilayer metamaterial absorber structure

4. Results and Discussions

Figure 3 shows the broadband characteristics of the multilayer metamaterial design that has been proposed in this paper. The results shows that the proposed optimized design achieved a 90%-absorption rate over a wide frequency bandwidth of 2.636 GHz to 18.717 under normal incidence

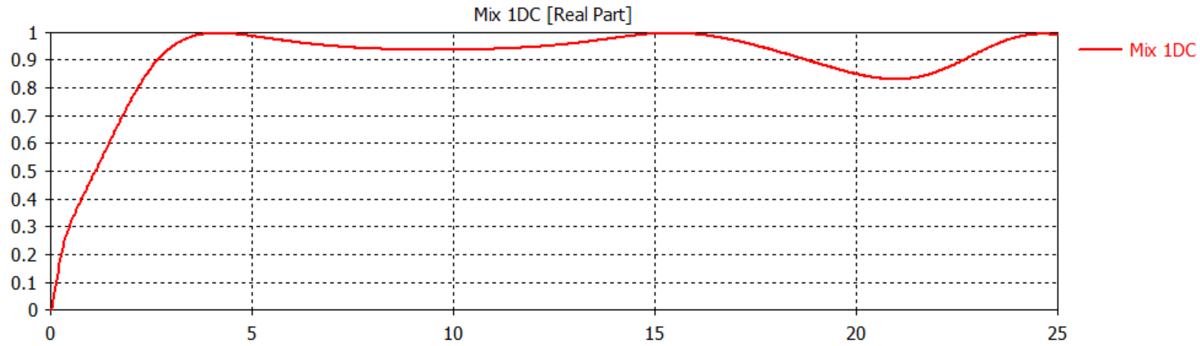

Figure 3. Simulated reflection coefficient of the proposed metamaterial absorber.

5. Conclusions

In this work the optimization of a scheme based on designing the metamaterial in multi-layered structure to get wideband absorber have been proposed. In the proposed design simple conventional metamaterial shape has been used to ease the fabrication of the proposed design. The absorber is a periodic array of cells which includes three patterns of a resistive films on two dielectric substrates. In the optimization process we choose the Seeker Optimization Algorithm to get the different dimensions of the structure to get the best absorption over the selected band. Our optimized design achieved a 90%-absorption rate over a wide frequency bandwidth of 2.636 GHz to 18.717 under normal incidence. Moreover, the absorber operates over a wide range of incidence angles for obliquely incident waves.

References

[1] L. Y. Jiang, X. Y. Li and J. Zhang , "Design of high performance multilayer mi-crowave absorbers using fast genetic algorithm," *Science in China Series E: Technological Sciences,* vol. 52, pp. 2749-2757, 2009.

[2] S. K. Goudos, Z. D. Zaharis, K. B. Baltzis, C. S. Hilas and J. N. Sahalos, "A comparative study of Particle Swarm Optimization and Differential Evolution on Radar Absorbing Materials design for EMC applications," in *International Symposium on Electromagnetic Compatibility - EMC Europe*, Athens, Greece, 2009.

[3] A. Toktas, D. Ustun, E. Yigit, K. Sabanci and M. Tekbas, "Optimally Synthesizing Multilayer Radar Absorbing Material (RAM) Using Artificial Bee Colony Algorithm," in *23rd International Seminar/Workshop on Direct and Inverse Problems of Electromagnetic and Acoustic Wave Theory (DIPED)*, Tbilisi, Georgia, 2018.

[4] S. Goudos, "Design of Microwave broadband absorbers using a self-adaptive differential evolution algorithm," *International Journal of RF and Microwave Computer-Aided Engineering,* vol. 19, no. 3, pp. 364-372, 2009.

[5] E. Yigit and H. Duysak, "Determination of Optimal Layer Sequence and Thickness for Broad-band Multilayer Absorber Design Using Double-Stage Artificial Bee Colony

Algorithm," *IEEE Transactions on Microwave Theory and Techniques,* vol. 67, no. 8, pp. 3306 - 3317, 2019.

[6] N. Dib, M. Asi and A. Sabbah, "On the optimal design of multilayer micro-wave absorbers," *Progress In Electromagnetics Research C,* vol. 13, pp. 171-185, 2010.

[7] L. JIANG, J. CUI, L. SHI and X. LI, "Pareto optimal design of multilayer microwave absorbers for wide-angle incidence using genetic algorithms," *IET microwaves, antennas & propagation ,* vol. 3, no. 4, pp. 572-579, 2009.

[8] A. Mujahed, "Design of multilayer microwave absorbers using evolutionary optimization techniques", Master Thesis, Jordan University of Science and Technology, 2010.

[9] H. Gargama, S. K. Chaturvedi and A. Thakur, "Design and Optimization of Multilayered Electromagnetic Shield Using a Real-Coded Genetic Algorithm," *Progress In Electromagnetics Research B,* vol. 39, pp. 241-266, 2012.

[10] S. Roy, S. D. Roy, J. Tewary, A. Mahanti and G. Mahanti, "Particle Swarm Optimization for Optimal Design of Broadband Multilayer Microwave Absorber for Wide Angle of Incidence," *Progress In Electromagnetics Research B,* vol. 62, pp. 121-135, 2015.

[11] M. H, M. V and N. D. M, "Design of Microwave Absorbers using Improvised Particle Swarm Optimization Algorithm," *Journal of Microwaves, Optoelectronics and Electromagnetic Applications ,* vol. 17, no. 2, pp. 188-200, 2018.

[12] C. Dai, W. Chen and Y. Zhu, "Seeker Optimization Algorithm," in *International Conference on Computational Intelligence and Security*, Guangzhou, China, 2006.

[13] S. Binitha and S. S. Sathya, "A survey of bio inspired optimization algorithms,," *International Journal of Soft Computing and Engineering,,* vol. 2, pp. 137-151, 2012.

[14] D. Karaboga and B. Basturk, "A powerful and efficient algorithm for numerical function optimization: Artificial bee colony (ABC) algorithm," *Journal of Global Optimization,* vol. 39, no. 3, pp. 459-471, 2007.

[15] D. Karaboga, B. Gorkemli, C. Ozturk and N. Karaboga, "A comprehensive survey: Artificial bee colony (ABC) algorithm and applications," *Artificial Intelligence Review,* vol. 42, no. 1, pp. 21-57, 2014.

[16] K. Guney and S. Basbug, "Seeker optimization algorithm for interference suppression of linear antenna arrays by controlling position-only, phase-only, and amplitude-only," *International Journal of RF and Microwave Computer-Aided Engineering,* vol. 21, no. 5, pp. 505-518, 2011.

[17] J. D. Hewlett, B. M. Wilamowski and G. Dundar, "Optimization Using a Modified Second-Order Approach With Evolutionary Enhancement," *IEEE Transactions on Industrial Electronics,* vol. 55, no. 9, pp. 3374-3380, 2008.

[18] V. Kumar and F. Sahin, "Cognitive maps in swarm robots for the mine detection application," in *SMC'03 Conference Proceedings. 2003 IEEE International Conference on Systems, Man and Cybernetics.*, Washington, DC, 2003.

[19] M. Wooldridge and N. R. Jennings, "Intelligent agents: Theory and practice,," *The Knowledge Engineering Review,* vol. 10, no. 2, pp. 115-152, 1995.

[20] I. Ajzen, "Residual Effects of Past on Later Behavior: Habituation and Reasoned Action Perspectives," *Personality and Social Psychology Review,* vol. 6, no. 2, pp. 107-122, 2002.

[21] B. Raphael and I. F. C. Smith, "A direct stochastic algorithm for global search," *Applied Mathematics and Computation,* vol. 146, no. 2-3, pp. 729-758, 2003.

[22] L. A. Zadeh, "The concept of a linguistic variable and its application to approximate reasoning," *Information Sciences,* vol. 8, no. 3, pp. 199-249, 1975.

[23] D. Li, D. Cheung, X. Shi and V. Ng, "Uncertainty reasoning based on cloud models in controllers," *Computers & Mathematics with Applications,* vol. 35, no. 3, pp. 99-123, 1998.

[24] "Software Electromagnetic Simulation," CST Microwave Studio, 2020. [Online]. Available: https://www.cst.com. [Accessed 10 January 2021].

MICROWAVE METAMATERIAL-BASED SENSOR DESIGN FOR DETECTION OF ADULTERATION IN OLIVE OIL

HUSEYİN KORKMAZ*[1], UGUR CEM HASAR[1]

[1]Gaziantep University, Department of Electrical and Electronics Engineering, 27310 Gaziantep, TURKEY.

Abstract

The benefits of olive oil to health, its taste and aroma have been effective in its popularity. For this reason, production and sales costs have increased accordingly, so increased costs lead to adulteration in olive oil. Since the dielectric coefficients of olive oil and other oils mixed with olive oil are very close to each other, detection of adulteration has costly and complex processes. In this study, we designed a metamaterial-based microwave sensor and simulated it for the detection of adulteration with olive oil in the x band (8.2-12.4 GHz) frequency region. We observed that the sensor we designed was able to detect adulteration of some low-cost oils with olive oil. Computer Simulation Technology (CST), which is popular in electromagnetic research was used to adjust the dimensions of the proposed sensor and simulate adulteration. As a result of our analysis and simulation, proposed sensor clearly detected liquid oils adulterated with pure olive oil by resonance frequency shift technique. We anticipate that this study may be a reference in industrial applications, especially for studies related to the detection of liquid adulteration.

Keyword: Microwave Metamaterial Sensor, Olive oil, X-band Frequency region, Dielectric Constant, Adulteration.

1.Introduction

Olive oil has gained popularity in regions where other edible oils are used a lot. Olive oil's health, aroma, taste and features such as being more nutritious than other edible oils have played an active role in the popularity of olive oil. Increasing demand for olive oil has brought with it the addition of other economic oils to olive oil (adulteration) to make a profit [1]. From this point of view, researchers have conducted and continue to conduct many studies on the detection of adulteration in olive oil.

On the other hand, metamaterials (MM) are artificial materials that can be adjusted periodically, whose dimensions are much smaller than the electromagnetic wave that comes to them [2]. In general, the variation of the incident electromagnetic wave is evaluated depending on two parameters, the electrical permeability (ϵ) and magnetic permeability (μ) of the materials. Metamaterials come to the fore in areas such as temperature, displacement, strain, density and material characterization [3]. Many sensors have been developed in many different areas using metamaterials that have negative refraction properties and are not found in their natural state at microwave frequencies [4]–[9]. In addition, MMs are frequently used in energy harvesting applications, antennas, signal absorbers, etc. [5], [10]–[14].

In the literature, there are studies to determine the electrical properties of some liquid oils by MM sensors. The first study includes the dielectric coefficients and resonance frequencies of some liquids such as clean and waste transformer oils, corn oil, cottonseed oil and olive oil in the x band frequency region (8 to 12 GHz) with the MM sensor [15]. However, in this study, we could not find an analysis or narrative about the adulteration of other oils with olive oil. Another study is related to planar microwave probe design for edible oils. More precisely, a complementary split-ring resonator (CSRR) has been proposed for the detection of adulteration of liquids. Roger RT 5880 substrate with a thickness of 0.8 mm was used in the proposed sensor and the measurements were made using a vector network analyzer [16].

As a result of our detailed literature search, we could not find any study or detailed analysis regarding the MM-based new generation microwave sensor that can detect other oils adulterated by olive oil for the x band frequency region. The main problem in this regard is that the dielectric coefficients of olive oil and other liquid oils are very close to each other. Therefore, mixed oils are difficult to detect by conventional and low-sensitivity sensors. The aim of this study design and analysis MM-based new generation microwave sensor that has ability to detect other oils adulterated with olive oil for the x band frequency region.

2. Design and Analysis

In this part of our study, details about MM based sensor design and determination of dielectric coefficients of liquids will be given. The dimensions of the proposed design for the detection of adulteration of liquids (especially oils) have been adjusted in the most effective and efficient way, and the final version is presented in Figure 1. The design and simulation were carried out with Computer Simulation Technology (CST), a computer program based on the finite integration technique and widely used in electromagnetic field studies [17], [18]. Our design consists of copper resonator, Flame Reterdant-4 (FR-4) dielectric layer, sensing layer, FR-4 dielectric layer and copper resonator, from back to front, respectively. The reason we use FR-4 dielectric layers in the design is because of low transmission loss, high mechanical strength and low cost. The Flame Reterdant-4 (FR-4) that used in the design has a thickness of 1 mm, a loss tangent of 0.02, and a relative permeability of 4.3. The sensing layer has a thickness of 3 mm and was initially defined as air (relative permeability is 1) (without sample addition). The copper resonator has a conductivity of $5.8x10^7 \frac{s}{m}$ and its thickness is determined as 35 μm.

Material selection is very important in detecting even the smallest dielectric coefficient changes. The most important criterion here is to design a sensitive sensor by minimizing the losses and capacitive effects on the material due to the very low dielectric coefficient and loss tangent values of the material [15]. As can be observed from Figure 2, the resonance frequency of the proposed MM-based sensor (without sample) is 10.116 GHz. The sensor operates in the x band frequency region, so the total area of the structure is 22.86x10.16 mm^2. As can be seen in Figure 3, the boundary conditions of the design in the simulation program are determined as Perfect Electric Conductor (PEC), Perfect Electric Conductor (PEC) and open (add space) for the x, y and z axes, respectively.

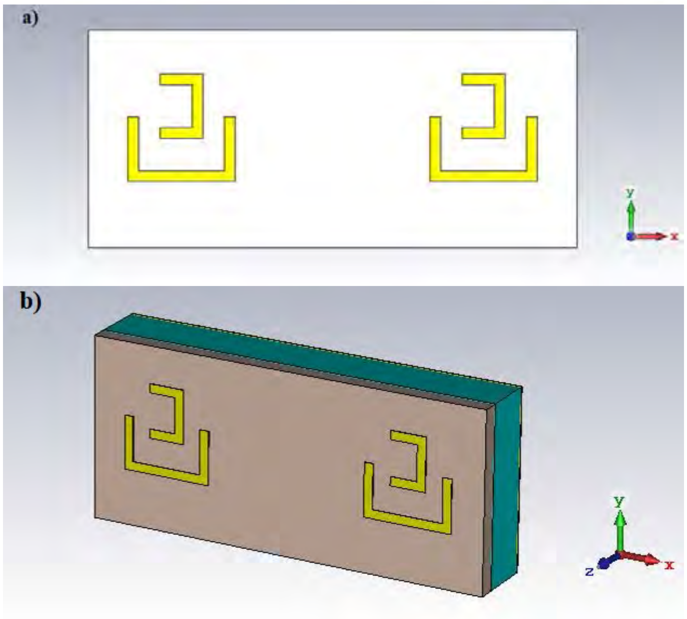

Figure 1. (a) Front and (b) perspective view of the proposed reflective resonance MM-based sensor

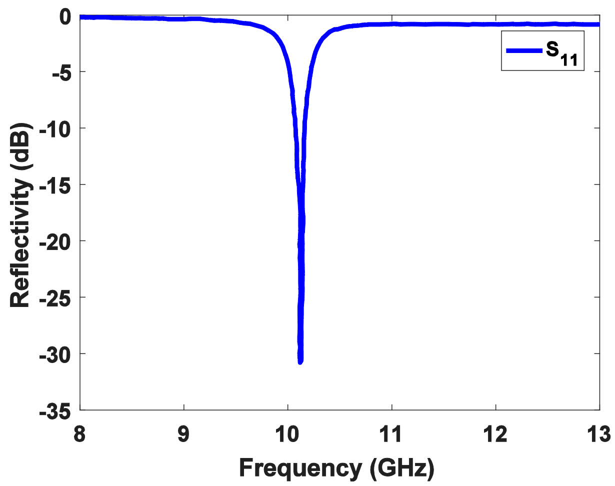

Figure 2. Reflectivity plot of the proposed reflective resonance MM based sensor (without sam

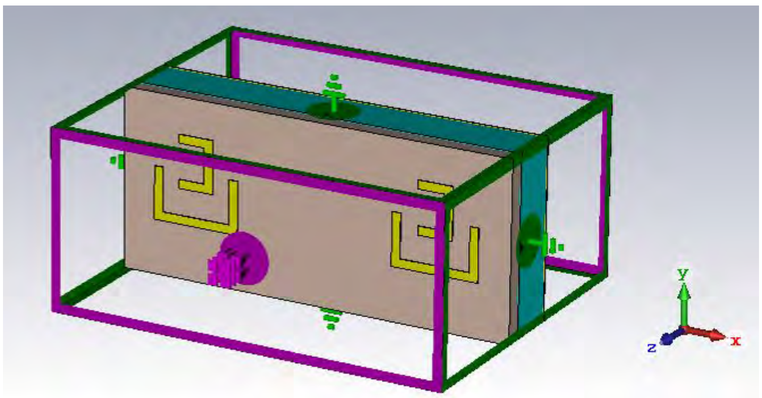

Figure 3. Boundary conditions for the x, y and z axes of the proposed reflection resonance MM based sensor

According to our literature and market research, we observed that sunflower oil is one of the most economical and one of the most adulterated oils with olive oil [19]. Based on this observation, we determined the dielectric coefficients of the samples using a calibrated network analyzer (Keysight-model N9918A) that available in our laboratory (Figure 4) and an open-ended coaxial dielectric probe kit (Keysight Technologies- Model no: N1501A) with calibration steps such as air, short circuit and water. We determined the dielectric coefficients of two different brands of sunflower oil and pure olive oil purchased from the supermarket by mixing 10% separately. Complex dielectric coefficients are calculated with the formula $\epsilon = \epsilon' - \epsilon''$. In this formula, ϵ' and ϵ'' denote real and imaginary part, respectively [15].

Figure 4. Experimental setup for dielectric constant measurement of oil samples

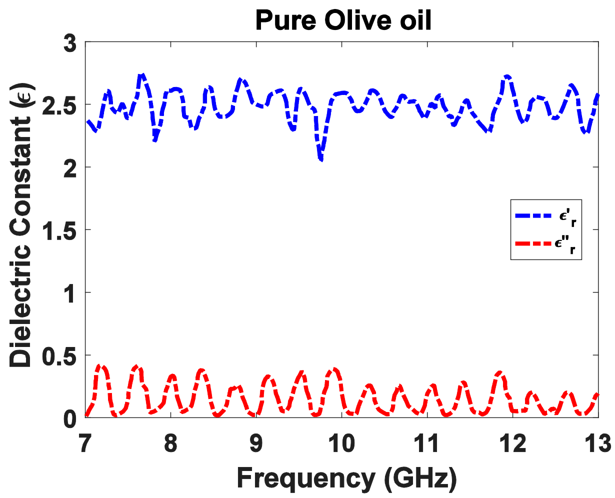

Figure 5. Dielectric probe measurement results (real and imaginary) of pure olive oil purchased from a supermarket chain measured between 7– 13 GHz frequency range

First of all, we carried out dielectric probe measurement of pure olive oil. The average measurement result for pure olive oil was found as $\epsilon' = 2.53$ and $\epsilon'' = 0.19$. Then, we performed dielectric probe measurements for two different sunflower oils (brand a and brand b) that we bought from the supermarket. As can be observed in Figure 6 and Figure 7, the average dielectric constants for brands a and b were determined as [ϵ′=2.77 and ϵ″=0.68] and [ϵ′=2.92 and ϵ″=0.65], respectively. These values, which we have expressed for the dielectric constants of oils, are the average of the values we obtained from the open-ended coaxial dielectric probe set (1001 values).

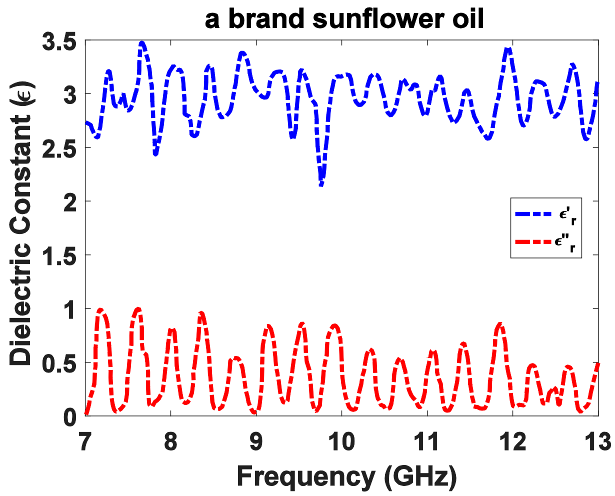

Figure 6. Dielectric probe measurement results (real and imaginary) of sunflower oil of brand a purchased from a supermarket chain measured between 7– 13 GHz frequency range

In order to test the sensitivity of proposed MM-based sensor, we defined the dielectric constants (ϵ′, ϵ″) of the samples to the CST program. By replacing the samples we prepared to the sensor layer in the design, we tried to observe whether the proposed sensor detects very small epsilon changes. In the first step, we replaced pure olive oil to the sensing layer, and then we simulated adulteration of 10% 'a' brand sunflower oil with olive oil. The same procedures were repeated for 10% b brand sunflower oil. Although the dielectric coefficients of the oils are very close to each other, the proposed MM-based sensor can detect very small epsilon changes with the resonance frequency shift technique.

3. Simulation Results and Discussion

The resonance frequency of the proposed sensor can be determined by using equation 1.

$$f = \frac{1}{2\pi\sqrt{LC}} \tag{1}$$

As can be understood from Equation 1, it can be seen that the total inductance and capacitance of the proposed sensor is inversely proportional to the resonance frequency of the resonator. From this point of view, these two parameters are very important in determining the sensitivity of the sensor. The working principle of the sensor is related to the interaction between the resonator and the sensing layer [15]. When we look at Figure 8, the resonance frequency of pure olive oil is 10.069 GHz, the resonance frequency of olive oil with 10% a brand sunflower oil is 10.025 GHz, and thus a resonance frequency shift of 44 MHz compared to pure olive oil. In addition, the resonance frequency of olive oil with 10% b brand sunflower oil is 9.939 GHz, and a frequency shift of 130 MHz was detected compared to pure olive oil. As can be observed from Figure 8, the proposed sensor detected the resonance frequencies of three different liquids separately. These results show that the proposed sensor can detect other oils adulterated with olive oil, even if the dielectric coefficients are very close. Thus, we proved that sunflower oil adulteration, which is the most used oil for adulteration with olive oil, can be observed with the resonance frequency shift method by means of the MM-based new generation microwave sensor.

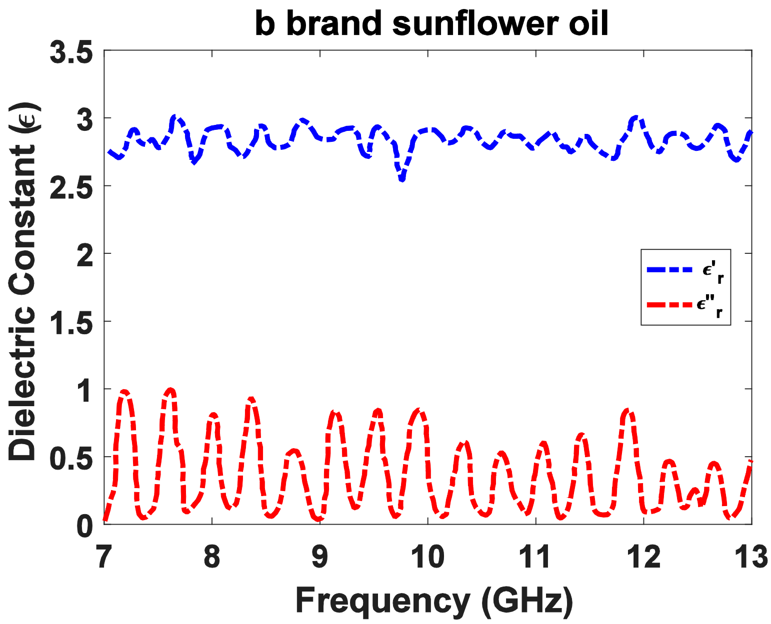

Figure 7. Dielectric probe measurement results (real and imaginary) of sunflower oil of brand b purchased from a supermarket chain measured between 7– 13 GHz frequency range

The resonance frequencies, dielectric constants and frequency shifts of the samples according to pure olive oil are presented in Table 1. According to our inference from the table 1, when the real dielectric constants of the samples increase, the resonance frequencies decrease. Since capacitance is directly proportional to electrical permittivity, any increase in dielectric parameters results in increased effective capacitance of the resonator. Therefore, increasing the capacitance causes the resonance frequency of the sample to decrease [15]. Thus, our results are verified by equation 1.

Table 1. Dielectric constants of samples, resonance frequency and resonance frequency shifts with respect to pure olive oil.

Sample	(ϵ', ϵ'')	Resonance Frequency (GHz)	Frequency Shift (MHz)
Pure Olive Oil	(2.53, 0.19)	10.069	0
10% adulteration (a brand)	(2.77, 0.68)	10.025	44
10% adulteration (b brand)	(2.92, 0.65)	9.939	130

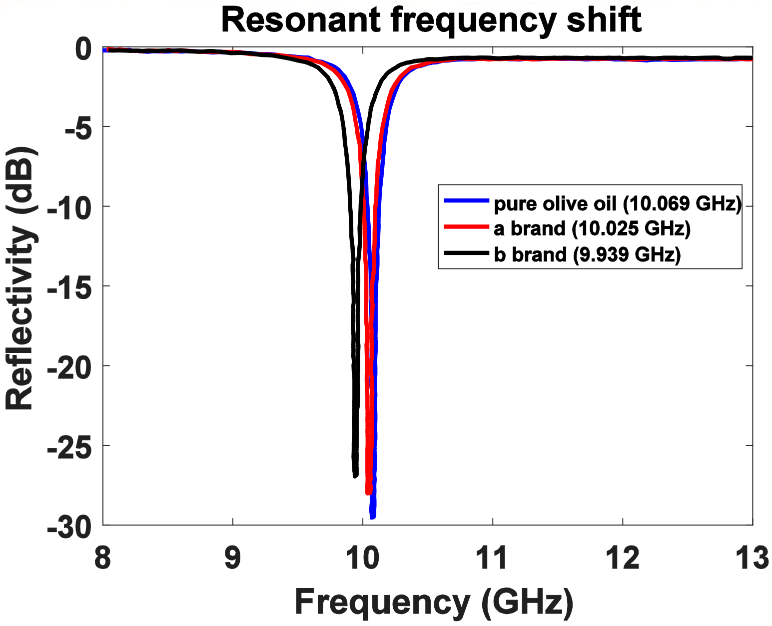

Figure 8. Simulation results of pure olive oil and samples with 10% a brand and 10% b brand sunflower oils adulterated with pure olive oil

4. Conclusions

The metamaterial-based microwave sensor is designed and simulated for the detection of adulteration of liquids (oil) in the x band frequency region. Although the dielectric coefficients of the samples are very close to each other, the proposed sensor detected a frequency shift of 44 MHz and 130 MHz for different brand adulteration process. The simulation results for the proposed sensor were analyzed and interpreted. We foresee that the proposed sensor will be in demand for industrial applications, especially for liquid contamination detection.

Acknowledgments: H. Korkmaz acknowledges the Scientific and Technological Research Council of Turkey (TUBITAK) BIDEB 2211/C program for supporting his studies.

References

[1] D. L. García-González, R. Aparicio-Ruiz, and R. Aparicio, “Olive Oil,” Gourmet Heal. Spec. Oils, pp. 33–72, 2009, doi: 10.1016/B978-1-893997-97-4.50007-3.

[2] A. Vivek, K. Shambavi, and Z. C. Alex, “A review: metamaterial sensors for material characterization,” Sens. Rev., vol. 39, no. 3, pp. 417–432, 2019, doi: 10.1108/SR-06-2018-0152.

[3] Aman, V. Singh, Nilotpal, and S. Bhattacharyya, “A free space frequency-time-domain technique for electromagnetic characterization of materials using reflection-based measurement,” Int. J. RF Microw. Comput. Eng., vol. 31, no. 1, pp. 1–12, 2021, doi: 10.1002/mmce.22490.

[4] M. Bakir, M. Karaaslan, F. Dincer, O. Akgol, and C. Sabah, “Electromagnetic energy harvesting and density sensor application based on perfect metamaterial absorber,” Int. J. Mod. Phys. B, vol. 30, no. 20, 2016, doi: 10.1142/S0217979216501332.

[5] A. Ebrahimi, W. Withayachumnankul, S. Al-Sarawi, and D. Aboott, “High-Sensitivity Metamaterial-Inspired Sensor,” IEEE Sens. J, vol. 14, no. 14(5), pp. 1345–1351, 2014.

[6] Y. I. Abdulkarim et al., “Utilization of a triple hexagonal split ring resonator (SRR) based

metamaterial sensor for the improved detection of fuel adulteration," J. Mater. Sci. Mater. Electron., vol. 32, no. 19, pp. 24258–24272, 2021, doi: 10.1007/s10854-021-06891-6.

[7] M. Karaaslan and M. Bakir, "Chiral metamaterial based multifunctional sensor applications," Prog. Electromagn. Res., vol. 149, no. July, pp. 55–67, 2014, doi: 10.2528/PIER14070111.

[8] C. Liu and F. Tong, "An SIW Resonator Sensor for Liquid Permittivity Measurements at C Band," IEEE Microw. Wirel. Components Lett., vol. 25, no. 11, pp. 751–753, 2015, doi: 10.1109/LMWC.2015.2479851.

[9] H. Lobato-Morales, A. Corona-Chavez, J. L. Olvera-Cervantes, R. A. Chavez-Perez, and J. L. Medina-Monroy, "Wireless sensing of complex dielectric permittivity of liquids based on the RFID," IEEE Trans. Microw. Theory Tech., vol. 62, no. 9, pp. 2160–2167, 2014, doi: 10.1109/TMTT.2014.2333711.

[10] T. S. Almoneef and O. M. Ramahi, "A 3-dimensional stacked metamaterial arrays for electromagnetic energy harvesting," Prog. Electromagn. Res., vol. 146, no. May, pp. 109–115, 2014, doi: 10.2528/PIER14031603.

[11] M. Mrnka, P. Vasina, M. Kufa, V. Hebelka, and Z. Raida, "The RF Energy Harvesting Antennas Operating in Commercially Deployed Frequency Bands: A Comparative Study," Int. J. Antennas Propag., vol. 2016, 2016, doi: 10.1155/2016/7379624.

[12] M. Schüßeler, C. Mandel, M. Puentes, and R. Jakoby, "Metamaterial inspired microwave sensors," IEEE Microw. Mag., vol. 13, no. 2, pp. 57–68, 2012, doi: 10.1109/MMM.2011.2181448.

[13] D. Shrekenhamer, W. C. Chen, and W. J. Padilla, "Liquid crystal tunable metamaterial absorber," Phys. Rev. Lett., vol. 110, no. 17, pp. 1–5, 2013, doi: 10.1103/PhysRevLett.110.177403.

[14] A. Vora, J. Gwamuri, N. Pala, A. Kulkarni, J. M. Pearce, and D. O. Güney, "Exchanging ohmic losses in metamaterial absorbers with useful optical absorption for photovoltaics," Sci. Rep., vol. 4, pp. 1–13, 2014, doi: 10.1038/srep04901.

[15] Y. I. Abdulkarim et al., "Design and study of a metamaterial based sensor for the application of liquid chemicals detection," J. Mater. Res. Technol., vol. 9, no. 5, pp. 10291–10304, 2020, doi: 10.1016/j.jmrt.2020.07.034.

[16] N. K. Tiwari, S. P. Singh, and M. J. Akhtar, "Novel Improved sensitivity planar microwave probe for adulteration detection in edible oils," IEEE Microw. Wirel. Components Lett., vol. 29, no. 2, pp. 164–166, 2019, doi: 10.1109/LMWC.2018.2886062.

[17] T. Wu, "Three-Dimensional Electromagnetic Parametric Modeling and Implementation of Miniaturized Lumped-Element PD Based on Symmetrical Configuration," p. 573185, 2022.

[18] E. M. Eldesouki, K. M. Ibrahim, and A. M. Attiya, "On the applicability of numerical tools for simulating wave-ports close to the cutoff frequency," Int. J. Electr. Comput. Eng., vol. 12, no. 2, pp. 1724–1731, 2022, doi: 10.11591/ijece.v12i2.pp1724-1731.

[19] E. Casadei et al., "Emerging Trends in Olive Oil Fraud and Possible Countermeasures," Riv. Ital. delle Sostanze Grasse, vol. 98, no. 4 Special Issue, pp. 252–254, 2021.

NOISE PREDICTION AND CONTROL UNDER JORDANIAN CONDITIONS

Khair Jadaan [1], Dania Alameh [2*], Mais Al-Abbadi [2], Baraa Al-Zaharna [2], Dareen Abu srour[2], Mohammad Obaid[3]

[1] Professor, University of Jordan, Civil Engineering Department, Amman, JORDAN.
[2] Research associate, University of Jordan, Civil Engineering Department, Amman, JORDAN.
[3]PhD candidate, Budapest University of Technology and Economics, HUNGARY.
*alamehdania97@gmail.com

Abstract

The transportation sector is growing rapidly in Jordan, and the number of vehicles on roads is increasing at a very fast rate leading to overcrowded road network, and serious environmental pollution in Amman, the capital of Jordan. Noise is one of the environmental pollutants encountered in daily life which has become a major concern of communities living in the vicinity of major highway corridors.

In this study, a noise prediction model based on the British Calculation of Road Traffic Noise (CRTN) method is developed allowing for the prediction of traffic noise level along busy urban arterials under local conditions. Total vehicle volume/hour, percentage of heavy vehicles, and average vehicle speed are the main model input parameters. The results of the study show that the CRTN noise prediction method can be applied satisfactorily under Amman's traffic conditions.
The model which was generated using multiple linear regressions for predicting L10 (1hr) gave an average error equal to 2.6 % for day time and 3.9% for night time which is a better result than CRTN model. Consequently, appropriate noise control and mitigation measures are recommended.

Keywords: Traffic noise, Modelling, Mitigation measures, JORDAN.

1. Introduction

The daily activities of urban communities have been invaded by noise from different sources with traffic noise being reported as the major source of the urban noise pollution [3] Recent studies have shown that noise can negatively affect human health and behaviour on the short and long scales [1, 2, 3, 4]. Noise levels were also found to have significant costs on surrounding properties as an indirect negative effect [5]. noise levels were also found to have significant costs on surrounding properties as an indirect negative effect especially house prices [2] In a recent study on the impact of noise pollution in Amman, various methods used to devise a monetary value to traffic noise in Jordan concluded a minimum-maximum band of JD 54 million-JD 170 million equivalent to $81million -$255 million annual cost [3].

One of the most known models to predict traffic noise levels is the British Calculation of Road Traffic Noise model (CRTN) which predicts the basic level L10 percentile and considers correction values due to several factors [6].

Federal Highway Administration (FHWA) Traffic Noise Model calculates noise level through a series of adjustments to a reference sound level. The reference sound level (L_O) is the energy mean emission level which is determine through field of individual vehicles pass by for each vehicles type (cars, medium trucks, heavy trucks). Adjustments are then made to this level to account for traffic movements, varying distances of receivers from the roadways and for barriers [7].

In India, noise prediction has been done on the basis of two models, FHWA and CRTN models. However, FHWA model results are found close to Indian conditions. Comparative paired t test was used on the FHWA model in which an equation for highway noise prediction for Indian conditions has been calibrated [8].

A study was carried out to develop a noise prediction model for Amman traffic conditions which took into account incorporated variables describing traffic and site conditions including traffic volume, composition and speed, gradient, and distance from the source as affecting factors, the trial model expresses noise level by the index L10 (1hr) [9]. The model was found to satisfactorily predict noise levels under Jordanian conditions

The issue of traffic noise in Jordan has been drawing an increasing attention over the last few years, due to its increasing magnitude, yet few comprehensive studies were carried out to accurately describe the current and the predicted magnitude of the problem, predict it's future impact and identify effective mitigation measures. Few studies on the same problem were conducted in Jordan. The attitudes of Jordanians toward traffic noise were investigated in a study by Jadaan and Dakhlallah (2005). The study was conducted along urban arterials in Amman, and the result indicate that traffic noise levels exceeded the permitted maximum levels. This issue was so annoying that more than half of the residents considered moving to a quieter area because of it [4].

This study tries to bridge this gap and investigates the magnitude of the problem in Amman, the capital of Jordan, develop a noise prediction model and identify the most effective mitigation measures.

2. Materials And Methods

In order to assess the distribution of noise level, field level noise monitoring was carried out in major noisy area of 20 locations within the Amman city. These sites were selected to represent major roads near to various residential areas of the city, which currently suffer from persisting traffic noise. Description of the selected sites is given in Table 1.

Traffic Noise measurement were measured during the 2 peaks periods in Amman city, the morning peak from 7:00 to 8:00 am and the night peak from 7:00-8:00 pm. A Bruel and Kjaer 2215 precision sound level meter was used for measuring the noise level L10 (1hr) noise level. All measurements were taken in a clear and sunny working days. The noise level meter has been planted 3.5m away from the near side curb of the road and 1.2 m above pavement level.

Noise measurements were taken as L10 (1hr) which is is the noise level that exceeded for 10% of the time of the measurement duration. Noise measurements were taken in decibel unit with weighting “A” which is the nearest weight to perceived by the human ear dB(A).

Classified manual counts of traffic volume were conducted at the selected locations by counting vehicles for both selected morning and evening intervals. Jordanian Traffic Institute has provided all the required speed data for each location in which they used a Laser Speed Detection Radar LTI 20-2 for the speed measurements.

Table 1. Selected sites.

Location ID	Location
1	Wasfi Al Tal Street
2	Al Sharif Naser Street
3	Princess Basma Street
4	Al Istiqlal Street
5	Abu Nsair Street
6	Al Madenah Al Munawarah Street
7	Airport Road
8	Al Sakhra Al Mosharafah Street
9	Queen Rania Al Abdallah Street
10	King Abd-Allah II Street
11	Prince Ali Bin Hussien Street
12	Prince Shaker Street
13	Al Sina'a Street
14	Jordan Street
15	Al Mahatta Street
16	King Hussain Street
17	Khalil Al Saket Street
18	Al Qahrah Street
19	Khaled Ben Al waled Street
20	Zahran Street

Google Earth was used for the measurement of the gradient for each location. The gradient varied between 0.30% at Al- Sakhra Al Mosharafa Street to 6.00% at King Hussain Street and all of the selected locations have a hard bituminous ground surface.

3. Development of Amman Noise Prediction Models

The basic elements of traffic noise modeling are the traffic source levels and the propagation or attenuation of sound between traffic and receiver. Typical source related inputs to traffic noise models are the speed and volume of vehicle types, operating mode of the vehicles and the length of roadway with line of sight to the receiver location. Propagation related inputs include the acoustic characteristics of the ground, the number of lanes of travel, site geometry and topography and the type of geometry of any barriers or buildings present.

The UK CRTN algorithm [6] is one of the most widely used models for the estimation/prediction of road traffic noise in urban areas. CRTN model predicts the level L10 percentile and considers correction values due to several factors such as the percentage of trucks, the distance between source and receiver, sound reflections on the surfaces, sound propagation and phase speed.

CRTN predicts noise level by calculating the basic noise level using equation 1 which depends on the flow in veh/hr (q) and assumes that the basic speed = V = 75 km/hour, the Gradient (slope) of the road = 0% and percentage of heavy vehicle = P = 0%.

$$L10 \text{ (hourly)} = 42.2+10 \log10 q \text{ dB (A)} \tag{1}$$

The next step is to calculate the necessary corrections for the various site conditions as explained above and add them to the calculated basic noise level.

Followings are steps followed for the development of Amman Road traffic noise model:

1. Data collection: data were collected for various parameters including Date & Time, Total vehicle count, Q (veh/hr), Average Speed, V (km/hr) Equivalent noise level, Leq dB(A), Gradient of the road, G (%), and Percentage of heavy vehicles, P (veh/hr).
2. Data Analysis: Analysis of the collected data was carried out using MICROSOFT EXCEL to find out the correlation between the various parameters and the noise level.
3. Plotting of graphs for Leq vs. Q, Leq vs. V, Leq vs. G, and Leq vs. P from the scatter diagram it is possible to visualize a nature of relationship between variables. Multiple regression analysis was done for Leq (1hr) with independent parameters (Q, P, V, and G) for day time and night time separately.

4. Results and Discussion

The day time statically noise level L10 (1hr) throughout Amman has an average of 79 dB(A) ranges between 71 dB(A) and 86 dB(A). The night time average was found to be 77 dB(A) with a range between 66 dB(A) and 86 dB(A).

Result of CRTN model is shown in table 2. Day time which showed an average error with the prevailing noise levels equals to 3.2% and night time showed an average error equal to 5.8%. These results show a high accuracy in using the British CRTN model for Amman traffic conditions.

A multiple linear regression model was developed for predicting equivalent noise level, and it was found that the model which has the highest capability has the following form:

For Day Time:

$$Leq= 64.42 + 0.00094Q + 0.0728V + 0.495P + 0.696G \tag{2}$$

For Night Time:

$$Leq= 66.97 + 0.00185Q + 0.107V - 0.358P + 0.687G \tag{3}$$

Where:

Leq: The equivalent noise level (dB(A)).

Q: Traffic volume (veh/hr).

P: Percentage of heavy vehicle (%).

V: Average speed (Km/hr).

G: Road gradient (%).

The developed model was statistically significant with a coefficient of multiple determination (R^2) equals 0.715 for day time and equals 0.33 for night time.

The developed models were used to predict noise levels for the traffic and geometric data collected. The comparison showed an average error equals to for day time and for night time. Table 3 shows the comparison between the prevailing noise levels and the predicted levels from the developed models.

Table 2. Comparison between prevailing noise levels and predicted noise levels using CRTN model for the selected sites for day and night times.

Location ID	Day Time		Night Time	
	Prevailing L10 (1hr)	**L10 (1hr) CRTN**	**Prevailing L10 (1hr)**	**L10 (1hr) CRTN**
1	78	78.2	76	81.9
2	77	80.5	79	82.2
3	75	79.5	66	78.9
4	85	84.1	79	82.5
5	81	78.2	79	79.7
6	76	82.0	72	81.9
7	86	84.9	84	83.9
8	79	78.5	71	79.0
9	78	85.6	78	84.0
10	84	86.1	82	84.5
11	77	78.9	76	78.8
12	71	75.6	77	76.2
13	79	78.8	76	79.2
14	83	82.6	80	83.4
15	86	83.7	78	83.7
16	82	79.8	80	78.3
17	73	73.9	75	74.5
18	76	75.3	76	76.0
19	77	80.4	71	80.0
20	85	84.1	86	81.1
	Average error = 3.2%		Average error = 5.8%	

5. Traffic Noise Control

Several mitigation measures are available for the control of traffic noise including:

1) The installation of barriers between the noise source and the receiver for the proper attenuation of noise levels is the most common noise abatement approach. In extreme cases, two layers of porous asphalt are employed as a noise-reducing strategy in place of noise barrier walls.

Noise barriers were found to be highly effective and can reduce noise level by an amount ranging between 5 and 20 dB(A) [7]. In addition, barriers suit Amman's Road network conditions where the right of way along many busy streets is limited.

Various factors need to be considered to produce an acoustically effective barriers i.e., a barrier that provides the required noise reduction without being "over-designed". The noise reduction goal is the first and an important element of the barrier design process which influence the acoustical considerations such as height, length, location and the material of the barrier.

Noise barriers 3m high were found adequate for the current but not for future conditions when more effective barriers (5m high for example) will be required. However, a more comprehensive study into the present and future magnitudes of the problem, potential mitigation measures and their cost estimates is necessary for appropriate decision-making.

Table 3. Comparison between the prevailing noise levels and the predicted noise levels from the developed models.

Day Time		**Night Time**	
Prevailing L10 (1hr)	**L10 (1hr) predicted**	**Prevailing L10 (1hr)**	**L10 (1hr) predicted**
78	75.7	76	77.3
77	76.6	79	78.0
75	78.4	66	73.3
85	84.8	79	79.0
81	79.5	79	77.0
76	77.3	72	79.2
86	85.2	84	80.3
79	77.0	71	75.1
78	82.1	78	81.1
84	86.0	82	80.7
77	78.4	76	77.0
71	73.3	77	72.7
79	82.7	76	71.7
83	81.7	80	79.7
86	84.0	78	75.4
82	79.3	80	76.5
73	74.4	75	74.5
76	74.6	76	75.1
77	75.8	71	76.1
85	80.7	86	79.0
Average error = 2.6%		Average error = 3.9%	

Other less costly mitigation measures include:
2) Natural barriers using plants like the hibiscus and Eugenia can be placed at a sufficient height and density to absorb sound together with serving aesthetic purposes [9].

3) A dense belt of trees and shrubs (30 m wide) was found to possibly reduce sound levels by as much as 4-8 dB. Such hedges, trees and shrubs can be planted adjacent to highways in order to reduce traffic noise.

4) The use of earthberms.

5) Noise-absorbing materials could be used in the design of buildings for the walls, doors, windows, ad ceiling.

6) Malaysia has implemented rubber road construction in several places, but it is in the trial stages and it was found that rubber road yield up to 7 dBA noise reduction [10].

6. Conclusion

This study investigates the levels of traffic noise along Amman urban road network, The study concluded that that the day time statically average noise level L10 (1hr) throughout Amman has increased from 69 dB(A) in 2005 study to 79 dB(A) and ranging between 71 dB(A) to as high as 86 dB(A). This may be a result of increasing trips, aging pavement, older vehicles.

Traffic noise levels were predicted using (CRTN) prediction model in order to validate it for the prediction of noise appropriate prediction under Amman traffic conditions. The results of the study show that the CRTN noise prediction method can be applied satisfactorily under Amman's traffic conditions with a mean prediction difference of only 2.2 dB(A). An average error equals to 3.2%for day time and 5.8% for night time.

Finally a model was generated using multiple linear regressions for L10 (1hr). The developed model was used to predict the noise level for each location and it gave an average error equals to 2.6 % for day time and 3.9% for night time which is a better results than CRTN model.

References

1. Banihani, Q. Jadaan, K.S. Assessment of Road Traffic Noise Pollution at Selected Sites in Amman, Jordan: Magnitude, Control and Impact on the Community. Jordan Journal of Civil Engineering. 2012; 6: 267-278.
2. Banerjee D. Research on road traffic noise and human health in India: Review of literature from 1991 to current. Noise Health 2012;14:113-8.
3. Jadaan, k., Gammoh, H., Okasha, A., Breizat, E., and Hadidi, T. Evolution of Traffic Noise Impacts In Amman, Jordan, International Journal of Automotive Engineering and Technologies, 2015; 4 (1): 7-11
4. Al-Dakhlallah, A., and Jadaan, K, Attitudes of Jordanian Population Towards Traffic Noise Int. J. of Appl. Sci. Eng. 2005, 3 (2):145-150.
5. Goussous, J., Al-Dakhlallah, A. Jadaan, K., and Al-zioud, M. Road Traffic Noise in Amman, Jordan: Magnitude and Cost investigation. Journal of Traffic and Logistics Engineering, 2014; 2: 104- 107.
6. Department of Transport Welsh Office, 1988, Department of Transport Welsh Office, 1988. Calculation of Road Traffic Noise. HMSO Books, London, UK.
7. Federal Highway Adminstration (FHWA), 2010, Highway Traffic Noise. FHWA-HEP-10-25.
8. Mukesh Chandra Mishra, 2010, Study and Development of road traffic noise model- A Thesis, Thapar University, Patiala, Page No.1-45.
9. Jadaan, K. and Okasha, A., Developing a Traffic Noise Prediction Model For Jordanian Conditions. Journal of Geotechnical and Transportation Engineering, 2016,2 (1):6- 13
10. Haron1 Z, Darus N, Yahya K, Halim H, Mazlan A,, Azri M, Zanariah H, 2019 Review on Traffic Noise Problem in Malaysia , IOP Conf. Series: Earth and Environmental Science 220.

AUTOMATED DRUG COLLECTION AND SERVICE OPERATIONS IN A PHARMACY ROBOT: A SOFTWARE APPROACH TO MEASURE THE DIMENSIONS OF MEDICINE BOXES

SİNAN ÇOLAK [1], ONAT HALİS TOTUK* [1,2], ÖZGÜN SELVİ[2]

[1] EBOT, Ankara, TURKEY.
[2]Çankaya University, Engineering Faculty, Mechanical Engineering Department, Ankara, TURKEY.

Abstract

This study presents a series of software works of computer vision to increase the reliability and speed of the automatic pharmacy robot called EBOT. Between the industrial shelves with compartments of varying widths, there is a receptacle that travels with a cartesian panel to handle the collection and service activities according to a specific command. This study uses specific applications to accomplish digital size measurement of medicine boxes, shelf number recognition, and data matrix decoding. A computer vision method has been produced that can measure the actual dimensions of the medicine boxes with an error rate of 1-1.5 millimeters. In addition, software has been developed that digitally analyzes and records the data matrix of drugs over the image according to Turkish Medicine and Medical Devices Agency standards. It was observed that the error rate was between 0.83% and 4.2%, which is an acceptable percentage for the digital measurement process thanks to the adequate space inside the compartments. Also, our software work is successful in terms of decoding the data matrix since there is no loss of information. Finally, another software for reading the shelf numbers handles the process fluently thanks to the fact that there is no missing or incorrect digit extraction.

Keyword: Digital Image Processing, Image Processing Applications, EBOT

1. Introduction

With technological developments, the use of software in design and analysis is increasing rapidly. Computer programs play an active role in design and analysis, minimizing the margin of error. Many applications like image understanding, object recognition, noise removal, visual data modeling, edge detection, and many others can be run thanks to image processing. This study uses specific applications to accomplish digital size measurement of medicine boxes, shelf number recognition, and data matrix decoding.

Several studies have been made in the area of digital size measurement. In the study of Işık and Güler (2003) [1], digital measurement of product dimensions while evaluating agricultural products is done using a camera. They used a measurement plate in a digital environment to compare with an apple (inside the image) to determine the dimensions. In a similar study, Yılmaz [2] aimed to digitally measure product dimensions in industrial production. To accomplish this, A CMOS camera has been used to track the movable panel. This work was completed by comparing the coordinate information obtained from the two-axis motion system via PCI and the measurement information obtained from the image taken with the camera.

Yanık and Haydar (2021) [3] have evaluated the digital distance measurement methods in two parts in terms of using pixels (with mono and stereo cameras) and without using pixels. Using different geometric approaches (like camera angles, distances, etc.), they have discussed the term “image-meter, " a digital distance measurement method.

In the second aspect of this study, which is number recognition from an image, there are some certain studies as well. In Samtaş and Gülesin (2012) [4], image processing techniques were analyzed and evaluated in different areas. One of the techniques that have been mentioned was the recognition of car plate characters which includes digits as well while discussing defense and security applications. A similar study about plate character recognition via image by using a CNN model called M-BESA has been done by Bayram (2020) [5], and the motivation of this project is the development of license plate control systems needed depending on the increase in the number of vehicles. Another study for this aspect is about utilizing various models for handwritten digit recognition developed with the help of a discriminant classifier to create boundaries between different characters. This work has been done by M. Revow, C. K. I. Williams, and G. E. Hinton (1996) [6], which is more relatable to our study in terms of the specified area since it is about recognizing numbers in a digital environment. In a related study, Lauer, F. & Suen, C. Y,. and Bloch, G. (2007) [7] focused on developing a convolutional neural network to extract and predict handwritten digits with the method of implementing a support vector machine on LeNet5 CNN model which is also a comparable work with ours.

The final and third aspect of this study is decoding the Data Matrix of a medicine box from an image. Of course, there are several works done in this scope as well. One of the studies has been accomplished by Brylka, R. & Schwanecke, U. and Bierwirth, B. (2020) [8] to decode a barcode from an image. The motivation of this study is to develop a model that makes the correct localization and decoding of the complete information even if the image is blurred or noisy. They used a real-time object recognition algorithm to do this work. Another study on this scope has been done by Y. Liu, Yang and M. Liu (2008) [9] to create a mobile system that recognizes a QR code from an image and decodes it. The method includes the techniques of binarizing, locating, segmenting, and decoding the QR Code from an image.

In this study, using digital image processing techniques, measuring the actual dimensions of the medicine box from an image with a low margin of error (the measurements obtained are compared with the measurements made by hand) has been aimed. Secondly, reading and saving the Data Matrix code of the medicine box, which is a 2-dimensional barcode type consisting of black and white cell arrays and square or rectangular modules (as indicated in “Drug Tracking System” [16]), in accordance with TITCK (abbreviation of “Turkish Medicines and Medical Devices Institution”) [15] standards using specific libraries have been intended. Finally, reading the shelf numbers from an image and displaying it as a digital output to the user is also aimed.

2. Materials and Methods

In this part, the 3 stage of the software work and their methodologies will be explained. In the first section, the geometric and digital approaches will be expressed. The other two sections will present the workflows, the use of open-source libraries, and their functionalities.

2.1 Size Measurement on Image

Measuring the medicine's dimensions in the robot's receptacle is a process required to determine which shelf the medicine will go to, and it is a process that ensures that the shelves of different widths keep the correct medicines.

Figure-1: Example Medicine Boxes with Visualization of Intended Measurements

With image processing, the dimensions of the medicines are measured in pixels, and then the camera image and the actual measurements are calculated using the reference points. This situation made it possible to control which shelf a medicine can enter on the panel. Since the dimensions of the shelves are different from each other, it is aimed to prevent a possible loading error by calculating the dimensions of the medicine.

To perform this operation, the image processing library "OpenCV" (an open-source library that is used in real-time computer vision applications) belonging to the "Python" language was used with the guidance of its official source code [13]. OpenCV has let us detect the image's rectangles (medicine boxes). Still, to perform rectangle detection better, the image has been converted into a binary image (gray-scaled image), as Sahir suggests in "Canny Edge Detection with Computer Vision" [10]. After detecting the rectangles, it was calculated with the ratio of the actual dimensions of the receptacle to the digital size (per pixel) with an error rate of 1-1.5 millimeters. The medicines in the receptacle were displayed in 2 dimensions.

In order to measure the 3rd dimension (depth) of the medicine, it is planned to use an analog distance sensor inside the receptacle chamber to see it from the opposite side. It aims to find the depth by subtracting the distance between the medicine box and the sensor; from the sensor's actual distance to the chamber's wall (which must be calculated when the chamber is empty).

The dimensions in the digital environment were calculated using the equations (1), (2), and (3) below. In this calculation, a simple geometric equation is used by expanding the ratio of the medicine box (based on the chamber wall) and the chamber wall to each other in the digital environment. by the distance of the box from the camera. Finally, the dimensions of the medicine were calculated digitally, taking into account the actual dimensions of the chamber. In order to measure the dimensions of the medicine box in pixels, the edge recognition (rectangle recognition) algorithm was used, and this data was proportional to the overall image. Edge detection/Rectangle detection is a method that aims to identify points in a digital image where image brightness changes sharply or, more formally, where discontinuities exist. After detecting the points, the distance between each location (in the cartesian coordinate system) was calculated in terms of pixels thanks to the "Euclidian Distance" technique. Then the lengths of the virtual box were ready to rate with the whole background (with known dimensions in the real world) in pixels.

$$A = \frac{Dimensions of Medicine \in Pixels(width,height)}{Dimensions of Receptacle \in Pixels(width,height)} \tag{1}$$

B = The Real Dimensions of Receptacle.

$$C = \frac{DistanceBetweenMedicine \wedge Camera}{DistanceBetweenChamberWall \wedge Camera} \tag{2}$$

$$Actual\ Size\ Measured\ From\ Image = A * B * C \tag{3}$$

Figure-2: Example of Dimension Measurement with Image Processing

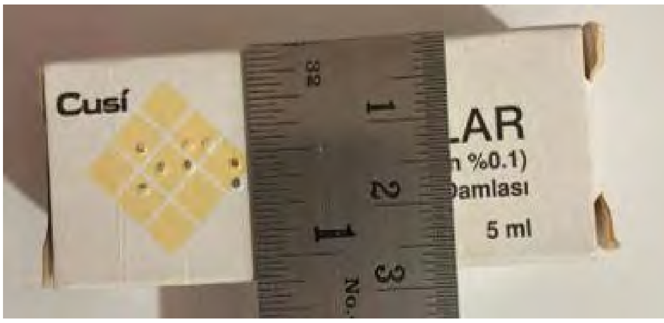

Figure-3: Real Size Measurement (Horizontal)

Figure-4: Real Size Measurement (Vertical)

In the first image, the dimensions of the medicine box in the digital environment were calculated. In the other two images, the actual dimensions were measured. It has been observed that the dimensions calculated in the digital environment and the exact dimensions are consistent.

2.2 Number Recognition on Image

This process is necessary for the digital recognition of the shelves on the panel, and the "PyTesseract" library is used to recognize the shelf numbers. Python Tesseract OCR (Optical

Character Recognition) transfers the texts in an image to the computer environment. Tesseract has constructed a recognition engine built on Long-Short Term Memory (LSTM). A type of recurrent neural network is the LSTM (RNN). Recurrent neural networks identify patterns in data and utilize them to anticipate the following most likely scenario. In this method, every digit has been expressed with their numerical representation with a matrix, as seen in the example figure below. So, the inputs will be evaluated with the respective form and predicted.

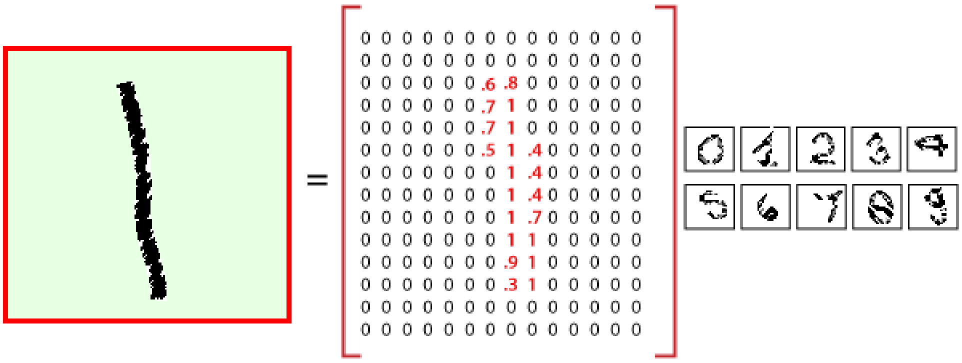

Figure-5: Example of Numerical Representation of a Digit Inside a Matrix (TensorFlow MNIST dataset in CNN [20])

In this study, the dataset consists of 10 different classes, and each class represents a number (0, 1, 2, 3, 4, 5, 6, 7, 8, 9). This library is a deep learning library and has a dataset. To increase the consistency of the process, the data set is supplemented with sample shelf numbers.

The library itself is trained with this dataset and is used as a deep learning model so that the numbers on the image can be transferred to the digital environment in a meaningful way.

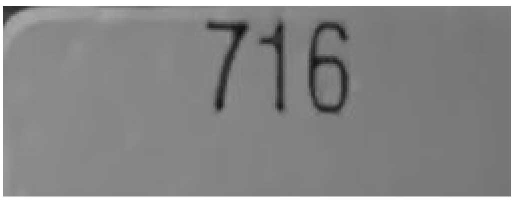

Figure-6: Sample Shelf Number

Figure-7: Example of Number Recognition from Image

2.3 Data Matrix Decoding on Image

A specific library, which was installed for Data Matrix analysis over Python, called "Pylibdtmx," was used. Pylibdtmx is a library compatible with Python programming language, and allows the reading and writing the information encoded inside the data matrix. The specific details on this library and its usage has been done according to its source code presentation [11].

The Data Matrix on the medicines contains the following information about the drug, according to TITCK standards (should not be confused with barcode or QR code);

- Expiration date,
- Party number,
- Serial number,
- Barcode number.

Figure-8: Example of QR Code Decoding

After the Data Matrix analysis is done, thanks to the “Python-OS” module, which is a built-in module in Python that allows us to perform operations on files and directories efficiently, the information can be entered into a notebook on the desired file path, and the operation date (day, hour, minute, seconds) was recorded. In this way, the track of the operated products is facilitated by recording. The source of the OS module (os - Miscellaneous operating system interfaces) [18] has been considered to accomplish the file operations.

3. Results and Discussion

In this project, we have created a series of software works of computer vision to speed up, increase credibility and automatize the collecting and serving processes of the pharmacy robot called EBOT. This series of software work includes three different stages, which are digitally measuring the medicine boxes (to fit the box inside the compartment that has been mentioned), number recognition (to check the shelf numbers), and data matrix decoding (to confirm the information that has been encoded). Similar works with these stages have been mentioned in the “1. Introduction” part. Of course, there are similarities and differences between those works and ours.

The methods developed for digital dimension measurement on an image are generally similar in calculating the distances within the image. At the same time, the differences occurred considering the methods of getting the actual dimensions. To accomplish this, a reference point must be determined, and the methods may vary depending on the location of the reference or the geometric approach. The size measurement technique in the work of Işık and Güler (2003) [1] is based on the digital comparison of the object whose size is desired to be calculated with the calibration plate inside the image (the actual dimensions are known). This work resembles ours in terms of pixel counting and comparing with a known reference, but, in our work, there is no plate inside the image. At the same time, the camera was calibrated to the whole background (with the known dimensions) inside the receptacle. Also, our objects were not irregular (like an apple) but in a rectangle shape (since they are boxes). So, we used rectangle detection and depth distancing algorithms in our work, which are more compatible with our motivation. The study of Yılmaz [2] aims to measure the dimensions by calculating the distances of the moving objects along with the panel (while having this process done, the actual dimensions are getting known since the movement of the panel has been tracked). The pixel distancing method in this study resembles ours as well. Still, since we do not have any moving panel or object inside the receptacle, the methodology of this work would not apply to our project. Also, line tracking is a more mechanical work because there are sliding objects, but our work is based more on the software side since there is only one known object, and the rest is done with digital algorithms. A different work, done by Yanık and Turan (2021) [3], discusses the geometric approaches for digital distancing, and the depth proportioning part reminds our approach. Still, we have done the depth measurement process by using a measurement sensor, and thanks to the data we had, we could do the geometric proportioning mentioned in the "2.1 Size Measurement on Image" section. Another difference about this work is that our work includes digital size measuring.

The methods created for number recognition from an image are generally similar to each other as well. In the work of Bayram (2020) [5], a CNN model called M-BESA was used to recognize car plate characters (which also includes numbers as well). In our work, another deep learning module called "Tesseract" has been used, which implements an LSTM model (mentioned in "2.2 Number Recognition on Image"). Since we did this project in Python, we had to use an application module with the language. Tesseract module includes a deep learning methodology similar to Revow, Williams, and Hinton (1996) [6], which discusses generative models to recognize handwritten characters. A similar work about handwritten character recognition has been done by Lauer, Suen, and Bloch [7]. Still, since Tesseract is a newer module, it has been getting updated until today in terms of its pre-trained data, making it more reliable.

Finally, there are many examples and libraries for decoding matrices codes, as in the work of Brylka, Schwaneck,e and Bierwirth (2020) [8], which is about camera-based barcode localization and decoding. In a similar study, Y. Liu, Yang, and M Liu (2008) [9] worked on recognizing another type of code, the QR code, and they handled the mobile applications. Yet, in this study, we have used "Pylibdmtx" to decode data matrices since they are included in medicine boxes. Still, we did not need to work on the localization process since the camera calibration had been set to recognize the codes. In addition to this process, an instant data recording system was created with an OS module which is a different procedure than the mentioned works. To sum up, we created a series of digital image processing methods to increase the reliability and speed of the automatic pharmacy robot called EBOT. As far as we know, all the aspects of this work are original and unique.

4. Conclusions

Digital image processing is a computer work that can be used in many industrial applications of computers. It occurs in most technological developments in today's world, as in this study. A computer vision method has been produced that can measure the actual dimensions of the medicine boxes with an error rate of 1-1.5 millimeters. In addition, the software has been developed that digitally analyzes and records the data matrix of drugs over the image according to TITCK standards. Finally, a similar method is used in number recognition and digital transfer processes. It was observed that the error rate was between 0.83% and 4.2%, which is an acceptable percentage for the digital measurement process thanks to the adequate space inside the compartments. Also, the software for data matrix decoding and number recognition worked with no incorrect or lost data with the proper camera calibration.

References

1. Işık, E. , Güler, T. Elma yüzey alanlarının görüntü işleme tekniği yöntemiyle saptanması. Uludağ Üniversitesi Ziraat Fakültesi Dergisi, **2003,** 17(1): 59-64.
2. Yılmaz, M. Kamerali görsel boyut ölçme otomasyonu, EMO.
3. Yanık, H. and Turan, B. Mesafe Ölçümünde Image-Metre: Görüntü İşleme ile Mesafe Tespit Yöntemlerinde Eksik Ne?. IV International Conference on Data Science and Applications (ICONDATA'21), June 4-6, 2021, Turkey, 2021, 474-480.
4. Samtaş, G. & Gülesin, M. (). Sayısal Görüntü İşleme ve Farklı Alanlardaki Uygulamaları . Ejovoc (Electronic Journal of Vocational Colleges), 2012, 2 (1), 85-97.
5. F, Bayram. Derin öğrenme tabanlı otomatik plaka tanıma, Politeknik Dergisi, 2020, 23(4): 955-960.
6. Revow, M. & Williams, C. K. I. and Hinton G. E. Using generative models for handwritten digit recognition, in IEEE Transactions on Pattern Analysis and Machine Intelligence, 1996, 18 (6), 592-606.
7. Lauer, F. & Suen, C. Y. and Bloch, G. A trainable feature extractor for handwritten digit recognition, Science Direct, Pattern Recognition, 2007, 40 (6), 1816-1824.
8. Brylka, R. & Schwanecke, U. and Bierwirth, B. (). "Camera Based Barcode Localization and Decoding in Real-World Applications," 2020 International Conference on Omni-layer Intelligent Systems (COINS), 2020, 1-8, doi: 10.1109/COINS49042.2020.9191416.
9. Liu, Y. & Yang, J. and Liu, M. Recognition of QR Code with mobile phones, Chinese Control and Decision Conference, 2008, 203-206, doi: 10.1109/CCDC.2008.4597299.
10. Sahir, S. (2019, January 27). Canny edge detection step by step in python-computer vision. Medium. Retrieved July 2022, from https://towardsdatascience.com/canny-edge-detection-step-by-step-in-python-computer-vision-b49c3a2d8123
11. NaturalHistoryMuseum. Pylibdmtx/pylibdmtx/tests at master · Naturalhistorymuseum/pylibdmtx. GitHub. 2021 Retrieved July 2022, from https://github.com/NaturalHistoryMuseum/pylibdmtx/tree/master/pylibdmtx/tests
12. Wikimedia Foundation. Kenar Algılama. Wikipedia. 2022. Retrieved July 2022, from https://tr.wikipedia.org/wiki/Kenar_alg%C4%B1lama
13. About OpenCv. OpenCV. (2020, November 4). Retrieved July 2022, from https://opencv.org/about/
14. Rectangle feature. Rectangle Feature - an overview | ScienceDirect Topics. (2022). Retrieved July 2022, from https://www.sciencedirect.com/topics/computer-science/rectangle-feature
15. Wikimedia Foundation. (, April 22). Türkiye ilaç Ve tıbbi cihaz kurumu. Wikipedia. 2022. Retrieved July 2022, from https://tr.wikipedia.org/wiki/T%C3%BCrkiye_%C4%B0la%C3%A7_ve_T%C4%B1bbi_Cihaz_Kurumu
16. İlaç Takip Sistemi (İTS). İlaç Takip Sistemi (İTS). 2017 Retrieved July 2022, from https://its.tiga.com.tr/data-matrix-nedir/
17. "How to measure the real size of an object from an unknown picture?" [Online]. 2022 Available: https://www.researchgate.net/post/How-to-measure-the-real-size-of-an-object-from-an-unknown-picture. [Accessed: 10-Jul-2022].
18. OS - miscellaneous operating system interfaces¶. os - Miscellaneous operating system interfaces - Python 3.10.5 documentation. (n.d.). Retrieved July 2022, from https://docs.python.org/3/library/os.html
19. EBOT. (2022). Retrieved July 2022, from https://www.ebot.com.tr/
20. TensorFlow MNIST dataset in CNN - javatpoint. www.javatpoint.com. (2021). Retrieved July 2022, from https://www.javatpoint.com/tensorflow-mnist-dataset-in-cnn

SURFACE FINISHING OF CEMENTED TUNGSTEN CARBIDE USING ABRASIVE FLOW MACHINING

OMER EYERCIOGLU [1], KURSAD GOV[2], ENGIN TEK [1], M. BURAK TOPARLI[3]

[1] Gaziantep University, Engineering Faculty, Mechanical Engineering Department, Gaziantep, TURKEY.
[2] Gaziantep University, Aeronautics and Aerospace Faculty, Aeronautics and Aerospace Engineering Department, Gaziantep, TURKEY.
[3] Norm Civata R&D Center, Izmir, TURKEY

Abstract

In this article, the abrasive flow machining (AFM) method is used for the surface finishing of tungsten carbide-cobalt (WC-Co) material. A total of six groups of abrasive flow media with different abrasive particle sizes and concentration ratios were used. Aluminum oxide was used as abrasive and a polymer-based carrier was used for the abrasive media. Tungsten carbide specimens were cut by electrical discharge machining and AFM processes were applied at various cycle numbers. Surface roughness and material remove rate were measured before and after processing with abrasive machining, and the variation of surface quality and material remove rate was investigated. The surface roughness values were decreased to (Ra)=0.5 µm levels in about 20 cycles.

Keywords: Abrasive flow machining, tungsten carbide, surface finishing, abrasives, surface roughness

1. Introduction

Despite the new technologies developed in recent years, traditional finishing processes, finishing complex shapes in hard, high strength, heat resistant alloys, die steels and fasteners have not yet reached the desired speeds and quality. Abrasive flow machining (AFM) is an uncommon new technique that has the potential to provide high precision and economical means to finish inaccessible areas and complex internal and external passages. This method has been applied in aviation, aircraft, medical, and other precision manufacturing fields, and successful results have been obtained[1].

The AFM technique has been carried out to enhance the floor integrity of the machined workpiece by the use of numerous machining methods along with milling, turning, grinding, and in particular electric discharge machining (EDM). AFM is used to do away with deburring, polishing, radius, and recast (white) layer [2],[3]. The Abrasive flow machining method enables the surface to be polished as the paste under pressure moves over the workpiece surfaces. Thanks to this method, it has been demonstrated by the studies that the surface roughness values that cannot be obtained with the classical polishing methods or that take a very long time are reached[4].

The main parameters in the abrasive fluid processing method; fluid parameters are classified as process parameters and workpiece parameters[4]. Process parameters; the pressure applied, the number of cycles, and the flow rate and volume of the abrasive paste used. Workpiece parameters; material properties of the workpiece, its geometry, and mechanical processing (turning, milling, electro-erosion, etc.) method. The fluid parameters are viscosity, temperature, abrasive grain size, abrasive ratio, and abrasive type. The most important parameters affecting the surface roughness are considered abrasive parameters [5].

The material to be used in this work is tungsten carbide with 15% Carbon. The composite of tungsten carbide and cobalt (WC–Co) has special importance in the production of cutting tools, dies, and other special tools and components due to its very high hardness and excellent resistance to shock and wear. . It is possible to process this material with some conventional methods; however, the high precision required for machining complex shapes cannot be achieved[5],[7]. Therefore, AFM was applied for surface finishing after EDM cutting.

In another study by Jain et al., a theoretical model was determined in which acceptable results could be obtained, close to the experimental results [8]. In a different study, they determined the parameters that depend on the paste viscosity. Accordingly, paste viscosity; It is directly proportional to the abrasive grain size and inversely proportional to the abrasive ratio and temperature. It has been observed that high viscosity provides higher material removal rate and lower surface roughness value [9]. Flenther and Fioravanti used polyborosiloxane as the polymeric carrier for the abrasive paste. In this study, it has been proven that the abrasive ratio is more effective than the abrasive size and polymetric carrier properties. In different studies using polyborosiloxane, abrasives such as aluminum oxide (AlO2), silicon carbide (SiC), and garnet were used.[10] A study by Gov and Eyercioglu examined the effects of abrasive types on abrasive flow machining surfaces [2]. In a study in which the forces acting on the surfaces during the AFM process were measured, the effects of the abrasive paste parameters on the surface roughness were tested[11].

In this study, AFM application was applied to coarse-grained tungsten carbide alloy with a 15% Carbon ratio using two different sizes of 180 mesh size and 400 mesh size Al2O3 abrasive. An abrasive is produced by mixing the polymer and AL2O3 abrasive at 50%, 60%, and 70% by mass for each mesh size of this abrasive. As a result of this application, the surface roughness and Material Remove Rate (MRR) values of the material were compared.

2. Materials and Methods

2.1 Workpiece Material

The samples were produced from Tungsten carbide material. The samples were cut with EDM from the same stock material as 20x10x5 mm and a total of 36 samples were prepared. Surface measurements and weight measurements were made from all samples before AFM and are given in Table 1. All technical specifications of the sample material are given in Table 2.

2.2 Abrasive Flow Machine

In this study, a two-way AFM processing bench was used. The bench consists of four parts the main body, hydraulic unit, control unit, and cooling unit (Figure 1.). The samples are placed in the pre-prepared dies. These dies are connected to the flow path of the abrasive fluid of the machine and are compressed by means of four pistons (Figure 2). The AFM process consists of two main pistons pushing the abrasive fluid through the die with forwarding and backward movement. The full forward and backward movement of these pistons is called a cycle. In this experimental study, one cycle takes 1.5 minutes.

Table 1. Surface roughness values and weights of samples before AFM.

Specimen No	R_a (µm)	Weight	Specimen No	R_a (µm)	Weight	Specimen No	R_a (µm)	Weight
s1	3,9	13,8883	s13	3,8	12,6032	s25	4,1	12,9724
s2	3,8	13,0023	s14	4,2	12,9795	s26	4,2	13,1516
s3	3,6	13,6090	s15	4,0	13,9230	s27	3,9	12,2252
s4	4,1	13,0377	s16	4,1	13,2264	s28	4,0	14,2198
s5	3,7	12,9573	s17	3,7	12,9687	s29	3,8	13,0917
s6	4,2	13,7179	s18	3,8	13,7182	s30	4,2	13,6462
s7	4,0	13,0721	s19	3,9	13,2783	s31	4,1	13,2332
s8	4,1	13,1673	s20	3,8	13,9637	s32	3,8	13,0771
s9	3,9	12,6757	s21	4,2	12,9919	s33	3,8	13,3118
s10	3,8	14,1594	s22	4,2	13,4144	s34	3,9	13,0329
s11	3,8	12,5368	s23	4,1	13,0420	s35	4,0	12,9458
s12	3,9	13,0551	s24	4,0	13,7214	s36	4,1	13,3831

Table 2. Workpiece Material Properties.

Properties	Unit	Value
Density	*g/cm³*	14
Hardness	*HV 30*	1100
Elastic Modulus	*kN/mm²*	550
WC	*%*	84,55
Co	*%*	15
TiC+TaNbC	*%*	0,45

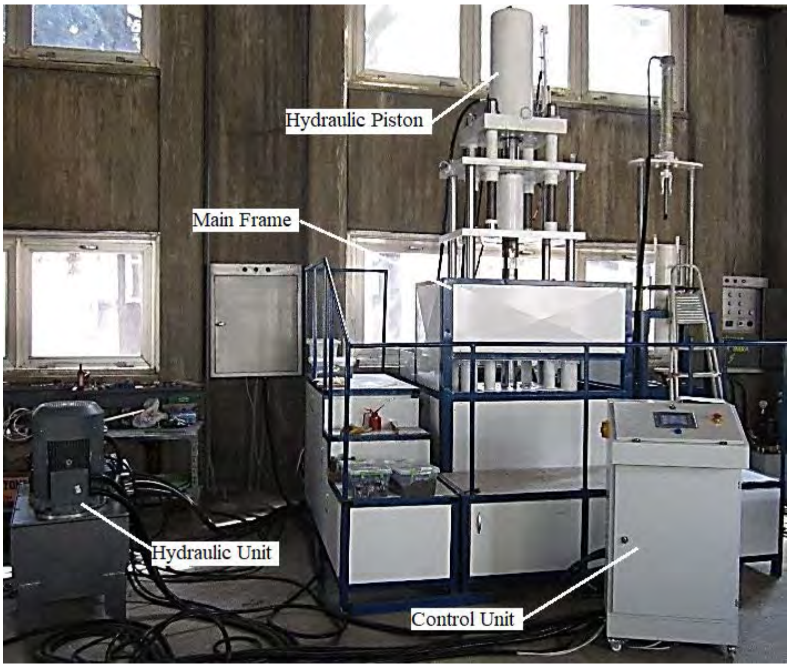

Figure 1. Abrasive flow machine.

Figure 2. Dies.

2.3 Abrasive media

In this experimental study, a mixture of Alal2O3 abrasive 180 mesh size and 400 mesh size, hydraulic oil, and the polymeric carrier was prepared. In order for the mixture to be homogeneous, 5 cycles were made with a die in AFM. The properties of the abrasive fluid are given in Table 3.

Table 3. Abrasive Properties.

	Al_2O_3
Mesh size	180, 400
Hardness (Mohs)	9
Density (g/cm3)	3.7
Apparent density (g/L)	1800
Viscosity (Pa s, 25 ºC)	60
Concentration (% wt)	50, 60, 70

2.4 Experimental Procedure

Experiments were made on six groups of samples. Six specimens in each experimental group were attached to the abrasive fluid machine. 1, 5, 10, 20, 60, and 100 cycles were applied to these samples for each abrasive. A total of six surface measurements were made from each sample, perpendicular to the flow direction and flow direction of the samples. These measurements were taken using a Mitutoyo SJ 401 surface measuring machine with a cutting length of 0.8 mm (ASTM D7127). Samples were weighed before and after the experiment using a SHIMADZU AUX220 balance to calculate the MRR.

3. Results and Discussion

3.1 Surface roughness

The surface roughness values of the WC-Co material, on which the AFM process was applied, were made and the measurements were taken. In Figure 3, the concentration ratios of 50%, 60%, and 70% of the abrasive and the surface roughness values of the abrasive flow direction are given for 180 mesh. It is seen that the surface roughness values show a similar trend here. It is seen that the Ra value of the 60% concentration ratio abrasive drops below 0.50 µm in 20 cycles and has the lowest surface roughness value.

The surface roughness values taken from the flow direction of 400 mesh, which is another abrasive, are given in figure 4. The surface roughness of the process applied with 50%, 60%, and 70% concentration ratios in 20 cycles of 70% concentration ratio was measured as Ra = 0.7 µm.

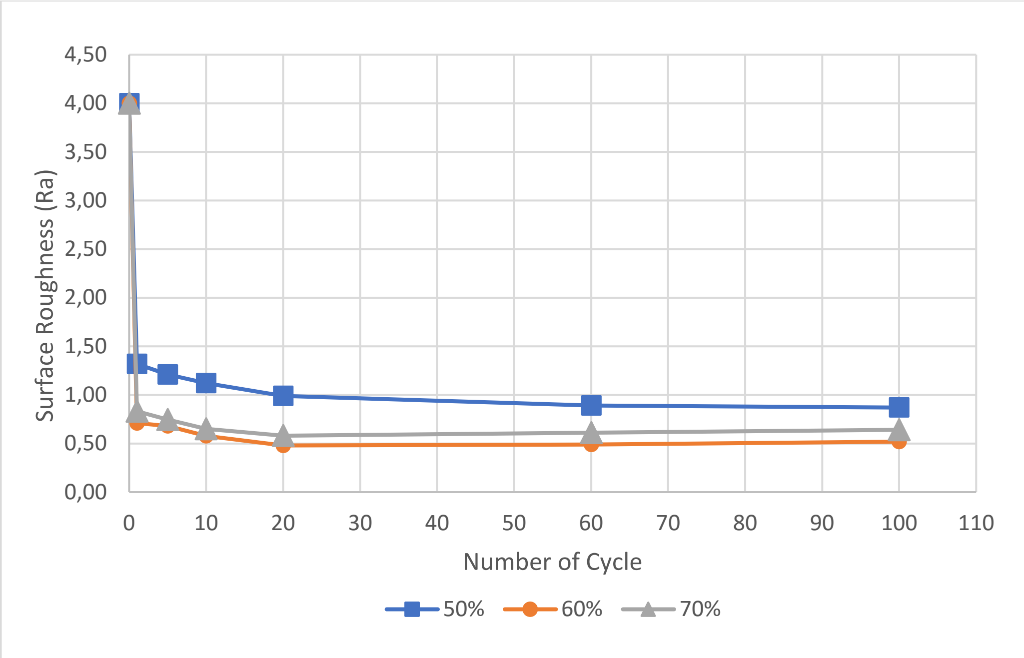

Figure 3. Surface roughness with respect to AFM cycle for 180 mesh size abrasive in the direction of media flow.

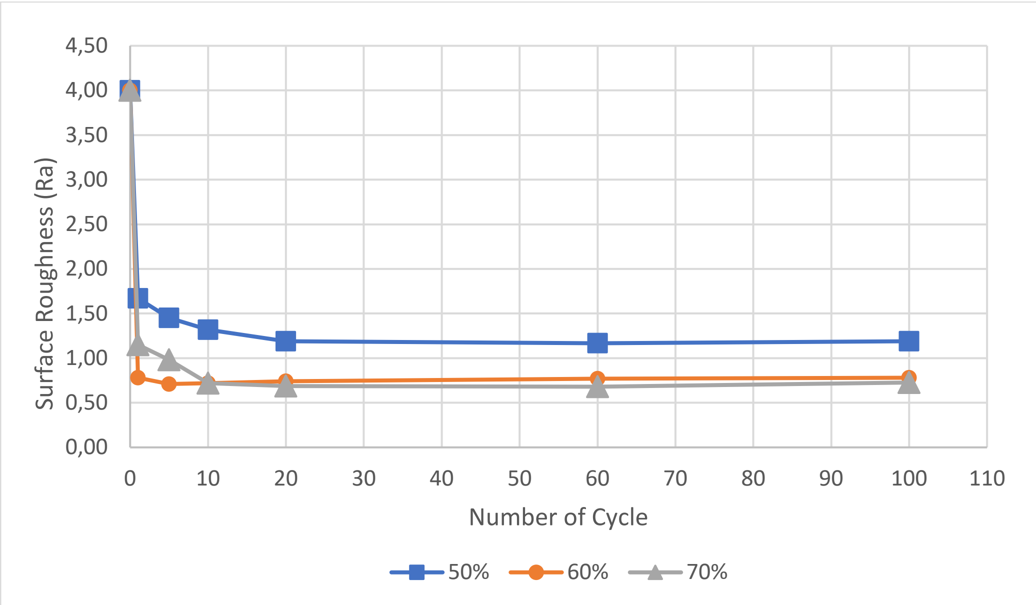

Figure 4. Surface roughness with respect to AFM cycle for 400 mesh size abrasive in the direction of media flow.

In Figure 5 and Figure 6, the graphs of the measured values with 3 repetitions perpendicular to the median flow direction are given. In Figure 5, the surface roughness value was measured as 0.53 in 20 cycles at a 60% concentration of 180 mesh size abrasive. Measurements perpendicular to the median flow direction and the median flow direction showed similar trends. Similarly, the surface roughness of 70% concentration ratio in 400 mesh size in 20 cycles was measured as approximately Ra = 0.8.

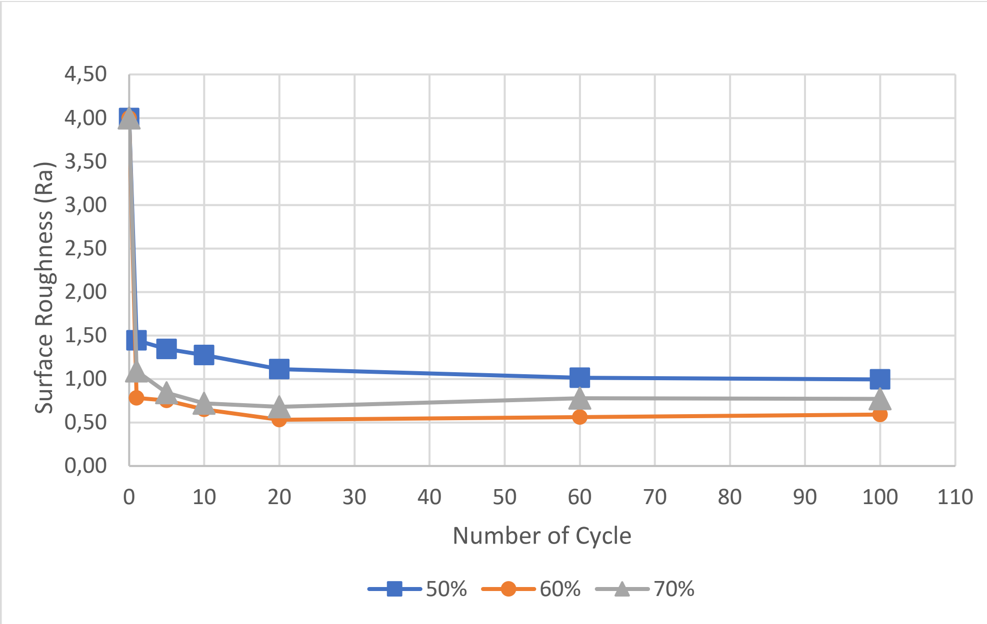

Figure 5. Surface roughness with respect to AFM cycle for 180 mesh size abrasive in the perpendicular direction of media flow.

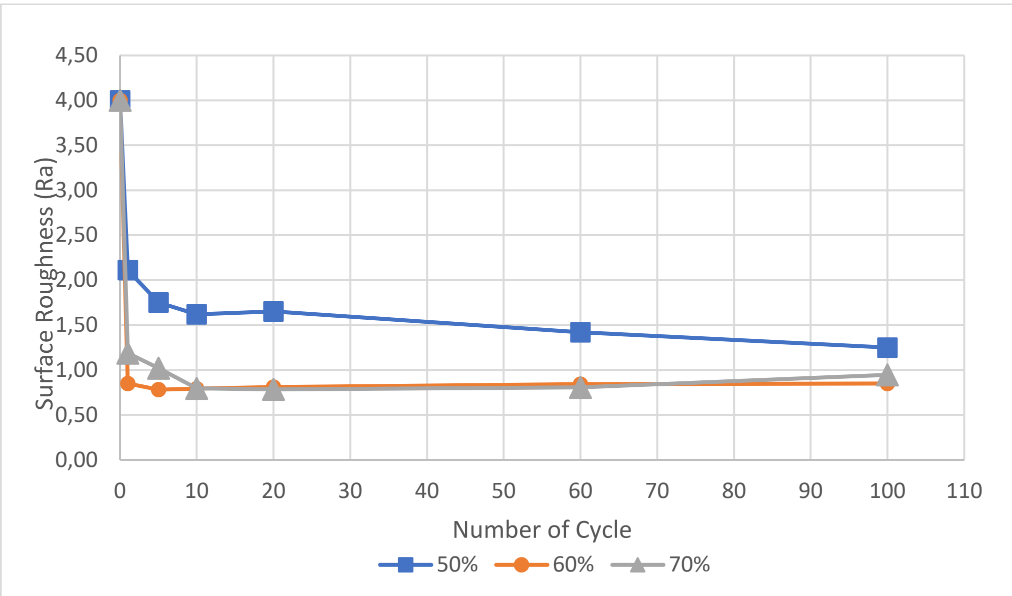

Figure 6. Surface roughness with respect to AFM cycle for 400 mesh size abrasive in the perpendicular direction of media flow.

3.2 Material remove rate (MRR)

The material removal rate is given in figure 7 and figure 8. A nonlinear increase in MRR was observed. The MRR acceleration did not increase as the number of cycles increased. This can be explained by the high surface roughness values of the specimen before AFM. A smoother surface is formed in the next cycle as the abrasive media flow particles flatten the crests on the material. Thus, it was seen that the number of cycles and MRR did not increase at the same rate.

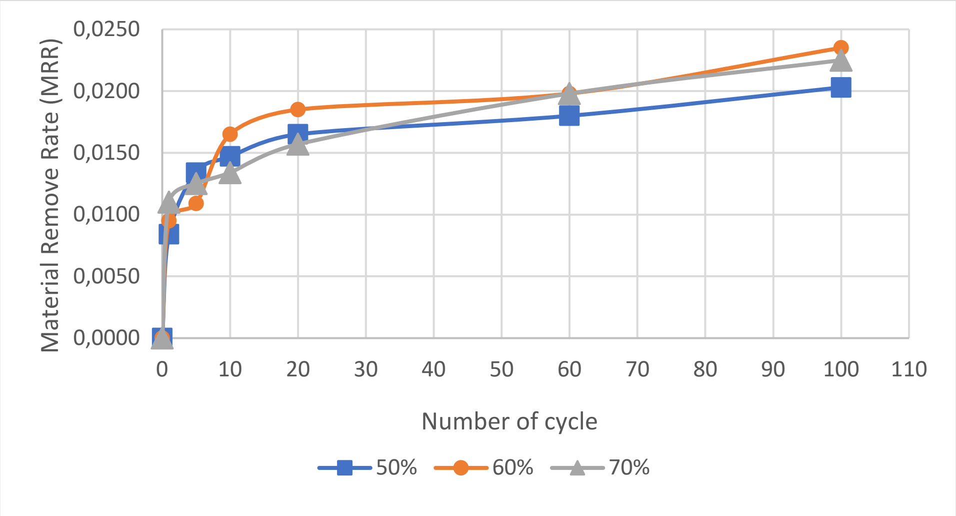

Figure 7. 180 Mesh size MRR

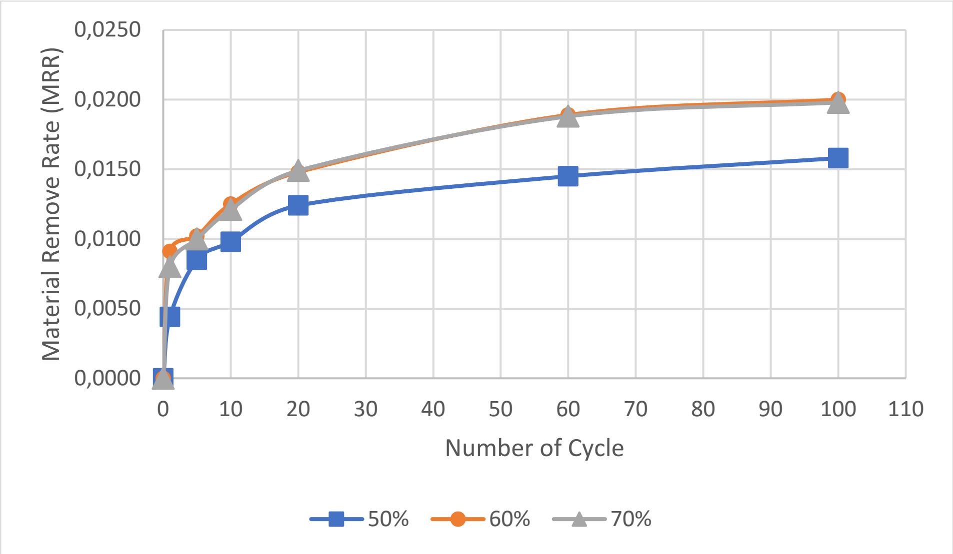

Figure 8. 400 Mesh size MRR

4. Conclusions

In this study, the effects of processing tungsten carbide material (WC-Co) with abrasive fluid on the surface quality were investigated experimentally. The following conclusions can be drawn from this study.

- The abrasive flow machining (AFM) method can be used as a fast and effective method for polishing WC-Co material.

- The average surface roughness (R_a) of the samples decreased from 4.0 µm to 0.50 µm in approximately 20 cycles.
- In the AFM process, Al_3O_2 180 mesh results in better surface quality than 400 mesh size.
- The abrasive media of 60% concentration ratio is the most effective compared to other ratios.
- 180 mesh size has the highest MRR among the other mesh sizes. The bigger abrasive size removes more asperities.
- The MRR is not constant, but the rate decreases with the number of cycles.

Acknowledgments
The authors would like to acknowledge the contributions of the TUBITAK TEYDEB (1505-PROJECT 5200068) and Norm Civata Company.

References

1. Venkatesh, G., Singh, T., Sharma, A.K., and Dvivedi, A. Finishing of micro-channels using abrasive flow machining. Lecture Notes in Mechanical Engineering, (2014), 15, 243–252.
2. Gov, K., and Eyercioglu, O. Effects of abrasive types on the surface integrity of abrasive-flow-machined surfaces. Proceedings of the Institution of Mechanical Engineers, Part B: Journal of Engineering Manufacture, (2018), 232 (6), 1044–1053.
3. Eyercioglu, O., Aksoy, A., and Aladag, M. Bağlantı Elemanları Şekillendirme Kalıplarının Aşındırıcı Akışkan Yöntemiyle Parlatılması. (2019), (November).
4. Rhoades, L. Abrasive flow machining: a case study. Journal of Materials Processing Tech., (1991), 28 (1–2), 107–116.
5. Jain, V.K., and Adsul, S.G. Experimental investigations into abrasive flow machining (AFM). International Journal of Machine Tools and Manufacture, (2000), 40 (7), 1003–1021.
6. Mahdavinejad, R.A., and Mahdavinejad, A. ED machining of WC-Co. Journal of Materials Processing Technology, (2005), 162–163 (SPEC. ISS.), 637–643.
7. Exnert, B.H.E., and Gurland, J. A REVIEW OF PARAMETERS INFLUENCING SOME MECHANICAL Exner and Gurland : Parameters Influencing Some. Powder Metallurgy, (1970), 13 (25), 13–31.
8. Jain, R.K., and Jain, V.K. Finite element simulation of abrasive flow machining. Proceedings of the Institution of Mechanical Engineers, Part B: Journal of Engineering Manufacture, (2003), 217 (12), 1723–1736.
9. Jain, V.K., Ranganatha, C., and Muralidhar, K. Evaluation of rheological properties of medium for AFM process. Machining Science and Technology, (2001), 5 (2), 151–170.
10. Fletcher, A.J., and Fioravanti, A. Polishing and honing processes : An investigation of the thermal properties of mixtures of polyborosiloxane and silicon carbide abrasive. Proceedings of the Institution of Mechanical Engineers, Part C: Journal of Mechanical Engineering Science, (1996), 210 (3), 255–265.
11. Gorana, V.K., Jain, V.K., and Lal, G.K. Experimental investigation into cutting forces and active grain density during abrasive flow machining. International Journal of Machine Tools and Manufacture, (2004), 44 (2–3), 201–211.

PERMITTIVITY EXTRACTION USING UNCALIBRATED MICROWAVE MEASUREMENTS OF SOIL SAMPLES FROM THE CITY GAZIANTEP

HAFIZE HASAR [*1], TASKIN OZTAS [2]

[1] Ministry of Agriculture and Forestry of Republic of Turkey, Gaziantep Directorate of Provincial Agriculture and Forestry, Gaziantep 27090, Turkey.
[2] Department of Soil Science and Plant Nutrition, Ataturk University, Erzurum 25240, Turkey.

Abstract

A microwave method is proposed for precise permittivity extraction of soil samples loaded over a bead within the EIA 1-5/8" coaxial measurement cell. The method does not need any formal calibration and uses one measurement cell for permittivity determination. Besides, it is a non-iterative method based on explicit expressions. The method is validated by experiments of a low-loss polyethylene sample, and its accuracy is compared with the accuracy of other microwave techniques in the literature. After validation, permittivity measurements of three soil samples with different moisture contents from the city Gaziantep are presented.

Keyword: Frequency-domain, permittivity, soil, uncalibrated measurements.

1. Introduction

Measurement of moisture content of soil samples attracts attention since such measurements could be directly associated with performance of seed development, plant evolution and nutrition, and nutrient transfer in the root zone [1]. For this goal, various methods, which could be categorized into direct and indirect methods, could be implemented. Methods in the former category (direct methods) provide information about water content by direct moisture measurements of soil samples. The thermo-gravimetric method, as a direct method, necessitates a huge number of samples-to-be-processed (time-consuming) and has problems associated with the transportation of soil samples from side to laboratory [2]. To overcome these problems, methods in the latter category (indirect methods) give moisture content through correlation of measured non-moisture content. The ground-penetrating radar (GPR) [3], time-domain reflectometry (TDR) [4], the open-ended coaxial or waveguide probe [2], and coaxial transmission line measurements [5]–[7] can be enumerated for the indirect methods.

The GPR method is a nondestructive method sensitive to the changes in moisture content of soil samples [3]. It is possible to relate these changes to volumetric moisture content of soil samples through some suitable empirical relationships. However, its measurements are influenced by non-ideal soil conditions including heterogeneity or conductive elements. On the other hand, the TDR method is another nondestructive method, which uses information of propagation delay and amplitude change of a pin-like pulse to evaluate moisture content [4]. Nonetheless, it requires a special probe design to perform accurate measurements. Furthermore, it is prone to the effect of air gap present between the probe and soil sample. Besides, open-ended coaxial or waveguide measurements can as well be utilized for determining moisture content within soil samples. These methods, however, necessitate a good contact between the probe and the soil sample [2].

Coaxial transmission lines, on the other hand, are a good candidate for water content measurement via a proper correlation [5]–[7]. These measurements have the advantage of providing broadband information about electromagnetic properties of soil samples, which are especially useful for the GPR and TDR methods. Effective medium approximation is generally used by these methods. According to this approximation, the wavelength must be at least time times greater than the maximum scatterer inside the soil sample. Satisfying this criterion could be problematic for coaxial transmission lines with smaller cross section. Electronic Industries Association (EIA) 1-5/8" coaxial transmission lines [5]-[7] could be used to overcome such limitation. These lines, however, need a suitable calibration procedure to eliminate the effect of adapters used for transforming electromagnetic signals to these lines. For example, a simple calibration procedure based on port extension was implemented in the study [6]. However, its accuracy was limited since port extension at the adapters (after short-open-load-thru (SOLT) calibration procedure) could only correct amplitude (but not the phase information) of the electromagnetic signals. To circumvent this problem, the multiline thru-reflect-line (TRL) calibration technique (five coaxial line standards of different lengths together with an open standard and a 50 match load) was implemented to eliminate the effects of adapters on water content measurements of soil samples [5]. However, a real benefit from these methods [5] and [6] can be exploited if accurate calibration standards are utilized. An imperfection in these calibration standards or usage of improper calibration standards, in return, seriously alters the accuracy of measurements of the methods [5] and [6]. To overcome this disadvantage, measurements relying on a de-embedding technique [7] can be used. Although accurate, the inhomogeneity of the second line and the shift in the position of the sample holder in the second line can alter the accuracy of this method. To remove both of these drawbacks simultaneously, in this study, another de-embedding technique based on uncalibrated measurements of one coaxial line is proposed.

2. Materials and Methods

The proposed method uses three measurement configurations of one coaxial line (or cell) (EIA 1-5/8") with length L_{cell}, as shown in Figs. 1(a)-1(c). While Fig. 1(a) shows the empty measurement cell, Fig. 1(b) illustrates the measurement configuration where the sample holder with length L_h is positioned at any position (L_{air1} and L_{air2} are not known) in the cell. The last configuration in Fig. 1(c) indicates the configuration after the soil sample with relative permittivity $\varepsilon_{rs} = \varepsilon_{rs}' - i\varepsilon_{rs}''$ and length L_s is poured over the sample holder. Here, the regions shown by X and Y designate two-port error networks representing frequency and source/load match errors of a vector network analyzer (VNA) and effects of adapters and transitions.

In our theoretical analysis, we assume the error networks X and Y do not change for each configuration in Figs. 1(a)-1(c). Applying the ABCD matrix presentation, it is possible to relate scattering (S-) parameters of the configurations in Fig. 1(a)-1(c) to air, sample and holder regions within the measurement cell as

$$M_a = T_X T_{\text{air}}^{(1)} T_{H0} T_{S0} T_{\text{air}}^{(2)} T_Y, \quad (1)$$

$$M_b = T_X T_{\text{air}}^{(1)} T_H T_{S0} T_{\text{air}}^{(2)} T_Y, \quad (2)$$

$$M_c = T_X T_{\text{air}}^{(1)} T_H T_S T_{\text{air}}^{(2)} T_Y. \tag{3}$$

Here, M_a, M_b, and M_c are, respectively, the ABCD parameters of the overall configurations in Figs. 1(a)-1(c), which are functions of measured S-parameters; T_X and T_Y denote the ABCD matrices of the error networks X and Y; $T_{\text{air}}^{(1)}$ and $T_{\text{air}}^{(2)}$ designate the ABCD matrices of air regions with lengths L_{air1} and L_{air2}; and T_{H0} and T_H are the ABCD matrices of air-filled and holder-filled sections in the measurement cell.

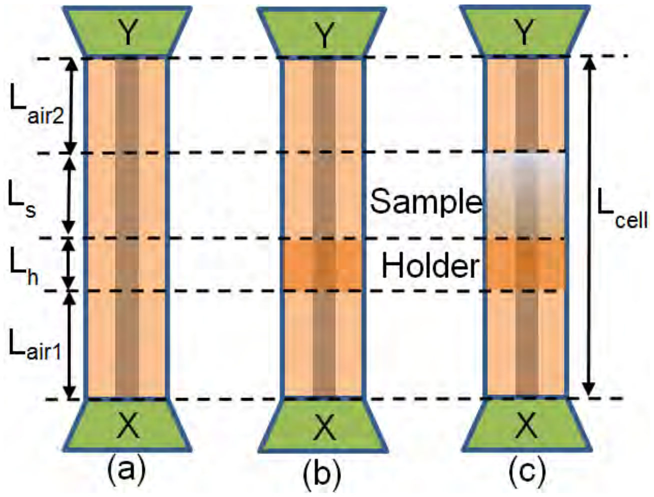

Fig. 1. (a) Empty line, (b) line with the holder of length L_h positioned at an arbitrary distance of L_{air1} from bottom of the line, and (c) the same as the configuration in (b) except for the soil sample with length L_s is loaded over the holder

The expressions for T_S, T_H, T_{S0}, and T_{H0} can be written as

$$T_S = \frac{1}{2}\begin{bmatrix} \left(\frac{1}{P_s}+P_s\right) & z_s\left(\frac{1}{P_s}-P_s\right) \\ \frac{1}{z_s}\left(\frac{1}{P_s}-P_s\right) & \left(\frac{1}{P_s}+P_s\right) \end{bmatrix}, \quad T_H = \frac{1}{2}\begin{bmatrix} \left(\frac{1}{P_h}+P_h\right) & z_h\left(\frac{1}{P_h}-P_h\right) \\ \frac{1}{z_h}\left(\frac{1}{P_h}-P_h\right) & \left(\frac{1}{P_h}+P_h\right) \end{bmatrix}, \tag{4}$$

$$T_{S0} = \frac{1}{2}\begin{bmatrix} \left(\frac{1}{P_{s0}}+P_{s0}\right) & \left(\frac{1}{P_{s0}}-P_{s0}\right) \\ \left(\frac{1}{P_{s0}}-P_{s0}\right) & \left(\frac{1}{P_{s0}}+P_{s0}\right) \end{bmatrix}, \quad T_{H0} = \frac{1}{2}\begin{bmatrix} \left(\frac{1}{P_{h0}}+P_{h0}\right) & \left(\frac{1}{P_{h0}}-P_{h0}\right) \\ \left(\frac{1}{P_{h0}}-P_{h0}\right) & \left(\frac{1}{P_{h0}}+P_{h0}\right) \end{bmatrix}, \tag{5}$$

$$z_s = \sqrt{\frac{1}{\varepsilon_{rs}}}, \quad z_h = \sqrt{\frac{1}{\varepsilon_{rh}}}, \tag{6}$$

$$P_s = e^{-jk_0\sqrt{\varepsilon_{rs}}L_s}, \quad P_h = e^{-jk_0\sqrt{\varepsilon_{rh}}L_h} \tag{7}$$

$$P_{s0} = e^{-jk_0 L_s}, \quad P_{h0} = e^{-jk_0 L_h}, \tag{8}$$

where P_s, P_h, z_s, and z_h are, respectively, the propagation factors and normalized wave impedances of the sample-filled and holder-filled regions; P_{s0} and P_{h0} are, respectively, the propagation factors of air regions with lengths L_s and L_h; ε_{rh} is the relative complex permittivity of the sample holder; and k_0 is the wavenumber of free-space.

We eliminate the effects of unknown terms $T_{\text{air}}^{(1)}$, $T_{\text{air}}^{(2)}$, T_X, and T_Y by applying the following two-step procedure. As a first step, effects of $T_{\text{air}}^{(2)}$ and T_Y are eliminated by using the inverse of matrix operations as

$$M_c M_b^{-1} = T_X T_{\text{air}}^{(1)} T_H T_S T_{S0}^{-1} \left(T_X T_{\text{air}}^{(1)} T_H \right)^{-1}, \tag{9}$$

$$M_c M_a^{-1} = T_X T_{\text{air}}^{(1)} T_H T_S T_{S0}^{-1} T_{H0}^{-1} \left(T_X T_{\text{air}}^{(1)} \right)^{-1}. \tag{10}$$

Here, '$*^{-1}$' designates the inverse of a square matrix `*'.

As a second step, effects of $T_{\text{air}}^{(1)}$ and T_X are removed from (9) and (10) by using the unitary property or the trace property of matrices as

$$\Omega_1 = \text{Tr}\left(M_c M_b^{-1} \right) = \text{Tr}\left(T_S T_{S0}^{-1} \right), \tag{11}$$

$$\Omega_2 = \text{Tr}\left(M_c M_a^{-1} \right) = \text{Tr}\left(T_H T_S T_{S0}^{-1} T_{H0}^{-1} \right), \tag{12}$$

where Tr(*) denotes the trace operation for a square matrix `*'.

When expressions in (4)-(8) are substituted into (11) and (12) and after some length operations, it is possible to determine an polynomial function for z_s as

$$F(z_s) = \xi_1 z_s^6 + \xi_2 z_s^5 + \xi_3 z_s^4 + \xi_4 z_s^3 + \xi_5 z_s^2 + \xi_6 z_s + \xi_7 = 0, \tag{13}$$

$$\xi_1 = \Lambda_6 \left[(\Omega_1 \Lambda_7 - \Omega_2 \Lambda_6)^2 - 4(\Lambda_1 \Lambda_6 - \Lambda_5 \Lambda_7)^2 \right], \tag{14}$$

$$\begin{aligned} \xi_2 = {} & \Lambda_5 \left[4(\Lambda_1 \Lambda_6 - \Lambda_5 \Lambda_7)^2 + (\Omega_1 \Lambda_7 - \Omega_2 \Lambda_6)^2 \right] \\ & + 2\left[\Lambda_6 (\Omega_1 \Lambda_1 - \Omega_2 \Lambda_5) - \Omega_1 (\Lambda_1 \Lambda_6 - \Lambda_5 \Lambda_7) \right] (\Omega_2 \Lambda_6 - \Omega_1 \Lambda_7), \end{aligned} \tag{15}$$

$$\begin{aligned} \xi_3 = {} & 2\Lambda_5 (\Omega_1 \Lambda_1 - \Omega_2 \Lambda_5)(\Omega_2 \Lambda_6 - \Omega_1 \Lambda_7) \\ & + \Lambda_6 \begin{bmatrix} 8(\Lambda_5 \Lambda_7 - \Lambda_1 \Lambda_6)(\Lambda_1 \Lambda_6 - \Lambda_5 \Lambda_8) \\ + (\Omega_1 \Lambda_1 - \Omega_2 \Lambda_5)^2 + 2(\Omega_1 \Lambda_7 - \Omega_2 \Lambda_6)(\Omega_1 \Lambda_8 - \Omega_2 \Lambda_6) \\ + (\Omega_1 \Lambda_7 - \Omega_2 \Lambda_6)^2 - 4(\Lambda_1 \Lambda_6 - \Lambda_5 \Lambda_7)^2 \end{bmatrix} \\ & - 2\Omega_1 (\Lambda_1 \Lambda_6 - \Lambda_5 \Lambda_7)(\Omega_1 \Lambda_1 - \Omega_2 \Lambda_5) \end{aligned} \tag{16}$$

$$\begin{aligned}\xi_4 &= \Lambda_5\left[\begin{aligned}&8(\Lambda_1\Lambda_6-\Lambda_5\Lambda_7)(\Lambda_1\Lambda_6-\Lambda_5\Lambda_8)+(\Omega_1\Lambda_1-\Omega_2\Lambda_5)^2\\&+2(\Omega_1\Lambda_7-\Omega_2\Lambda_6)(\Omega_1\Lambda_8-\Omega_2\Lambda_6)\end{aligned}\right]\\&+2\Lambda_6(\Omega_1\Lambda_1-\Omega_2\Lambda_5)\left[(\Omega_2\Lambda_6-\Omega_1\Lambda_7)+(\Omega_2\Lambda_6-\Omega_1\Lambda_8)\right]\\&+2\Omega_1\left[\begin{aligned}&(\Lambda_1\Lambda_6-\Lambda_5\Lambda_7)(\Omega_1\Lambda_8-\Omega_2\Lambda_6)\\&+(\Lambda_1\Lambda_6-\Lambda_5\Lambda_8)(\Omega_1\Lambda_7-\Omega_2\Lambda_6)\end{aligned}\right],\end{aligned} \tag{17}$$

$$\begin{aligned}\xi_5 &= 2\Lambda_5(\Omega_1\Lambda_1-\Omega_2\Lambda_5)(\Omega_2\Lambda_6-\Omega_1\Lambda_8)\\&+\Lambda_6\left[\begin{aligned}&8(\Lambda_1\Lambda_6-\Lambda_5\Lambda_7)(\Lambda_5\Lambda_8-\Lambda_1\Lambda_6)+(\Omega_1\Lambda_1-\Omega_2\Lambda_5)^2\\&+2(\Omega_1\Lambda_7-\Omega_2\Lambda_6)(\Omega_1\Lambda_8-\Omega_2\Lambda_6)+(\Omega_1\Lambda_8-\Omega_2\Lambda_6)^2-4(\Lambda_1\Lambda_6-\Lambda_5\Lambda_8)^2\end{aligned}\right]\\&-2\Omega_1(\Lambda_1\Lambda_6-\Lambda_5\Lambda_8)(\Omega_1\Lambda_1-\Omega_2\Lambda_5)\end{aligned} \tag{18}$$

$$\begin{aligned}\xi_6 &= \Lambda_5\left[4(\Lambda_1\Lambda_6-\Lambda_5\Lambda_8)^2+(\Omega_1\Lambda_8-\Omega_2\Lambda_6)^2\right]\\&+2\Lambda_6(\Omega_1\Lambda_1-\Omega_2\Lambda_5)(\Omega_2\Lambda_6-\Omega_1\Lambda_8)\\&+2\Omega_1(\Lambda_1\Lambda_6-\Lambda_5\Lambda_8)(\Omega_1\Lambda_8-\Omega_2\Lambda_6),\end{aligned} \tag{19}$$

$$\xi_7 = \Lambda_6\left[(\Omega_1\Lambda_8-\Omega_2\Lambda_6)^2-4(\Lambda_1\Lambda_6-\Lambda_5\Lambda_8)^2\right], \tag{20}$$

where

$$Q = P_{s0}P_{b0}+\frac{1}{P_{s0}P_{b0}}, \qquad R = P_{s0}P_{b0}-\frac{1}{P_{s0}P_{b0}}, \tag{21}$$

$$\Lambda_1 = \frac{Q}{4}\left(P_b+\frac{1}{P_b}\right)-\frac{R}{8}\left(z_b+\frac{1}{z_b}\right)\left(P_b-\frac{1}{P_b}\right), \tag{22}$$

$$\Lambda_2 = \frac{R}{8}\left(P_b+\frac{1}{P_b}\right)\left(z_s+\frac{1}{z_s}\right)-\frac{Q}{8}\left(P_b-\frac{1}{P_b}\right)\left(\frac{z_s}{z_b}+\frac{z_b}{z_s}\right) \tag{23}$$

$$\Lambda_3 = \Lambda_5+\Lambda_6\left(z_s+\frac{1}{z_s}\right), \tag{24}$$

$$\Lambda_4 = \Lambda_5-\Lambda_6\left(z_s+\frac{1}{z_s}\right), \tag{25}$$

$$\Lambda_5 = \frac{1}{2}\left(P_{s0}+\frac{1}{P_{s0}}\right), \qquad \Lambda_6 = \frac{1}{4}\left(P_{s0}-\frac{1}{P_{s0}}\right), \tag{26}$$

$$\Lambda_7 = \frac{1}{8}\left[R\left(P_p+\frac{1}{P_p}\right)-\frac{1}{z_p}Q\left(P_p-\frac{1}{P_p}\right)\right], \tag{27}$$

$$\Lambda_8 = \frac{1}{8}\left[R\left(P_p + \frac{1}{P_p} \right) - z_p Q\left(P_p - \frac{1}{P_p} \right) \right]. \tag{28}$$

Once z_s is calculated from (13) for $\mathrm{Re}\{z_s\} \geq 0$ by a suitable 2D numerical technique such as Newtons method, the value of P_s can be determined from

$$P_s = \frac{(\Lambda_1 - \Lambda_2)\Lambda_3 - (\Lambda_1 + \Lambda_2)\Lambda_4}{\Omega_1(\Lambda_1 - \Lambda_2) - \Omega_2\Lambda_4}. \tag{29}$$

Finally, the complex permittivity of the soil sample ε_{rs} can be determined from

$$\varepsilon_{rs} = \left(\frac{j\ln(P_s) \mp 2\pi m}{k_0 L_s} \right)^2, \tag{30}$$

where m is the branch index term.

3. Results and Discussion

We constructed a measurement setup, as shown in Fig. 2, to perform coaxial line measurements in Figs. 1(a)-1(c). The setup involves the VNA (purchased from the Keysight Technologies with model N9918A), two phase-stable 3.5 mm Type-N coaxial lines each with a length of 100 cm, two Type-N-to-EIA 1-5/8” adapters, two flanges, and a measurement cell with a length of 171.5 cm (inner diameter of the outer conductor of 38.8 mm and the outer diameter of the inner conductor of 16.9 mm). The VNA can be operated from 30 kHz to 26.5 GHz (a dynamic range of approximately 90 dB and a directivity larger than 32 dB). As a sample holder, a polyethylene (PE) material with length L_h = 3.85 mm was utilized in measurements.

An accuracy analysis was carried out before starting to real permittvity measurements of three soil samples with different water contents. In this regard, a PE sample, which is considered to be a dielectric material used as a metric, with length L_s = 3.85 mm was considered in our analysis. Our proposed method was applied to determine ε_{rs}' and ε_{rs}'' of this sample, as shown in Figs. 3(a) and 3(b), using uncalibrated S-parameters (average of five independent measurements) of the configurations in Figs. 1(a)-1(c). The methods in [6] and [7] were also applied to assess the accuracy of the proposed method. It is noted that the method in [5] requires at least five coaxial measurement lines (or cells). Therefore, this method is not implemented by limited number of coaxial lines in our laboratory. In implementation of the method in [6], the SOLT calibration procedure was first utilized for calibration of the measurement setup to ends of the 3.5 mm Type-N coaxial lines, and then the port extension feature of the VNA was operated. Besides, in implementation of the method in [7], two coaxial lines with lengths 150 mm and 171.5 mm (with the same cross sections) were utilized. Furthermore, in our method and the method in [7], the moving average was applied over approximately 30 MHz frequency region to smooth the extracted parameters [8].

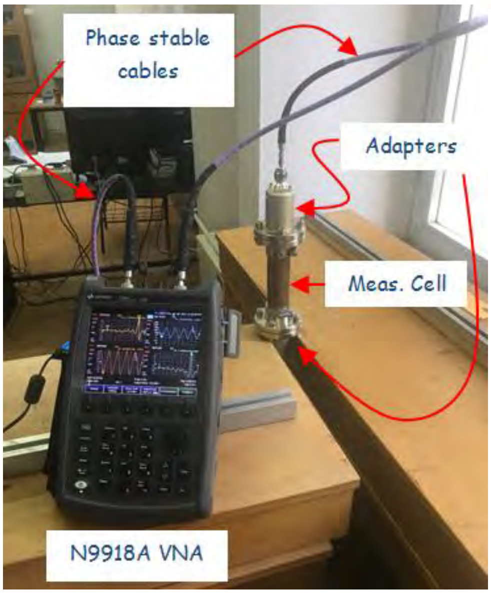

Fig. 2. A picture of the measurement setup

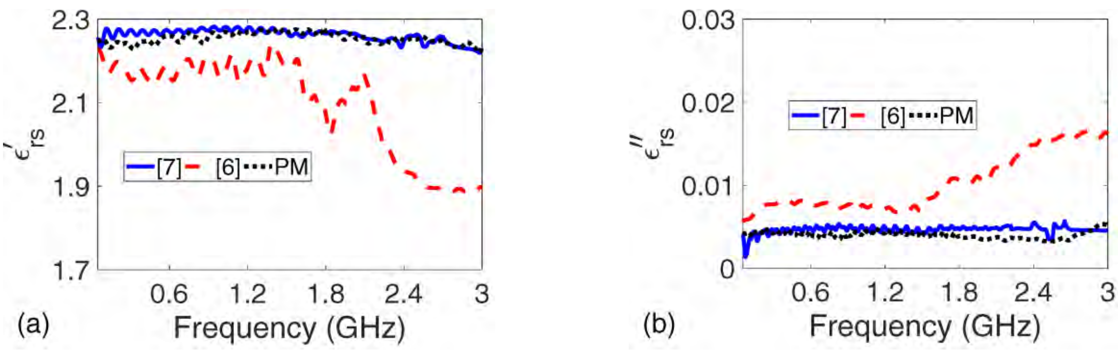

Fig. 3. Extracted (a) ε_{rs}' and (b) ε_{rs}'' of the PE sample by our method (PM) and the methods in [6] and [7].

We note from the dependencies in Figs. 3(a) and 3(b) that extracted ε_{rs}' and ε_{rs}'' of the PE sample by our method and the method in [7] are in good agreement with each other and are close to reference values of 2.26 and 0.0002 (measured by a resonator method at 1 kHz, 1 MHz, 100 MHz, and 3 GHz frequencies) [9]. Besides, it is seen from Figs. 3(a) and 3(b) that extracted ε_{rs}' and ε_{rs}'' of the PE sample by the method in [6] introduce some oscillations and diverge from reference values which we think are mainly due to the applied port extension in elimination of adapters.

Effects of L_s and L_{air1} on measurements were also evaluated by performing additional measurements. Fig. 4(a) presents the influence of a 5% increase (offset) in L_s on ε_{rs}' extraction of the PE sample by our method and the method in [7]. Besides, Fig. 4(b) illustrates extracted ε_{rs}' of the PE sample after L_{air1} was modified from 10.0 mm to 20.0 mm for our method and when the sample holder was shifted 5% in the second coaxial line (171.5 mm) for the method in [7].

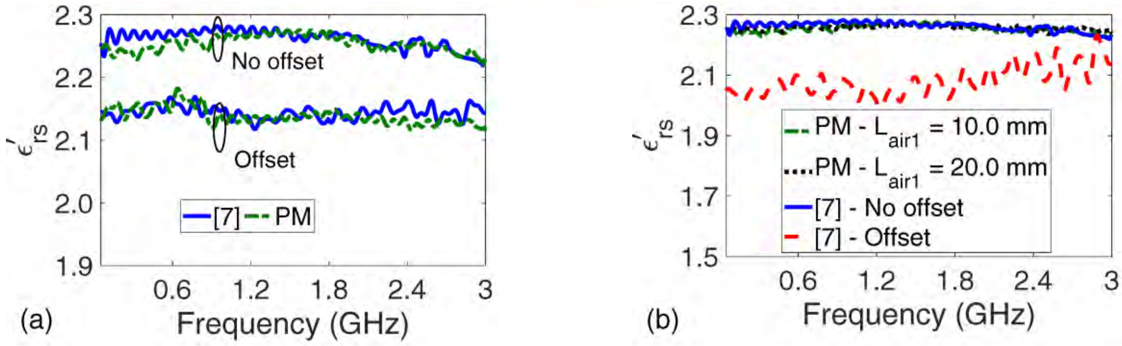

Fig. 4. Extracted ε_{rs}' of the PE sample by our method (PM) and the method [7] (a) when there is 5% increase (offset) in L_s and (b) when the sample holder is shifted 5% in the second coaxial line.

It is noted from Fig. 4(a) that accurate knowledge of L_s is needed for our method and the method in [7], indicating that care should be given in measurement of accurate L_s. A 5% increase (offset) in L_s approximately follows a 5% reduction in extracted ε_{rs}' for our method and the method in [7]. On Besides, as seen from Fig. 4(b), our method is essentially independent of the position (from 10.0 mm to 20.0 mm) of the sample holder in the second measurement cell. Unlike our method, the accuracy of the method in [7] is greatly altered by a 5% increase in the holder position. The difference between the extracted ε_{rs}' values by the method in [7] with and without this offset can reach up to 12.6% at 1.23 GHz.

Finally, after validating and accuracy evaluation of our proposed method using the permittivity measurements of the PE sample, we continued with the permittivity measurement of three soil samples (labeled by S_I, S_{II}, and S_{III}), each composed of 90% or more sand content, from different areas of the city Gaziantep in Turkey. Electrical conductivities of these samples are 95.70 mS/m, 341 mS/m, and 490 mS/m while their pH values are 7.62, 8.14, and 7.82. Conductivity values of the soil samples were measured by the conductivity bridge technique [10] at the Pistachio Research Institute of Republic of Turkey Ministry of Agriculture and Forestry in Gaziantep, Turkey.

Figs. 5(a)-5(c) illustrate the extracted ε_{rs}' of S_I with a volumetric water content of $\theta_V = 0.20$, S_{II} with a volumetric water content of $\theta_V = 0.30$, and S_{III} with a volumetric water content of $\theta_V = 0.42$ by our method. All these volumetric contents of soil samples were measured by the thermo-gravimetric method. It is seen from Figs. 5(a)-5(c) that, as expected from the studies in the literature [6], extracted ε_{rs}' value of soil samples have a smoother exponentially decaying dependence with frequency.

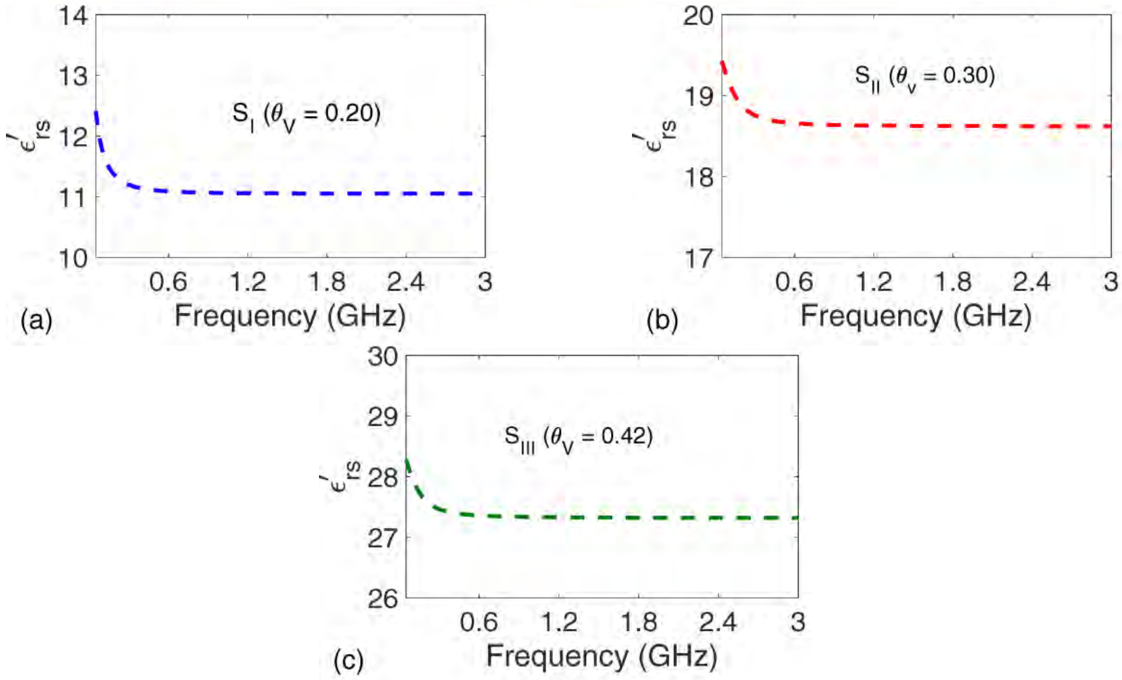

Fig. 5. Extracted ε_{rs}' of (a) the soil S_I with $\theta_V = 0.20$, (b) the soil S_{II} with $\theta_V = 0.30$, and (c) the soil S_{III} with $\theta_V = 0.42$ by our method.

4. Conclusion: A microwave de-embedding method has been proposed for accurate complex permittivity extraction of soil samples. There are two main advantages of the proposed method. First, it only needs uncalibrated measurements of three different configurations of one measurement cell. Second, it does not need any numerical toolbox for permittivity measurement. Effects of holder position, sample length, and using different measurement cells are all examined to evaluate its accuracy using the measurements of a PE sample, which is generally considered as a metric dielectric material for evaluating the accuracy of methods. It is noted from this analysis, our method is position-insensitive to the sample holder but requires precise knowledge of its length. As a future study, we will apply calibration curves (dependence of the volumetric water content of θ_V versus ε_{rs}') to determine indirectly the water content of soil samples through ε_{rs}' measurements.

Acknowledgments: Authors thank Dr. Ugur Cem Hasar at the Department of Electrical and Electronics Engineering in Gaziantep University, Turkey for helping performing microwave measurements.

References:

1. Bittelli, M., Measuring soil water content: A review, Horttechnology, **2011**, 21(3):293-300.
2. Luciani, G., Berardinelli, A., Crescentini, M., Romani, A., Tartagni, M., and Ragni, L. Non-invasive soil moisture sensing based on open-ended waveguide and multivariate analysis, Sens. Actuator A.: Phys., **2017**, 265:236-245.

3. Babaeian, E., Sadeghi, M., Jones, S. B., Montzka, C., Vereecken, H., and Tuller, M. Ground, proximal, and satellite remote sensing of soil moisture, Rev. Geophys., **2019,** 57(2):530-616.
4. Majcher, J., Kafarski, M., Wilczek, A., Szypłowska, A., Lewandowski, A., Woszczyk, A., and Skierucha, W. Application of a dagger probe for soil dielectric permittivity measurement by TDR, Meas., **2021**, 178:109368.
5. Lewandowski, A., Szyplowska, A., Kafarski, M., Wilczek, A., Barmuta, P., and Skierucha, W. 0.05-3 GHz VNA characterization of soil dielectric properties based on the multiline TRL calibration, Meas. Sci. Technol., **2017**, 28(2):024007.
6. Lauer, K., Wagner, N., and Felix-Henningsen, P. 2012. A new technique for measuring broadband dielectric spectra of undisturbed soil samples, Eur. J. Soil Sci., **2012**, 63: 224-238.
7. Hasar, H., Hasar, U. C., Kaya, Y., Oztas, T., Canbolat, M. Y., Aslan, N., Ertugrul, M., and Ramahi, O. M. Broadband soil permittivity measurements using a novel de-embedding line-line method, IEEE Geosci. Remote Sens. Lett., **2022**, 19: 5002605.
8. Jebbor, N., Bri, S., Sanchez, A. M., and Chaibi, M. A fast calibration independent method for complex permittivity determination at microwave frequencies, Meas., **2013**, 46(7):2206-2209.
9. Chin, G. Y. and Mechtly, E. A. Properties of Materials. Indianapolis, IN: Howard W. Sams Co., **1986**.
10. Richards, L. A. Diagnosis and improvement of saline and alkali soils. Agriculture handbook 60. US Department of Agriculture, Washington, DC, **1954**.

GRAPHNE IN CEMENTIOUS MATERIALS FOR BUILT ENVIRONMENT APPLCATIONS

SHOUKAT ALIM KHAN[1*], MOHAMMAD JASSIM JASSIM[2], MUAMMER KOC[1]

[1]Division of Sustainable Development College of Science and Engineering, Hamad Bin Khalifa University, Doha, Qatar
[2]Mechanical Engineering Department, University of Engineering and Technology Taxila, Pakistan
[*]shoukat.alimkhan@gmail.com

Abstract

The aim of this study is to find out the potential benefits that Graphene Oxide (GO) can add to cementitious composites. Graphene Oxide being a nanoparticle has dimensions less than 100 nm. Studies have proved that the use of GO can improve the mechanical properties at microstructure level in construction and building applications. There are several types of cement composites such as concrete, mortar, cement paste and engineered cementitious composites (ECC). These cementitious composites are used in a wide range in the building and construction industry. As time has passed these cementitious composites have lost their strength and the need to develop stronger and enhanced binders were aroused. As time passed by several materials and additives were developed which are to be added to cement binders and cementitious composites to increase their strength. Researchers have been doing a lot of work to measure the enhanced strength of these composites. The addition of these additives has provided vital results. The crack propagation was greatly controlled by the addition of additives. This study provides a brief introduction of using Graphene and Graphene Oxide in cementitious composites to increase the strength of binders. The use of GO in these cement composites has provided many advantages. It has greatly reduced the growth of cracks in cementitious composites. The spreading of cracks among the walls was also greatly reduced by this method. All these advantages were studied at the nano-scale level which proved the results. The use of GO in such composites has paved a new way for researchers. It has opened some new ways to develop further enhancement in concrete, mortar, cement paste and engineered cementitious composites. The strength of cement composites discussed above is exemplary. We will also see that the addition of GO in such composites will further add up to its strength.

Keyword: Geopolymers, Construction Waste, Mechanical Process, Energy Efficiency, Environmental Sustainability, Circular Economy

ENHANCED BOILING HEAT TRANSFER ON SILVER NANOWIRE NETWORKS

NURETTİN SEZER[1*], YUSUF BİCER[1], MUAMMER KOÇ[1]

[1]Hamad Bin Khalifa University - , Qatar
[*]nsezer@hbku.edu.qa

Abstract

The heat load on electronic devices is increasing with the growing trend of miniaturization and the continuous development of the electronics industry. Thus, the dissipation of heat fluxes from high energy density devices becomes crucially important to sustain safe and efficient operations. Nucleate boiling is a prominent passive heat transfer mode for cooling high heat flux systems. The capacity and efficiency of nucleate boiling can be enhanced by improving the hydrodynamics and bubble dynamics through modifying the characteristics of the heating surface such as the surface morphology, roughness, wettability, and capillarity. This study proposes an open porous interconnected silver nanowires network as an effective heating surface for enhanced nucleate boiling heat transfer. The boiling-induced deposition of silver nanowires from aqueous dispersions and its impact on the boiling heat transfer performance were investigated. Experiments were conducted on a custom-made boiling setup with a flat plate heating surface by stepwise increasing the supplied heat flux until the critical heat flux was reached. The surface deposition layers were investigated for morphology, topology, wettability, and capillarity to provide insights into understanding the nucleate boiling enhancement mechanisms. An interconnected porous nanowire network was formed on the heating surface that improved the bubble nucleation site density, lateral heat conduction, and capillary wicking, resulting in enhanced heat transfer capacity and efficiency. The boiling heat transfer coefficient and critical heat flux of nanostructured surface were increased by 93.7% and 200%, respectively.

Keyword: Nucleate boiling, Critical heat flux, Heat transfer coefficient, Silver nanowires, Boiling-induced deposition

NUMERICAL CHARACTERIZATION OF THE MECHANICAL PROPERTIES OF FGM USING THE MULTI PHASE FINITE ELEMENT METHOD

ABDELKADER BOUDJEMLINE[1*], SAMIR CHOUARFIA[1], KAMEL MEFTAH[2], WAHID KADDOURI[2], LAKHDAR SEDIRA[1]

[1]Mohamed Khider University of Biskra, Algeria
[2]University of Batna 2, Algeria
[*]abdelkader.boudjemline@univ-biskra

Abstract

The present work qi;ed to be a contribution to the characterization of the homogenized elastic properties of the funnctionaly graded materials (FGM). It deals with the developement of a numerical homogenization approach based on 2D micrographic analysis of several materials. A specific subroutine has been implemented in a finite element code to take in consideration the gradual variation of elastic properties of the FGMs. The four-node Q4 quadrangle element is developped in a multiscale formulation, and validated through a tensile test simulations. The obtained results are compared to experimental measurements [1,2 and 3] with excellent agreement.

Keyword: Homogenized elastic properties, Functionaly graded materials, Numerical homogenization approach, Micrographic analysis, Finite element, Multiscale, Tensile test simulation

TAGUCHI METHOD WITH ANOVA ANALYSIS of HEAT-TREATED 4140 STEEL

HALIL IBRAHIM KURT[1*], UTKU BERK AKYUZ[2] AND ENGIN ERGUL[3]

[1]Aerospace Engineering, Faculty of Aeronautics and Astronautics, University of Samsun, Turkey
[2]Department of Metallurgical and Materials Engineering, Engineering Faculty, Gaziantep University, Turkey
[3]Mechanical Department, İzmir Vocational High School, Dokuz Eylul University, Turkey

Abstract

In this work, the heat treatment process is applied on the 4140 steel to see how the samples show mechanical changes under various conditions. The samples have a height and diameter of 20 mm and 10 mm. The samples are heated up to 800 and 850 °C and then cooled in oil or oil and water mixture. The samples are annealed at 150 and 300 degrees for 1 and 3 hours, respectively. After these stages, the microscope images of the samples are taken by optical and SEM microscopes. In addition to these, hardness test is conducted on the specimens and results are analyzed by Taguchi method with ANOVA. As a result of these tests, the properties of the samples are fixed and discussed. The process variations affected the hardness values of the samples. The maximum hardness is obtained on the sample the hardened in the mixture of the oil and water. The DOE analysis confirmed the experimental results and showed the minimum error and maximum consistency.

Keywords: 4140 Steel, Heat Treatment, Tempering, Taguchi, ANOVA

A STUDY ON AL-CU ALLOY REINFORCED BY STEEL POWDER

MUSTAFA GUVEN GOK[1*], HALIL IBRAHIM KURT[2], OKAN SERT[1] AND ENGIN ERGUL[3]

[1] Department of Metallurgical and Materials Engineering, Engineering Faculty, Gaziantep University, TURKIYE
[2] Aerospace Engineering, Faculty of Aeronautics and Astronautics, University of Samsun, TURKIYE
[3] Mechanical Department, İzmir Vocatioanl High School, Dokuz Eylul University, TURKIYE

Abstract

Aluminum is one of the important materials with a wide range of usage. Because it has important features such as lightness, corrosion resistance, compatibility with heat treatment, easy formability and affordable price. On the other hand, Al-Cu alloys are widely used in the aerospace industry due to their high specific strength and excellent machining properties. In this alloy, copper increases the strength of the material as it forms intermetallic compounds with alloying elements. Moreover, precipitation hardening is possible by dissolving copper in aluminum in the solid phase. In this study, it was aimed to investigate the microstructure and mechanical properties of Al-Cu alloy. For this, firstly, Al-Cu alloy was melted at 800 °C and 0.3% and 0.5% by weight steel powder was added into this melt. The Al-Cu melt, mixed at 300rpm for 10 minutes, was controlled with aluflux and degassing tablets and then poured into a steel mold. Heat treatment for the Al-Cu alloys was fulfilled at 500 degrees for 2 hours and then they were cooled in water. The aging process was carried out by keeping it in an annealing furnace at 150 and 200 degrees for 1 and 3 hours. After the manufacturing processes, the samples were polished and etched for microstructural studies. The obtained Vickers hardness values were analyzed with the Taguchi method and the results were evaluated.

Keywords: Al-Cu, Taguchi, ANOVA, Steel powder, Casting, MMCs, AMCs

A STUDY ON AL-CU-MG ALLOY REINFORCED BY CERAMIC CLAY

HALIL IBRAHIM KURT[1*], MUSTAFA GUVEN GOK[2], DAMRA NISA DAL[2] AND ENGIN ERGUL[3]

[1]Aerospace Engineering, Faculty of Aeronautics and Astronautics, University of Samsun, TURKİYE
[2] Department of Metallurgical and Materials Engineering, Engineering Faculty, Gaziantep University, TURKİYE
[3] Mechanical Department, İzmir Vocatioanl High School, Dokuz Eylul University, TURKİYE

Abstract

Aluminum and its alloys are used in many tools and equipment that are part of daily life. In addition, they find a wide application area in important sectors such as automotive, aerospace, defense and food industry. The most important features of aluminum that make it important and give it such a wide usage area are its low density and relatively good level of durability and functionality. However, the strength of aluminum is relatively low. Fortunately, different methods have been developed to overcome this. In this study, Aluminum-Copper-Magnesium alloys are reinforced with ceramic clay. The composites are produced via stir casting method. After casting, the samples are heat treated in the furnace to 500 degrees for 2 hours and then cooled in water. Then, the aging process is applied to the samples at 150 and 200 degrees for 1 and 3 hours. Microstructures of the samples are examined by optical microscope and SEM. In addition, the densities, porosity content and Vickers hardness analysis are performed and the results are evaluated with the Taguchi method.

Keywords: Al-Cu-Mg alloy, Taguchi, Casting, Composite.

MATERIAL PARAMETERS OF GASB ALLOYS FOR SILICON PHOTONICS APPLICATIONS

MURAT ODUNCUPĞLU[1*], GÖKÇE KARANFİL[1]

[1]Yildiz Technical University, İstanbul, Turkey
murato@yildiz.edu.tr

Abstract

The silicon based photonic devices operating in the communication bands are produced by integrating different semiconductor materials for ultrafast data transfer. Incorporation of aforementioned devices can also lower the cost considerably. When designing novel photonic integrated circuits, there are some problems, one being the semiconductor materials having a direct/indirect band gap and a chance of mismatching the properties of constituent materials. Firstly, the direct bandgap semiconductor materials are needed for new device architectures. Secondly, material incompatibility between the host and integrated materials causing faulty transactions. In this study, we theoretically investigated the temperature and hydrostatic pressure dependence of material parameters of the gallium antimonide (GaSb) based materials. The GaSb-based lasers can be grown directly on a silicon platform for photonic integrated circuits. The evaluation, simulation, and understanding of the parameters on this material system provided us the opportunity to create Si-based electronics with desired properties to optimise device designs.

Keyword: GaSb, Semiconductors, Temperature, Hydrostatic pressure, InGaSb

INTRODUCING AND COMPARING TWO KEY ENABLING TECHNOLOGIES: INDUSTRY4.0 AND CLOUD MANUFACTURING

KHAIR JADAAN[1*], JUMAN AL-FALAHAT[2], BATOOL MAQABLEH[2]

[1]University of Jordan, Engineering Faculty, Civil Engineering Department, Amman, JORDAN.
[2]University of Jordan, Engineering Faculty, Civil Engineering Department, Amman, JORDAN.

Abstract

A worldwide movement in advanced manufacturing countries, such as Germany, is to improve productivity and efficiency in industrial manufacturing by incorporating the latest advances in information and communications technology (ICT). The introduction of the internet into the manufacturing environment has led to proposing two concepts in the field of advanced manufacturing namely Industry 4.0 and cloud manufacturing. The two concepts have some similarities but adopt different approaches to promoting the development of manufacturing industry.
Realizing the great significance of the two concepts to the manufacturing industry, this paper provides an understanding of Industry 4.0 and cloud manufacturing concepts and their relationship. It introduces and presents an overview of both concepts and their major technologies then explores the relationship between the two concepts in terms of similarities and differences.

Keyword: Industry 4.0, Cloud Computing, Cyper-Physical Systems (CPS), Internet of Things (IoT).

DEEP MACHINE LEARNING ANALYSIS for ATOMIC COORDINATE PREDICTION of CARBON NANOTUBES

EMINE AKPINAR[1*], BILGIN KESERCI[2]

Yildiz Technical University, Turkey
Universiti Sains Malaysia, Malaysia
emineakpinar28@gmail.com

Abstract

Developments in the field of carbon nanotube technology have expanded the area of application from the medical field such as cancer diagnosis to hydrogen storage and nanotube transistors. Due to their chemical, electrical and mechanical properties, carbon nanotube technology also have many applications in nanotechnology and materials science. However, the scale at which the physical phenomena of carbon nanotubes are visible is too small to conduct physical investigations due to their size. Therefore, the aim of this study was to compare different machine learning techniques for precisely determining the coordinates of carbon nanotubes and to minimize the computation time for atomic coordinates from days to minutes utilizing established prediction models. Eighteen Traditional, Tree and Boosting based machine learning regression methods — Linear regression, Passive Aggressive regressor, Linear Discriminant Analysis, Linear Support Vector regression, Support Vector regressor (SVR), K-Neighbors regressor (KNN), Gaussian Naive Bayes, Decision Tree regressor, Random Forest (RF) regressor, Extra Trees regressor, Bagging regressor, Adaptive Boosting (AdaBoost) regressor, Gradient Boosting regressor, Extreme Gradient Boosting (XGBoost) regressor, CatBoost regressor, Light Gradient Boosted Machine (LightGBM) regressor, Histogram Gradient Boosting (HistGBM) regressor and ensemble model that consist of the combination of these methods were used. The performance of the proposed models is evaluated with Mean Absolute Error (MAE), Root mean squared error (RMSE) and R-squared (R2) score. The methods with the best performance in finding the three coordinates separately are given as follows: Linear regression and KNN regressor from traditional based methods, RF from tree based methods and CatBoost regressor, LightGBM regressor and Gradient Boosting regressor from boosting based methods. R2 score, RMSE, MAE values changes from, 0.53 to 0.80, 0.16 to 0.21, 0.08 to 0.12, respectively. This preliminary study indicates that the atomic coordinates of carbon nanotubes can be predicted with a low-error and lower computational time using machine learning methods.

Keywords: Atomic Coordinate, Carbon Nanotube, Machine Learning

THE CLASSIFICATION PERFORMANCE COMPARISON OF CLASSICAL AND QUANTUM SUPPORT VECTOR MACHINE IN PREDICTING THE TREATMENT OUTCOME OF HIGH INTENSITY FOCUSED ULTRASOUND ABLATION OF UTERINE FIBROIDS

EMİNE AKPINAR[1*],BİLGİN KESERCİ

[1*]Yildiz Technical University, Turkey
[2]Universiti Sains Malaysia, Malaysia
*emineakpinar28@gmail.com

Abstract

Magnetic resonance imaging (MRI)-guided high-intensity focused ultrasound (HIFU) performs an important clinical role in the treatment of uterine fibroids. One of the biggest challenges in this treatment is the selection of patients suitable for HIFU treatment. Therefore, the aim of this study was to comparatively evaluate the role of classical and quantum support vector machine (SVM) for predicting the treatment outcome of HIFU ablation with an immediate nonperfused volume (NPV) ratio of at least 80%, which was defined a measure of clinical treatment success. We, in this study, used multiparametric (mp) MRI features including anatomical characteristics of patients and tissue characteristics of lesion outlining its cellularity, diffusivity, and vascularity. The screening MR examinations of 73 women (mean age, 38.8 years; range, 22–49 years) were included in the analysis. Kernel methods for machine learning are important for pattern recognition, with support vector machines (SVMs) being the most well-known method for classification problems. So, in the quantum part, we set up the quantum kernel class to calculate a kernel matrix using the ZZFeatureMap and we ran our model using 1024 shots in Qasm simulator. In the classical part, we utilized radial basis function as kernel and also, we split the datasets into 8 groups by performing the 8-fold cross validation to evaluate generalizability and accuracy of the model. Quantum SVM gave the superior performance with 0.87 test score value compared the classical SVM with test score value 0.84. However, process time (training and testing) was lower in classical SVM with 13 seconds. Our study confirms that the Quantum SVM method can use for tumor classification problems instead of classical SVM with higher performance.

Keywords : High-intensity focused ultrasound, Quantum support vector machine, SVM,uterine fibroids

AN ASSESSMENT OF THE EFFECT OF VISCOSITY, SOLUBILITY, AND MISCIBILITY RATIOS ON COP IN VAPOR COMPRESSION REFRIGERATION COMPRESSOR OILS

HASAN MITHAT DELIBAS[*1], EMRAH DENIZ[2], GURSAH GURUF[2]

[1]Hasan Kalyoncu University, Engineering Faculty, Mechanical Engineering, Gaziantep, TURKEY.
[2] Karabuk University, Engineering Faculty, Mechanical Engineering, Karabük, TURKEY.
*hmithat.delibas@hku.edu.tr

Abstract

Refrigerating machines, air conditioners, and heat pumps using the vapor compression refrigeration cycle are systems that operate according to the laws of thermodynamics. These systems offer a wide range of services for both domestic and industrial use in many different industrial areas from the food industry to the pharmaceutical industry. Therefore, the amount of energy consumed by systems using this cycle is more than 15% of the energy consumed worldwide. Considering these systems, which have a high energy consumption potential, and the increasing energy production-distribution costs, it is very important to determine the conditions that affect the COP value of the systems using this cycle. Especially the compressor, which has the highest energy consumption for these systems, is one of the most important elements to be considered due to the working oil in its volume. These oils can be affected by the slightest temperature changes in the system and must work in complete harmony with the refrigerant technology. The incompatibility between the compressor oil technology and the type of refrigerant causes problems such as the formation of unsuitable viscosity, solubility, and miscibility ratio in the refrigeration system, and thus causes significant disruptions in the system. In this study, the data of previous studies has been compiled and made into a meaningful interpretation as a whole. The effect of oil accumulation on the system COP and system elements is explained by considering the viscosity, solubility, and miscibility ratios. In line with the extensive literature studies, it is seen that such an assessment has not been made on this title so far

Keyword: Refrigeration cycle, Vapor compression system, Compressor oils, Coefficient of performance (COP), Solubility, Miscibility, Viscosity.

3B yazıcıda üretilen polilaktik asit (PLA)/peroksit kompozitinin mekanik davranışının incelenmesi

Musa Yılmaz*[1], Necip Fazıl Yılmaz[1, 2], Ali Kılıç[1] ve Hidayet Mazı[3]

[1]Makine Mühendisliği, Mühendislik Fakültesi, Gaziantep Üniversitesi, Gaziantep
[2]Mütevelli Heyeti, Hasan Kalyoncu Üniversitesi, Gaziantep
[3]Kimya Bölümü, Fen Edebiyat Fakültesi, Gaziantep Üniversitesi, Gaziantep
*msyilmaz@gantep.edu.tr.

Özet

Eklemeli imalat, bir dizi endüstriyel sektörde kullanımı günden güne hızla artan bir üretim teknolojisidir. Eriyik yığma modelleme (FDM) ise düşük maliyet ve tasarım özgürlüğü avantajı ile karmaşık geometrilere sahip ürünlerin üretilmesinde yaygın olarak kullanılan bir eklemeli imalat yöntemidir. Bununla birlikte, FDM ile üretilmiş polimer ürünlerin ara yüzey yapışma mukavemetlerinin düşük olması bu yöntemin zayıf yönünü oluşturmaktadır. Bu çalışmada, FDM teknolojisi ile çalışan 3B yazıcıda PLA filamentinin serilmesi esnasında peroksit takviye edilerek yeni bir kompozit malzeme üretimi gerçekleştirilmiştir. Peroksit ile çapraz bağlanan PLA polimerinin katmanları arasında ki ara yüzey mukavemetinin artırılması amaçlanmış ve üretilen bu kompozit malzemelerin çekme dayanım ve sertlik gibi mekanik özellikleri araştırılmıştır. Ayrıca, çekme testi sonrasında kompozit numunelerin kopma yüzeyleri taramalı elektron mikroskobu (SEM) ile incelenmiştir. Deneysel sonuçlar, peroksit ile çapraz bağlı PLA kompozitinin ara yüzey mukavemetinin arttığını ve buna bağlı olarak mekanik özelliklerinin geliştiğini göstermiştir.

Anahtar Kelimeler: Çapraz bağlanma, Eklemeli imalat, Kompozit, 3D yazıcı, PLA

RESEARCH ON THE ELECTRICAL EFFECT OF FERROMAGNETIC MATERIAL ON THE COIL

MEHMET ALİ ÖZÇELİK*[1], AHMET AYCAN[1]

[1]Gaziantep University, Technical Science, Department Electric and Energy, Gaziantep, Turkey.

Abstract

Applying an electric current to the coils causes a magnetic field to around them. The self-induction electromotive force occurring in this magnetic field depends on time, coil current, and the number of turns. Ferromagnetic materials such as iron, cobalt, and nickel can be magnetized in this magnetic field. In the study, different values of Alternating and Direct current were applied to the coil wound on the square-shaped carcass under core and coreless conditions. Obtained values are interpreted with tables and graphics. In the application made by placing the silicon core in the coil under varying values, it was observed that the values obtained in the core and coreless cases were the same. In alternating current measurements, it was determined that the electrical current values obtained under both conditions were different. In this study, the effect of the core on the coil has been demonstrated experimentally in electrical system.

Keywords: Electric motor, Magnetic field, Ferromagnetic material

CLASSIFICATION OF NEONATAL EPILEPTIC SEIZURE FROM ELECTROENCEPHALOGRAPHY SIGNALS USING DEEP NEURAL NETWORK

ABDULLAH ÇALIŞKAN[1,2], SÜLEYMAN RENCUZOĞULLARI[3], HASAN BADEM[4]

[1]Dept. of Computer Enginnering, Hasan Kalyoncu University, Gaziantep, Turkey
[2]IMaR Technology Gateway, Munster Technological University, Kerry, Ireland
[3]Department of Electrical and Electronics Engineering, Institute of Science and Engineering, Iskenderun Technical University, Hatay, Turkey
[4]Dept. of Computer Enginnering, Kahramanmaraş Sütçü İmam University, Kahramanmaraş, Turkey

Abstract

This study used a deep neural network to predict newborns' epileptic seizures. The proposed deep neural network is based on a convolutional neural network. Today, deep neural networks are used in many fields, such as voice recognition, object recognition, pattern recognition, disease diagnosis, etc., due to their effectiveness in classification problems. Neonatal seizures with severe neurological dysfunctions, including hypoxic-ischemic encephalopathy, stroke, meningitis, infarction, etc. Unlike adults, newborns' epileptic seizures are not easily understood because they are confused with normal behaviours such as yawning and thumb sucking. For this reason, there is a need for neurologists specialized in this field. However, training a well-trained neurologist is a highly time-consuming and costly process. Therefore, for the detection of epileptic seizures in newborns, an assistive system can be recommended to the physician by utilizing good machine learning techniques. This system begins with collecting and recording electroencephalography (EEG) signals. Then, noises originating from EEG signals, network, interference during transmission, unwanted movements during recording, eye movements, etc., are removed. The next step is the feature extraction process. Various features are extracted that can best represent the EEG signal. After feature extraction, these features are used for classification purposes. In the classical approach, the data set for the classification process is divided into two parts: the training and the test data set. The weights of the deep neural network are fixed by optimizing the training set. Deep neural networks then allow new classifications to be made. However, in this study, 38 EGG data obtained from 39 newborns were used for training and one for testing. This process was continued so that each newborn was in the test data once. Thus, the model is made to be able to make inferences from data that it has not encountered before. According to the results obtained, over 90% success was achieved in classifying epilepsy. The results were also confirmed statistically. Classification of neonatal seizure from electroencephalography signals by using deep neural network.

Keywords: Deep Learning, Epileptic Seizure, electroencephalography

THE EFFECT of "B" TARGET VOLTAGE on WEAR PROPERTIES of TiCrNb-hBN COATINGS

YAŞAR SERT [*1], TEVFİK KÜÇÜKÖMEROĞLU [1], HÜCCET KAHRAMANZADE[1], LEVENT KARA[2]

[1*] Karadeniz Technical University, Engineering Faculty, Mechanical Engineering Department, Trabzon, TURKEY.
[2] Erzincan Binali Yıldırım University, Engineering Faculty, Mechanical Engineering Department, Erzincan, TURKEY.
*yasarsert@ktu.edu.tr

Abstract

This paper goals to determine the effect of boron target voltage on elevated temperature wear behavior of newly designed (Ti, Cr, Nb)-hBN PVD coatings. For this purpose, this layer is growth on the AISI L6 (55NiCrMoV7) with various target voltage (600 V, 700 V) using high impulse magnetron sputtering setup. The coating layer has a graded design and has been coated on the substrate surface as Cr - CrN - TiCrN - TiCrNbN and finally TiCrNb-hBN (working layer), respectively. The surface properties of the layer were determined by SEM and optical profilometer. It is seen that the coatings are deposited on the surface in a granular structure away from the deposition defect (such as droplet or hole), and the roughness values increase as the target voltage increases. Phase analysis is determined by XRD, and average grain size calculations are performed using the XRD data. The coating layer has grown to the surface by the TiN (112), CrN (311), NbN (111) and h-BN (001) orientations. Then, mechanical tests including micro-hardness and scratch tests were conducted on the specimens. Although the layer that produces with both different parameters improves the hardness of the substrate (4.7 GPa), the hardness of the coating layer with 700 V voltage (24.67 GPa) is higher than the others. Based on scratch tests, scratch crack propagation resistance (CPR_s) values were determined as 40 N^2 and 1650 N^2 for coatings produced at 600 V and 700 V, respectively. Wear behavior of specimens are specified using ball on disc type tribometer at 450 °C. It is seen that the coating with high hardness and scratch resistance offers unique contributions to the wear performance of the substrate. The optimum value of the target voltage to be used in the production of this innovative coating has been brought to the literature.

Keyword: TiCrNb-hBN, Target voltage, Elevated temperature, Scratch, Wear

DISTANCE EFFECT OF THE ROWS OF TUBES INSERTED ON THE ABSORBER OF A SOLAR COLLECTOR: NUMERICAL AND EXPERIMENTAL APPROACH

HAMIDOU BENZENINE[1,2], FETHI MOUSSA BOUDJEMA[1], SAID ABBOUDI[3]

[1]Department of Mechanical Engineering, faculty of science and technology, University of BELHADJ Bouchaib, P.O.B. 284 RP, Ain Témouchent, 46000, Algeria,
[2]Laboratory of Energetic and Applied Thermal (ETAP), Faculty of Technology,B.P 230, University of Tlemcen, 13000, Algeria,
[3]ICB, UMR 6303 CNRS, Department COMM UTBM, University of Bourgogne Franche-Comte, 90010 Belfort Cedex, France,

Abstract

The article presents a numerical and experimental study of heat exchanges in forced convection in a solar air collector equipped with an absorber made from used cans. This collector was designed and produced at the University of Ain Temouchent. Measurements of ambient temperature, solar flux and airflow were made, presented and interpreted. The influence of the distance of the rows of tubes on the thermal efficiency has been analyzed and compared to the case of a simple solar collector. The thermo-convective structure and the dynamic behavior of the flow were also presented and interpreted for the whole geometry and for selected sections.

Keyword: Simple air collector, Experimental, Forced convection, Thermal efficiency, Can, Drying, Agricultural products.

THERMAL WEAR PERFORMANCE EVALUATION OF FNC TREATED AND STAINLESS STEEL COATED BRAKE DISC

EKREM ALTUNCU [*1], RECEP AKYÜZ [2], ÇİĞDEM DİNDAR [2,3], HAKAN AYDIN[3]

[1*]Materials and Manufac. Tech. App. & Research Center-SUMAR, Sakarya University of Applied Sciences, Sakarya, Turkey.
[2] Centre of Research & Development, TOFAS, Bursa, Turkey
[3]Uludag University, Mechanical Eng., Bursa, Turkey

Abstract

Expectations from new generation automobile brake discs are increasing rapidly. Gray cast iron-based brake discs are safe and economical parts that are exposed to high wear and corrosion in the face of increasing vehicle speeds and road conditions. Disc life and brake performance are reduced due to varying harsh weather and aggressive road conditions. Trends and developments in electric vehicles; weight reduction, higher wear and corrosion resistance, lower replacement costs, and minimum brake dust are desired without loss of brake performance on the new generation brake discs. For this reason, advanced surface treatment or coating applications on brake discs are an inevitable necessity. Within the scope of this experimental studies, laser cladding and ferritic nitrocarburizing (FNC) processes were separately applied to the pad-disc friction surface of the cast iron brake discs. Then pad-disc friction properties and the brake performance were measured by a dynamometer test at different temperatures. Test results are presented comparatively. The findings are quite satisfactory in terms of both wear resistance and brake performance. Coating brake discs by the thermal process instead of uncoated discs is a great way with high application potential for improving brake performance.

Keyword: Brake disc, Laser Cladding, Ferritic Nitrocarburizing (FNC), Wear Resistance, Stainless steel

CHARACTERIZATION OF FRESH STATE PROPERTIES OF CONSTRUCTION AND DEMOLITION WASTE BASED GEOPOLYMER FOR NUMERICAL MODELLING AND SIMULATION

HUSEYIN ILCAN[1], SHOUKAT A KHAN[2], OGUZHAN SAHIN[3], MUAMMER KOC[2], MUSTAFA SAHMARAN[1]

[1]Hacettepe University - huseyin.ilcan@hacettepe.edu.tr, Turkey
[2]Hamad Bin Khalifa University - shoukatalim.khan@gmail.com, Qatar
[3]Ankara University - ohsahin@ankara.edu.tr, Turkey

Abstract

Construction and demolition waste (CDW)-based geopolymers are newly-developed green binding materials providing reduction in the carbon footprint of the Ordinary Portland cement-based materials by eliminating their utilization in the construction industry. In addition to alternative green materials for the materials with high environmental impact, advanced production methods including 3-dimensional (3D)-printing also contribute to environmentally friendly construction operations. Because of the advantages of 3D-printing for built-environment applications such as reduction in waste production, time-efficiency, low-labor requirement, cost-efficiency, and low environmental impact, development of materials suitable for 3D-printing and research on improvements of 3D-printing application-related issues has attracted great interest in recent years and, for the studies for these areas of interest, predicting the applications before the actual printing made by using the materials developed provides great convenience. In this regard, numerical modelling&simulation is a promising technique to observe the possibility of 3D-printing for CDW-based geopolymer materials. However, the fresh properties of the developed geopolymer materials are the key factors to develop an accurate numerical model. This study focuses on the characterization of newly-developed CDW-based geopolymer materials by conducting triaxial compression testing and their numerical modelling. For accurate modelling, young modulus (E), poisson ratio (v), cohesion factor (C), friction angle (phi), and the density of the fresh geopolymer materials are determined and numerical modelling of 3D-printing application is performed especially for assessing the buildability performance of the targeted materials. The study also performs a comparative analysis of the model developed with the experimental study. Different geometries such as circular, semi-circular and square cross-sections have been tested for verification. According to the results of the study, experimental results are in line with the numerical results from numerical modelling largely.

Keywords: Construction and Demolition Waste, Geopolymer, Three-Dimensional Printing, Fresh Properties, Numerical Modelling, Simulation.

FPGA IMPLEMENTATION OF SENSORLESS SPEED DETECTION FORINDUCTION MOTOR

ABDÜLKADİR ÇAKIR [*1], EYÜP ÇAKI [2]

[1*] Isparta University Of Applied Sciences, Technology Faculty, Electrical and ElectronicsEngineering Department, Isparta, TURKEY.
[2] Gaziantep University, Naci Topçuoğlu Vocational School, Electronics and AutomationDepartment, Gaziantep, TURKEY.

Abstract

In this study, a sensorless, real-time speed detection method for induction motors which are frequently used in industry based on FPGA is proposed. The three-phase stator current variation at zero crossing time (ZCT) is transferred in real-time from the proposed method to the FPGA. Fast Fourier transform is used to perform spectrum analysis on the ZCT signal in the FPGA environment. The spectrum representing the motor speed is identified as (fr). The suggested method has been put into practice using the MATLAB environment and an NI FPGA board and has been validated on a 4 kW, 4 pole induction motor at various speed values.

Keyword: Induction Motor, FPGA, Sensorless Speed Detection, Zero Crossing Time

YABANI HAYVANLARININ TARIM ARAZILERINE VERDIGI ZARARLARI AZALTMAK AMACIYLA OLUSTURULAN ARDUINO KONTROLLU YABANI HAYVAN KOVUCU SISTEM

SEYİT AKPANCAR[1*], ABDULKADİR CAKİR[2], EYUP CAKİ[3]

[1*]Isparta Uygulamali Bilimler Universitesi - Atabey Meslek Yuksekokul, Isparta, Turkey
[2]Isparta Uygulamali Bilimler Universitesi - Teknoloji Fakultesi Elektrik Elektronik Muhendisligi, Isparta, Turkey
[3]Gaziantep Universitesi - Naci Topcuoglu Meslek Yuksekokulu, Gaziantep, Turkey
*seyitakpancar@isparta.edu.tr

Abstract

Tarım ürünlerinin üretilmesi ve yetiştirilmesinde karşılaşılan problemlerin yanı sıra yaban hayvanlarından korunması da günümüzün önemli problemlerinden birisidir. Günümüzde kullanılan yaban hayvanı kovucu sistemler belirli zaman aralıklarında ses çıkarıp korkutma mantığında çalışmaktadır. Bu sistemler zamanla canlılar için alışılagelmiş sesler olmakla birlikte canlılar bu sese karşı duyarsızlaşmaktadırlar. Tarım alanlarının genellikle geniş alanlar olması fiziksel olarak korumasını güçleştirmektedir. Otomatik kontrol teknolojisinin gelişimi ile birlikte otomatik sistemler bu tip sistemlerin kontrolü açısından önem kazanmıştır. Bu çalışmada, lazer ışıklar ile tarım arazilerinin çevresel olarak kontrolünü sağlayan bir otomatik sistem gerçekleştirilmiştir. Sistem tek bir noktadan arduino denetimi ile gerçekleştirilmektedir. Sistemin enerji gereksinimi arazi şartları düşünüldüğünde oldukça zordur. Bu nedenle sisteme güneş enerjisi şarj kontrolü dâhil edilmiştir.

Keywords : Gömülü Sistem, Yaban Hayatı, Arduino,Lazer Işık

FPGA BASED BATTERY MANAGEMENT SYSTEM DESIGN

ABDULKADIR SADAY[1*], ILKER ALI OZKAN[1]

[1]Selcuk University - Konya, Turkey
*asaday@selcuk.edu.tr

Abstract

Battery management systems (BMS) are becoming an important part of all types of electric vehicles using battery packs. There are various factors such as battery temperature and balance that directly affect the life, safety, and efficiency of batteries used in vehicles. For security and robustness, these factors should be monitored and adjusted instantly. Today, battery management systems are constantly being developed using different production methods and algorithms. In the studies, calculations are made by measuring parameters such as temperature, current, current balance, load status, and health status of the battery cells, and the control of the battery group is provided with these calculations. Instant and continuous measurement and processing of all these data and the creation of a control algorithm according to the calculation result are possible with the use of powerful processors. FPGA is a processor that can provide the speed and functionality required for BMS. In the battery management system, the FPGA is responsible for receiving and processing all signals from the battery cells and producing results. It processes the data coming from temperature, current and voltage sensors instantly and applies the control stage required for balancing. In addition, the charge and discharge capacity of the battery is calculated by measuring the state of charge (SOC) instantly. SOC is of great importance in the battery management system to ensure the safety of the battery pack. Therefore, the SOC needs to be estimated accurately and in real-time. Thanks to its parallel processing capability, the FPGA can simultaneously perform the operations of reading data from the sensors and performing the related calculations. In this study, a versatile system design with real-time, high computational speed for BMS was carried out on FPGA. The voltage and current of an experimental battery based on the embedded system were monitored in real-time in a simulation environment. Experimental results show that the instantaneous SOC estimation is successful, and the system returns instant results to the incoming sensor data. The use of FPGA as a management unit will provide significant advantages in BMS with its high operating speed, real-time monitoring, low power consumption, and re-programmability.

Keywords: BMS, Battery management system, FPGA

SOGUK DOVME PROSESINDE KULLANILAN BIR SIVAMA KALIBININ SONLU ELEMANLAR YONTEMI ILE INCELENMESI

SARPER DOGAN[1*], CENK KİLİCASLAN[2], SEZGİN YURTDAS[3], BURAK TOPARLİ[1]

[1*]Norm Fasteners, Turkey
[2]Norm Additive, Turkey
[3]Norm Fasteners Co, United States
*sarper.dogan@normfasteners.com

Abstract

Sıvama operasyonu; soğuk dövme yöntemi ile üretilen ürünlerde tercih edilen bir şekillendirme metodudur. Sıvama işlemi, önceki istasyonlarda silindirik ve daha büyük çapa şişirilen veya bu şekilde elde edilen iş parçasının, çapından küçük ve genelde eksenel simetrik olmayan bir forma dolmaya zorlanması/ilerletilmesi ile gerçekleştirilmektedir. Bağlantı elemanı üretimi düşünüldüğünde; sıvama işlemi, genelde kafa altında bulunan formların oluşturulmasında (kare, altı köşe vb.) kullanılmaktadır. Sıvama işlemi kalıp açısından düşünüldüğünde zorlayıcı bir operasyondur. Özellikle malzeme akışı kaynaklı aşınma ve şekillenme işlemi sırasında oluşan yükleme koşulları nedeniyle kalıbın ince cidarlarında veya gerilme birikmesi olabilecek yerlerinde mikro çatlak oluşumu gözlenebilmektedir. Sonuç olarak, kalıplar hasara uğramakta ve kullanılamaz hale gelmektedir. Bu çalışmada, M14X115 özel bir cıvatanın kafa altında bulunan ve rondela montajında kullanılan altı köşe kademe formunun sıvama operasyonu detaylı olarak incelenmiştir. Kalıp performansının artırılması için öncelikle mevcut durumda kulanılan kalıplar; hem sonlu elemanlar yöntemi ile modellenmiş hem de üretim ortamında performansı takip edilmiştir. Kırılan kalıplar üzerinde yapılan baskın hasar mekanizması incelemeleri ve simülasyon sonuçları eşleştirilerek kalıp ömrünün artırılması için yapılması gereken tasarım revizyonları ve olası kalıp malzemesi değişiklikleri belirlenmiştir. Sonlu elemanlar yöntemi ile alternatif kalıp revizyonları incelenmiş ve nihai kalıp tasarımı ortaya çıkarılmıştır. Revize edilen formun üretiminin ardından performansın belirlenmesi için kalıplar denenmiştir. Yapılan üretim denemelerinde kalıp performansının 3 kat artırıldığı ortaya konmuştur. Ayrıca, kullanılamaz hale gelen kalıplar incelendiğinde revizyon ile birlikte kalıpta meydana gelen baskın hasar mekanizmasının değiştiği saptanmıştır. Kalıpların aşınmadan dolayı kullanılamaz hale geldiği, çatlak veya kırılma gibi bir hasar oluşmadığı belirlenmiştir.

Keywords: Soğuk dövme, Sonlu Elemanlar Yöntemi, Kalıp, Hasar Mekanizması

INFLUENCE OF A NATURAL FILLER ON PROPERTIES OF A POLYMER COMPOSITE BASED ON THERMOPLASTIC POLYURETHANE TPU MATRIX

Mehmet Aladag[1*], Klaudia Lubko[1], Magdalena Joka Yildiz[1], Rafal Molak[2], Izabela Zglobicka[1], Marek Jalbrzykowski[1], Krzysztof J Kurzydlowski[1]

Bialystok University of Technology, Poland
Warsaw University of Technology, Poland
*mmehmetaladag@gmail.com

Abstract

Extrusion is a very common method of fabrication of advanced composite materials, which has been successfully used in synthesizing various materials. In the present study, an attempt was made to use an extruder for consolidating systems with natural filler – buckwheat husk. The rationale for using this filler was its natural origin and ecological approach to manufacturing the innovative polymer matrix composites. A novel buckwheat husk composites have been consolidated with thermoplastic polyurethane (TPU) as a matrix by extrusion method in form of filaments. Composites have been prepared with various weight-based concentrations (0, 5, 10, and 15%). The physio-chemical, as well as mechanical properties of the manufactured filaments, have been investigated.

Keywords: Composite materials, Polymer matrix, Thermoplastic polyurethane, Physico-chemical properties, Mechanical properties

MACHINE LEARNING FOR EFFICIENT SWARM INTELLIGENCE

MEHMET EMIN AYDIN [*1], RAFET DURGUT [2]

[*1]University of the West England, Faculty of Environment and Technology, Department Computer Science and Creative Technologies, Bristol, UK.
[2] Bandirma Onyedi Eylul University, Engineering Faculty, Computer Engineering Department, Bandirma, TURKIYE.

Abstract

Problem solving is one of renown artificial intelligence fields, which has kept attracting research for decades, while swarm intelligence is recognised as the family of the state-of-art approaches in problem solving. The main challenge appears to be in the speed of algorithmic approximation where many approaches were proposed to accelerate and not to spin in local optima. Recent research demonstrates that inefficiencies in search procedures can be avoided using the experiences gained while search is undergoing utilising machine learning approaches. We have demonstrated that reinforcement learning facilitates very capable and powerful tools to gain experience for immediate use and to generalise for later use.

Keyword: Adaptive Operator Selection, Machine Learning, Reinforcement Learning, Swarm Intelligence, Artificial Bee Colonies, Combinatorial Optimisation.

PHYSICAL PROPERTIES OF RING AND AIR VORTEX YARNS MADE OF SOYBEAN RECYCLED POLYESTER POLYESTER AND VISCOSE

GULISTAN BANU GOKGONUL[1*], EMEL CEYHUN SABIR[1], MEHMET KERTMEN[2], AYBUKE SEN[2]

[1*]Cukurova Universitesi - , Turkey
[2]Iskur Tekstil Enerji Tic Ve San A S, Turkey
bgokgonul@gmail.com

Abstract

Vortex spinning technology is a modified form of air-jet spinning, which is preferred due to its advantages in production speed and yarn quality. The aim of this research is to compare Vortex and Ring spinning yarns produced from different fibers. Soybean protein fiber, recycled polyester, polyester and viscose fibers were used in the study. Soybean fiber has superior comfort properties. The production of soybean protein fiber by Vortex spinning method will be analyzed and a contribution will be made to the literature. Produced Ne 28 yarns from 6 different fiber blends using Vortex air-jet spinning and ring spinning methods were examined and the suitability of the spinning methods according to the fiber type was revealed. The results showed that the structural differences of both spinning methods according to the fiber blend give different strength, evenness and hairiness values. As a result of the yarn performance tests, it has been revealed that the strength values of 20% soybean, 80% polyester or 80% r PET blended yarns produced with Vortex spinning technology are lower than Ring. The hairiness values of soybean blended yarns produced with Vortex is also lower than Ring. Low hairiness will positively affect pilling in the fabric. This project was supported by Çukurova University Scientific Research Projects Unit. (Project ID FDK-2022-14473)

Keywords : Soybean, Recycle polyester, Vortex, Ring, Performance test

SOLVOTHERMAL SYNTHESIS OF TITANIUM DIOXIDE URCHINS

DERYA KAPUSUZ YAVUZ[1]

[1]Gaziantep University, Gaziantep, Turkey
*dkapusuz@gantep.edu.tr

Abstract

Currently, the controlled synthesis of semiconductor nanoceramics, specifically titanium dioxide (TiO2) is of considerable interest due to their superior photocatalytic performance [1]. In this work, urchin-like TiO2 particles were obtained by a simple solvothermal reaction at temperatures lower than 200 °C. Chloroform and acetone were utilized as solvents. In addition, urea, hydrochloric acid, and water were used at different proportions to control the crystallization and growth behavior of the particles. The crystalline and chemical properties, as well as the morphology, were investigated by XRD, XPS, SEM, TEM, and BET. Results indicated that solvent type was notably effective on the particle size and morphology. The use of acetone led to the formation of micro/nanospheres with needles on their surfaces. Whereas chloroform led to the formation of microfibers or smooth microspheres. The addition of water and urea changed the morphology by controlling the rate of crystallization inside the solution. Hollow urchins smaller than 200 nm could be prepared using acetone.

Keywords: Titanium dioxide, Solvothermal, Urchin-like, Hollow

This work was funded by The Scientific and Technological Research Council of Turkey (TUBITAK) under project number 118M195.

ELECTROCHEMICAL GROWTH OF ALLOYS FROM IONIC LIQUIDS ON COPPER TO PREVENT CORROSION

ABDULCABBAR YAVUZ[1]

[1]Gaziantep University, Gaziantep, Turkey
*abdulcabbaryavuz@gmail.com

Abstract

The literature has plenty of studies regarding the electrodeposition of metals and alloys from aqueous solutions in great detail. Ionic liquids which do not have solvent and have only anions and cations could be employed as baths for metal and alloy electrodeposition. The surface features of coatings may be considerably changed by growth conditions. In this study, stoichiometric 1:2 mixes of choline chloride and ethylene glycol called Ethaline were used to create metal and alloy-based electrodes on copper surfaces. Cyclic voltammograms were used to analyze the growth potentials of metal and alloy electrodes. Metals and alloys were electrodeposited separately by using constant potential and ionic liquid electrolytes containing the salt of these metals. Fourier Transform Infrared spectrophotometer, X-ray Photoelectron Spectroscopy, Energy-Dispersive X-ray Spectroscopy and X-ray Diffractometer were used to investigate the surface morphologies, compositions, and structures of the synthesized coatings. Microlayer having nano particles were obtained for both metals and alloys. It was noticed that the alloy particles that were electrodeposited at the nano- and micrometer sizes could be agglomerated but these thin film coatings having nanostructured on copper surfaces were uniform. The Tafel method was used to reveal the corrosion behavior of coatings. Potentiodynamic polarization of the films were evaluated in a 3.5 % NaCl electrolyte. The corrosion resistance of the films depended on the electrodeposition conditions such as applied potential.

Keywords: Alloys, Electrodepostion , Corrosion, Ionic liquids

SUPERCAPACITIVE BEHAVIOUR OF ALLOYS ELECTRODEPOSITED BY APPLYING DIFERENT GROWTH POTENTIAL

ABDULCABBAR YAVUZ[1*], MURAT ARTAN[2], NECIP FAZIL YILMAZ[2]

[1*]Gaziantep University - , Turkey
[2]Gaziantep University – Mechanical Engineering Department, Turkey
ayavuz@gantep.edu.tr

Abstract

The growing demand for clean, sustainable energy that comes from non-fossil sources are studied by researchers. Additionally, the phenomenon of energy storage and conversion has become seriously important because energy from wind and solar could be storade for later use. Electrochemical energy storage and conversion systems including supercapacitors, batteries, and fuel cells have been studied. Batteries are currently regarded as the primary electrochemical energy storage technologies as they have high energy density. However, batteries could have some disadvantages such as short lifetime, low specific power, environmental impact, and safety concerns. Therefore, recently supercapacitors are considered as one of the most promising energy storage solutions because they could have high specific power and capacitance retention. In this study flexible alloy coated electrodes were obtained for supercapacitor applications. On a graphite substrate, materials based on two metals were potentiostatically electrodeposited using a bath having the ions (salts) of both metals. Alloy coated graphite films were scanned in alkaline electrolyte at various scan rates between 5 mV s-1 and 100 mV s-1. Scanning electron microscopy, Fourier transform infrared spectroscopy, and X-ray diffraction were used to evaluate the modified alloy-based electrodes. EDX analysis was used to calculate the metal production ratios on graphite substrate depending on various deposition voltages. Galvanostatic charge-discharge behaviour of the modified electrodes at various applied voltages support the supercapacitor behavior of the coatings. The self-discharge behavior of electrodes is one of the main problems of supercapacitors for probable applications. The modified electrodes' self-discharge curves showed that lowering of the deposition potential can reduce the self-discharge problem.

Keywords: Alloys, Electrodepostion, Supercapacitor, Metals

PRODUCTION OF HEAT TREATED METAL SHEET FOR ENERGY STORAGE DEVICES

METIN BEDIR[1*], ABDULCABBAR YAVUZ[1], ALI TUNC[1]

[1*]Gaziantep University, Gaziantep, Turkey
*bedir@gantep.edu.tr

Abstract

The need for energy has increased with the development of technology. Fossil fuels are the main source of non-renewable energy and it is easy to transfer these sources and use them instantly when needed. Storage of fossil fuels is not a significant problem as they can generally be handled and store easily. Renewable energy sources have been naturally used but they mostly depend on location and climate conditions. For example, dams and windmills cannot build everywhere and it is not possible to produce electricity from a photovoltaic cell at night or generate electricity from dams if there is drought. Therefore, it is necessary to store the electrical energy produced by these sources to use anytime. Energy storage is also important for mobile devices and electrical vehicles. With the development of technology, numerous types of mobile devices including cell phones, mobile computers, mobile drills, and hair cutters have been invented. Most of these devices use batteries. Fuel cells, batteries, and capacitors can be the main devices to store and use electrical energy in the application of mobile devices. Supercapacitors could be in between these two types of devices as they can have both high power and energy density. When supercapacitors currently used are compared to the most common type of batteries (lithium-ion batteries), the benefits of supercapacitors outweigh their drawbacks. The charging duration of a supercapacitor could generally be less than 10 seconds whereas it takes about 60 minutes to fully charge a lithium-ion battery. The cycle life of supercapacitors could be around one million cycles but batteries capacity significantly drop after 500 cycles and when batteries reach around 1000 cycles, they can become almost useless. People may usually observe dead batteries because of their capacity problems when using smart phones after several hundreds of charge-discharge. Annealing method was applied to fabricate metal oxide based thin coating on a metal substrate. The metal oxide was cycled in various baths to find an appropriate electrolyte. Metal based electrolyte was cycled by applying different scan rate in order to elucidate electrochemical behaviour of the electrodes. Some important characteristics of the films were investigated by using XRD, SEM, XPS, FTIR and cyclic voltammetry measurement. It was found that annealing temperature and time could be critical for the performance of the energy storage devices. Metals could be heated in a muffle furnace to form its oxide layer which could be used in an energy storage devices.

Keywords: Electrochemistry, Annealing, Cyclic Voltammetry, Energy Storage

HYBRID FAILURE CRITERIA APPLICATION FOR COLD FORGING DIES

BURAK TOPARLI[1*], BAYBARS SARICA[1]

[1]Norm Fasteners - Turkey
*burak.toparli@normfasteners.com

Abstract

Low energy consumption and high efficiency production have become more crucial in recent years since the COVID pandemic increases environmental awareness, commodity and energy costs. In this study, a new failure criteria approach was presented for cold forging dies for the sake of improvement in die performance leading to increase in efficiency in production, i.e. OEE (Overall Equipment Effectiveness) and decrease in cost. Particular interest was directed to die inserts and stress rings which are assembled with pre-stressing. Since, the mechanical behaviour of the materials preferred for die inserts (WC-Co metal ceramic composite) and stress rings (tool steels) deviates under tension and compression, application of different failure criteria was required. In this study, particular interest was directed to WC-Co hard materials and various failure criteria available in the literature. A standard DIN 6921 M12 hexagonal bolt with flange was chosen in this scope. After finite element modelling of the cold forging process, die analysis was carried out and different failure criteria were applied for die insert and stress ring. As a result, die design was modified and new dies were produced. At the production floor, new dies were employed and performance was monitored. About 80% performance increase was achieved with the new design leading to significant increase in OEE and decrease in cost of both dies and overall production.

Keywords: Failure criteria, WC-Co hard metals, Die design

DETERMINATION OF TWO PORT NETWORK PARAMETERS BY UNCALIBRATED SCATTERING PARAMETERS

HAMDULLAH OZTURK[1], UGUR CEM HASAR[1]

[1]Gaziantep University, Gaziantep, Turkey
*hamdullah.ozturk@hotmail.com

Abstract

In this study, a methodology is proposed to determine all scattering (S-) parameters of a two-port device (or network) using uncalibrated measurements. To verify the method used, analyzes were made for an X-band waveguide (8.2-12.4 GHz). To apply the proposed method, we used three different topologies such as a reflecting line, (direct and reversed configurations) a non-reflecting line, and (direct and reversed configurations) a device. As different from previous studies, it determines all S-parameters of the device without any sign ambiguity. Additionally, it has the ability of evaluating the terms of error networks, as a byproduct, up to constant terms. A vector network analyzer (VNA) purchased from the Keysight Technologies (N9918A) was used to perform measurements for validation of the proposed method. The preferred method was validated by extracting the S parameters of a bianisotropic metamaterial sheet constructed by some discrete resonators.

Keywords: Microwave measurements, S-parameters, Metamaterial.

INVESTIGATION OF BENDING STRENGTH IN FML COMPOSITES PRODUCED USING STEEL MESH WIRE

MEHMET ALI AKELOGLU[1*], MELIH BAYRAMOGLU[2]

[1]University of Gaziantep - Gaziantep, Turkey
[2]Cukurova University - Adana, Turkey
*makeloglu@gantep.edu.tr

Abstract

Fiber Metal Laminate (FML) composites were primarily developed to improve fatigue strength in the modern civil aerospace industry. Further studies have shown that, with the help of different configurations, it also has other advantages such as excellent impact and damage resistance, fire resistance and light weight impact resistance. In this study, the bending strength behavior of the fiber-metal composition was investigated by determining its flexural properties. Test samples were fabricated using extremely thin stainless steel mesh material in place of sheet metal layers as a traditional component of FML composites. The specimens were produced as FML (Fiber Metal Laminate) composites with steel meshes and FRP (Fiber Reinforced Polymer) composites produced also in the same combination but without steel mesh layers. In experimental stage, specimens were investigated with `Flexural Bending Tests` were conducted in a Universal Testing Machine, having three-point test fixtures such as specimen, support and loading nose. Testing parameters were conducted according to ASTM D7264 Standarts, Flexural Properties of Polymer Matrix Composite Materials.

Keywords: Composites, Fiber reinforced polymer (FRP), Fiber metal laminate (FML), Steel mesh, Bending strength, Flexural properties.

DISTRIBUTION OF ALUMINA IN BULK POLYMERS PRODUCED BY TRADITIONAL MOLDING AND 3D PRINTING: A COMPARATIVE STUDY

OMER EYERCIOGLU[*1], DERYA KAPUSUZ YAVUZ[2], DIMA BABI[1]

[1]Dept. of Mechanical Engineering, Gaziantep University, 27310 Gaziantep, Turkey.
[2]Dept. of Metallurgical and Materials Engineering, Gaziantep University, 27310 Gaziantep, Turkey.

Abstract

This research compared the effectiveness of digital light processing (DLP) and traditional molding (TM) techniques on the uniform dispersion of ceramic particles within bulk polymers. 50 wt.% alumina-reinforced 3D printing-sensitive resins were manufactured using both techniques under identical conditions. Scanning electron microscope equipped with energy dispersive spectrometer was used to characterize bulk resins (SEM-EDS). SEM images and EDS mapping results demonstrated that alumina micro-particles were dispersed more evenly in the DLP-derived photopolymer than in the resins manufactured by traditional molding (TM), which exhibited large aggregates and an inability to break alumina aggregates. Overall, the results demonstrated the superiority of DLP over TM for the manufacture of uniform ceramic/polymer composites, which can facilitate the fabrication of large, uniform ceramic pieces after the photopolymer is removed.

Keywords: DLP, 3D printing, Photopolymer, Alumina, Green parts.

POTENTIAL OF SPECTRUM SELECTIVE NANOFLUID FOR SUSTAINABLE COOLING OF AGRICULTURAL GREENHOUSES AN EXPERIMENTAL EVALUATION

MUHAMMAD USMAN SAJID[1*], YUSUF BICER[1]

[1]Hamad Bin Khalifa University, Qatar
*ybicer@hbku.edu.qa

Abstract

The agricultural greenhouses in hot arid climates require energy-intensive cooling systems to maintain optimum temperature for the optimal growth of plants. Plants utilize only visible portion of the solar spectrum during photosynthesis. In contrast, infrared radiations in the solar spectrum are trapped inside greenhouse and cause a significant rise in the cooling load of greenhouse. This study experimentally evaluates the impact of application of spectrum selective nanofluid on the inside temperature of greenhouse, heat gained by the cooling system, and photothermal conversion efficiency of the system. Spectrum selective CuS-ZnO/water hybrid nanofluid having a concentration of 0.0025wt.% was prepared using two-step method. The CuS and ZnO nanoparticle ratios were 95% and 5%, respectively. The optical transmission of prepared nanofluid confirmed the higher transmittance in the visible region and lower transmission in the infrared region of spectrum. The experimental setup consists of a duct (having 8 mm distance between front and back sheet) installed in front of a greenhouse unit, thermocouples to measure the temperature at various locations, a datalogger to record the measured temperature values, a cooling unit, pumps for circulation of water and nanofluid, DC power supply, air heater to raise temperature of air, spectrophotometer to find the transmittance of sunlight through the duct and solar simulator to provide artificial sunlight. The experimental results showed that the inside temperature of greenhouse unit was lower when nanofluid was flowing through the duct than water flowing through the duct or empty duct case. The cooling system gained an average of 23.45% less heat for duct containing nanofluid than the empty duct case under similar conditions. The CuS-ZnO/water hybrid nanofluid displayed about 24% higher photothermal conversion efficiency than the water for a flow rate of 8.1 liters per hour.

Keywords: Agriculture, Food Security, Heat, Nanomaterials, Spectrum splitting

MICROWAVE COAXIAL PROBE MEASUREMENTS OF METAKAOLIN GEOPOLYMERS AT THEIR EARLY CURING TIMES

UGUR CEM HASAR [*1], HAMDULLAH OZTURK [1], HUSEYIN KORKMAZ[1], MUSA BUTE[1], ANIL NIS[2], AHMET TASDEMIR[3], ABDULKADIR CEVIK[3], MUHARREM KARAASLAN[4]

[*1]Department of Electrical and Electronics Engineering, Gaziantep University, Gaziantep 27310, Turkey [2]Department of Civil Engineering, Istanbul Gelisim University, Istanbul 34315, Turkey [3]Department of Civil Engineering, Gaziantep University, Gaziantep 27310, Turkey [4]Department of Electrical and Electronics Engineering, Iskenderun Technical University, Hatay 31200, Turkey

Abstract

Geopolymer samples, as compared with ordinary Portland cement samples, generally gain mechanical strength at early ages, show good resistance to acid and sulfate reactions, and have less creep and shrinkage. In addition, these samples are environmentally friendly because they can reduce CO_2 emissions in the world and additionally decrease industrial waste consumption. In this regard, they have great potential in the construction of infrastructures. However, information about fundamental reaction mechanisms and phase transformations taking place in the geopolymerization process has been insufficient yet. To fill this gap, in this study, we carried out microwave coaxial probe measurements of metakaolin geopolymer samples with two different sodium silicate to sodium hydroxide ratios of 1 (Set-1) and 2.5 (Set-2) to examine the role of water during the geopolymerization process within geopolymer samples. From microwave measurements, it is observed that the dielectric constant ( ) of the metakaolin Set-1 geopolymer sample is smaller for about 2 hours of curing than of the metakaolin Set-2 geopolymer sample. This can be interpreted as the faster reaction of activators with water for the metakaolin Set-2 geopolymer sample for the first few hours of curing, compared with the reaction of activators with water for the metakaolin Set-1 geopolymer sample.

Keyword: Microwave measurements, Coaxial probe, Permittivity, Metakaolin, Geopolymer.

YARN QUALITY INVESTIGATION OF COMPACT COTTON YARNS WITH DIFFERENT COMBING NOIL PERCENTAGE

HALIL İBRAHIM ÇELIK[1], ÖZHAN ÇOBAN[1], ESIN SARIOĞLU[2]

[1]Faculty of Engineering, Department of Textile Engineering, Gaziantep University, Gaziantep, 27310, Turkey
[2]Fine Arts Faculty, Department of Textile and Fashion Design, Gaziantep University, Gaziantep, 27310, Turkey

Abstract

The noil percentage of the combing process can be varied 8-25% depending on the cotton quality and combing machine adjustments to obtain desired cotton yarn quality parameters. In this study, the effect of combing noil percentage on yarn quality for different linear densities (19.7 and 14.8 tex) and twist coefficients (3, 3.5 and 4) in the production of the compact spun yarn was investigated. Comber noil percentage was chosen in accordance with optimum combing machine setting as 14, 16 and 18%. The amount of noil percentage to be extracted at comber was achieved by forward feeding detaching which means the material is fed whilst the nipper is rocking towards the detaching roller to obtain better fiber control. Then, the tenacity, elongation, unevenness, imperfection index (IPI) and hairiness values of the yarn samples were determined. Analysis of variance and multiple regression analysis was carried out to analyze the relationship between a yarn quality variables and linear density, twist coefficient, noil percentage independent variables.

Keyword: Comber noil, Forward feeding, Compact yarn, Yarn quality, Twist coefficient.

INVESTIGATION OF EFFECT OF PRE-CONSUMER RECYCLING ACRYLIC FIBER RATIO ON YARN AND FABRIC PROPERTIES

ESIN SARIOĞLU[1*], SERDAR SAYCAN[2], PERIHAN TEKIN[2], HALIL İBRAHIM ÇELIK[3], HATICE KÜBRA KAYNAK[3]

[1]Fine Arts Faculty, Department of Textile and Fashion Design, Gaziantep University, Gaziantep, Türkiye
[2]Melike Tekstil San. ve Tic. A.Ş., Gaziantep, Türkiye
[3]Faculty of Engineering, Department of Textile Engineering, Gaziantep University, Gaziantep, Türkiye

Abstract

Within the framework of the European Green Deal, with the adoption of the circular economy model, it is necessary to investigate the recyclable possibilities of the wastes produced in the production of residual products. We can classify textile industry wastes as fiber, yarn, fabric waste, and post-consumer waste of the product in terms of raw materials. Raw material wastes formed during production before consumer use are expressed as pre-consumer, and wastes formed after use are expressed as post-consumer. Both pre-consumer and post-consumer wastes can be recycled and used at certain rates in the production of new textile products. In this way, the waste of textile products before and after use is recycled, contributing to the ecological environment. This study covers the recycling of 100% acrylic yarn waste, which is pre-consumer waste, by mechanical method and reuses in acrylic yarn production. For this purpose, Ne 20/1 yarns were produced with the same production parameters by blending acrylic fiber recycled from yarn waste with acrylic virgin fiber at 20, 30, and 40% ratios. Furthermore, a control sample was produced from virgin acrylic fiber. The tenacity, elongation, unevenness, IPI and hairiness properties of these produced yarns were determined. Single jersey fabrics were produced using these yarns in the SDL ATLAS sample knitting machine. Fabric weight, course and wale per cm, air permeability, bursting strength, bursting height and pilling properties were analyzed. Test results show that the blend ratio of recycled acrylic fiber ratio has a statistically significant effect on yarn properties. On the other hand, it was found that this parameter has no significant effect on fabric properties.

Keywords: European Green deal, pre-consumer, Acrylic, Recycling, Yarn.

DETERMINATION OF INTERACTIVE INFLUENCE OF NANOPARTICLE SIZE, AMOUNT AND TEMPERATURE FOR THE UTILITY OF NANOFLUIDS

MELDA OZDINC CARPINLIOGLU[*1], MAHMUT KAPLAN [2]

[1]Gaziantep University, Faculty of Engineering, Department of Mechanical Engineering,
Gaziantep, TÜRKİYE.
[2] Gaziantep University, Naci Topçuoglu Vocational School, Department of Machine and Metal Technology,
Gaziantep, TÜRKİYE.

Abstract

Interactive influence of nanoparticle diameter, d_p and volumetric fraction, φ on major thermophysical characteristics of relative thermal conductivity, k_r and dynamic viscosity, μ_r of nanofluids as a primary function of temperature, T is determined to assess the utility of nanofluids. In the case study common base fluids of water (W) and ethylene glycol (EG) are used. Spherical shape Ag and Al_2O_3 with a selected d_p range of (20 nm -100 nm) are used in the covered φ range of (0.25% -5%). Influence of T is set by considering 293 K and 323 K. The referred data ranges are applied for the calculation of k_r and μ_r of nanofluids Ag-W, EG and Al_2O_3-W, EG in reference to a calculation procedure provided previously by the authors. The calculated magnitudes of k_r and μ_r are expressed as a function of d_p, φ and T .It seems that there exists limiting magnitudes of d_p, φ as a function of T for the effective utilization of nanoparticles in base fluids. The interactive influence of d_p, φ and T should be referred for the utility of nanofluids.

Keyword: Nanofluid Utility, Thermal Conductivity, Dynamic Viscosity, Nanoparticle Size, Volumetric Fraction, Temperature

A CNN BASED STUDY ON KERF ANGLE ESTIMATION IN PLASMA CUTTING PROCESS

AYKUT BİLİCİ [*1], NECİP FAZIL YILMAZ [2]

[1] Gaziantep University, Naci Topçuoğlu Vocational School, Gaziantep, TÜRKİYE.
[2] Gaziantep University, Engineering Faculty, Mechanical Engineering Department, Gaziantep, TÜRKİYE.

Abstract

Plasma arc cutting systems are widely used in steel construction manufacturing enterprises. In this study, in which the factors affecting the surface quality and kerf angle in these systems were examined, experiments were carried out according to the 3-level full factorial experimental design by changing the arc voltage and current values on materials of different thicknesses, and the data set was obtained by performing 90 drilling operations.

In this study, comparing the FIS tree model and the CNN models was carried out on this dataset. The convolutional neural network (CNN) architecture has been preferred because the training and testing time is shorter than other architectures. Thanks to this model, the results of the parameter values were estimated and the optimization range was extended.

Keyword: CNN, FIS, Kerf Angle, Drilling

TICMET'22

8-10 SEPTEMBER, 2022

YTÜ DAVUTPAŞA CONGRESS AND CULTURE CENTER

The 4th International Conference of Materials and Engineering Technology

4. Uluslararası Malzeme ve Mühendislik Teknolojileri Konferansı

Konferans Hakkında Detaylı Bilgi

Detailed Information About the Conference

www.ticmet.org